Karl W. Böer

SPRINGER SERIES IN SOLID-STATE SCIENCES 160

Introduction to Space Charge Effects in Semiconductors

Springer

Springer Series in
SOLID-STATE SCIENCES 160

Springer Series in

SOLID-STATE SCIENCES

The Springer Series in Solid-State Sciences consists of fundamental scientific books prepared by leading researchers in the field. They strive to communicate, in a systematic and comprehensive way, the basic principles as well as new developments in theoretical and experimental solid-state physics.

Karl W. Böer

Introduction to Space Charge Effects in Semiconductors

With 168 Figures

Springer

Professor Dr. Karl W. Böer
University of Delaware
Dept. Physics & Astronomy
Newark DE 19711
USA
E-mail: solpax@aol.com

Series Editors:

Springer Series in Solid-State Sciences ISSN 0171-1873
ISBN 978-3-642-02235-7 e-ISBN 978-3-642-02236-4
DOI 10.1007/978-3-642-02236-4
Springer Heidelberg Dordrecht London New York

Library of Congress Control Number: 2009929029

Cover design: SPi Publisher Services

Printed on acid-free paper

Springer is part of Springer Science+Business Media (www.springer.com)

Preface

This short *Introduction into Space Charge Effects in Semiconductors* is designed for teaching the basics to undergraduates and show how space charges are created in semiconductors and what effect they have on the electric field and the energy band distribution in such materials, and consequently on the current–voltage characteristics in semiconducting devices.

Such space charge effects were described previously in numerous books, from the classics of Spenke and Shockley to the more recent ones of Seeger and others. But many more detailed information were only available in the original literature and some of them not at all. It seems to be important to collect all in a comprehensive Text that can be presented to students in Physics, Electrical Engineering, and Material Science to create the fundamental knowledge that is now essential for further development of more sophisticated semiconductor devices and solar cells.

This book will go through every aspect of space charge effects and describe them from simple elementaries to the basics of semiconductor devices, systematically and in progressing detail.

For simplicity we have chosen this description for a one-dimensional semiconductor that permits a simple demonstration of the results graphically without requiring sometimes confusing perspective rendering.

In order to clarify the principles involved, the book starts with a hypothetical model, by assuming simple space charge distributions and deriving their effects on field and potential distributions, using the Poisson equation. It emphasizes the important sign relations of the interreacting variables, space charge, field, and potential (band edges).

It then expands into simple semiconductor models that contain an abrupt nn-junction and gives an example of important space charge limited currents, as observed in nn^+-junctions.

In the following chapters, the developing of space charges in more realistic semiconductors are discussed. For this discussion it is assumed that the student is already familiar with the energy band model in solids, knows the difference between electron and hole transport and understands the basics of

the transport equations, including the carrier mobility and the action of an (external) electric field. It is also assumed that he is familiar with the basic thermodynamics of solids, including the concept of Fermi levels, as well as of nonequilibrium conditions when external excitations, e.g., optical excitations are present. We will, therefore, refer in the following presentation only briefly to the concept of quasi-Fermi levels which then will be used extensively here.

Such space charges will be first discussed in simple Schottky barriers, where these processes are most easily understood. The book will begin in a simple n-type semiconductor with one type of donors that can trap charges and are the principle facilitators of space charges when the conditions at the semiconductor surface are fixed and are different from the volume. The book then proceeds to include multiple trap levels at different energies and discusses in more detail the shape of current–voltage characteristics.

It then includes optical excitation and its influence on the space charge, and gives as a practical example a Schottky barrier description as part of an abrupt heterojunction.

The book proceeds with including electrons and holes In the next chapters. It expands the discussion to include minority carriers, carrier generation, recombination, and trapping, and uses quasi-Fermi and demarcation levels to distinguish between traps and recombination centers and their relevance to optical excitation and carrier transport. Here the differences between thermal equilibrium and steady state are explained and current continuity equations are introduced. The effect of carrier lifetimes on currents is described. Minority carrier currents and their interrelation with majority carrier currents are discussed and generation–recombination currents are analyzed under a variety of conditions, including surface recombination.

The concepts of diffusion velocity and drift-assisted diffusion, as well as drift-assisted generation–recombination currents are discussed.

Here it becomes important to distinguish between different types of fields, the built-in fields as they occur in space charge regions, and the external fields created by an applied voltage.

Now the book proceeds to a more comprehensive discussion of a variety of pn-junctions, their behavior with and without light in a number of typical devices. The analytical description, presenting solution curves of the complete set of transport – Poisson and continuity equations is divided into thin devices and thick devices in which two parts of the devices have different dominant transport properties.

All chapters are appended with a brief Summary and Emphasis section and with a number of Exercise Problems for students to familiarize themselves with the important findings discussed in the preceding chapter.

The book contains two chapters as appendix that may be added to the curriculum, depending on the background of the students, dealing with the basic carrier transport equations.

I would like to thank my friend Professor Dieter Bimberg for reminding me that my material he had on his desk needs some upgrading and editing to make it available to future generations of students as a text.

I would like to acknowledge the dedicated help I received from Ms. Anita Schwartz of the Information Technology Department of the University of Delaware to assist me in composing the text of this book.

My special thanks goes to Renate, my wife, who expected me to be truly retired and spend more time relaxing with her, while I was most of the days in my office, trying to find the proper way to explain in writing to future students and colleagues the intricacy of the field of space charges in semiconductors.

Newark *Karl W. Böer*
June 2009

Contents

1 Space Charges in Insulators 1
1.1 Basic Electrostatic Relations 1
1.1.1 The Poisson Equation 2
1.2 Fixed Space-Charge Distributions 5
1.2.1 Sinusoidal Continuous Space-Charge Distribution 5
1.2.2 Abruptly Changing Space-Charge Distribution 6
1.2.3 Space-Charge Double Layer with Neutral Interlayer 9
1.2.4 Asymmetric Space Charge Double Layer 10
1.2.5 Single Space-Charge Layer 11
1.2.6 Space-Charge Double Layer, Nonvanishing Net Charge . 12
Summary and Emphasis 13
Exercise Problems 13

2 Creation of Space-Charge Regions in Solids 15
2.1 One Carrier Abrupt Step-Junction 17
2.1.1 Electron Density, Space Charge, and Field Distribution 18
2.2 Significance of Basic Barrier or Junction Variables 31
2.2.1 Interdependence of Carrier Densities, Fields, and Currents 31
2.3 Space-Charge Limited Current 33
2.3.1 Majority Carrier Injection 35
2.3.2 Minority Carrier Injection 36
2.3.3 Trap-Controlled Space-Charge-Limited Currents 36
Summary and Emphasis 37
Exercise Problems 38

3 The Schottky Barrier 41
3.1 The Classical Schottky Barrier 41
3.1.1 Schottky Approximation: Field and Potential Distributions 42
3.1.2 Zero Current Solution of the Electron Distribution 46

3.1.3 Nonvanishing Currents 49
3.1.4 Current–Voltage Characteristics 55
3.2 Modified Schottky Barrier 57
3.2.1 The Schottky Barrier with Current-Dependent Interface Density 57
3.2.2 Schottky Barrier with Two or More Donor Levels 65
3.2.3 Schottky Barriers with Multiple Donors, and Field Excitation 75
3.3 Schottky Barrier with Optical Excitation 77
3.3.1 Partially Compensated Schottky Barrier 77
3.3.2 Compensated Barrier with Optical Excitation 77
3.3.3 Schottky Barrier with Optical Excitation and Field Quenching 79
3.4 Quasi-Schottky Barrier as Part of a Heterojunction 81
3.4.1 Electron Boundary Condition at the Heterojunction Interface 83
3.4.2 Current-Voltage Characteristics for an Abrupt Heterojunction 85
3.4.3 Heterojunction with Interface Recombination 87
Summary and Emphasis 88
Exercise Problems 90

4 Minority Carriers in Barriers 93
4.1 Carrier Generation and Recombination 94
4.1.1 Thermal Excitation 95
4.1.2 Optical Excitation 96
4.1.3 Field Ionization 97
4.2 Trapping and Recombination 100
4.2.1 Electron and Hole Traps 100
4.2.2 Recombination Centers 101
4.3 Quasi-Fermi Levels, Demarcation Lines 101
4.3.1 Thermal Equilibrium and Steady State 104
4.3.2 Current Continuity 106
4.4 Carrier Lifetimes 109
4.4.1 Large Generation, Optical Excitation 111
Summary and Emphasis 112
Exercise Problems 113

5 Minority Carrier Currents 115
5.1 Minority Carrier Currents in the Bulk 116
5.1.1 Thermal Excitation GR-Currents 116
5.2 GR-Current with Surface Recombination 121
5.2.1 Thermal GR-Current with Surface Recombination 122
5.2.2 The Effective Diffusion Velocity 124

5.2.3 Optical Excitation GR-Currents with Surface Recombination . . . 125
5.2.4 Optical Excitation GR-Currents with Recombination at Right and Barrier at Left . . . 126
5.2.5 Effective Diffusion Velocity for Optical Excitation . . . 131
5.2.6 Optical vs. Thermal Carrier Generation . . . 132
5.3 Drift-Assisted GR-Currents . . . 132
5.3.1 Field-Influence in the Bulk . . . 132
5.3.2 Analytical Solution of Diffusion with Constant Field . . . 133
5.3.3 Drift-Assisted GR-Currents Without Surface Recombination at Right Electrode . . . 134
5.3.4 Total Drift-Assisted Minority Carrier Current . . . 136
Summary and Emphasis . . . 139
Exercise Problems . . . 140

6 Schottky Barrier in Two-Carrier Model . . . 143
6.1 Electron and Hole Currents in Barriers . . . 143
6.1.1 Divergence-Free Electron and Hole Currents . . . 144
6.1.2 GR-Currents in Schottky Barrier Devices . . . 145
6.2 Schottky Barrier with Two Carriers . . . 150
6.2.1 The Governing Set of Equations . . . 151
6.2.2 Example Solutions for a Thin Device . . . 154
6.2.3 Schottky Barrier Device . . . 163
6.2.4 The Relative Contribution of Divergence-Free and GR-Currents in Schottky Barrier Devices . . . 166
Summary and Emphasis . . . 168
Exercise Problems . . . 168

7 pn-Homojunctions . . . 171
7.1 Simplified pn-Junction Model . . . 171
7.1.1 Basic Features of the Simplified Model . . . 172
7.1.2 Simplified Junction Model in Steady State . . . 174
7.1.3 Junction Capacitance . . . 175
7.1.4 The Current–Voltage Characteristic of the Simplified Junction . . . 175
7.1.5 Relevance to Actual pn-Junctions . . . 178
7.2 Abrupt pn-Junction in Ge . . . 179
7.2.1 Governing Set of Equations and Example Parameters . . . 179
7.2.2 Solution Curves for Thin Germanium pn-Junction . . . 180
7.2.3 The Current–Voltage Characteristic . . . 188
7.3 Thick pn-Junction Device (Ge) . . . 189
7.3.1 Changes in Current Contributions with Device Thickness . . . 189
7.3.2 The Quasi-Fermi Levels of the Thicker Device . . . 191
7.4 Si-Homojunction . . . 193

7.5 More Complex Homojunctions . . . 195
7.5.1 Linearly Doped Junction . . . 196
7.5.2 High Minority Carrier Injection . . . 197
7.5.3 Series Resistance Limitation . . . 197
7.5.4 Position-Dependent Material Parameters . . . 198
Summary and Emphasis . . . 198
Exercise Problems . . . 199

8 The Photovoltaic Effect . . . 201
8.1 Enhanced Carrier Generation and Recombination with Light . . . 202
8.1.1 Photoconductors . . . 203
8.1.2 Photo-emf and Photocurrents . . . 204
8.1.3 Quasi-Equilibrium Approximation . . . 205
8.2 Reaction Kinetic, Balance . . . 206
8.2.1 Trap-Controlled Carrier Densities . . . 208
8.3 Simple Model of the Photodiode . . . 210
8.3.1 Derived Photodiode Parameters . . . 213
8.3.2 Resistive Network Influence on the Diode Characteristics . . . 214
Summary and Emphasis . . . 217
Exercise Problems . . . 217

9 The Schottky Barrier Photodiode . . . 219
9.1 A Thin Schottky-Barrier Photodiode . . . 219
9.1.1 Solution Curves of the Transport Equations . . . 220
9.1.2 Current–Voltage Characteristics . . . 223
9.1.3 Lessons Learned from a Thin Schottky-Barrier Photodiode . . . 223
9.1.4 Thicker Schottky Barrier Device . . . 224
Summary and Emphasis . . . 225
Exercise Problems . . . 226

10 The pn-Junction with Light . . . 227
10.1 Open Circuit Conditions . . . 227
10.1.1 Thin, Symmetric Si-Diode with Abrupt Junction . . . 228
10.2 Thin Asymmetric Si Diodes with Abrupt Junction . . . 241
10.2.1 Recombination Through Charged Recombination Centers . . . 242
10.2.2 Inhomogeneous Optical Excitation . . . 244
10.2.3 Asymmetric Doping . . . 249
10.2.4 Thick Asymmetric Devices, Si Solar Cells . . . 251
10.3 Nonvanishing Bias . . . 254
10.3.1 Thin Symmetrical pn-Junction Device With Bias . . . 255
Summary and Emphasis . . . 259
Exercise Problems . . . 261

11 The Heterojunction with Light 265
11.1 The Cu_2S/CdS Solar Cell 267
11.1.1 The Current–Voltage Characteristics 268
11.1.2 Space Charge Effects in the Heterojunction 270
11.1.3 Kinetic Effects of Solar Cell Characteristics 276
11.1.4 Influence of Interface Recombination 281
11.1.5 Information from the Exponential A-Factor 283
11.1.6 Lessons Learned from the CdS/Cu_2S Solar Cell 286
Summary and Emphasis 287
Exercise Problems 288

A External and Built-In Fields 289
A.1 Penalties for a Simple Transport Model 290
A.2 Built-In or External Fields 291
A.2.1 Distributions in Built-In or External Fields 291
A.2.2 Mobilities in Built-In or External Fields 293
A.3 Device Cooling when Electric Energy Is Extracted from Devices Exited with Light 293
A.3.1 Detailed Energy Balance 294
Summary and Emphasis 296

B Generalized Transport Equations 299
B.1 Modified Poisson Equation 300
B.2 Continuity Equation 300
A Few Words at the End 300

Bibliography 303

Index 317

1

Space Charges in Insulators

Summary. The space charges in insulators directly determine the built-in field and electron energy distribution, as long as carrier transport can be neglected.

In this chapter we present a few arbitrarily introduced space-charge profiles and point out some of the basic resulting field and band edge distributions with consequences to device applications.

1.1 Basic Electrostatic Relations

The basic electrostatic relations connect charges, forces, fields and potential with each other under static (as opposed to dynamic) conditions.

We start from the *Coulomb relation* describing the force between two fixed point charges, e_1 and e_2.

$$\mathcal{F} = c_u \frac{e_1 e_2}{r_0^2} \tag{1.1}$$

with r_0 as the distance between the two charges. The units-related constant c_u (*in vacuo*) is set, in the rational four-parameter system used in this book, to $c_u = 1/(4\pi\varepsilon_0)$ with the vacuum permittivity $\varepsilon_0 = 8.8543 \times 10^{-14}$ $\left(\mathrm{AsV^{-1}cm^{-1}} = \mathrm{Farad\,cm^{-1}}\right)$. For $e_1 = e_2 = e$ one obtains[1]

$$\mathcal{F} = \frac{e^2}{4\pi\varepsilon_0 r_0^2} = \begin{cases} 2.3 \times 10^{-16}\ \mathrm{dyn} & \text{for } r_0 = 1\,\mathrm{cm} \\ 1\ \mathrm{dyn} & \text{for } r_0 \simeq 1.5\ \text{Å}; \end{cases} \tag{1.2}$$

[1] Since the force is measured in dyn $= \mathrm{g\,cm\,s^{-2}}$ (1 dyn is equivalent to the force exerted by 1.0197 mg on its supporting surface), it is convenient to express the mass in $\mathrm{Ws^3cm^{-2}}$ with 1 $\mathrm{Ws^3cm^{-2}} = 10^{-7}$g.

e is the elementary charge[2] $(= 1.6022 \times 10^{-19}\text{As})$. This force[3] can be related to an electric field, F, via[4]

$$\mathcal{F} = eF; \tag{1.4}$$

hence one has

$$F = \frac{e}{4\pi\varepsilon_0 r_0^2} \tag{1.5}$$

as the (constant) field on the intersecting line between the two point charges at distance r_0 between these charges.

1.1.1 The Poisson Equation

When applying *Gauss' law*, we can relate a region containing many charged particles (i.e., a space-charge region, neglecting the microscopic position of each individual particle), with $\varrho = ne$, to the field on a closed surface (of any shape) surrounding this space charge, and one obtains:

$$\oint \mathbf{F}\mathrm{d}\mathbf{S} = \int \frac{\varrho}{\varepsilon_0}\mathrm{d}\mathcal{V} \tag{1.6}$$

where $\mathcal{V}$ is the volume containing thespace charge ne with n the density of charged particles, and $\mathrm{d}\mathbf{S}$ is an element of the enclosing surface. For a sphere of the radius r_0 one can easily solve the closed surface integral $\oint \mathrm{d}S = 4\pi r_0^2$; hence the field normal to such a sphere at its surface is

$$F = \frac{\varrho\mathcal{V}}{4\pi\varepsilon_0 r_0^2} = 1.44 \times 10^{-7}\,\frac{n\,(\mathrm{cm}^{-3})}{r_0^2\,(\mathrm{cm}^2)} \quad \left(\frac{\mathrm{V}}{cm}\right) \tag{1.7}$$

which, for a sphere of 1 cm radius results is a field[5] of $\simeq 1.44 \times 10^{-7} n\ \mathrm{V\,cm^{-1}}$.

The electric field is a vector that points from a positive to a negative charge, i.e., it points inward, normal to the surface of this sphere when its charge is negative. It decreases with increasing distance from the center of the sphere $\propto 1/r^2$. An *electrostatic potential difference* $\psi_{1,2}$, which describes

[2] The charge of an electron is $(-e)$.

[3] It is interesting to recognize that the electrostatic force between two ions at a distance of 1.5 Å is ≈1 dyn, i.e., on an order of magnitude that is well within the means of macroscopic sensors. This permits one to manipulate single atoms in an atomic force microscope.

[4] The correct way to introduce the field–force relation is via a test charge in the limit of zero charge:

$$\mathbf{F} = \lim_{e\to 0} \vec{\mathcal{F}}/e. \tag{1.3}$$

[5] It should be recognized that these fields are exceedingly large for uncompensated charges. For instance, when charging a sphere of 1 cm radius with only $10^{13}\,\mathrm{cm^{-3}}$ electrons, one approaches already breakdown fields of the best insulators (a few times $10^6\ \mathrm{V\,cm^{-1}}$).

the work required to move a positive test charge in this electric field from a position r_1 to r_2 is defined as

$$\psi_{1,2} = -\int_{r_1}^{r_2} F \mathrm{d}r. \tag{1.8}$$

Since this work is defined to be negative when a positive test charge moves in direction of the field, 1.8 requires the $(-)$ sign for $r_2 > r_1$.

When an electron is moved from $r_2 = \infty$ to r_1, one obtains the *absolute electrostatic electron potential*, which for the above given example is

$$\psi_n = -\int_{r_1}^{\infty} \frac{\varrho \mathcal{V}}{4\pi\varepsilon_0 r^2} \mathrm{d}r = +\frac{\varrho \mathcal{V}}{4\pi\varepsilon_0 r_1}, \tag{1.9}$$

or, for a sphere of 1 cm radius, is $\psi \simeq 0.1\ \mu\mathrm{V}$ for every excess electron on the sphere.

In general one has

$$\oint \mathbf{F} \mathrm{d}\mathbf{S} = \int \mathrm{div}\, \mathbf{F} \mathrm{d}\mathcal{V} = \int \frac{\varrho}{\varepsilon_0} \mathrm{d}\mathcal{V}, \tag{1.10}$$

or,

$$\mathrm{div}\, \mathbf{F} = \frac{\varrho}{\varepsilon_0}, \tag{1.11}$$

which is referred to as the *Poisson equation*. The relation between electric field and electrostatic potential can be written in general form as

$$\mathbf{F} = -\mathbf{grad}\psi = -\nabla\psi; \tag{1.12}$$

hence, Poisson's equation is often also given as

$$\mathrm{div}\, \mathbf{grad}\psi = \nabla^2\psi = -\frac{\varrho}{\varepsilon_0}. \tag{1.13}$$

This equation holds when the distance r to a probing charge is sufficiently large compared to the distance between individual charges of the space-charge ensemble, so that a homogeneous, smeared-out collective of charges acts on the probing charge. The *granular texture* of the space charge can then be neglected.[6]

[6] Modern devices become progressively smaller and represent typically a volume on the order of 10^{-4} cm in diameter. With a carrier density of $10^{16}\,\mathrm{cm}^{-3}$ they contain a total of only 10^4 carriers in the bulk. In addition, the actual space-charge region has only a typical thickness of 10^{-5} cm and therefore contains less than 1,000 charged defects with an average distance between these charges of 1/30 of the device dimension. Statistical fluctuations ($\propto \sqrt{N}/N$) then become large. For smaller device dimensions, or lower space-charge densities, the granular texture of the charges can no longer be neglected. Here the continuum model is expected to approach its limits, and must be replaced by an atomistic picture, the carrier transport by a ballistic rather then diffuse transport.

In a semiconductor or insulator the force between two charges is reduced because of the *shielding influence* of the atoms between these charges. Such a shielding is described by the dielectric constant ε (more precisely by the static dielectric constant ε_{st} here):

$$\mathcal{F} = \frac{e^2}{4\pi\varepsilon\varepsilon_0 r^2}; \tag{1.14}$$

hence, the relation between field and space charge within a semiconductor is given by

$$\boxed{\operatorname{div}\mathbf{F} = \frac{\varrho}{\varepsilon\varepsilon_0},} \tag{1.15}$$

and between electrostatic potential and space charge by

$$\boxed{\nabla^2\psi = -\frac{\varrho}{\varepsilon\varepsilon_0}.} \tag{1.16}$$

In the following chapters we will only use one relevant space coordinate between these charges. The relationship between space charge and field is then given by the one-dimensional Poisson equation

$$\boxed{\frac{\mathrm{d}F}{\mathrm{d}x} = \frac{\varrho}{\varepsilon\varepsilon_0}.} \tag{1.17}$$

Such a field distribution determines the electrostatic potential distribution for electrons via

$$\boxed{\frac{\mathrm{d}\psi(x)}{\mathrm{d}x} = -\left[F(x) - F(x=0)\right] = -\int_0^x \frac{\varrho(\xi)}{\varepsilon\varepsilon_0}\,\mathrm{d}\xi,} \tag{1.18}$$

with

$$\boxed{\psi(x) = \int_{d_1}^{x} F(\xi)\mathrm{d}\xi.} \tag{1.19}$$

and for $\xi = d_1$, the corresponding $\psi(d_1)$ serves as reference point for the electrostatic potential.

In summary, we have shown that space-charge regions result in field inhomogeneities. The importance of such field inhomogeneities lies in their ability to influence the current through a semiconductor. With the ability to change space charges by changing a bias, as we will see later, they provide the basis for designing semiconducting devices.

Since a wide variety of space-charge distributions are found in semiconductors, many of which are of technical interest, we will first enumerate some of the basic types of these distributions and start with a catalogue of the interrelationships of various given $\varrho(x)$, resulting in corresponding distributions of electric field $F(x)$ and electrostatic potential $\psi(x)$.

Because of the common practice to plot the distribution of the band edges for devices, we will follow this habit throughout the following sections. The band edge follows the electron potential $\psi_n(x)$ and this relates to the electrostatic potential as

$$E_c(x) = e\psi_n(x) + c = -e\psi(x) + \text{const.} \tag{1.20}$$

1.2 Fixed Space-Charge Distributions

In the examples given in this section, the *space-charge profiles* are arbitrarily introduced as fixed, explicit functions of the independent coordinate (x). The space charge can be kept constant in an insulator that does not contain free carriers. Here all charges are assumed to be trapped in now charged lattice defects.

1.2.1 Sinusoidal Continuous Space-Charge Distribution

A simple sinusoidal space-charge double layer can be described by

$$\varrho(x) = \begin{cases} ea \sin[2\pi x/d] & \text{for} \quad -d/2 \le x \le d/2 \\ 0 & \text{elsewhere} \end{cases} \tag{1.21}$$

with $d = d_1 + d_2$ the width of the space charge layer; d_1 and d_2 are the widths of the negative and positive regions of the space charge double layer (here, $d_1 = d_2$). The space charge profile is shown in Fig. 1.1a.

The corresponding field distribution is obtained by integration of (1.21), and assuming $F(x = \pm\infty) = 0$ as boundary conditions:

$$F(x) = \begin{cases} -(ead)\cos[2\pi x/d] & \text{for} \quad -d/2 \le x \le d/2 \\ 0 & \text{elsewhere;} \end{cases} \tag{1.22}$$

it is shown in Fig. 1.1b, and presents a negative field with a symmetrical peak; its maximum value lies at the position where the space charge changes its sign. The maximum field increases with increasing space-charge density ea and width d.

The corresponding electron energy (band edge) distribution is obtained by a second integration of 1.21, yielding with an assumed $E_c(\infty) = 0$ as boundary condition:

$$E_c(x) = \begin{cases} e^2ad^2/(4\varepsilon\varepsilon_0) & \text{for} \quad x < -d/2 \\ -e^2ad^2 \sin[2\pi x/d]/(4\varepsilon\varepsilon_0) & \text{for} \quad -d/2 \le x \le d/2 \\ 0 & \text{for} \quad x > d/2, \end{cases} \tag{1.23}$$

that is, a band edge step down of height $ead^2/(4\varepsilon\varepsilon_0)$, as shown in Fig. 1.1c.

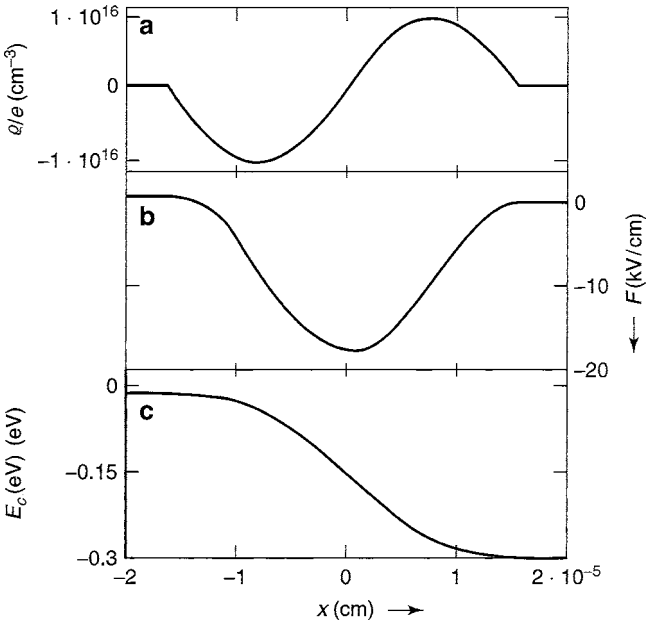

Fig. 1.1. Sinusoidal space charge, and resulting electric field and electron energy distributions. Computed for a maximum charge density, $a = 10^{16}\,\mathrm{cm}^{-3}$, a width $d = 3 \cdot 10^{-5}\,\mathrm{cm}$, and for a relative dielectric constant, $\varepsilon = 10$

Such behavior is typical: a **space-charge double layer** produces a *field spike* and a *band edge step*. For a $(-+)$ sequence of the space charge with increasing x (from left to right), the step is downward and the field spike is negative. The reversed space charge sequence $(+-)$ produces a positive field spike and a band edge step upward as shown in Fig. 1.2.

1.2.2 Abruptly Changing Space-Charge Distribution

All distributions of F and ψ are smooth when caused by the integration of a smooth space-charge distribution. As will be shown in Sect. 2.1, however, the charge distributions change abruptly from one sign to the other in many solids. A sinusoidal distribution with an abrupt change at $x = 0$ is therefore presented as an example in Fig. 1.3, curve set a:

$$\varrho = \begin{cases} 0 & \text{for} & & x < -d/2 \\ -ea\cos\left(\frac{2\pi x}{d}\right) & \text{for} & -d/2 \leq & x < 0 \\ ea\cos\left(\frac{2\pi x}{d}\right) & \text{for} & 0 \leq & x < d/2 \\ 0 & \text{for} & d/2 \leq & bx. \end{cases} \tag{1.24}$$

As a result, the field distribution is now given by a triangle and has a sharp peak (i.e., an abrupt change in slope) at $x = 0$ with equal values of

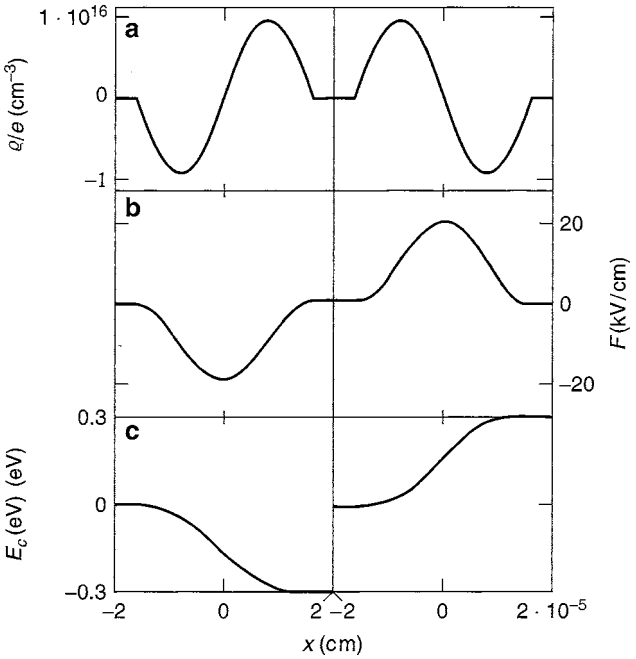

Fig. 1.2. Field extrema and band edge step signs depending on space-charge double layer sequence (computed as in Fig. 1.1)

the slope on either side. However, the potential distribution is still a smooth distribution and its shape is rather similar to the one produced by a smooth rather than abrupt change of the space charge.

Another often observed form of the space-charge distribution can be approximated by two step-functions:

$$\varrho = \begin{cases} 0 & \text{for} & & x < -d/2 \\ -ea & \text{for} & -d/2 \leq & x < 0 \\ ea & \text{for} & 0 \leq & x < d/2 \\ 0 & \text{for} & d/2 \leq & x. \end{cases} \tag{1.25}$$

We assume again $d_1 = d_2$ for a symmetrical distribution, as shown in Fig. 1.3a, curve b. Here the value of the field increases linearly in the range of constant space-charge according to

$$F(x) = F_c - \frac{ea}{\varepsilon\varepsilon_o}x \quad \text{for} - d/2 \leq x < 0 \tag{1.26}$$

$$F(x) = F_c + \frac{ea}{\varepsilon\varepsilon_o}x \quad \text{for} \quad 0 \leq x < d/2 \tag{1.27}$$

with the maximum value of the field F_c given by

$$F_c = -\frac{ead_1}{\varepsilon\varepsilon_o}, \tag{1.28}$$

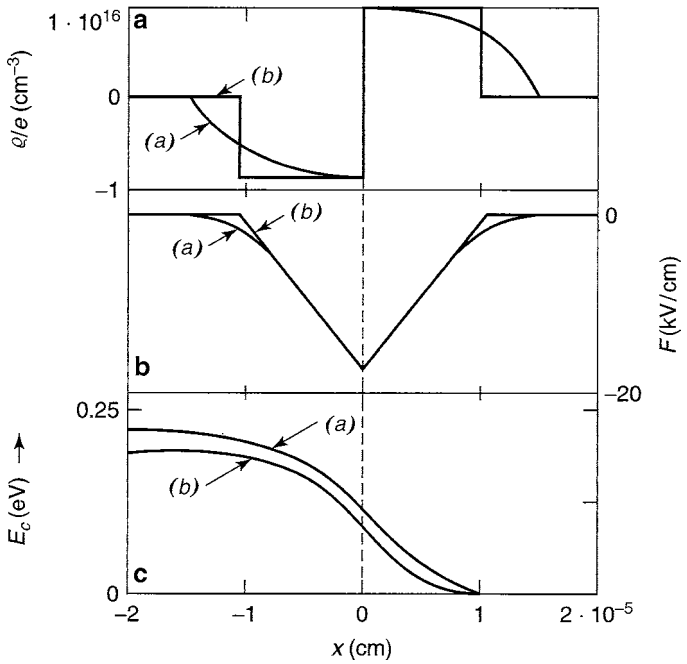

Fig. 1.3. (**a**) Space charge with an abrupt change of sign, resulting in corresponding (**b**) field and (**c**) band edge distributions: shown for (a) sinusoidal; and (b) step-like space charge distribution

shown in Fig. 1.3b, curve b. The band edge potential distribution, obtained by integration of (1.28) [using $E_c(x = \infty) = 0$ as boundary condition], changes parabolical:

$$E_c(x) = \begin{cases} \dfrac{e^2 a d_1^2}{\varepsilon\varepsilon_o} & \text{for} \quad x < -d_1 \\ \dfrac{e^2 a d_1^2}{\varepsilon\varepsilon_o} + F_c x - \dfrac{ea}{2\varepsilon\varepsilon_o} x^2 & \text{for} \quad -d_1 \leq x < 0 \\ \dfrac{e^2 a d_2^2}{\varepsilon\varepsilon_o} + F_c x + \dfrac{ea}{2\varepsilon\varepsilon_o} x^2 & \text{for} \quad 0 \leq x < d_2 \\ 0 & \text{for} \quad d_2 \leq x; \end{cases} \tag{1.29}$$

the total height of the band edge step for a symmetrical distribution with $d_1 = d_2$ is given by:

$$E_c(x = -d_1) - E_c(x = d_2) = \frac{e^2 a d_1^2}{4\varepsilon\varepsilon_o}. \tag{1.30}$$

This simple shape evaluation of the field distribution within, and the potential drop across a step-like space-charge distribution is helpful in the evaluation of potential barriers and many junctions (see Sect. 3.1).

From (1.30) it is evident that a large potential drop (supporting a large applied voltage) can be obtained by either a large space-charge density ea or a wide space-charge width d. However, both quantities also cause a similar increase in the maximum field F_c (1.28), which may become too large and consequently could lead to an electrical breakdown of the device. An increase of the potential step *without* the increase in F_c can be obtained by inserting a neutral layer between the two space-charge regions, as will be discussed below.

1.2.3 Space-Charge Double Layer with Neutral Interlayer

Under certain conditions (e.g., via appropriate doping profiles or through field quenching, described in Sect. 3.3), the two space-charge regions can be separated by an extended range of vanishing space charges (see Fig. 1.4a). In this charge-neutral region the field remains constant (Fig. 1.4b), and the band edge step increases linearly (Fig. 1.4c). Large potential drops can be achieved by simply increasing the distance $(x_2 - x_1)$ between the two space-charge regions,

$$E_c^{(2)} - E_c^{(1)} = F_c\Big[\frac{x_2 - x_1}{2} + \frac{d_1}{2} + \frac{d_2}{2}\Big], \tag{1.31}$$

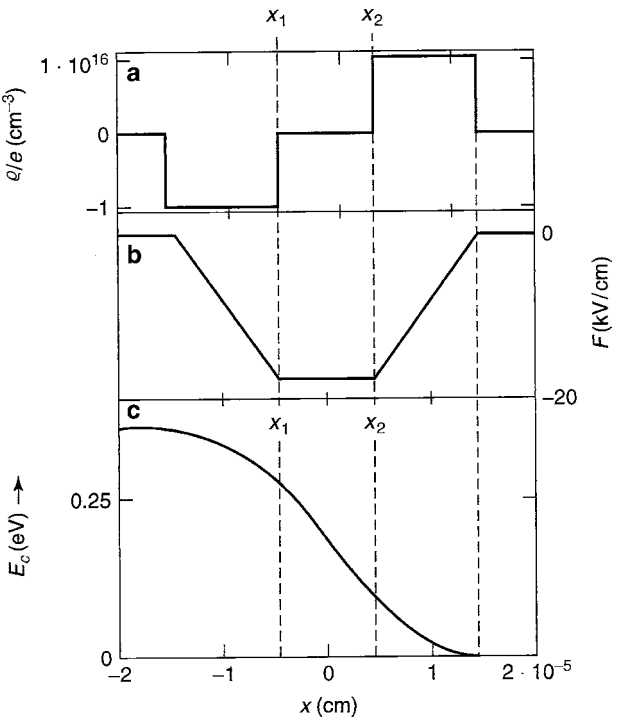

Fig. 1.4. (**a**) Step-like space-charge double layer with a neutral interlayer, resulting (**b**) a field distribution with constant center region and (**c**) a band edge change with a linear range in the middle distributions

d_1 and d_2 are the widths of each of the space-charge regions (see Sect. 3.3.3.1). The maximum field remains the same (for $d_1 = d_2 = d$) as given in (1.28):

$$F_c = -\frac{ead}{\varepsilon\varepsilon_o}. \tag{1.32}$$

This is an important means to increase the reverse blocking voltage of certain semiconducting devices.

1.2.4 Asymmetric Space Charge Double Layer

In all of the previous examples, a symmetrical charge double layer was assumed. With an asymmetrical space charge profile, the resulting field spike also becomes asymmetric and the band edge distribution becomes skewed (see Fig. 1.5, curve set a.)

In cases of highly asymmetrical profiles, the contribution of the high density part of the space-charge double layer can be neglected with respect to the band edge drop, as seen in Fig. 1.5, curve set b. In the region with $a = 10^{15}\,\mathrm{cm}^{-3}$, this band edge drop is 0.24 V; in the adjacent region with $a = 2 \cdot 10^{16}\,\mathrm{cm}^{-3}$, the additional band edge drop is only 1% of that and is barely visible in Fig. 1.5c, curve set b.

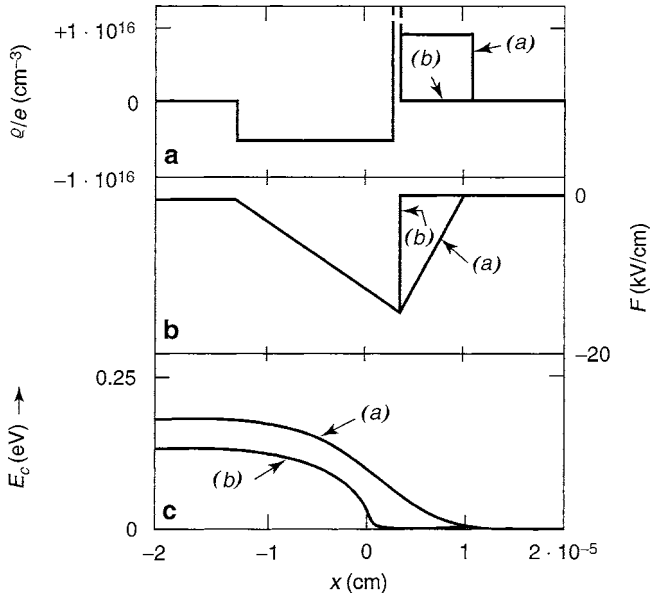

Fig. 1.5. (**a**) Asymmetric space-charge double layer and resulting (**b**) field and (**c**) band edge distributions with minor (a) and major (b) asymmetry, the latter results in a steeper change of the band edge distribution

In actual semiconductor junctions the doping of p- and n-type parts of the junction is usually asymmetric and the resulting space charge profile is similar to such highly asymmetrical double layers. The results shown in Fig. 1.5, curve set b, with resulting field and band edge distributions in the low charge density region *only*, are often used as a reasonable approximation to describe asymmetrical junctions.

1.2.5 Single Space-Charge Layer

In all previous examples we have assumed total charge neutrality within the given solid, i.e.,

$$\int_{-l_1}^{l_2} \varrho(x)\,\mathrm{d}x = 0,$$

with l_1 and l_2 as the distance form the space-charge interface to the left or right semiconductor boundary (e.g., to its electrodes). If this neutrality condition is not fulfilled within one solid (e.g., some of the compensating charges of a semiconductor are located on the surface of the adjacent metal electrode), then the *effective* (net) *space charge* can be represented by a single layer within the bulk of the semiconductor.

Such a single space charge layer (Fig. 1.6a) causes a field-ramp as shown in Fig. 1.6b. Depending on the distance of this layer from the metal electrode

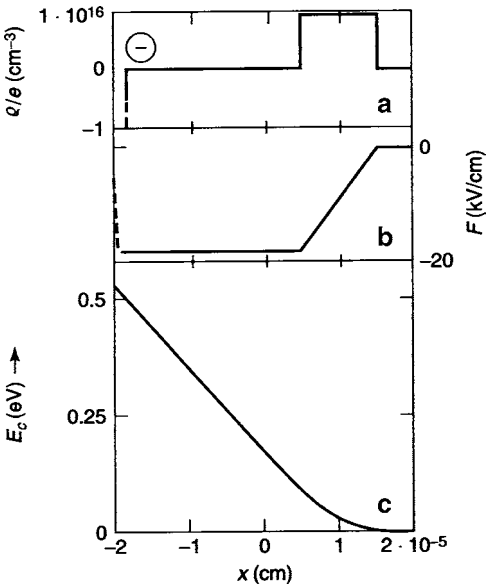

Fig. 1.6. (**a**) Single space-charge layer in the bulk with corresponding surface charge on the left electrode and resulting in a (**b**) field ramp and a (**c**) linear band edge slope in the field ramp region

where the compensating charges[7] are located, the band edge drop increases in a manner similar to the example of an ordinary double layer with charge separations (1.31). In other words, the band edge increases parabolical (to the left) in the region of the field-ramp and then linearly in the adjacent space charge-free region toward the (left) electrode as shown in Fig. 1.6c. The field collapses at the surface of the left electrode due to the fact that it is a surface charge rather than a distributed space charge which would result in a more gradual decrease of $F(x)$. This collapse is indicated by the dashed line in Fig. 1.6b.

For reasons of maintaining a constant field in the homogeneous part of an actual semiconductor, a corresponding space charge separation with net charges sitting on both electrodes, is always present for nonvanishing net currents (see Sect. 2.1.1).

1.2.6 Space-Charge Double Layer, Nonvanishing Net Charge

We now extend the previous example to a nonsymmetrical double layer with a remaining net charge. The net charge is compensated by surface charges on the two electrodes. We assume that these surface charges are different in the two electrodes, resulting in a field distribution as shown in Fig. 1.7.

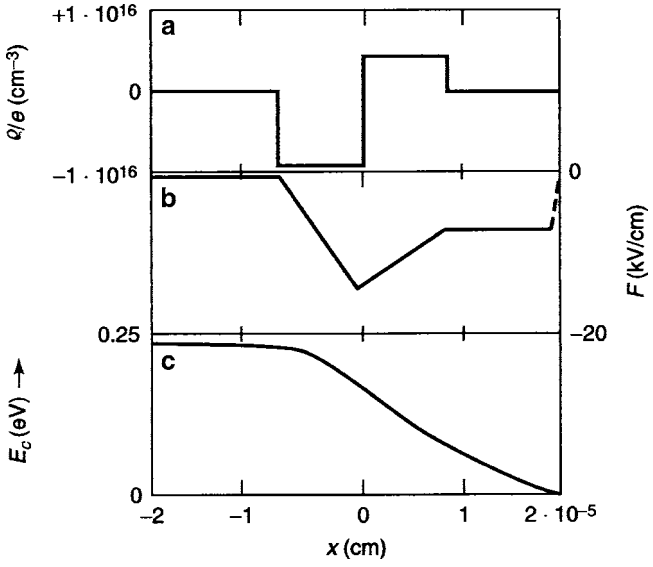

Fig. 1.7. (**a**) Asymmetrical space-charge double layer with asymmetric compensation on the two electrode surfaces and corresponding (**b**) field distribution showing the constant field range near the right electrode and (**c**) the band edge distribution with the linear range again corresponding to the constant field range distributions

[7] It is assumed that such charges are at the surface of the left electrode in this example and indicated by the "−" sign in Fig. 1.6a.

Such a space-charge distribution is quite common for asymmetrical junctions with different conductivities in the adjacent bulk regions, hence causing different, but constant, fields in these regions when a bias voltage is applied. The major band edge drop usually occurs within the space-charge double layer, and the band edge drop[8] in the adjacent bulk regions is considered a *series-resistance* perturbation.

Summary and Emphasis

Eight arbitrarily introduced space charge profiles are discussed as idealized examples to demonstrate the typical behavior that can be observed in various types of semiconductor devices. Though somewhat modified through the influence of mobile carriers, the principal trend remains the same and determines a number of device properties.

For instance, the field distribution in space charge double layers has usually a triangular shape with its maximum value at the double layer interface. The band edge shows a step.

If a diode is to be used at high bias conditions, a neutral interlayer between the positive and negative space-charge layers is necessary to achieve a sufficient voltage drop without running into breakdown fields.

Highly asymmetrical field and band edge distributions are common in asymmetrically doped *pn*-junctions. The potential drop in the highly doped (high space charge) region is usually negligible.

Series resistance effects, though undesired, are often a by-product of yet un-optimized solar cells or in some high-speed devices, e.g., in the base of bipolar transistors.

A clear understanding of the interrelation between space-charge distribution, the resulting field, and electron potential, corresponding to the band edge distribution assists in the task of designing devices with improved characteristics.

Exercise Problems

1.(e) Design an Si-diode with an n-type region, doped with 10^{16} cm^{-3} donors and a p-type region with 10^{17} cm^{-3} acceptors with an appropriate interlayer in which the field cannot exceed 10^5 V cm^{-1} and which can support a reverse bias of 10^3 V. Assume an ideal step-like space charge.

(a) How wide are the space charge layers in the n-type and p-type regions?

(b) How large are the voltage drops in both space charge regions?

[8] Here enlarged for better clarity.

(c) How thick must the neutral layer be?
(d) How large is the voltage drop in the interlayer?

2.(r) List a number of semiconductor devices and classify them according to the examples given in this chapter. Explain the idealization in respect to the actual device.

3.(e) Relate the electrostatic potential distribution, electrostatic electron potential distribution, and band edge distribution for a given homojunction; identify an external bias (applied voltage). Watch for proper sign, and energy vs. potential denotation.

4. Design an idealized space-charge distribution of your own that represents a typical semiconductor device. Insert typical space charge density values and layer thickness. Give field distribution and voltage drop quantitatively.

5. Derive the equivalence of the mass in units of $\mathrm{Ws^3cm^{-2}}$.

2

Creation of Space-Charge Regions in Solids

Summary. The basic relations of the creation of space-charge regions caused by inhomogeneous doping can best be studied in a semiconductor with an abrupt step in the density of shallow donors (an nn^+-junction). The interrelations to electric fields and currents are transparent and present the foundation for more complex space-charge effects.

Space-charge regions, which were arbitrarily introduced in Sect. 1.2, occur normally in solids as a consequence of inhomogeneous doping or of the boundary conditions at the contact.

Here, carriers can *leak out* from a region of higher carrier density into a region of lower carrier density. Since the average electron density in thermal equilibrium is equal to the density of ionized uncompensated donors in a homogeneous n-type solid, the leaking out of mobile electrons into an adjacent region of a lesser donor density must create a positive space charge

$$\varrho = e(N_{d2} - n) \tag{2.1}$$

in the more highly doped region where some of the charge-compensating electrons are now missing and a negative space charge

$$\varrho = e(N_{d1} - n), \tag{2.2}$$

in the adjacent, lower doped region, caused by the excess electrons, with an abrupt flip[1] of sign of the space charge at the doping boundary between the two regions,[2] as shown in Figs. 2.1a, b.

The space-charge distribution, and hence the field and potential distributions (see Fig. 2.1c, d), look somewhat similar to the abrupt space-charge

[1] The flip of signs is caused by the fact that $N_{d2} > n$ while $N_{d1} < n$, hence it is negative at the left (1) side and positive on the right side of the junction

[2] The left-hand region is identified with a parameter index 1, the right-hand region with an index 2.

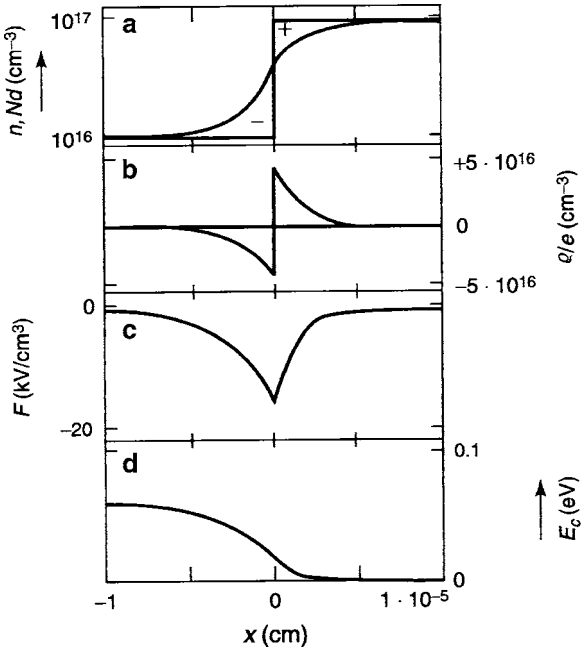

Fig. 2.1. Step-like doping distribution in an nn^+-junction with higher doping density at right, and resulting carrier density (**a**), space charge (**b**), field (**c**), and band edge (**d**) distributions shown below

distributions shown in Fig. 1.3. In Fig. 2.1 the carrier distribution is still arbitrarily drawn, so as to provide neutrality over the junction.

The exact shape of these distributions, however, is given by the distribution of the mobile carriers which is caused by carrier diffusion out of the highly doped region ($x > 0$). In equilibrium, such diffusion is counterbalanced by carrier drift in the opposite direction, due to the field induced by the space charge, which was created by the initial carrier diffusion. Hence, in addition to the Poisson equation discussed in the previous section, one must now consider the **carrier transport equation**[3] including drift and diffusion currents, here for electrons:

$$\boxed{j_n = e\mu_n nF + \mu_n kT\frac{\mathrm{d}n}{\mathrm{d}x},} \tag{2.3}$$

where n is the electron density and μ_n, the electron mobility. Equations (1.17), (1.18), and (2.3) are now the **governing set of differential equations** that

[3] For an extensive discussion of the transport equation and its derivation see Appendix Part I of this Volume.

for convenience we will repeat here in their basic formulation:

$$j_n = e\mu_n nF + \mu_n kT\frac{\mathrm{d}n}{\mathrm{d}x} \tag{2.4}$$

$$\frac{\mathrm{d}F}{\mathrm{d}x} = e\frac{\varrho}{\epsilon\epsilon_o} \tag{2.5}$$

$$\frac{\mathrm{d}\psi_n}{\mathrm{d}x} = F. \tag{2.6}$$

These determine quantitatively the space-charge distribution and consequently the entire electrical behavior of any junction in which only one carrier is mobile. In this example, it is a simple nn$^+$-junction.[4]

We will now analyze in more detail the behavior of such an idealized nn^+-junction, which illustrates the main behavior that in a modified form is the basis for the carrier transport in all other barriers or junctions.

Such junctions have technical relevance as high–low junctions, or nn^+-junctions in many devices. The notation n^+ is used to identify a highly doped, or often degenerate region in which the Fermi-level is close to, or inside the conduction band.

2.1 One Carrier Abrupt Step-Junction

In rewriting (2.4)–(2.6) one obtains a set of four **simultaneous nonlinear differential equations**:[5]

$$\frac{\mathrm{d}n}{\mathrm{d}x} = \frac{j_n - e\mu_n nF}{\mu_n kT} \tag{2.7}$$

$$\frac{\mathrm{d}F}{\mathrm{d}x} = \frac{e(N_{d1} - n)}{\varepsilon\varepsilon_0} \qquad \text{for} \qquad x < 0 \tag{2.8}$$

$$\frac{\mathrm{d}F}{\mathrm{d}x} = \frac{e(N_{d2} - n)}{\varepsilon\varepsilon_0} \qquad \text{for} \qquad x \geq 0 \tag{2.9}$$

$$\frac{\mathrm{d}\psi_n}{\mathrm{d}x} = F. \tag{2.10}$$

Equations (2.7)–(2.10) cannot be integrated in closed form and certain approximations, that are used in Sect. 3.1, are not sufficiently accurate for the problem presented here. Therefore, the solution curves of (2.7)–(2.10)

[4] Most other doping inhomogeneities also need consideration of minority carriers and will have to involve another important equation, the current continuity equation. This will be discussed in Chap. 4.

[5] With $x = 0$ at the interface between materials 1 and 2. The density of positively charged donors p_d is approximately equal to the total density of these donors N_d when they are assumed to be shallow enough to be fully ionized: $p_{d1} \approx N_{d1}$ and $p_{d2} \approx N_{d2}$. This assumption is used in this chapter and, if not otherwise stated, throughout the entire Part I of this book.

are obtained by numerical integration. Such integration needs six boundary conditions[6] for selecting a set of physically meaningful solution curves. To illustrate such solutions, let us assume the existence of very thick slices of materials 1 and 2 so that the solutions approach the *singular point* far away from the interface:

$$\frac{\mathrm{d}n}{\mathrm{d}x} = \frac{\mathrm{d}F}{\mathrm{d}x} \equiv 0 \tag{2.11}$$

i.e., the electron density and the electric field become constant:

$$n_{(x\to-\infty)} = n_{10} \to N_{d1} \tag{2.12}$$

$$n_{(x\to\infty)} = n_{20} \to N_{d2} \tag{2.13}$$

$$F_{(x\to-\infty)} \to \frac{j_n}{e\mu_n N_{d1}} \tag{2.14}$$

$$F_{(x\to\infty)} \to \frac{j_n}{e\mu_n N_{d2}} \tag{2.15}$$

because far from the interface, the diffusion current vanishes and the electron density is equal to the density of shallow uncompensated donors.

The initial value for the electrostatic electron potential is set arbitrarily to zero for $x = d_2$ in this section.

The results of the numerical integration of (2.7)–(2.10) for an *nn*-junction with relatively low doping step and with the set of parameters given in Table 2.1 are shown in Fig. 2.2. The family parameter of the curves in each of the sub figures is the current density. The center curve is obtained for zero current, i.e., for thermodynamic equilibrium. The selection of the current as a family parameter is necessary for obtaining the numerical solution of the set of controlling differential equations. Then, as a result, one reads from the solution curves the potential difference at both electrodes. With these one can draw a current–voltage characteristics (see the following chapter) as it is a common characterization of semiconductor devices. In an experimental setup, however, one supplies the voltage difference (bias) to both electrodes and measures directly the resulting current. We should remember this difference between the mathematical analysis and the experiment.

2.1.1 Electron Density, Space Charge, and Field Distribution

A closer look at the set of solution curves given in Fig. 2.2 show the difference of the polarity of the bias: With the anode at the left, the electrons in the lower

Table 2.1. Parameters used for Fig. 2.2

Parameters	μ_n	T	ε	N_{d1}	N_{d2}	d_1	d_2
Values	100	300	10	10^{16}	10^{17}	-2×10^{-5}	10^{-5}
Dimensions	$\mathrm{cm^2\,Vs^{-1}}$	K	–	$\mathrm{cm^{-3}}$	$\mathrm{cm^{-3}}$	cm	cm

[6] Three boundary conditions for (2.7), (2.8) and (2.10) in region 1, and three conditions for (2.7), (2.9) and (2.10) in region 2.

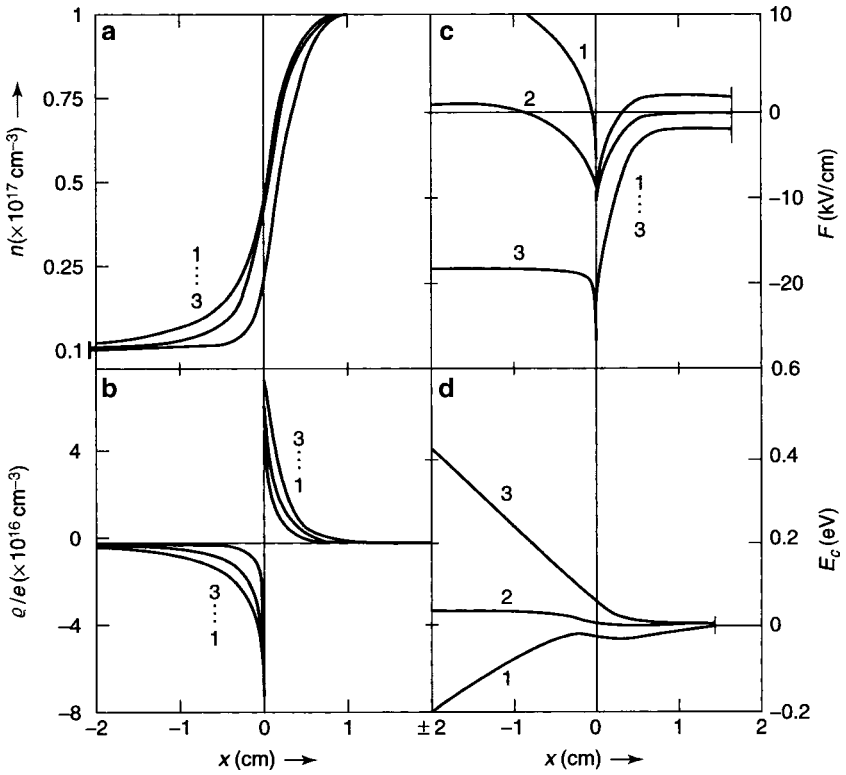

Fig. 2.2. *nn*-junction with small doping step of only a factor of 10, with resulting $n(x)$, $\varrho(x)$, $F(x)$, and $E_c(x)$, for the net current as family parameter: curves 1–3 for $j_n = 3$, 0, and $-3\,\mathrm{kA\,cm^{-2}}$, respectively (observe the large current densities necessary that were assumed here in order to find a significant changes in the other distributions with j_n. The *center curve* for zero current)

doped region (1) are pulled away from the junction interface (the oppositely charged donors here are fixed in space), thereby making this *depletion region* a wider space charge region with "higher resistance," while on the higher doped side (2) the electrons are "blown" into that *surplus* or *accumulation* space charge region, making it smaller. In series connection of both sides, the effect of the widened region with its increased resistance dominates.

In contrast, with the anode at the right electrode, the higher resistance left region (1) will have electrons blown into the donor region, thereby neutralizing more donors and reducing the space charge width and consequently its resistance, while the higher space charge region (2) is widened; though increasing its resistance, its effect is smaller than in *reverse bias.*[7] Hence, the current is (slightly) asymmetric with regard to the applied voltage, or, in the

[7] Defined by applying a negative bias to the lower doped region (1)

rendering of Fig. 2.2 one needs a higher reverse bias (0.4 V) than in forward bias (−0.2 V) to achieve the same value of the current ($\pm 3\,\mathrm{kA\,cm^{-2}}$)

The resulting *space-charge distribution* is tailing into the low density region and is wider than the depletion in the high density region (see Fig. 2.2b); the reason for this behavior will be explained in Chap. 3.1. The total positive space charge, however, is equal to the total negative space charge in the junction for vanishing net current, i.e., quasi-neutrality in the entire device is maintained.

When a bias is applied, quasi-neutrality, when integrated over the entire junction, no longer holds. With forward bias the negative charge becomes larger while the positive one decreases, resulting in a negative net charge of the double layer. Inversely, with reverse bias a positive net charge of the double layer results, as can be seen in Fig. 2.2b.

We will discuss the typical behavior of these solution curves for other more typical doping profiles and also optical excitation in the following sections and chapters.

2.1.1.1 Electrode-Surface Charges

The corresponding "missing" charges, to render the total device neutral, are located at the two electrodes (not shown[8] in Fig. 2.2b), following the arguments given in Sect. 1.2.3. These charges are split between both electrodes in such a way that the fields (Fig. 2.2c) created by these charges provide drift current continuity in the bulk parts of regions 1 and 2.

The current outside of the space-charge region is given by drift alone:

$$j = \sigma F \simeq e\mu N_\mathrm{d} F = \mathrm{const}, \tag{2.16}$$

hence, current continuity requires:

$$\frac{F_{20}}{F_{10}} = \frac{\sigma_1}{\sigma_2} = \frac{N_{d1}}{N_{d2}} \tag{2.17}$$

(= 0.1 for the parameters used in this example). From the integration of Poisson's equation one obtains for the left electrode a surface charge

$$\Omega_1 = \varrho\,\delta x = \varepsilon\varepsilon_0 F_{10} \tag{2.18}$$

with $\varrho\,\delta x$ as the surface charge in a surface layer of thickness δx (a few Å). After eliminating F_{10} from (2.18) using the drift current equation, one obtains for the surface charges at the left and right electrodes, respectively

$$\Omega_1 = -\frac{|j_n|\varepsilon\varepsilon_0}{\sigma_1}; \qquad \Omega_2 = +\frac{|j_n|\varepsilon\varepsilon_0}{\sigma_2}. \tag{2.19}$$

[8] These surface charges balance the net charge of the double layer but do not change the zero space-charge line shown in Fig. 2.2b.

For the given parameters and a current density of 2,000 A cm^{-2}, the surface charge at the right electrode is $\approx 10^{-9}$ As cm^{-2}, or $\approx 10^{10}$ electrons cm^{-2}, i.e., a widely dispersed charge with 1,000 Å average distance between electrons at the electrode surface.

Surface charges adjacent to bulk semiconductors are common in many applications, including external surfaces and semiconductor insulator interfaces. As an example, see for an analysis of surface charge between semiconductor and insulator (Kassah and Bouarissa 2000).

2.1.1.2 Field Distribution

The field distributions for these *nn*-junctions are shown in Fig. 2.2c with the given currents as family parameter. The field in the junction is approximately triangle-shaped, though slightly skewed, at zero bias. Its maximum value increases (decreases) with increasing reverse (forward) bias. With bias, the field distribution becomes more asymmetrical. At larger reverse bias the relative maximum of the field value decreases and high field values extend to the cathode. At very high reverse bias (not shown in Fig. 2.2) essentially all excess electrons are swept out from region 1, rendering this region space-charge-free, and consequently eliminating the field spike, i.e., making $F(x)$ monotonic. Now the space-charge double layer has turned into a positive single space-charge layer with compensating negative charges at the left electrode surface. Such behavior, however, can only be realized at relatively small N_{d2}/N_{d1} ratios for reasonable bias and current densities.

2.1.1.3 Electrostatic and Fermi Potentials

The *electrostatic electron potential* distribution[9] for the *nn*-junction shows the typical potential step down for a $(+-)$ space-charge double layer and is shown in Fig. 2.2d with j_n as family parameter. This potential distribution represents the shape of the edge of the conduction band $E_c(x)$

$$e\psi_n(x) = E_c(x) + c_1, \tag{2.21}$$

as shown in Fig. 2.3 for zero bias, indicating a larger distance from the horizontal Fermi level in region 1 than in region 2, hence a smaller electron density there.

[9] The electrostatic electron potential follows the conduction or valance band distribution, but has the opposite sign of the electrostatic potential which conventionally is taken as the potential energy of a positively charged particle:

$$\psi_n(x) = -\psi(x). \tag{2.20}$$

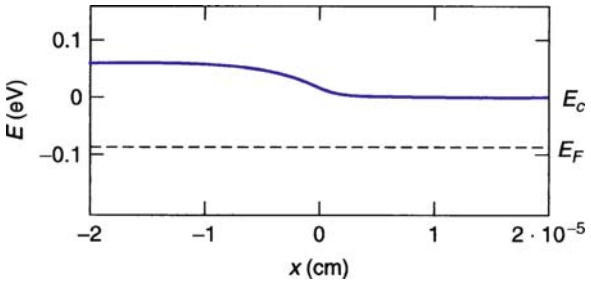

Fig. 2.3. Conduction band edge corresponding to Fig. 2.2d for zero bias with position of the Fermi level, showing a larger energy distance between band and Fermi level on the left side (1) because of the lower electron density here

With forward current the potential step is lowered; with reverse current it is increased. At a sufficiently high reverse current the potential step disappears[10] as its slope in the low conductive region becomes identical with the potential slope impressed by the external field (Fig. 2.2d, curve 3).

For zero current the potential step between regions 1 and 2 (Fig. 2.3) can be obtained from the integration of the transport equation (2.3) (without involving the Poisson equation):[11]

$$e\mu_n n\frac{\mathrm{d}\psi_n}{\mathrm{d}x} = \mu_n kT\frac{\mathrm{d}n}{\mathrm{d}x}, \tag{2.22}$$

permitting separation of variables,

$$\frac{e}{kT}\mathrm{d}\psi_n = \frac{1}{n}\mathrm{d}n. \tag{2.23}$$

After integration this yields:

$$\boxed{\psi_{n,\mathrm{D}} = \psi_{n,10}(j=0) - \psi_{n,20}(j=0) = \frac{kT}{e}\ln\left(\frac{n_{20}}{n_{10}}\right).} \tag{2.24}$$

This potential difference $\psi_{n,\mathrm{D}}$ for zero currents is called the *electron diffusion potential*. For the given parameters with a density ratio of 10, it is approximately 60 mV.

In addition to the electrostatic electron potential $\psi_n(x)$, one recognizes as a very useful variable the **electrochemical potential**, also referred to as the **Fermi potential**, $(1/e)E_\mathrm{F}$, which relates to the electrostatic electron

[10] This does not imply that the effect of the junction on the current (see Sect. 2.1.1.4) disappears: Even though in the field and potential distributions the *nn*-junction with sufficient reverse bias looks like a smooth connection between low and highly conductive semiconductors, the *width* of the highly conductive material is reduced with further increased reverse bias, thereby reducing the device conductance.

[11] For justification of this neglect, see Sect. 3.1.3 and (3.14).

potential and the free electron density in the classical approximation (see below), here expressed as **Fermi energy**:

$$E_{\mathrm{F}} = E_c(x) - kT \ln \left[\frac{N_c}{n(x)} \right]. \tag{2.25}$$

This relation can be derived from the equation for the equilibrium electron density at the lower edge of the conduction band, using Fermi–Dirac statistics:

$$n = \frac{N_c}{1 + \exp\left(\dfrac{E_c - E_{\mathrm{F}}}{kT} \right)}, \tag{2.26}$$

or, for $(E_c - E_{\mathrm{F}}) > 3kT$:

$$n \simeq N_c \exp\left(-\frac{E_c - E_{\mathrm{F}}}{kT} \right), \tag{2.27}$$

where N_c is the *effective density of states* at the lower edge of the conduction band, given by

$$\boxed{N_c = 2\left(\frac{m_n kT}{2\pi\hbar^2} \right) = 2.5 \times 10^{19} \left(\frac{m_n}{m_o} \frac{T(K)}{300} \right)^3 /2} \tag{2.28}$$

and m_n is the effective mass of electrons at the edge of the conduction band (see Appendix 1). Equation (2.25) holds in thermal equilibrium throughout the space-charge region.

With nonvanishing bias, the Fermi level will split into two quasi-Fermi levels as will be explained in Sect. 6.2.2.3. However, in a sufficiently doped single carrier device the majority carrier quasi-Fermi level remains so close to the Fermi level, that the latter may be used as a reasonable approximation[12] (see Sect. 3.1), even for nonvanishing bias. With bias then E_{F} becomes space-dependent $E_{F_n}(x)$, here $\simeq E_{\mathrm{F}}(x)$.

The distribution of the Fermi levels with j_n as a family parameter is shown in Fig. 2.4 for the nn-junction given in Fig. 2.2. The two slopes in bulk regions 1 and 2 are directly proportional to the different conductivities there.

The difference of the Fermi potentials at the interfaces to the two electrodes is equal to the applied voltage difference:

$$\boxed{\Delta V = \frac{1}{e}\big[E_{\mathrm{F}}(x = -d_1) - E_{\mathrm{F}}(x = d_2)\big].} \tag{2.29}$$

[12] Its use is permissible also in an nn^+-junction and to some extent throughout some Schottky barriers, provided that the carrier depletion in the Schottky barrier remains "moderate", i.e., even within this range, the electron density remains larger than the free hole density.

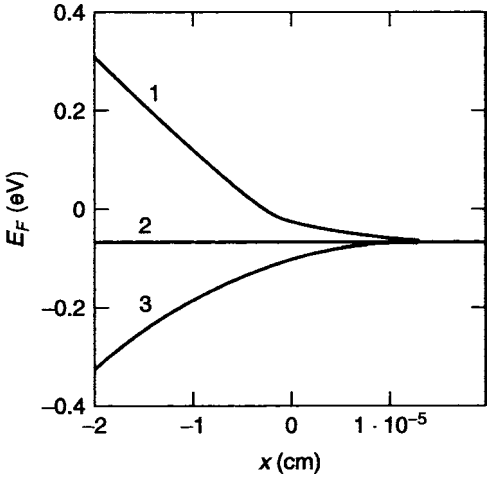

Fig. 2.4. Fermi-potential distribution using (2.25) is given here with j_n as family parameter as in Fig. 2.2; compare these with $E_c(x)$ given in (**d**) of that figure

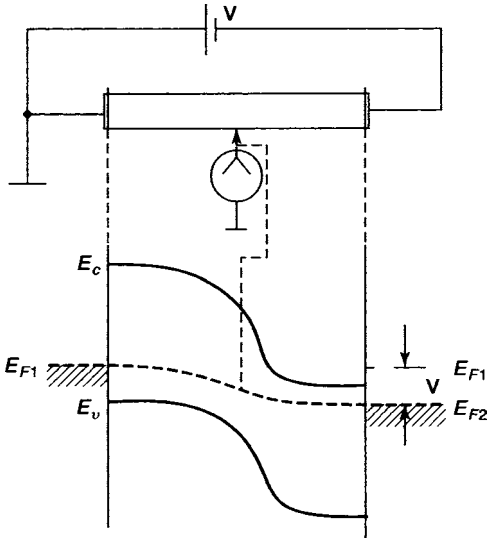

Fig. 2.5. Probing of the Fermi-level distribution along the surface of a semiconductor with a metal point contact connects the probe to the Fermi level

Probing with a point contact along the semiconductor surface connects the metal probe to the electrochemical potential of the semiconductor, as indicated in Fig. 2.5.[13] In contrast, the electrostatic potential distribution is *not* accessible to outside probing.

[13] and not to any of the quasi-Fermi levels

The constant c_1 of (2.21) can be determined by using the electron density in the bulk, thereby fixing the distance $E_c - E_F$ according to (2.25), e.g., with the ratio N_c/n_{20}, and using the applied voltage at the corresponding electrode to determine E_F.[14]

2.1.1.4 Currents

The total current, including drift and diffusion can be obtained from the product of the conductivity and slope of $E_F(x)$. This can be seen by differentiating the Fermi-distribution (2.25) with respect to the spatial coordinate:

$$\frac{\mathrm{d}}{\mathrm{d}x}\left(E_c - E_F\right) = kT\frac{\mathrm{d}}{\mathrm{d}x}\left[\ln\left\{\frac{N_c}{n(x)}\right\}\right], \tag{2.30}$$

yielding

$$\frac{\mathrm{d}E_c}{\mathrm{d}x} - \frac{\mathrm{d}E_F}{\mathrm{d}x} = -kT\frac{1}{n}\frac{\mathrm{d}n}{\mathrm{d}x}, \tag{2.31}$$

which, after multiplying with μ_n and rearranging, yields:

$$\mu_n n\frac{\mathrm{d}E_F}{\mathrm{d}x} = n\mu_n\frac{\mathrm{d}E_c}{\mathrm{d}x} + \mu_n kT\frac{\mathrm{d}n}{\mathrm{d}x}. \tag{2.32}$$

After replacing $\mathrm{d}E_c/\mathrm{d}x$ with e times the electric field,[15] the right-hand side of (2.32) represents the sum of drift and diffusion current. Therefore, the **total current** is given by the product of conductivity with the gradient of the electrochemical potential.[16]

$$\boxed{j_n = \frac{\sigma_n}{e}\frac{\mathrm{d}E_F}{\mathrm{d}x}.} \tag{2.33}$$

This is a similar expression to the **drift current**, which is given by the product of conductivity with the gradient of the *electrostatic electron potential*

$$\boxed{j_{n,\mathrm{Drift}} = \frac{\sigma_n}{e}\frac{\mathrm{d}E_c}{\mathrm{d}x} = \sigma_n\frac{\mathrm{d}\psi_n}{\mathrm{d}x}.} \tag{2.34}$$

When a bias is applied, a current is drawn and $E_F(x)$ is tilted. In the *bulk* of regions 1 and 2, the *drift current*

$$j_{n,\mathrm{Drift}} = e\mu_n n_{10}F, \quad \text{or} \quad = e\mu_n n_{20}F \tag{2.35}$$

[14] In the given example, however, we arbitrarily normalized $E_c(x = d_2) = 0$; hence, $E_F(x = d_2) = -kT\ln(N_c/n_{20}) \simeq -60\,\mathrm{mV}$.

[15] This holds strictly only for electron-fields, but, except for graded band gap semiconductors or highly doped regions with inhomogeneous dopant distribution, this distinction needs not be made.

[16] One, thereby, confirms that, in thermodynamic equilibrium, requiring $j = 0$ (here $j_n = 0$), the Fermi level is horizontal throughout the semiconductor: $\mathrm{d}E_F/\mathrm{d}x \equiv 0$.

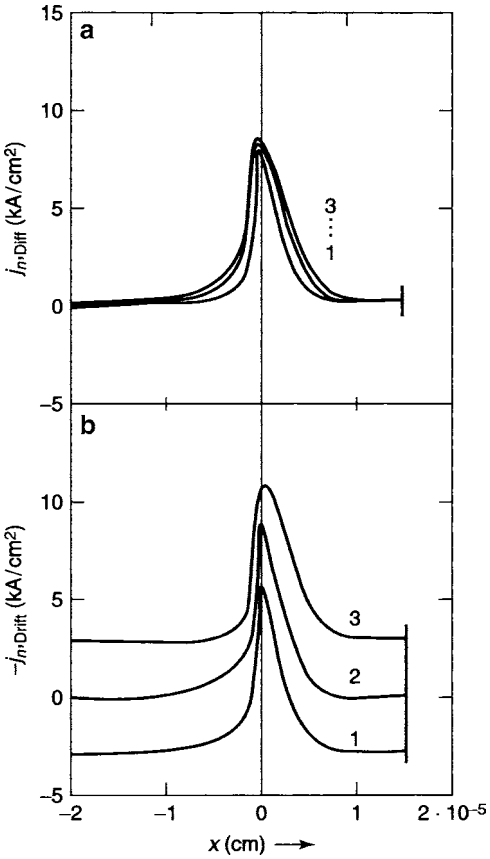

Fig. 2.6. Here, the distribution of the values of the drift currents (*lower graph*) and the diffusion currents (*upper graph*) are given within the *nn*-junction, with the net current as family parameter as shown in Fig. 2.2. One should recognize that both currents act in opposite direction, so that, e.g., for vanishing bias, they compensate each other exactly

is the dominant part of the current; hence, the slopes $\mathrm{d}E_\mathrm{F}/\mathrm{d}x$ and $\mathrm{d}E_c/\mathrm{d}x$ must be equal to each other: here, $E_c(x)$ and $E_\mathrm{F}(x)$ are parallel to each other.

Within the junction, however, the distributions of $E_c(x)$ and $E_\mathrm{F}(x)$ are no longer parallel (see Fig. 2.5). The slope of $E_c(x)$ here is larger than that of $E_\mathrm{F}(x)$, i.e., the drift current ($\propto \mathrm{d}E_c/\mathrm{d}x$) is larger than the total current (that is $\propto \mathrm{d}E_\mathrm{F}/\mathrm{d}x$) and therefore needs compensation from the diffusion current.

The diffusion current becomes very large at the doping interface (Fig. 2.6). It is typically on the order of 10^4 A cm^{-2} and changes little with applied bias.[17]

[17] Its distribution is slightly deformed, according to the changes in $n(x)$ with applied bias, while its amplitude remains nearly unchanged. This reflects the fact that at a first approximation the electron distribution is pushed "sideways" (in the

The drift current distribution is shown in Fig. 2.6b. It matches the diffusion current, however, is shifted parallel to the current axis resulting in the constant net current. For $j_n = 0$ both currents are exactly equal in magnitude and cancel each other.

2.1.1.5 Current–Voltage Characteristics

Connecting the obtained[18] differences in applied voltage (obtained from the Fermi-level distribution – Fig. 2.4) with the corresponding currents used as parameters in (2.7) yields the *current–voltage characteristic*. Curve 1 in Fig. 2.7 is obtained from the solutions of $E_F(x)$ given in Fig. 2.4 for the described

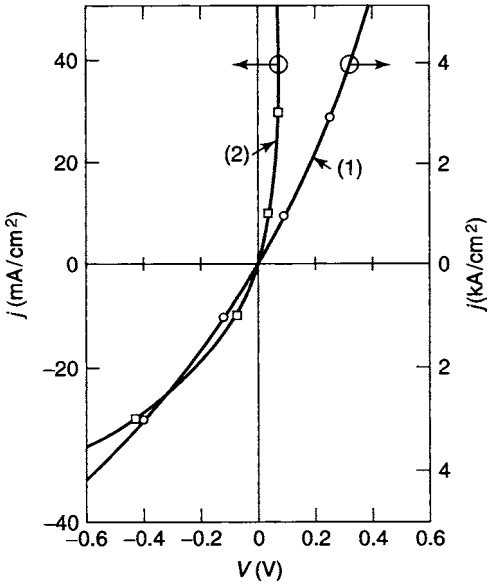

Fig. 2.7. Current–voltage characteristic for an *nn*-junction corresponding to the solutions shown in Fig. 2.2 as *curve 1* with the right current scale; and, for a higher step ($N_d = 10^{17}$–$10^{11}\,cm^{-3}$) of an nn^+-junction, with their solution curves shown in Fig. 2.9 and its current–voltage characteristic given here for comparison as *curve 2* corresponding to the left current scale. Observe the different scales with $mA\,cm^{-2}$ on the *left* and $kA\,cm^{-2}$ on the *right* and the much stronger curvature (rectifying shape) of curve 2

x-direction) with changing bias, with little deformation at the point of its steepest slope, as shown in Fig. 2.2a.

[18] In mathematical computation, the current is given as a parameter and the bias is then obtained by numerical integration as the difference between the Fermi-level at both electrode interfaces; in contrast, experimentally the bias is (mostly) given and the current is obtained as a result (except for some current-driven devices).

nn-junction. This curve shows a (slightly) nonohmic behavior due to the expansion or contraction of the more resistive region 1 in reverse or forward bias, respectively.[19]

Such a characteristic is easily obtained experimentally. It presents the key information to judge the performance of many semiconductor devices. Therefore, most theoretical analyses attempt to obtain as final output the current–voltage characteristics for comparison between theory and experiment. The computation of the current–voltage characteristic, however, is a tedious process: for each point, the solution curves of the set of (2.7)–(2.10) must be found. Only rarely can the system of governing equations be simplified sufficiently so that it can be integrated, yielding an analytic expression of sufficient accuracy; some examples where such explicit integration is possible will be given in Sects. 2.3, 3.14, 3.2.1.2, 3.4.2, and 7.1.4.

Current Rectification. The nonlinearity of such a current–voltage characteristic has an important practical implication: it can be used for rectification of an ac (alternating current) input. Such a characteristic is, therefore, also referred to as a *rectifying characteristic*.

Rectification occurs when a sinusoidal voltage bias is supplied to a device in which the current in forward bias is larger than in reverse bias, thereby causing a net forward *dc* component (Fig. 2.8).

There is a large body of publication dealing with devices designed for efficient current rectification. For a more exotic device involving a p/p^+-diamond diode that is capable to operate at high temperatures and high current rectification ratios, see (Esser et al. 1993).

2.1.1.6 Dependence on the Doping Step-size

In Fig. 2.9, a set of solution curves is shown for a substantially higher step-size of an nn^+-junction:[20] the donor density in region 1 is reduced by a factor of 10^5 from the value in Fig. 2.2 to $N_{d1} = 10^{11}\,\mathrm{cm}^{-3}$, while all other parameters remain the same as in Fig. 2.2, except for the current densities that also are correspondingly reduced by a factor of 10^5 to obtain a set of curves for forward, zero, and reverse bias that can be more easily compared with solution curves shown in Fig. 2.2 for the *nn*-junction.

The general behavior depicted in Fig. 2.9 is similar to the one shown for the much smaller step-size; however, now a much smaller current causes a similar, large spread in the carrier leakage that is shown in a logarithmic and a linear scale in Fig. 2.9a, b. The corresponding field and potential distributions are given in Fig. 2.9d–f. The magnitude of space charge, field, and current peaks

[19] This is distinctly different from the influence of a Schottky barrier or a *pn*-junction on the current voltage characteristic, which introduce *new*, more highly resistive regions that expand or contract with bias.

[20] We are using the denotation as an nn^+-junction somewhat loosely in this chapter, merely to indicate that the electron density in the n^+-region is orders of magnitude larger than in the *n*-region.

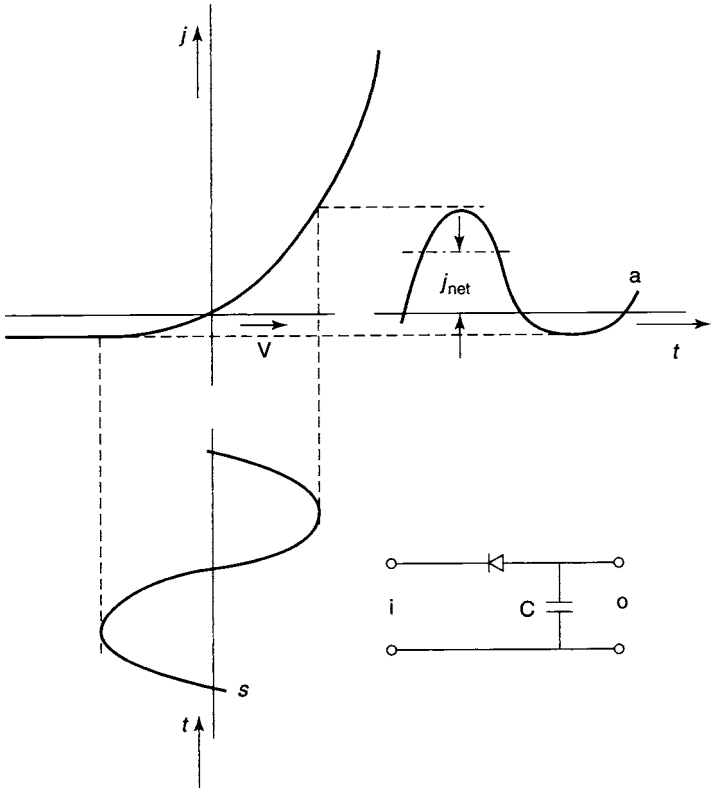

Fig. 2.8. Rectifier characteristics with a net forward dc output: (s) symmetric ac bias input; and (**a**) asymmetric current output. j_{net} is indicated inside the asymmetric current graph as the "net dc output current" obtained across a sufficiently large capacitor, as shown in the corresponding circuit diagram, with (i) input ac, and (o) output dc

shown in Fig. 2.9 are almost the same as the ones given in Fig. 2.2 for the lower step, but the relative shift between drift and diffusion for nonvanishing bias is substantially reduced.[21] The resulting characteristic consequently is much more asymmetric, and is presented in Fig. 2.7 as curve 2.

As more carriers are swept from the higher to the lower doped region with forward bias, the substantial increase in carrier density, as seen in Fig. 2.9a, permits a much increased current in region 1. The higher the N_{d2}/N_{d1} ratio, the higher is the ratio of forward to reverse current; the lower the N_{d1}, the lower is the current at which rectification becomes noticeable. However, if the lightly doped region is too wide, so that the limited number of carriers swept

[21] This similarity relates to the fact that we left the donor density in the highly doped region unchanged.

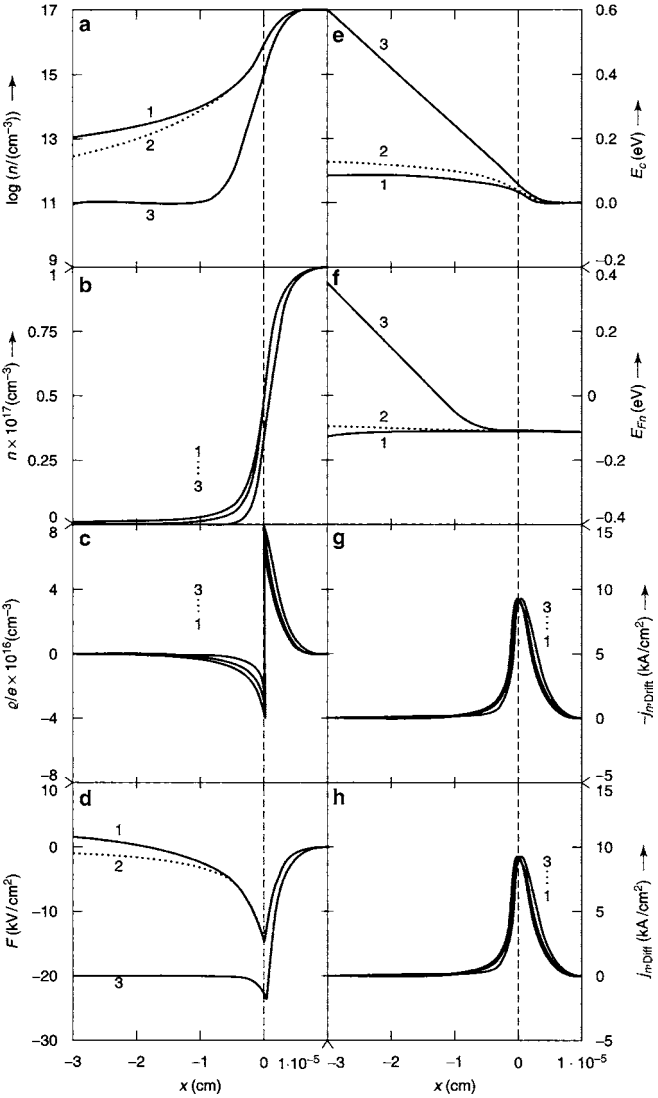

Fig. 2.9. nn^+-junction with a large doping step, with resulting distributions: $n(x)$, $\varrho(x)$, $F(x)$, $\psi(x)$, $E_{\mathrm{F}}(x)$, $j_{n,\mathrm{Drift}}(x)$, and $j_{n,\mathrm{Diff}}(x)$ for j_n as family parameter; curves 1–3 for 30, 0, and $-30\,\mathrm{mA\,cm^{-2}}$, respectively. The curve set shows somewhat similar behavior as the curve set for the nn-junction shown before, except that the spread for different bias is larger (that is even more pronounced at higher bias values) and the asymmetry is larger

into it[22] cannot sufficiently raise the average free carrier concentration there, then little rectification will occur, since the nonlinearity of the characteristic is caused by the change in the integrated resistance of the low-conductivity region; the current in the nn^+-junction is then series-resistance limited.

In most practical devices, nn^+-junctions are caused by unintentional doping inhomogeneities or by intentional boundary layer doping. The influence of such junctions on the current–voltage characteristics is small, except for extreme cases involving very high current densities or extremely high doping density ratios.

2.2 Significance of Basic Barrier or Junction Variables

In the previous sections, we have described in a few examples how the diffusion of carriers from a highly doped region causes the development of a space-charge double layer that relates to all other device variables via Poisson and transport equations. We shall now summarize these relations in a general description.

2.2.1 Interdependence of Carrier Densities, Fields, and Currents

There is a direct interdependence of the primary variables n, ϱ, F, and the two conventional currents $j_{n,\mathrm{Drift}}$ and $j_{n,\mathrm{Diff}}$.

The out-diffusion of electrons from a highly doped region creates a space-charge double layer. This space-charge layer produces an electric field, which causes a *drift current* opposite to the *electron diffusion*, and thus provides a containment of the electrons. The interdependence of these primary variables is direct and results in a steady-state electron density distribution.

2.2.1.1 Dependence on Other Parameters

The set of the governing equations contains parameters that influence the solution curves. These are the

- basic parameters $T, \varepsilon, \mu_n, N_{d1}$, and N_{d2},
- derived parameter j_n, and
- externally impressed parameter $\Delta V = (1/e)[E_\mathrm{F}(d_2) - E_\mathrm{F}(d_1)]$.

The solution curves, and consequently the current–voltage characteristics, show different sensitivity with respect to changes of these parameters.

[22] We will see later that the distance to which such carriers can be swept into the lowly doped region is given by the diffusion length (Sect. 5.1.1.1) or at higher fields by the drift length (Sect. 5.3.2) which may be smaller than the device thickness.

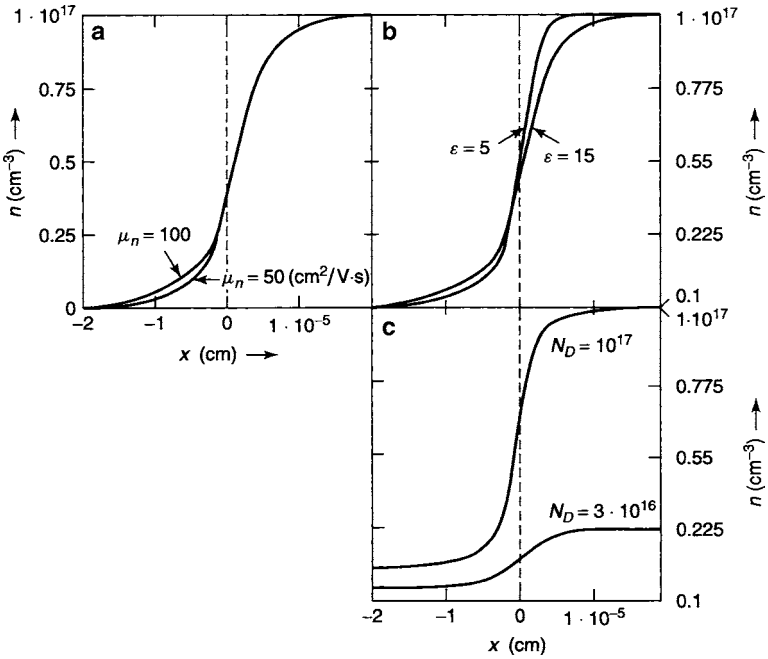

Fig. 2.10. Changes of the carrier distribution in an *nn*-junction for a step size of 10 in (**a**) and (**b**). With two different mobilities $\mu_n = 50$ and $100\,\mathrm{cm^2\,Vsec^{-1}}$ for $j_n = 30\,\mathrm{mA\,cm^{-2}}$ in (**a**); with two dielectric constants, $\varepsilon = 5$ and 15 in (**b**); and for donor densities of $3 \cdot 10^{16}$ and $1 \times 10^{17}\mathrm{cm^{-3}}$ in the high density range and with the same step size of 1 : 5 to the low density range in (**c**). The changes are minute and are explained in the text

We present in Fig. 2.10 a few examples for the influence of carrier mobility, relative dielectric constant, and donor densities on the solution curves: μ_n influences only the transport equation, ε only the Poisson equation, and N_d (through ϱ and n) both the equations.

For zero net currents most solution curves of (2.7)–(2.10) are independent of the *mobility*. Drift and diffusion currents are both proportional to μ_n; therefore, μ_n cancels out if $j_n = 0$. A similar independence on μ_n is expected for "small" net currents, i.e., when $j_n \ll (j_{n,\mathrm{Drift}}, j_{n,\mathrm{Diff}})$.

With an increase in the *donor density*, the distribution becomes steeper for the same relative step-size, as indicated in Fig. 2.10. This is caused by a decreased Debye length, as will be discussed quantitatively in Sect. 3.1.2.

A similar increase in steepness of the distribution is obtained when the relative *dielectric constant* is decreased (from 15 to 5 in Fig. 2.10c), thereby causing an increase in field by the same ratio. In the Poisson equation, this is equivalent to a similar change of N_d; however, it has no *direct* influence on the carrier density in the transport equation (an *indirect* influence via F causes the change in $n(x)$).

We will close this chapter by presenting an example of an nn^+-junction in which the current–voltage characteristic can be obtained in an analytic form. This example has practical significance in a variety of applications using carrier injection.

2.3 Space-Charge Limited Current

With the tools given in the previous sections we are now able to analyze the behavior of some semiconductors that are conventionally described as space charge limited currents. Such behavior is observed in certain nn^+-junctions in sufficient forward bias.

Under such conditions, Poisson and transport equations (1.17) and (2.3) can be integrated in closed form. We will discuss such important example below.

If, in an nn^+-junction device with sufficient forward bias, the electron density in the entire lowly doped region can become much larger than the donor density in this region; then the current through the device becomes controlled by the surplus carriers originating from the adjacent highly doped region. This current behaves much like the current in a vacuum diode [23] in which electrons are injected from the cathode and carried to the anode following the electric field, although limited by the space charge near the injecting cathode. This current is, therefore, often referred to as an *injected current*, or as a *space-charge limited current*[24](Mott and Gurney, 1940; Lampert, 1956; and Rose, 1978).

For spectroscopy of local states using space charge limited currents see also Nespurek and Sworakowski (1990). For the theory of space-charge limited currents in materials with an exponential distribution of capture coefficients see Gildenblat et al. (1989). The temperature dependence of space-charge limited currents in amorphous and disordered semiconductors is discussed by Schauer et al. (1996)

Figure 2.9a shows that $n \gg N_{d1}$ in the entire region 1 with sufficient forward bias; therefore, the space charge in the lower conducting region may be approximated as

$$\varrho = e(N_{d1} - n) \simeq -en. \tag{2.36}$$

Consequently, the Poisson equation becomes independent of the doping in this region:

$$\frac{\mathrm{d}F}{\mathrm{d}x} = -\frac{en(x)}{\varepsilon\varepsilon_0}. \tag{2.37}$$

[23] Though modified by the scattering of electrons in the semiconductor.

[24] The subject of space-charge limited currents was first discussed when the carrier injection occurs from injecting (nonblocking) electrodes. We have chosen here the injection from highly doped (n^+) region since it presents less ambiguities near the junction than neighboring an electrode (see the discussion later in this section).

In addition, the drift current becomes much larger than the diffusion current in the lowly doped region with large enough forward bias, as one can see from a comparison of Figs. 2.6a, b. This permits, with sufficient forward bias, an approximation of the total current by the drift current alone:

$$j_n = e\mu_n n(x)F(x). \tag{2.38}$$

After replacing $n(x)$ in (2.38) with the Poisson equation (2.37) one obtains

$$j_n = -\varepsilon\varepsilon_0\mu_n F(x)\frac{\mathrm{d}F}{\mathrm{d}x} \tag{2.39}$$

which can be integrated after separating variables, yielding

$$(x_0 - x)j_n = \varepsilon\varepsilon_0\mu_n\frac{[F(x) - F_0]^2}{2}. \tag{2.40}$$

Whenever $F_0 \ll F(-d_1)$, one can evaluate (2.40) at $x = -d_1$ for sufficient forward bias and directly obtain with[25] $F(d_1) \simeq V/d_1$ an analytical expression for the current–voltage characteristic:

$$j_n \simeq \varepsilon\varepsilon_0\frac{\mu_n V^2}{2d_1^3}; \tag{2.41}$$

that is, the current increases proportionally to the square of the applied *voltage* and decreases with the third power of the width of the low conductivity region.

From the assumption used, it is evident that space-charge-limited currents occur with sufficient forward bias in devices that have a *thin enough* region 1 to have the entire low-conducting region swamped with electrons, and have a density of carriers at the injecting boundary which lies sufficiently above the bulk carrier density in region 1 of the device. Such a device may alternatively consist of a homogeneous semiconductor of length L with an *injecting contact* (see Sect. 3.2.1.1); its current follows the same, well-known **space-charge-limited current equation**:

$$\boxed{j_n = \varepsilon\varepsilon_0\frac{\mu_n V^2}{2L^3}.} \tag{2.42}$$

From the relation $n \gg N_{d1}$ throughout the device, that is used to evaluate the space charge (2.36) and the characteristics given in Fig. 2.11, one sees that the space-charge-limited current equation holds only for "thin devices" in which the entire low-doped region can be swept over by electrons from the n^+- region. The injected currents then become rather large in such thin

[25] Neglecting the voltage drop in the highly conducting region 2. A somewhat better approximation yields $F(-d_1) \simeq (3/2)V/d_1$, yielding 9/8 as numerical factor in (2.41).

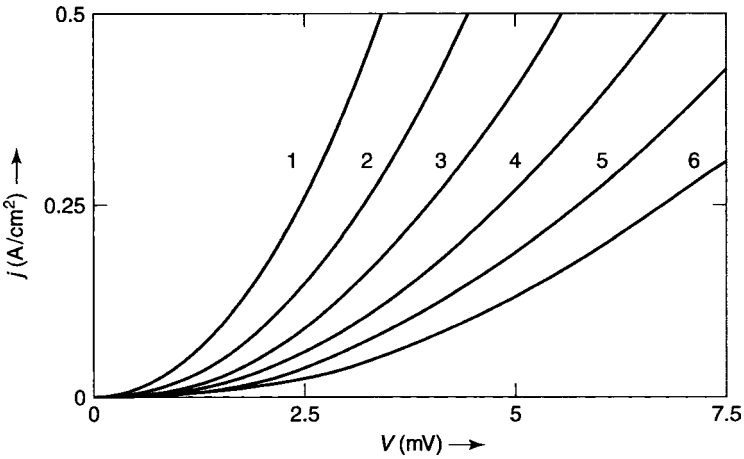

Fig. 2.11. Space-charge-limited currents calculated from (2.42) with $\mu_n = 100\,\mathrm{cm^2\,Vs^{-1}}$, $\varepsilon = 10$, and the device thickness as family parameter with $L = 1$, 1.2, 1.4, 1.6, 1.8, and $2 \cdot 10^{-5}$ cm for curves 1–6, respectively (the thinner the device, the steeper is the increase of the current with bias, the more electrons are swept through the entire device)

devices even in the mV bias range as shown in Fig. 2.11 and, in the given approximation do not depend on the doping density or the step size beyond a minimum range.

However, one should recognize that the space-charge-limited currents are part of the ordinary current–voltage characteristics in forward bias discussed in the previous section. The often-cited *majority carrier injection*[26] presents no special, new mechanism, but describes the normal "blowing over" of surplus carriers from the region of high carrier density into the region of lower doping. Under the given approximation, it permits explicit integration of the transport and Poisson equations and results in an analytical expression of the current–voltage characteristics.

2.3.1 Majority Carrier Injection

Majority carrier injection is used as a technical term to describe any boundary to a semiconducting region which supplies more than the equilibrium density of majority carriers in this semiconductor region. This boundary can be given as

- An nn^+-junction, described in the previous sections of this chapter (for more details, see Lampert and Mark, 1970),

[26] It is an expression coined to indicate similarity to the current in a vacuum diode.

- A metal-semiconductor contact in which the metal work function is so low that the electron density at the interface is substantially larger than in the semiconductor bulk (Taylor and Lalevic, 1977), or by external means, such as
- By optical excitation with photon energies in excess of the band-gap that increases the majority carrier density near the illuminated surface substantially (Silver and Shaw, 1976).

In each of these cases, electrons will leak into the lowly conducting region of the semiconductor and cause an increase in its conductance which can become marked when the thickness of the semiconductor is comparable to the distance to which the injected electrons can diffuse. This distance is the diffusion length or the drift enhanced diffusion length, as described in Sects. 5.1.1.1 or 5.3.2, respectively.

In case of an optical injection, this assumption is not always satisfied. With additional minority carrier diffusion one also has to consider carrier lifetime limitation by an increased recombination. This makes the discussion a bit more complex and shall be postponed to Sect. 8.3.

2.3.2 Minority Carrier Injection

Minority carrier injection appears more frequently as a part of the operation of conventional devices. It refers to the leaking-out of minority carriers from any boundary that supplies more minority carriers than are present in the adjacent semiconductor region. This is the case for

- Any *pn*-junction where minority carriers are considered as being injected across the doping interface of the junction. Such process is usually dealt with in the conventional junction theory (see Sect. 7.2) without specific reference to an injection process
- Any "blocking" electrode, i.e., an electrode of sufficiently high work function so that the majority carrier density at the interface is much smaller than in the bulk of the semiconductor, or in extreme cases, where we have
- An inversion layer. Such a layer is a very substantial source of minority carriers which are injected beyond the field-free region close to the inversion layer and in forward bias then continue to *drift* into the bulk of the semiconductor, following the bulk field, until they recombine (Higman et al. 1991).

2.3.3 Trap-Controlled Space-Charge-Limited Currents

When a sufficient fraction of the injected electrons can become trapped they need to be considered in the Poisson equation. The space charge is then given as

$$\varrho = e(n + n_t) \tag{2.43}$$

with n_t the density of electrons in traps (as long as one can neglect N_{d1}). Under certain conditions (see Sect. 8.2.1), n_t is proportional to the electron density in the conduction band:

$$n_t = \frac{nN_t}{n + n_0} \tag{2.44}$$

with N_t the density of these traps, and $n_0 = n(E_F = E_t)$ the electron density in the conduction band when the Fermi level coincides with the trap level. For $N_t \gg n$, (2.44) can be simplified and the space charge is given by

$$\varrho \simeq en\left(1 + \frac{N_t}{n_0}\right). \tag{2.45}$$

Introducing this space charge into (2.39) yields after integration a *modified space charge limited current* equation that is given by

$$\boxed{j_n = \frac{n_0}{N_t}\frac{\varepsilon\varepsilon_0\mu_n V^2}{2L^3},} \tag{2.46}$$

with a current that is reduced from the trap-free case by the ratio n_0/N_t.

In many semiconductors, a trap distribution rather than a single trap level is present, rendering the relationship between n and n_t more complicated. This modifies the relation in (2.46), and can be evaluated analytically if the trap distribution is known. However, the general behavior of the forward current is preserved.

Summary and Emphasis

We first introduced several typical space-charge profiles to demonstrate the general behavior that can be observed in various types of semiconductor devices.

The field distribution in space charge double layers has usually a triangular shape with its maximum value at the double layer interface.

A neutral interlayer between the positive and negative space-charge layers is shown to achieve a sufficient voltage drop across a junction device without increasing the field into the electric breakdown range.

The interrelation between space-charge distribution, the resulting field and electron potential corresponding to the band edge distribution is unique and is delineated.

We then discussed how the space-charge double layer is created in an *nn*-junction by leakage of mobile electrons from the region of a high density of shallow donors into the adjacent region with a low donor density. The space charge shows a sign-flip at the doping interface.

The space-charge double layer produces an electric field which counteracts via electron drift the out-diffusion of electrons from the highly to lowly doped region.

The field distribution shows the characteristic triangular shape with the maximum of the built-in field *at* the doping interface. Here also, the drift and diffusion currents have their maximum values (but opposite signs), which are typically many orders of magnitude larger than the net currents.

When a bias is applied, the electron profile is shifted. Concurrent with the change in electron (space charge) profile, all other variable distributions change and cause a nonlinear change of the net current with applied bias. The resulting current voltage characteristic is a rectifying one.

Current injection can be analyzed most transparently in an nn^+-junction. A steeply increasing current in forward bias is caused by swamping of a thin, lowly doped layer with electrons from the adjacent, highly doped region. The injection current has a similar behavior in forward bias as the current in a vacuum diode.

Some of the basic phenomena of space-charge development of inhomogeneously doped semiconductors can be studied in a rather transparent fashion in an nn^+-junction and provide clues for the understanding of the operation of a variety of semiconductor devices.

Exercise Problems

1.(r) List a number of examples where nn^+-junctions (or pp^+-junctions) occur unintentionally in semiconductor devices. What is the purpose of such junctions when they are created intentionally?

2.(*) In thermodynamic equilibrium, the Fermi level is always horizontal. The distribution of the band edge mirrors the distribution of electrons. When a bias is applied, the Fermi-level becomes tilted. Describe $E_\mathrm{F}(x)$ in both n and n^+ bulk regions and in the junction. Describe $E_c(x)$ in these three regions and observe the changes in the junction region carefully. $n(x)$ is no longer mirrored by $E_c(x)$ alone. Discuss the specific changes.

3.(x) The field distribution shows a spike exactly at the doping interface between the n and n^+ region.
   (a) Is this always the case? Define the involved principle.
   (b) With an applied bias, describe the changes of $F(x)$.
   (c) Give the conditions for which $F(x)$ becomes monotonic.

4.(e) The diffusion potential is defined in thermal equilibrium. Is there an upper limit for the diffusion potential? Give it for Si and for Ge at 300 K.

5.(l) In problem 4, the upper limit of the diffusion potential was analyzed. Does this simple estimate also hold for large band gap materials, e.g., for ZnO at 300 K, or even for Si at 4 K?

(a) What does this mean if you do not limit the time to achieve thermodynamic equilibrium?
(b) What does that mean if quantitatively you want to complete your experiment within 10 h?
(c) What does the result of the previous question signalize in respect to "frozen-in equilibria"? Where would you place the energy limits for trap levels above which equilibrium could be expected for typical experiments?

6. Compare carrier injection in an nn^+-junction
(a) with the thermionic emission in a vacuum diode; point out similarities and differences
(b) with a semiconductor between injecting electrodes (assume that $n(x = -d_1) = n(x = +d_2) = n_c \gg n_0$, with n_0 the electron density in the homogeneous semiconductor.

3

The Schottky Barrier

Summary. A metal of sufficiently high work function causes the electron density of an n-type semiconductor to be much lower than determined by its doping in the bulk, causing a space charge near the electrode. The bias-induced shift and deformation of this space charge determines the corresponding changes in the current. An understanding of this interrelation is the key for deriving the current–voltage characteristics of such a Schottky barrier device.

In this chapter, we will analyze the space charge induced by the metal–semiconductor boundary and its deformation by an applied bias, yielding the typical diode characteristics. We analyze the mathematical relations given by the transport and Poisson equations which yield as approximative solutions the diode equation. We will approach this problem by starting from a rather simple model, and will later introduce more realistic modifications that yield results more in tune with experimental observation.

3.1 The Classical Schottky Barrier

When an n-type semiconductor is connected to a metal of a sufficiently high work function, electrons from the semiconductor leak out into the adjacent metal.[1] The electron density at the interface between the metal electrode and the semiconductor is reduced below its equilibrium bulk value n_{10}, and thereby a positive space-charge region is created within the semiconductor near the metal contact. The corresponding negative charge, to render the total device neutral is located at the metal/semiconductor interface.

[1] Even though the electron density *inside* a metal is much higher than in the semiconductor, at its boundary to the semiconductor this density is substantially reduced according to its effective work function. It is this electron density which causes a reduction of n in the semiconductor at the interface.

The space-charge layer in the semiconductor results in a field ramp and a potential step, referred to as the *Schottky barrier*.[2]

The electron density at the metal/semiconductor interface is given by

$$n_c = n(x = 0) = N_c \exp\left(-\frac{e\,\phi_{\mathrm{MS}}}{kT}\right) \tag{3.1}$$

where $\phi_{\mathrm{MS}} (= \phi_{\mathrm{M}} - \chi_{\mathrm{Sc}}$ in the linear model) is the *metal/semicon-ductor work function* and N_c is the effective level density at the metal–semiconductor interface.[3] This interface electron density n_c is initially assumed to be independent of current and applied voltage:

$$n_c = n_j(x = 0^+, j \neq 0), \tag{3.2}$$

where n_j is the electron density at the semiconductor side of the interface which will later be allowed to change as a function of the current (see Sects. 3.2.2.2 and 3.4.1). The electron density in the bulk is given by the density of the shallow, uncompensated donors

$$n_{10} \simeq N_{d1}. \tag{3.3}$$

When n_c is *lower* than the electron density in the bulk, a depletion region results near the electrode that has properties similar to the depletion region in the highly doped half of the nn^+-junction discussed in Sect. 2.1.1. It produces a rectifying (*blocking*) contact, which can be substantially more rectifying than in an nn^+-junction since the ratio n_c/n_{10} is usually much smaller than n_{10}/n_{20} caused by doping gradients.

First, we discuss an example with the same parameters for the highly doped region as in Sect. 2.1, but with a *lower* electron density at the boundary: $n_c = 10^{10}\,\mathrm{cm}^{-3}$ (see Table 3.1), resulting in a pronounced Schottky barrier behavior.

3.1.1 Schottky Approximation: Field and Potential Distributions

In Fig. 3.1a we show the electron distribution computed from (3.5)–(3.7) with parameters listed in Table 3.1 (Electrode interface at $x = 0$). Because of the

Table 3.1. Parameters used for Fig. 3.1

Parameter	μ_n	ε	T	N_{d1}	n_c
Value	100	10	300	10^{17}	10^{10}
Dimensions	$\mathrm{cm}^2\,\mathrm{Vs}^{-1}$	–	deg K	cm^{-3}	cm^{-3}

[2] A similar Schottky barrier appears in p-type semiconductors near a metal electrode with *low* work function, again when the hole density near the electrode is much smaller than in the bulk. Here the space-charge region is negatively charged and the resulting field is positive.

[3] This is slightly different from N_c within the semiconductor bulk (see (2.26)) because of a different effective mass at the interface.

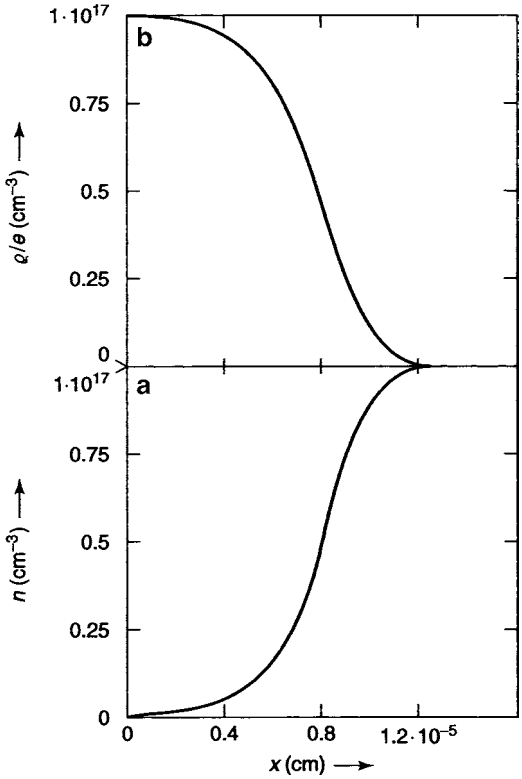

Fig. 3.1. Typical electron density (**a**) and space-charge distribution (**b**) in a Schottky barrier computed from (3.5)–(3.7) (parameters are listed in Table 3.1)

large ratio of the bulk-to-surface carrier densities n_{10} and n_c, the electron density in the space-charge region rapidly decreases to values very small compared to the donor density N_d, thus rendering the space charge

$$\varrho(x) = e[p_\mathrm{d} - n(x)] \simeq e[N_\mathrm{d} - n(x)] \simeq eN_\mathrm{d} \quad \text{for} \quad 0 \leq x < x'_\mathrm{D}, \tag{3.4}$$

independent of n in a substantial fraction of this junction-region (with $x'_\mathrm{D} < x_\mathrm{D}$ – see below); p_d is the density of positively charged, ionized donors.

In using this constant space charge[4] within the entire width of the Schottky barrier (i.e., assuming $x'_\mathrm{D} = x_\mathrm{D} \simeq 8 \cdot 10^{-6}\,\mathrm{cm}$) in this example, the resulting

[4] The error encountered at the boundary of this range ($8.10^{-6}\,\mathrm{cm}$) seem to be rather large (factor 2) when judging from the plot in linear scale of Fig. 3.1. The accumulative error, when integrating from the metal/semiconductor interface, however, is tolerable, as shown in Fig. 3.2. The substantial simplification in the mathematical analysis justifies this seemingly crude approach.

Schottky approximation permits a major simplification[5] of the governing set of equations[6]:

$$\frac{\mathrm{d}n}{\mathrm{d}x} = \frac{j_n - e\mu_n nF}{\mu_n kT} \tag{3.5}$$

$$\frac{\mathrm{d}F}{\mathrm{d}x} = \frac{eN_\mathrm{d}}{\varepsilon_\mathrm{st}\varepsilon_0} \tag{3.6}$$

$$\frac{\mathrm{d}\psi_n}{\mathrm{d}x} = F. \tag{3.7}$$

This allows decoupling of the Poisson equation from the transport equation. Integration of (3.6) yields

$$\boxed{F(x) = F_c + \frac{eN_\mathrm{d}}{\varepsilon_\mathrm{st}\varepsilon_0}x;} \tag{3.8}$$

that is, the field decreases linearly with increasing distance from the metal/semiconductor interface (see dashed line in Fig. 3.2b), with F_c, the *maximum value of the field* at $x = 0$, used here as the integration constant. From the integration of (3.7) after insertion of (3.8), one obtains the electrostatic electron potential

$$\boxed{\psi_n(x) = \psi_{n,\mathrm{D}} + F_c x + \frac{eN_\mathrm{d}}{2\varepsilon_\mathrm{st}\varepsilon_0}x^2,} \tag{3.9}$$

which decreases parabolically with increasing x, shown as dashed parabola in Fig. 3.2c. As integration is constant we used the *electron diffusion potential* $\psi_{n,\mathrm{D}}$ which is appropriate for zero current, as we will show in Sect. 3.1.2.1. For a finite current, the solutions $F(x)$ and $\psi_n(x)$ have exactly the same form ((3.6) and (3.7) don't depend on j_n), however, with integration constants that are current-dependent, as will be shown in Sect. 3.1.3. This results in a parallel shift of $F(x)$ and $\psi_n(x)$ in x with changing j_n (Fig. 3.5c, d).

For a positive space charge ($+eN_\mathrm{d}$), i.e., for an n-type semiconductor, F_c is negative and $\psi_{n,\mathrm{D}}$ is positive; their values are calculated in Sect. 3.1.2.1. When inserting F_c from (3.18) (see below), the potential distribution can also be written as

$$\psi_n(x) = \frac{1}{\sqrt{2}}\frac{kT}{e}\left[\sqrt{\frac{2e\psi_{n,\mathrm{D}}}{kT}} - \frac{x}{L_\mathrm{D}}\right]^2, \tag{3.10}$$

an expression that is sometimes helpful. L_D is the *Debye length* (3.20), which is a characteristic length for changing $\psi_n(x)$ and $F(x)$ (see Sect. 3.1.2.2).

[5] A comparison with the previously discussed example of majority carrier injection, in which $n \gg N_\mathrm{d}$, presents the other alternative for the two cases for which the discussion of this one-carrier space-charge distribution can be drastically simplified.

[6] We have rewritten the first transport equation as a function of $\mathrm{d}n/\mathrm{d}x$ to identify this set as a set of three differential equations that need to be solved

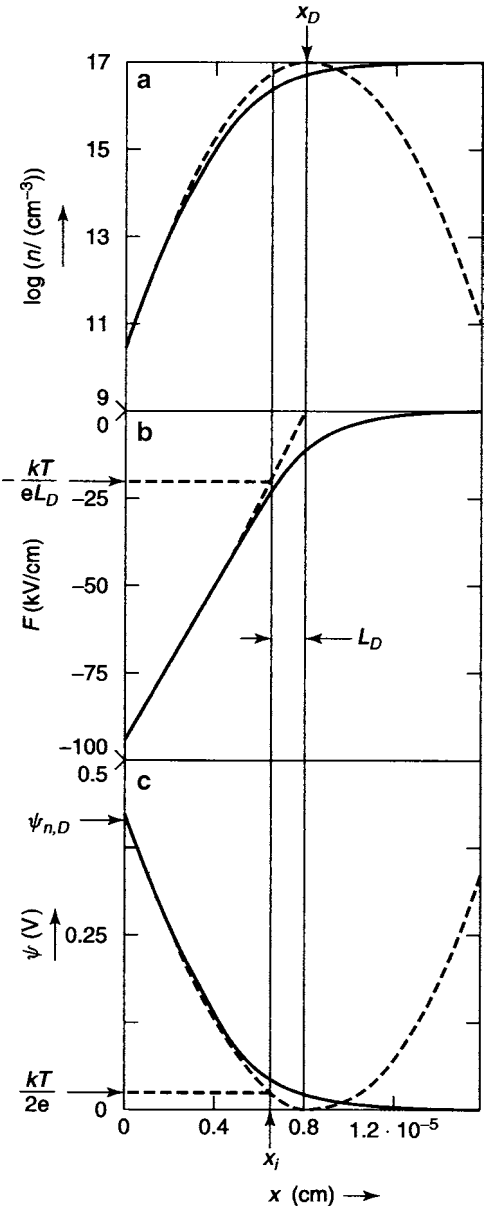

Fig. 3.2. Electron density, field, and potential distributions of a Schottky barrier with parameters given in Table 3.1. The *Solid curves* show the exact solutions of (3.5)–(3.7); the *dashed curves* show the Schottky approximations, using (3.8), (3.9), or (3.14). The approximation and shown as *continued dashed curve* for $x > x_{\mathrm{D}}$ is physically meaningless

Figures 3.2b, c show a comparison between the Schottky-approximation (dashed) and the exact solutions (solid curves) obtained by numerical integration of (3.5)–(3.7) with $\varrho(x) = e[N_\mathrm{d} - n(x)]$ in the Poisson equation. Near the electrode this approximation is quite satisfactory (see Sect. 3.1.2), and consequently is mostly used.

The Schottky approximation permits the definition of a barrier layer thickness x_D from the linear extrapolation of $F(x)$ with $F(x_\mathrm{D}) = 0$, as indicated in Fig. 3.2b. For a computation of x_D, see Sect. 3.1.2.2.

3.1.2 Zero Current Solution of the Electron Distribution

The electron density distribution can be obtained for $j_n = 0$ from the transport equation (3.5):

$$\frac{\mathrm{d}n}{\mathrm{d}x} = -\frac{e}{kT} n F(x). \tag{3.11}$$

After replacing $F(x)$ by $\mathrm{d}\psi_n/\mathrm{d}x$ one obtains the Boltzmann distribution by integration

$$\boxed{n(x) = n_{10} \exp\left(-\frac{e\psi_n(x)}{kT}\right).} \tag{3.12}$$

When inserting $F(x)$ from (3.8) and using as a convenient parameter

$$\frac{1}{L_\mathrm{D}^2} = \frac{e}{kT} \cdot \frac{eN_\mathrm{d}}{\varepsilon_\mathrm{st}\varepsilon_0}, \tag{3.13}$$

with L_D the *Debye length*

$$n(x) = n_{10} \exp\left[-\left(\frac{e\psi_{n,\mathrm{D}}}{kT} + \frac{eF_c x}{kT} + \frac{x^2}{2L_\mathrm{D}^2}\right)\right], \tag{3.14}$$

which is shown as dashed curve in Fig. 3.2a.

This holds for zero currents or, as a good approximation, as long as the net current is small compared to both drift and diffusion currents: $j_n \ll (j_{n\,\mathrm{Drift}}, j_{n\,\mathrm{Diff}})$. This range is referred to as the **Boltzmann range** (see Sect. 3.1.2.2).

3.1.2.1 Diffusion Potential, Junction Field

The solutions (3.8) and (3.9) contain two integration constants, the electron potential and the electric field at the metal/semiconductor interface.

The electron potential step between bulk and metal/semiconductor interface is obtained from (3.12) by setting $x = 0$, yielding the "diffusion potential" for **zero current** with $n(x = 0) = n_c$:

$$\boxed{\psi_{n,\mathrm{D}} = \frac{kT}{e} \ln\left(\frac{n_{10}}{n_c}\right).} \tag{3.15}$$

This *electron diffusion potential* depends only on the ratio of the bulk and interface densities of carriers.

From Fig. 3.2 one sees that the diffusion potential can also be approximated by the product of maximum barrier field and barrier width:

$$\psi_{n,\mathrm{D}} = -\frac{F_c x_\mathrm{D}}{2}. \tag{3.16}$$

For the barrier field[7] at $x = x_\mathrm{D}$ one obtains from (3.8):

$$F_c = -\frac{eN_\mathrm{d} x_\mathrm{D}}{\varepsilon_\mathrm{st}\varepsilon_0}. \tag{3.17}$$

After combining (3.16) and (3.17) and eliminating x_D, one can express the *barrier field at zero current* as a function of $\psi_{n,\mathrm{D}}$:

$$\boxed{F_c = -\sqrt{\frac{2eN_\mathrm{d}\psi_{n,\mathrm{D}}}{\varepsilon_\mathrm{st}\varepsilon_{0.}}}} \tag{3.18}$$

For reasonable values of doping ($N_\mathrm{d} \simeq 10^{16}\,\mathrm{cm}^{-3}$) and of the electron diffusion potential, F_c is on the order of $40\,\mathrm{kV\,cm}^{-1}$:[8]

$$F_c = -42.3\sqrt{\frac{N_\mathrm{d}}{10^{16}}\frac{\psi_{n,\mathrm{D}}}{0.5}\frac{10}{\varepsilon_\mathrm{st}}} \qquad (\mathrm{kV\,cm}^{-1}). \tag{3.19}$$

3.1.2.2 Debye Length and Barrier Width

The Debye length is introduced from (3.13), as the distance from x_D in which the electron potential has increased by $kT/(2e)$:

$$\boxed{L_\mathrm{D} = \sqrt{\frac{\varepsilon_\mathrm{st}\varepsilon_0 kT}{e^2 N_\mathrm{d}}}} \tag{3.20}$$

[7] That is, the maximum field which lies in this approximation at the metal/semiconductor boundary (neglecting image forces).

[8] However, at higher doping densities, especially close to the metal interface, tunneling fields may be reached when $N_\mathrm{d} > 10^{18}\,\mathrm{cm}^{-3}$. This often is desired to make a contact "ohmic" and such increased defect density can be reached, e.g., by gas discharge treatments (Buttler, 1956)

and typically is on the order of a few hundred or thousand Å:

$$L_{\mathrm{D}} = 381\sqrt{\frac{\varepsilon_{\mathrm{st}}}{10}\cdot\frac{T}{300}}\sqrt{\frac{10^{16}}{N_{\mathrm{d}}}} \quad (\text{Å}). \tag{3.21}$$

The *barrier layer thickness* can be expressed in terms of L_{D} by combining (3.16) and (3.17), while eliminating F_c:

$$\boxed{x_{\mathrm{D}} = L_{\mathrm{D}}\sqrt{\frac{2e\psi_{n,\mathrm{D}}}{kT}},} \tag{3.22}$$

which means that x_{D} is usually a few (typically 3–6) Debye lengths thick, since $\psi_{n,\mathrm{D}}$ is typically on the order of $10kT/e$.

The Debye length is also the position (counting from $x = x_{\mathrm{D}}$) at which $n(x)$ for zero current has its *maximum slope*, i.e., the opposing diffusion and drift currents have their maximum value (see Figs. 3.5f, g, curve 1), as one obtains from differentiation of (3.11):

$$\frac{\mathrm{d}^2 n}{\mathrm{d}x^2} = -\frac{e}{kT}\left(\frac{n\mathrm{d}F}{\mathrm{d}x} + \frac{F\mathrm{d}n}{\mathrm{d}x}\right) = 0, \tag{3.23}$$

which yields for the inflection point of $n(x)$, located at $x = x_i$

$$F(x_i) = F_c\sqrt{\frac{kT}{2e\psi_{\mathrm{D}}}} = -\sqrt{\frac{kTN_{\mathrm{d}}}{\varepsilon_{\mathrm{st}}\varepsilon_0}} = -\frac{kT}{eL_{\mathrm{D}}}, \tag{3.24}$$

which, when compared with the value obtained from the Poisson equation:

$$F(x_i) = \frac{eN_{\mathrm{d}}(x_{\mathrm{D}} - x_i)}{\varepsilon_{\mathrm{st}}\varepsilon_0}, \tag{3.25}$$

yields:

$$x_i = x_{\mathrm{D}} - L_{\mathrm{D}}; \tag{3.26}$$

both x_i and $F(x_i)$ are identified in Fig. 3.2b. This result was already used in Sect. 2.1.1.4 without derivation.

Using (3.12) and (3.24), the maximum current at the inflection point can be written as

$$j^{\max}_{n,\mathrm{Drift}} = e\mu_n n_{10}\left(\frac{kT}{eL_{\mathrm{D}}}\right)\exp(-0.5) = -j^{\max}_{n,\mathrm{Diff}}. \tag{3.27}$$

With a field $F(x_i) \simeq kT/(eL_{\mathrm{D}})$ which is on the order of $10^4\,\mathrm{V\,cm^{-1}}$, the maximum current is typically on the order of tens of $\mathrm{kA\,cm^{-2}}$, i.e., very large compared to the net current through Schottky barrier devices.

3.1.2.3 The Accuracy of the Schottky Approximation

In the part of the junction near $x = x_D$, the Schottky approximation is not satisfactory, since ϱ has not yet reached its constant value eN_D (see Figs. 3.1 and 3.2). The error made by computing the maximum field F_c or the barrier width x_D, using the expressions (3.18) or (3.22), respectively, can be substantial when n_c is not (at least) several orders of magnitude smaller than N_D.

We determine the error by comparing F_c obtained from the computed solutions of (3.5)–(3.7) with the approximated value obtained from (3.15) and (3.18) for a variety of n_c values. The *computed solutions* of (3.5)–(3.7) for $j_n = 0$ are shown in Fig. 3.3 for $n(x)$, $\varrho(x)$, $F(x)$, and $\psi(x)$, with n_c as family parameter. Space-charge saturation is achieved for curves 3–5 (**b**). The saturation region, however, is much narrower than the total width of the barrier, even for the lowest value of n_c. Nevertheless, the Schottky approximation yields a substantially linear branch of the field distribution near the metal/semiconductor interface as long as n_c/N_d is below $\approx 10^{-2}$ (**c**).

The error for the barrier field in the Schottky approximation ($\Delta F_c/F_c$) is plotted in Fig. 3.4 as function of n_c/N_d. It is less than 5% for $n_c/N_d < 10^{-5}$, but increases rapidly above 10% when n_c/N_d increases above 10^{-2}.

3.1.3 Nonvanishing Currents

For nonvanishing currents, the carrier and field distributions are deformed, similar to those of the nn^+-junction. However, since n at $x = 0$ is kept constant (at n_c), independent of the bias, the $n(x)$ curve is substantially deformed near $x = 0$ (see Fig. 3.5 and discussed below). Other distributions [$F(x)$, $\varrho(x)$, and $\psi(x)$] look similar to the highly doped region (i.e., for $x > 0$) of the nn^+-junction (compare Fig. 3.5 with Fig. 2.9).

3.1.3.1 The Electron Density Distribution

When introducing the Schottky approximation (3.8) for $F(x)$ into the transport equation (3.5), one obtains a linear differential equation for $n(x)$:

$$\frac{\mathrm{d}n}{\mathrm{d}x} + \frac{e}{kT}\left(F_c + \frac{eN_d}{\varepsilon_{st}\varepsilon_0}x\right)n(x) - \frac{j_n}{\mu_n kT} = 0. \tag{3.28}$$

Integration of (3.28) yields the general solution[9]

$$n(x') = n_c \exp\left(-\frac{e[\psi_n(x') - \psi_{n,D}]}{kT}\right) + \frac{j_n}{e\mu_n F_c}\cdot 2\cdot\left[\sqrt{\frac{e\psi_{n,D}}{kT}}\cdot D\left(\sqrt{\frac{e\psi_n}{kT}}\right)\right] \tag{3.29}$$

[9] We have introduced here a shifted coordinate system (x', n). The amount of the shift in x is determined by the boundary condition, as will be discussed later in this section.

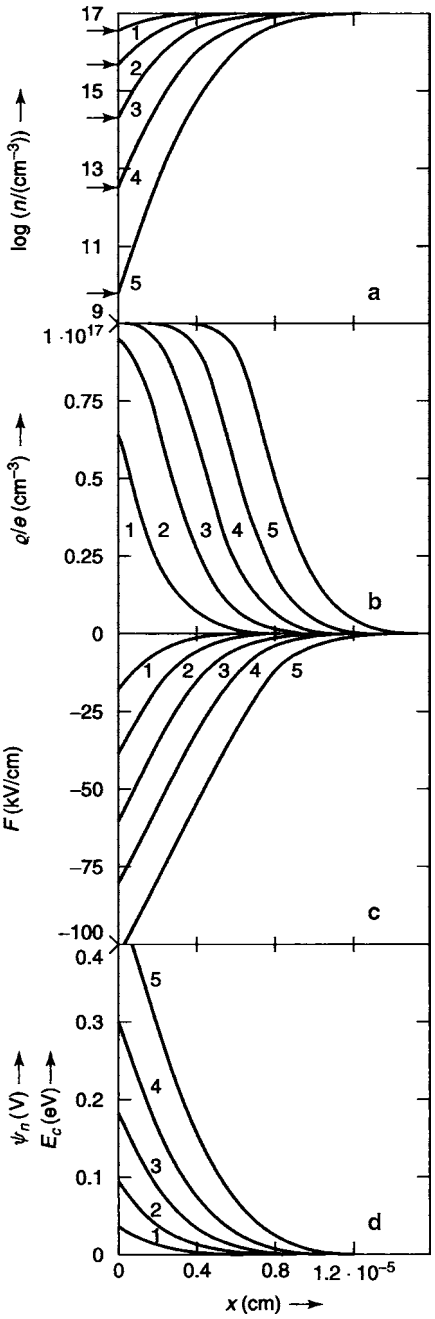

Fig. 3.3. Schottky barriers for $j = 0$ with different n_c as family parameter, as pointed out by arrows for $x = 0$ in (**a**). Curves $n(x)$, $\varrho(x)$, $F(x)$, and $\psi(x)$ are obtained by numerical integration of (3.5)–(3.7) with other parameters listed in Table 3.1

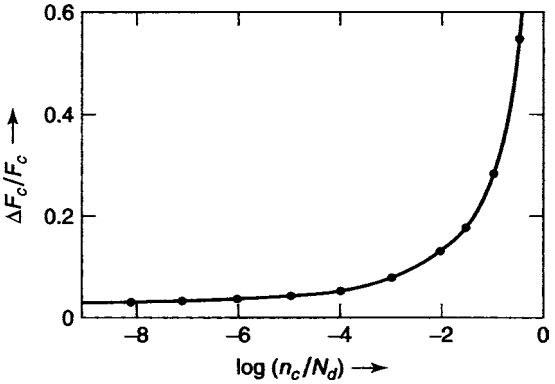

Fig. 3.4. Computed relative error of $F_c = F(x = 0, j = 0)$ between exact solutions and Schottky approximation is the function of n_c/N_d

where $D(\xi)$ is Dawson's integral:

$$D(\xi) = \exp(-\xi^2) \int_o^\xi \exp(t^2)\mathrm{d}t, \tag{3.30}$$

as shown in Fig. 3.6 and tabulated in the *Handbook of Mathematical Functions* (Abramowitz and Stegun, 1970). For $\xi > 2$, Dawson's integral can be approximated by

$$D(\xi) = (1/2\xi)(1 + 1/2\xi^2 + 3/4\xi^4 + \ldots), \tag{3.31}$$

the first term of which is sufficiently accurate for $\xi > 4$, as can be judged from Fig. 3.6, yielding

$$D(\xi) \approx \frac{1}{2\xi} \qquad \text{for} \quad \xi > 4. \tag{3.32}$$

The solution $n(x)$ given in (3.29) consists of a Boltzmann term (3.12),[10] and a correction term that is linear in current and has the shape shown in Fig. 3.7. This term is zero for $x = x_\mathrm{D}$, i.e., at the beginning of the Schottky barrier, goes through its maximum at $x' \approx x_\mathrm{D} - L_\mathrm{D}$, and drops hyperbolically for $x' < x_\mathrm{D} - 3L_\mathrm{D}$. In reverse bias ($j_n < 0$), the term is added to the zero current solution, causing the electron density distribution to become S-shaped (Fig. 3.8). In forward bias, this term is subtracted, which causes the Boltzmann solution (Fig. 3.8b) to steepen.

Using only the first term of the Dawson's integral approximation, one can reduce (3.29) to a simple expression:

$$\boxed{n(x') = n_c \exp\left[\frac{-e\{\psi_n(x') - \psi_{n,\mathrm{D}}\}}{kT}\right] + \frac{j_n}{e\mu_n F(x')},} \tag{3.33}$$

[10] The first term of (3.29) is identical with (3.12) when replacing $\psi_{n,\mathrm{D}}$ using (3.15).

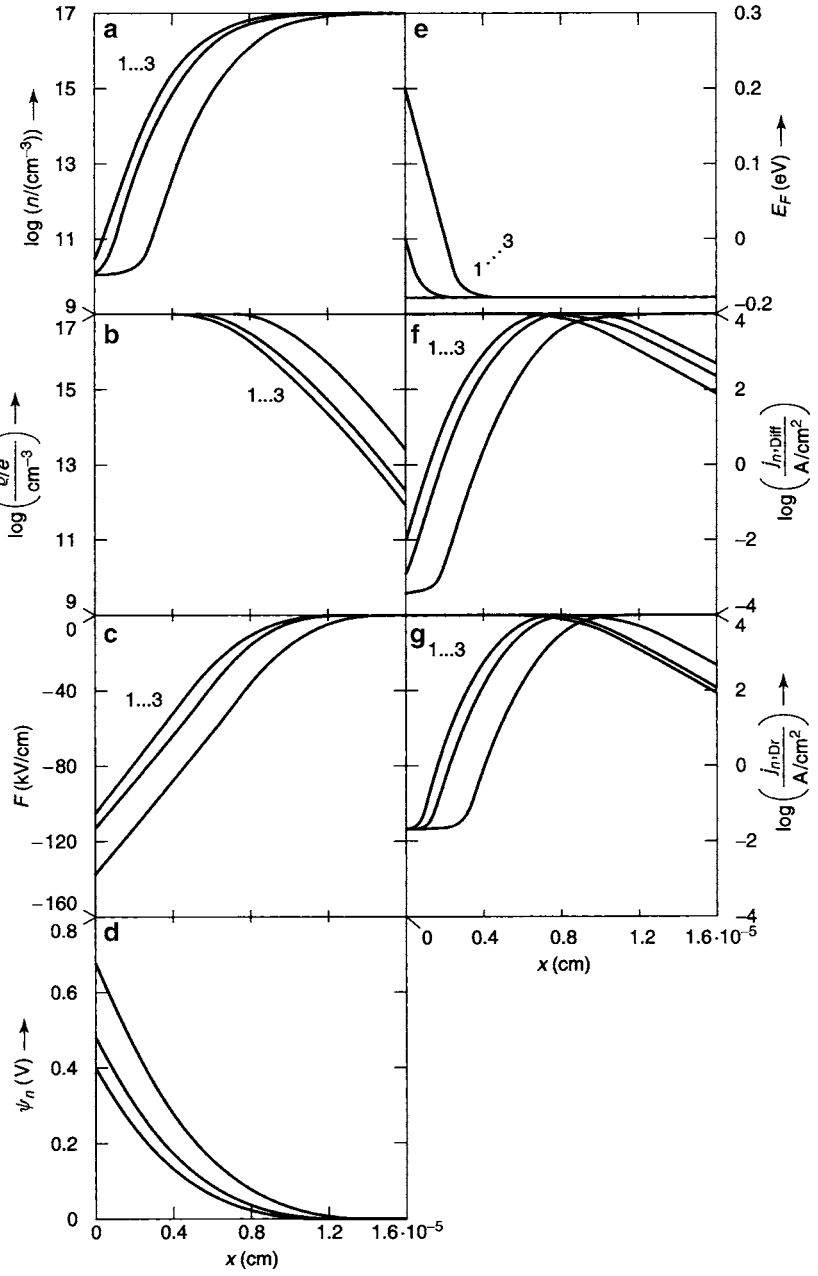

Fig. 3.5. Schottky barrier with $N_\mathrm{d} = 10^{17}\,\mathrm{cm}^{-3}$, $n_c = 10^{10}\,\mathrm{cm}^{-3}$; other parameters are the same as listed in Table 3.1. The exact solution curves of (3.5)–(3.7): $n(x)$, $\varrho(x)$, $F(x)$, $\psi(x)$, $E_\mathrm{F}(x)$, $j_{n,\mathrm{Drift}}(x)$, and $j_{n,\mathrm{Diff}}(x)$ are given in (**a**)–(**g**), respectively. Family parameter in each sub figure is the current: curves 1–3 for 0, −10, and $-20\,\mathrm{mA\,cm}^{-2}$, respectively

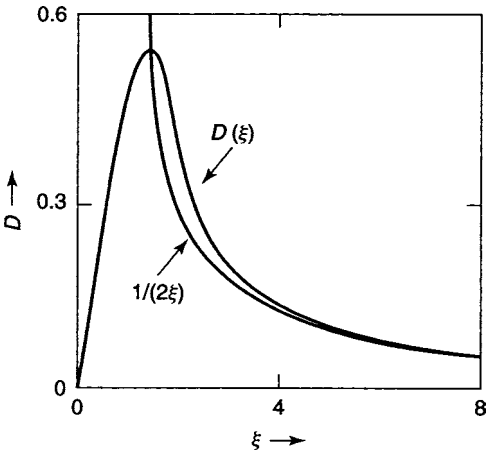

Fig. 3.6. Dawson's integral ($D(\xi)$) compared with a simple hyperbolic function, indicating excellent agreement for $|\xi| > 4$

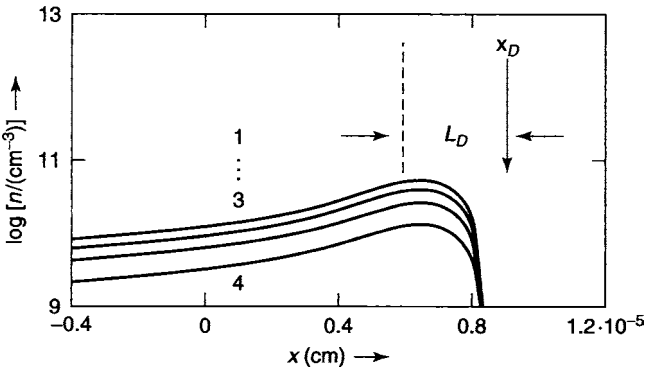

Fig. 3.7. Current term in $n(x)$ (3.29) with j_n as family parameter: curves 1–4 for $-20, -15, -10$, and $-5\,\mathrm{mA\,cm^{-2}}$, respectively. Observe the sign inversion of, and shift in the x-axis by, the width of the Schottky barrier x_D (for $j_n = 0$) compared to Fig. 3.8

with $F(x')$ obtained similar to (3.18):

$$F(x') = \sqrt{\frac{2eN_\mathrm{d}\psi_n(x')}{\varepsilon_\mathrm{st}\varepsilon_0}}. \tag{3.34}$$

One can determine $\psi_n(x)$ from (3.9) and obtain $\psi_n(x')$ after the shift $x - x'$ is known. This shift is a function of j_n and can be obtained for each curve from the boundary condition $n(x = 0) = n_c$. When this is done graphically from Fig. 3.8, one obtains a replotted set $n(x)$ as shown in Fig. 3.9.

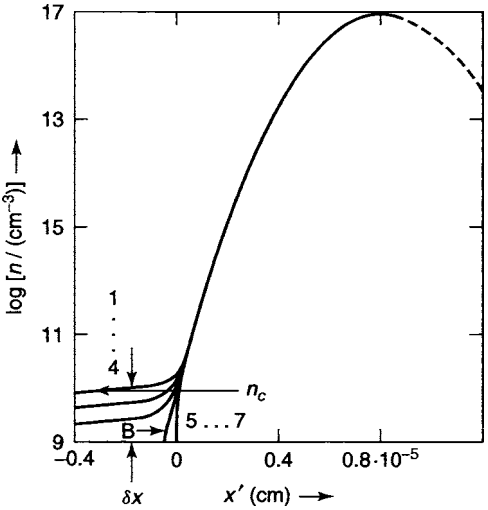

Fig. 3.8. Electron density distribution in a Schottky barrier with j_n as the family parameter; the curves are obtained from the Schottky approximation, yielding (3.33) with x' as the abscissa, defined so that the Boltzmann parts of the solutions coincide. Curves 1–5 for $j_n = -20,\ -10,\ -5,\ 0$, and $10\,\mathrm{mA\,cm^{-2}}$, respectively. B identifies the Boltzmann solution for $j_n = 0$

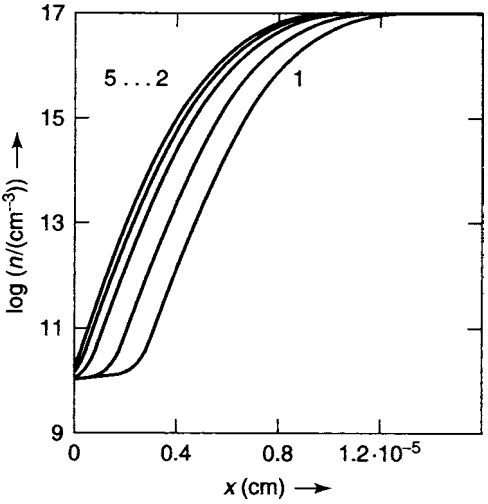

Fig. 3.9. Electron density distribution for Schottky barrier as in Fig. 3.8, however, shifted by $x - x'$ for each curve to start at $n(x = 0) = n_c$. This set also contains the exact solutions of (3.5)–(3.7) and drawn with x as abscissa; j_n is the family parameter: curves 1–5 for $j_n = -20, -15, -10,\ 0$, and $10\,\mathrm{mA\ cm^{-2}}$, respectively. The exact and Schottky-approximation curves fall within the width of the plotted lines on top of each other

This approximation is excellent for $N_d/N_c > 10^3$ and cannot be distinguished within the width of the plotted curves from the exact solutions of (3.5)–(3.7), which are also computer-drawn in Fig. 3.9. Therefore, (3.33) will be used as the key equation in the following discussions describing the behavior of $n(x)$ within the Schottky barrier.

An analysis of this solution exposes an important behavior. The Boltzmann term of (3.33) is independent of j_n and describes the exponential decrease of n in the bulk-adjacent part of the barrier. The second term shown in Fig. 3.7 depends linearly on the current, and, when added to (or subtracted from) the Boltzmann term (Fig. 3.8b), permits an expansion (or compression) of the barrier with increased reverse (or forward) bias by moving the Boltzmann region away from (or closer to) the metal/semiconductor interface in order to fulfill the boundary condition $n(x = 0) = n_c$. In the coordinate system used for the integration, $x' = 0$ is identified in Fig. 3.7 and Fig. 3.8 as the position in which the *Boltzmann solution* crosses n_c. In all the discussions given in this chapter and the approximation given here, n_c is left unchanged with changing j_n that is used simply as a family parameter.

This means that starting from the bulk and approaching the barrier, the shape of the solution curve $n(x)$ does *not* depend on bias; it is only shifted in x. A noticeable deformations of the shape of $n(x)$, however, occurs closer to the contact interface only.

With the increasing width of the junction, the value of the field between $x' = 0$ and $x = 0$ continues to increase linearly (3.8). The electrostatic potential at the interface, and consequently the voltage drop across the junction, therefore continues to increase parabolically with increasing width as given by (3.34).

This analysis is important to obtain a better description for the often discussed Schottky barrier and can be compared with the experiment more satisfactorily.

3.1.4 Current–Voltage Characteristics

One obtains an analytical expression of the current–voltage characteristic when solving (3.33) for j_n and using the boundary condition $n(x = 0) = n_c$. This yields

$$j_n = e\mu_n n_c F_j \left\{ \exp\left[-\frac{e(\psi_{n,j} - \psi_{n,\mathrm{D}})}{kT} \right] - 1 \right\} \tag{3.35}$$

with

$$F_j = F(x = 0) = \sqrt{\frac{2eN_d\psi_{n,j}}{\varepsilon_{st}\varepsilon_0}} \tag{3.36}$$

and

$$\psi_{n,j} = \psi_n(x = 0). \tag{3.37}$$

The index j identifies the value of the variable at the interface for a given current j_n.

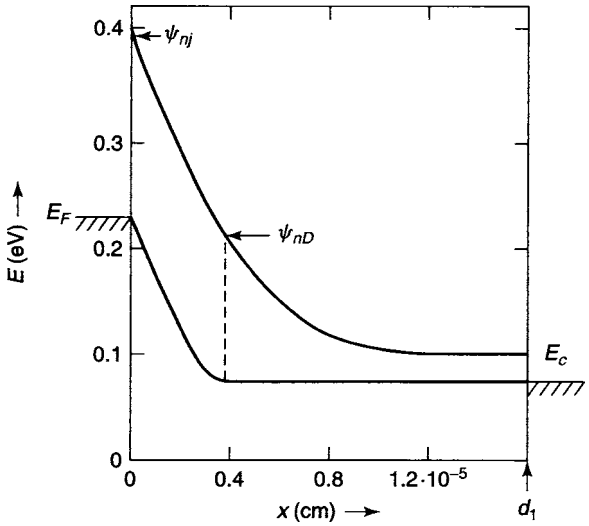

Fig. 3.10. Band-model of a Schottky barrier for reverse bias with conduction band and Fermi-potential distribution computed from (3.5)–(3.7) for a bias of $V = (1/e)[E_F(d_1) - E_F(d_2)] = -0.15\,\mathrm{V}$ and the values of the Parameters given in Table 3.1

This (3.35) is the **diode equation** for which the expression [exp () − 1] is typical. The applied voltage, defined as

$$V = -\frac{1}{e}\left[E_F(x=0) - E_F(x=d_1)\right] \tag{3.38}$$

can be easily obtained in the range where $E_c(x)$ and $E_F(x)$ run parallel to each other (Fig. 3.10) which yields

$$V = \psi_{n,j} - \psi_{n,D}. \tag{3.39}$$

When introducing (3.39) into (3.35) one obtains as an approximation, the often used **classical diode equation** of *drift-current-limited Schottky barriers.*[11]

$$\boxed{j_n = e\mu_n n_c F_j \left[\exp\left(\frac{eV}{kT}\right) - 1\right],} \tag{3.40}$$

and with the field at the barrier interface given by

$$\boxed{F_j = \sqrt{\frac{2eN_d(\psi_{n,D} - V)}{\varepsilon_{st}\varepsilon_0}}.} \tag{3.41}$$

[11] Since its pre-exponential factor is the drift current, which for a large reverse bias (i.e., for a vanishing exponential) is the limiting current.

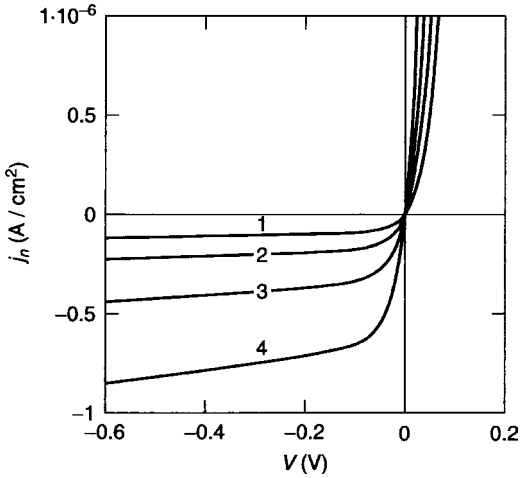

Fig. 3.11. Drift-limited diode characteristics (3.40) with n_c as family parameter: curves 1–4 for $n_c = 3.2,\ 6.3,\ 12.6,$ and $25 \cdot 10^4\,\mathrm{cm}^{-3}$, respectively. $N_\mathrm{d} = 10^{17}\,\mathrm{cm}^{-3}$, $\mu_n = 100\,\mathrm{cm}^2\,\mathrm{Vs}^{-1}$, $\varepsilon_\mathrm{st} = 10$

A set of these characteristics with n_c as family parameter is given in Fig. 3.11. These curves show the typical diode behavior but no true current saturation in reverse bias, for reason of the bias dependence of the pre-exponential factor, containing F_j. We will return to the behavior of the current in reverse bias in Sect. 3.2.

3.2 Modified Schottky Barrier

The basic approximation and conclusions, derived in Sects. 2.1 and 3.1 for the classical nn^+-junction and the Schottky barrier, apply for numerous metal/semiconductor barriers and a large number of heterojunctions (see Sect. 3.4). From here, several modifications relating to boundary conditions, drift velocity limitation, and space charge generation expand the basic model and will be discussed in the following sections.

3.2.1 The Schottky Barrier with Current-Dependent Interface Density

In the previous section, we have assumed a constant carrier density at the metal/semiconductor boundary which does not depend on the current through the barrier. We will now modify this condition.

3.2.1.1 Metal/Semiconductor Boundary Condition

The potential barrier at the metal/semiconductor boundary prevents the leaking-out of metal electrons into the semiconductor.

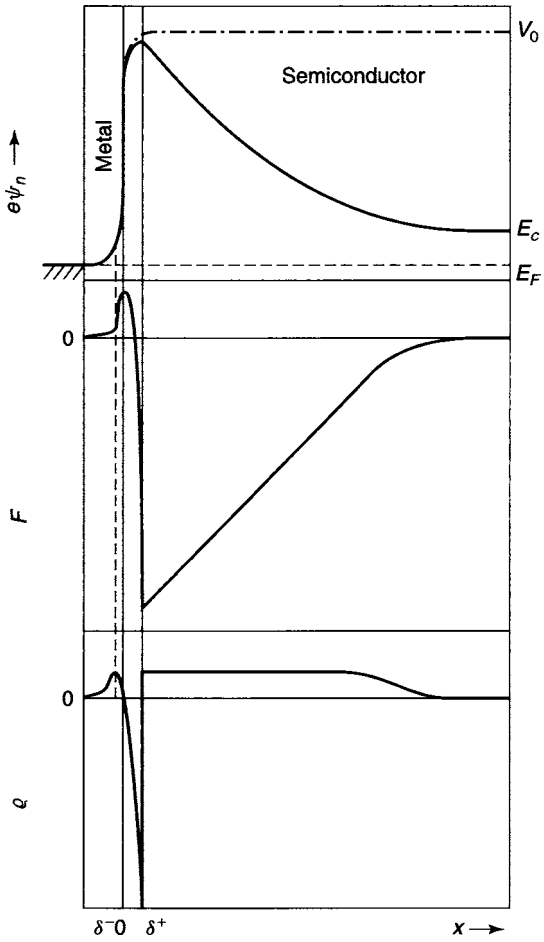

Fig. 3.12. Classical representation of the electron potential, field, and space-charge distributions near the metal/semiconductor interface, excluding image forces (Schematic, not to scale)

Figure 3.12 illustrates in a simplified schematic and not-to-scale presentation the space charge, field, and electron potential distributions near the metal/semiconductor interface. The potential barrier keeps the conduction electrons in the metal. This barrier is created by a (+−)space-charge double layer at the surface, caused by some of these electrons escaping through the metal surface, thereby charging the metal ($x < 0$) positive and the adjacent space ($x > 0$) negative.

With an adjacent semiconductor, this dipole layer merges with a similar one at the semiconductor surface, which prevents its conduction electrons from leaking out. The resulting triple layer (+ − +) at the interface

is asymmetric, since it is created by the superposition of two double layers of different magnitude. This can be seen if the interface is opened and we have to separate surfaces, metal to vacuum and vacuum to semiconductor each one having its own double layer. When these surfaces merge, the triple layer results can be regarded as a net double layer with an effective $(+-)$ charge given by the difference of the charges in the two double layers. This (effective) *double layer "at" the metal/semiconductor "interface"* retains most of the conduction electrons in the metal and results in the **work function between metal and semiconductor**.

We will here forego the more detailed considerations discussed in the second Volume of this Text, and assume a simplified potential distribution shown in Fig. 3.12 with a maximum at $x = \delta^+$; here the field vanishes, and the current is carried by diffusion only. The maximum diffusion current that can be drawn from this metal surface is given by the Richardson-Dushman emission (Schumacher et al. 2000)

$$j_n = e n_c v_n^* \tag{3.42}$$

with $v_n^* = v_n/\sqrt{6\pi}$ and v_n as the rms velocity of electrons:

$$v_n = \sqrt{\frac{3kT}{m_n}} \tag{3.43}$$

With a bias, the current at $x = \delta^+$ can be described as the difference of two components, one which passes through this interface from left to right ($\overrightarrow{j}_n$) and one which passes from right to left ($\overleftarrow{j}_n$):

$$j_n = \overrightarrow{j}_n - \overleftarrow{j}_n \,. \tag{3.44}$$

When assuming each of these currents to be Richardson–Dushman currents[12] at $x = \delta^+$, with

$$\overrightarrow{j}_n = e n_c v_n^* \quad \text{and} \quad \overleftarrow{j}_n = e n_j v_n^*, \tag{3.45}$$

one obtains a jump of n from $n(x = \delta^{+-}) = n_c$ at the metal side to $n(x = \delta^{++}) = n_j$ at the semiconductor side of the interface at $x = \delta^+$.

This **jump of the carrier density** at the interface, between the metal and the semiconductor is essential to be recognized for any discussion of such electrical contact. In recognizing this we obtain for the net current through the interface

$$j_n = e v_n^* (n_j - n_c). \tag{3.46}$$

[12] The formalism used here is similar to the one used to develop the expression for the diffusion currents inside a semiconductor with gradually varying carrier density. However, the rather abrupt (in less than a mean free path) change in carrier density at both sides of the surface interlayer justifies the use of the Richardson–Dushmann electron emission relation here.

With (3.46) we have now introduced a *modified boundary condition* for the electron density at the semiconductor side[13] of this junction, $n_j(j_n)$ that is current-dependent.

3.2.1.2 Current–Voltage Characteristic in a Modified Schottky Barrier

With the modified boundary condition (3.46) we can now calculate the current–voltage characteristics from (3.33) and, replacing $n(x = \delta^+)$ with n_j from (3.46); this yields

$$j_n = \frac{ev_n^* n_c \left\{ \exp\left[\frac{e(\psi_{n,\mathrm{D}} - \psi_{n,j})}{kT} \right] - 1 \right\}}{1 - \frac{v_n^*}{\mu_n F_j}}. \tag{3.47}$$

The replacement of $\psi_{n,\mathrm{D}} - \psi_{n,j}$ follows the same procedure used in Sect. 3.1.4, yielding again (3.39) which leads to the *modified Schottky diode equation*

$$\boxed{j_n = \frac{ev_n^* n_c \left\{ \exp\left[\frac{eV}{kT} \right] - 1 \right\}}{1 + \frac{v_n^*}{|\mu_n F_j|}}}. \tag{3.48}$$

For low fields ($|\mu_n F_j| \ll v_n^*$) in forward and low reverse bias, this equation reverts back to the *drift-limited Schottky diode equation*:

$$j_n = en_c \mu_n F_j \left\{ \exp\left[\frac{eV}{kT} \right] - 1 \right\}. \tag{3.49}$$

For high fields[14] ($\mu_n F_j \gg v_n^*$), i.e., for sufficiently high reverse bias, (3.48) converts to the *diffusion-limited Schottky diode equation*:

$$j_n = en_c v_n^* \left\{ \exp\left[\frac{eV}{kT} \right] - 1 \right\}. \tag{3.50}$$

A family of such characteristics are given in Fig. 3.13 with n_c as the family parameter. They show a simple exponential behavior with forward bias, but with *perfect current saturation* in reverse direction. Such characteristic is commonly referred to as **ideal characteristics**.

[13] We assume that n_c (at the metal side of the junction) remains constant and is given by (3.1).

[14] This approach is mathematically correct; however, one should recognize that, even though the drift velocity is limited to approximately the rms velocity in bulk semiconductors (Böer, 2002, Chap. 26) resulting in a factor 1/2 in (3.50), conditions at the thin boundary layer are more complex, and need detailed studies to also become physically appropriate.

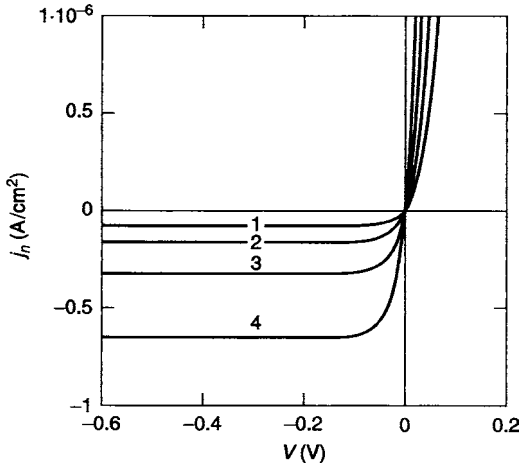

Fig. 3.13. Diffusion-limited diode characteristics (3.50)] with n_c as family parameter: curves 1–4 for $n_c = 12.6$, 25, 50, and $100 \times 10^4\,\mathrm{cm}^{-3}$, respectively; $v_n^* = 4 \cdot 10^6\,\mathrm{cm\ s}^{-1}$

The transition from the drift- to the diffusion-limited diode is determined by the denominator in (3.48). This denominator is of the form[15] $1 + v/|\mu F|$, which is typical of the characteristics of Schottky-like barriers with current-dependent boundary conditions (see Sects. 3.2.1–3.4). It determines the shape of the characteristic, and $1/[1 + v/|\mu F|]$ shall therefore be called the *shape factor* (Böer 1981).

The Shape Factor. When introducing the shape factor

$$\boxed{SF = \frac{1}{1 + \dfrac{v_n^*}{|\mu_n F_j|}},} \tag{3.51}$$

one can separate the classical diode equation from its modifying factor

$$\boxed{j_n = j_s \left\{ \exp\left[\frac{eV}{kT}\right] - 1 \right\} SF,} \tag{3.52}$$

One can also interpret this as the result of equalizing the current at the left and right sides of the metal/semiconductor interface. The current at the left side is emission-limited and determined by v_n^*. At the right side it is bias-dependent because of the drift component $\mu_n F_j$. As a result, the current is lowered from the ideal diode current by the shape factor ($SF < 1$).

[15] Here we have used a general velocity v and a general field to indicate the type of relationship rather than the specific one explained in this section.

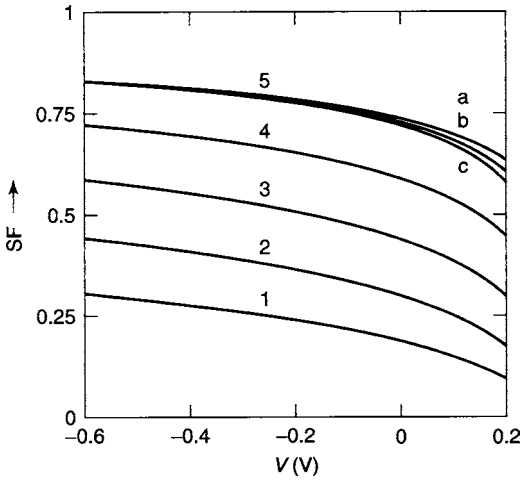

Fig. 3.14. Shape factor (3.51) as function of bias for N_d as main family parameter: curves 1–5 for $N_\mathrm{d} = 10^{15},\ 3 \cdot 10^{15},\ 10^{16},\ 3 \cdot 10^{16}$, and $10^{17}\,\mathrm{cm}^{-3}$; for a subfamily, curves 5a–c with $n_c = 10^4,\ 10^5$, and $10^6\,\mathrm{cm}^{-3}$, respectively as a subfamily parameter. $\mu_n = 100\,\mathrm{cm}^2\,\mathrm{Vs}^{-1},\ \varepsilon = 10$. F_j is computed from (3.34)

The shape factor depends on several diode parameters, mostly contained in F_j. It modifies the characteristic from the ideal case, the more it does so, the smaller μ_n, V, N_d, and T and the larger ε and n_c. The shape factor is shown for N_d and n_c as family parameters in Fig. 3.14. It is of the order of one and approaches unity for large reverse bias.

For further discussion, that will be helpful in later discussions of current–voltage characteristics, we will divide the characteristic into two ranges in which different transport mechanisms predominate, the Boltzmann and the DRO range that will be defined below.

Modified Boltzmann Range. The current within the Schottky barrier is composed of drift and diffusion currents, each of which exhibits a large maximum at one Debye length from the onset of the barrier (see Sect. 3.1.2).

For a sufficiently low bias, the drift and diffusion currents in most of the barrier are very large compared to the net current. In this part of the junction, the current term in (3.33) can be neglected, and $n(x)$ becomes a simple exponential function of $\psi_n(x)$:

$$\boxed{n(x) = n_c \exp\left[-\frac{e(\psi_n(x) - \psi_{n,\mathrm{D}})}{kT}\right].} \tag{3.53}$$

This approximation is identical to the one applied in Sect. 2.1.1.3 with $n(x)$ following the *Boltzmann distribution*. This region is therefore called the *Boltzmann region*.

However, when calculating the *current*, the drift current-term in (3.33) can no longer be neglected near $x = 0$. Replacing $n(x = 0)$ with n_j from (3.46),

as was done for deriving the characteristic (3.47), but here leaving the terms separated to identify their origin, one obtains

$$\frac{j_n}{ev_n^*} = n_c \left\{ \exp\left[\frac{(e\psi_{n,\mathrm{D}} - \psi_{n,j})}{kT} \right] - 1 \right\} - \frac{j_n}{e\mu_n F_j}, \tag{3.54}$$

and recognizes that near $x = 0$ the drift current term on the right hand side (i.e., the current term in $n(x)$) remains important, even for low currents, as long as v_n^* is of the same order as, or larger than, the drift velocity $\mu_n F_j$. This drift current term in (3.54) influences the shape of the characteristic near zero bias and in the entire forward bias range, since here F_j is smallest. In order to emphasize this influence, we refer to this bias range as the *modified Boltzmann range*, and the resulting current–voltage characteristic as the *nonideal characteristic*.

DRO-Range. A major deformation of $n(x)$ appears with *larger reverse bias* near $x = 0$, as shown in Figs. 3.7 and 3.8. When the drift current term on the right side of (3.54) becomes *dominant*, and carrier diffusion can be neglected. Here, the net current is almost exclusively carried by drift in this region. We therefore identify this region in contrast to the Boltzmann region as the *DRO-region*, since it is controlled by DRift Only. When this region determines the current through the barrier, we call the corresponding bias range the *DRO-range*.

When with increased reverse bias ($-V \geq 2kT/e$) the exponential term in (3.54) can be neglected, and as long as $\mu_n F_j$ is small compared to v_n^*, the DRO-range determines the current, with

$$j_n = e\mu_n n_c F_j. \tag{3.55}$$

The bias dependence of j_n is obtained explicitly by introducing F_j from (3.41):

$$j_n = -e\mu_n n_c \sqrt{\frac{2eN_\mathrm{d}(\psi_{n,\mathrm{D}} - V_\mathrm{DRO})}{\varepsilon_{st}\varepsilon_0}}, \tag{3.56}$$

yielding the typical *square-root dependence* of the reverse current on bias in this DRO-range.[16] Nearly all of the voltage drop then occurs across the DRO-region; hence $V \simeq V_\mathrm{DRO}$.

The DRO-range of the current–voltage characteristics is the bias range between the modified Boltzmann range and the saturation range. In Fig. 3.15 the square root behavior in this range is shown with the donor density as family parameter. It shows an increase of the reverse current and an *increase of the slope* with increasing N_d for a given n_c. This is typical for a change in space charge within the DRO-range.

With some caution, this can be used to *determine the density of depleted donors* N_d as long as the other parameters of this (3.56) (namely ε_{st}, μ_n

[16] Therefore this range is also referred to as the *square root range*.

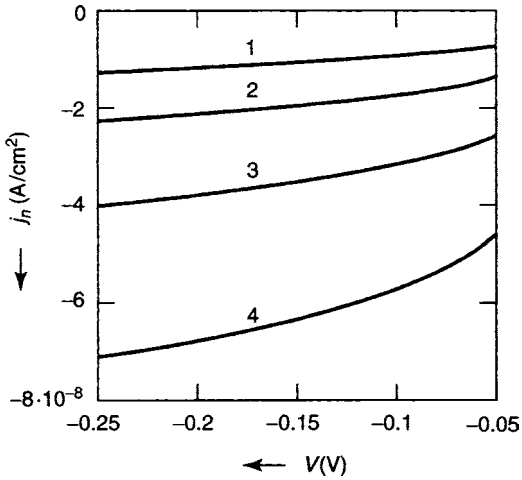

Fig. 3.15. Square root branch of the characteristic, in a relatively small, limited bias range using (3.56) for the same parameters as in Fig. 3.14, except $n_c = 2 \cdot 10^6\,\mathrm{cm}^{-3}$. The family parameters N_d for curves 1–4 are 10^{14}, 10^{15}, 10^{16}, and $10^{17}\,\mathrm{cm}^{-3}$ respectively

and n_c) are known. Or, inversely, if N_d is better estimated from other information, one can use this range to verify n_c and hence obtain more information about the *work function*. This fact should be remembered as a tool for barrier material analysis, rather than an interesting mathematical clarification.

The DRO-region can be identified by carefully viewing the semilogarithmic plot of $n(x)$, since in this region n decreases only hyperbolically[17] with decreasing x (see Figs. 3.5a, 3.7 and 3.8). The identification of the DRO-range in a current–voltage characteristic is more difficult, since the square-root dependence of the DRO-region joins smoothly with current saturation at larger reverse bias when the drift velocity at $x = 0$ approaches v_n^*; consequently, the shape factor then approaches unity.

Figure 3.16 summarizes the different ranges of a typical Schottky diode characteristic. It contains in small reverse and in forward bias the modified Boltzmann range, with larger reverse bias the DRO-range, and finally at high reverse bias, the saturation range.[18]

Electrostatic and Electrochemical Potentials in a Schottky Barrier. The electrostatic electron potential distribution is parabolic, reaches the diffusion potential $\psi_{n,\mathrm{D}}$ for vanishing current, and increases (decreases) with reverse (forward) bias according to (3.14).

[17] Since $F(x)$ increases linearly with decreasing x and the product $n(x)\,F(x)$ must remain constant in the DRO-range; namely $nF = j_n/e\mu_n$ and $j_n = j = \mathrm{const}$.

[18] We neglect here the pre-breakdown effects which cause a steep increase of the current at still higher reverse bias.

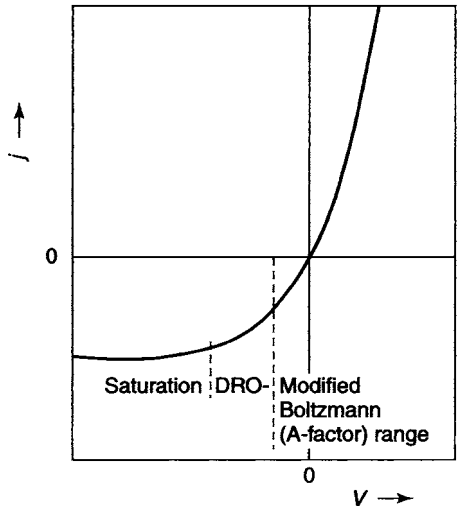

Fig. 3.16. Typical nonideal diode characteristic with the characteristic saturation, DRO, and Boltzmann ranges identified (schematically plotted)

The electrochemical potential, however, is flat for $j_n = 0$ (i.e., in thermodynamic equilibrium) but it becomes tilted[19] with nonvanishing currents in the bulk and in the Boltzmann region. With increased reverse bias, the electrochemical potential bends away in the DRO-region from the rather flat range and obtains a nearly constant slope, and remains almost parallel to $E_c(x)$, since here n decreases only hyperbolically with decreasing x, causing comparatively little change in $E_c - E_F$.

The applied voltage $V = \psi_{n,D} - \psi_{n,j}$ across a Schottky barrier device drops mostly in the region adjacent to the metal/semiconductor interface (see Fig. 3.5e). With sufficient reverse bias, almost the entire bias drops in the DRO-range (see Fig. 3.10). This becomes important in later discussions when higher bias cases are analyzed since most *carrier heating occurs only in the DRO-region* (see Sect. 7.2.2.3).

The description of the potentials will later (Sects. 4.3 and 6.2.2) be extended when two carriers are considered, and a split of the Fermi level into two quasi-Fermi levels is discussed.

3.2.2 Schottky Barrier with Two or More Donor Levels

A semiconductor with one type of shallow donors show a depletion of these donors within the Schottky barrier. However, when the semiconductor contains several donors of different ionization energies (i.e., a donor distribution, that is typical for most semiconductors), a sequential donor-depletion

[19] This tilting is too small to be visible in Fig. 3.5e.

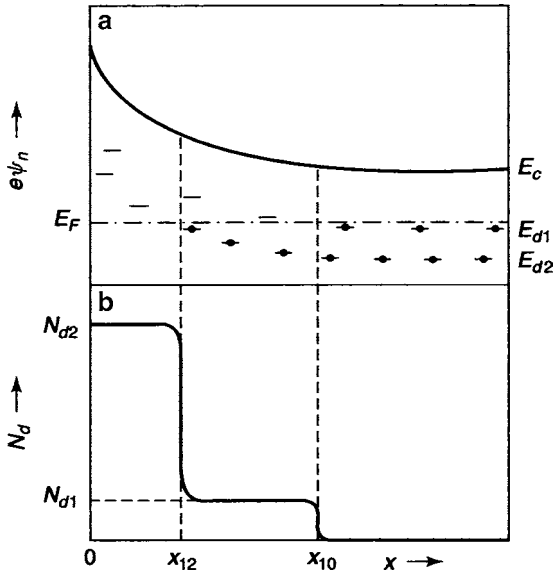

Fig. 3.17. Electron potential (**a**) and space-charge (**b**) distributions in a two-donor model (in a schematic presentation)

complicates the barrier behavior. We will discuss first a simple example of two types of donors at separate energy levels.

A semiconductor containing shallow and deep donors with densities N_{d1} and N_{d2}, respectively, shows an increase of the space charge near the metal/semiconductor interface by a step[20] $\varrho \simeq eN_{d1}$ and another step of eN_{d2} as soon as the deeper levels are raised above the Fermi level as shown in Fig. 3.17: the shallow levels are depleted for $0 < x < x_{10}$ and the deeper levels are also depleted closer to the electrode $0 < x < x_{12}$. Consequently, the field slope increases abruptly at x_{12} and $\psi_n(x)$ rises more steeply (see Fig. 3.20d). Therefore the slope of the current–voltage characteristic increases, and current saturation will be reached sooner (see Sect. 3.2.2.4).

With increased reverse bias the barrier expands; after depletion of the deep donor starts, only the width of the *high* space-charge region increases; the *low* space-charge region is shifted, but its width remains unchanged (see Fig. 3.20b); the increased bias drops almost entirely across the high space-charge region.

3.2.2.1 Junction Field in Double-Donor Barrier

Corresponding to the stepwise increase of $\varrho(x)$ at $x = x_{12}$, a kink in $F(x)$ occurs as shown in Figs. 3.18 and 3.20c. The additional voltage drop $\psi_{n,12}$,

[20] See Sect. 3.2.2.2 for a better approximation.

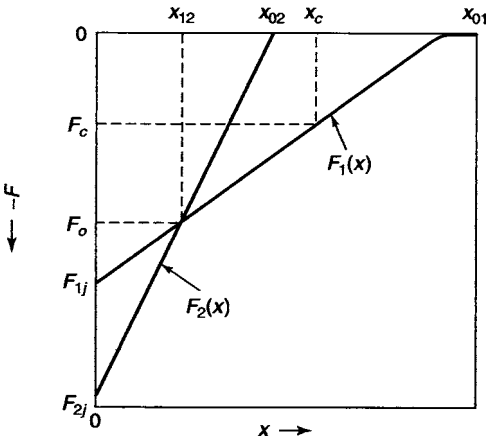

Fig. 3.18. Field distribution in a two-donor Schottky barrier (schematic). For actual computation, see Fig. 3.20c. For further discussion of the identified values of x and F see text

given by the field triangle for $x > x_{12}$ between $F_1(x)$ and $F_2(x)$ is obtained from trignometric reasoning (see Fig. 3.18):

$$\psi_{n,12} = F_o \frac{x_{02} - x_{01}}{2}, \tag{3.57}$$

with $x_{01} = x_{\mathrm{D}}$ the barrier width of a single-donor barrier (3.22) and x_{02} obtained from the slopes of $F_1(x)$ and $F_2(x)$, thereby yielding:

$$x_{02} = x_{01} \frac{N_{d1}}{N_{d2}}. \tag{3.58}$$

The voltage drop in this triangle can therefore be expressed as

$$\psi_{12} = \frac{1}{e}(E_c - E_{d2}) \left(1 - \frac{N_{d1}}{N_{d2}}\right). \tag{3.59}$$

Consequently, the field at the metal/semiconductor interface is given by

$$F_j = \sqrt{\frac{2e}{\varepsilon\varepsilon_0} \left\{ p_{d1}(\widetilde{V}_{\mathrm{D}} - V_2) + [p_{d1} + p_{d2}(V)](V_2 - V) \right\}}, \tag{3.60}$$

with V_2 and $\widetilde{V}_{\mathrm{D}}$ given by

$$V_2 = \frac{1}{e}(E_c - E_{d2}) \quad \text{and} \quad \widetilde{V}_{\mathrm{D}} = \frac{kT}{e} \ln\left(\frac{N_c}{n_c}\right). \tag{3.61}$$

The hole density in deep donors $p_{d2}(V)$ is approximated by

$$p_{d2}(V) = \begin{cases} 0, & \text{for } |V| > |V_2| \\ N_{d2} & \text{for } |V| \le |V_2|. \end{cases} \tag{3.62}$$

3.2.2.2 Gradual Depletion of Deep Donors

In actual semiconductors, the depletion of the deep level depends not only on bias and level depth, but also on the temperature, and occurs more gradually than assumed for (3.62). It is thermal depletion and it is described by the Fermi function

$$n_{d2} = \frac{N_{d2}}{1 + \exp\left(\dfrac{E_{d2} - E_{\mathrm{F}}}{kT}\right)}, \tag{3.63}$$

yielding for the space charge (always assuming complete ionization of the shallow donor here, for simplicity)

$$\varrho(x) = e\left[N_{d1} + \frac{N_{d2}}{1 + \exp\left\{\dfrac{E_{\mathrm{F}}(x) - E_{d2}(x)}{kT}\right\}} - n(x)\right], \tag{3.64}$$

with $E_{\mathrm{F}}(x)$ being a function of the bias (see Fig. 3.19):

$$E_{d2}(x) - E_{\mathrm{F}}(x) = E_c(x) - E_{\mathrm{F}}(x) - [E_c(x) - E_{d2}(x)] \tag{3.65}$$

which can be replaced in the modified Boltzmann range[21] by (using (3.61)).

$$E_{d2}(x) - E_{\mathrm{F}}(x) = kT \ln\left[\frac{N_c}{n(x)}\right] - eV_2. \tag{3.66}$$

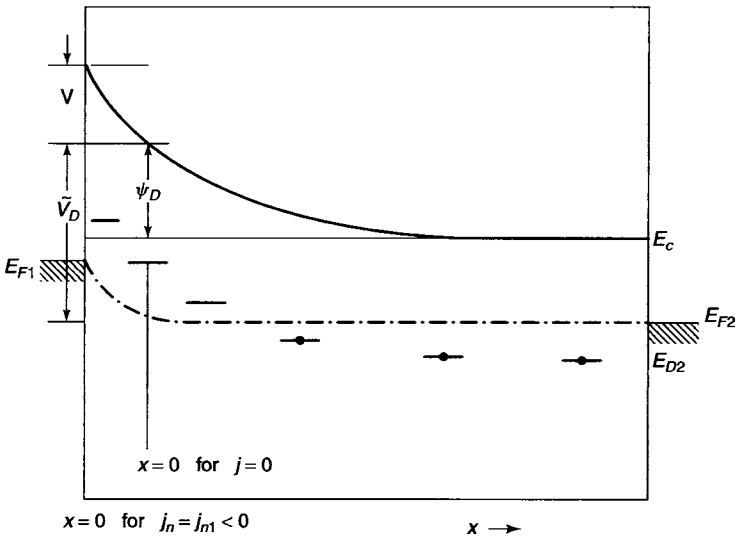

Fig. 3.19. Potential notation in barrier

[21] Such depletion has to start in the modified Boltzmann range, since with further increased reverse bias in the DRO-range, $E_c(x)$ and $E_{\mathrm{F}}(x)$ run essentially parallel to each other, preventing deeper traps from becoming depleted (see end of this section for more).

When evaluating (3.66) at the metal/semiconductor interface, one obtains

$$(E_{d2} - E_{\mathrm{F}})_{(x=0)} = kT \ln\left(\frac{n_c}{n_j}\right) + eV_{\mathrm{D}} - eV_2, \tag{3.67}$$

with n_j as the electron density at $x = 0$ for nonvanishing current (3.46); the bias dependence is contained in $kT \ln(n_c/n_j)$:

$$V = \frac{kT}{e} \ln\left(\frac{n_j}{n_c}\right). \tag{3.68}$$

With $E_{\mathrm{F}}(x = d)$ set arbitrarily = 0, one then has for the bias dependence of

$$(E_{\mathrm{F}} - E_{d2})_{x=0} = e(V - V_{\mathrm{D}} + V_2). \tag{3.69}$$

That is, with forward or small reverse currents (in the modified Boltzmann range), the Fermi level shifts linearly with bias.

As a consequence, one observes first a rapid lowering of the Fermi level with concurrent level depletion when the bias is reduced from forward to reverse until the DRO range is reached and current saturation is approached; then, the distance from the Fermi-level to the conduction band becomes frozen and no deeper centers can be depleted.

3.2.2.3 Exact Solutions of Double-Donor Barriers

The distributions of $n(x)$, $\varrho(x)$, $F(x)$, $\psi(x)$, and $E_{\mathrm{F}}(x)$ of such a two-donor model are shown in Fig. 3.20 as obtained by numerical integration of (3.5)–(3.7) with ϱ given in (3.64). $E_c - E_{d2}$ is chosen to exceed $\phi_{\mathrm{MS}} = 0.316\,\mathrm{eV}$ by 84 meV. The figure shows a step-like increase of $\varrho(x)$, and a kink in the slope of $F(x)$ when depletion of the deeper donor starts. The width of the layer with deep-level depletion increases with increasing reverse bias.

The general behavior of the solution curves shown in Fig. 3.20 is much akin to the behavior of the solution curves given in Fig. 3.5 in a single donor model, except for the space-charge and field distributions which now shows a step and a kink respectively. There are only slight changes in $n(x)$ and $\psi_n(x)$ caused by the presence of a second donor. Significant differences, however, occur for the current–voltage characteristics, as will be discussed below.

3.2.2.4 Current-Voltage Characteristics for Double-Donor Barriers

The current–voltage characteristic can be obtained in an analytic approximation (3.48) after replacing F_j in (3.48) with (3.60), yielding an explicit equation in V for a step like increase in depletion:

$$j_n = \frac{en_c v_n^* \left\{\exp\left(\dfrac{eV}{kT}\right) - 1\right\}}{1 + \dfrac{v_n^*}{\mu_n \sqrt{\frac{2e}{\varepsilon\varepsilon_0}\left[p_{d1}(\widetilde{V}_{\mathrm{D}} - V_2) + (p_{d1} + p_{d2}(V))(V_2 - V)\right]}}}; \tag{3.70}$$

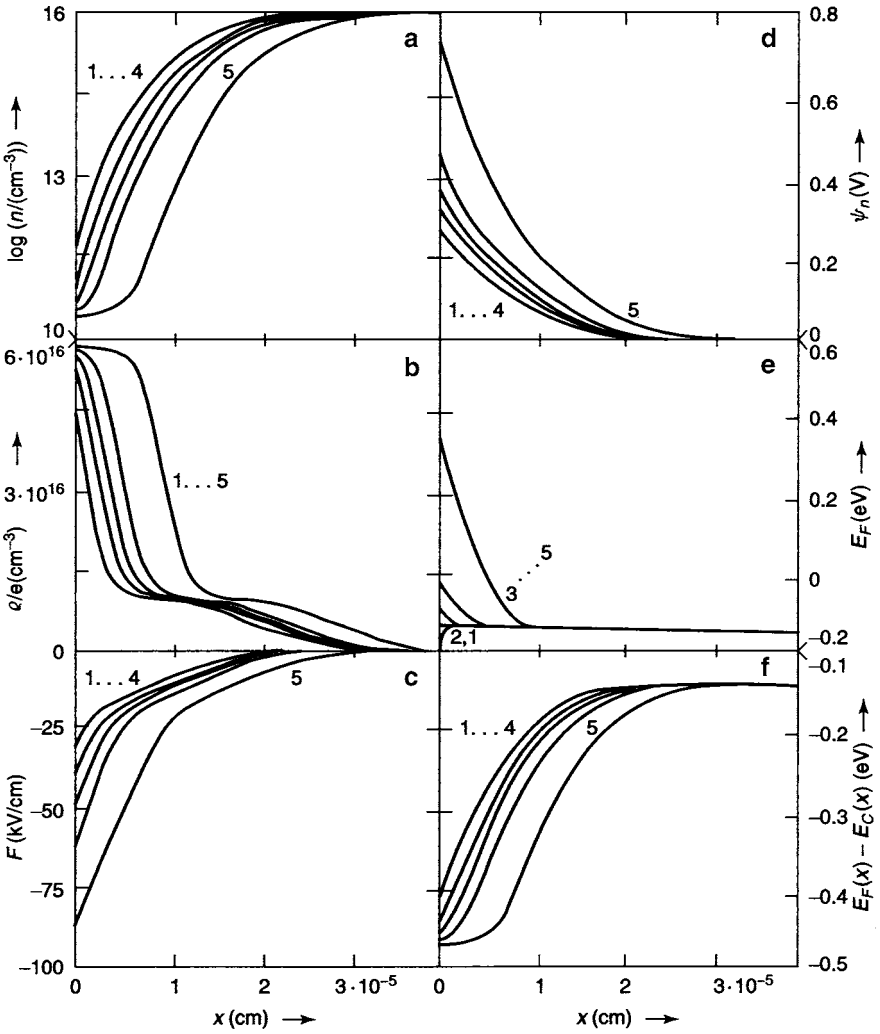

Fig. 3.20. Schottky barrier with two donor levels. Solution curves obtained from numerical integration of (3.5)–(3.7) with the space charge given by (3.64): $n(x)$, $\varrho(x)$, $F(x)$, $\psi(x)$, $E_{\mathrm{F}}(x)$, and $E_c(x) - E_{\mathrm{F}}(x)$ for j_n as family parameter: curves 1–5 for 100, 0, −15, −20 and −25 mA cm^{-2}, respectively. Other parameters are: $E_c - E_{d2} = 0.4\,\mathrm{eV}$, $N_{d1} = 10^{16}\,\mathrm{cm}^{-3}$, $N_{d2} = 5 \cdot 10^{16}\,\mathrm{cm}^{-3}$, $\varepsilon = 10$, $\mu_n = 100\,\mathrm{cm}^2\,\mathrm{Vs}^{-1}$, $T = 300\,\mathrm{K}$, $n_c = 5 \cdot 10^{10}\,\mathrm{cm}^{-3}$, and $N_c = 2 \cdot 10^{18}\,\mathrm{cm}^{-3}$

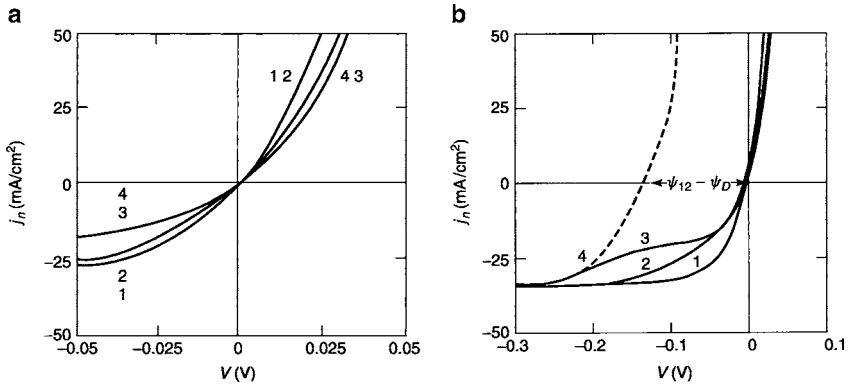

Fig. 3.21. (**a**) Current–voltage characteristics for two-donor Schottky barrier calculated from (3.71) with $v_n^* = 5 \cdot 10^6\,\mathrm{cms}^{-1}$, $n_c = 5 \times 10^{10}\,\mathrm{cm}^{-3}$, $\mu_n = 100\,\mathrm{cm}^2\,\mathrm{Vs}^{-1}$, $N_{d1} = 10^{16}\,\mathrm{cm}^{-3}$, $N_{d2} = 3 \cdot 10^{17}\,\mathrm{cm}^{-3}$, $\widetilde{V}_\mathrm{D} = 0.4\,\mathrm{V}$, $\varepsilon = 10$, and $eV_2 = E_c - E_{d2} = 0.35$, 0.45, 0.5, and 0.65 eV as family parameter for curves 1–4, respectively. For small bias, the characteristics are rather similar to the ones for a single donor model. However, in an extended voltage range, shown in (**b**) for the current–voltage characteristics with the same parameters as in (**a**), it develops a knee when the second donor level lies substantially deeper

when using the approximations $p_{d1} \simeq N_{d1}$ and $p_{d2} = N_{d2} - n_{d2}$ with n_{d2} given by (3.63), one obtains for a gradual depletion:

$$j_n \simeq \frac{en_c v_n^* \left\{\exp\left(\dfrac{eV}{kT}\right) - 1\right\}}{1 + \dfrac{v_n^*}{\mu_n \sqrt{\dfrac{2e}{\varepsilon\varepsilon_0}\left\{N_{d1}(\widetilde{V}_\mathrm{d} - V_2) + \left[N_{d1} + \dfrac{N_{d2}}{1 + \exp[e(V_2 - V_\mathrm{D} + V)/(kT)]}\right](V_2 - V)\right\}}}}. \tag{3.71}$$

As a result of deeper donor depletion, the characteristic steepens in the modified Boltzmann range as shown in Fig. 3.21a. It may also result in a knee of the jV curve as shown in Fig. 3.21b. A knee rather than a break in slopes is observed, when the second level lies at a substantially lower energy, since the depletion of deeper donors results in an effective shift in the voltage scale[22] by ψ_{12} (see (3.57) and Fig. 3.21), as shown by the dashed curve for the second donor at $E_c - E_\mathrm{d} = 0.6\,\mathrm{eV}$ in Fig. 3.21b.

Figure 3.22 shows the corresponding behavior of the shape factor with the deep donor density as family parameter. This family shows more clearly, the development of this knee. The higher the density ratio N_{d2}/N_{d1} is, the more pronounced is the knee.

[22] In the jV-characteristic such a shift can be obtained from extrapolating the characteristic from the onset of the knee (see dashed curve in Fig. 3.21b for the most pronounced knee).

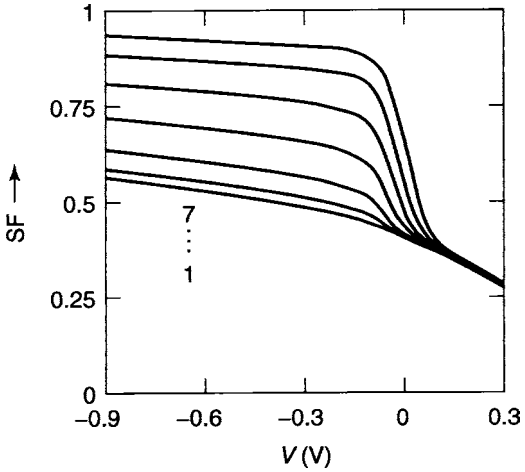

Fig. 3.22. Shape factor for the same parameters as in Fig. 3.21 except for $E_c - E_{d2} = 0.4\,\text{eV}$ and with N_{d2} as family parameter, with $N_{d2} = 10^{15}$, $3 \cdot 10^{15}$, 10^{16}, $3 \cdot 10^{16}$, 10^{17}, $3 \cdot 10^{17}$, and $10^{18}\,\text{cm}^{-3}$ for curves 1–7, respectively

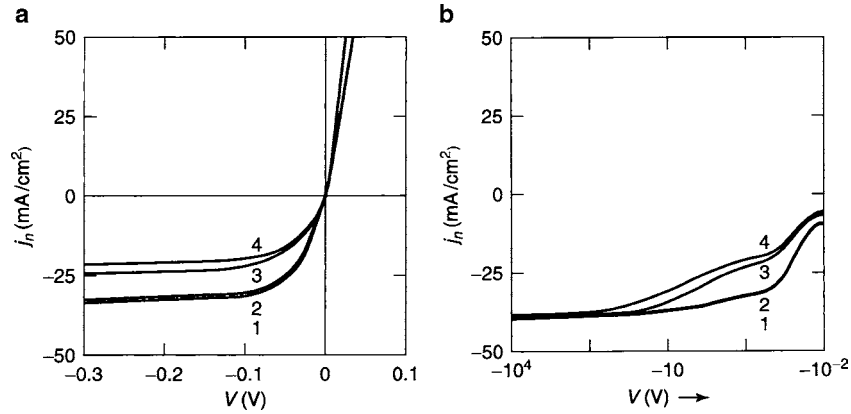

Fig. 3.23. Current–voltage characteristics for a two-donor model in which the depletion of the second donor occurs within the DRO-range limitation of n_j and for the same parameters as in Fig. 3.21. Shown in (**a**) with family parameter $E_c - E_{d2} = 0.3$, 0.4, 0.5, and 0.6 eV for curves 1–4, respectively; and in (**b**) for the same family of curves, but here with a logarithmically expanded abscissa

When the deep donor depletion occurs closer to the DRO-range, the depletion occurs more gradually and one observes seemingly a shift of saturation rather than a decrease in steepness with increasing $E_c - E_{d2}$ (Fig. 3.23). With much further increased reverse bias, however, n_j continues to decrease. Consequently, $(E_c - E_F)_{x=0}$ will continue to increase, and a knee in the characteristic occurs at much higher reverse bias, as shown for a semi-logarithmic plot in Fig. 3.23b. Here, for deeper donors with $E_c - E_{d2} > 0.5\,\text{eV}$, a significant

sloping of $j(V)$ extends to a reverse bias in excess of $-100\,\mathrm{V}$ before current saturation is reached (neglecting breakdown effects).

In summary, deep donor depletion causes a steepening of the characteristic. Such transition occurs rapidly in the modified Boltzmann-range and only gradually in the DRO-range. In all cases, however, the same saturation current will be finally reached, independent of the donor distribution. The steepening is a result of the drift velocity ($\mu_n F_j$) competition with v_n^* in the modified diode equation (3.60).

3.2.2.5 The Exponential A-Factor

In Fig. 3.21a we have seen that the slope of the jV characteristic in the modified Boltzmann range is reduced when a deeper donor level is gradually being depleted. Such a reduced exponential slope is frequently observed in many other *real diodes* and is usually described by an exponential correction factor A

$$j_n = j_s \left[\exp\left(\frac{eV}{AkT}\right) - 1 \right]. \tag{3.72}$$

This A-factor is of great technical interest and since it can here be described in its most transparent form, we will emphasize its description here.

A-factors well in excess of one have been observed in a wide variety of diodes. Since such A-factors cause a degradation of the diode characteristic, A is also referred to as the *diode quality factor*. An A-factor of $A \simeq 2$ has generally been linked in the literature with junction recombination (Helleman 1999; Rodnyi 1997), this will become evident and will be discussed later in Sect. 11.1.2.

We will here connect this commonly used A-factor with the shape factor derived in the previous sections, or, more generally, with the nonideal diode equation that is caused by *carrier depletion* in the barrier.[23] When equating (3.72) with the nonideal Schottky diode equation (3.48) resulting in the definition of the shape factor SF, (3.51) and (3.52), one now obtains a similar condition for the A-factor, again relating to gradual donor depletion: With sufficient forward bias for $\mu_n F_j$ to be small enough to neglect the 1 in the shape factor (3.51) and in the diode equation with the A-factor, one obtains

$$-\frac{\mu_n F_j}{v_n^*} \exp\left(\frac{eV}{kT}\right) \simeq \exp\left(\frac{eV}{AkT}\right); \tag{3.73}$$

hence

$$-\mu_n F_j = v_n^* \exp\left(\frac{eV}{kT} \cdot \frac{1-A}{A}\right). \tag{3.74}$$

[23] Such carrier depletion in a junction for which one has to consider electrons and holes is, in addition influenced by recombination. It becomes then understandable that the A-factor is for such devices referred to as "caused" by recombination, while both, redistribution, described here, and recombination may contribute, and one should distinguish in each case which one dominates.

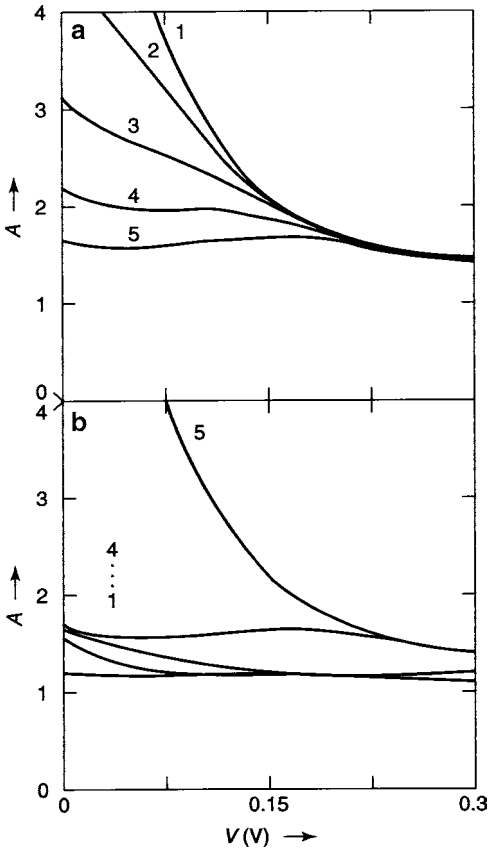

Fig. 3.24. A-factor as function of forwardbias for a two-donor model using the diode equations (3.71) and (3.72) in the Boltzmann range with parameters $\varepsilon = 10$, $\mu_n = 30\,\mathrm{cm^2\,Vs^{-1}}$, $N_{d1} = 10^{15}\ \mathrm{cm^{-3}}$, $N_{d2} = 10^{18}\ \mathrm{cm^{-3}}$, $\widetilde{V}_\mathrm{D} = 0.4\,\mathrm{V}$, $V_2 = 0.401$ V, except as listed as family parameters: (**a**) $N_{d2} = 10^{16}, 3\cdot 10^{16}, 10^{17}, 3\cdot 10^{17}$ and $10^{18}\,\mathrm{cm^{-3}}$ for curves 1–5, respectively. (**b**) A-factor as function of forward bias with same standard values, except for *curve 1*: $N_{d2} = 10^{18}$; *curve 2*: $V_2 = 0.3$; *curve 3*: standard; curve 4: $N_{d1} = 10^{14}\,\mathrm{cm^{-3}}$; curve 5: $\mu_n = 100\,\mathrm{cm^2\,Vs^{-1}}$ and $N_{d1} = 10^{16}\,\mathrm{cm^{-3}}$

In Fig. 3.24, we have plotted the computed ideality factor A as obtained from the complete double-donor characteristic (3.71) and (3.72): a depletion of a high density, deep donor with decreasing forward bias results in a reduction of the slope in the exponential part of the characteristic by a quality factor between 1 and 2 that is nearly constant over a substantial bias range for some typical values of the parameters (curves 4 and 5 as shown in Fig. 3.24a, curves 1–4 shown in Fig. 3.24b). However, for certain parameter combination as e.g., for a donor at an energy $E_c - E_{d2} \simeq e\widetilde{V}_\mathrm{D}$ (see (3.61)) and drawn for curve 5 of Fig. 3.24a, changes of A as a function of V are obtained in a wide range $1 \le A < 5$.

A-Factor in Junctions with Donor Distributions. If instead of one predominant deep donor, the donors are distributed over a wider energy range, or if any of the additive terms cannot be neglected, then the quality factor deviates more substantially from 2. For instance, the introduction of a donor (hence ϱ-) distribution function

$$\varrho_0 = \varrho_{01} \exp(\alpha V) \tag{3.75}$$

into F_j, and keeping the same approximations as above, yields

$$\frac{2(A-1)}{A \simeq 1 + \dfrac{\alpha e}{kT}}. \tag{3.76}$$

This results in values of A larger or smaller than 2, depending on whether α is positive or negative respectively, i.e., when the donor distribution increases or decreases with increasing distance from the conduction band.

3.2.3 Schottky Barriers with Multiple Donors, and Field Excitation

In Sect. 3.2.2, thermal ionization of deep donors was assumed when the deep donor was lifted above the Fermi level. But deeper donors can also be ionized with a sufficiently large electric field e.g., by Frenkel-Poole ionization (Franz and Naturforsch 1958; Poole 1922), impact ionization, or tunneling. Frenkel-Poole ionization (Sect. 4.1.3) affects Coulomb-attractive centers and responds to rather low critical fields that are typically in the order of 10–50 kV cm^{-1}. These fields are easily attained in typical barrier layers long before breakdown occurs. Hence, such field excitation becomes an important contributor to the behavior of current–voltage characteristics in many barriers and junctions and should be considered. The depletion of deeper donors due to field ionization causes an increase in the space-charge density close to the metal/semiconductor interface where the threshold field is exceeded.

The Frenkel-Poole ionization causes an increase of the space charge when the critical field for such ionization is reached and thereby forces a contraction of the depletion region and a further increase of the electric field that is shown together with the other the solution curves in Fig. 3.25. The curves are computed by using an empirical space-charge function

$$\varrho_{\mathrm{FP}} = \varrho_0 \left(1 + 0.5 \frac{\varrho_{FP}}{\varrho_0} \left\{ 1 + \tanh \left[C(F - F_{\mathrm{FP}}) \right] \right\} \right). \tag{3.77}$$

with $\varrho_{\mathrm{FP}}/\varrho_0$ as the assumed step of the increased space charge, F_{FP} the critical field for Frenkel-Poole ionization and C as an empirical steepness factor for the onset of the ionization. This function is added to the space charge in the Poisson equation (see Sects. 4.1.3 and 11.1.2.4).

When the critical field (here 50 kV cm^{-1}) is reached, the deep level is rapidly ionized, ϱ increases nearly stepwise, and the field-slope increases accordingly as shown in Figs. 3.25b, c. Such steepening occurs here in the DRO-range, where thermal ionization alone no longer can deplete deeper levels.

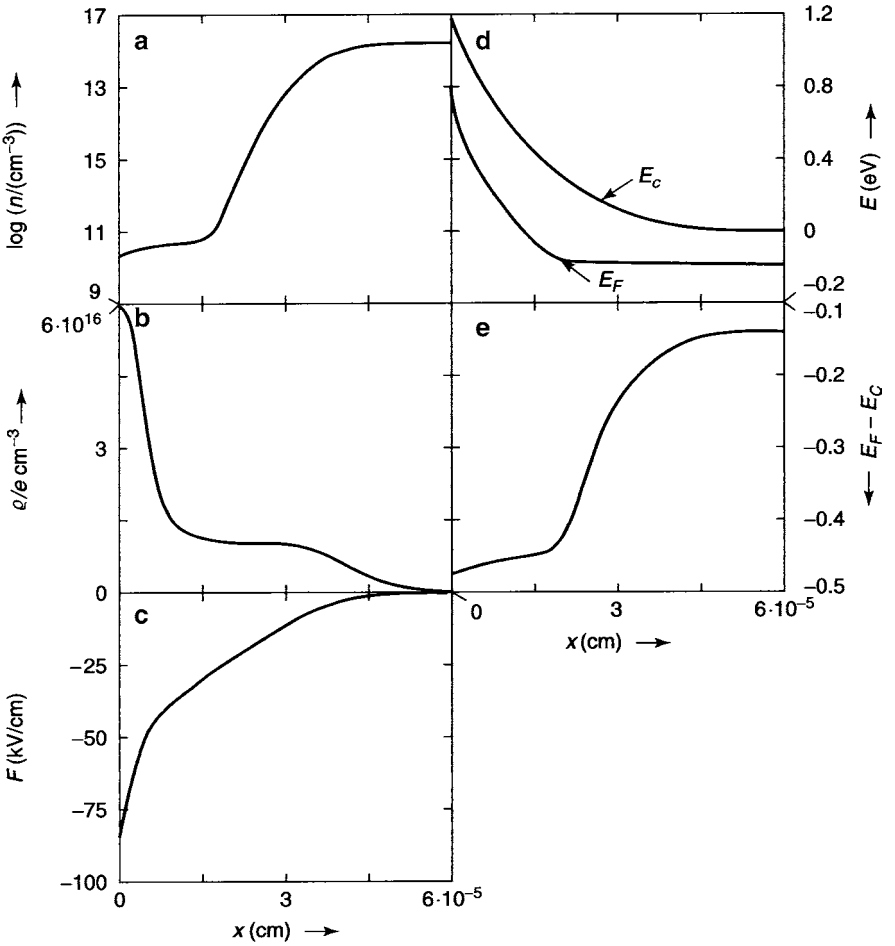

Fig. 3.25. Schottky barrier with depletion of Coulomb-attractive deep center via Frenkel-Poole effect in the DRO-range; computation as in Fig. 3.20 with same parameters except for $E_c - E_{d2} = 0.7\,\mathrm{eV}$, $F_{FP} = 5{\cdot}10^4\,\mathrm{V\,cm^{-1}}$, $\varrho_{FP}/e = 6{\cdot}10^{16}\,\mathrm{cm^{-3}}$, $C = 10^{-4}\,\mathrm{cm\,V^{-1}}$, using (3.77) for the given $n(x)$, $\varrho(x)$, $F(x)$, $\psi(x)$, $E_\mathrm{F}(x)$, and $E_c(x)$

A simple thermal ionization of the deep level is precluded in this example since the assumed $E_c - E_{d2} = 0.7\,\mathrm{eV}$ is larger than the largest achieved value of $E_c - E_\mathrm{F} \simeq 0.5\,\mathrm{eV}$ for thermal equilibrium.

Correspondingly, this causes a more rapid depletion and hence, a decrease in $n(x)$ which thereby leads to a more rapid decrease of the width of the barrier, since n_j is reached earlier. The increased space charge causes an increase in the electric field near the metal/semiconductor interface. It thereby also causes a corresponding increase in the shape factor A, hence reducing the

reverse bias at which saturation is reached: *the Frenkel-Poole depletion in the modified Boltzmann range causes a steepening of the characteristic*[24].

3.3 Schottky Barrier with Optical Excitation

In the previous two sections, we described an increase of the space charge with increasing reverse bias via thermal ionization, or via field ionization when a critical potential or field was reached. We will now introduce an optical excitation, and depending on the photon energy this can result in a change of excitation from deep electron traps (infra red irradiation) or exciting electrons from still deeper traps (usually called hole traps), or creating holes in the valence band as well. We will here progressively proceed to more advanced models and will first consider only redistribution of electrons over deep donors in competition between depletion and the three excitation processes: thermal, field, and optical. But all of this can be dealt with in a similar manner as before.

3.3.1 Partially Compensated Schottky Barrier

When, in an n-type semiconductor with shallow donors, deep acceptors are added with a density N_a which is slightly less than the donor density, a fraction of the electrons from these donors will fill these acceptors, and they will no longer participate in creating the space charge in the barrier region:

$$\varrho = e(p_\mathrm{d} - n_\mathrm{a} - n) \simeq e(N_\mathrm{d} - N_\mathrm{a}). \tag{3.78}$$

Consequently, one observes a lower space charge in such (partially) *compensated* semiconductors, and a lower field-slope results, causing the barrier to expand as a consequence of compensation. The effect is similar to now including optical excitation of deep donors that result in an additional depletion, hence an increase in space charge density close to the electrode.

3.3.2 Compensated Barrier with Optical Excitation

Optical excitation across the band gap tends to restore the uncompensated case by generating electrons in the conduction band and holes in the valence band which in turn are trapped in donors (electron traps) and acceptors (hole traps) respectively. The degree of space charge generation depends on the generation, recombination and trapping parameters of donors and acceptors.

[24] Note that such a steepening of the characteristic is only observed in single carrier model, i.e., for instance in an n-type semiconductor in which holes are negligible. In many other semiconductors both carriers need to be considered and here minority carrier recombination induced by Frenkel Poole ionization of Coulomb-attractive centers become more important, causing the opposite effect, namely a widening of the space charge region (see Sect. 3.3.2).

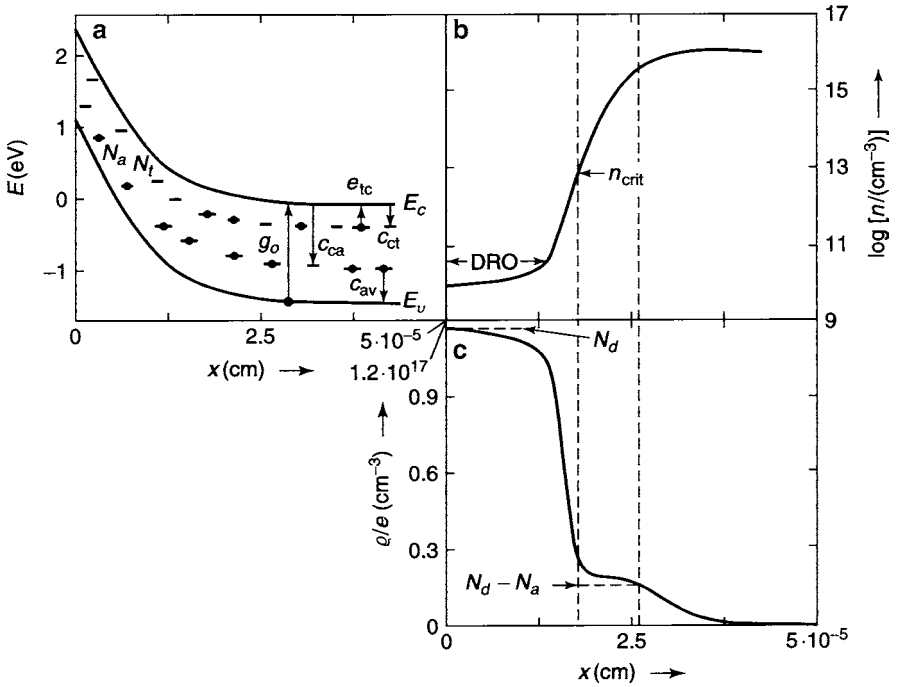

Fig. 3.26. Band-model, $n(x)$, and $\varrho(x)$ including optical carrier generation, trapping and recombination, causing changes in compensation. The computation with the same parameters as in Fig. 3.25, however, with partial compensation (3.78) shows a similar behavior of $n(x)$ and $\rho(x)$, with a different width of the plateaus (see text)

An analysis of the model, shown in Fig. 3.26, explains this behavior. This model contains donors N_d, deep acceptors N_a, and an optical generation of electrons and holes with a generation rate g. In addition, the most important electron transitions are indicated in Fig. 3.26a with transition rates[25] c_ct and e_tc for trapping and thermal ionization from shallow donors and c_ca and c_av for recombination through deep acceptors. The electron density in the bulk is given in steady state by the sum of electrons originating from uncompensated donors (3.78) plus the electrons from the optical generation:

$$n_{10} = N_\mathrm{d} - N_\mathrm{a} + g_o \tau_n \tag{3.79}$$

with g_o as the optical generation rate and τ_n the lifetime of electrons in the conduction band. The lifetime of the optically-generated excess carriers is given by

$$\tau_n = \frac{1}{c_\mathrm{ca} p_\mathrm{a}} \tag{3.80}$$

[25] With letters e and c representing excitation and capture, and subscripts c, t, a, and v representing conduction band, trap (shallow donor), acceptor, and valence band (first and second subscripts for originating and final states, respectively).

with p_a as the density of holes in deep acceptors into which the optically generated electrons recombine. The space charge in the depletion region now becomes

$$\varrho = e(N_d - N_a + g_o \tau_n) \tag{3.81}$$

which, dependent on the intensity of the exciting light, lies between the compensated and the uncompensated case, for moderate light intensities. However, since τ_n depends on p_a and the density of these holes increases with the decreasing density of electrons in the conduction band, as seen from the detailed balance equation (generation = recombination $c_{ca} p_a n$), one obtains

$$p_a = \frac{g_o}{c_{ca} n}, \tag{3.82}$$

and observes an important feedback in the depletion region: when n decreases below a critical value n_{crit}, p_a approaches the density of acceptors:

$$p_a \simeq N_a; \tag{3.83}$$

hence in this part of the barrier region the material reverts back to an uncompensated semiconductor with a space charge

$$\varrho = eN_d. \tag{3.84}$$

The uncompensated case is reached at a critical electron density that can be estimated from (3.83) and (3.82), yielding

$$n_{crit} = \frac{g_o}{c_{ca} N_a}. \tag{3.85}$$

The typical behavior of a Schottky barrier in a partially compensated semiconductor with moderate optical excitation is shown in Fig. 3.26. At the beginning of depletion, the initial space charge is given by the density of compensated donors plus optically-generated carriers that can be expressed as $e(N_d - N_a)$. When with decreasing electron density, one proceeds toward the electrode, (see Fig. 3.26b), $n = n_{crit}$ is reached, and compensation starts to decrease and $\varrho(x)$ increases until it reaches the uncompensated case eN_d (Fig. 3.26c). In the computed example, $n_{crit} \simeq 10^{13}\,\mathrm{cm}^{-3}$. The width of the plateaus in the sub figures (b) and (c) depend on the relative values of the parameters. For more, see Sects. 4.2 and 8.2

3.3.3 Schottky Barrier with Optical Excitation and Field Quenching

Quenching typically describes the reduction of photoconductivity or of luminescence in materials that contain several competing recombination paths for optically excited electrons. We will discuss the consequences of such quenching for the space-charge behavior in the following section.

The simplest model for quenching of an optically excited electron distribution in the barrier assumes, as a competing mechanism with the normal recombination transition, the depletion of holes (minority carriers) by an electric field into the adjacent electrode and the consequent recombination there, as discussed below.

3.3.3.1 Compensated Barrier with Optical Excitation and Field Extraction of Holes

When n has decreased below n_{crit} (see Sect. 3.3.2) in an optically excited barrier, thereby eliminating the effect of compensation via deep acceptors, this compensation can be restored when the holes trapped in the deep acceptors are removed by excitation into the valence band and consequently drift into the adjacent electrode with no significant influence of these holes on the space charge, since $p \ll N_{\mathrm{a}}$. Excitation can be induced thermally, optically, or by an electric field.

Field-induced ionization of holes from deep acceptors is achieved as soon as the field has increased above its threshold field for the Frenkel-Poole effect of Coulomb-attractive acceptors to become competitive,[26] the critical field is typically on the order of $50\,\mathrm{kV\,cm^{-1}}$.

When the field is high enough to extract a major fraction of the holes that are stored in the hole traps, in order to reduce p_{a} well below N_{a}, then the original compensation is restored, and the space charge density reduces to:

$$\varrho = e(N_{\mathrm{d}} - N_{\mathrm{a}}). \tag{3.86}$$

This is shown in Fig. 3.27 which is computed for the same parameters as in Fig. 3.26, but with additional field quenching starting at $F_{\mathrm{crit}} \simeq 70\,\mathrm{kV\,cm^{-1}}$. In Fig. 3.27b, one distinguishes three regions: the compensated region with optical excitation for $2 < x < 2.5 \cdot 10^{-5}\,\mathrm{cm}$, an intermediate region near $x \simeq 1.5 \times 10^{-5}\,\mathrm{cm}$ where the compensation becomes eliminated, and the field-quenching region for $x < 10^{-5}\,\mathrm{cm}$ where the space charge is again reduced to the compensated case (3.86). Here, the *field slope is significantly reduced*, permitting a further *widening of the barrier layer*.

This is technically a most important effect that is utilized in many devices with barriers (or junctions) with light and field-quenching: it permits a substantially larger voltage drop within the barrier before breakdown occurs, and results in much **better rectification**.

[26] A strong Frenkel-Poole excitation is needed to compete significantly with the other transitions. Even though the threshold field for Frenkel-Poole excitation is usually on the order of $10^4\,V\,\mathrm{cm^{-1}}$, the critical field cited here is almost an order of magnitude larger (Dubey and Ghosh 1997).

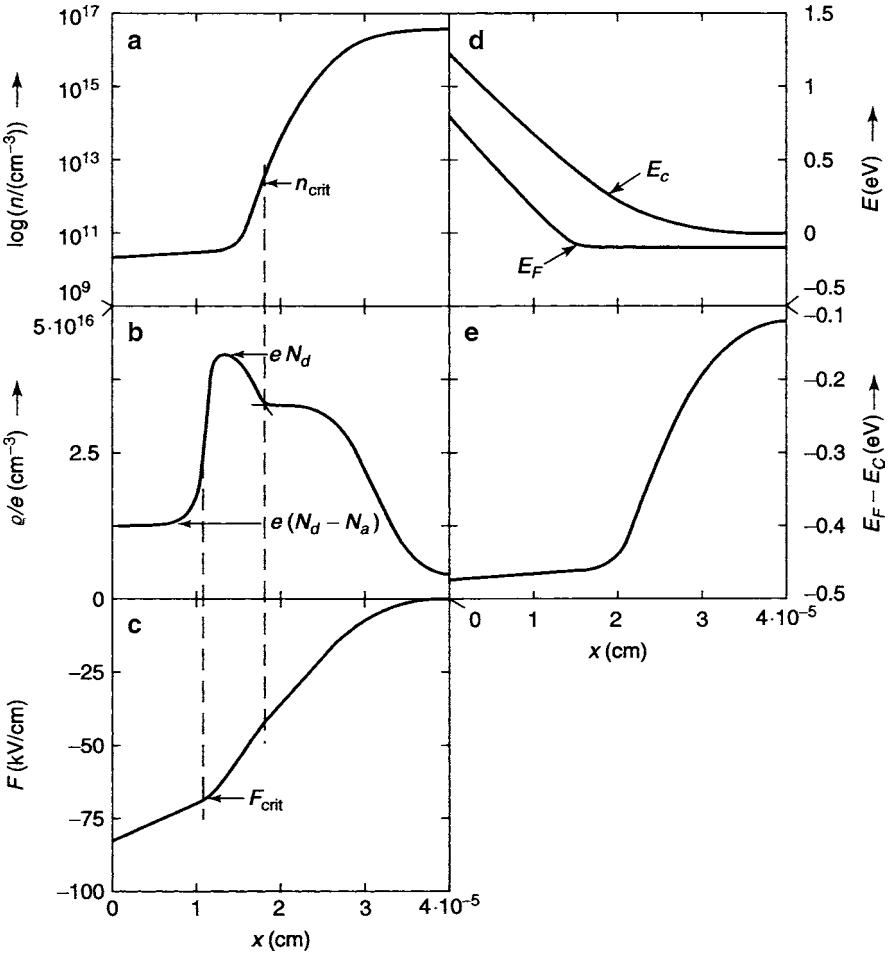

Fig. 3.27. Compensated Schottky barrier with optical excitation and field-quenching and the same parameters as in Fig. 3.25 except: $N_{\rm d}-N_{\rm a}=1.2\times10^{16}$, $N_{\rm d}-N_{\rm a}+p_{\rm a}^{(\rm opt)}=3\times10^{16}$, $N_{\rm d}=4\times10^{16}$, and $n_{\rm crit}\simeq5\times10^{12}\,{\rm cm}^{-3}$; $F_{crit}=70\,{\rm kV\,cm}^{-1}$. It shows first an increase in the space charge when the deeper center becomes depleted, but then, closer to the electrode when the critical field is reached, it shows a substantial decrease of the space charge below the density of both shallow and deep donors (**b**). Here the space charge region is widened as it takes more space before the electron density given by n_j is reached (**a**). Since the space charge is reduced in this region close to the cathode, the field slope is also reduced (**c**)

3.4 Quasi-Schottky Barrier as Part of a Heterojunction

The main property of a Schottky barrier is based on a well-defined metal/semiconductor boundary that forces the electron density at the boundary to be reduced significantly below the density in the bulk. Its

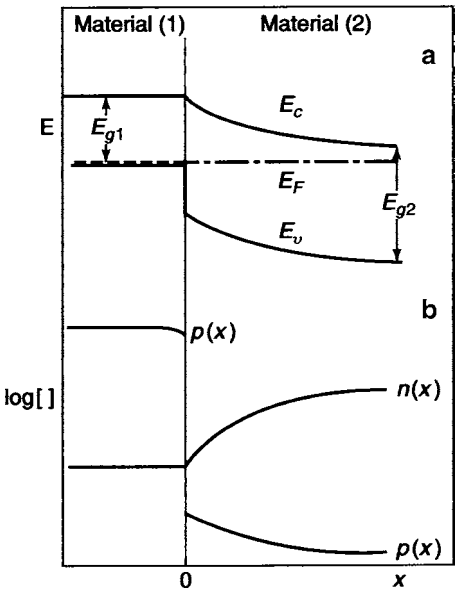

Fig. 3.28. High-blocked abrupt heterojunction band-model assuming a connection of the bands with a jump only of the valence bands (**a**) and the corresponding carrier distribution with continuity of the electron density and a major jump of the hole density at the interface (**b**)

electrical behavior is determined by only one carrier within the entire barrier. We will later see (Sect. 7.1) that in *pn*-homojunctions the conditions are substantially different, so that the main approximations used here to yield an analytical expression for the space charge, field, and current–voltage characteristics are no longer justified.

One type of heterojunction, however, fulfills similar conditions as a Schottky barrier, which permits the use of the same approximations as used in the previous sections in the lower conductivity and wider band gap material of the heterojunction. This can be an abrupt np^+ heterojunction. Here the higher conductivity p^+ material replaces the metal, e.g., the p^+ region in such a p^+n-heterojunction. When the n-side is the wider-gap, lower-doped material (Fig. 3.28), it harbors the part of the junction that is quite similar to the Schottky barrier. Assuming continuity of the conduction band at the heterojunction interface[27], the entire band-gap jump occurs in the valence band at the interface. This jump provides a substantial barrier for the holes in the p^+-region and causes a large jump of the hole density at the interface,

[27] we will later on show that this is the case when the electron current continuity is the controlling condition for the interface band connection that is given by a thin space charge double layer at the interface, related to the electron affinity

while the electron density is continuous[28] through this boundary (Fig. 3.28). Such a heterojunction is referred to as a *high-blocked heterojunction* since the higher carrier density from the p^+ region is effectively blocked from entering the lowly doped n-type region.

The conductivity in the p^+ region is described by an essentially constant, large density of holes; the electrical properties of the n-type region are described by electrons alone, if the jump in p at the interface is large enough to render $p(x = 0^+) \ll n(x = 0^+)$. Consequently, the conditions determining the behavior of the n-part of the heterojunction are identical in this approximation to those in the Schottky barrier. The field in the n-type region is thus obtained by integrating the Poisson equation with constant ϱ (3.6) in the depletion region, as long as we can neglect generation or recombination in the n-type region, and (3.5)–(3.7) are again the governing set of equations for the electrical properties of this n-type region. The electrical properties of the p^+ region are described as being similar to a metal, fixing the density of electrons at the interface and providing negligible series resistance.

The main difference between the low conductive material in a *high-blocked heterojunction* and the semiconductor in a simple Schottky barrier is a slightly more involved boundary condition, since the p^+-semiconductor permits a more extensive sliding of the minority carrier density at the boundary $n(x = 0^-) = n_j$, as will be discussed in the following section.

A set of solution curves for (3.5)–(3.7) is obtained by numerical integration and is shown in Fig. 3.29 in the n-type region.[29] We have assumed a single-donor model and used the same set of material parameters as used for the Schottky barrier in Sect. 3.1. Except for a wider range of $n_j(j_n)$, resulting in a wider spacing of the $n(x)$ curve family near $x = 0$, the curves look similar to the curves obtained in a metal/semiconductor Schottky barrier. This means that if such heterojunction interface permits a larger gliding of n_j, the current–voltage characteristic becomes significantly steeper, or, in other words, an high/low **abrupt heterojunction is a much better rectifier** than a Schottky barrier.

3.4.1 Electron Boundary Condition at the Heterojunction Interface

In Sect. 3.2.1 we have shown that the boundary condition for the electron density at the interface is given by the carrier transport from the metal into the semiconductor. At a heterojunction interface, a similar relationship holds, for the continuity of the electron current. Because of the high hole density in the p^+-region, the electric field is limited here to low values, causing the

[28] For more realistic modifications of this assumption, this also results in some discontinuity of the electron density, as we will discuss later.

[29] The solutions in the p^+ part are not shown here, since they need additional consideration of both carriers, which will be discussed later.

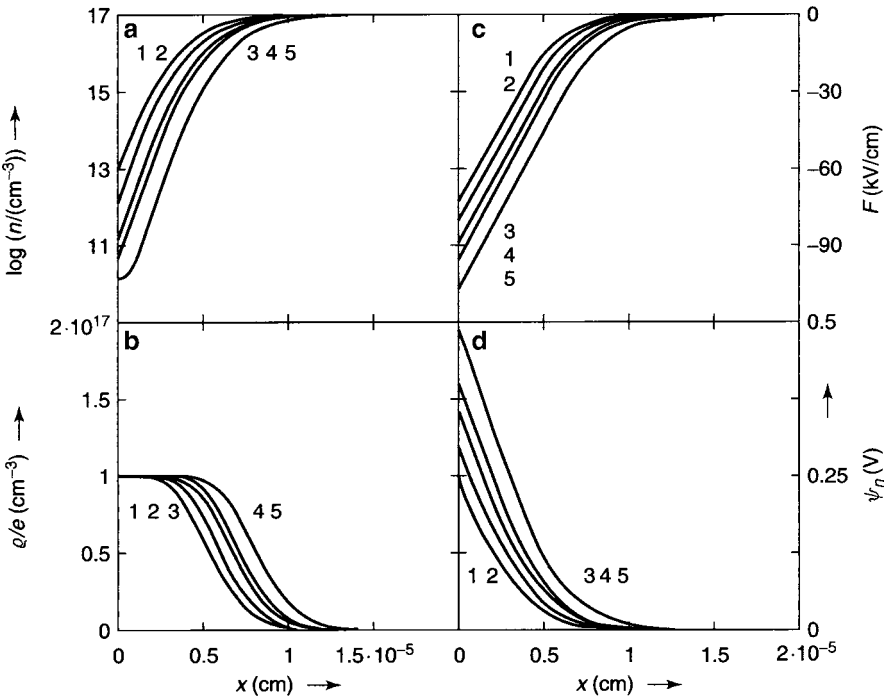

Fig. 3.29. n-region of a p^+n heterojunction; computation of $n(x)$, $F(x)$, and $\psi(x)$ for same parameters as in Fig. 3.5 (Table 3.1) from (3.5)–(3.7) and boundary condition (3.87). Observe, however, that currents are much closer spaced to the saturation current ($j_{\mathrm{nsat}} = 23.85\,\mathrm{mA\,cm^{-2}}$); $j_n = 0, -23.5, -23.75, -23.83$, and $-23.84\,\mathrm{mA/cm^2}$ to obtain a similar spread for curves 1–5, respectively, that means the resulting current–voltage characteristic is much steeper than for the typical Schottky barrier

electron current for $x < 0$ to be carried by diffusion only. This diffusion current can be expressed in terms of the electron density at the interface, n_j, and in the bulk of the p^+-region, n_{10}, as will be derived in Sect. 5.1 (Böer 1975; Böer 1977).

$$j_n = ev_{\mathrm{D}}^*(n_j - n_{10}). \tag{3.87}$$

This expression is formally identical to the expression at the metal/semiconductor interface, except that the thermal electron velocity v_n^* is now replaced by an effective diffusion velocity v_{D}^*, and n_c is replaced with the equilibrium minority carrier density n_{10} in the bulk of the p^+-region.

The effective diffusion velocity is given (see Sect. 5.2.5, (5.41)) by

$$v_{\mathrm{D}}^* = \frac{L_{n1}}{\tau_{n1}} \tanh\left(\frac{d_1}{L_{n1}}\right) \tag{3.88}$$

with d_1 as the thickness of the p^+ -region, and L_{n1} and τ_{n1} as the minority carrier diffusion length and lifetime in this region. The density n_{10} is given either by

$$n_{10} = \frac{n_i^2}{p_{10}} \tag{3.89}$$

with n_i the intrinsic carrier density and p_{10} the density of holes in the bulk for thermal equilibrium, or by

$$n_{10} = g_o \tau_{n1} \tag{3.90}$$

for optical carrier generation. We will derive expressions for the diffusion length, carrier lifetime, and intrinsic carrier density in Sects. 4.4, 5.1.1, and 8.1.

The effective diffusion velocity v_{D}^* is usually several orders of magnitude smaller than v_n^*; therefore, the reverse saturation current is lower by the fraction v_{D}^*/v_n^* in a high-blocked heterojunction than in the ordinary Schottky barrier if we assume the same $n_c = n_{10}$. Therefore, the diffusion current at the heterojunction interface, is that much smaller than at a metal/semiconductor interface, or, if a certain current needs to be drawn, then the difference between n_c and N_{10} must be larger by the same amount. This is the very reason for the steepening of the current voltage characteristics, as referred to in the previous section and will be computed in the following section.

3.4.2 Current-Voltage Characteristics for an Abrupt Heterojunction

In an *ideal high-blocked heterojunction* with a single shallow donor lower doped n-type region, the field distribution is triangle-like (see Fig. 3.29c); thus the Schottky approximation can be used, and $n(x)$ can be obtained explicitly by integrating the transport equation for electrons, yielding (3.33). When evaluating $n(x)$ at $x = 0$ and introducing $n(x = 0^+) = n_j$ from (3.87), one obtains the current equation:

$$j_n = \frac{j_s \left\{ \exp\left[\frac{e(\psi_{n,\mathrm{D}} - \psi_{n,j})}{kT} \right] - 1 \right\}}{1 + \frac{v_{\mathrm{D}}^*}{\mu_n F_j}}, \tag{3.91}$$

which is identical to the modified-diode equation for Schottky barriers except that v_{D}^* replaces v_n^* in theshape factor (Sect. 3.2.1.2) and the electron density (i.e., the minority carrier density) n_{10} in the p-type region replaces n_c at the interface for the saturation current:

$$\boxed{j_s = e n_{10} v_{\mathrm{D}}^*.} \tag{3.92}$$

The electrostatic electron potential $\psi_{n,\mathrm{D}} - \psi_{n,j}$ in (3.91) can be replaced by the applied voltage, using the same considerations given in Sect. 3.2.2. This

yields for the current–voltage characteristic

$$\boxed{j_n = \frac{j_s \left\{ \exp\left(\frac{eV}{kT}\right) - 1 \right\}}{1 + \frac{v_{\mathrm{D}}^*}{\mu_n F_j}}.} \tag{3.93}$$

This is the *ideal high-blocked heterojunction diode equation*, which is of the same form as the modified Schottky diode equation.

However, since v_{D}^* is usually much smaller than v_n^*, the term $v_{\mathrm{D}}^*/\mu_n F_j$ can more readily be neglected, and therefore, the bias-range in which the shape factor deforms the shape from the ideal characteristic is greatly reduced. In addition, $n_{10} = n_i^2/p_{10}$ is usually much smaller than n_c. Both factors cause a substantial *improvement of the ideal diode characteristics* for the high-blocked heterojunction compared to that of a metal/semiconductor barrier.

This fact identifies the large advantage of a (hetero)junction compared to a Schottky barrier diode, and inversely indicates, that so-called Schottky diodes that show reasonable rectifying characteristics are in all probability hidden heterojunction diodes[30].

A comparison of effective diffusion velocity v_{D}^* in relation to the drift velocity $\mu_n F_j$ will further illustrate this influence.

3.4.2.1 Magnitude of the Effective Diffusion Velocity

With the diffusion length L_n given as

$$L_n = \sqrt{\frac{\mu_n kT\tau_n}{e}} \tag{3.94}$$

(see Sect. 5.1.1), one can rewrite the effective diffusion velocity (3.88) as a function of μ_n, τ_n, and d_1 (Böer, 1975):

$$v_{\mathrm{D}}^* = \sqrt{\frac{\mu_n kT}{e\tau_n}} \tanh\left(\frac{d_1}{\sqrt{\mu_n kT\tau_n/e}}\right). \tag{3.95}$$

It increases with μ_n, decreases with τ_n, and increases (and saturates) with increasing width d_1 of the p^+-region as shown in Fig. 3.30. Typically, the effective diffusion velocity is on the order of 10^4–$10^5\,\mathrm{cm\,s^{-1}}$, while the thermal electron velocity v_n^* is on the order of $10^7\,\mathrm{cm\,s^{-1}}$, that is typically two to three orders of magnitude higher.

[30] Often a thin interlayer of an oxide or metal/semiconductor alloy separates the metal from the semiconductor, and the actual rectifying junction lies at that interface rather than at the metal/semiconductor interface.

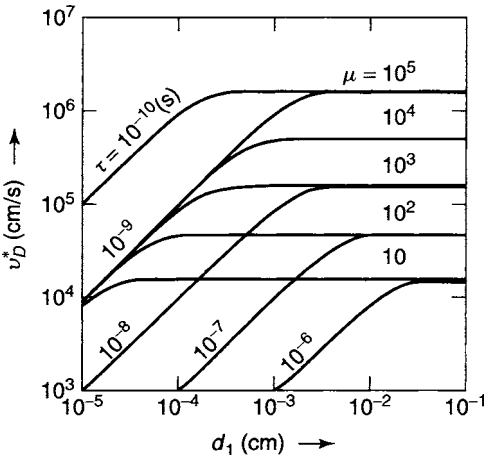

Fig. 3.30. Effective diffusion velocity (at 300 K) in the p^+ region as function of the thickness of this region d_1. This is computed for the minority carrier mobility μ_n and lifetime τ_n in this p^+-region as family parameters. This presentation shows the wide range of several orders of magnitude in which v_{D}^* can vary

3.4.3 Heterojunction with Interface Recombination

In actual heterojunctions, however, the lattice mismatch between two semiconductors and other interface defects often cause a significant increase of recombination at the interface. The recombination results in an electron and hole leakage-current of equal amount and opposite sign at the interface, given by:

$$j_{\mathrm{ns}} = en_j s_j = -j_{\mathrm{ps}} \tag{3.96}$$

with s_j as the interface recombination velocity.

This recombination current is subtracted from the electron current passing from the p^+- into the n-part of the junction:

$$j_n(x = 0^+) = j_n(x = 0^-) - j_{\mathrm{ns}}. \tag{3.97}$$

With the diffusion-limited current (3.87) at $x = 0^-$, one obtains for the current in the n-part of the junction:

$$j_n(x = 0^+) = en_j(x = 0^+)(v_{\mathrm{D}}^* + s_j) - en_{10}v_{\mathrm{D}}^*. \tag{3.98}$$

3.4.3.1 Nonideal Heterojunction Characteristics

When the current equation *with interface recombination* (3.98) is used to eliminate n_j in the electron density distribution (3.33), one obtains the *nonideal*

high-blocked heterojunction characteristic

$$\boxed{j_n = \frac{j_s \left\{ \exp\left[\frac{eV}{kT}\right] - 1 \right\}}{1 + \frac{v_{\mathrm{D}}^* + s_j}{\left|\mu_n F_j\right|}};} \tag{3.99}$$

this equation is similar to the modified-diode equation, except that v_n^* is now replaced by the sum of diffusion and interface recombination velocities. Since s_j usually exceeds v_{D}^* and is on the order of $10^6\,\mathrm{cm\,s^{-1}}$ in heterojunctions with more than 1% lattice mismatch, the shape factor now deviates more readily from 1, thus causing a more pronounced deviation from the ideal characteristic, and contains an extended DRO-range.

These typical deviations from the ideal characteristic are shown in Fig. 3.31 for a family with s_j as family parameters. From this figure it becomes evident that for interface recombination velocities below the effective diffusion velocity and for (effective) donor densities above a critical value[31] one obtains almost perfect ideal diode characteristics. There remains only

$$v_{\mathrm{D}}^* + s_j \ll \left|\mu_n F_j\right| \tag{3.100}$$

within the entire reverse bias range of the characteristic, and the shape factor here remains close to unity.

One therefore concludes the importance of selecting heterojunctions (or junctions) with low interface recombination (or junction recombination) when one wants to produce devices with high rectification (or solar cells with high "fill factors," as we will explain later).

Summary and Emphasis

The basic Schottky barrier is a good example for the initial analysis of a real space-charge region in semiconductors that has a long history of discussions in literature and shows the principles for rectification. It also is the simplest example that demonstrates all essentials of space charge behaviors and can be analyzed in a one-carrier model. Here only the one-carrier transport and Poisson equations are necessary to obtain the main features of the Schottky barrier, in contrast with a *pn*-junction, where both carriers need to be considered, and the current continuity equation becomes an additional element in the analysis.

The space charge in a Schottky barrier is created by the leaking out of conduction electrons into a metal with sufficiently large work function. In many

[31] The critical value, of N_{d} depends on T, ε, μ_n (3.36) and v_{D}^* in order to keep (3.100) satisfied.

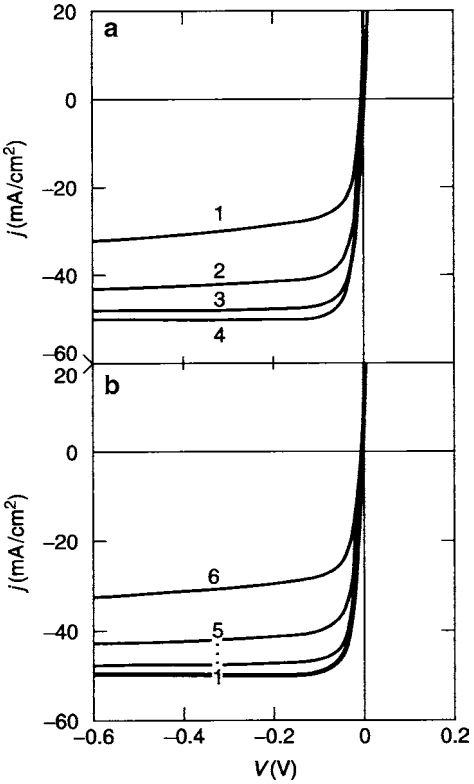

Fig. 3.31. Current–voltage characteristics for single donor, high-blocked, nonideal hetero-junction with parameters as in Fig. [f2512/3]. Shown is a family of characteristics with s_j as family parameters for $s_j = 10^4,\ 3 \times 10^4,\ 10^5,\ 3 \times 10^5,\ 10^6$ and $3 \times 10^6\,\mathrm{cm\,s^{-1}}$ for curves 1–6, respectively, indicating that for low interface recombination velocities, the curves are essential ideal diode characteristics and decrease in "quality" only when $s + j$ approaches or exceeds the effective electron diffusion velocity

semiconductors, coupled with it is the depletion of deeper and deeper defect centers (donors, electron traps) as one approaches the metal/semiconductor interface. This results in a ramp-shaped (triangular) increase of the electric field within each layer of constant space charge (Schottky approximation). Widening or contracting of the space-charge layer with increasing reverse or forward bias, respectively, determines the corresponding voltage drop. This causes a raising or lowering of the potential barrier height, which effectively controls the current and results in a rectifying characteristic.

The characteristic is "ideal" when the carrier density at the metal/semiconductor interface is kept constant, determined by a bias-independent work function.

Current continuity through the barrier requires a changing carrier density at the interface, resulting in a nonideal diode characteristic with an exponential ideality factor $A > 1$. This ideality factor is determined by the donor (trap) distribution in the barrier region.

With light and the ionizing effect of an electric field, significant changes occur in the characteristic result, which can easily be analyzed in the framework of the Schottky approximation.

The basic elements of the Schottky approximation can be extended to a high-blocked heterojunction which has superior rectifying characteristics because of an easily gliding carrier density at the interface with changing bias and lesser interface recombination than at the metal/semiconductor interface.

The rather transparent relation between defect parameters and the resulting current–voltage characteristics in Schottky barriers provides the basis for designing barrier-related devices with improved properties. Specifically, the influence of doping and of field-related ionization provides tools, which can advantageously be used to improve rectifying characteristics and maximum permissible bias before breakdown. A better understanding of the specific metal/semiconductor boundary, including the design of appropriate inter layers between metal and semiconductor has significant potential for improved Schottky barrier devices.

Field ionization of Coulomb-attractive traps or recombination centers permitting Frenkel-Poole ionization of such centers at fields well below the breakdown field strength is shown as an important means to limit the electric fields in such barriers and substantially improve the device performance.

Exercise Problems

1.(e) Express the field in a Schottky barrier in terms of the Debye length. What is the physical significance of $kT/(eL_\mathrm{D})$? Give its value for typical doping densities.

2.(e) Show explicitly that the integration of the transport equation (3.28) yields (3.29) which can be written as the diode equation (3.40).

3.(*) Discuss the error using the Schottky approximation in $F(x)$ and $\psi_n(x)$ for an insufficiently flat (box-shaped) space charge distribution, and compare these results with $\psi_n(x)$ obtained from the Boltzmann distribution.

4. Discuss the validity range of the nonideal current–voltage characteristic with special attention to Dawson's integral approximation.

5.(e) Plot the field at the metal/semiconductor boundary of a Schottky barrier as a function of the bias for $N_\mathrm{d} = 10^{16}$ and $10^{17}\,\mathrm{cm}^{-3}$ and for $n_c = 10^{10}$ and $10^{12}\,\mathrm{cm}^{-3}$. What are the limitation in forward bias?

6.(e) Express the shape factor (3.52) in terms of the bias for a typical example and discuss its influence on the characteristic.

7.(*) Express the width of the DRO-range in terms of the bias and its significance for estimating the current–voltage characteristic for medium reverse bias. Refer to the relative distribution of electrostatic and electrochemical electron potentials.
8.(*) Give an explicit expression for the width of the Schottky barrier x_{D}, as in (3.22), however as a function of a nonvanishing bias.
9.(*) Discuss the expected changes in the solution curves of the transport and Poisson equations, and in the resulting characteristics when two discrete donor levels are replaced by a continuous donor distribution.
10.(r) Under what conditions can a second donor level be neglected regarding its influence on the jV-characteristic?
11.(r) What signalises a diode quality factor larger than one for the shape of the current voltage characteristics; and under what conditions could one expect the diode quality factor (3.72) to be larger than two?
12.(*) Discuss the influence of optical excitation in a partially compensated semiconductor on the development of a Schottky barrier with increasing reverse bias and with fields extending into the range of field quenching. Design a doping profile of a Schottky-barrier device that limits the field to $10^5\,\mathrm{V\,cm^{-1}}$ in reverse bias up to $-100\,\mathrm{V}$.
13.(r) Discuss the difference between the shape factor for a Schottky barrier adjacent to a metal and to a high-blocked heterojunction. Give a quantitative comparison between the different characteristic velocities in terms of the competing currents.
14.(*) What is the physical significance of a diffusion velocity compared to the rms velocity of electrons? Relate both velocities quantitatively with each other.
15.(r) Relate the interface recombination velocity to the rms velocity and the relevant capture parameters of the recombination centers at the interface. Compare this with the volume recombination.
16.(*) Discuss in your own words the difference between the boundary conditions of an n-type semiconductor to a metal and to a p^+-type semiconductor with, and without interface recombination. Since there is complete interface recombination at a semiconductor/metal interface, where can you find this term in the Schottky barrier discussion?
17.(*) In the light of the discussion of trap-depletion, how will
(a) interface recombination, and
(b) recombination within a space charge layer modify the shape factor?
(c) How would such changes translate into changes of the diode quality factor?
18.(e) In Fig. 3.31 the density of donors is not given explicitly as a family parameter. Assuming shallow, noncompensated donors, $\varepsilon = 10$, $\mu_n = 500\,\mathrm{cm^2\,Vs^{-1}}$, $T = 300\,\mathrm{K}$, and $v_{\mathrm{D}}^* = 10^5\,\mathrm{cm\,s^{-1}}$, calculate the N_{d}-values for the four curves of panel a and the N_{d}-value for panel b.

4

Minority Carriers in Barriers

Summary. Minority carriers have a significant influence on the carrier transport through space–charge regions when these carriers are created by light or are present in sufficient concentration as, e.g., in the neighborhood of inversion layers or within *pn*-junctions. Minority carrier currents of technical interest are predominantly diffusion currents. These currents are in competition with recombination currents at device surfaces or interfaces.

In the discussions of the previous chapters, we have neglected the influence of minority carriers. This is justified when throughout the entire device the Fermi level remains well above the midpoint of the band gap (for electrons as majority carriers) and there are no excitation mechanisms active to generate electron–hole pairs with a significant rate, specifically, when there is no optical excitation.

We will now extend this discussion to include examples where minority carriers play an important role. These include

- The influence of generation and recombination on the steady state carrier distribution
- The influence of minority carriers on the space-charge variation with an applied bias
- The additive current of minority carriers in junction devices
- The continuity condition for minority and majority currents and their crossover in junctions

The discussion presented in this chapter will provide the groundwork for the inclusion of minority carriers into a more comprehensive model of the carrier transport through space–charge layers.

We will first briefly summarize carrier generation and recombination and then introduce demarcation lines to distinguish between carrier trapping and recombination, and quasi-Fermi levels to conveniently describe steady state carrier distributions.

We finally will analyze carrier lifetimes and their use in describing steady state relations.

We will then analyze the current contribution of minority carriers, while interacting with majority carriers.

4.1 Carrier Generation and Recombination

Carriers are redistributed over con-ducting (bands) and nonconducting (levels in the band gap) states via generation and recombination mechanisms. They are also influenced by local currents from the surrounding of each volume element:[1]

$$\frac{\partial n}{\partial t} = g - \frac{n}{\tau_{no}} + \frac{1}{e}\mathbf{div} j_n. \tag{4.1}$$

Carrier generation needs a supply of energy; one consequently distinguishes thermal, optical or field-induced generation. It can originate from localized or nonlocalized states and proceed into localized or nonlocalized states.

Carrier recombination)[2] is the opposite transition and occurs mostly with a transition from a nonlocalized state into a localized state; it sets free energy as thermal energy or as luminescence.

Local currents follow the changes in carrier distribution from thermal equilibrium caused by a bias across space–charge regions, or by optical or field excitation.

In Fig. 4.1, a number of typical transitions are shown between a variety of such states. For consistency in the following description, we will identify

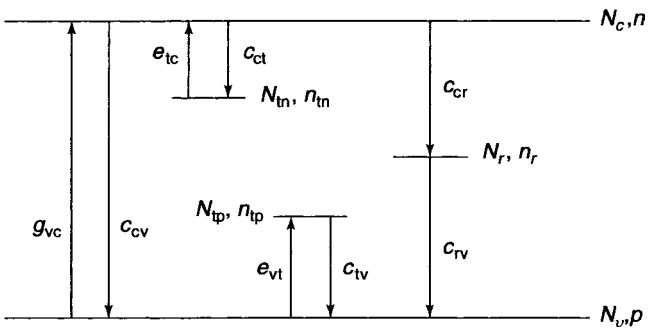

Fig. 4.1. Electron transitions between localized (in band gap) and nonlocalized states (bands)

[1] The following analogy may help to remember the formula: the change in population is given by the birth rate (g) minus death rate (= population over life expectancy) plus the drop-off from travelers through the region (change in current multiplied by $-1/e$).

[2] We are using here the term recombination somewhat loosely before defining the distinction between trapping and recombination in Sect. 4.1.3.

only electron transitions; hole transitions proceed in the opposite direction. The transition coefficients c_{ik} are unambiguously defined by the first index indicating the originating state and the second index indicating the final state. In order to facilitate comprehension, we have identified transition coefficients for "e"xcitation transition as e_{ik} to set them apart from recombination or "c"apture transitions as c_{ik}.

The transition rate R_{ik} is defined as the product of the electron density in the originating state, the hole density in the final state and the transition coefficient,

$$R_{12} = c_{12} n_1 p_2, \tag{4.2}$$

with the transition rate measured in $\mathrm{cm}^{-3}\ s^{-1}$. As an example, the capture of an electron from the conduction band (n – following the convention, we have left off the index c here) into an electron trap is given by

$$R_{\mathrm{tc}} = c_{\mathrm{ct}} n (N_t - n_t), \tag{4.3}$$

with N_t and n_t as the densities of electron traps and of captured electrons in these traps, respectively[3].

The transition coefficients c_{ik} or e_{ik} have the dimension $\mathrm{cm}^3\mathrm{s}^{-1}$; the product of such a coefficient with the electron or hole density in the final state, for instance $c_{ik} p_k$, is the transition probability, which has the dimension s^{-1}.

The different excitation mechanisms to populate higher energy states will now be briefly reviewed.

4.1.1 Thermal Excitation

Thermal excitation probabilities can be obtained from thermodynamic arguments. Transition between two levels (or a level and a band) always comes in pairs, as a transition into the level and a transition out of this level. In thermal equilibrium, they must be equal to each other. This *detailed balance principle* applied to an electron trap yields (see Fig. 4.1)

$$e_{\mathrm{tc}} n_t p_c = c_{\mathrm{ct}} n (N_t - n_t). \tag{4.4}$$

This equation can be used to obtain an explicit expression for e_{tc}: in thermal equilibrium the population of these traps is 1/2 when the Fermi level coincides with the energy of the trap level; thus, with $(N_t - n_t)/n_t = 1$, and for the nondegenerate case in which essentially all conduction band states are empty, $p_c \simeq N_c$, one obtains

$$e_{\mathrm{tc}} N_c = c_{\mathrm{tc}} n \tag{4.5}$$

[3] Capital letters are consistently used to identify the density of states and lower case letters to identify the density of electrons or holes in these states.

or, when using (4.4) and $E_F = E_t$,

$$e_{tc} N_c = c_{tc} N_c \exp\left(-\frac{E_c - E_t}{kT}\right), \tag{4.6}$$

yielding for the

$$\frac{e_{tc}}{c_{ct}} = \exp\left(-\frac{E_c - E_t}{kT}\right). \tag{4.7}$$

Even though this condition was obtained for a specific case, namely thermal equilibrium, this ratio holds true in general, since both coefficients are constants and do not change with trap population. One obtains therefore for the **thermal excitation coefficient**

$$\boxed{e_{tc} = s_n v_{rms} \exp\left(-\frac{E_c - E_t}{kT}\right)}, \tag{4.8}$$

using $c_{ct} = s_n v_{rms}$, i.e., the **capture coefficient** as the product of capture cross section and rms velocity of the electron. The thermal excitation is consequently determined by *two parameters*: the *energy* of the level and its *capture cross section*. The *population of this center in thermal equilibrium*, however, is determined by its *energy alone*. The attainment of this equilibrium (i.e., the time it takes to follow changes in excitation) or the change in population to obtain steady state, e.g., after changes of external excitation, is determined also by its kinetic parameters c_{ct} and e_{tc}. These changes may take long times (frozen-in equilibria) and need to be carefully considered for deeper centers.

4.1.2 Optical Excitation

We will briefly summarize here only those aspects of the optical excitation which are commonly used to create free electrons and holes, and thereby increase the density of minority carriers and of majority carriers in photoconductors. Such optical excitation typically involves band-to-band transitions. The optical absorption coefficient $\alpha_o(\lambda)$ near the band edge of direct band gap semiconductors[4] is on the order of $10^5\,\mathrm{cm}^{-1}$; i.e., the light is substantially absorbed in a layer of 1,000 Å thickness. The flux ϕ of photons of a certain wavelength λ inside a solid is given by

$$\phi(\lambda, x) = \phi_0(\lambda) \exp[-\alpha_o(\lambda) x], \tag{4.9}$$

where $\phi_0(\lambda)$ is the photon flux per unit wavelength ($\Delta\lambda$) that penetrates through the top layer[5] of the solid and is given in $\mathrm{cm}^{-2}\,\mathrm{s}^{-1}\Delta\lambda^{-1}$.

[4] In corresponding photon energy ranges of indirect band gap semiconductors, the absorption coefficient is roughly three orders of magnitude smaller.

[5] After reflection is subtracted.

When polychromatic light is used, the total photon flux as a function of the penetration depth x is obtained by integration,

$$\phi(x) = \int_{\lambda_1}^{\lambda_2} \phi_\lambda(\lambda, x)\,\mathrm{d}\lambda, \tag{4.10}$$

with ϕ in $\mathrm{cm}^{-2}\,\mathrm{s}^{-1}$.

The optical generation rate $g_o(x)$ is given by the absorbed light in each slab of infinitesimal thickness; thus,

$$g_o(x) = -\frac{\mathrm{d}\phi(x)}{\mathrm{d}x}. \tag{4.11}$$

For monochromatic light (λ_0), the optical generation rate depends exponentially on x:

$$g_o(x, \lambda_0) = \alpha_o(\lambda_0)\phi_0(\lambda_0)\Delta\lambda\,\exp[-\alpha_o(\lambda_0)x], \tag{4.12}$$

with $\Delta\lambda$ a small wavelength range in which $\alpha_o(\lambda)$ is constant.

For polychromatic excitation, a constant (space-independent) generation rate is often a sufficient approximation: Even though ϕ_λ depends exponentially on the penetration depth, $\phi(x)$ usually does not, since, with polychromatic light of various absorption coefficients $\alpha_o(\lambda)$, the superposition of a wide variety of such exponential functions causes a substantially lesser-than-exponential dependence of ϕ on x. For excitation with sunlight, as used in solar cell application, a wide spectrum of active light is employed; and for indirect band gap material, one often uses as a reasonable approximation an average generation rate (Böer 1976):

$$g_o = \overline{g} \qquad\qquad \mathrm{cm}^{-3}\,\mathrm{s}^{-1}. \tag{4.13}$$

Such average generation rates for AM 1 sunlight[6] and 1 eV band gap semiconductors are typically on the order of 10^{21} for indirect band gap materials. For direct band gap materials where the exponential distribution needs to be considered, under certain condition an average generation rate close to the surface of $10^{23}\,\mathrm{cm}^{-3}\,\mathrm{s}^{-1}$ is often used. For more specific information on sunlight excitation see (Böer 2002).

4.1.3 Field Ionization

The three major field ionization mechanisms – Frenkel–Poole, impact and tunnel ionisations – all produce free carriers, predominantly by inducing bound-to-free transitions. Band-to-band transitions require substantially higher fields

[6] AM 1 stands for air mass 1 and indicates the optical absorption by an air column when the sun stands at the zenith. In total power, this absorption amounts to 28.6%, namely from $\simeq 140\,\mathrm{mW\ cm}^{-2}$ above the earth's atmosphere to $100\,\mathrm{mW\ cm}^{-2}$ at AM 1. With decreased elevation φ the light path through the atmosphere becomes longer as $1/\cos(90^\circ - \varphi)$ which is used as the corresponding air mass value. E.g., for $\varphi = 42^\circ$, one has sunlight of AM 1.5, a value often used as more realistic for solar cell calibration in solar simulators.

which are not present in normal space charge regions, except for tunneling junctions that are specifically designed for that purpose. Field-ionization is thereby distinguished from optical generation of both types of carriers; it does not generate pairs of mobile carriers as a primary process.

In conjunction with other generation mechanisms, however, field ionization can interfere and thereby shift the population of carriers in defect centers with an applied bias. This, in turn, can influence recombination traffic and space–charge distributions. Field-enhanced deep donor depletion (Sect. 3.2.3) and field quenching (Sect. 3.3.3) are two examples for such important field-induced changes that were already mentioned. We will, therefore here briefly summarize the most important relations for field ionization.

As indicated earlier, the **Frenkel–Poole effect** (Franz and Naturforsch 1958; Pisani et al. 1988) needs by far the lowest field[7] for ionizing Coulomb-attractive centres. Such ionization is achieved by tilting the bands and thereby lowering the energy of such a center at which thermal ionization becomes possible (see Fig. 4.2).

The potential barrier lowering can be described by superimposing the Coulomb potential with an external field,

$$\psi_n(x) = \frac{eZ}{4\pi\varepsilon\varepsilon_0 x} - Fx, \tag{4.14}$$

with Z the charge of the defect. The barrier lowering as shown in Fig. 4.2 can then be expressed as

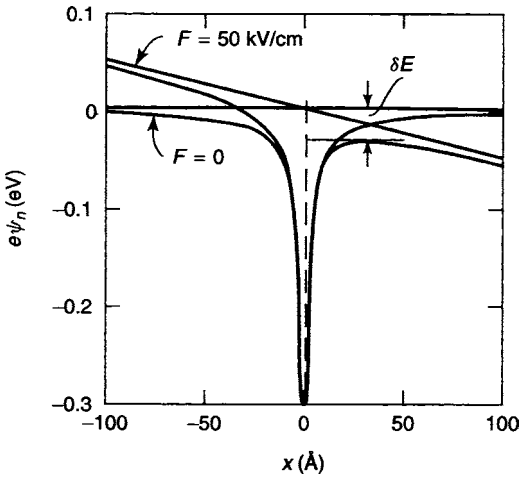

Fig. 4.2. Lowering of the electron binding energy of a Coulomb-attractive center by $\delta e \simeq 30\,mV$ with an external electric field of $50\,kV\,cm^{-1}$ and a distance of $\simeq 35$ Å from the funnel center of the barrier maximum over which the electron can leak out in field direction (Frenkel–Poole effect), as computed for $\varepsilon = 10$ and $F = 50\,\mathrm{kV\,cm^{-1}}$

[7] Except for high mobility semiconductors at low temperatures where impact ionization competes favorably.

$$\delta E = e\sqrt{\frac{eFZ}{\pi\varepsilon\varepsilon_0}} = 2.4\times10^{-4}\sqrt{F(\mathrm{V\,cm^{-1}})}\sqrt{\frac{10}{\varepsilon}Z}. \tag{4.15}$$

This lowering is equal to kT for a field of

$$F_{kT} = 1.165\varepsilon Z \quad (\mathrm{kV\,cm^{-1}}) \tag{4.16}$$

which is on the order of 10 kV cm^{-1} for typical semiconductors. The Frenkel–Poole effect causes an enhancement of the thermal ionization which may be approximated by an increase of the thermal ionization coefficient

$$e_{\mathrm{tc}} = s_n v_{\mathrm{rms}} \exp\left(-\frac{E_c - E_t - \delta E}{kT}\right) \quad \mathrm{(s)}. \tag{4.17}$$

Impact ionization occurs when, between scattering events, the carriers can accumulate sufficient energy from an external field to markedly change their energy distribution, and become "heated." Fast electrons in this distribution when colliding with a defect center, may transfer sufficient energy to free a trapped carrier from the center.

The ionisation rate per unit path length[8] due to impact ionization can be approximated as

$$\alpha_i = C\,\exp\left[-\frac{B(E_c - E_t)}{F^2}\right] \ (\mathrm{cm^{-1}}) \tag{4.18}$$

with C a constant on the order of 1, $B \simeq 4\hbar\omega_{\mathrm{LO}}/(e^2{\lambda_e}^2)$, ω_{LO} the longitudinal optical phonon frequency and λ_e the carrier mean free path (Wolff, 1954).

Tunneling occurs at very high fields, usually across thin insulating layers (typically on the order of $10^6\,V\ cm^{-1}$). The transmission probability of a one-dimensional rectangular barrier of height V_0 and thickness d (in Å) is given by

$$\begin{aligned} T_t &\simeq 16\frac{E}{eV_0}\exp\left\{-d\sqrt{\frac{2m_n}{\hbar^2}(eV_0 - E)}\right\} \\ &\simeq 16\frac{E}{eV_0}\exp\left\{-0.512d\,(\text{Å})\sqrt{(eV_0 - E)\frac{m_n}{m_0}},\right\} \end{aligned} \tag{4.19}$$

where E is the average electron energy, e.g., kT, for thermal electrons.

In an electric field, the barrier becomes triangular and the transition probability can be estimated from

$$T_{t\Delta} \simeq \widetilde{C}\exp\left\{-\frac{4}{3}\sqrt{\frac{2m}{\hbar^2}}\frac{\Delta E^{3/2}}{eF}\right\} \simeq \widetilde{C}\exp\left\{-6.8\times10^7\frac{[\Delta E(V)]^{3/2}}{F(\mathrm{V/cm})}\right\} \tag{4.20}$$

with a pre-exponential $\widetilde{C}$ on about the same magnitude as in (4.19). For a review see, e.g., (Wiersma et al. 1997).

[8] With increased path length in an electric field, more energy is accumulated. The ionization rate per unit path length is measured in cm^{-1}.

4.2 Trapping and Recombination

In the previous sections, we have identified the transitions that require absorption of energy. The inverse transitions that generate energy (e.g., heat or luminescence), shown in Fig. 4.1, are referred to as either trapping or recombination transitions; a differentiation between the two will be discussed in the following section.

4.2.1 Electron and Hole Traps

There are numerous transitions possible between any center and other states. All such transitions can be described by their corresponding rates. These rates are additive and describe the change in population of this center. For example, the change of the electron density in an electron trap can be influenced in four ways: by ionization into, and electron capture from, the conduction band; by recombination with holes from the valence band and by an electron transfer to another localized state of a nearby defect to which such a transition is sufficiently probable.

For reason of *detailed balance*, in each pair of transitions shown in Fig. 4.3, the excitation transition must be equal to the recombination in thermal equilibrium. Usually their magnitude varies from pair to pair over a wide range; e.g., thermal excitation of an electron from the more distant valence band into the electron trap is much less probable than thermal excitation of a trapped electron into the closer conduction band. Therefore, one can usually neglect all pairs of transitions compared to the pair interacting with the nearest band.

With external excitation, or a shift in the carrier distribution by an applied bias, this is no longer necessary. In *steady state*, the total net influx to the center must now equal the net out flux, in order to maintain a constant trap population. Again, with a variation of transition coefficients over many orders of magnitude, one can pick two transitions which are near equal to each other, here, however, not necessarily connecting the center to the same band. This identifies different classes of such centers according to the kind of predominant transition.

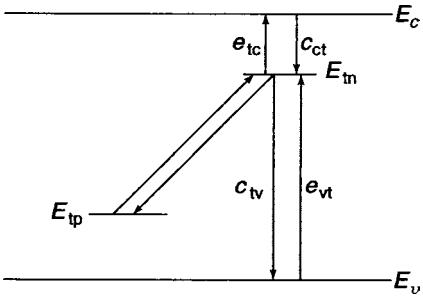

Fig. 4.3. Various possible transitions from and to a localized state

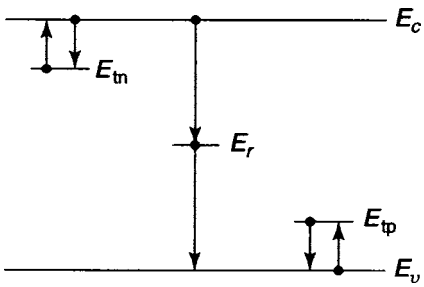

Fig. 4.4. Electron and hole traps at energies E_{tn} and E_{tp} close to the respective bands and recombination centers at an energy E_r closer to the center of the gap

When the predominant pair of transitions communicates with the same band as, e.g., through e_{tc} and c_{ct} the center is identified as a *trap*. Customarily, traps close to the conduction band are identified as *electron traps* and traps close to the valence band as *hole traps*.

4.2.2 Recombination Centers

When the predominant transitions communicate between two bands as, e.g., through c_{ct} and c_{tv}, the center is called a *recombination centre* (Fig. 4.4). Recombination centers usually lie closer to the middle of the band gap and communicate readily with both bands since it is easier for a captured electron to recombine with a hole in the valence band than to be thermally re-emitted into the conduction band. It is expected that such recombination centers are activated only when sufficient holes are available, e.g., with optical excitation or in certain regions of a junction with an external bias. We will analyse this relation in the following section.

4.3 Quasi-Fermi Levels, Demarcation Lines

With external means, e.g., light or bias, the electron distribution over levels and bands is changed from the thermodynamic equilibrium distribution. Given sufficient time, the changed distribution becomes stationary, and the *steady state* is achieved. This new electron distribution near the band edges can again be approximated by a Fermi-type distribution, however, replacing the Fermi level with two quasi-Fermi levels, one for electrons E_{Fn} and one for holes E_{Fp}. The measured electron density in the conduction band can now be used to define E_{Fn} via[9]

$$n \simeq N_c \frac{1}{1+\exp\left(\frac{E_c - E_{Fn}}{kT}\right)}; \tag{4.21}$$

[9] The exact relation contains the Fermi integrals $F_{1/2}$ (see (Böer 1985)). The approximation only holds for the nondegenerate case, i.e., for $E_c - E_{Fn} > kT$.

the hole density in the valence band defines E_{Fp} via

$$p \simeq N_v \frac{1}{1+\exp\left(\frac{E_{Fp}-E_v}{kT}\right)}. \tag{4.22}$$

With external excitation, n and p will both be larger than the equilibrium densities; hence, E_{F} will be split into E_{Fn} and E_{Fp} with[10]

$$E_{Fp} < E_{\mathrm{F}} < E_{Fn}. \tag{4.23}$$

With intrinsic ($h\nu > E_g$) optical excitation, electrons and holes are generated in equal rates. The increase of the steady state carrier densities above the thermal equilibrium densities in typical semiconductors[11] is usually only a small fraction for majority carriers, while it is very large for minority carriers. Therefore, most semiconductors show only a slight split of the majority quasi-Fermi level from E_{F}, while the minority quasi-Fermi level is changed substantially.

We will now analyst the relative strength of the various transitions for a level in the band gap. With external excitation, the changing occupation of the level and bands causes the transition rates to change, making, for deeper levels, the recombination transitions more probable than the re-emission into the adjacent bands. Since that re-emission depends exponentially on the energy difference between the level and the nearest band edge, one can now define a *demarcation line* between traps and recombination centers by the condition that the transition rates of electrons from this center to the two bands become equal to each other. For example, for electron traps one can compare the excitation rate into the conduction band with the recombination transition into the valence band and require,

$$n_t e_{\mathrm{tc}} N_c = n_t c_{\mathrm{tv}} p. \tag{4.24}$$

Using (4.8) for e_{tc} and (4.22) for p, one obtains the condition that defines the *electron demarcation line* when setting $E_t = E_{Dn}$ for this specific trap level that fulfills (4.24). This yields

$$E_c - E_{D_n} = E_{F_p} - E_v + \delta_i, \tag{4.25}$$

with

$$\delta_i = kT \ln\left[\frac{m_n s_n}{m_p s_p}\right]. \tag{4.26}$$

The demarcation line for electrons defines the energy that separates electron traps above and recombination centers below E_{Dn}. The reference to a *hole*

[10] The inequality of (4.23) holds for optical excitation but not for shifted distribution in *pn*-junctions in reverse bias (see Sect. 6.2).

[11] In good photoconductors, however, the majority quasi-Fermi level is also substantially changed.

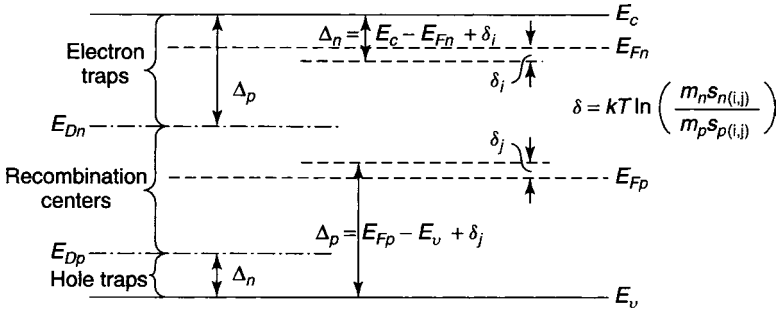

Fig. 4.5. Band-model with quasi-Fermi levels and demarcation lines for one kind of electron traps (with capture cross sections for electrons and holes s_{ni}, s_{pi}) and a corresponding kind of hole traps (with s_{nj}, s_{pj})

quasi-Fermi level for determining the *electron* demarcation line is understandably confusing at first, but it is based on the fact that the recombination path which competes with thermal ionization depends on the availability of free holes which in turn relates to E_{Fp}. A look at Fig. 4.5 helps to clarify this dependency: the distance of the demarcation line for electrons from the conduction band is the same as the distance of the quasi-Fermi energy for holes from the valence band plus a corrective energy δ_i, which is logarithmically related to the ratio of capture cross sections for electrons and for holes of this center and their effective masses.

A similar relationship holds for the *hole demarcation* line:

$$E_{Dp} - E_v = E_c - E_{Fn} + \delta_j \tag{4.27}$$

(see Fig. 4.5). Neglecting the influence of the correction terms[12] δ_i and δ_j, the anti-symmetric relation of the quasi-Fermi and demarcation lines is obvious:

[12] For estimating δ_i and δ_j, one needs to know the center's cross section, which may be estimated from the center's charge and bonding character. For example, a center that is neutral without an electron in it has a cross section for an electron on the order of $10^{-16}\,\mathrm{cm}^2$. After it has captured the electron, it is negatively charged; thus, its capture cross section for a hole has increased to $\approx 10^{-14}\,\mathrm{cm}^2$. For this example, $s_n/s_p \simeq 10^{-2}$ and $\delta_j \simeq -0.12\,\mathrm{eV}$ will be used. For hole traps, the charge character may turn from neutral to positive after hole capture, making $s_n/s_p \simeq 100$ and $\delta_j \simeq +0.12\,\mathrm{eV}$. The shifts δ_i and δ_j in Fig. 4.5 have been chosen accordingly. Other charge characters are possible, such as for Coulomb-repulsive centres, which have capture cross sections of $\approx 10^{-20}$ to $10^{-22}\,\mathrm{cm}^2$. Tightly bound centers usually provide relatively small cross sections (typically $10^{-18}\,\mathrm{cm}^{-2}$ or below for centers with deep relaxation – see (Böer 1985)). Since the capture cross section may vary from center to center from $\approx 10^{-13}$ to $\approx 10^{-22}\,\mathrm{cm}^2$, δ_i varies for these different centers by as much as $\approx 0.5\,\mathrm{eV}$; hence the demarcation lines of these centers are spread over a wide range within the band gap. Therefore, it is not customary to plot demarcation lines of all possible centers, but, if at all only those demarcation lines are shown that provide the most important transitions in the given device model.

for n-type material with a comparatively narrow $E_c - E_{Fn}$ range, there is a wide range of electron traps and a narrow range of hole traps (and vice versa).

4.3.1 Thermal Equilibrium and Steady State

Thermodynamic (thermal) equilibrium is present when a semiconductor is kept at a constant temperature without any outside bias or excitation for a sufficient length of time. Deviations from thermal equilibrium can occur because of nonthermal excitation by light or electrical field, or by a shift of the carrier distribution in junctions with nonvanishing currents. When such deviations occur, and have become stationary, a steady state nonequilibrium is reached. We will first discuss the thermal equilibrium condition in more detail.

4.3.1.1 Zero Net-Current, Thermal Equilibrium

In thermal equilibrium, electrons and holes are generated by thermal ionization only. The same amount of carriers generated in any volume element must recombine in the same volume element. There is no net transport of carriers, except for statistical fluctuations.

When a space–charge region is introduced, the densities of carriers change from their bulk value. The balance between generation and recombination, however, is still maintained throughout the bulk and in the entire space–charge region as long as there is no external force, e.g., there is no bias applied. The net[13] electron and hole currents in each volume element are individually zero; aside from fluctuations, electrons or holes are not brought in or carried away from any volume element. With vanishing bias, thermal equilibrium is maintained throughout the space–charge region.

For thermal equilibrium, the carrier distribution is given by one Fermi level E_{F}. Consequently, when using $E_{Fn} = E_{Fp} = E_{\mathrm{F}}$ in (4.25) and (4.27), the resulting demarcation lines also coincide: $E_{Dn} = E_{Dp} = E_{\mathrm{D}}$, i.e., causing electron and hole traps to join borders with each other with no recombination centre range existing in between.

In thermal equilibrium, an important relation between n and p can be derived for nondegenerate semiconductors. From $n = N_c \exp[-(E_c - E_{\mathrm{F}})/(kT)]$ and $p = N_v \exp[-(E_{\mathrm{F}} - E_v)/(kT)]$, one obtains,[14]

$$\boxed{n_0 p_0 = N_v N_c \exp\left(-\frac{E_c - E_v}{kT}\right) = n_i^2.} \tag{4.28}$$

[13] A diffusion current of each carrier is exactly compensated by an opposing drift current.

[14] In order to emphasise the equilibrium values of n and p, we have attached a subscript zero.

This condition permits the calculation of $p_0(x)$ throughout a device *in thermal equilibrium* if $n_0(x)$ is known, since n_i, the intrinsic carrier density, is a constant given by the band gap and temperature alone.

4.3.1.2 Nonvanishing Current, Steady State

When a bias is applied, the flow of a net current results. The carrier density distribution is deformed from equilibrium; then, the carriers generated in one volume element are moved to another one by the current before they recombine. In forward bias, this results in a carrier surplus, while in reverse bias it results in a carrier depletion within a Schottky barrier. The balance between the two transitions of a center to its adjacent band is disturbed, and a net generation or recombination through such centers results.

As a consequence, the Fermi level splits into two quasi-Fermi levels, and the two demarcation lines separate; hence, some levels which acted as traps before will now act as recombination centers.

When changing the bias, this distribution changes. One, therefore, needs to include all four transitions to the two bands for deeper centers that may become recombination centers (Fig. 4.6)[15]. These centers are called Schottky–Read–Hall centres. The net traffic through these centers is conventionally identified as U, given by

$$U = \frac{c_{\mathrm{cr}} c_{\mathrm{rv}} N_r (np - n_i^2)}{c_{\mathrm{cr}} \left[n + n_i \exp\left(\frac{E_r - E_i}{kT}\right)\right] + c_{\mathrm{rv}} \left[p + n_i \exp\left(\frac{E_i - E_r}{kT}\right)\right]} \tag{4.29}$$

or

$$\boxed{U = \frac{c_{\mathrm{cr}} c_{\mathrm{rv}} N_r (np - n_i^2)}{c_{\mathrm{cr}} (n + n_i^+) + c_{\mathrm{rv}} (p + n_i^-)}} \tag{4.30}$$

with

$$n_i^{\pm} = \exp\left(\pm \frac{E_r - E_i}{kT}\right) \tag{4.31}$$

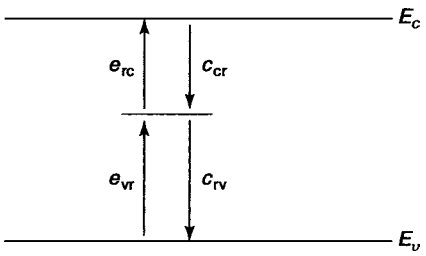

Fig. 4.6. Shockley–Read–Hall center with all transitions to both bands

[15] Since these centers are more important when they become recombination centres, they are identified here with the subscript r.

and the *intrinsic energy level*, E_i,:

$$E_i = \frac{E_c - E_v}{2} + \frac{kT}{2} \ln\left(\frac{N_v}{N_c}\right). \tag{4.32}$$

This equation is representative for the sequential nature of the recombination through a recombination center: an electron from the conduction band *and* a hole from the valence band must both find their way to the recombination centre; the equation for the net recombination traffic (4.30) is therefore of the type $(1/n + 1/p)^{-1}$. Thus, only when both carrier densities are high, is the recombination traffic large; the minority carrier limits the recombination. This will be of importance in *pn*-junctions, where only in the inner part of the junction region both densities are on the same order of magnitude, causing a substantially higher recombination here than in the adjacent bulk regions (see Sect. 4.4 and Fig. 4.9).

From (4.29), one confirms also that U vanishes for thermal equilibrium; i.e., for $np = n_i^2$

U represents a *net thermal generation* when, with reverse bias, the np product in the space charge region has decreased below its equilibrium value[16] n_i^2. A *net recombination* through the center occurs when with forward bias[17] the np-product exceeds n_i^2.

A simplified relation is occasionally used, assuming a center with equal capture coefficients[18] for electrons and holes ($c_{cr} = c_{rv} = c$). Equation (4.29) can then be reduced to

$$\boxed{U = \frac{cN_r(np - n_i^2)}{n + p + 2n_i \cosh\left(\frac{E_r - E_i}{kT}\right)}.} \tag{4.33}$$

4.3.2 Current Continuity

The difference between generation and recombination is carried as an increment to the current (Fig. 4.7a). For example, one obtains for the change of the incremental[19] electron current

$$\frac{\mathrm{d}\delta j_n}{\mathrm{d}x} = -eU = -e(g - r) \tag{4.34}$$

[16] Here both $n(x)$ and $p(x)$ have decreased below the equilibrium distribution, while the space-charge region has widened.

[17] Here, both $n(x)$ and $p(x)$ have increased above the equilibrium values.

[18] This assumption is **not** a very realistic one since the charge character of the center changes when capturing a carrier (see Sect. 4.2.2). However, the qualitative behavior deduced from (4.33) will remain valid.

[19] We are using here the notation of an incremental current since in some of the devices only a fraction of the total electron or hole current is influenced, as will be described below.

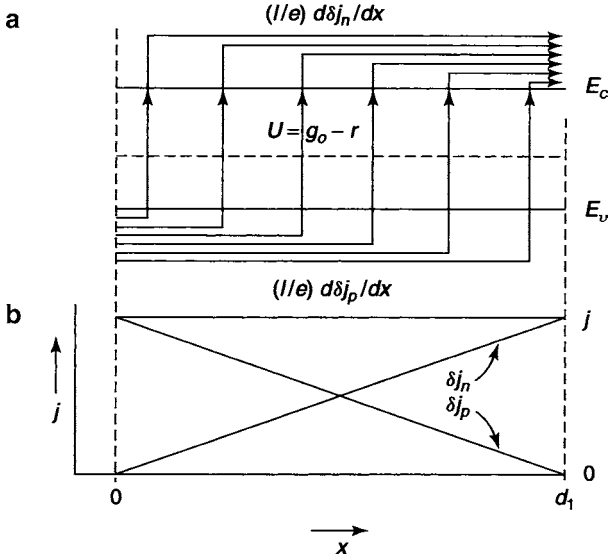

Fig. 4.7. Current generation with bias in a homogeneous region of $r < g_o$ ($g_o =$ optical excitation is assumed here) with resulting positive electron current increment. (**a**) Band-model; (**b**) incremental current distribution

and consequently, for the change of the incremental hole current

$$\frac{\mathrm{d}\delta j_p}{\mathrm{d}x} = eU = e(g - r), \tag{4.35}$$

with the *total incremental current* to remain constant,

$$\frac{\mathrm{d}\delta j}{\mathrm{d}x} = \frac{\mathrm{d}(\delta j_n + \delta j_p)}{\mathrm{d}x} \equiv 0. \tag{4.36}$$

Figure 4.7b shows the contributions of the incremental hole and electron currents, which are complementary to each other, to the total current. The figure gives a simple example of a constant, net generation rate U, which can be realised by a uniform optical carrier generation within a homogeneous semiconductor and a sufficient lifetime to render the diffusion length long compared to the width of the device. In the given example the electron current then increases linearly from $x = 0$ to $x = d_1$, while the hole current decreases with the same rate: the incremental current changes from a hole current at the left side to an electron current at the right side of the semiconductor. This crossover and the current continuity are indicated in the band-model of Fig. 4.7a.

In most semiconductors, and at normal optical excitation rates, the majority carrier density is changed only to a small fraction from its equilibrium

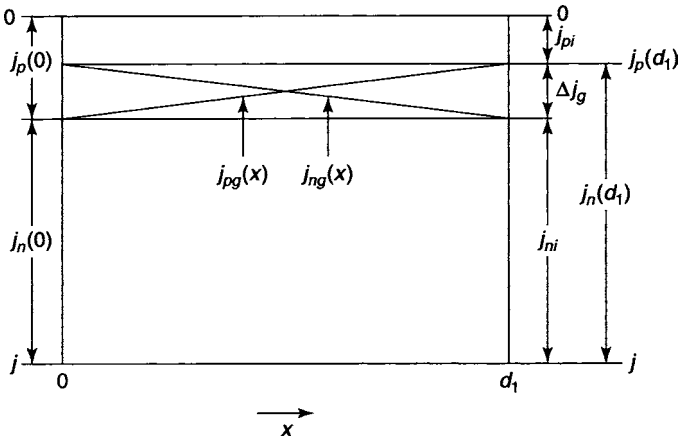

Fig. 4.8. Current distribution; generation/recombination currents are assumed for a homogeneous optical excitation and therefore are simple linear functions of x. The divergence-free hole and electron currents are shown as bands above and below the generation/recombination part

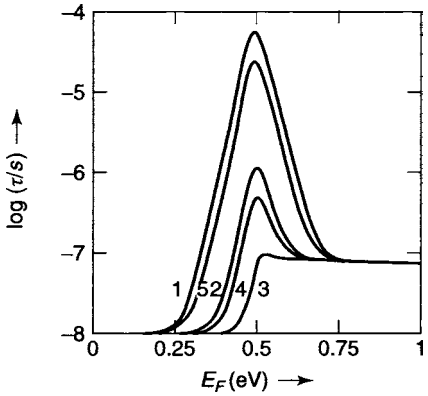

Fig. 4.9. The distribution of lifetimes in a pn-junction is shown as a function of the position of the Fermi-level (i.e., its composition) in a Shockley–Read–Hall model according to (4.47) for $N_c = 10^{19}\,\mathrm{cm}^{-3}$, $N_v = 5 \cdot 10^{18}\,\mathrm{cm}^{-3}$, $E_c - E_v = 1\,\mathrm{eV}$, $\tau_{p0} = 10^{-7}\,\mathrm{s}$, $\tau_{n0} = 10^{-8}$ when, $\delta n = \delta p = 0$. Family parameter is the location of the recombination center $E_r = 0.25$, 0.35, 0.45, 0.55, and 0.65 eV for curves 1–5, respectively

value. This means that the incremental currents as shown in Fig. 4.7 and given by

$$\delta j = \delta j_n(x_i) + \delta j_p(x_i) \quad \text{at any} \quad 0 < x_i < d_1 \tag{4.37}$$

have to be added to the divergence-free majority carrier current j_{ni} (see Fig. 4.8).

In this figure, we have also included for completeness a small equilibrium minority carrier current j_{pi} as a divergence-free contribution. The total current is then given by

$$j = j_{ni} + j_{pi} + \delta j = e\mu_n n_0 F + e\mu_p p_0 F + \delta j \tag{4.38}$$

with n_0 and p_0 as the carrier densities in equilibrium in a homogeneous semiconductor.[20]

The generation/recombination (gr-) contribution which can be dealt with in the fashion given here only for narrow devices [with $d_1 < (L_n,\ L_p)$], however, becomes essential for the current–voltage characteristics of junctions and will be discussed extensively in Sect. 5.

4.4 Carrier Lifetimes

The carrier lifetime is an important parameter, especially in a semiconductor in which minority carriers cannot be neglected. In the analysis of such a carrier lifetime, we will include the carrier transport in an inhomogeneous semiconductor in which this discussion is essential for the understanding of its electrical behavior.

When external forces, such as a bias or light are applied to cause deviations from the thermodynamic equilibrium, the distribution returns to equilibrium after these forces are removed with a characteristic time constant. If, for example, the electron density at a certain position x_0 in the space-charge region changed from n_0 to $n_0 + \delta n_i$ with forward bias, the return to its original value can be described by

$$\delta n(t) = \delta n_i \exp\left(-\frac{t}{\tau_n}\right), \tag{4.39}$$

with τ_n, the lifetime of the excess electrons.

Such exponential decay can be obtained from the reaction kinetic equation including current continuity; for electrons, one obtains,

$$\frac{\partial n}{\partial t} = g - r + \frac{1}{e}\frac{\mathrm{d}\delta j_n}{\mathrm{d}x} = -U + \frac{1}{e}\frac{\mathrm{d}\delta j_n}{\mathrm{d}x}; \tag{4.40}$$

i.e., the change in electron population at a certain volume element is given by the difference of "birth" minus "death rates" plus the net "drop-off" of carriers from surrounding regions of the semiconductors.

After steady state is reached, one has

$$\frac{\partial n}{\partial t} \equiv 0. \tag{4.41}$$

[20] In an inhomogeneous semiconductor, the determination of the divergence-free electron or hole current is a bit more involved and is discussed in Section 6.1.2.1.

When the bias is removed, δj_n and $\mathrm{d}\delta j_n/\mathrm{d}x$, vanish, and the change in carrier density is given by

$$\frac{\partial n}{\partial t} = -U, \tag{4.42}$$

with U given by (4.29). In order to orient ourselves about the influence of this rather than the complex net recombination, let us first replace (4.29) by the simplified approximation (4.33) and observe the decay of a minority carrier density after the termination of a forward bias. Here, at the beginning of the decay, one has $np \gg n_i^2$ and in the p-type region with $p \gg (n, n_i \cosh[(E_t - E_i)/(kT)])$, one obtains

$$U = c_{\mathrm{cr}} N_r n, \tag{4.43}$$

which yields the well-known relation

$$\frac{\partial n}{\partial t} = -c_{cr} N_r n. \tag{4.44}$$

The solution of (4.44) is of the form given in (4.39) with a time constant, and the electron (i.e., the minority carrier) lifetime:

$$\boxed{\tau_{n0} = \frac{1}{c_{cr} N_r} = \frac{1}{v_n s_n N_r}.} \tag{4.45}$$

From (4.29), it is obvious that up to eight cases of different carrier lifetimes may be distinguished, depending on whether the deviation from thermal equilibrium was caused by forward or reverse bias, or which of the terms in the denominator of (4.29) is dominant.

The hole lifetime can be obtained in the same fashion in the n-type part of the junction, where holes are the minority carriers, after release of forward bias, yielding

$$\boxed{\tau_{p0} = \frac{1}{c_{rv} N_r} = \frac{1}{v_p s_p N_r}.} \tag{4.46}$$

In any region of the semiconductor, the minority lifetime can then be described as a polynomial in[21] τ_{n0} or τ_{p0}; e.g., for electrons one has

$$\tau_n = \frac{\tau_{n0}(p_0 + p_1 + \delta p) + \tau_{p0}(n_0 + n_1 + \delta n)}{n_0 + p_0 + \delta n}. \tag{4.47}$$

In general, the carrier lifetime in a two-carrier semiconductor is given by

$$\boxed{\tau_n = \frac{n}{U}} \tag{4.48}$$

[21] Equation (4.47) can be obtained from (4.30), (4.45), and (4.46) with $n = n_0 + \delta n$ and $p = p_0 + \delta n$ and using $n_0 p_0 = n_i^2$ and $\delta n = \delta p$, when traps can be neglected, since electrons and holes are mutually created, and for n as minority carrier, assuming $\delta n \gg n_0$.

or

$$\boxed{\tau_p = \frac{p}{U}} \tag{4.49}$$

and U can be expressed, when using τ_{n0} and τ_{p0} given in (4.45) and (4.46), from (4.30) by

$$\boxed{U = \frac{np - n_i^2}{\tau_{p0}(n + n_i^+) + \tau_{n0}(p + n_i^-)}.} \tag{4.50}$$

From (4.48) and (4.49), it is obvious that in thermal equilibrium ($U = 0$) the carrier lifetime is infinity. Only when deviating from equilibrium do τ_n and τ_p become finite, depending on the spread of the demarcation lines that is a measure of the density of the acting recombination centers. That is, as shown above, *carrier lifetimes, are never the same throughout a semiconducting device including a junction*; they depend on the spread of the demarcation lines and may change substantially from part to part of the semiconductor. When using a given value for such a lifetime throughout an entire n- or p-type region, one must be aware that this is an approximation that may or may not be justified (see next section).

Examples for this computed lifetime distribution are given in Fig. 4.9, as a function of the position of the Fermi level in a semiconductor of an assumed band gap of $E_g = 1\,eV$. There are two ways in which this figure can be read:

(a) for a set of homogeneous semiconductors in which the Fermi level was changed by various doping or
(b) in one semiconductor in which the doping changes as a function of the position, producing a pn-junction.

The figure shows nearly constant lifetimes τ_{n0} and τ_{p0} in the bulk of the p- and n-type materials respectively, a slope when the Fermi level moves toward the center of the band gap and a maximum, when E_F coincides with the intrinsic level E_i. This occurs in well compensated intrinsic semiconductors or at the interface of a pn-junction.

We will return to a discussion of the net generation rate and lifetimes when we analyze the solution curves for the junction variables in Sect. 6.1.2.1.

4.4.1 Large Generation, Optical Excitation

When a large enough optical generation is considered, the deviation of both the carrier densities from the equilibrium value can become large; i.e., when $\delta n \gg n_0$ or $\delta p \gg p_0$. Then, one has $p_1 \ll p = p_0 + \delta p$ and $n_1 \ll n = n_0 + \delta n$; hence, here, only the two main lifetimes τ_{p0} and τ_{n0} apply as long as the recombination of the minority carriers proceeds via these recombination centres.

With optical excitation in excess of the thermal generation rate, the total generation rate can be approximated by g_o (Sect. 4.1.2). This is a reasonable

assumption in homogeneous good photoconductors, e.g., in CdS. The steady state minority carrier density is then simply given by

$$n_{10} = g_o \tau_{n0} \quad \text{or} \quad p_{10} = g_o \tau_{p0} \tag{4.51}$$

with τ_{n0} and τ_{p0} given by (4.45) and (4.46), respectively.

When the minority carrier density approaches the majority carrier density, so that

$$\frac{c_{\mathrm{cr}}}{c_{\mathrm{rv}}} \frac{n}{p} \simeq \frac{s_n n}{s_p p} \simeq 1, \tag{4.52}$$

a "clogging" of this recombination path can occur by reducing the fraction of available recombination centers. Consequently, the respective lifetime increases. This may occur for centers with largely different cross sections, e.g., for repulsive vs. neutral centers where s_n can be four to six orders of magnitude different from s_p, counteracting the usually large differences of n and p. Again, a good example is CdS where such centers appear with copper doping and are usually referred to as fast and slow recombination center with their charge character changing by changing their (here) hole occupation.

Summary and Emphasis

In contrast to the homogeneous semiconductor, minority carriers have a major influence on the carrier transport in most inhomogeneous semiconductors, except for a few instances where an appropriate description can still be given from a single carrier model.

The influence of minority carriers is exerted through the balance between generation and recombination including a net transport of carriers from one to another volume element as soon as their density deviates substantially from thermodynamic equilibrium.

The most important deviation from equilibrium is caused by optical excitation or by the application of a bias in devices with space-charge regions. Here, the equilibrium balance becomes significantly distorted. Recombination becomes enhanced wherever the carrier density exceeds thermodynamic equilibrium.

Quasi-Fermi levels are a convenient means to describe the changed carrier distribution within a device in steady state. The magnitude of the split between the quasi-Fermi levels for electrons and holes indicates the degree of deviation from thermal equilibrium.

Demarcation lines are introduced as additional indicators to separate traps from recombination centers. Even though related to quasi-Fermi levels, that are well defined by the carrier densities in each band, the demarcation lines are far less general, since they depend on the specific capture cross section and, therefore, are individually shifted for different types of recombination centers. They are consequently rarely used for the characterisation of the device behavior, except when specific centers are dominant.

Recombination through such centers depends on their relative positions in the band gap and the position of the Fermi level. They are most active when they are close to the center within the part of the device that is nearly compensated (e.g., in the center plane of a *pn*-junction).

Generation, recombination and the internal currents play an important role for the device performance. The intricate interplay between majority and minority carriers, easily separated in semi-empirical models, need to be augmented by microscopic defect-center information to provide a more realistic guidance to the evaluation of generation and recombination traffic in actual devices. Specifically, the change of capture parameters of recombination centers after capturing the first carrier need to be considered carefully when estimating the completion of the recombination event with the capture of the complimentary carrier in another now recharged center.

Exercise Problems

1.(*) For carrier generation, three types of energies (thermal, optical and electric field) are mentioned as important contributors in semiconductor devices. Are there other forms of energy to excite electrons? Name two. Discuss when these can play a measurable role in the performance of semiconductor devices.

2.(l) We have not mentioned Auger recombination in this chapter. Under what circumstances would Auger recombination be an important contributor? What are the physical characteristics of Auger recombination?

3.(l) Estimate the optical generation rate $g_o(x)$ for AM1 sunlight in a Si single crystal platelet at room temperature.

4.(e) Calculate the threshold Frenkel–Poole generation rate (i.e., when δE reaches kT) as a function of the electric field for $T = 4$, 100, and 300 K for Coulomb attractive centers in Si and GaAs.

5.(e) Determine the field strength at which tunneling through the upper part of the barrier of a Coulomb-attractive center would have to be considered in addition to the Frenkel-Poole barrier lowering.

6.(*) Steady state can be reached after changes in excitation within a reasonable elapsed time if the quasi-Fermi level is closer than 0.8 eV from the corresponding band edge. What does this statement mean for minority carriers in a GaAs device? Specifically,

   (a) How much of an optical generation rate do you need to guarantee achievement of steady state across the device within 1 s with a minority carrier lifetime of 10^{-7} s?

   (b) What does this mean for a *pn*-junction device without optical excitation for alternating current bias?

7.(*) There are three classes of recombination centers in an actual device. In GaAs with $E_{Fp} - E_v = 0.5\,\text{eV}$ and $E_c - E_{Fn} = 0.2\,\text{eV}$, where would the demarcation lines fall
   (a) For a Coulomb-attractive center for electrons, with a corresponding funnel cross section of $10^{-13}\,\text{cm}^2$?
   (b) For a Coulomb-attractive center for holes with the same capture cross section?
   (c) For a deep center with a capture cross section for both carriers of $10^{-18}\,\text{cm}^2$?
   (d) For a neutral center with a capture cross section of $10^{-16}\,\text{cm}^2$ for capturing the first carrier. Then, it turns into Coulomb-attractive center for capturing the oppositely charged carrier, with a capture cross section as described in (a) or (b).

8. Derive (4.26) from the condition for the demarcation line given in (4.24).

9.(e) Usually, the divergence-free minority carrier current is totally negligible compared to the majority carrier current in a homogeneous semiconductor. In the linear plotting of Fig. 4.8, it is not.
   (a) Calculate the position of the Fermi level that would correspond to the given figure.
   (b) How much light would you need to obtain the given generation/recombination currents in a semiconductor with $E_\text{g} = 1\,\text{eV}$ and a carrier lifetime of $10^{-7}\,\text{s}$?
   (c) What is the maximum device width to permit the figure to be essentially correct? Assume $\mu = 100\,\text{cm}^2\,\text{Vs}^{-1}$ and $T = 300\,\text{K}$.

10. Derive the simple lifetime condition (4.45) from the generation/recombination traffic through a Hall–Shockley–Read center and discuss the necessary conditions required.

11.(*) Discuss the validity of (4.48) and (4.49) for the carrier lifetime and its implication in respect to kinetic changes in carrier density after termination of the optical excitation.

5

Minority Carrier Currents

Summary. Minority carrier currents of technical interest are predominantly diffusion currents and are controlled by the boundary concentration of minority carriers that can be influenced by the bias across an adjacent space-charge region. These currents are in competition with recombination currents at device surfaces or interfaces.

Minority carrier currents are insignificant in homogeneous semiconductors, since the density of minority carriers is usually smaller by orders of magnitude compared to that of majority carriers. However, when a space-charge layer is introduced, e.g., as a Schottky barrier or a *pn*-junction, then the majority carrier current is dramatically reduced in reverse bias and can be augmented markedly by the minority carrier current. Such current contributes to the *diode leakage current*, or, with external optical excitation results in the *photodiode current*.

In order to lay the groundwork for an understanding of the minority carrier current contribution, we will first separate the discussion of these currents from other influences within a space-charge layer. This requires the introduction of a substantially simplified model.

We will assume a thin *n*-type Ge slab with a metal electrode on the right and a optically transparent surface on the left that may be covered with a transparent, neutral electrode. We first deal with the thermally generated minority carriers and later with the optically generated ones. The minority current near the transparent electrode and the bulk is controlled by the minority carrier density at the surface boundary. Let us first focus on that boundary. Depending whether the density on this boundary lies above ($p_c^{(u)}$) or below ($p_c^{(l)}$) the bulk density p_{10}, a diffusion current of minority carriers (holes) flows from this boundary into (injection) the bulk or from the bulk (carrier collection) into the boundary (Fig. 5.1)[1].

[1] These conditions can be realised by optical excitation with intrinsic light that is absorbed close to the surface (carrier injection), or for the opposite case by excessive carrier recombination at the surface.

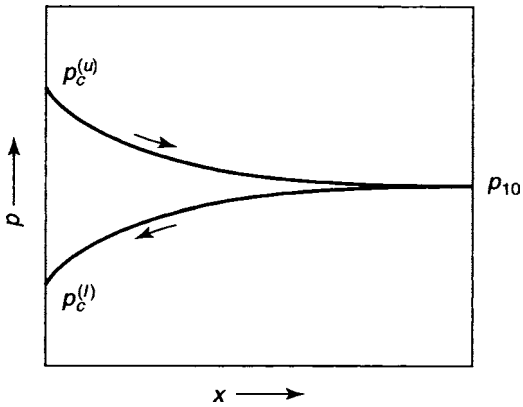

Fig. 5.1. Schematic sketch of the minority carrier distribution with the left boundary held at $p_c^{(u)}$ or $p_c^{(l)}$ for an upper (u) or lower (l) boundary density, and a diffusion current flowing toward or from the bulk, respectively (*arrows*)

5.1 Minority Carrier Currents in the Bulk

The majority carrier density in the bulk regions of most semiconductor devices is much larger than the minority carrier density. Therefore, any field that produces a reasonable drift current of majority carriers here, produces a negligible drift current of minority carriers. There are, however, occasions in which the minority carrier gradients are large enough to make the corresponding minority carrier diffusion current compatible with the net majority carrier current. We will analyze this current here in more detail and will assume throughout the chapter that the electrons are majority and the holes are minority carriers.

The hole (minority carrier) diffusion current is given by

$$j_{\mathrm{gr}} = -\mu_p kT \frac{\mathrm{d}p}{\mathrm{d}x}, \tag{5.1}$$

and with carrier generation or recombination, must also follow the current continuity equation (see Sect. 4.3.2)

$$\frac{dj_{\mathrm{gr}}}{\mathrm{d}x} = -eU. \tag{5.2}$$

These currents are related to concurrent changes of the electron current and therefore referred to as *generation/recombination currents* (gr-currents).

5.1.1 Thermal Excitation GR-Currents

When the hole density at the left boundary is lowered below the thermodynamic equilibrium value p_{10}, a net generation rate results (4.29) in the adjacent bulk region that can be approximated[2] by

[2] This approximation results from the fact that in the bulk the majority carrier density $n \gg \{p,\ 2n_i \cosh[-(E_i - E_t)/(kT)]\}$.

$$U = \frac{np - n_i^2}{\tau_{p0} n_{10}} = \frac{p - p_{10}}{\tau_{p0}} = g_{\text{th}} - r, \tag{5.3}$$

with a thermal generation rate

$$g_{\text{th}} = \frac{p_{10}}{\tau_{p0}}, \tag{5.4}$$

that exceeds the recombination rate

$$r = -\frac{p}{\tau_{p0}}. \tag{5.5}$$

When the hole density at the left boundary is raised above p_{10}, then $U > 0$, and it represents a net recombination rate.

5.1.1.1 The Diffusion Equation and its Solution

By differentiating (5.1), inserting it into (5.2) and replacing U with (5.3), one obtains the *minority carrier diffusion equation*,

$$\frac{\mathrm{d}^2 p}{\mathrm{d}x^2} = \frac{p_{10} - p}{L_p^2}, \tag{5.6}$$

where, L_p is the *diffusion length*:

$$\boxed{L_p = \sqrt{\frac{\mu_p k T \tau_{p0}}{e}} \simeq 0.15 \sqrt{\frac{\mu_p}{1000}} \sqrt{\frac{T}{300}} \sqrt{\tau_p},} \tag{5.7}$$

i.e., the average distance to which a carrier can proceed during a random walk in its lifetime.

The diffusion equation has the solution

$$p(x) = A \sinh\left(\frac{x}{L_p}\right) + B \cosh\left(\frac{x}{L_p}\right) + p_{10}. \tag{5.8}$$

A and B are obtained from the boundary conditions at the two surfaces, respectively. We obtain B from[3] $p(x = 0) = p_{j\text{D}}$:

$$B = p_{j\text{D}} - p_{10}. \tag{5.9}$$

We obtain the second boundary condition from the current at the other surface $x = d_1$. We will first assume that $j_{\text{gr}}(d_1) = 0$, which yields from (5.1)

$$\frac{\mathrm{d}p}{\mathrm{d}x} = 0 \quad \text{at} \quad x = d_1, \tag{5.10}$$

[3] We have used, here, $p_j D$ to indicate that the hole density at the boundary may depend on the current through the boundary.

hence,

$$A = B \tanh\left(\frac{d_1}{L_p}\right). \tag{5.11}$$

This yields from (5.8)

$$p(x) = p_{j\mathrm{D}} - p_{10}\left[\tanh\left(\frac{d_1}{L_p}\right)\sinh\left(\frac{-x}{L_p}\right) + \cosh\left(\frac{-x}{L_p}\right)\right] + p_{10}, \tag{5.12}$$

which is shown computed in this section with parameters that are the same as for the Schottky barrier which will be discussed in the following section to permit a simple comparison of the figures in these chapters. Specifically we have chosen $n_i = p_{10} = 5\times10^{10}\,\mathrm{cm}^{-3}$, $\mu_p = 1,900\,\mathrm{cm}^2/\mathrm{Vs}$ for germanium and if not otherwise stated, $\tau_{p0} = 10^{-7}\,\mathrm{s}$. In Fig. 5.2, a set of such solution curves is shown with $p_{j\mathrm{D}}$ as a family parameter. p decreases or increases monotonically from its initial value $p_{j\mathrm{D}}$ at $x = 0$ and approaches the thermal equilibrium value $p_{10}(= 5 \times 10^{10}\,\mathrm{cm}^{-3})$ for x larger than L_p.

When introducing $p(x)$ into the diffusion current equation (5.1), one obtains:

$$\boxed{j_{\mathrm{gr}}(x) = ev_{\mathrm{D}}(p_{j\mathrm{D}} - p_{10})\left[\tanh\left(\frac{d_1}{L_p}\right)\cosh\left(\frac{-x}{L_p}\right) + \sinh\left(\frac{-x}{L_p}\right)\right],} \tag{5.13}$$

with the *diffusion velocity*

$$\boxed{v_{\mathrm{D}} = \frac{L_p}{\tau_p} = \sqrt{\frac{\mu_p kT}{e\tau_p}} \simeq \sqrt{\frac{8.3\cdot10^{-8}}{\tau_p}}\sqrt{\frac{\mu}{1000}\frac{T}{300}}.} \tag{5.14}$$

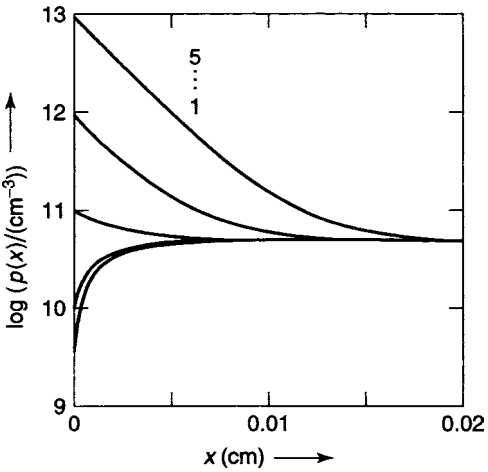

Fig. 5.2. Minority carrier density distribution as a function of the distance from the left surface. Family parameter is the boundary density $p(x = 0) = p_{j\mathrm{D}}$, for a slab of width $d_1 = 2 \times 10^{-2}\,\mathrm{cm}$ plotted in a semi-logarithmic scale

It is important to recognise that this diffusion velocity is on the order of 3 cm/s at $\tau_p = 10^{-8}$ s and *decreases* with increasing minority carrier lifetime. Though the diffusion length *increases* proportional to the diffusion, the velocity decreases proportional to τ_p, since it takes longer for the random walk of holes to move through the increased diffusion length, causing the diffusion velocity to decrease proportional to $\sqrt{\tau_p}$.

The gr-current now decreases exponentially[4] from the left boundary into the bulk when its thickness d_1 exceeds the diffusion length:

$$j_{\mathrm{gr}}(x) \simeq e v_{\mathrm{D}} (p_{j\mathrm{D}} - p_{10}) \exp\left(-\frac{x}{L_p}\right), \tag{5.16}$$

as shown in Fig. 5.3.

5.1.1.2 Maximum GR-Currents

Figure 5.4 shows how, with increased minority carrier lifetime, the current slope increases and more and more carriers are collected at the left electrode,

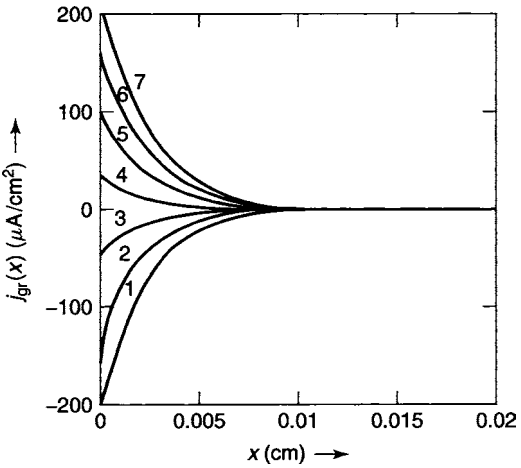

Fig. 5.3. Gr-current given by (5.12) with parameters as in Fig. 5.2 yielding $L_p \sim 0.02$ cm and $v_{\mathrm{D}} = 2.22 \times 10^4$ cm/s and with $p_{j\mathrm{D}}$ as a family parameter given as $p_{j\mathrm{D}} = 0,\ 2\times10^{10},\ 4\times10^{10}$ *and* 6×10^{10} yielding current injection $8\times10^{10},\ 10^{11}$ and with 1.2×10^{11} cm^{-3}, yielding current collection from the left electrode, for curves 1–7, respectively. $p_{10} = 5 \times 10^{10}$ cm^{-3}

[4] For $d_1 > L_p$, $\tanh(d_1/L_p) \to 1$, hence $A \to B$ [see (5.11)], and

$$j_{\mathrm{gr}}(x) \simeq e v_{\mathrm{D}} (p_{j\mathrm{D}} - p_{10}) \left[\cosh\left(-\frac{x}{L_p}\right) - \sinh\left(-\frac{x}{L_p}\right)\right], \tag{5.15}$$

which can be simplified to yield (5.16).

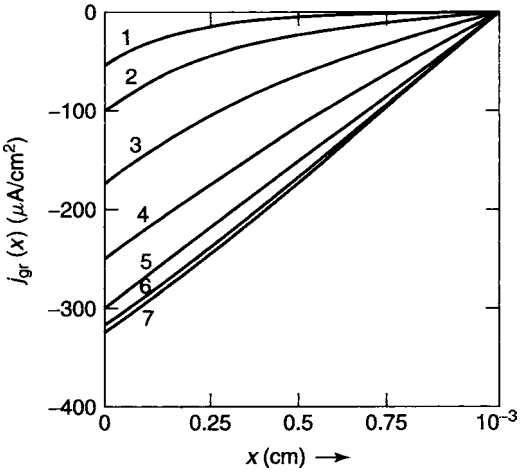

Fig. 5.4. Gr-current as in Fig. 5.3 for $p_{j\mathrm{D}} = 10^{11}\,\mathrm{cm}^{-3}$ for current collection, however, with τ_{p0} as a family parameter, with $\tau_{p0} = 10^{-8},\ 3\times10^{-8},\ 10^{-7},\ 3\times10^{-7},\ 10^{-6},\ 3\times10^{-6}$ and 10^{-5} s for curves 1–7, respectively. For discussion see text

until it approaches its maximum value across the slab when τ_{p0} has increased to render $L_p > d_1$. The maximum of the gr-current collected at $x = 0$ is then obtained from simplifying (5.13)

$$\boxed{\Delta j_{\mathrm{gr,max}} = j_{\mathrm{gr}}(x=0) = ev_{\mathrm{D}}(p_{j\mathrm{D}} - p_{10})\tanh\left(\frac{d_1}{L_p}\right).} \tag{5.17}$$

This maximum integrated gr-current as observed to flow across the entire slab of width d_1 is shown in Fig. 5.4 as a function of that slab thickness (and not as the local gr-cur within a slab of constant thickness $d_1 = 0.02\,\mathrm{cm}$).

The maximum increment of the gr-current increases with decreasing lifetime although it is collected from a shorter distance from the surface, but it relates directly to the diffusion velocity which increases hyperbolically with decreasing lifetime (5.14).

5.1.1.3 Pure Generation or Recombination Currents

When $p_{j\mathrm{D}}$ is pulled down sufficiently as a result of a reverse bias, the current becomes a **pure generation current** (here is $n_i^2 \gg np$) that reaches its maximum value when $p_{j\mathrm{D}}$ becomes negligible compared to p_{10}:

$$\Delta j_{\mathrm{g,max}} = -ev_{\mathrm{D}}p_{10}\tanh\left(\frac{d_1}{L_p}\right). \tag{5.18}$$

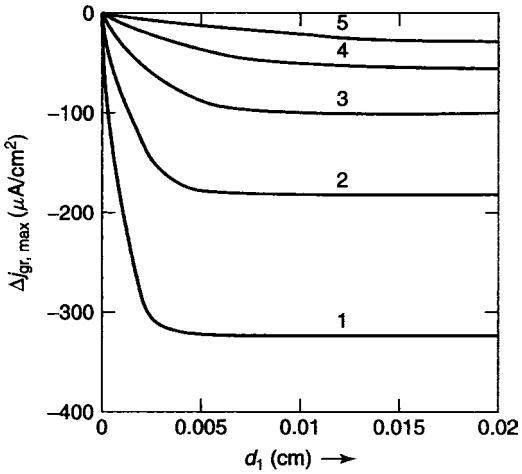

Fig. 5.5. Total gr-current increment as a function of the total slab width d_1, as given in (5.17) with the parameters as given in Fig. 5.4, now with $p_j D = 10^8\,\mathrm{cm}^{-}3$ and with τ_p as a family parameter for $\tau_p = 3\times10^{-8}$ 10^{-7} 3×10^{-7} 10^{-6} and 3×10^{-6} for curves 1–5, respectively. For discussion see text

This generation current saturates for $d_1 \gg L_p$ as shown in Fig. 5.5 at

$$\boxed{\Delta j_{\mathrm{g,max}}^{(\mathrm{sat})} = -ev_{\mathrm{D}}p_{10} = -egL_p.} \tag{5.19}$$

In contrast, with forward bias, i.e., for ($p_{j\mathrm{D}} > p_{10}$), the injection current becomes a **pure recombination current** (here is $np \gg n_i^2$) that increases linearly with increasing $p_{j\mathrm{D}}$ without bound (5.17):

$$\boxed{\Delta j_{r,\mathrm{max}} = ev_{\mathrm{D}}p_{j\mathrm{D}}.} \tag{5.20}$$

5.2 GR-Current with Surface Recombination

Surface recombination tends to restore the thermal equilibrium, when it is disturbed by an applied bias: In order to separate the influence of both, we discuss surface recombination to the right surface first. It forces the hole density $p(d_1)$ here to approach the equilibrium density p_{10}.

The influence of the surface recombination is introduced via the surface recombination current boundary condition,[5]

[5] In order to separate the effects of a bias controlled $p_{j\mathrm{D}}$ and a surface-recombination-controlled p_s, we have chosen consistently the left surface as being bias-controlled and the right surface as being recombination-controlled. In actuality, the conditions are interwoven, as shown in Sect. 6.2 and the relevant subsections.

$$j_p(x = d_1) = e(p_s - p_{10})s, \tag{5.21}$$

with $p_s = p(x = d_1)$ and s the surface recombination velocity.

5.2.1 Thermal GR-Current with Surface Recombination

When combining the surface boundary condition with (5.1), one obtains

$$\left(\frac{\mathrm{d}p}{\mathrm{d}x}\right)_{x=d_1} = \frac{es(p_s - p_{10})}{\mu_p kT}. \tag{5.22}$$

With this and the continuity equation, one obtains a modified diffusion equation which yields a solution[6] similar to that given in (5.13):

$$p(x) = (p_{j\mathrm{D}} - p_{10})\left[\left\{\tanh\frac{d_1}{L_p} + SR(s)\right\}\sinh\left(-\frac{x}{L_p}\right) + \cosh\left(-\frac{x}{L_p}\right)\right] + p_{10}, \tag{5.24}$$

but now with a modifying surface recombination term,

$$SR(s) = \frac{\frac{s}{v_\mathrm{D}}}{\left[1 + \frac{s}{v_\mathrm{D}}\tanh\left(\frac{d_1}{L_p}\right)\right]\cosh^2\left(\frac{d_1}{L_p}\right)}. \tag{5.25}$$

The minority carrier density at the surface is obtained by evaluating (5.24) at d_1:

$$p(x = d_1) = p_s = p_{10} + \frac{p_{j\mathrm{D}} - p_{10}}{\left[1 + \frac{s}{v_\mathrm{D}}\tanh\left(\frac{d_1}{L_p}\right)\right]\cosh\left(\frac{d_1}{L_p}\right)}, \tag{5.26}$$

which is plotted in Fig. 5.6 as a function of the surface velocity s. It shows that this surface density of minority carriers decreases below the thermal equilibrium value the more so, the more it exceeds the diffusion velocity v_D and is almost independent of surface recombination when the surface recombination velocity is kept below v_D. This important fact can be a measure of the defect density at the surface and its specific recombination cross section.

The surface density p_s approaches the thermal equilibrium value p_{10} when s becomes much larger than v_D, as shown in Fig. 5.7.

As shown in (a), the effect of s on $p(x)$ extends towards the left side of the device for a distance determined by the diffusion length: any effect induced by a boundary condition at $x = 0$ or $x = d_1$ has essentially died out after a few

[6] The integration constants are again given as (5.9) for B and, similar to (5.11):

$$A = B\left[\tanh\left(\frac{d_1}{L_n}\right) + SR(s)\right]. \tag{5.23}$$

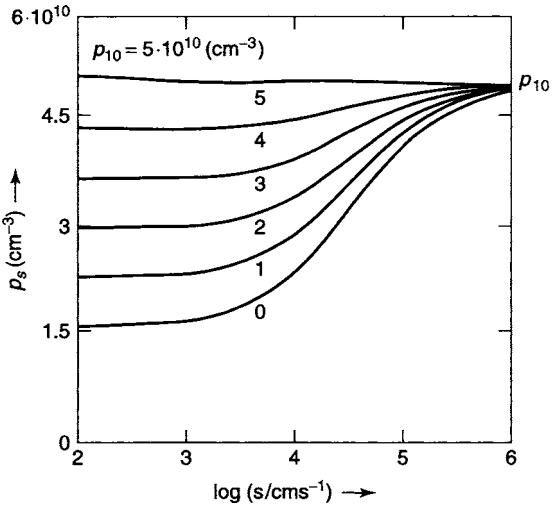

Fig. 5.6. Minority carrier density p_s at the right surface (d_1) as a function of the surface recombination velocity according to (5.26) with parameters as in Fig. 5.2, $d_1 = 2 \times 10^{-3}$ cm and $p_{j\mathrm{D}}$ as a family parameter, that can be read from the figure at the intersect with the ordinate

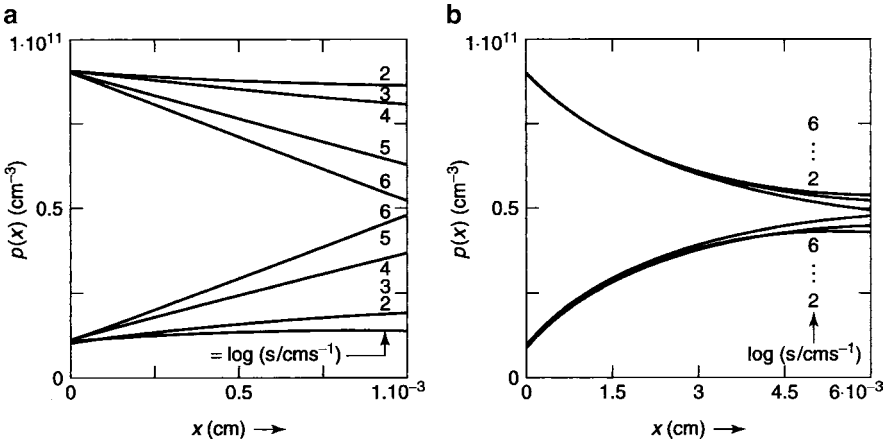

Fig. 5.7. Minority carrier density distribution as a function of the spatial coordinate according to (5.24) with the same parameters as in Fig. 5.2; $p_{j\mathrm{D}} = 10^{10}$ and $9 \times 10^{10}\,\mathrm{cm}^{-3}$ in forward and reverse bias, respectively, and s as a family parameter. (**a**) thin slab of 10^{-3} cm thickness, showing the surface recombination extending through the entire slab, while thick slab of 6×10^{-3} cm thickness shown in (**b**) the surface recombination effect is limited to only a thin, surface-near region

diffusion lengths. A slab much thicker than the diffusion lengths shown in (b) separates two regions near the two surfaces which react essentially independent of each other. In a thinner slab this inter-reaction, however, determines $p(x)$ throughout the device.

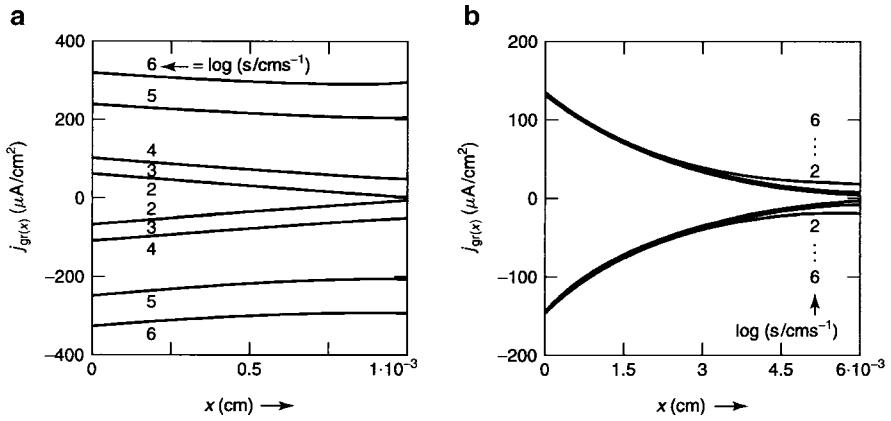

Fig. 5.8. Gr-current distribution according to (5.27) with same parameters and family parameters as given in Fig. 5.2 and with the surface recombination velocity as a family parameter. This emphasises that the minority carrier current is influenced significantly by surface recombination only in a slab of thickness comparative to the diffusion length

When differentiating (5.24) and multiplying it with $\mu_p kT$, one obtains the current distribution, which is similar to (5.13), however, modified by $SR(s)$:

$$j_{pg}(x) = ev_{\mathrm{D}}(p_{j\mathrm{D}} - p_{10})\left[\left\{\tanh\left(\frac{d_1}{L_p}\right) + SR(s)\right\}\cosh\left(\frac{-x}{L_p}\right) + \sinh\left(\frac{-x}{L_p}\right)\right]. \tag{5.27}$$

and is shown in Figs. 5.8a and 5.8b. It again gives a similar picture for the current distributions that change for a thin ($d_1 = 10^{-4}\,\mathrm{cm}$) slab throughout the device, while for a thicker ($d_1 = 6 \times 10^{-4}\,\mathrm{cm}$) slab the current is only minimal influenced by the surface recombination, corresponding to the carrier density distributions given in Fig. 5.6.

5.2.2 The Effective Diffusion Velocity

When using the expression for the current at $x = 0$, including surface recombination, one can formally write,

$$\Delta j_{\mathrm{gr}} = e(p_{j\mathrm{D}} - p_{10})v^*_{Ds}, \tag{5.28}$$

which has the same form as for vanishing surface recombination (5.18), but with an effective diffusion velocity, modified by surface recombination:

$$v^*_{Ds} = v_{\mathrm{D}}\left[\tanh\left(\frac{d_1}{L_p}\right) + SR(s)\right]; \tag{5.29}$$

the saturation current is also *increased* accordingly:

$$\Delta j_{\mathrm{r,max,s}}^{(\mathrm{sat})} = e p_{10} v_{Ds}^{*}. \tag{5.30}$$

Therefore, at high surface recombination, a much higher current can be drawn and the reverse saturation current for thin slabs is dominated by the surface recombination velocity:

$$\Delta j_{r,\mathrm{max},s}^{(s)} = e p_{10} s, \tag{5.31}$$

while the gr-contribution from within the slab becomes negligible.

5.2.3 Optical Excitation GR-Currents with Surface Recombination

With optical excitation, a similar behavior is expected, however, since the steady state minority carrier density $p_{10}^{(o)}$ is increased substantially above the thermal equilibrium density $p_{10}^{(\mathrm{th})}$, the surface recombination current,[7]

$$j_s = e\left(p_s - p_{10}^{(\mathrm{th})}\right) s, \tag{5.32}$$

which for $p_1 0^{(o)} \gg p_1 0^{(\mathrm{th})}$ can be simplified to

$$j_s \simeq e p_s s. \tag{5.33}$$

One now obtains as minority carrier density at $x = d_1$,

$$p_s = \frac{p_{j\mathrm{D}} - p_{10}^{(o)}\left[1 - \cosh\left(\frac{d_1}{L_p}\right)\right]}{\left[1 + \frac{s}{v_{\mathrm{D}}}\tanh\left(\frac{d_1}{L_p}\right)\right]\cosh\left(\frac{d_1}{L_p}\right)}, \tag{5.34}$$

which is shown in Fig. 5.9 as a function of the surface recombination velocity for different $p_{j\mathrm{D}}$ (larger and smaller than $p_{10}^{(o)}$, shown arrow pointing to the left) as a family parameter. The density p_s decreases below the steady state value $p_{10}^{(o)} = 10^{13}\,\mathrm{cm}^{-3}$ for the bulk even in a thick slab and approaches the much lower thermodynamic equilibrium value $p_{10}^{(\mathrm{th})} = 5.13 \cdot 10^{10}\,\mathrm{cm}^{-3}$ for s approaching the thermal velocity (shown as an arrow pointing to the right side of the box in Fig. 5.9).[8]

[7] Recombination always tends to restore thermal equilibrium. Therefore, $p_{10}^{(\mathrm{th})}$ is contained in (5.32) and not $p_{10}^{(o)}$.

[8] Here, (5.32) should be used instead of (5.33), which causes a levelling-off, near $p_{10}^{(\mathrm{th})}$, of the lowest curves in Fig. 5.9.

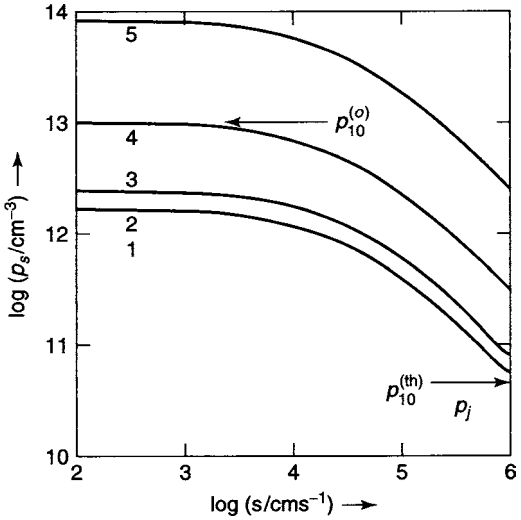

Fig. 5.9. Minority carrier density at the surface as a function of the surface recombination velocity with the optically generated steady state minority carrier density $p_{10}^{(o)} = 10^{13}\,\mathrm{cm}^{-3}$; all other parameters are the same as in Fig. 5.2. Family parameter is $p_{j\mathrm{D}}$ with $p_{j\mathrm{D}} = 10^{10},\ 10^{11},\ 10^{12},\ 10^{13}$ and $10^{14}\,\mathrm{cm}^{-3}$ for curves 1–5, respectively. The equilibrium density $p_{10}^{(\mathrm{th})} = 5 \times 10^{10}\,\mathrm{cm}^{-3}$ is indicated

5.2.4 Optical Excitation GR-Currents with Recombination at Right and Barrier at Left

We now return to a device with a Schottky barrier at the left with fixed surface recombination and a transparent electrode at the right for optical excitation with various surface recombinations. When this surface recombination s is sufficiently large, the hole density distribution $p(x)$ shows in reverse bias a maximum at $x = x_m$ (Fig. 5.10), since part of the holes diffuses to the right surface (for $x > x_m$) and part of the holes (for $x < x_m$) diffuses towards the left, the barrier surface. The position of this maximum[9] x_m permits replacing the slab width d with x_m and rewriting of the integration constant A in (5.11) as

$$A = (p_{j\mathrm{D}} - p_{10}) \tanh\left(\frac{x_m}{L_p}\right). \tag{5.35}$$

Consequently, one can express the gr-current at $x = 0$, using the hole contribution only to the left of the maximum in reverse bias, resulting in a rather simple equation:

$$\boxed{\Delta j_{\mathrm{gr,o,s}} = e v_{\mathrm{D}} (p_{j\mathrm{D}} - p_{10}^{(o)}) \tanh\left(\frac{x_m}{L_p}\right).} \tag{5.36}$$

[9] Equation (5.35) can be verified by differentiating $p(x)$ with B given in (5.9) and setting $\mathrm{d}p/\mathrm{d}x = 0$.

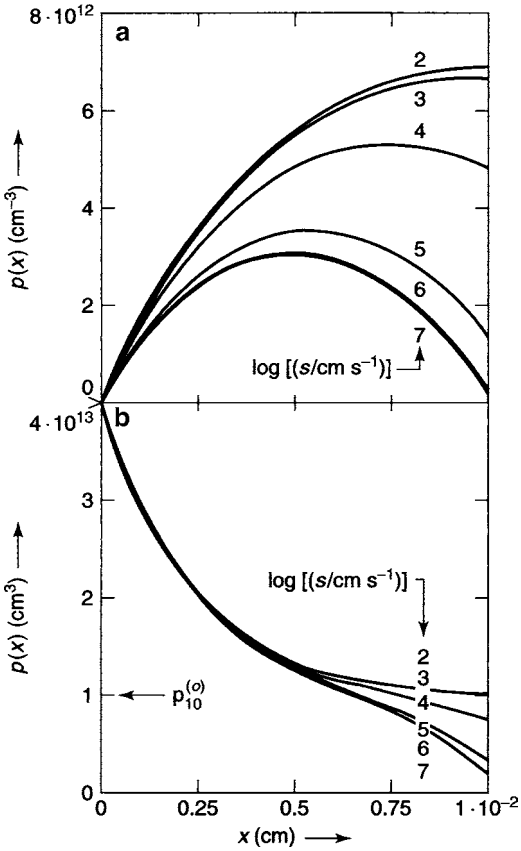

Fig. 5.10. Minority carrier distribution (same parameters as in Fig. 5.2, but $p_{10}^{(o)} = 10^{13}\,\mathrm{cm}^{-3}$) and with the surface recombination velocity s at the *right side* as a family parameter. (**a**) in reverse bias with $p_{j\mathrm{D}} = 10^{10}\,\mathrm{cm}^{-3}$ at the *left side* fixed; (**b**) in forward bias again with the *left side* fixed but at $p_{j\mathrm{D}} = 4 \times 10^{13}\,\mathrm{cm}^{-3}$

Figure 5.10a shows the hole distribution in reverse bias (with $p_{j\mathrm{D}} = 10^{10}\,\mathrm{cm}^{-3}$) for a thin slab and with the surface recombination velocity as the family parameter. When s becomes larger than v_{D}, the hole density distribution becomes nonmonotonic with x_m shifting to the centre of the slab.

In forward bias (i.e., for $p_{j\mathrm{D}} > p_{10}$), the hole density distribution $p(x)$ is monotonic with an inflection point at $x = x_i$ where $p(x)$ crosses $p_{10}^{(o)}$ (see Fig. 5.10b). Again, the current at $x = 0$ can be written as

$$\boxed{\Delta j_{\mathrm{gr,o,s}} = e v_{\mathrm{D}} (p_{j\mathrm{D}} - p_{10}^{(o)}) \tanh\left(\frac{x_i}{L_p}\right);} \tag{5.37}$$

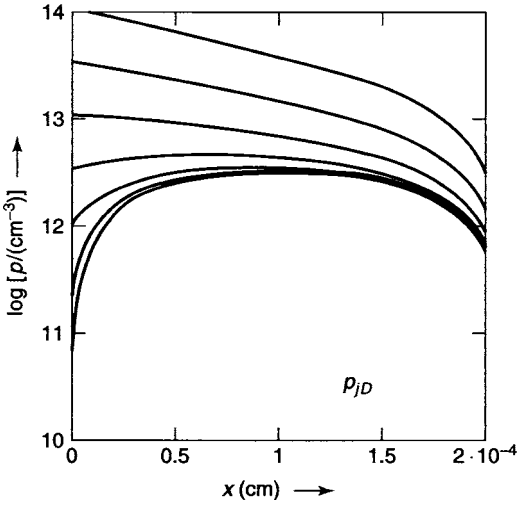

Fig. 5.11. Minority carrier distribution as in Fig. 5.10 for $p_{10}^{(o)} = 10^{13}\,\mathrm{cm}^{-3}$ and $s = 10^6$ cm/s, however, with various values of $p_{j\mathrm{D}}$ at the left as the family parameter, as can be seen from $p(x)$ at $x = 0$

x_m and x_i are functions of the surface recombination velocity and move closer to the middle of the slab, the larger s is(see Fig. 5.10) and the larger the difference between $p_{j\mathrm{D}}$ and $p_{10}^{(o)}$ (Fig. 5.11).

5.2.4.1 Currents in Short and Long Devices

The current distribution is linear for a *thin slab* as shown in Fig. 5.12. It crosses the zero line, since part of this current flows to the left into the barrier, and part flows to the outer, right surface. The current distribution remains essentially parallel and shifts to lower values with increasing s, as shown in Figs. 5.12a and 5.12b.

In reverse bias, gr-current and surface recombination currents have opposite signs, with forward bias, however, they have the same sign, and $j_p(x = 0)$ *increases* with increasing s as shown in Fig. 5.12c.

For a *thicker slab* ($d_1 \gg L_p$), the region close to the junction is separated from the region close to the outer surface by a neutral, inactive bulk region as shown in Fig. 5.13. The junction and near-surface regions are then influenced independently by $p_{j\mathrm{D}}$ and p_s, respectively.

5.2.4.2 Collection Efficiency of Minority Carriers

With optical generation, it becomes an instructive parameter to see what fraction of the generated minority carriers can be extracted in such a (photovoltaic) device. By comparing the current from a slab of insufficient thickness

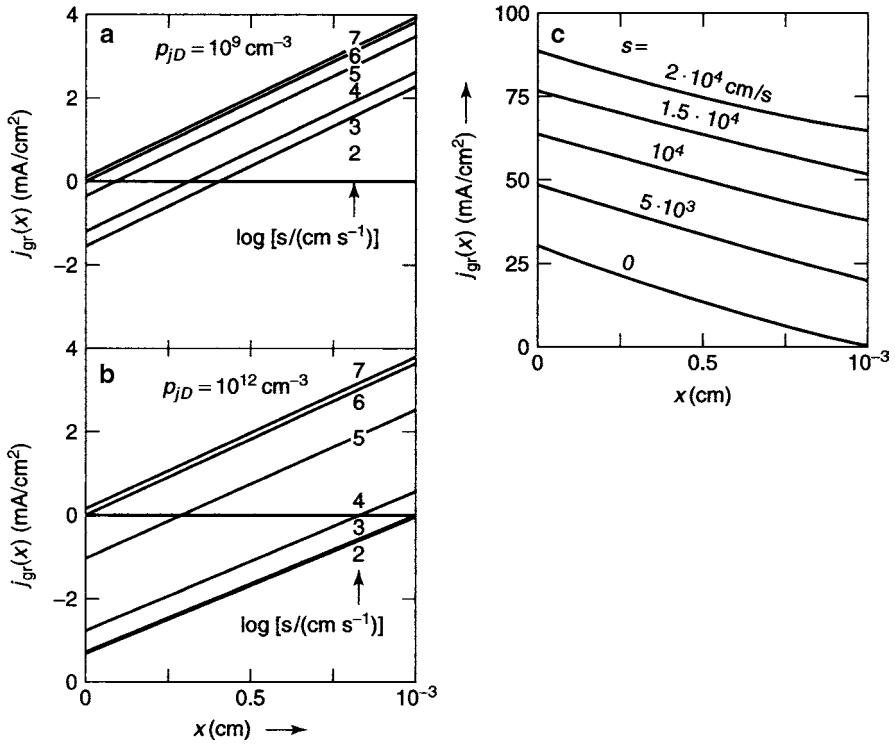

Fig. 5.12. Minority carrier current distribution for the same parameters as Fig. 5.10 with s as family parameter. (**a**) $p_{j\mathrm{D}} = 10^9\,\mathrm{cm}^{-3}$ for reverse bias; (**b**) with a larger value of $p_{j\mathrm{D}} = 10^{12}\,\mathrm{cm}^{-3}$, again for a lesser reverse bias. Observe the crossing of the zero current line, clearly showing that part of the current flows to the right and part to the left electrode. In (**c**), we show the current distribution for $p_{j\mathrm{D}} = 10^{14}\,\mathrm{cm}^{-3}$ representing a forward bias; hence, the current is monotonic and pointing to the left electrode

with surface recombination with the maximum optically generated minority current that can be extracted from a sufficiently thick slab (5.19) one defines as a collection efficiency at the barrier interface:

$$\eta_c = \frac{\Delta j_{\mathrm{g,s}}}{\Delta j_{\mathrm{g,max}}^{(\mathrm{sat})}(s=0)}, \tag{5.38}$$

with (5.19) and (5.36), yielding:

$$\boxed{\eta_c = \frac{L_p}{d_1} \tanh\left(\frac{x_m}{L_p}\right).} \tag{5.39}$$

The collection efficiency as a function of surface recombination with different ratios of L_p/d_1 is shown in Fig. 5.14. It is important to remember that

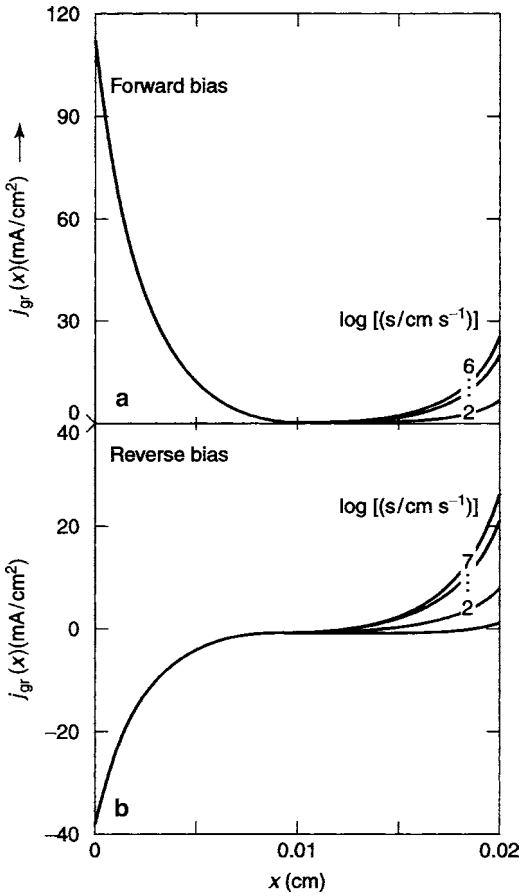

Fig. 5.13. Generation/recombination current as in Fig. 5.12, however, for a much thicker slab; (**a**) for forward and (**b**) for reverse bias. Parameters and family parameter as in Fig. 5.10.

collection efficiencies in excess of 95% are obtained when the diffusion length exceeds three times the slab thickness and the surface recombination velocity is smaller than the diffusion velocity.

From Fig. 5.15, one can see that even for high surface recombination velocities, the collection efficiency does not drop below 0.5 as long as $L_p/d_1 > 2$. The collection efficiency as a function of L_p/d_1 is shown in Fig. 5.15 for different surface recombination velocities as a family parameter[10]

[10] design parameters for good solar cells are $s < \frac{d_1}{\tau_{p0}}$ and $L_p > 3d_1$.

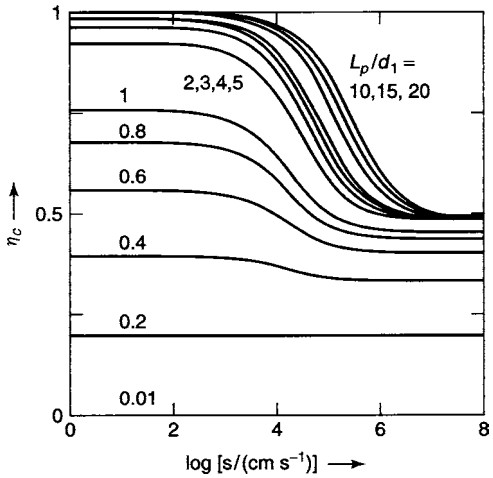

Fig. 5.14. Collection efficiencies for collecting minority carriers as a function of the surface recombination velocity for reverse saturation currents with L_p/d_1 as a family parameter, as given in the figure. η_c according to (5.39)

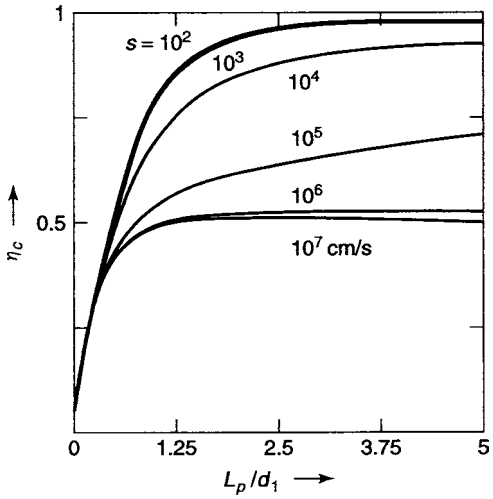

Fig. 5.15. Collection efficiency of minority carriers as in Fig. 5.14 as a function of diffusion length, for s, as given in the figure, as a family parameter

5.2.5 Effective Diffusion Velocity for Optical Excitation

In the preceding sections, we have seen that also the optically generated gr-current at the collecting barrier can be described by a single formula:

$$\Delta j_{\mathrm{gr}} = j_{\mathrm{gr}}(x=0) = ev_{\mathrm{D}}(p_{j\mathrm{D}} - p_{10}) \tanh\left(\frac{x_c}{L_p}\right), \tag{5.40}$$

where, x_c is the distance to the maximum (x_m) or inflection point (x_i) of $p(x)$ for reverse or forward bias, respectively.

We can now introduce a corresponding *effective diffusion velocity*,

$$\boxed{v^*_{Ds,o} = v_{\mathrm{D}} \tanh\left(\frac{x_c}{L_p}\right),} \tag{5.41}$$

which describes the diffusion current as a function of the minority carrier density at the left boundary:

$$\boxed{\Delta j_{\mathrm{gr}} = e v^*_{Ds,o}(p_{j\mathrm{D}} - p_{10}).} \tag{5.42}$$

This is the key diffusion equation for minority carriers with optical generation which will be used throughout the following sections.

5.2.6 Optical vs. Thermal Carrier Generation

The different characters of the collection of the photogenerated carriers, from the thermally excited minority carriers with and without surface recombination is emphasised (compare Figs. 5.8 and 5.12).

With *optical excitation*, part of the generated carriers are diverted to the outer surface, resulting in a loss for the *carrier collection*, i.e., in a reduced current.

With *thermal excitation*, the density at the surface deviates from the equilibrium density with sufficient bias and for a thin enough slab, resulting in an additional *leakage current*.

5.3 Drift-Assisted GR-Currents

In devices that contain an extended compensated region (an *i*-region), the electric field can have a substantial influence on the minority carrier transport. This will be discussed in the following sections.

5.3.1 Field-Influence in the Bulk

When the drift velocity, given by $\mu_p F$ (that is larger than 10^3 cm/s for fields in excess of only 1 V/cm), approaches or exceeds the diffusion velocity[11], the region from which the minority carriers can be extracted before they recombine in a thick slab can be significantly increased. This causes an increase of the gr-current, which will be the subject of discussion below.

[11] Since such fields can extend by many Debye lengths beyond a Schottly barrier or junction, one must consider such field-influence on the diffusion in much thicker device slabs.

The characteristic length from which carriers are extracted before they recombine is the diffusion length for negligible fields, as defined in Sect. 5.1. With field, this length is increased by the *"Schubweg"* or *drift length*

$$\boxed{L_s = \mu_p F_{10} \tau_{p0}.} \tag{5.43}$$

In the bulk region with a constant field, the so modified diffusion is accessible to an analytic calculation.

5.3.2 Analytical Solution of Diffusion with Constant Field

We obtain from the transport equation including the drift contribution, here for simplicity assumed with a constant external field, F_{10}, for the current:

$$j_p = e\mu_p p F_{10} - \mu_p kT \frac{\mathrm{d}p}{\mathrm{d}x}. \tag{5.44}$$

Together with the continuity equation [see (4.35)]

$$\frac{\mathrm{d}j_p}{\mathrm{d}x} = \frac{e(p_{10} - p)}{L_p^2}, \tag{5.45}$$

one obtains the basic field-enhanced-diffusion equation for the minority carriers and constant external field:

$$\frac{\mathrm{d}^2 p}{\mathrm{d}x^2} - \frac{eF_{10}}{kT}\frac{\mathrm{d}p}{\mathrm{d}x} + \frac{p_{10} - p}{L_p^2} = 0, \tag{5.46}$$

which has the solution

$$p(x) = c_1 \exp\left(\frac{x}{L_{pf1}}\right) + c_2 \exp\left(\frac{x}{L_{pf2}}\right) + p_{10} \tag{5.47}$$

with the effective *downstream diffusion length* (here the diffusion is assisted by the field):

$$L_{pf1} = L_p \frac{2L_p}{L_s + \sqrt{4L_p^2 + L_s^2}} \tag{5.48}$$

and the *upstream diffusion length* (here the diffusion is opposed by the drift):

$$L_{pf2} = L_p \frac{2L_p}{L_s - \sqrt{4L_p^2 + L_s^2}}. \tag{5.49}$$

These downstream and upstream diffusion lengths L_{pf1} and L_{pf2} are plotted in Fig. 5.16 as a function of the electric field F_{10} (contained in L_s), and with the diffusion length L_p as the family parameter.

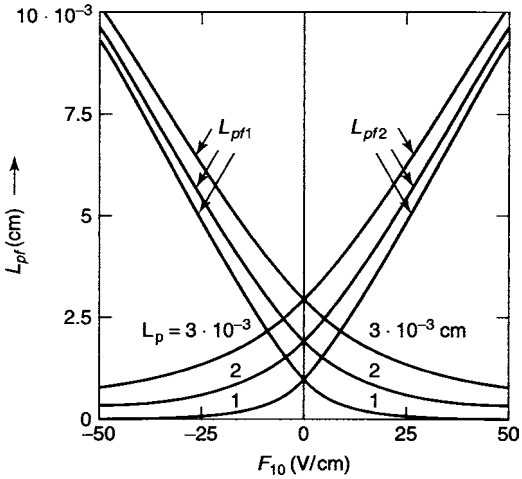

Fig. 5.16. Effective diffusion lengths L_{pf1} and L_{pf2} according to (5.48) and (5.49) as a function of the constant external field F_{10}; with L_p as the family parameter (for $\mu_p = 1900\,\mathrm{cm}^2/\mathrm{Vs}$, $T = 300\,\mathrm{K}$ and $\tau_{p0} = 10^{-7}\,s$). From this Figure, it is evident that even at small electric fields, the effective diffusion lengths are significantly changed the more so, the higher the diffusion length is without external field

5.3.3 Drift-Assisted GR-Currents Without Surface Recombination at Right Electrode

The drift-assisted gr-currents can now be given in closed form and, for simplicity, should be discussed for zero surface recombination at the right electrode. The integration constants c_1 and c_2 are determined from the boundary conditions, and for zero surface recombination; hence, with $p(x = 0) = p_{j\mathrm{D}}$ and $\mathrm{d}p/\mathrm{d}x|_{x=0} = 0$, one obtains,

$$c_1 = \frac{p_{j\mathrm{D}} - p_{10}}{1 + \frac{L_{pf2}}{L_{pf1}} \exp\left(\frac{d_1}{L_p^*}\right)} \tag{5.50}$$

and

$$c_2 = \frac{p_{j\mathrm{D}} - p_{10}}{1 - \frac{L_{pf1}}{L_{pf2}} \exp\left(-\frac{d_1}{L_p^*}\right)} \tag{5.51}$$

with

$$L_p^* = -\frac{L_p^2}{\sqrt{4L_p^2 + L_s^2}}. \tag{5.52}$$

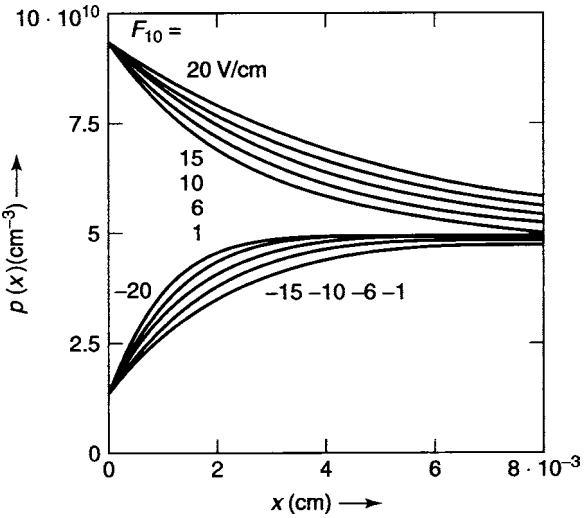

Fig. 5.17. Carrier distribution according to (5.53) with the same parameters as used for Fig. 5.2 and the external field, F_{10}, as a family parameter, as listed in the figure. $p_j D = 10^{10}$ for reverse and $p_j D = 9 \times 10^{10}$ for forward bias are fixed. $p_{10} = 5 \times 10^{10}\,\mathrm{cm}^{-3}$ with a neutral surface with $\mathrm{d}p/\mathrm{d}x = 0$ at $x = d_1$ is assumed

This yields for the minority carrier density distribution

$$p(x) = p_{10} + (p_{j\mathrm{D}} - p_{10}) \frac{\left[\frac{L_{pf1}}{L_{pf2}} \exp\left(-\frac{d_1}{L_p^*}\right) \exp\left(\frac{-x}{L_{pf1}}\right) - \exp\left(\frac{-x}{L_{pf2}}\right)\right]}{\left[\frac{L_{pf1}}{L_{pf2}} \exp\left(-\frac{d_1}{L_p^*}\right) - 1\right]}, \quad (5.53)$$

which is similar to the solution obtained for the field-free case (5.12), however, with field-dependent effective diffusion lengths.

In Fig. 5.17, a family of solution curves of (5.53) is shown for different external fields as the family parameter, arbitrarily keeping the boundary concentration constant at $p_{j\mathrm{D}} = 10^{10}\,\mathrm{cm}^{-3}$ and $p_{j\mathrm{D}} = 9 \times 10^{10}\,\mathrm{cm}^{-3}$ for reverse and forward bias, respectively. The influence of the field is seen by shrinking (in reverse) or widening (in forward bias) the region of the changing minority carrier density in reverse and forward bias, respectively.

The corresponding currents are plotted in Fig. 5.18 for the boundary condition,[12] $p(d_1) = 5 \times 10^{10}\,\mathrm{cm}^{-3}$ in reverse and $5.26 \times 10^{10}\,\mathrm{cm}^{-3}$ in forward bias with $p_{10} = 5.13 \times 10^{10}\,\mathrm{cm}^{-3}$.

[12] $p(d_1)$ is kept constant in forward and in reverse bias in order to simplify the following discussion.

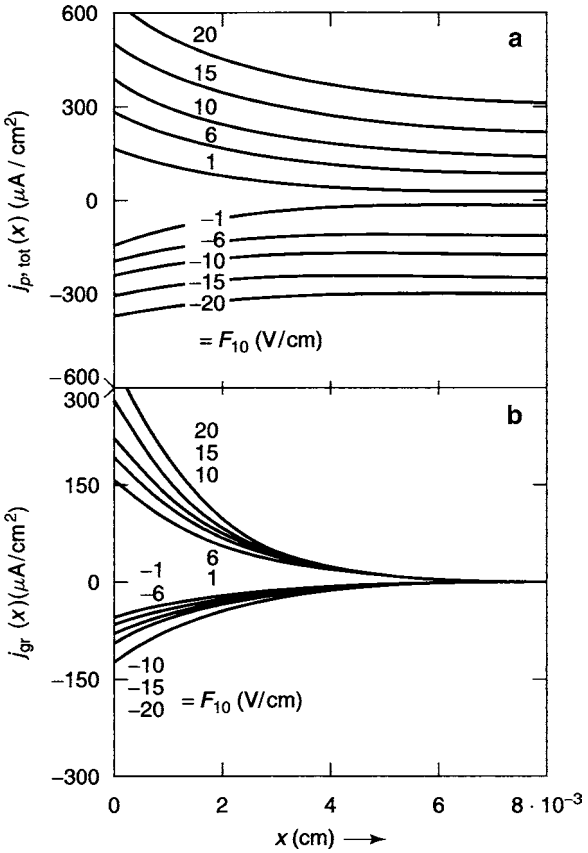

Fig. 5.18. Current distribution corresponding to Fig. 5.17 except $p_{10} = 5.13 \times 10^{10}$, $p(d_1)_{\mathrm{forw}} = 5.26 \times 10^{10}$ and $p(d_1)_{\mathrm{rev}} = 5 \times 10^{10}\,\mathrm{cm}^{-3}$. (**a**) total hole currents $[j_{p,\mathrm{tot}}(x)]$; (**b**) gr-currents $[j_{\mathrm{gr}}(x)]$; both figures with the external field as a family parameter

5.3.4 Total Drift-Assisted Minority Carrier Current

When evaluating the hole current obtained from (5.53) at $x = 0$, one obtains the *total hole current*; it has the same form as (5.17) except for the factor and the diffusion length that is now replaced by the downstream diffusion length L_{pf1}:

$$\boxed{j_{p,\mathrm{tot}}(x=0) = e\frac{L_{pf1}}{\tau_{p0}}(p_{j\mathrm{D}} - p_{10}).} \tag{5.54}$$

Figure 5.19 shows the currents as the functions of the external field F_{10}. The *generation/recombination* (part of the) *current* is obtained by using the upstream diffusion length L_{pf2} as the effective diffusion length:

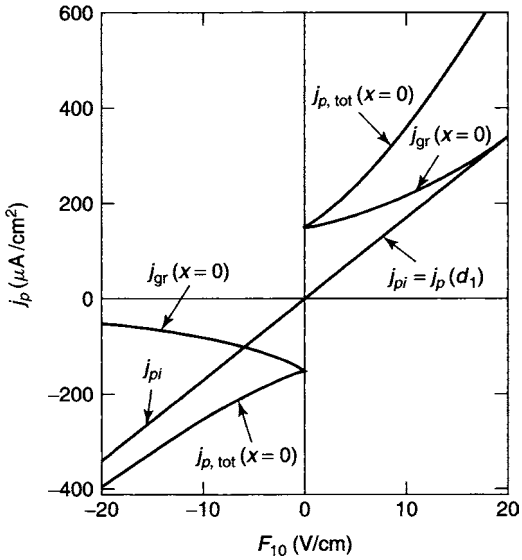

Fig. 5.19. Hole currents with the same parameters as in Fig. 5.16 as obtained for $p_{j\mathrm{D}} = 10^{10}\,\mathrm{cm}^{-3}$ in reverse and for $9 \times 10^{10}\,\mathrm{cm}^{-3}$ in forward bias, and for $p(d_1) = 5 \times 10^{10}\,\mathrm{cm}^{-3}$ in reverse and $5.26 \times 10^{10}\,\mathrm{cm}^{-3}$ in forward bias as a function of a constant external field, F_{10}. The Figure shows as three branches the generation-recombination branch j_{gr}, the divergence-free drift branch $j_p i$ and the sum of both j_p, tot all evaluated at $x = 0$ in reverse (*left side*) and in forward bias (*right side of the figure*)

$$j_{\mathrm{gr}}(x=0) = \Delta j_{\mathrm{gr}} = e\frac{L_{pf2}}{\tau_{p0}}(p_{j\mathrm{D}} - p_{10}). \tag{5.55}$$

The *divergence-free* (part of the) *current*, as defined by $j_{p,\mathrm{tot}}(x=0) - j_{\mathrm{gr}}(x=0) = j_{pi}$, is given by

$$\boxed{j_{pi} = e\frac{L_{pf1} - L_{pf2}}{\tau_{p0}}(p_{j\mathrm{D}} - p_{10}).} \tag{5.56}$$

From (5.48) and (5.49), one has for sufficiently high fields, when $L_s \gg L_p$,

$$L_{pf1} - L_{pf2} = L_s; \tag{5.57}$$

hence,

$$j_{pi} = e\mu_p F_{10}(p_{j\mathrm{D}} - p_{10}), \tag{5.58}$$

which is in agreement with (5.44) for $p_{j\mathrm{D}} \ll p_{10}$.

A homogeneous external field, therefore, causes an increase in the minority carrier current which, with increasing field, becomes more and more a simple drift current.

In **forward bias**, the gr-current increases linearly with the field for $L_s \gg L_p$:

$$L_{pf2}^{\text{forw}}(L_s \gg L_p) \to L_s. \tag{5.59}$$

For high fields, the gr-current approaches the drift current

$$j_{\text{gr}}^{\text{forw}} \to e\mu_p F_{10}(p_{j\text{D}} - p_{10}). \tag{5.60}$$

In addition, one has the divergence-free current

$$j_{pi} = e\mu_p F_{10}(p_{j\text{D}} - p_{10}); \tag{5.61}$$

hence, the total minority current with sufficient forward bias equals twice the drift current for thick devices. When the field is further increased, the effective diffusion length increases and will finally surpass the device thickness. The device then becomes a thin device, reducing the additional contribution of the gr-current; the total hole current then becomes the *simple drift current*:

$$j_p(x = 0, L_s > d_1) \to j_{pi} = e\mu_p(p_{j\text{D}} - p_{10})F_{10}, \tag{5.62}$$

an equation which now holds for sufficiently large forward bias in the homogeneous part of the device.

In **reverse bias**, L_s is negative and L_{pf2} decreases hyperbolically with the field,

$$L_{pf2}^{\text{rev}}(-L_s \gg L_p) \to \frac{L_p^2}{L_s}. \tag{5.63}$$

This means that in reverse bias, $L_{pf1} - L_s$ goes asymptotically to zero. At large enough reverse bias, again (5.62), i.e. the simple drift current holds.

The *influence of the device thickness* can be included explicitly by introducing the above neglected tanh factor, i.e., by using $v_{Ds,o}^*$ (5.41) for optical minority carrier generation, but with L_{pf2} instead of L_p in its argument

$$\boxed{j_{\text{gr}} \simeq e(p_{pD} - p_{10})\frac{L_{pf2}}{\tau_{p0}} \tanh\left(\frac{x_m}{L_{pf2}}\right),} \tag{5.64}$$

with x_m depending on the surface boundary condition as described in Sect. 5.2.5.

5.3.4.1 Justification for the Separation of Injection and Generation Currents

In principle, we can use field-assisted diffusion with L_{pf1} and L_{pf2} as effective diffusion lengths using only (5.53) and its spatial derivative for all further discussion.

This leaves the gr- and drift-part entangled. We have chosen to separate these two currents from the beginning, since they represent different transport

mechanisms. Such separation is possible, since the divergence-free current j_{pi} remains constant throughout the device ($L_{pf1} - L_{pf2}$ is independent of x). The drift-part is divergence-free and uniquely determined by the hole density and the field[13] at d_1.

On the other hand, only the gr-current contributes to the interchange between minority and majority carriers. Only to the extent that j_{gr} for holes changes in x will j_{gr} for electrons also change, causing a corresponding changeover between electron and hole currents as discussed in Sect. 4.3.2. If Δj_{gr} is small compared to the total current, j_n will be essentially divergence-free. This aspect will be helpful in the distinction between the behavior of Schottky barriers and *pn*-junctions. Only in the latter, a nearly complete changeover occurs between predominant hole current in the *p*-type material and a predominant electron current in the *n*-type part, and only here the divergence-free part becomes negligible. In many Schottky barriers, the divergence-free current remains significant and often provides most of the reverse saturation current.

Our approach permits a cleaner separation of different current contributions as they relate to device operation.

Summary and Emphasis

Minority carrier currents of technical interest are almost always predominant diffusion currents, controlled by the minority carrier density in a barrier or junction that in turn is determined by the applied bias. When this barrier density is above or below the density of minority carriers in the bulk, the current will flow from (in reverse bias) or towards the bulk (in forward bias). It is referred to as a collection or an injection current, respectively. The change in minority carrier density follows an exponential decay with the diffusion length as a characteristic distance parameter.

The current towards or from a controlling barrier is superimposed by the recombination currents at the surfaces of the device. The recombination current tends to restore the steady state equilibrium minority carrier density. It is proportional to the surface recombination velocity and the deviation of the carrier density from its steady state equilibrium value.

In large devices with dimensions of several diffusion lengths, the diffusion currents at the surface and at the controlling barrier (when separated at different surfaces) are well separated by a transport-neutral bulk region.

In thinner devices, there is a substantial interplay between the surface-related currents, and this interplay reduces the collection efficiency of photogenerated carriers at the controlling barrier: surfaces with high recombination

[13] The selection of d_1 here is due to the specific example in which we assumed a neutral electrode at d_1 with a flat-band (no space charge) connection to the semiconductor/metal interface. When a space-charge layer is also present at d_1, the identification of j_{pi} is more involved (see Sect. 6.2.2.3).

always act as competing sinks for minority carriers and are detrimental to the photodiode performance. A reduction of the surface recombination velocity s to or below the diffusion velocity v_D is beneficial to minority carrier collection in thin devices, causing an increase in the effective minority carrier lifetime.

Drift-fields in an i-layer provide another advantage in minority carrier collection; however, they need to be adjusted carefully to avoid excessive contribution of a divergence-free drift current component which is a passive (resistive) rather than an electronically active contribution to the device performance.

An understanding of the interplay between the controlling effect of the minority carrier density at the barrier and of the competing surface recombination provides the basis for designing diodes and photodiodes of improved performance characteristics. Careful evaluation of drift components in devices with i-layers maximises benefits while avoiding series resistance losses.

Exercise Problems

1.(e) Give the condition under which the minority carrier drift current can be neglected ($< 1\%$ of the majority carrier current) in a homogeneous semiconductor. Discuss the influence of mobilities, effective masses and the Fermi-level position.

2. What conditions need to be fulfilled to obtain from an Si-platelet of $1\,\mathrm{cm}^2$ with a transparent front electrode surface and 0.1 mm electrode distance a minority carrier diffusion current of $40\,\mathrm{mA/cm}^2$ for an optical generation rate, calculated from $40\,\mathrm{mW/cm}^2$ photon flux at band gap energy, assumed to be completely and homogeneously absorbed within this platelet.

3.(r) Derive explicitly the diffusion length and relate it quantitatively to the change of carrier densities given by diffusion only.

4. Discuss the relation between gr-currents of minority and majority carriers and explain the sign relation for forward and reverse bias.

5. Develop the equation for current competition between collection and surface recombination in relation to the maximum x_m or the inflection point x_i of $p(x)$ (5.36) and (5.37).

6.(*) Develop an explicit expression for x_m and x_i for gr-currents with optical excitation and surface recombination.

7.(l) How does the collection efficiency of minority carriers given in Sect. 5.2.4.2 compare with the collection efficiency of solar cells?

8.(*) Describe in your own words the physical meaning of the diffusion velocity (5.14) and of the effective diffusion velocity considering surface recombination given in (5.41). Compare the diffusion velocity with the drift velocity in its microscopic description, using the concept of random walk.

9.(*) Develop explicitly the expression for the effective upstream and downstream diffusion lengths given in (5.48) and (5.49), and compare these to the simplified picture with an effective diffusion length as the geometric means $\sqrt{L_p^2 \pm L_s^2}$. Point out the differences, limiting cases and microscopic reasons.

10.(*) Develop the equation for the minority carrier distribution with drift field contribution (5.53) from the basic diffusion equation (5.46).

11. Derive the hole current equations (5.54), (5.55) and (5.56) from the equation for the minority carrier distribution (5.53).

12. Develop the equations for minority carrier distribution corresponding to (5.36), considering optical excitation and surface recombination and using $p_{j\mathrm{D}}$ as boundary condition at $x = 0$.

6

Schottky Barrier in Two-Carrier Model

Summary. In Schottky barriers one needs to consider the influence of minority carriers when the barrier is sufficiently large. Here carrier generation and recombination become important.

We will now extend the analysis of the transport properties of a two-carrier model to a Schottky barrier. One of the main differences between a one-carrier Schottky barrier discussed earlier and the two-carrier Schottky barrier is the electron-hole inter-relation to its currents that was discussed for a homogeneous semiconductor in the previous chapter. We will again assume here an n-type Schottky barrier.

6.1 Electron and Hole Currents in Barriers

The majority carrier current (j_n) is controlled by the properties of the barrier, as discussed in Chap. 3. The minority carrier current (j_p), though also controlled by the barrier, is mostly generated in the bulk region near the barrier, as described in the preceding chapter. Both regions have a different thickness, the barrier relating to the Debye length L_D, and the active part of the bulk relating to the minority carrier diffusion length L_p.

In most devices, L_p is much larger than L_D. In the Schottky barrier discussed here as an example (see Table 6.1) $L_\mathrm{D} = 480$ Å and $L_p = 22\,\mu\mathrm{m}$, with a ratio L_p/L_D of ~ 500, so that the different properties in these regions can be well separated for transparency of the following discussion.

In order to identify the different contributions to the current j, we have subdivided[1] the current into several contributions, even though there are inter reactions between several of them.

[1] For justification of this unconventional approach see Sect. 5.3.

Table 6.1. Parameters of Germanium-Barrier

Parameters	N_d	N_r	N_c	N_v	n_{10}
Values	10^{16}	10^{16}	10^{19}	$6 \cdot 10^{18}$	10^{16}
Dimensions	cm^{-3}	cm^{-3}	cm^{-3}	cm^{-3}	cm^{-3}
Parameters	E_g	$E_i - E_r$	$\psi_{\mathrm{MS},n}$	$\psi_{\mathrm{MS},p}$	p_{10}
Values	0.66	0.10	0.319	0.341	5.13×10^{10}
Dimensions	eV	eV	V	V	cm^{-3}
Parameters	c_{cv}	μ_n	μ_p	n_c	p_c
Values	10^{-9}	3900	1900	4.48×10^{13}	1.15×10^{13}
Dimensions	$\mathrm{cm}^3 s^{-1}$	$\mathrm{cm}^2/\mathrm{Vs}$	$\mathrm{cm}^2/\mathrm{Vs}$	cm^{-3}	cm^{-3}
Parameters	v_n^*	ε	T	n_i^*	n_i
Values	5.7×10^6	16	300 K	1.077×10^{15}	2.265×10^{13}
Dimensions	cm/s	—		cm^{-3}	cm^{-3}

We distinguish four contributions to the total currents:

- the $n(x = 0) = n_j$-controlled, divergence-free majority-current, j_{ni};
- the $p(x = d_1) = p_j$-controlled, divergence-free minority-current, j_{pi}; and
- the gr-current for minority-carriers $j_\mathrm{gr}^{(p)}(x)$, and
- the complementary gr-current for majority-carriers $j_\mathrm{gr}^{(n)}(x)$.

These currents are plotted schematically in Fig. 4.8 for reverse bias to indicate the general relationship. In a device containing a space charge region, each of these currents has, in part of the device, drift and diffusion contributions.

6.1.1 Divergence-Free Electron and Hole Currents

The divergence-free current is a part of the current that does not interact via generation or recombination with the opposite carrier. Its separation provides an immediate check on the influence of minority carriers: in a one-carrier model, only the divergence-free majority carrier current j_{ni} exists. In the bulk it is carried by drift, in the barrier by the difference between drift and diffusion. $j_{ni} = j_n$ is used as an input parameter for numerical integration of the system of governing differential equations, e.g., in (3.5) – (3.7) as described in Sects. 6.2 and 3.1. It will be used later in a similar fashion in (6.12)–(6.17) for the two-carrier model (Sect. 6.2).

In the two-carrier model, there are two divergence-free current contributions j_{ni} and j_{pi}. These currents can be determined at any convenient position of the device in which the gr-current contribution can be neglected. Without surface recombination, this could be at the cathode for j_{ni} and at the anode for j_{pi} since $j_\mathrm{gr}^{(n)}(x = 0) = j_\mathrm{gr}^{(p)}(x = d_1) = 0$. When including surface recombination, the task of current separation is more involved, as will be shown in Sect. 6.2.3.1.

6.1.2 GR-Currents in Schottky Barrier Devices

The gr-current contribution can be subdivided into four parts:

- gr-currents from the bulk region (as discussed in Chap. 5);
- gr-currents from the space charge region;
- gr-currents from metal/semiconductor interfaces; and
- gr-currents from other surfaces.

We separate the contribution of the gr-currents in the space-charge region and in the bulk region in this discussion and present some typical device examples later in this chapter. The interface recombination will be discussed in different Sections, emphasizing its contributions to the diode leakage.

6.1.2.1 GR-Currents in the Space-Charge Regions

In the space-charge region, the net gr-rate U changes as a function of x. In order to show the main features, we separate generation and recombination. We first approximate the generation rate $g(x)$ for thermal excitation by [see (4.33)]

$$g(x) = \frac{c_{cv} N_r n_i^2}{n(x) + p(x) + 2n_i \cosh\left(\frac{E_r - E_i}{kT}\right)} \tag{6.1}$$

or

$$\boxed{g(x) = \frac{1}{\tau_{p0}} \frac{n_i^2}{n(x) + p(x) + n_i^*}.} \tag{6.2}$$

In the Schottky barrier region, $n(x)$ decreases below $n_{10}^{(\mathrm{th})} \simeq N_\mathrm{d}$ to approach n_c at the metal/semiconductor interface. Consequently the generation rate increases, until $n(x)$ crosses $p(x)$ or n_i^* in the denominator of (6.2), depending on which of these terms predominates.

One, therefore, distinguishes two regions, the n-type bulk with the generation rate

$$g_1(x) = g_n = \frac{n_i^2}{\tau_{p0} n_{10}} = \frac{p_{10}}{\tau_{p0}}, \tag{6.3}$$

and the barrier where n becomes comparable to p, with $g_1(x)$ increasing. For $E_r - E_i \neq 0$, the third term in the denominator finally becomes the largest, and one obtains a flat maximum of the generation rate with

$$g_2(x) = g_j = \frac{n_i^2}{\tau_{p0} n_i^*}. \tag{6.4}$$

A typical generation rate distribution is shown in Fig. 6.1 with these two ranges depicted.

The recombination rates, corresponding to the above mentioned generation rates, are given by

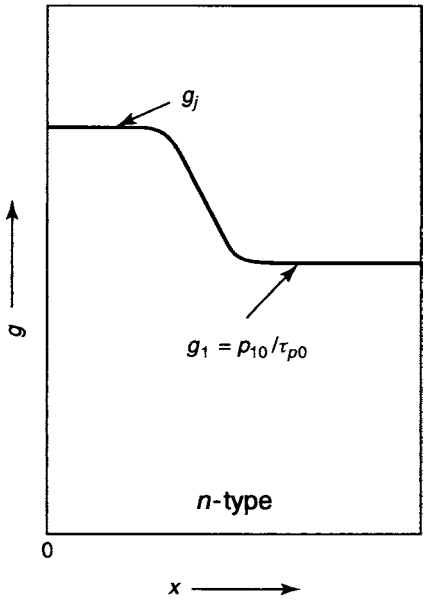

Fig. 6.1. Generation rate that show a step-like behavior between bulk and barrier (schematic)

$$\boxed{r(x) = \frac{1}{\tau_{p0}} \frac{np}{n(x) + p(x) + n_i^*}} \tag{6.5}$$

and change within the barrier region in a similar manner. For zero bias (i.e. in thermodynamic equilibrium), the recombination rate is the same as the generation rate distribution (since $np = n_i^2$). It shows the same step like behavior.

With *reverse bias*, both $n(x)$ and $p(x)$ decrease below the equilibrium distribution, thus causing $r(x)$ to become smaller than $g(x)$, and resulting in a positive *net* gr-rate U of similar shape. The opposite relation appears with *forward bias*: $n(x)$ and $p(x)$ becomes larger than the equilibrium distribution; hence, the recombination dominates: $r(x) > g(x)$ and $U(x)$ becomes negative.[2] Figure 6.2 shows an example of such a distribution for $g(x)$, $r(x)$, and $U(x)$ as computed for an actual Schottky barrier with parameters listed in Table 6.1 (observe the changing sequence of g, r, and U in panels a–c).

[2] Observe that in Fig. 6.2 the absolute values of $r(x)$ and $U(x)$ are plotted in order to permit an easy comparison of the shape of these two curves. The change in sign for U in forward bias is indicated by $-U$ in Fig. 6.2a and by $+U$ in reverse bias in Fig. 6.2b and c.

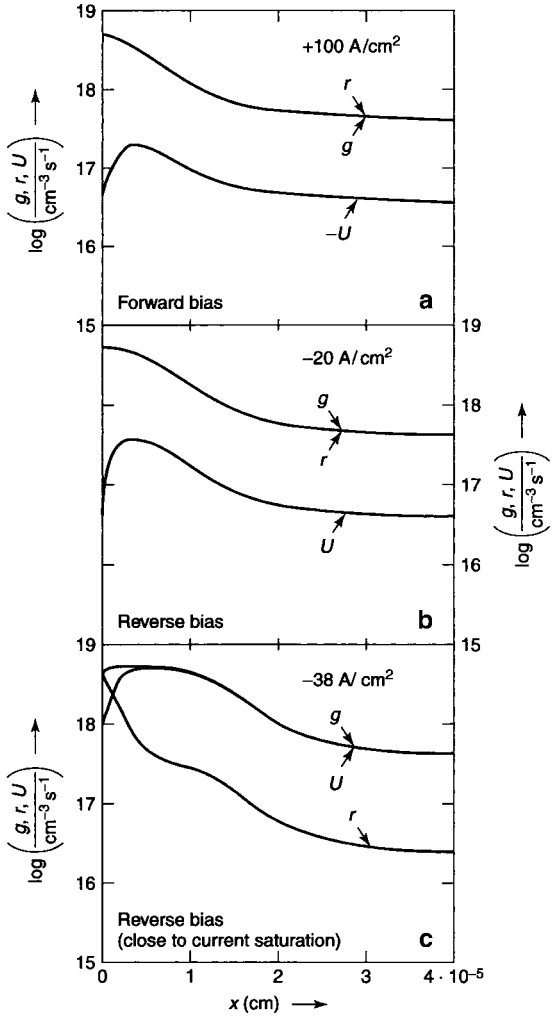

Fig. 6.2. Generation, recombination, and net gr-rates in a Schottky barrier, as computed from (6.12) to (6.17) with parameters given in Table 6.1; for forward bias: (**a**) with $j = 100\,(\mathrm{A/cm^2})$; and for reverse bias in (**b**) with $j = -20\,(\mathrm{A/cm^2})$; or in (**c**) with $j = -38\,(\mathrm{A/cm^2})$

The net gr-rate U can also be approximated by two (nearly) Constant space-independent values, joining each other in a step like fashion,[3] in the bulk by U_{10}:

[3] Even though (6.7) should contain the space-dependent minority carrier densities, we have replaced these by the constant $p_{j\mathrm{D}}$ and later in (6.8) by n_j; this is justified to an improved approximation with reverse bias as can be seen from the computed result of a step like $U(x)$.

$$\boxed{U_{10} \simeq \frac{p_{j\mathrm{D}} - p_{10}}{\tau_{p0}};} \tag{6.6}$$

and in the barrier,[4] by U_j:

$$\boxed{U_j \simeq \frac{p^*_{j\mathrm{D}} - p^*_{10}}{\tau_{p0}}} \tag{6.7}$$

with

$$p^*_{j\mathrm{D}} = p_{j\mathrm{D}} \frac{n_j}{n^*_i} \quad \text{and} \quad p^*_{10} = p_{10} \frac{n_{10}}{n^*_i}; \tag{6.8}$$

for n^*_i see (6.1) and (6.2). The variation of the bias influences the boundary density $p_{j\mathrm{D}}$ (or $p^*_{j\mathrm{D}}$), hence the net gr-rate. This causes a change in the step-height; by influencing the changeover from $p_{j\mathrm{D}}$ to $p^*_{j\mathrm{D}}$, it makes the step in the barrier region wider or narrower in reverse or forward bias, respectively.

The step like behavior permits the use of the same diffusion equation as discussed in Sect. 5.1.1.1 within the horizontal range of each step. Δj_{gr} to be approximated by line segments as shown in Fig. 6.3:

$$\Delta j_{\mathrm{gr}} = e \int_0^{d_1} U(x)\mathrm{d}x \simeq -e\left[U_j x_{\mathrm{D}} + U_{10}(d_1 - x_{\mathrm{D}})\right]. \tag{6.9}$$

For wider slabs, $U(x)$ in the bulk starts to vanish for $x > L_p$, as discussed in Sect. 5.1.1.

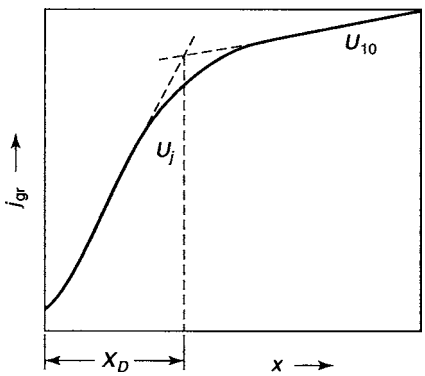

Fig. 6.3. Schematics of gr-current with bias in the barrier of width x_{D} and in the bulk with barrier and bulk *net-generation rates* U_j and U_{10}, respectively shown

[4] For simplicity of the mathematical description, we have chosen modified carrier densities $p^*_{j\mathrm{D}}$ and p^*_{10} rather than the modified minority carrier lifetime τ_p [given in (4.49)], which would result in a somewhat longer expression.

6.1.2.2 Field Influence in the Barrier Region

In the space-charge region, the field is much larger than in the bulk, and thus, its influence on the minority carrier current needs to be considered. The changes of the effective diffusion length due to the *Schubweg* are mostly negligible, since the length in which the field acts, the Debye length, is usually much smaller than the minority carrier diffusion length in which most of the minority carrier collection occurs.

A significant influence of the field, however, on $p(x)$ requires a large minority carrier gradient near the interface to the electrode, in order to compensate the ensuing drift current. We will discuss this balance in the following section.

6.1.2.3 The Definition of the Carrier Density at the Splicing Boundary

The minority carrier distribution in the bulk as a function of the density $p_{j\mathrm{D}}$ at the barrier-to-bulk interface is discussed in Chap. 5. The connection of this density with the computed $p(x)$ distribution in the barrier region was indicated in Fig. 5.2 and was mentioned as a means of the bias to control the minority carrier current through the bulk. We need now to refine the discussion of the boundary condition $p_{j\mathrm{D}}$.

The steep increase of the minority carrier density toward the density p_j at the metal boundary is shown in Fig. 6.4 (see also Sect. 6.2.2.1). Such increase is required for obtaining a balancing diffusion current toward the bulk to counteract the drift current toward the metal boundary. Depending on the bias, the field-ramp and therefore the minority carrier density slope, changes in the barrier region, in order to maintain almost exact cancellation of drift

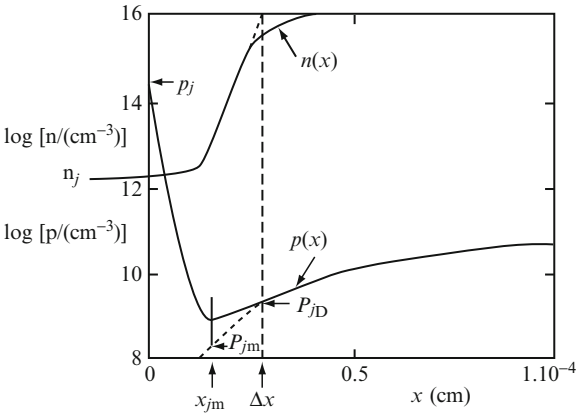

Fig. 6.4. Minority carrier and majority carrier distribution in the junction as given by the computed solution of (6.12)–(6.17) with parameters given in Table 6.1, and for $j_{ni} = -39\,\mathrm{A/cm^2}$. The solution curves for $p(x)$ with $x > \Delta x$ are also shown as obtained from the approximation of [e2632] $p_{10} = 5.13 \times 10^{10}\,\mathrm{cm}^{-3}$

and diffusion. This results in a shift of the density $p_{j\mathrm{D}}$ at the end of the barrier where the barrier field vanishes and the minority current becomes almost exclusively diffusion-controlled.

In reverse bias, this transition is clearly visible in Fig. 6.4, as $p(x)$ goes through a minimum with the diffusion current changing sign at x_{jm}. Between x_{jm} and Δx, a small and decreasing drift field maintains current continuity.

For computational reasons, we treat the Schottky barrier region and the bulk region separately in the approximation given earlier, and splice the solution curves at the boundary Δx. Such splicing is shown in reverse bias in Fig. 6.4: One can define a density p_{jm} on the extrapolated diffusion curve at the position x_{jm} of the minimum of the exact $p(x)$ distribution in reverse bias. For the diffusion analysis in the bulk, given in the previous chapter, we would have obtained exactly the same answer if we started at x_{jm} with p_{jm} rather than at Δx with $p_{j\mathrm{D}}$ as we did.

Whenever $p_{\min}$ is easier to determine than $p(\Delta x) = p_{j\mathrm{D}}$, we may indeed do so. For most devices, however, $\Delta x - x_{jm}$ is very small compared with L_p and with the device thickness, so that the error introduced by omitting Δx altogether is small.

6.1.2.4 Minority Carrier Density at the Metal/Semiconductor Interface

The metal/semiconductor interface acts as a perfect recombination surface which forces the *two quasi-Fermi levels* (see Sect. 6.2.2.4) to *collapse* and connect to the Fermi level of the metal. The product of the of minority and majority carrier densities at the interface, is therefore, given by n_i^2. With zero bias, this means

$$p_c = \frac{n_i^2}{n_c}. \tag{6.10}$$

With bias, the majority carrier density slides near this boundary according to (3.46). When assuming that the interface recombination also determines the shifted boundary densities, one has as a condition for the holes

$$p_j = \frac{n_i^2}{n_j} \tag{6.11}$$

which we will use consistently in the following sections. This condition holds as long as $j_p(x = 0) \ll j_n(x = 0)$, that means the electron current controls the minority carrier relation at the metal/semiconductor interface.

6.2 Schottky Barrier with Two Carriers

The interaction between the two carriers in a Schottky-barrier device now becomes transparent. Its discussion will guide further understanding about the minority carrier contribution in *pn*-junction devices, where this interaction becomes essential for controlling the total current.

6.2.1 The Governing Set of Equations

The entire behavior of the space charge region is analytically described by one set of six first order differential equations: This governing set of differential equations includes the transport equations for both carriers (given here in a form to emphasize the set of governing differential equations):

$$\frac{\mathrm{d}n}{\mathrm{d}x} = \frac{j_n - e\mu_n nF}{\mu_n kT} \tag{6.12}$$

and

$$\frac{\mathrm{d}p}{\mathrm{d}x} = \frac{-j_p + e\mu_p pF}{\mu_p kT}; \tag{6.13}$$

the continuity equations[5]

$$\frac{\mathrm{d}j_n}{\mathrm{d}x} = -eU \tag{6.14}$$

and

$$\frac{\mathrm{d}j_p}{\mathrm{d}x} = eU, \tag{6.15}$$

and the Poisson equation, which now includes electrons and holes (assuming only minor compensation: $N_\mathrm{a} \ll N_\mathrm{d}$):

$$\frac{\mathrm{d}F}{\mathrm{d}x} = \frac{e(N_\mathrm{d} - n + p)}{\varepsilon\varepsilon_0} \tag{6.16}$$

with

$$\frac{\mathrm{d}\psi_n}{\mathrm{d}x} = F. \tag{6.17}$$

6.2.1.1 Example Set of Parameters

In order to make minority carrier contributions more important, we have chosen as the first example a small band-gap material (Germanium) with $E_g = 0.66\,\mathrm{eV}$ in which the majority and minority carrier densities can be kept in closer proximity to each other (Figs. 6.5 and 6.6).

For reasons of initial simplicity, the metal/semiconductor work function was chosen, so that the electron density at the metal/semiconductor interface in equilibrium at $T = 300\,\mathrm{K}$ is only slightly larger than the corresponding hole density (see Fig. 6.6). A shallow, totally ionized donor is assumed to produce n-type semiconductivity. The complete set of parameters used in the computation is summarized in Table 6.1.

[5] One of the continuity equations can be replaced by the total current equation $j = j_n + j_p$.

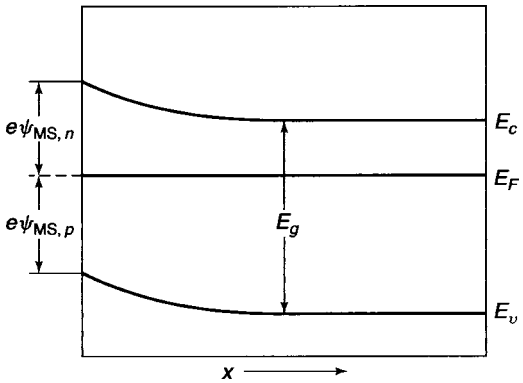

Fig. 6.5. Band-model of the Schottky barrier used in this Section

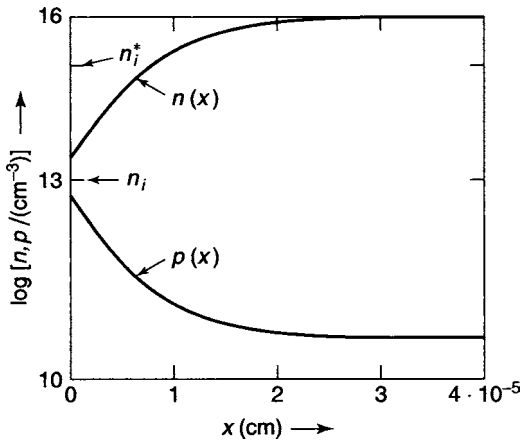

Fig. 6.6. Electron and hole distributions for thermal equilibrium as computed from (6.12) to (6.17) with parameters given in Table 6.1, with n_i and n_i^* indicated in the figure

6.2.1.2 Boundary Conditions

One distinguishes several cases depending on the excitation (whether it is thermal only, or predominant optical), the width of the device d_1 (short or long compared to the minority carrier diffusion length), and the surface condition (negligible or predominant surface recombination). Accordingly, different approximations may be employed.

With six first order differential equations describing the problem, we need six boundary conditions, n_b, F_b, ψ_b, p_b, j_{nb}, and j_{pb}, which would conventionally be given for one side of the device, i.e., either at $x = 0$ or at $x = d_1$. Unfortunately, some of these boundary conditions are sufficiently known only

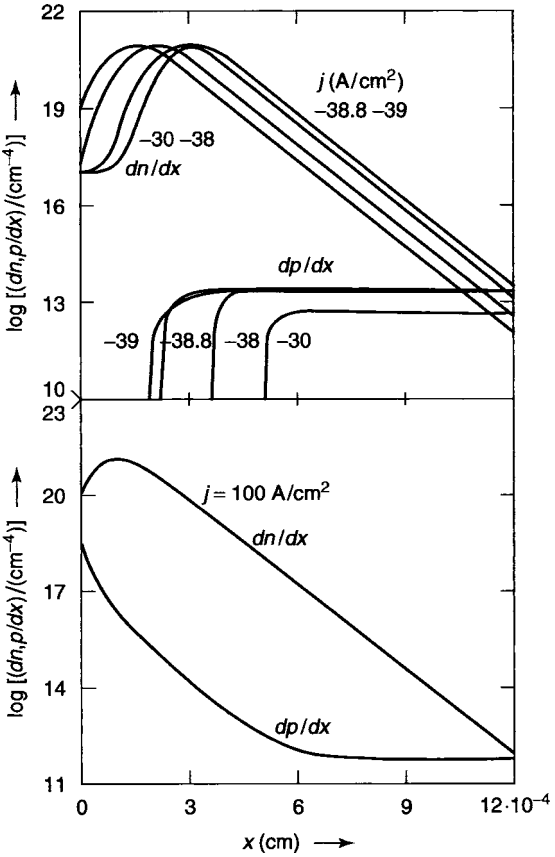

Fig. 6.7. Slopes of n and p as obtained from numerical integration of (6.12)–(6.17) and parameters of Table 6.1 with the total current as family parameter. (**a**) for reverse bias with $j = -30,\ -38,\ -38.8$, and $-39\,\mathrm{A/cm^2}$ for curves 1–4, respectively; (**b**) for forward bias with $j = 100\,\mathrm{A/cm^2}$

at one side, others at the other side. This requires a mixed condition approach, necessitating iteration.[6]

The boundary conditions for the thin device are first chosen for a neutral right surface with $s(d_1) = 0$, $n(d_1) = N_\mathrm{d} - \delta n$ (δn obtained by iteration to assure an exponential decrease of $\mathrm{d}n/\mathrm{d}x$ with increasing x, as shown in Fig. 6.7 beyond the maximum — for more see Sect. 6.2.3.2), $F(d_1) = j_{ni}/[e\mu_n n(d_1)]$, $\psi_n(d_1) = 0$, $j_{pi} = e\mu_p p(d_1)F(d_1)$ and $j_{ni}(d_1)$ as

[6] For educational purposes, it is advantageous to use a forward numerical integration of the governing set of differential equation rather than a more conventional finite element method (Snowden, 1985). Straightforward integration permits one to study the interaction of different variables and the cause-and-effect relation of changing boundary conditions.

input parameter. The remaining $p(d_1)$ is first guessed and then iterated so that $p(0) = p_j = n_i^2/n_j$, assuring perfect recombination at $x = 0$.

6.2.2 Example Solutions for a Thin Device

In Figs. 6.8 and 6.9, we present a family of example solutions for the Schottky barrier within a thin slab of the n-type Germanium as described above.

These solution curves show a similar behavior for $n(x)$, $\varrho(x)$, $F(x)$, and $\psi_n(x)$ as given in Fig. 3.29 for the single carrier model. $p(x)$ is essentially flat within the bulk with a barely visible slope toward the barrier in reverse and

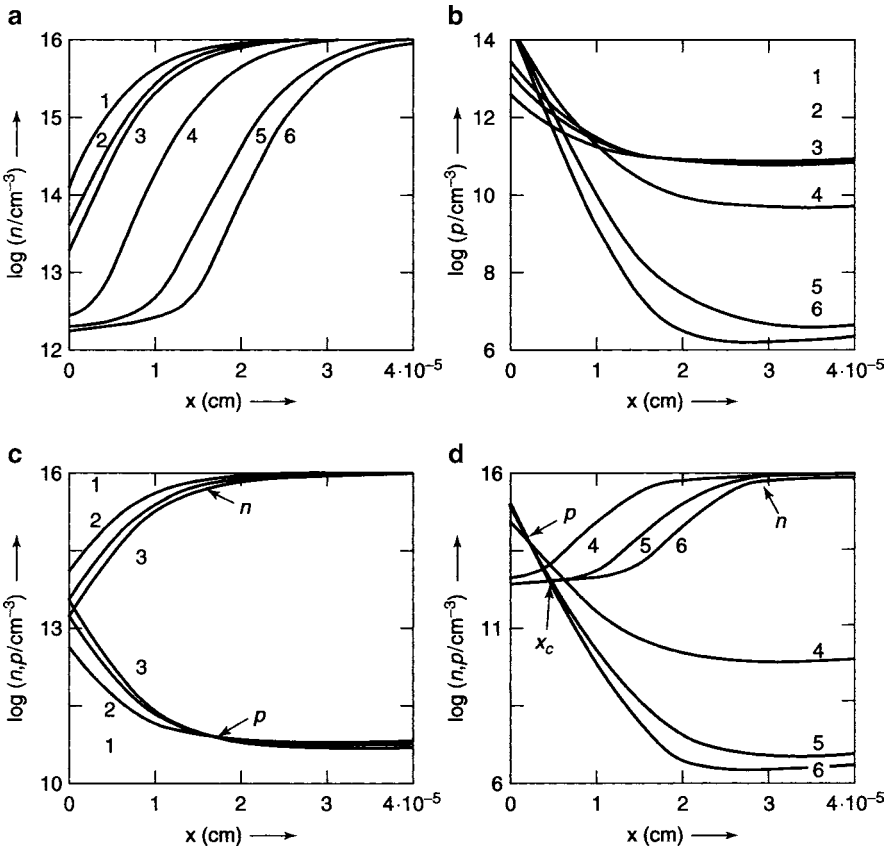

Fig. 6.8. Carrier density distribution curves obtained as solutions of (6.12)–(6.17), with parameters given in Table 6.1 for the total current as family parameter. Curves 1, 3,4, and 6 for $j = 100,\ 0,\ -38$, and $-39\ \mathrm{A/cm^2}$, respectively. (**a**) Electron density distribution; (**b**) hole density distribution; (**c**) electron and hole distributions for curves 1 and 3 only; and (**d**) electron and hole distributions for larger reverse currents (curves 4 and 6 only). (**c**) and (**d**) are plotted to demonstrate the relation between $p(x)$ and $n(x)$ with a cross-over near $x = 0$ at higher reverse bias

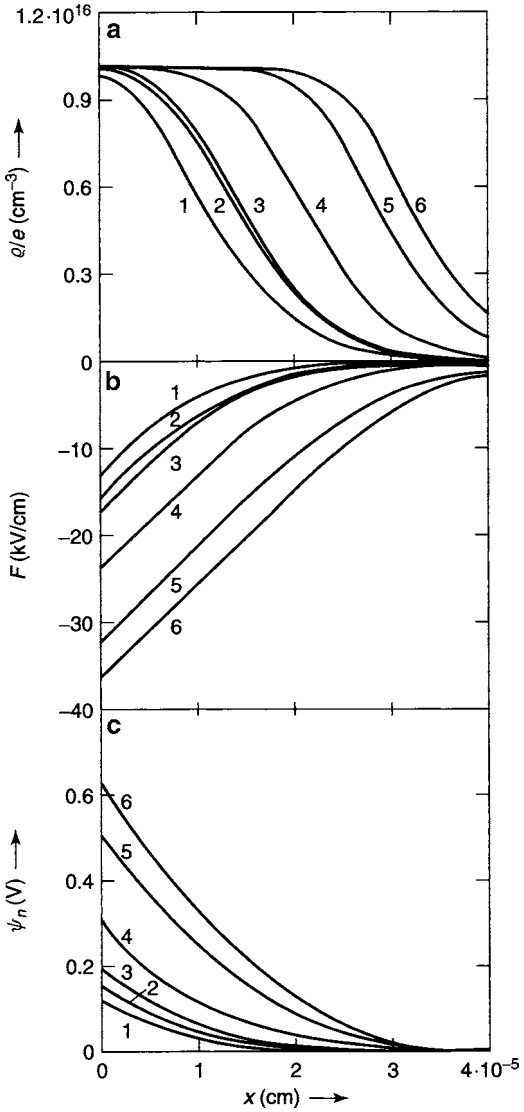

Fig. 6.9. Space-charge, field, and electrostatic electron potential distributions as solutions of (6.12)–(6.17) with parameters given in Table 6.1; the total current as family parameter for curves 1, 3,4, and 6 as listed in Fig. 6.8

away from the barrier in forward bias. Most remarkable is the steep increase of $p(x)$ in the barrier with a cross-over of $n(x)$ at higher reverse bias. However, the influence of p on other variables is negligible well within the width of the drawn curves except for ϱ at the highest reverse bias and close to $x = 0$ when $p(x)$ has risen above N_d (not shown in Fig. 6.8).

6.2.2.1 Carrier Distributions

The steeply changing carrier distribution is caused by the increasing field and, thereby, increasing drift that needs to be almost exactly compensated by an increasing diffusion current in the opposite direction to keep the total current essentially[7] constant throughout the device. This problem is not unlike the one discussed in Sect. 5.3 and governed by (5.44) and (5.45), but here with an impressed (fixed) field distribution $F(x)$ as given by the majority carrier distribution, i.e., by (3.8), yielding an inhomogeneous differential equation for the minority carriers

$$\frac{\mathrm{d}^2p}{\mathrm{d}x^2} - 2\left[\frac{1}{L_\mathrm{D}}\frac{2e(\psi_{n,\mathrm{D}}-V)}{kT} + \frac{x}{L_\mathrm{D}^2}\right]\frac{\mathrm{d}p}{\mathrm{d}x} - \left[\frac{1}{L_p^2}+\frac{1}{L_\mathrm{D}^2}\right]p + \frac{p_{10}}{L_p^2} = 0 \qquad (6.18)$$

with L_D the Debye length–see (3.20) and $\psi_{n,\mathrm{D}}$ the diffusion electron potential–see (3.15). The solution of (6.18) now contains a mixture of bulk- (hole-related–L_p) and junction- (electron-related–L_D) characteristic lengths.

Boltzmann Region for Minority Carriers. A substantially simple approximation can be obtained within the barrier region where the net current j_p is small compared to the drift and diffusion of holes; here one obtains from the transport equation, by neglecting j_p,

$$\frac{\mathrm{d}p}{\mathrm{d}x} = \frac{epF}{kT}, \qquad (6.19)$$

From the balance between drift and diffusion currents for holes in the entire barrier region namely $ep\mu_p F = \mu_p kT\,\mathrm{d}p/\mathrm{d}x$, one can obtain the Boltzmann solution for holes, that is very similar to the Boltzmann solution for electrons:

$$p(x) = p_j \exp - \left[\frac{e\psi_{n,j}}{kT} + \frac{eF_j x}{kT} + \frac{x^2}{2L_\mathrm{D}^2}\right], \qquad (6.20)$$

with all parameters $\psi_{n,j}$, F_j, and L_D, however, controlled by the electron-distribution. One can then substitute $\psi_{n,j} = (kT/e)\ln(n_{10}/n_j)$, using $n_{10}p_{10} = n_i^2$ and introducing F_j from (3.40), to obtain for the *Boltzmann distribution of minority carriers*

$$\boxed{p(x) = \frac{n_i^2}{n_j}\exp - \left[\frac{x}{L_\mathrm{D}}\sqrt{2e\frac{\psi_{n,\mathrm{D}}-V}{kT}} + \frac{x^2}{2L_\mathrm{D}^2}\right]}, \qquad (6.21)$$

which describes the exponentially decreasing branch of $p(x)$ within the Schottky barrier. Since this distribution is Boltzmann-like[8] and, consequently,

[7] The gr-current is a very small fraction of the currents.

[8] The crossing of $p(x)$ for different bias within the barrier region is a direct result of the control of the boundary concentration p_j by the electron density n_j via

the hole quasi-Fermi level is flat[9] in reverse bias in the entire barrier region, as can be seen in Figs. 6.10 and 6.11a.

In Fig. 6.10b, the DRO range is identified close to the left electrode where the drift dominates, and toward the bulk the DO range (for (D)iffusion (O)nly) is identified where diffusion dominates. In between these two regions is at high reverse bias the relatively small Botzmann region where drift and diffusion compensate each other.

In Fig. 6.11b, the two quasi -Fermi levels are given that show a distinct parallel sloping toward the right electrode.

6.2.2.2 Demarcation Lines and Shockley–Franck–Read Recombination Centers

The Fig. 6.10 also include the two demarcation lines E_{Dn} and E_{Dp}. They lie well below the two quasi-Fermi levels and spread over a relatively wide energy range. Centers within the energy range of the demarcation lines are considered recombination centers and consequently discussed in the Shockley-Frank-Read accounting. But for this, one needs to know the specific energy level and its capture cross sections. It is probable that such a wide energy range is also a significant distribution of energy levels with a variety of capture cross sections. Under limited circumstances, one may approximate all of them with one effective recombination center and one set of capture cross sections. But, as seen from Fig. 6.11 this energy range shifts with respect to the band edges as one moves from the electrode boundary into the bulk of the semiconductor. This makes even that approximation more problematic.

This may be remembered as a warning, that, whenever one resorts to the Shockley-Frank-Read approximation to compute the behavior in barriers or junctions, a much better understanding of the recombination traffic is necessary to avoid misleading result. There is no consolation from the fact that such demarcation lines are usually not shown, because they are at best confusing for different sets of centers. But since recombination becomes an important factor in determining the efficiency of solar cells, it must be emphasized to

$n_j p_j = n_i^2$ required by perfect recombination at the interface. n_j, however, is controlled by the dominant majority carrier current which forces a decrease of n_j with increased reverse bias, and, in turn, causes an increased p_j. This, together with an increased slope of $p(x)$ due to the increased barrier field, results in the crossing of the different $p(x)$ curves in the family of curves of Fig. 6.8b. In contrast, $n(x)$ is the dominant variable with an increasing fraction of drift current as the bias is reduced, causing the $n(x)$ profile to widen, the $n(x)$ slope thereby to reduce hence avoiding an $n(x)$-crossover (the solution curves of the dominant variables must be unique– Fig. 6.8a).

[9] The quasi-Fermi level remains flat wherever drift and diffusion currents are large compared with the net current, i.e., for holes almost in the entire barrier region until $x = x_D$ is approached.

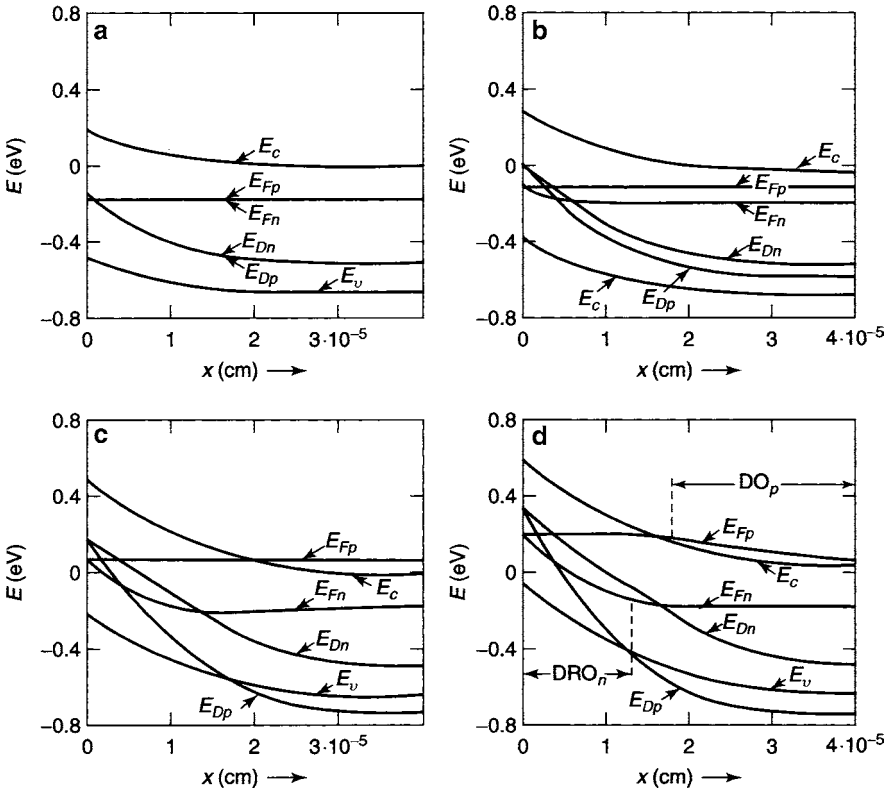

Fig. 6.10. Band-model with quasi-Fermi and demarcation lines computed from (6.12) to (6.17) and parameters listed in Table 6.1 for the Ge-Schottky barrier for different reverse bias conditions with $j = -38.8$ and $-39\,\mathrm{A/cm^2}$ for panels (**a**) and (**b**), respectively. In panel (**c**) the quasi-Fermi level for holes is flat throughout, the Boltzmann, or DRO region, while at higher reverse bias in panel (**d**) a bending down of E_{Fp}, following essentially parallel to E_c is observed, identified as DO region for diffusion only. Observe that the demarcation lines have dropped below both quasi-Fermi levels and are even extending into the valence bands

pay sufficient attention to independently determine their position within the material, their energy spectrum, and recombination cross sections.

6.2.2.3 Currents in the Schottky Barrier

The main current in the Schottky barrier[10] is the *divergence-free electron current* j_{ni},

$$j_{ni} = ev_n^*(n_j - n_c); \tag{6.22}$$

[10] The chosen example of a Ge-diode with a relatively high barrier density results in an unfavorable diode characteristic with high reverse saturation current. A much improved Schottky barrier can be obtained with a substantially lower n_c.

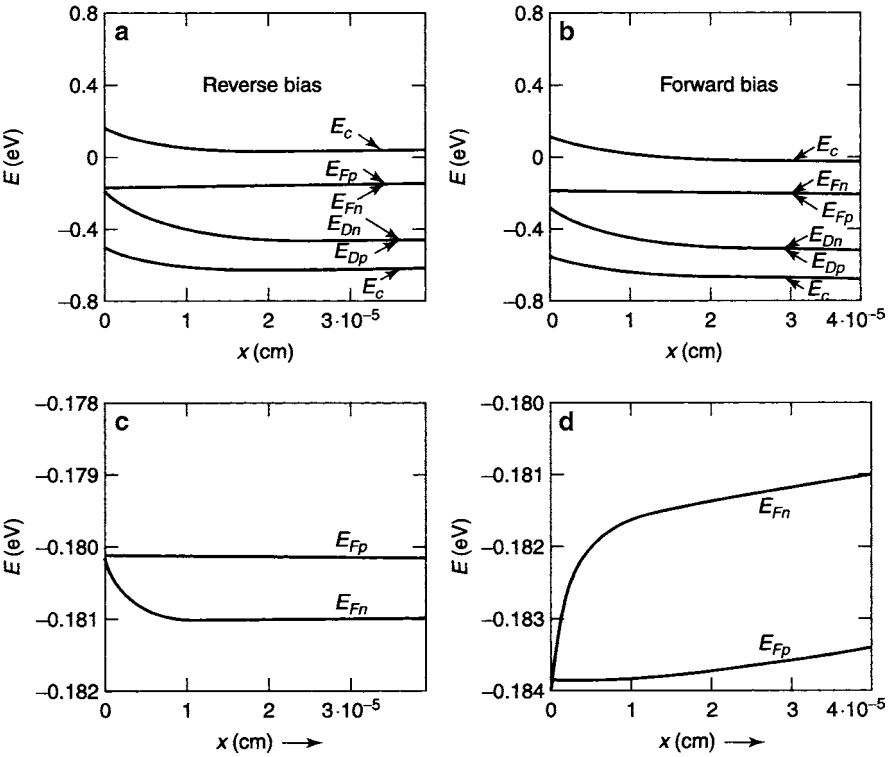

Fig. 6.11. The quasi-Fermi levels, computed for the Ge-Schottky barrier device as in Fig. 6.10, but with enlarged energy resolution, here for reverse bias in panel (**a**) with $j = -10\,\mathrm{A/cm^2}$ and in forward bias in panel (**c**) and (**d**) with $j_{ni} = 100\,\mathrm{A/cm^2}$ in panel (**b**). Observe the marked sloping up of both quasi-Fermi levels in forward bias

with $n_c = 4.48 \times 10^{13}\,\mathrm{cm^{-3}}$ and $v_n^* = 5.7 \times 10^6\,\mathrm{cm/s}$, one obtains a rather large saturation current in reverse bias of $j_{ni}^{(s)} = -40.6\,\mathrm{A/cm^2}$. To support such a current through the bulk,

$$j_{ni} = en_{10}\mu_n F_{10}, \tag{6.23}$$

a reverse saturation field of $F_{10} = 6.55\,\mathrm{V/cm}$ must be maintained in the bulk with an electron drift velocity of $\mu_n F_{10} = 2.55 \times 10^4\,\mathrm{cm/s}$.

The *divergence-free hole current* in the bulk is given by

$$j_{pi} = ep(d_1)\mu_p F_{10}. \tag{6.24}$$

Because of the much lower minority carrier density in the bulk, it is more than five orders of magnitude smaller than j_{ni}.

The *gr-current* obtained by numerical integration is shown in Fig. 6.12 for four bias conditions. Near electron reverse saturation, we obtain the maximum

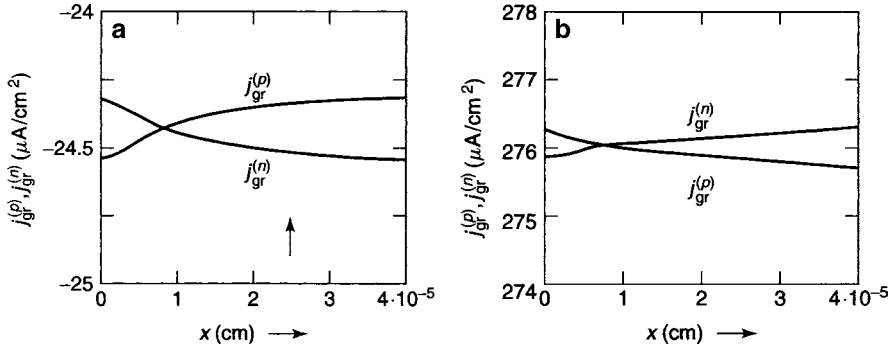

Fig. 6.12. Electron and hole gr-current distribution for different total current: $j = -38$, and $+100\,\mathrm{A/cm^2}$ with reverse and forward bias for panels (**a**) and (**b**), respectively. Observe that the ordinate scale is shifted by j_{pi} on top of which $j_{\mathrm{gr}}^{(p)}$ and starts at $x = d_1$

contribution of $\Delta j_{\mathrm{gr}} \simeq 20\,\mu\mathrm{A/cm^2}$. This current is also more than six orders of magnitude smaller than the divergence-free electron current since, in spite of the larger net gr-rate it develops only in a thin slab of only $4 \times 10^{-5}\,\mathrm{cm}$ width (Fig. 6.12c). The electron gr-current is complementary to the hole gr-current. The sum of both add up to the same Δj_{gr} at any position of the slab, as shown in Fig. 6.12.

The total gr-contribution does not saturate but increases with reverse bias as shown in Fig. 6.13, since U increases with increasing width of the barrier region.

6.2.2.4 Quasi-Fermi Levels and Demarcation Lines

With the information given in this chapter, it is important to review some of the detail of the most important quasi-Fermi levels in the understanding of the barrier behavior that can easily be expanded to junctions, as we will see in the next chapter. It also gives another opportunity to reflect on the change of the behavior of defect centers from being carrier traps to becoming recombination centers, and the possibility of the wide range of energy in which such changes can take place, but also warns again to be careful in using a simple Shockley-Read -Hall model for computing the barrier or junction behavior since the energy range in which new recombination centers become activated, that is, the range between the demarcation lines usually changes significantly throughout such space charge layers. This means that in different regions of the device the recombination traffic takes place through different centers that may have quite different recombination parameters.

Let us first review again the quasi-Fermi levels. As $n(x)$ and $p(x)$ deviate from their equilibrium distribution for nonvanishing currents, the Fermi level splits into two quasi-Fermi levels E_{Fn} and E_{Fp}, and two demarcation lines

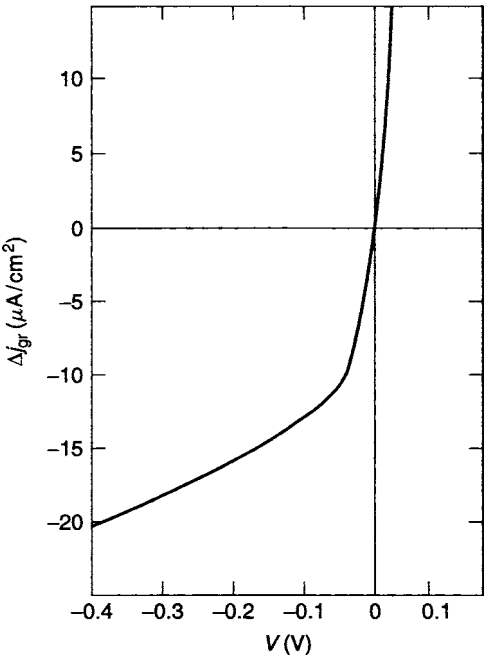

Fig. 6.13. Total gr-current Δj_g as function of the applied voltage, obtained by integrating (6.12)–(6.17) with parameters listed in Table 6.1

E_{Dn} and E_{Dp} separate to identify the recombination centers in between, as computed for four reverse currents and plotted in Fig. 6.10.

At the metal/semiconductor interface, the *quasi-Fermi levels collapse* because of the complete recombination at the metal surface. In reverse bias, the quasi-Fermi level for electrons, E_{Fn} drops *below* the Fermi level E_{Fp} that remains essentially constant.

When near the electrode the quasi Fermi level for majority car E_{Fn} changes parallel to the band edge $E_c(x)$, a DRO-range for majority carriers appears. Where the quasi-Fermi level remains independent of x, the Boltzmann range appears. At higher reverse bias (sub figure b), E_{Fp} also starts to slope downward. Here the hole current is exclusively carried by diffusion only,[11] indicating a DO-range for minority carriers. These DO and DRO ranges are identified in Fig. 6.10d.

The main portion of the voltage drop[12] (Sect. 3.1.3) occurs in the barrier near the metal/semiconductor interface, where the majority quasi-Fermi level $E_{Fn}(x)$ shows a similar sloping as the Fermi level for the single carrier

[11] We have introduced the DO-range, which is similar to the DRO-range: i.e., the total carrier current is given by one of the contributing currents only.

[12] The total voltage drop across the entire device is equal to the drop of the majority quasi-Fermi potential: $V = [E_{Fn}(x = 0) - E_{Fn}(d_1)]/e$.

model (compare with Fig. 3.5b): almost all of the voltage drop occurs in the DRO-range. The sloping becomes marked for a larger reverse currents and can be clearly identified in sub Fig. 6.10c and d.

In reverse bias, the quasi-Fermi level for holes lies *above* the one for electrons, indicating *minority carrier depletion*, i.e., this region is substantially less minority carrier than in equilibrium. In forward bias (shown in Fig. 6.11c), the majority carrier quasi-Fermi level E_{Fn} lies above E_{Fp} as expected when additional majority carriers are pulled from the bulk into the barrier (*carrier accumulation*).

With large enough reverse bias, the hole density in the bulk is sufficiently reduced so that the minority quasi-Fermi level enters the majority carrier (conduction) band. This strong depletion has no other significance[13] attached to it.

The *demarcation lines* given in Figs. 6.10 and 6.11 lie close to the valence band and for the given example (with the assumed $c_{ct} = c_{tv}$), are almost a mirror-image of the quasi-Fermi levels.

It is striking that at higher reverse bias (Fig. 6.10b) there are *no hole traps* as the hole demarcation line approaches and enters the valence band. Here, near the bulk, the preferred recombination can extend into the valence band (intrinsic recombination, band-to-band recombination). This is understandable when referring to the very low hole density in this region in high reverse bias (Fig. 6.8d).

Near the metal/semiconductor interface, the sets of quasi- Fermi levels and demarcation lines cross each other, indicating the rapidly changing role of different levels[14] in the gap in the first part of the barrier. This again emphasizes the need for precaution to use a too simplified recombination model for an entire device.

Electron and Hole Density Crossings. We have chosen in the preceding sections an example in which ending near a Schottky barrier a cross-over of electron and hole densities may occur under certain bias condition. It is important to point out that such a cross-over per se does not mean the existence of pn-junction that will be discussed in the following chapter and is caused by a change in doping but, most importantly, is identified by a change in the sign of the space charge causing a change in the sign of the slope of the field. One must remember that the space charge is determined by the *sum of free and trapped charges*. Though the carrier density may change the entire distribution, it does not signify a parallel change over of the sign of the sum of all charges.

[13] In contrast to the entry of the majority carrier Fermi-level into its band, that signifies degeneracy.

[14] In this example, only two kinds of levels were assumed: very shallow electron donors and deep recombination centers. In actual practice, a larger variety of levels exist, making such an analysis more important.

We have shown that close to the metal/semiconductor interface, $n(x)$ and $p(x)$ cross each other at a higher reverse bias at a bias-dependent position x_c (Fig. 6.8b).

The transport properties remain unchanged for $x < x_c$, where p becomes larger than n: j_n remains more than five orders of magnitude larger than j_p. An inspection of the solution curves shown in Figs. 6.8 and 6.9 does not reveal significant changes in any of these curves[15] at x_c.

We, therefore, ignore such a crossing of n and p, and describe the entire Schottky barrier as an n-type barrier, independent of whether $n > p$, or a *carrier inversion* to $p > n$ occurs close to the interface.

Carrier Inversion Layer with Consequences on the Space Charge. When in strongly blocking electrodes at sufficient reverse bias minority carrier injection becomes large enough to compensate the donor density, one speaks of a true *inversion layer* near the contact. In the given example of an n-type Ge, the hole density at sufficient reverse bias becomes comparable to the donor density N_d, and consequently the space charge increases beyond the donor density, that otherwise determines the positive space charge when depleted close to the metal/semiconductor interface. This is shown close at the left in (Fig. 6.14). As a consequence, the field slope increases and n decreases to keep j_n constant in the DRO-region:

$$n(x) = \frac{j_n}{e\mu_n F(x)}. \tag{6.25}$$

This inversion layer has only a slight effect on the barrier as it reduces the increment in barrier width with further increasing reverse bias; i.e, the solution will not expand as readily as it would without such a carrier inversion. The influence on the voltage drop, however, can become noticeable since the DRO-region shrinks, even though the change of $F(x)$ is minute.

6.2.3 Schottky Barrier Device

Any real Schottky barrier device has two metal electrodes. Earlier, we have neglected such a contact at d_1. We will now introduce perfect recombination also at d_1, however, still assuming a neutral contact with a flat band connection at d_2. Such influence of the second electrode is usually negligible in long devices with a width substantially exceeding the Debye length and the diffusion length. However, under certain circumstances, e.g., in solar cells with indirect band gaps, having a nearly homogeneous optical excitation throughout the cell, the second electrode may also exert its influence because of the carrier recombination there. To analyze the effects of the second electrode, we will analyze a few examples below.

[15] The only expected change would be in U from being n-controlled to becoming p-controlled; however, this changeover is hidden near n_c by n^* in the denominator of $U(x)$.

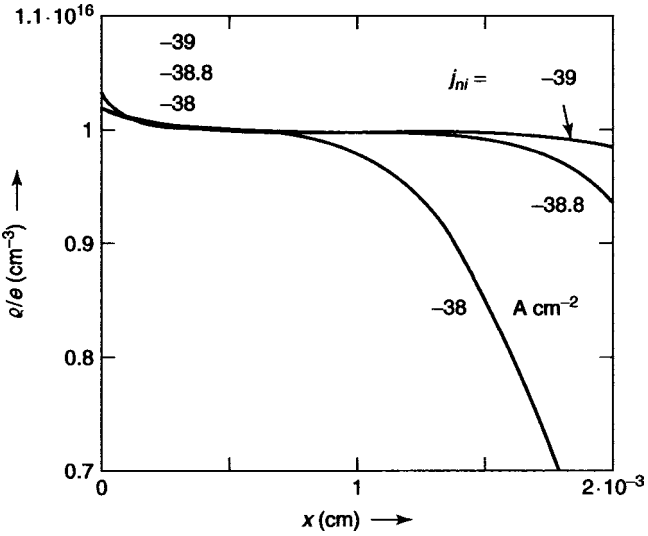

Fig. 6.14. Space-charge distribution in the Ge-Schottky barrier computed as for Figs. 6.8 and 6.9; shown in an enlarged scale with high reverse currents as family parameter indicating the increase of space charge above eN_d near $x = 0$ due to the contribution of free holes

6.2.3.1 Medium Width Device, Boundary Conditions

We first assume a thin device of 10^{-4} cm thickness with the set of parameters given in Table 6.1, with a neutral metal contact at $x = d_1$ and a surface recombination velocity of $s(d_1) = 2 \times 10^7$ cm/s to provide perfect recombination at that surface, and leaving $n(d_1) = n_{10}$ and $F(d_1) = F_{10}$, but forcing $p(d_1) = n_i^2/n_{10}$, hence forcing both quasi-Fermi levels also at the right surface to collapse.

General Solution Behavior. Figure 6.15 shows the influence of this increased surface recombination the right electrode (at d_1).

The hole density is increased in the bulk; the minimum is shifted further into the bulk and is not as deep compared to Fig. 6.4. This can be understood by the increased diffusion current toward the right surface, which brings $p(d_1)$ closer to p_{10}. The electron density distribution, however, is essentially unchanged since $n \gg p$.

The quasi-Fermi levels collapse now at $x = 0$ *and* at $x = d_1$. Close to the neutral contact, E_{Fn} remains constant (as n does) while $E_{Fp}(x)$ decreases in reverse bias until it joins E_{Fn} at $x = d_1$.

In summary, strong surface recombination influences minority carriers throughout the thin device: $p(x)$, $E_{Fp}(x)$, and therefore also $j_p(x)$ are substantially changed. The majority carrier properties, however, are essentially unchanged, except for a comparatively small reduction of the DRO-range

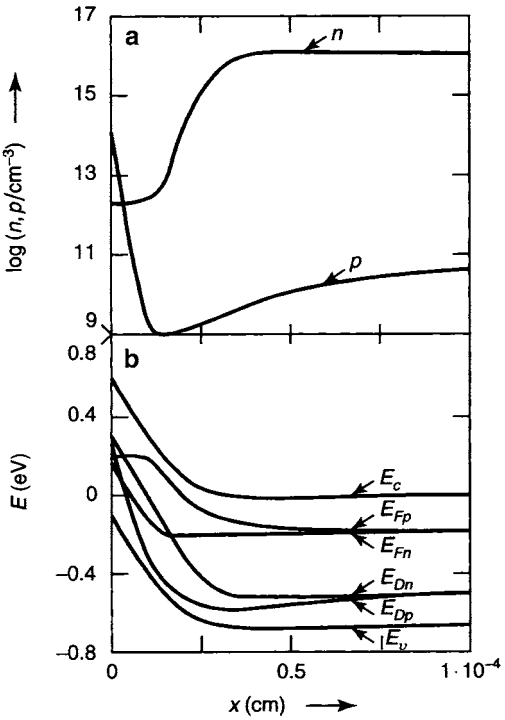

Fig. 6.15. Solution curves of (6.12)–(6.17) with parameters given in Table 6.1 and surface recombination at $d_1 = 10^{-4}$ cm with $s = 2 \times 10^7$ cm/s that shows relatively little influence on $n(x)$ but an increase of $p(x)$ toward the right electrode (panel **a**). The quasi-Fermi levels shown in panel (**b**) collapse at both metal surfaces

width when the minority carrier density exceeds the majority dopant density. This causes a slight steepening of the characteristics before attaining saturation.

6.2.3.2 Schottky Barrier in Wider Device and Violation of the Roosbroek Approximation

Earlier, we analyzed a device that extended only little beyond the barrier width. The integration much beyond the barrier width analysis can be simplified substantially by assuming $n(x) = n_{10}$ and $F(x) = F_{10}$ as soon as both variables have approached the constant values within sufficient accuracy.

How close $n(x)$ has approached the constant n_{10} can be estimated from the transport and Poisson equations for electrons (after differentiation of the first and substituting the second):

$$\frac{\mathrm{d}^2 n}{\mathrm{d}x^2} \simeq \frac{n}{L_\mathrm{D}^2} \frac{N_\mathrm{d} - n}{N_\mathrm{d}}, \tag{6.26}$$

yielding the approximate solution

$$\frac{\mathrm{d}n}{\mathrm{d}x} \simeq \frac{N_\mathrm{d} - n(x=0)}{L_\mathrm{D}} \exp\left(-\frac{x}{L_\mathrm{D}}\right), \tag{6.27}$$

and decreases exponentially. After a second integration, one obtains for $\delta n = n_{10} - n(x)$:

$$\delta n = N_\mathrm{d} - n(x) = N_\mathrm{d} \exp\left(-\frac{x}{L_\mathrm{D}}\right). \tag{6.28}$$

with $n_{10} = N_\mathrm{d}$. Equation (6.27) agrees well for $x \gg L_\mathrm{D}$ with the exponential slopes obtained from the "exact" computation shown in Fig. 6.7.

In contrast, the slope $\mathrm{d}p/\mathrm{d}x$ changes comparatively little (see below) for $x > x_\mathrm{D}$ as it is necessary to support the continuous gr-current. In our example, $\mathrm{d}p/\mathrm{d}x$ is on the order of $10^{12}\,\mathrm{cm}^{-4}$, as shown in Fig. 6.7.

In the bulk region, the slope of minority carriers decreases linearly as can be estimated from

$$\frac{\mathrm{d}p}{\mathrm{d}x} = \frac{e}{\mu_p kT} \int_x^{d_1} U(x)\mathrm{d}x \simeq \frac{e}{\mu_p kT} \frac{p_{10}}{\tau_{p0}} (d_1 - x). \tag{6.29}$$

The large difference of $\mathrm{d}n/\mathrm{d}x$ and $\mathrm{d}p/\mathrm{d}x$ in regions extending beyond the diffusion lengths precludes the use of the approximation of *ambipolar diffusion* only when the condition $\mathrm{d}n/\mathrm{d}x \simeq \mathrm{d}p/\mathrm{d}x$ is fulfilled (the well-known van Roosbroek assumption, can one use as a reasonable approximation for an *ambipolar transport equation* with the corresponding *ambipolar diffusion coefficient* $D^* = (n+p)D_nD_p/[nD_n + pD_p]$ and an *ambipolar mobility* $\mu^* = (n-p)\mu_n\mu_p/[n\mu_n + p\mu_p]$ in a very small parts of such devices.

In order to avoid misleading conclusion, we have therefore refrained from using the ambipolar approximation.

6.2.4 The Relative Contribution of Divergence-Free and GR-Currents in Schottky Barrier Devices

At the end of the chapter of Schottky barrier devices, we should emphasize the enormous difference between the magnitude of the usually minute generation-recombination current to the divergence-free current that is constant throughout the crystal. We have shown the solution curves for the generation and recombination rate as well as for the sum of both $U(x)$ in Fig. 6.16 for the same parameters as before used in this chapter but for a wider device.

Even for such wider devices, the g-r currents amount only to about $\pm 20\,\mu\mathrm{A/cm}^2$ at a reasonable forward or reverse bias (see Fig. 6.17) while the divergence-free currents are $= 100$ or $-39\,\mathrm{A/cm}^2$ respectively. Consequently, in the total current is negligible except for large optical excitation that will be discussed in later chapters.

For a more detailed analysis of Schottky structures see e.g., Racko et al. (Poole and Farach 1994); for effects of surface space charge on the shape of the potential barrier see Feng (Feng 1990) for bipolar injection, see Swistacz (Suetaka 1995).

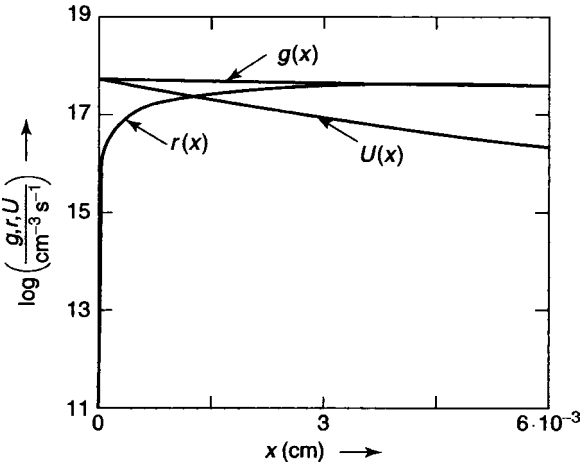

Fig. 6.16. $g(x)$, $r(x)$, and $U(x)$ for a total current of $-38\,\mathrm{A/cm^2}$ plotted for comparison in an unbroken linear scale

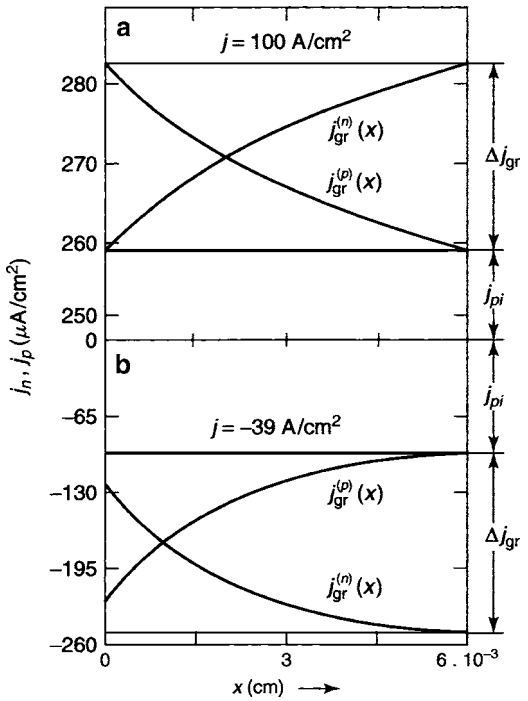

Fig. 6.17. Gr-currents for -39 and $100\,\mathrm{A/cm^2}$ in (**a**) and (**b**), respectively. Observe the ordinate break at $250\,\mu\mathrm{A/cm^2}$ in (**a**)

Summary and Emphasis

The influence of minority carriers is exerted on the properties of Schottky barriers through the recombination at the metal/semiconductor interfaces that contributes to the diode leakage current. The generation current within the barrier can compete in wider band gap semiconductors with the divergence-free majority carrier current in reverse bias, causing a slanting "saturation" branch.

The separation of divergence-free electron and hole currents from the gr-currents is helpful to judge the relative contributions to the total current.

As minority carriers cannot compete with majority carrier currents in homogeneous semiconductors, so is their contribution to the forward current negligible in devices with classical Schottky barriers. Only when most of the majority carrier current is suppressed with sufficient reverse bias has the minority carrier a chance to be observed. This chance is enhanced, the smaller the divergence-free majority carrier current, which is determined by the carrier density at the boundary. That is, minority carrier contributions are more visible in Schottky barrier devices with a larger metal/semiconductor work function (for n-type semiconductors) and therefore in wider gap materials, or at lower temperatures.

Schottky photodiodes and solar cells are examples of a highly desirable contribution of minority carriers. When these minority carriers are collected at the barrier, they provide the output current for the photoelectric power conversion. A careful evaluation of the basic competing currents will permit an estimate of the comparative advantages or disadvantages of Schottky barriers compared with pn-junction devices.

Exercise Problems

1.(r) List the determining parameters for the divergence-free electron and hole currents, and for the gr-currents through a Schottky barrier device. Assume one blocking ($n_c \ll n_{10}$) and one neutral ($n_c = n_{10}$) contact.

2.(e) Describe how the minority carrier density at the boundary between Schottky barrier and the bulk is changed as a function of bias, and how this density controls the minority carrier diffusion from the bulk.

3.(*) We have discussed in this chapter a simplified generation- (6.2) and recombination- (6.5) rate with equal capture cross sections for electrons and holes in the Hall-Shockley-Read centers. How would the present picture change when a center is assumed that is Coulomb-attractive to electrons. Remember that it changes its capture cross section after it has trapped an electron.

4. In Fig. 6.2 we have shown a crossing of $r(x)$ and $U(x)$ near $x = 0$ at large reverse bias. Explain the reasons for such a crossing and its relevance to interface recombination.

5.(e) Explain the slight differences between $g(x)$ and $r(x)$ for reverse and forward bias given in Fig. 6.2a and c, and comment on the resulting sign reversal of $U(x)$.

6. Estimate the magnitude of the gr-current for thermal excitation at reverse saturation bias in a Schottky barrier of your choice, following (6.9).

7.(*) Explain in your own words why a crossover of n and p would not constitute the position of a pn-junction:
   (a) When focusing your attention on currents, what would be the appropriate definition of the boundary of a pn-junction?
   (b) What are the properties of a conventional inversion layer?
   (c) How do you differentiate carrier inversion?

8.(e) The space charge distribution at high reverse bias has a little spike near $x = 0$. Explain the reason and its effects on the electronic barrier properties:
   (a) In a Schottky barrier with perfect current saturation;
   (b) Before saturation is reached.

9.(e) What are the basic differences between majority and minority currents in the barrier in forward and in reverse bias?

10.(e) The Debye length enters into the diffusion equation for holes (6.18) as minority carriers:
   (a) Is the hole density involved in L_{D}?
   (b) If so, under what circumstances?
   (c) Are these realistic for some actual devices?

11.(r) The divergence-free hole current is bias-dependent and nonmonotonic in reverse bias. Why?

12. The band edge and characteristic energy distributions are computed for four different bias conditions, and are shown in Fig. 6.10. Analyze these sets of curves:
   (a) Identify traps and recombination centers.
   (b) Identify the regions for different current contributions.
   (c) Identify the Boltzmann region and justify your identification.

13. Why is the curvature of $E_{Fn}(x)$ larger than the curvature of $E_{Fp}(x)$ near $x = 0$ in Fig. 6.11c and d? What does the slight slant and curvature of $E_{Fp}(x)$ in these two figure panels indicate?

14.(*) Give quantitatively the conditions under which the minority carrier contribution would equal the majority carrier contribution for reverse bias in a Schottky barrier device.

15.(*) When thermal minority carrier generation is augmented by optical generation (assume $g_o(x) = \text{const.}$), how much of this generation is needed to render the gr-current larger than the divergence-free current?

7

pn-Homojunctions

Summary. *pn*-junctions are the single most important part of almost all semiconductor devices. They are highly efficient in controlling the current as a function of the bias and yield excellent diode characteristics.

The *pn*-homojunction is produced by a doping transition from an acceptor-doped *p*-type region to a donor-doped *n*-type region of the same semiconductor. This doping transition creates a space charge double layer with a built-in field and a potential barrier to separate the majority carriers from one to the other part of the device.

We will first orient ourselves along the classical depletion layer approximation in steady state which yields analytical solutions and has guided generations of researchers and engineers in the field.

We will then briefly compare this model with two Schottky barriers, one *p*-type and one *n*-type, which are connected back-to-back with each other, except for a thin metal inter layer. Such an analysis will help us indicate similarities and emphasize the main differences between the Schottky barrier and the *pn*-junction.

We will then analyze computer solutions of an *abrupt pn-homojunction* as an example, i.e., a junction in which the doping changes abruptly from *p*- to *n*-type. Here we can follow some of the characteristic junction properties in more detail.

Finally, we will briefly discuss the properties of more complex *pn*-junctions.

7.1 Simplified pn-Junction Model

We first present a simple depletion-type model for analyzing the main features of a *pn*-junction. This model permits a general overview of the *pn*-junction which will assist us later in discriminating more detail of the actual device behavior.

7.1.1 Basic Features of the Simplified Model

We assume a semiconductor with two adjacent regions of homogeneous doping, one with shallow donors and the other with shallow acceptors that are joining each other with an abrupt transition as shown in Fig. 7.1a, b:

$$N_{\mathrm{a}}(x) = \begin{cases} N_{\mathrm{a}} & \text{for } x < 0 \\ 0 & \text{for } x \geq 0 \end{cases} \qquad N_{\mathrm{d}}(x) = \begin{cases} 0 & \text{for } x < 0 \\ N_{\mathrm{d}} & \text{for } x \geq 0. \end{cases} \tag{7.1}$$

In the process of joining these two parts, electrons diffuse from the n-type region into the adjacent p-type region, producing a positively charged region in the depleted part of the n-type region. In a similar manner, the holes diffuse from the p-type into the n-type region, producing a negatively charged depletion region as indicated in Fig. 7.1b.

We now assume a rather abrupt and complete depletion so that both adjacent depletion regions have a box-like space charge profile as shown in Fig. 7.1c:

$$\varrho(x) = \begin{cases} -\varrho_p = -eN_{\mathrm{a}} & \text{for } l_p \leq x < 0 \\ \varrho_n = eN_{\mathrm{d}} & \text{for } 0 \leq x \leq l_n. \end{cases} \tag{7.2}$$

For the reason of total neutrality in equilibrium, one requires in an asymmetric junction (here $N_{\mathrm{a}} > N_{\mathrm{d}}$)

$$N_{\mathrm{d}} l_n = N_{\mathrm{a}} l_p \tag{7.3}$$

with l_p and l_n the widths of the depletion regions in the p- and n-type parts of the junction (here $l_n > l_p$). In each of these space charge regions, we obtain the field distribution from the Poisson equation

$$F(x) = \frac{e}{\varepsilon\varepsilon_0} \varrho(x) x. \tag{7.4}$$

This field distribution is triangular (Fig. 7.1d) and is familiar to us in each half of the junction from the Schottky barrier: with two back-to-back depletion layers, it yields two joining triangles with the same height

$$|F_{\max}| = \frac{e}{\varepsilon\varepsilon_0} N_{\mathrm{a}} l_p = \frac{e}{\varepsilon\varepsilon_0} N_{\mathrm{d}} l_n. \tag{7.5}$$

The electron potential distribution can be obtained by integrating once more the Poisson equation, yielding

$$\psi_n(x) = \begin{cases} \psi_n(-\infty) & \text{for } x < l_p \\ \psi_n(-\infty) + \frac{e}{\varepsilon\varepsilon_0} N_{\mathrm{a}} (x + l_p)^2 & \text{for } l_p < x \leq 0 \\ \psi_n(+\infty) - \frac{e}{\varepsilon\varepsilon_0} N_{\mathrm{d}} (x - l_n)^2 & \text{for } 0 < x \leq l_n \\ \psi_n(+\infty) & \text{for } x > l_n. \end{cases} \tag{7.6}$$

Continuity of the electrostatic potential at $x = 0$ yields the diffusion electron potential across the p- and n-type region of the junction (Fig. 7.1e):

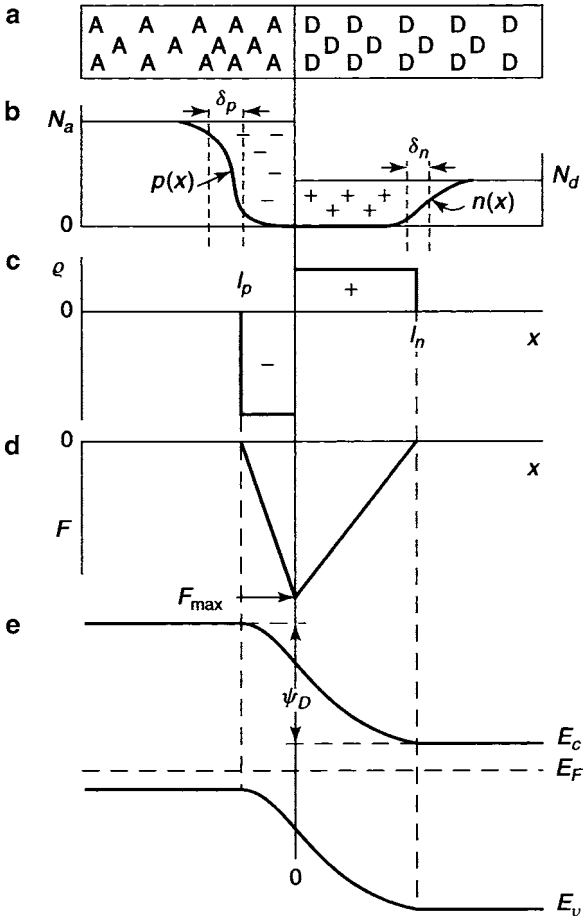

Fig. 7.1. Simplified model of a *pn*-junction in thermal equilibrium. (**a**) Doping distribution; (**b**) doping and carrier distribution with δ_n and dδ_p the widths of the transition regions to achieve complete carrier depletion; (**c**) space-charge distribution in the two depletion regions of width l_p and l_n in the *p*- and *n*-type material, respectively; (**d**) triangular field distribution; and (**e**) potential distribution (band model) with the diffusion potential ψ_D identified. δ_n and δ_p are neglected in panels c and d. A more careful inspection of panels d and e shows that the higher doped, thinner *p*-type region has a steeper field slope but has a lower fraction of the diffusion potential than the lower doped, wider *n*-type region

$$\psi_{n,\mathrm{D}} = \psi_n(\infty) - \psi_n(-\infty) = \frac{e}{\varepsilon\varepsilon_0}\left(N_\mathrm{d} l_n^2 + N_\mathrm{a} l_p^2\right); \tag{7.7}$$

the sum of the diffusion potentials can also be expressed as

$$\boxed{\psi_{n,\mathrm{D}} = \frac{kT}{e} \ln\left[\frac{N_\mathrm{d}}{n(x=0)}\right] + \frac{kT}{e} \ln\left[\frac{N_\mathrm{a}}{p(x=0)}\right] = \frac{kT}{e} \ln\left[\frac{N_\mathrm{d} N_\mathrm{a}}{n_i^2}\right]} \tag{7.8}$$

since in thermal equilibrium at any position of the junction $n(x)p(x) = n_i^2$.

The width of the depletion regions in equilibrium, as obtained from (7.3) and (7.7), yields

$$l_{n,p} = \sqrt{\frac{\varepsilon\varepsilon_0 \psi_{n,\mathrm{D}}}{e(N_\mathrm{a} + N_\mathrm{d})} \left(\frac{N_\mathrm{a}}{N_\mathrm{d}}\right)^{\pm 1}} \tag{7.9}$$

for l_n and l_p with the upper and lower sign in the exponent, respectively.

7.1.2 Simplified Junction Model in Steady State

With reverse bias, both depletion layers expand (Fig. 7.2), and with forward bias[1] they shrink according to (see Sect. 7.2.2)

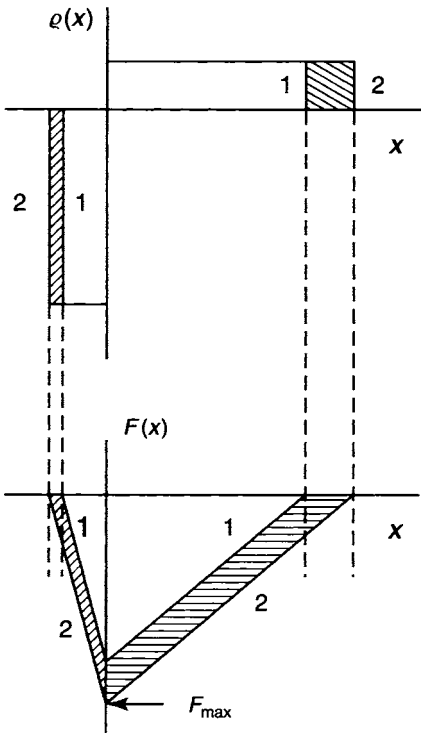

Fig. 7.2. Changes of space charge and field distribution in the simplified *pn*-junction model. Thermal equilibrium (curves 1) and reverse bias applied (curves 2)

[1] However, the depletion layer approximation becomes inadequate for larger forward bias.

$$\boxed{l_{n,p} = \sqrt{\frac{\varepsilon\varepsilon_0(\psi_{n,\mathrm{D}} - V)}{e(N_\mathrm{a} + N_\mathrm{d})}\left(\frac{N_\mathrm{a}}{N_\mathrm{d}}\right)^{\pm 1}}.} \tag{7.10}$$

The maximum field varies as

$$\boxed{F_\mathrm{max} = \sqrt{\frac{eN_\mathrm{d}N_\mathrm{a}}{\varepsilon\varepsilon_0(N_\mathrm{a} + N_\mathrm{d})}(\psi_{n,\mathrm{D}} - V)};} \tag{7.11}$$

in this simple model, the entire applied bias drops across the barrier with

$$\psi_n(\infty) - \psi_n(-\infty) = \psi_{n,\mathrm{D}} - V. \tag{7.12}$$

7.1.3 Junction Capacitance

With the junction depletion layer embedded between two highly conducting layers, namely the p- and n-type bulk semiconductor, this depletion layer acts as the dielectrics of a capacitor, which, per unit area, has a capacitance of[2]

$$C = \left|\frac{\mathrm{d}Q}{\mathrm{d}V}\right| = \left|\frac{\mathrm{d}(e[N_\mathrm{d}l_n + N_\mathrm{a}l_p])}{\varrho\mathrm{d}(\psi_{n,\mathrm{D}} - V)}\right| \tag{7.13}$$

$$C = \frac{\varepsilon\varepsilon_0}{l_n + l_p} = \sqrt{\frac{\varepsilon\varepsilon_0 eN_\mathrm{a}N_\mathrm{d}}{(N_\mathrm{a} + N_\mathrm{d})(\psi_{n,\mathrm{D}} - V)}}. \tag{7.14}$$

This provides for an often used method to determine the diffusion voltage by plotting $1/C^2$ vs. bias voltage, as can be seen by reordering (7.14):

$$\boxed{\psi_{n,\mathrm{D}} - V = e\varepsilon\varepsilon_0\frac{N_\mathrm{a}N_\mathrm{d}}{N_\mathrm{a} + N_\mathrm{d}} \cdot \frac{1}{C^2}.} \tag{7.15}$$

In an asymmetric junctions with $N_\mathrm{a} \gg N_\mathrm{d}$, one obtains also from the slope of $\psi_{n,\mathrm{D}} - V$ vs. $1/C^2$:

$$\psi_{n,\mathrm{D}} - V = e\varepsilon\varepsilon_0 N_\mathrm{d} \cdot \frac{1}{C^2} \tag{7.16}$$

the *lower* of the two doping densities (see Fig. 7.3 as an example for some measurements of an actual abrupt *pn*-junction Si device).

7.1.4 The Current–Voltage Characteristic of the Simplified Junction

The current through such a junction device is the sum of electron and hole current

[2] Equation (7.14) is identical to the result of the more general expression.

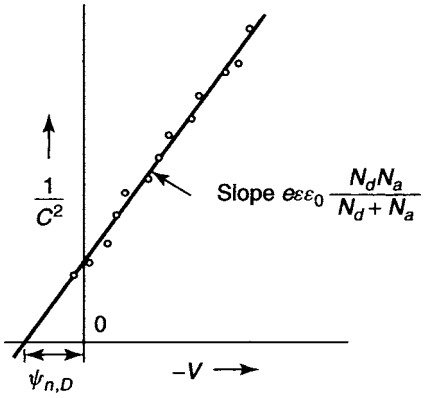

Fig. 7.3. Example of a capacitance measurement of an abrupt *pn* junction in an Si device as a function of the applied bias from which the diffusion voltage and the lesser space charge in a highly asymmetric *pn*-junction can be determined

$$j = j_n + j_p. \tag{7.17}$$

Each one of these currents is composed of a *generation current* caused by minority carriers that are generated close enough to the junction so that they can diffuse to the junction where they can be swept by the junction field to the other side, and a *recombination current* caused by majority carriers that have enough energy to surmount the barrier and then recombine with the oppositely charged majority carrier on the other side of the junction. In addition, generation and recombination within the junction can make a significant contribution under certain circumstances.

In the simplified model (essentially representing two back-to-back connected simplified Schottky barriers), described in the previous section, we can obtain an analytical description by separating three regions of the device, the *n*-type and the *p*-type bulk, and the junction region (see, e.g., Sze, 1985).

Since the *bulk regions* are essentially field-free, the current of the minority carriers is a diffusion current, as given in Sect. 5.1.1.1. In the *p*-type region, one has an electron current

$$j_n(x) = -\mu_n kT \frac{\mathrm{d}n}{\mathrm{d}x} = ev_{\mathrm{D}}(n_{j\mathrm{D}} - n_{p0}) \exp\left(-\frac{x}{L_n}\right) \tag{7.18}$$

(see (5.15)). With the boundary condition

$$n_{j\mathrm{D}} - n_{p0} = n_{p0}\left[\exp\left(\frac{eV}{kT}\right) - 1\right] \tag{7.19}$$

one obtains for the electron current

$$j_n = \frac{\mu_p kT n_{p0}}{L_n}\left[\exp\left(\frac{eV}{kT}\right) - 1\right] \tag{7.20}$$

with $n_{p0} = n_p(x = \infty)$ assuming here a "long device" with $d_2 \gg L_n$. The majority current is complementary to $j_n(x)$ rendering $j_n(x) + j_p(x) = j =$ const.

A similar hole current is contributed from the n-type bulk

$$j_p(x) = \frac{\mu_p k T p_{n0}}{L_p} \left[\exp\left(\frac{eV}{kT}\right) - 1 \right]. \tag{7.21}$$

As long as the contribution of the junction region is negligible,[3] the current voltage characteristic of such a device is consequently given by:

$$j = j_s \left[\exp\left(\frac{eV}{kT}\right) - 1 \right] \text{ with } j_s = \left(\frac{\mu_n p_{n0}}{L_n} + \frac{\mu_p p_{n0}}{L_p} \right) kT, \tag{7.22}$$

where we introduced the saturation current j_s that is the sum of the two saturation diffusion currents from each bulk region.

This is the **diode current–voltage characteristic** which has the typical form $j \propto [exp(eV/kT) - 1]$ with a pre-exponential factor that is subject to further modification dependent on the type of approximation that is used and other contributions that need to be considered.

7.1.4.1 Contribution of the GR-Currents

The contribution within the *junction region* is a generation/recombination current which can be approximated by

$$j_n = j_p = eUW \quad \text{with} \quad U = \frac{np - n_i^2}{\tau \left(n + p + n_i^{\pm}\right)} \tag{7.23}$$

In **reverse bias** with $W = l_n + l_p$, both n and p are reduced so that $np \ll n_i^2$ and the junction current becomes a generation current:

$$j_g = \frac{e n_i^2 W}{\tau n_i^{\pm}} \tag{7.24}$$

with

$$n_i^{\pm} = 2 n_i \exp \pm \left(\frac{E_i - E_r}{kT} \right)$$

the maximum contribution to the generation rate is obtained for recombination centers close to the middle of the band gap, thereby, with $E_r \simeq E_i$, yielding approximately

$$j_g \simeq \frac{e n_i W}{\tau} \tag{7.25}$$

[3] This can indeed occur for long devices with narrow band gap.

In **forward bias** with $np \gg n_i^2$, the current in the junction is described by recombination:

$$j_r = e\frac{npW}{n+p} \tag{7.26}$$

with

$$np = n_i^2 \exp\left(\frac{eV}{2kT}\right); \tag{7.27}$$

this results in a recombination current of

$$j_r \simeq \frac{n_i W}{2\tau}.\exp\left(\frac{eV}{2kT}\right); \tag{7.28}$$

The **total current–voltage characteristic** consists of the three contributions and is given by

$$j = j_s\left[\exp\left(\frac{eV}{kT}\right) - 1\right] + \frac{en_iV}{\tau}\left[1 + \exp\left(\frac{eV}{2kT}\right)\right] \tag{7.29}$$

or

$$j = en_i\left(\frac{L_n n_i}{\tau_n N_\mathrm{a}} + \frac{L_p n_i}{\tau_p N_\mathrm{d}}\right)\left[\exp\left(\frac{eV}{kT}\right) - 1\right] + \frac{W}{\tau}\left[\exp\left(\frac{eV}{2kT}\right) + 1\right]. \tag{7.30}$$

With sufficiently small band gap (larger n_i) and large diffusion lengths, the **bulk contribution** dominates. When the generation/recombination term in the junction region prevails, the generation term dominates in reverse and the recombination term dominates in forward bias.

7.1.4.2 The Diode Quality Factor

This leads to a characteristic that can be approximated in forward bias by

$$j \propto \exp\left(\frac{eV}{AkT}\right) \tag{7.31}$$

with a **quality factor** $A \simeq 2$; its origin is associated with the second term in (7.30), i.e., with junction recombination.

In summary, when in a *pn*-junction the bulk region dominates, the quality faxtor $A \simeq 1$, however, with the junction dominating $A \to 2$. We will return to this often used diode factor in the following sections.

7.1.5 Relevance to Actual pn-Junctions

The simplified *pn*-junction model with two box-like space charge layers joining each other back-to-back describes reasonably well the general features of a *pn*-junction device. The relations given in the preceding sections are,

therefore, often used to obtain first estimates about junction fields, barrier heights, capacitance, and current–voltage characteristics and some indication of the importance of junction recombination.

However, a quantitative agreement cannot be expected with an actual *pn*-junction device. This is especially important when attempting to obtain information on the space charge distribution from capacity measurements or a critical evaluation of reverse saturation currents or of curve shapes from the diode characteristics. For such an analysis, a more sophisticated model needs to be referenced which will be discussed in Sect. 7.5.1; however, we will remain on the topic of a rather simplified *pn*-junction throughout the following three sections.

7.2 Abrupt pn-Junction in Ge

In this study, we present computer generated solution curves for a specific Ge device that show more directly the interrelations between the different junction variables.

7.2.1 Governing Set of Equations and Example Parameters

For convenience, here we have collected and rewritten all time-invariant equations for the *pn*-junction, assuming Boltzmann gas statistics for carriers within the bands, and tabulated all of the parameters used for an abrupt Ge *pn*-junction in Table 7.1.

$$\frac{\mathrm{d}n}{\mathrm{d}x} = \frac{j_n - e\mu_n nF}{\mu_n kT} \tag{7.32}$$

$$\frac{\mathrm{d}p}{\mathrm{d}x} = \frac{-j_p + e\mu_p pF}{\mu_p kT} \tag{7.33}$$

$$\frac{\mathrm{d}j_n}{\mathrm{d}x} = -eU; \qquad \frac{\mathrm{d}j_p}{\mathrm{d}x} = eU \tag{7.34}$$

$$U = U_1 = \frac{np - n_i^2}{\tau_{p0}^{(1)}\left(n + n_i^+\right) + \tau_{n0}^{(1)}\left(p + n_i^-\right)} \quad \text{for} \quad d_1 \le x < 0 \tag{7.35}$$

$$U = U_2 = \frac{np - n_i^2}{\tau_{p0}^{(2)}\left(n + n_i^+\right) + \tau_{n0}^{(2)}\left(p + n_i^-\right)} \quad \text{for} \quad 0 \le x \le d_2 \tag{7.36}$$

$$\frac{\mathrm{d}F}{\mathrm{d}x} = \frac{e(p - N_\mathrm{a})}{\varepsilon\varepsilon_0} \qquad \text{for} \quad d_1 \le x < 0 \tag{7.37}$$

$$\frac{\mathrm{d}F}{\mathrm{d}x} = \frac{e(N_\mathrm{d} + p - n)}{\varepsilon\varepsilon_0} \qquad \text{for} \quad 0 \le x \le d_2 \tag{7.38}$$

$$\frac{\mathrm{d}\psi_n}{\mathrm{d}x} = F \tag{7.39}$$

Table 7.1. Parameters used for the abrupt Ge *pn*-junction

Parameters	N_a	N_d	N_{r1}	N_{r2}	N_c	N_v
Values	10^{17}	10^{16}	10^{17}	10^{16}	1.04^*10^{19}	5.76^*10^{18}
Dimensions	cm^{-3}	cm^{-3}	–	cm^{-3}	cm^{-3}	cm^{-3}
Parameters	n_{10}	p_{10}	n_{20}	p_{20}	μ_{n0}	μ_{p0}
Values	5.138^*10^9	10^{17}	10^{16}	5.138^*10^{10}	3900	1900
Dimensions	cm^{-3}	cm^{-3}	cm^{-3}	cm^{-3}	cm^2/Vs	cm^2/Vs
Parameters	E_g	$E_l - E_r$	$C = C_{cr} = C_{cv}$	$v_n^* = v_p^*$	ε	T
Values	0.66	0.1	10^{-9}	5.7^*10^6	16	300
Dimensions	eV	eV	cm^3s^{-1}	cm^3s^{-1}	–	K

$$n_i^{\pm} = n_i \exp\left(\pm\frac{E_i - E_r}{kT}\right) \tag{7.40}$$

$$n_i^2 = np \quad \text{in equilibrium} \tag{7.41}$$

$$\tau_{n0}^{(1,2)} = \frac{1}{c_{cr}N_{r(1,2)}}; \qquad \tau_{p0}^{(1,2)} = \frac{1}{c_{rv}N_{r(1,2)}}. \tag{7.42}$$

7.2.2 Solution Curves for Thin Germanium pn-Junction

We analyze first a thin device with $(d_1, d_2) \ll (L_n, L_p)$, which emphasizes the contributions of the junction and the two electrodes while de-emphasising the bulk. Figure 7.4 shows the solution curves for such a thin[4] Ge *pn*-junction device, $n(x)$, $p(x)$, $\varrho(x)$, $F(x)$, and $\psi_n(x)$ with the total current j as a family parameter, as obtained by numerical integration of (7.32)–(7.42) with the parameters listed in Table 7.1 and the boundary conditions given by surface recombination at d_2 or d_1 with $s(d_1) = s(d_2) = 5\times10^6\,\mathrm{cm\ s^{-1}}$, and a flat-band outer electrode connection.[5] This behavior of the solution curves is typical for *pn*-junction devices with a sharp peak of the field at the junction interface and a crossover of the carrier density extending substantially beyond this interface into the lower doped region.

7.2.2.1 The Position of the pn-Junction

The carrier densities $p(x)$ and $n(x)$ show a crossover, i.e., a change between the respective majority carriers that lies within the lower doped part of the device.

[4] The device extends only slightly beyond the junction region.

[5] Such a flat band electrode connection requires a metal/semiconductor work function $\psi_{\mathrm{MS}} = E_0 - E_c - E_{\mathrm{d}}$ for the *n*-type side and $\psi_{\mathrm{MS}} = E_0 - E_v + E_{\mathrm{a}}$ for the *p*-type side (E_0 is the vacuum level).

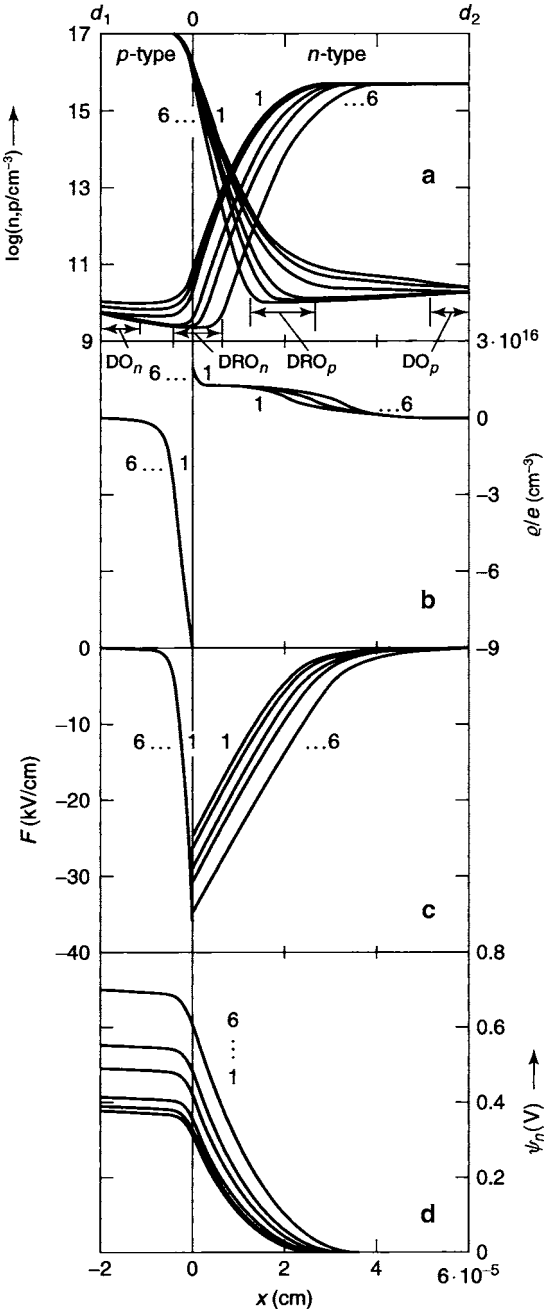

Fig. 7.4. Solution curves for a Germanium thin *pn*-junction device obtained by computation from (7.32)–(7.40). Parameters given in Table 7.1; $j = 6, 0, -9.15$, and $-9.84\,\mathrm{mA\,cm^{-2}}$ for curves 1–4, respectively. For curve 4, the extent of the DO- and DRO-regions for holes and electrons are identified in panel (**a**) (see Sect. 7.2.2.C for further explanation)

The boundary between the p- and n-type regions, however, is precisely at the doping boundary. To emphasize: The metallurgical interface is the locus of the pn-junction boundary and not the crossover between $p(x)$ and $n(x)$, as will be explained below.

The space charge shape in an asymmetrically doped junction is itself asymmetric and is in the higher doped region and no longer block-shaped. The carriers diffusing out from this region produce here a triangular space charge layer, as shown in Fig. 7.4b. In addition, the hole density in the n-type bulk increases above the donor density in this lower doped region, thereby causing a spike of the positive space charge near the junction interface (see Fig. 7.4b).

This modifies the Schottky-type solution: in the higher doped region, the field distribution is nonlinear, and it shows a gradual field slope in the lower doped region up to a spike exactly at the doping boundary, as shown in Fig. 7.4c. Consequently, the field distribution is best estimated from the lowly doped side of the junction.

The width of the lower doped space charge region is approximately given by the Schottky relation

$$l_n = \Delta x_2 = L_{Dn}\sqrt{2e\frac{\psi_{n,Dn} - V}{kT}}, \tag{7.43}$$

while the width of the higher doped space charge region is comparatively small. For the diffusion potential $\psi_{n,Dn}$ see (7.45).

7.2.2.2 Junction Field and Potential Distribution

The field distribution in the junction is triangular shaped with a curved branch in the higher doped side and a mostly linear branch in the lower doped side, except for a small spike (barely visible in panel c) close to the interface, caused by the overshoot of the space charge here (Fig. 7.4c). The maximum field, except for this spike, is given by

$$F_{\max} \simeq \sqrt{\frac{2eN_{\mathrm{d}}(\psi_{n,Dn} - V)}{\varepsilon\varepsilon_0}} \tag{7.44}$$

with

$$\psi_{n,Dn} = \frac{kT}{e}\ln\left(\frac{N_{\mathrm{d}}}{n_i}\right), \tag{7.45}$$

using the lower doped side for the estimate.

The electrostatic potential distribution is obtained by integrating $F(x)$ and is shown in Fig. 7.4d. It has the typical potential step shape which increases or decreases with applied bias, but with most of the changes in barrier width and step hight occurring in the lower doped region.

The total diffusion potential is given by

$$\psi_{n,\mathrm{D}} = \psi_{n,\mathrm{D}n} + \psi_{n,\mathrm{D}p} = \frac{kT}{e} \ln\left(\frac{N_\mathrm{a}N_\mathrm{d}}{n_i^2}\right) \tag{7.46}$$

or, using (4.28),

$$\boxed{\psi_{n,\mathrm{D}} = \frac{E_g}{e} - \frac{kT}{e}\ln\left[\frac{N_v N_c}{N_\mathrm{a}N_\mathrm{d}}\right].} \tag{7.47}$$

The diffusion potential is 0.38 V in the given example.

With bias, the electrostatic electron potential distribution is deformed, resulting in a bias-dependent step size according to

$$\psi_n(d_1) - \psi_n(d_2) = \psi_{n,\mathrm{D}} - V, \tag{7.48}$$

again with most of the changes occurring in the lower doped n-type region.

7.2.2.3 Quasi-Fermi Level and Current Distributions in the pn-Junction

At each of the Ge/metal interfaces, the two quasi-Fermi levels collapse at the majority quasi-Fermi level, which coincides with the Fermi level of the adjacent metal. Thus, the applied voltage can be expressed by:

$$V = \frac{1}{e}\left\{E_\mathrm{F}\left(d_1^-\right) - E_\mathrm{F}\left(d_2^+\right)\right\} \simeq \frac{1}{e}\left\{E_{F_p}(d_1) - E_{F_n}(d_2)\right\}, \tag{7.49}$$

with d_1^- and d_2^+ indicating the position inside the metal.

Instructive information about the operation of a pn-junction device can be obtained by analyzing the different current ranges within the junction. These can best be identified in conjunction with the band-model, shown in reverse bias in the composite drawing of Fig. 7.5 as computed from (7.32)–(7.42) with parameters listed in Table 7.1. This figure deserves full attention since it explains clearly the operation of the pn-junction. It includes in its top and bottom panel the current distributions and in its central panel the band edges and quasi-Fermi levels. The example shown is computed for sufficient reverse bias to show well-developed DRO- (drift only) and DO- (diffusion only) regions. The forward current distributions are relatively benign and will be mentioned briefly later.

Boltzmann-Ranges, DRO-Ranges, and DO-Ranges. In the upper (a) and lower (c) panel of Fig. 7.5, the current distributions are given for holes and for electrons, respectively. The current scales in panels a and c are broken at 10 mA cm^{-2} and 5 mA cm^{-2}, respectively, to present the Boltzmann range in the upper part in a logarithmic scale and to demonstrate the split between drift and diffusion currents in the lower parts of these panels in a linear scale.

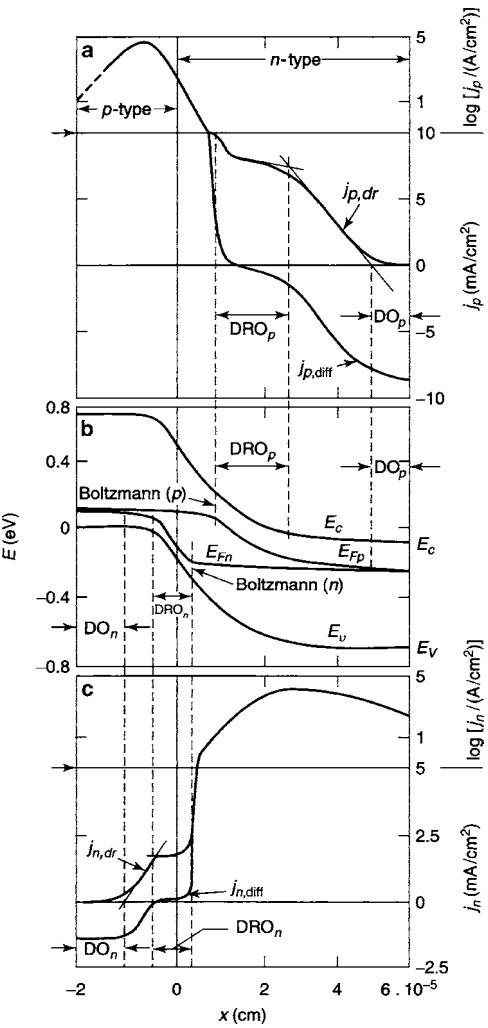

Fig. 7.5. Current distributions and band-model in a Ge *pn*-junction with quasi-Fermi level distribution for reverse bias near current saturation: $j = -9.5\,\mathrm{mA\ cm^{-2}}$. (**a**) Hole current distribution showing the split between drift and diffusion current, also indicating DRO- and DO-regions for holes where these are the minority carriers. (**b**) Band-edge and quasi-Fermi level distributions showing their split near the junction, but mainly in the lower conducting *n*-side, and their collapse close to each electrode. (**c**) Electron current distribution showing the split between drift and diffusion, again starting in the junction and being most pronounced where electrons are minority carriers, again indicating DRO- and DO-regions for electrons. Observe the break of the ordinate at the top of each current graph to show the full extend of the current

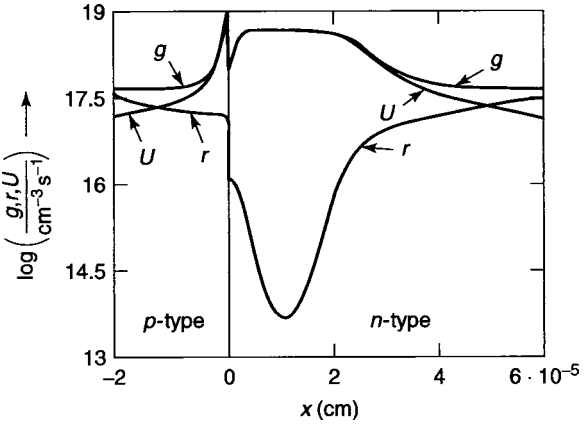

Fig. 7.6. Generation-, Recombination-, and net gr-rates plotted for the reverse saturation current $j = -9.84\,\mathrm{mA\ cm^{-2}}$.

These show the typical step like behavior of the currents with sufficient reverse bias: they drop from the high-current Boltzmann range, where drift and diffusion current almost completely compensate each other to a distinct DRO-range, where the drift current predominates and then near the outer contact in another step to the DO-range, where the diffusion current predominates. This rather complex figure needs more elaboration.

In panel b, the split of the quasi-Fermi levels is shown: the majority quasi-Fermi levels[6] in reverse bias remain flat in the Boltzmann regions. The extent of these regions differs in the p- and n-type parts of the junction; their ranges are slightly overlapping for electrons and holes.

The major drop of the quasi-Fermi levels occurs in the DRO-regions of holes and electrons, identified as DRO_p and DRO_n where they change parallel with the respective band edges. In these regions, the corresponding carriers become *minority carriers*.

The DRO-regions for electrons and holes are well separated from each other and start near the crossover point of n and p (compare with curves 5 of Fig. 7.4a), i.e., where the carriers have become minority carriers (and not at $x = 0$).

In the bulk-related DO-regions, one also observes a sloping of the quasi-Fermi levels, however, a much reduced one. The DO-range is caused by the predominant diffusion of minority carriers in the bulk and near the electrodes.

7.2.2.4 Carrier Heating in *pn*-Junctions

As can be seen from Fig. 7.5, major gradients of the quasi-Fermi levels occur only where the carriers have become minority carriers; only here in a

[6] There are two majority quasi-Fermi levels in a pn-junction, E_{Fp} in the p-type region and E_{Fn} in the n-type region.

well-developed DRO-region does major carrier heating occur due to the action of the external field; this then becomes strictly a minority carrier heating. Majority carrier heating in *pn*-junctions, however, is negligible as long as series resistance can be neglected (Böer, 1985).

Figure 7.5 shows the separation of the Boltzmann regions for electrons and for holes; in these regions both drift and diffusion currents are very large compared with the net current as shown in panels a and c. The overlap of these Boltzmann regions decreases[7] with increasing reverse bias (see Fig. 7.11).

In contrast to the Schottky barrier, where a DRO-region only appears for majority carriers at currents close to reverse current saturation, the DRO-region in the *pn*-junction surrounds the minimum of the minority carrier density where the diffusion current vanishes (see Sect. 7.3 for more details). In this DRO-range, minority carriers are heated.

In forward bias, there is no DRO-range for n or p. Both electron and hole currents maintain the same sign throughout the entire bulk and junction. Near the end of the junction, in the adjacent bulk, the minority carrier current becomes a DO-current. However, the electrochemical fields are usually too small here to cause any significant carrier heating.

The spread of the drift and diffusion currents for electrons at d_1 is smaller in the higher doped p-side than the spread for hole currents at d_2 in the n-side of the junction.

7.2.2.5 GR-Currents and Divergence-Free Currents

In a thin device, the minority carrier density in reverse bias is substantially lower than the equilibrium density throughout each bulk and up to the surface. This causes substantial *surface recombination currents*:

$$j_s(d_1) = e\,[n_{10} - n(d_1)]\,s(d_1) \simeq 1.58\ \text{mA cm}^{-2} \tag{7.50}$$

and

$$j_s(d_2) = e\,[p_{20} - p(d_2)]\,s(d_2) \simeq 8.20\ \text{mA cm}^{-2} \tag{7.51}$$

with $s = 5 \times 10^6\,\text{cm s}^{-1}$, for a total reverse current contribution of $9.8\,\text{mA cm}^{-2}$.

The *gr-current* in bulk and junction region is much smaller than the recombination currents at the electrode interfaces in thin devices which contribute by far the largest part of the current.

The **gr-rates** in the main part of the device show steps between bulk and junction similar to the ones for Schottky barriers. Three steps[8] are clearly identified. The jump at the metallurgical interface is caused by the step in the density of recombination centers at this interface. The surface recombination causes a slanting of the net gr-rates towards the outer surfaces.

[7] For vanishing current, both Boltzmann regions fill the entire device width.

[8] A fourth step in the highly doped region is not fully developed because of the triangular steep decline of $p(x)$.

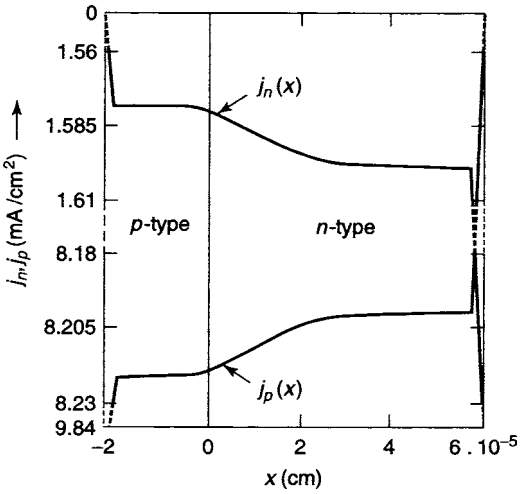

Fig. 7.7. Current distribution in the thin Ge *pn*-junction device, including recombination currents at $x = d_1$ and d_2 for a total of $j = -9.84\,\mathrm{mA\ cm^{-2}}$. Observe the broken ordinate scale at the upper, lower and middle part of the figure, to show the behavior of the gr-current within the device. Near the metal boundaries, the surface recombination parts are indicated. Also observe the crossover of the currents at the right electrode

The **gr-currents**, shown in Fig. 7.7, are composed in each part of the device of the two slopes in bulk and junction, with dominant contribution in the lower doped material. Near reverse saturation, the total contribution of the gr-current is approximately $20\,\mu\mathrm{A\ cm^{-2}}$; with its largest contribution of almost $15\,\mu\mathrm{A\ cm^{-2}}$ generated in the *n*-part of the junction.

In comparison, the divergence-free currents in *pn*-junctions are negligible. They are determined by the *divergence-free minority carrier currents* $j_{\mathrm{ni}}^{(p)}$ and $j_{\mathrm{pi}}^{(n)}$, presenting the bottleneck, and can be estimated from the fields in the bulk near the outer surfaces: $F(d_1) \simeq j_s/[e\mu_p p(d_1)] \simeq 10^{-3}\,\mathrm{V\ cm^{-1}}$ and $F(d_2) \simeq j_s/[e\mu_n n(d_2)] \simeq 10^{-2}\,\mathrm{V\ cm^{-1}}$ and the minority carrier densities of $n(d_2) \simeq 5 \times 10^9$ and $p(d_1) \simeq 5 \times 10^{10}\,\mathrm{cm^{-3}}$ yielding

$$j_{ni}^{(p)} = e\mu_n n_{10} F(d_1) \simeq 3 \times 10^{-9}\ \mathrm{A\ cm^{-2}} \tag{7.52}$$

and

$$j_{pi}^{(n)} = e\mu_p p_{20} F(d_2) \simeq 1.5 \times 10^{-7}\ \mathrm{A\ cm^{-2}}. \tag{7.53}$$

The total current distribution in this device is shown in Fig. 7.7 in a broken ordinate scale. It demonstrates the vast dominance of the surface recombination current that is of the order of $10\,\mathrm{mA\ cm^{-2}}$ at the metal interfaces (7.50) and (7.51). Inside the device, only a very small (0.2%) fraction of the gr-current is generated ($\Delta j_{\mathrm{gr}} \simeq 20\,\mu\mathrm{A\ cm^{-2}}$). This is typical for small devices.

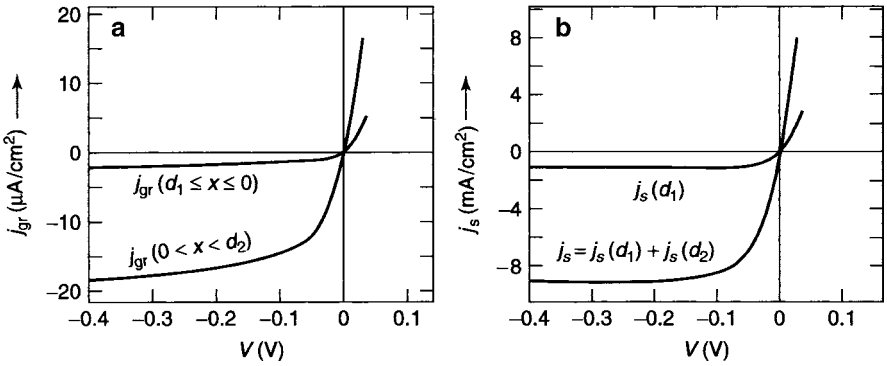

Fig. 7.8. Current–voltage characteristic for the same thin Ge *pn*-junction as in Figs. 7.4–7.7 with parameters as given in Table 7.1. (**a**) Gr-current increments for *p*-type part and for *n*-type parts of the device. (**b**) Surface recombination currents at d_1 and sum of these at d_1 and d_2; the total $j(V)$ is essentially equal to $j_s(d_1)+j_s(d_2)$ because of the vast differences of the currents in panel a and panel b

7.2.3 The Current–Voltage Characteristic

In Fig. 7.8, four current–voltage characteristics are plotted, as computed from the solutions of (7.32)–(7.42). We have here separated the *different contributions* to the characteristic because of their vastly different magnitude. The gr-currents in bulk and junction are shown in panel a. The increment in the higher doped *p*-type part is smaller because of the lower generation rate and the smaller width of the bulk region. The current shows good saturation as can be traced to the sufficient reduction of $r(x)$ below $g(x)$, shown in Fig.7.6. The gr-current in the *n*-type region is not yet saturated: with increasing reverse bias, the width of the barrier region in which the generation rate is larger, slowly increases until it fills the entire width of the *n*-type region; this results in a maximum gr-current (current saturation) in the *n*-type region of $\Delta j_{\rm gr}^{(n)} \simeq 40\,\mu{\rm A\ cm}^{-2}$ which is reached only at still higher reverse bias.

The contributions of the surface recombination to the current–voltage characteristics are shown in panel b of Fig. 7.8. They are approximately 500 times larger than the gr-currents but show a surprisingly similar diode-like shape (compare panels a and b). The total current–voltage characteristic for a thin *pn*-junction device is in good approximation given by the sum of the two surface recombination currents, i.e., they are essentially the leakage currents from the semiconductor/metal interfaces, and reach each metal surface by diffusion from the junction, and thereby, causes a similar diode-type shape.[9]

[9] The difference between the minority carrier density at the outer surface and the equilibrium density (7.56) and (7.57) that controls the surface recombination current is proportional to the difference at the bulk/junction interface (at l_n or l_p) that controls the diode current (7.18)

This remarkable interrelation totally escapes the simple junction analysis presented in Sect. 7.1. It amplifies the importance of a detailed check of the complete set of solution curves to identify the reasons for a behavior that could otherwise be attributed to completely different causes, as it is easily mistaken for its similar diode type shape to (7.30). Again, this is typical only for thin devices, where surface recombination dominates.

7.3 Thick pn-Junction Device (Ge)

We now increase the width of the device on both sides of the junction interface (to $d_1 = 2 \times 10^{-3}$ and $d_2 = 6 \times 10^{-3}$ cm) to make each side thicker by a factor of 2 or 2.7, respectively than the minority carrier diffusion length ($L_n = 10^{-3}$ and $L_p = 2.2 \times 10^{-3}$ cm).

7.3.1 Changes in Current Contributions with Device Thickness

With increasing width of the device, the surface recombination currents decrease, as $n(d_1)$ and $p(d_2)$ approach the equilibrium densities. This is a sensitive measure that relates to the thickness to diffusion length ratio. On the other hand, the gr-currents increase to approach their limit value for reverse bias, that is in the n-type region

$$\Delta j^{(p)}_{\mathrm{gr,max}} = egL_p \simeq 175\ \mu\mathrm{A\ cm}^{-2} \tag{7.54}$$

and in the p-type region

$$\Delta j^{(n)}_{\mathrm{gr,max}} = egL_n \simeq 80\ \mu\mathrm{A\ cm}^{-2}. \tag{7.55}$$

The computed $n(x)$ and $p(x)$ show the same typical behavior as shown for the thin device except now the carrier densities near the device surface $n(d_1)$ and $p(d_2)$ have increased to within less than 1% of the equilibrium densities, rendering (at -0.3 V bias) the recombination current small but not yet negligible:

$$j_s(d_1) = e\,(n(d_1) - n_{10})\,s \simeq 22 \quad \mu\mathrm{A\,cm}^{-2} \tag{7.56}$$

and

$$j_s(d_2) = e\,(p(d_2) - p_{20})\,s \simeq 26 \quad \mu\mathrm{A/cm}^2. \tag{7.57}$$

Therefore, the total current, which was dominated by the large recombination current at the outer electrodes of the thin device, is now reduced by two orders of magnitude and the sum of all four of the above listed currents can now be drawn at the same ordinate scale:[10]

[10] The divergence-free current is now reduced to below 10^{-8} A cm^{-2}, i.e., to completely negligible values in reverse bias.

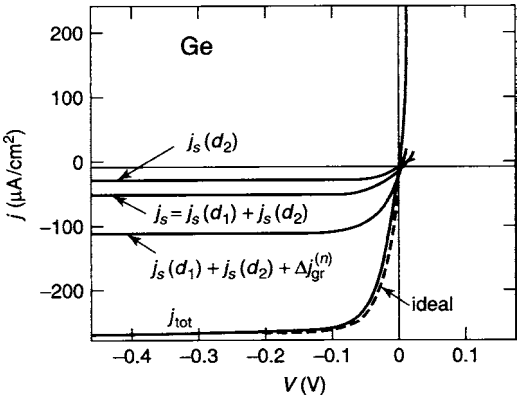

Fig. 7.9. Current–voltage characteristic computed from (7.32)–(7.39) here for a thick Ge-diode. Here surface recombination and bulk gr-currents can be drawn within the same figure. For more see text

$$j_{\mathrm{tot}} = j_s(d_1) + j_s(d_2) + \Delta j_{\mathrm{gr}}^{(n)} + \Delta j_{\mathrm{gr}}^{(p)}. \tag{7.58}$$

In Fig. 7.9, the bulk gr-current of holes $\Delta j_{\mathrm{gr,max}}^{(p)}$ gives the largest contribution to the total current j_{tot}, because of the larger diffusion length of holes in the n-type region.

The device width no longer enters the gr-current behavior, as both bulk currents are now saturated and the junction currents have become comparatively small. However, even for a device with dimensions two times larger than the minority carrier diffusion length, the interface recombination at the electrodes is not yet negligible and contributes about 15% to the total current.

The shape of the current–voltage characteristic composed of these four different contributions is surprisingly close to an ideal diode characteristic

$$j = j_0 \left[\exp\left(\frac{eV}{kT}\right) - 1 \right], \tag{7.59}$$

which is shown as a dashed curve in Fig. 7.9.

The spatial distribution of these currents is shown for a forward current in the upper panel, and for a reverse current in the lower panel of Fig. 7.10. These curves identify the additive contribution from electrode recombination and gr-currents in the p-type and n-type parts of the device. The surface recombination is emphasized by plotting it within a small band of the surface layer (sl) symbolizing the metal/semiconductor interface, and extending beyond the central part of the figure on each side. In order to identify the contribution of the junction region and the two bulk regions, this and the

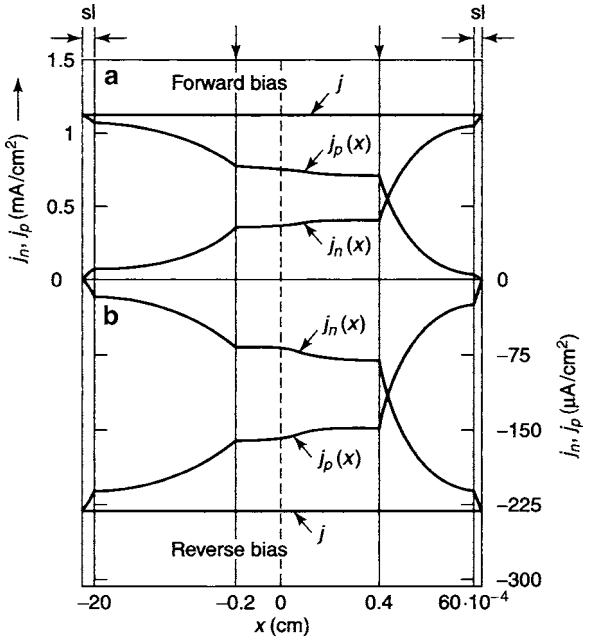

Fig. 7.10. Electron and hole current distribution in a thick Ge-diode computed from (7.32)–(7.40) with parameters listed in Table 7.1; $d_1 = 2 \times 10^{-3}$ cm, $d_2 = 6 \times 10^{-3}$ cm, and $s(d_1) = s(d_2) = 5 \times 10^6$ cm/s. (**a**) forward bias with $j = 1.14$ mA cm^{-2}; (**b**) reverse bias near saturation with $j = -230\,\mu$A cm^{-2}. Observe the asymmetric abscissa scale break at -2×10^{-5} and $+4 \times 10^{-5}$ cm that is chosen to show clearly the entire behavior in one figure. The crossover of the currents are now clearly visible within the figure in the n-type region. The thin slabs at both electrodes marked sl indicate the region of surface recombination

following figures in this section are plotted with two breaks of the abscissa at -0.2×10^{-4} and at $+0.4 \times 10^{-4}$ cm.[11] The junction interface is located at $x = 0$.

7.3.2 The Quasi-Fermi Levels of the Thicker Device

The quasi-Fermi levels remain spread much beyond the junction region (Fig. 7.11) and join each other more gradually as the electrodes are approached. The distinction between the rapid changes in the DRO-region, where quasi-Fermi levels and band edges slope parallel to each other, and

[11] Such a scale break results in a break of slopes at the break point. The actual curves, however, have continuous slopes.

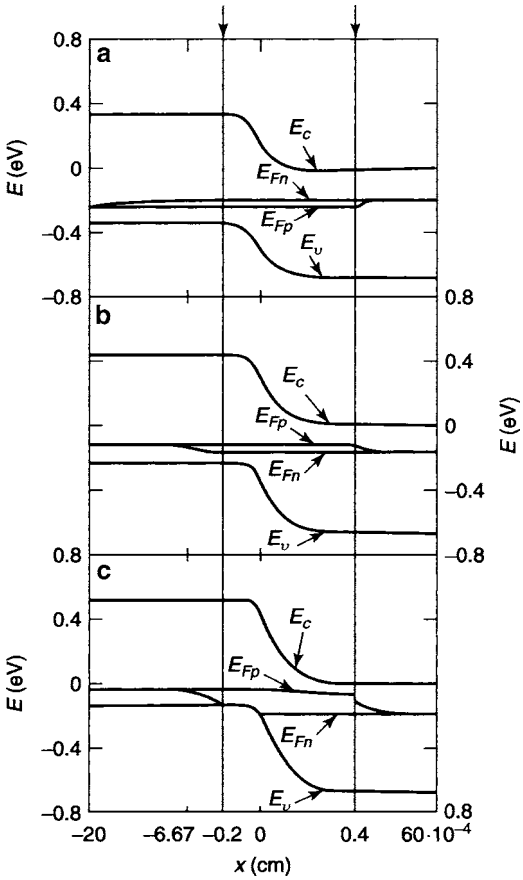

Fig. 7.11. Band and quasi-Fermi level distributions in the bulk and junction regions of the thick Ge-diode computed as in Fig. 7.10. (**a**) Forward bias with $j = 1.14\,\text{mA cm}^{-2}$; (**b**) reverse bias with $j = -230\,\mu\text{A cm}^{-2}$; and (**c**) reverse bias with $j = -262\,\mu\text{A cm}^{-2}$. The spread of the quasi-Fermi levels represents the distribution of the solution curves $n(x)$ and $p(x)$ that show the typical junction behavior, but here, for the thicker device, the bulk and surface regions are more clearly separated, as indicated by the spread and the collapse of the quasi-Fermi levels before the boundary is reached

the more gradual changes[12] of the quasi-Fermi levels in the DO-region, where the band edges remain essentially horizontal.

The generation and recombination rates in the central part of the device are similar to the curves of the thin device shown in Fig. 7.6 except that the

[12] Consider the scale break of the figure in your comparison between the DRO and DO ranges.

recombination rates drop more readily and thereby permit the net gr-rate $U(x)$ to attain the shape of $g(x)$ at lower reverse bias.

In summary, the recombination currents at the outer surfaces of a thicker device are greatly reduced as soon as the widths of both bulk regions substantially exceed the diffusion lengths of the minority carriers; the surface recombination current can be neglected when the bulk width exceeds ≈ 4 diffusion lengths. The total current is then given by the sum of the two gr-currents as discussed for the ideal junction model in Sects. 5.1 and 5.2. These currents increase with bias as $r(x)$ is shifted away from $g(x)$. In reverse bias, the net gr-rate $U(x)$ approaches readily $g(x)$ and the current saturates as the maximum of the minority carriers diffusion is reached. This current is many orders of magnitude smaller than the saturation current of a Schottky barrier device of the same material.

Thus, a *pn*-diode (with thermal carrier generation) is a much better rectifying device than a simple Schottky diode, since the recombination leakage current at the metal/semiconductor interface can be shifted to a region far away from the junction where it vanishes when the carrier densities approach their thermal equilibrium value. This is not possible for an electrode that is part of the current-controlling barrier in the Schottky diode.

7.4 Si-Homojunction

In the previous chapters and sections, we have described a narrow band-gap semiconductor in order to identify the intricate relationship of the different contributions to the current–voltage characteristics which influence their shape in an actual device, and to avoid the complications caused by a frozen-in carrier distribution, which appear in wider band gap semiconductors and often hinders a general discussion using a simple quasi-Fermi level model. We also have avoided the discussion of a highly asymmetric *pn*-junctin with only a very thin highly doped one side of the junction.

The Si-homojunction device is a borderline example for such devices since it has a wider band gap of 1.16 eV that could put a quasi-Fermi level in reverse bias away from the corresponding band edge by more than 1 eV. This is the critical energy distance for which frozen-in equilibria need to be considered. We will do this in following chapters and here will only refer to cautions when low reverse currents are to be discussed that depend on the minority carrier density and this density is limited by the position of the quasi-Fermi level. This means that it is usually higher than expected when a quasi-Fermi level approach is used, disrespecting frozen-in equilibria. As a first approximation, one may use the above mentioned 1 eV limit for such frozen-in disitribution resulting in a minimum minority carrier density on the order of $10^2\,\mathrm{cm}^{-3}$

Another limitation stems from the fact that a very thin highly doped layer tends to put one side of the junction in too close proximity to the metal contact to permit the recombination current there to be neglected in reverse bias.

Since this has in principle been discussed with thin devices already, we do not need to go into more detail here, except to mention that in some conventional Si devices the front p-type layer is only 500 Å thick with $10^{18}\,\mathrm{cm}^{-3}$ shallow acceptors. Here the minority carrier density is about $200\,cm^{-3}$ close to the froze-in equilibrium, and about acceptable for room temperature experiments, while the thickness of the highly doped layer is not large enough to neglect surface recombination for reverse bias.

And finally, if one side of the pn-junction is much larger than the diffusion length, then the additional contribution to the gr-current from the field enhanced diffusion needs to be considered in reverse bias that shifts the onset of the reverse current saturation to higher bias.

All these contributions have been discussed in separate examples before, and even though the solution curves of the set of transport equations that determine the junction behavior are quite similar to the set of solution curves discussed before, except for quantitative differences, we will here skip the figures showing such examples, but include the current voltage characteristic for such a device that summarizes the effects mentioned above for the example of the specific Si diode.

A The Current–Voltage Characteristics

The current–voltage characteristic is determined mainly by the gr-current in the junction. However, because of the comparatively thin p-type layer, a non-negligible recombination contribution of $\sim -5 \times 10^{-11}\,\mathrm{A\ cm}^{-2}$ from the surface of the p-type side must be added in reverse saturation (see Fig. 7.12).

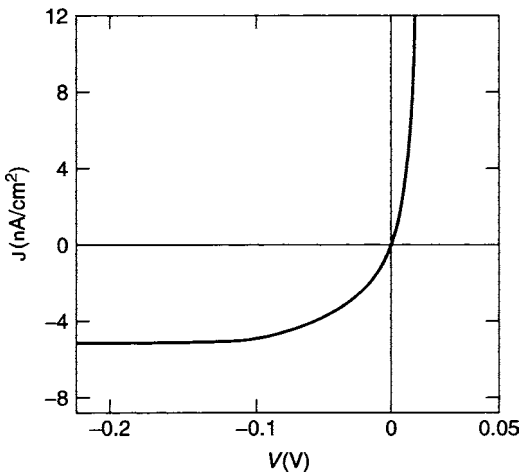

Fig. 7.12. Computed current–voltage characteristics of an Si-diode as described in the text with $j_s(d_1)$ and ${}^{(p)}\Delta j_{\mathrm{gr}}$ shown; $j_s(d_2)$ and ${}^{(n)}\Delta j_{\mathrm{gr}}$ are negligible. The marked contribution of the surface recombination is shown separately

Any additional contributions can be neglected: the current caused by the surface recombination at d_2 is $< 10^{-12}$ A cm^{-2}, the gr-current in the p-type region is $< 10^{-14}$ A cm^{-2} and the divergence-free current is $< 10^{-16}$ A cm^{-2}.

The lack of current saturation for the total current shown in Fig. 7.12 is caused by the gr-current generated in the junction that expands with increasing bias, as described in the previous section. The current will, therefore, continue to increase until the junction fills the entire bulk of the n-type region, or other high-field effects not considered in this section, terminate the validity range of the discussed model.

This example indicates once more the relationship of the different contributions to the current–voltage characteristics which influence their shape in an actual device. This includes the influence of the recombination current at the front contact of an asymmetrically doped devices, and the bias influence of the widening junction, that is responsible for the lack of an ideal current saturation.

We have intentionally selected here a device in which a variety of contributions determine the current–voltage characteristics, to demonstrate the intricate interrelationship of the different junction variables, but not necessarily to exemplify the more typical devices.

7.5 More Complex Homojunctions

In the preceding sections, we analyzed steady state effects of rather simple homojunctions with homogeneous and moderate doping profiles. Effects that influence the properties and operation of a pn-junction include

- Doping gradients
- Inhomogeneous distribution of recombination centers
- Series resistance contribution, and
- High injection effects.

In addition, one needs to consider modifications of the governing set of equations when material parameters become position-dependent, caused by inhomogeneous heavy-doping, graded composition or substantial surface treatments. The position-dependent material parameters can be

- The relative position of the conduction and valence band edges $E_c(x)$ and $E_v(x)$ with respect to each other, and thereby the band edge distribution $E_g(x)$;
- The density-of-state distribution within the bands $g_c(x)$ and $g_v(x)$;
- The carrier mobility $\mu_n(x)$ and $\mu_p(x)$, and
- The optical constants $\varepsilon(x)$, $\kappa(x)$, and $n_k(x)$.

These extensions present opportunities for designing new devices. The first set requires a study of more involved device properties. With limited space, we will only give a few selected examples here. The second set of extensions

requires a more generalised set of equations which we will briefly introduce; (see also Neudeck, 1983; Gray, 1967). For some detail on space charge recombination see, e.g., Anon, (1996); and on abrupt and linear junction see Van Halen, 1994.

7.5.1 Linearly Doped Junction

In the previous sections, we have assumed a constant doping within the n- and the p-type region. In most devices, at least one of the regions has a substantial doping gradient. As an example, we discuss here a linear grading of the doping profile[13] as shown in Fig. 7.13a.

With carrier depletion, one obtains from the corresponding Poisson equation

$$\frac{\mathrm{d}F}{\mathrm{d}x} = \frac{eax}{\varepsilon\varepsilon_0} \tag{7.60}$$

and after integration, the field distribution:

$$F(x) = -\frac{ea}{\varepsilon\varepsilon_0} \cdot \frac{(W/2)^2 - x^2}{2}, \tag{7.61}$$

as shown in Fig 7.13b, with a *rounded* maximum value of the field

$$|F_{\max}| = \frac{eaW^2}{8\varepsilon\varepsilon_0}. \tag{7.62}$$

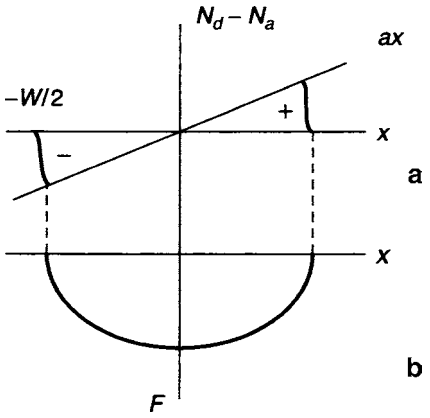

Fig. 7.13. a: Doping profile of a *pn*-junction with a linear doping gradient. Depletion region and sign of space charge indicated; **b**: corresponding built-in field distribution

[13] Such profile can (rarely) be achieved by cross diffusion of dopands for compensation; even though this is usually not symmetric, we will assume such symmetric compensation here.

The barrier width W can be expressed as

$$W = \sqrt[3]{\frac{12\varepsilon\varepsilon_0 V_\mathrm{D}}{ea}} \tag{7.63}$$

with V_D the diffusion potential, given by

$$V_\mathrm{D} = \frac{eaW^3}{12\varepsilon\varepsilon_0} = \frac{2kT}{e} \ln\left(\frac{aW}{2n_i}\right). \tag{7.64}$$

The diffusion potential increases logarithmically with the doping gradient. The width of the depletion layer varies according to the third root of $V_\mathrm{D} - V$. The qualitative behavior of the electronic properties of the linearly doped junction, however, remains similar to the abrupt junction discussed before.

7.5.2 High Minority Carrier Injection

With sufficiently large forward bias, the minority carrier density near the start of the junction (at l_n) can become comparable to the majority carrier density:

$$p_n(l_n) \simeq n_n = N_\mathrm{d} \tag{7.65}$$

This permits an approximation of the current-controlling minority carrier density as

$$p_n(l_n) \simeq n_i \exp\left(\frac{eV}{2kT}\right) \tag{7.66}$$

and consequently

$$j \propto \exp\left(\frac{eV}{2kT}\right), \tag{7.67}$$

i.e., a reduction of the slope of the characteristics with a quality factor of ≈ 2.

7.5.3 Series Resistance Limitation

In high forward bias, the current becomes large enough to induce a voltage drop across the space charge-free part of the device that can no longer be neglected. The voltage drop across the lower doped bulk region needs to be considered in the current–voltage characteristic:

$$j = j_s \exp\left[\frac{e(V - IR)}{kT}\right] \tag{7.68}$$

and causes a significant reduction in the slope, as indicated for some nontypical Si and GaAs diodes in Fig. 7.14.

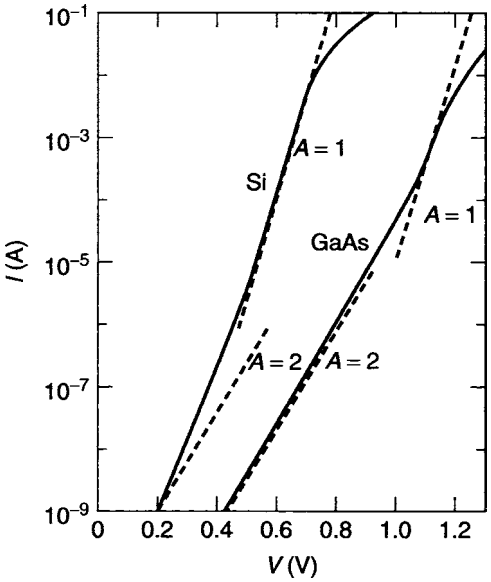

Fig. 7.14. Current–voltage characteristics of a typical Si- and GaAs-*pn*-junction-diode in forward bias. At small bias, the junction recombination predominates with quality factors close to $A \approx 2$; at higher bias, the diffusion current predominates with $A \approx 1$; at still higher bias, minority injection and finally series resistance limitation reduce the slope significantly

7.5.4 Position-Dependent Material Parameters

When material parameters are position-dependent, one needs to use a set of appropriately extended transport equations that are capable of dealing with such inhomogeneities. These will be presented in the Appendix 3 for the basic set of transport equations to indicate their consequences for device performance (see, e.g., Marshak, 1989).

Summary and Emphasis

The *pn*-junction is characterized by a space charge double layer caused by diffusion of electrons and holes into the oppositely doped region. The position of the electric field maximum remains at the metallurgical boundary between *n*- and *p*-type doping, independent of the doping ratio or bias.

The current–voltage characteristic of a *pn*-junction shows a much lower reverse saturation current and, therefore, a much better rectification than a Schottky barrier that has a detrimental recombination current leakage at the metal/semiconductor interface. The remaining leakage current due to recombination at the two electrodes of the *pn*-junction device can be reduced

by increasing the distance between junction and electrodes beyond several diffusion lengths of both minority carriers. The reverse bias branch of the jV-characteristic is then determined by the gr-current in the bulk or in the junction region. Which of the two regions predominates depends on the ratio of Debye length to diffusion length.

When the bulk predominates for minority carrier generation, the resulting jV-characteristics show nearly ideal behavior. When the junction region predominates, the reverse "saturation" current increases slightly since the junction region expands with increased reverse bias, resulting in less than perfect current saturation.

The reverse saturation current decreases exponentially with increasing band gap and soon reaches values below 10^{-10} A cm^{-2}. Spurious excitation and frozen-in steady state minority carrier densities are then responsible for limiting a further decrease of the saturation current for semiconductors with larger band gaps. These higher reverse saturation currents are more in tune with the experiment of better *pn*-diodes.

The quality factor of a *pn*-diode approaches 2 when junction recombination becomes predominant.

pn-junctions are the single most important part of almost all highly efficient semiconductor devices. The basic understanding of the interplay between the junction variables clearly distinguishing cause and effect relations and the decisive influence of boundary conditions is key to distinguishing between important and unimportant design parameters for the improvement of such devices. This becomes essential in smaller devices in which outer boundaries exert a more deteriorating influence.

Exercise Problems

1.(*) Why is the inter spaced metal layer much more effective in producing a deteriorating reverse bias leakage current in a back-to-back Schottky device than two outer electrodes, even for a "thin" device with $d_1 \ll L_n$ and $d_2 \ll L_p$? Give a quantitative answer.

2.(r) Why is the region adjacent to a high work function metal, independent of doping, more effective in controlling the voltage drop with increasing reverse bias in a back-to-back Schottky barrier device, while it is the lower doped region in a *pn*-junction?

3. Give the most important performance differences between a Schottky barrier and a *pn*-junction.

4. Which are the most important variables describing the actual position of the *pn*-junction interface?
   (a) How do electron and hole currents relate to the position of the junction interface?
   (b) Is there a possibility for the doping profile which permits a shift of the junction interface with bias?

(c) What are the necessary and sufficient condition for an inversion layer to be formed at an outer device surface?

5.(*) How much of an error is made by replacing the more triangular space charge region in the higher doped part of a *pn*-junction with a box-like region, using the neutrality condition for estimating its width, and applying the simple Schottky approximation in order to obtain field and potential distribution in this part, compared to the numerical solution of the exact system of controlling equations (7.32) to (7.40).

6.(*) To what extend does $\mu(F_e)$ influence the jV-characteristic of a typical *pn*-junction? Support your judgment by referring to Fig. 7.5.

7.(*) Discuss the extend of the DO- and DRO-ranges in Fig. 7.5.

(a) Why is the intermediate region between the DO- and DRO-regions in Fig. 7.5 not referred to as Boltzmann region?

(b) In what region does the major voltage drop within a device occur with reverse bias?

(c) In what region does most of the voltage drop occur with forward bias?

(d) Which region is most effective in carrier heating? What kind of fields are acting in this region?

(e) Why is carrier heating much less pronounced in the DO-region than in the DRO-region?

8. What means can you think of to reduce the surface recombination at the two electrodes of a typical *pn*-junction device?

9.(e) In Fig. 7.10, the crossover of electron and hole currents occurs at $\approx 10^{-3}$ cm from the junction interface in the *n*-type region. What changes can you suggest to move the crossover to -5×10^{-4} cm into the *p*-type region?

10. Make a list of all important parameters that influence the jV-characteristics.

(a) Identify the parameters that substantially increase the reverse saturation current.

(b) Identify the parameters that prevent clean current saturation. Give quantitative criteria.

(c) How does N_r influence the characteristics? Include the N_{r1} to N_{r2} ratio in your discussion.

(d) What is the quantitative influence of the band gap?

11.(*) Why has the current–voltage characteristic of a very thin *pn*-junction the typical diode shape, even though it is dominated by recombination currents at its contact surface? Provide a quantitative answer.

8

The Photovoltaic Effect

Summary. When a semiconductor is exposed to greater than band gap optical excitation, minority and majority carriers are produced which can be separated within the built-in field of a junction or barrier, thereby producing a photo-emf and/or generating a photocurrent in an external circuit. This is a sensitive device to detect light and an efficient means to convert light into electric power.

We will now introduce an additional optical excitation and wait until stationarity is achieved. We will discuss the influence of this optical excitation on the behavior of a variety of typical semiconductor devices. We will first introduce light with an energy in excess of the band gap that generates with equal rates majority and minority carriers[1]. Without an external bias applied, both types of carriers diffuse and when reaching the built-in field region of a junction or barrier, they become separated before they recombine. This causes a relative charging of both sides of the junction with respect to each other, or, when an external pathway is provided, it results in a photo-generated current.

The efficiency of this *photovoltaic effect* depends on the balance between generation, recombination, and carrier transport to the built-in field region, as well as the ability of this space charge region to separate both types of carriers effectively.

We will devote this chapter to a general overview of the photovoltaic effect with a basic reaction kinetic discussion relating to the lifetime of the photo-generated minority carriers and its related diffusion, and discuss this first in a

[1] Since we disregard in this first section the inhomogeneity of the optical absorption constant, this approach is justified only for thin platelets of a thickness of less than the optical absorption constant at the excitation energy. However, for indirect bandgap materials, such as Si, this absorption constant is on the order of a typical thickness of such devices (a few hundred micrometers); hence this approach is justified.

simplified photodiode model. This model connects the bulk diffusion with the junction-controlled minority carrier density, resulting in the basic photodiode equation.

8.1 Enhanced Carrier Generation and Recombination with Light

When light is introduced in addition to the thermal excitation, both majority and minority carrier densities will rise until the generation rate equals the recombination. The increased carrier densities can be obtained from the basic set of *reaction kinetic equations*:[2]

$$\frac{\mathrm{d}n}{\mathrm{d}t} = g - r - \frac{1}{e}\frac{\mathrm{d}j_n}{\mathrm{d}x} \tag{8.1}$$

and

$$\frac{\mathrm{d}p}{\mathrm{d}t} = g - r + \frac{1}{e}\frac{\mathrm{d}j_p}{\mathrm{d}x}, \tag{8.2}$$

with g, the sum of optical and thermal generation rate, given by

$$g = g_o + \frac{n_i^2}{\tau_{p0}\left(n + n_i^+\right) + \tau_{n0}\left(p + n_i^-\right)} \tag{8.3}$$

for a simple model with a one-level recombination center (see Sect. 4.3.1.2 and Fig. 4.6). The recombination rate follows the same formula as for thermal excitation alone; however, now with increased carrier concentration:

$$r = \frac{np}{\tau_{p0}\left(n + n_i^+\right) + \tau_{n0}\left(p + n_i^-\right)}. \tag{8.4}$$

The additional recombination traffic into regions of increased recombination needs to be considered in inhomogeneous semiconductors containing junctions or recombination surfaces and is represented by the $\mathrm{d}j/\mathrm{d}x$-term.

In Fig. 8.1, a typical reaction kinetic model for optical carrier generation in an n-type semiconductor is shown.

The balance between the different transitions depends on the optical generation rate in addition to the transition parameters, and on the boundary conditions in inhomogeneous semiconductors. This in turn will influence the changes of space charges and the development of currents in such semiconductors.

We will first describe the redistribution of carriers over the different levels as the result of optical generation in a **homogeneous semiconductor**.

[2] Also referred to as *continuity equations*, that contain generation and recombination, and traffic out of each volume element into junction or interfaces for additional recombination.

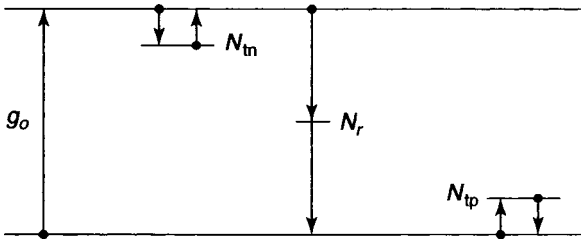

Fig. 8.1. Band and defect level model with optical carrier generation, recombination and trapping

In this case there are no net carrier currents involved, except for fluctuations; hence, one has

$$\frac{\mathrm{d}j_n}{\mathrm{d}x} = \frac{\mathrm{d}j_p}{\mathrm{d}x} \equiv 0. \tag{8.5}$$

We refer to semiconductors that change their conductivity significantly with light as **photoconductors** and will discuss these first, even though there is no space charge involved, but we need the reaction kinetic discussion to prepare for the following discussion including space charge regions.

8.1.1 Photoconductors

Optical generation increases the density of both minority and majority carriers. Depending upon doping and recombination, two types of materials may be distinguished: *semiconductors* and *photoconductors*.

In typical semiconductors, the density of thermally created *majority carriers* is so high that the optical generation causes only an insignificant increase of their density. The major changes are observed in a large increase of the density of *minority carriers*, resulting in a split of the quasi-Fermi levels by shifting the minority Fermi level only[3] with negligible shift of the majority quasi-Fermi level.

In typical photoconductors, the density of thermally created majority carriers is usually low: in the dark the material acts as an insulator. CdS is an example which, when properly doped, may have a dark resistivity in excess of $10^{10}\,\Omega$cm; it is n-type with $n \lesssim 10^7\,\mathrm{cm}^{-3}$. Even with low intensity[4] light the *majority carrier* density increases significantly. In a photoconductor, the band

[3] This state is often referred to as *low injection* state. With sufficient optical generation, e.g., for solar cells with concentrator, *high injection* can be reached, in which both carrier densities increase significantly above the equilibrium concentration.

[4] With a typical majority carrier lifetime of $10^{-4}\,\mathrm{s}$, a generation rate of $10^{11}\,\mathrm{cm}^{-3}\mathrm{s}^{-1}$ is sufficient to double the majority carrier density of $10^7\,\mathrm{cm}^{-3}$ in the dark. When exciting with band edge light (in CdS with $h\nu = 2.4\,\mathrm{eV}$) with an absorption constant of $10^5\,\mathrm{cm}^{-1}$, this represents a photon flux of $\sim 10^6\,\mathrm{cm}^{-2}\mathrm{s}^{-1}$, or about 10^{-11} of the photon flux in sunlight.

gap is wider than in typical semiconductors, the distance of the donor from the conduction band is larger, and most of the donors are depleted because of a large degree of compensation. With light the compensation is partially lifted, donors and acceptors are partially filled with electrons and holes, respectively, and both quasi-Fermi levels are shifted significantly. In addition, good photoconductors are *sensitized*, i.e., they are doped with minority carrier traps, which have a very small cross section to capture majority carriers, and consequently result in a *very low recombination rate* (e.g., Cu-doping in CdS), increased carrier lifetime and causes a very high photosensitivity.

8.1.2 Photo-emf and Photocurrents

In principle, either photoconductors or semiconductors produce a *photo-emf* when a space charge region is incorporated in the device. The built-in field of the space charge region separates some of the optically generated minority and majority carriers from each other, causing a relative charging of the two sides of the space charge region, or causing a *photocurrent* with carrier recombination within the external circuit when a path through an external circuit is provided (Fig. 8.2).

These *photovoltaic devices* have gained substantial commercial interest when using sunlight for carrier generation. They are called *solar cells* and convert solar energy into electrical energy with a respectable conversion

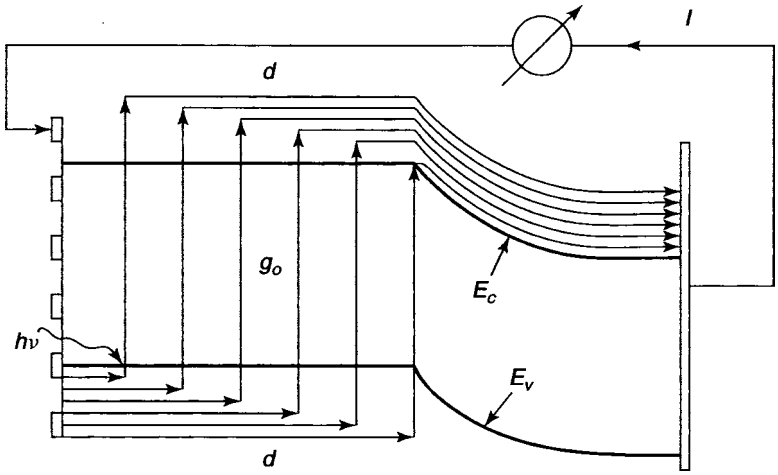

Fig. 8.2. Schematic of a photovoltaic device, indicating optical generation (g); separation of minority and majority carriers in the built-in field via minority carrier diffusion (d); and consequent recombination current (r) in the external circuit. The *arrows* represent electron paths (holes in the valence band move in the opposite direction)

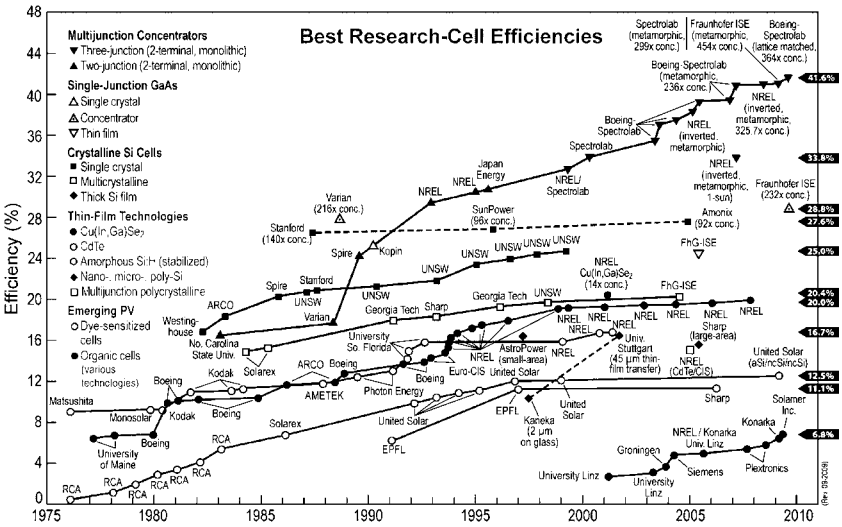

Fig. 8.3. History of developing highest efficiencies of various solar cells from 1975 to 2009 (curtesy of Lawrence Kazmerski, NREL, 2009, for specific quotation see (M.A. Green 1997)

efficiency[5]; with sunlight concentration solar cells have exceeded 40% (R.K. Gartia et al. 1992; D.S. Kim et al. 1992a), and recently, as $GaInP_2$/GaAs/Ge triple junction cells reached 40% see Fig. 8.3.

Highly efficient solar cells need a lower band gap in the 1.0–1.5 eV range to convert a large fraction of the solar light, and therefore are more typical *semiconductors*. Examples are Si, Cu_2S, $CuInSe_2$, CdTe, and GaAs as the material in which most of the sunlight is absorbed and the desired minority carriers are generated.

8.1.3 Quasi-Equilibrium Approximation

At the high generation rate associated with sunlight absorption,[6] the density of optically generated minority carriers

$$p = g_o \tau_p, \tag{8.6}$$

[5] Better solar cells (Si and GaAs) have presently achieved in excess of 24% conversion efficiencies (van 1993), and, with more sophisticated technology; such InGaP/GaAs tandem cells exceeded 30% (Yamaguchi and Wakamatsu (1996) and add it to the reference list.

[6] The photon flux impinging on a semiconductor is on the order of $10^{17}\,\mathrm{cm^{-2}s^{-1}}$ in the active part of the solar spectrum at AM 1. Indirect gap semiconductors with an absorption coefficient (weighted average) of $\sim 10^4\,\mathrm{cm^{-1}}$ thus have an effective generation rate (averaged) of $10^{21}\,\mathrm{cm^{-3}s^{-1}}$ and (thin) direct band gap semiconductors with an absorption efficient of $3 \times 10^5\,\mathrm{cm^{-1}}$ have an average generation rate of $3 \times 10^{22}\,\mathrm{cm^{-3}s^{-1}}$.

varies between 10^{10} for low lifetime (10^{-11} s) direct gap material to in excess of 10^{16} for high lifetime ($>10^{-6}$ s) indirect band gap material. This minority carrier density is proportional to the light intensity as long as the lifetime is independent of the generation rate; then the split of the quasi-Fermi levels is proportional to the logarithm of the light intensity

$$E_{Fn} - E_{Fp} = E_g - kT \ln \left(\frac{N_c N_v}{N_\mathrm{d} g_o \tau_p} \right), \tag{8.7}$$

assuming that the majority quasi-Fermi level remains essentially unchanged and is given by the density of shallow donors.

A constant lifetime is observed when the density of available recombination centers is constant; i.e., when the capture of electrons (in this example) into recombination centers is more rapid than that of minority carriers (holes). A constant density $n_r \simeq N_r$ of available centers is then provided. This can be achieved when the product of carrier density and capture cross section s fulfills the condition

$$n s_{rn} \gg p s_{rp}. \tag{8.8}$$

It also requires that most of the generated minority carriers remain in the valence band rather than being trapped in hole traps.

If substantial hole trapping needs to be considered, a pinning of the quasi-Fermi level for holes may occur with increasing optical generation rate until these hole traps are filled.

8.2 Reaction Kinetic, Balance

Whenever the recombination path for recombining holes becomes saturated ($n_r \ll N_r$) (e.g., at higher light intensities) or a major fraction of the optically generated holes is trapped at hole traps, the minority carrier lifetime becomes a function of the generation rate. A balance evaluation permits the determination of the minority carrier lifetime $\tau_p(g_o)$. The balance is determined by the difference between generation and recombination for each center, and is influenced by the carrier distribution over other centers via the neutrality condition, making more generated electrons available[7] for recombination than free holes (most of them are trapped). The change in minority carrier density with generation rate can be estimated from the formalism developed in Sect. 4.4 (see also Böer 2002).

In general, all competing transitions need to be considered. This yields for steady state a set of balance equations[8]

[7] This effect becomes active only at high enough light intensities, when the majority carrier density increases markedly.

[8] The capture and emission coefficients are identified by c and e, respectively, with subscripts identifying origin and target level (see Sect. 4.2).

$$g_o - [c_{cd} n p_{\rm d} - e_{dc} N_c n_{\rm d}] - [c_{cr} n p_r - (e_{rc} N_c n_r)] = \frac{dn}{dt} \equiv 0 \tag{8.9}$$

$$c_{cd} n p_{\rm d} - e_{dc} N_c n_{\rm d} = \frac{dn_{\rm d}}{dt} \equiv 0 \tag{8.10}$$

$$[c_{cr} n p_r - (e_{rc} N_c n_r)] - [c_{rv} n_r p - (e_{vr} N_v p_r)] = \frac{dn_r}{dt} \equiv 0 \tag{8.11}$$

$$c_{av} n_{\rm a} p - e_{va} N_v p_{\rm a} = \frac{dn_{\rm a}}{dt} \equiv 0 \tag{8.12}$$

$$g_o - [c_{av} n_{\rm d} p - e_{va} N_v p_{\rm a}] - [c_{rv} n_r p - (e_{vr} N_v p_r)] = \frac{dp}{dt} \equiv 0. \tag{8.13}$$

The terms in square parenthesis are usually negligible because of insufficient thermal excitation from the deep levels.

In addition to (8.9)–(8.13), one has the neutrality condition

$$n + n_{\rm a} + n_r = p + p_{\rm d}, \tag{8.14}$$

with

$$\begin{aligned} N_{\rm d} - p_{\rm d} &= n_{\rm d} \\ N_r - p_r &= n_r \\ N_{\rm a} - n_{\rm a} &= p_{\rm a}; \end{aligned} \tag{8.15}$$

we have here assumed an acceptor-like charging of the recombination centers.

One obtains from the balance of electrons in the conduction band, using (8.9) and (8.10) by neglecting the term in parenthesis:

$$g_o = c_{cr} n (N_r - n_r). \tag{8.16}$$

In a similar fashion, one obtains from the balance of holes, using (8.13) and (8.12), and neglecting the term in parenthesis:

$$g_o = c_{rv} n_r p. \tag{8.17}$$

Equations (8.16) or (8.17) can be used under certain conditions to estimate the carrier density generated by light. For instance, the minority carrier density for $n_r \simeq N_r$ is then simply given by

$$\boxed{p = \frac{g_o}{c_{rv} N_r}} \tag{8.18}$$

which is identical to the well-known relation (8.6), with the hole life time

$$\tau_{p0} = \frac{1}{c_{rv} N_r}. \tag{8.19}$$

In case n_r is no longer $\simeq N_r$ a better analysis of the system of (8.9)–(8.13) is required. When substituting the unknown densities of the trapped carriers

$$
\begin{aligned}
p_{\mathrm{d}} &= \frac{e_{dc} N_c N_{\mathrm{d}}}{c_{cd} n - e_{dc} N_c}, \\
n_r &= \frac{c_{cr} n N_r}{c_{rv} p - c_{cr} n}, \\
n_{\mathrm{a}} &= \frac{e_{va} N_v N_{\mathrm{a}}}{c_{av} p - e_{va} N_v},
\end{aligned}
\tag{8.20}
$$

and using total neutrality, one obtains

$$
\frac{g_o}{c_{cr}(N_r - n_r)} + \frac{e_{va} N_v N_{\mathrm{a}}}{c_{cv} p - e_{va} N_r} + \frac{c_{cr} n N_r}{c_{rv} p - c_{cr} n} = \frac{g_o}{c_{rv} n_r} + \frac{e_{dc} N_c N_{\mathrm{d}}}{c_{cd} n - e_{dc} N_c}. \tag{8.21}
$$

This equation can be converted into an implicit polynomial expression for computing the carrier densities n or p as function of the optical generation rate g_o by using (8.16) and (8.17). For certain cases (8.21) can be simplified as explicit polynomials:

$$
n = n(g_o) \qquad \text{or} \qquad p = p(g_o). \tag{8.22}
$$

For instance, at very high generation rates, where $n \simeq p$ one obtains from the first terms on each side of (8.21):

$$
n_r = N_r \frac{c_{cr}}{c_{cr} + c_{rv}} \quad \text{or} \quad N_r - n_r = N_r \frac{c_{rv}}{c_{cr} + c_{rv}}. \tag{8.23}
$$

From this condition one obtains an often used relation

$$
\boxed{n = p = \frac{g_o}{N_r} \left[\frac{1}{c_{cr}} + \frac{1}{c_{rv}} \right]} \tag{8.24}
$$

for the density of mutually created carriers, neglecting trapping. This is a typical bottleneck equation which determines the carrier density from the smaller of the two capture coefficients c_{cr} and c_{rv}.

The discussion given here is given merely to indicate the general trend and is by no means exhaustive. In a broader discussion, a larger variety of defect levels need to be included and their spatial distribution needs to be considered as well as other transitions and recombination mechanisms, including field depended excitation and Auger recombination (see Böer, 2002).

8.2.1 Trap-Controlled Carrier Densities

Traps may act as storage reservoirs to take part of the optically generated carriers out of circulation. Shallow traps usually are in quasi-thermal equilibrium with the corresponding band, with their degree of filling determined by the position of the quasi-Fermi level, ranging from $n_t \simeq N_t$ for $E_{Fn} < E_t$

to $n_t \ll N_t$ for $E_{Fn} > E_t$ for an electron trap. But with changing optical excitation the position of the quasi-Fermi level can be shifted, and hence the degree of occupation of these traps.

In order to illustrate the involved principle, let us assume a simple n-type photoconductor with electron traps and recombination centers as the only important defect centers. The corresponding reaction kinetic equations are

$$g_o - [c_{ct} n(N_t - n_t) - e_{tc} n_t N_c] - c_{cr} n(N_r - n_r) = \frac{dn}{dt} \equiv 0 \tag{8.25}$$

$$c_{ct} n(N_t - n_t) - e_{tc} n_t N_c = \frac{dn_t}{dt} \equiv 0 \tag{8.26}$$

$$g_o - e_{vr} p n_r = \frac{dp_t}{dt} \equiv 0 \tag{8.27}$$

with the corresponding neutrality equation

$$n + n_t + n_r = p. \tag{8.28}$$

When assuming predominant carrier trapping, one can simplify (8.28) to

$$n + n_t = p \tag{8.29}$$

and obtains from (8.25) and (8.26) the simple relation

$$g_o = c_{cr} n(N_r - n_r) \tag{8.30}$$

After replacing n_r from (8.27) and p from (8.29) one obtains a modified equation between carrier density and optical generation rate

$$n(n + n_t) = \frac{g_o}{N_r} \left[\frac{n + n_t}{c_{cr}} + \frac{n}{c_{rv}} \right] \tag{8.31}$$

which is nonlinear in n and shows a modified bottleneck relation in square brackets. For higher generation, $n \gg n_t$, (8.31) reverts back to (8.24) and shows that n rises proportional to g_o. For lower generation, $n_t \simeq N_t \gg n$, one obtains from (8.31):

$$n = \frac{g_o}{N_r} \left[\frac{c_{rv}}{c_{cr}} \cdot \frac{N_r N_t}{c_{rv} N_r N_t - g_o} \right] \tag{8.32}$$

which shows a sublinear rise[9] of n with g_o.

A similar relation can be developed for minority carriers.

We will now discuss in a simplified model how the photogenerated minority carriers produce the photodiode current in a photodiode.

[9] However, when optical generation at longer wavelength is applied, a superlinear branch can be observed, when optical *excitation* from filled traps increases.

8.3 Simple Model of the Photodiode

A simplified model for the photodiode can be derived from the diode model discussed in Sect. 7.1, which yields the basic diode equation (7.59). In addition to the diffusion current of thermally generated minority carriers that provided the saturation current in reverse bias, we have now to add the photo-generated carriers.

We will take here a modified formalism from the one used in earlier sections (Sects. 5.1, 6.1, and 8.1). This approach permits direct comparison between the thermal ionization (dark current) and the optical excitation (photovoltaic current).

The controlling equation for the minority carriers in the bulk is the current continuity equation (in steady state)

$$\frac{\mathrm{d}j_p}{\mathrm{d}x} = e(U + g_o) \tag{8.33}$$

with g_o the optical generation rate of electrons and holes, and

$$U = \frac{np - n_i^2}{\tau_{p0}\left(n + n_i^+\right) + \tau_{n0}\left(p + n_i^-\right)} \tag{8.34}$$

the net gr-rate, which, for $n \gg p$ becomes

$$U \simeq \frac{p - \frac{n_i^2}{n}}{\tau_{p0}} = \frac{p - p_0}{\tau_{p0}} \tag{8.35}$$

as long as the majority carrier density n remains close to its thermal equilibrium value n_0, which permits the use of $p_0 = n_i^2/n_0$.

In the space charge-free region, the minority carrier current is exclusively given by diffusion:

$$j_p = -\mu_p kT \frac{\mathrm{d}p}{\mathrm{d}x}; \tag{8.36}$$

with (8.33) and (8.35) one obtains the diffusion equation for minority carriers, including thermal and optical excitation

$$\frac{\mu_p kT}{e} \frac{\mathrm{d}^2 p}{\mathrm{d}x^2} = \frac{p - p_0}{\tau_{p0}} - g_o, \tag{8.37}$$

which has the general solution:

$$p(x) = p_0 + g_o + A \exp\left(\frac{x}{L_p}\right) + B \exp\left(-\frac{x}{L_p}\right) \tag{8.38}$$

with the diffusion length

$$L_p = \sqrt{\frac{\mu_p kT}{e} \tau_{p0}}. \tag{8.39}$$

By providing two boundary conditions, the particular solution curve can be picked from this set of general solutions. In a long device, we require

$$p(x \to \infty) = \text{finite} \tag{8.40}$$

which renders $A = 0$.

At the other side of the device, we are now connecting the minority carrier density to the density at the boundary of the barrier which is obtained from integrating the transport equation

$$j_p = e\mu_p p \frac{\mathrm{d}V}{\mathrm{d}x} - \mu_p kT \frac{dp}{\mathrm{d}x} \tag{8.41}$$

for small net currents,[10] resulting in

$$p(x_B) = p_0 \exp\left(\frac{eV}{kT}\right), \tag{8.42}$$

where $p_0 = p_0(x_B)$ is the equilibrium density at the barrier boundary x_B and V is the applied voltage (neglecting series resistances). Neglecting also the thickness of the barrier[11] for current generation, i.e., setting $x_B = 0$, one obtains for the particular solution after substituting (8.42) into (8.38)

$$p(x) = p_0 + g_o\tau_{p0} + \left[p_0\left(\exp\left\{\frac{eV}{kT}\right\} - 1\right) - g_o\tau_{p0}\right]\exp\left(-\frac{x}{L_p}\right). \tag{8.43}$$

When using this hole distribution in (8.36) one obtains for the minority carrier current:

$$j_p(x) = \frac{\mu_p kT}{L_p} p_0 \left[\exp\left(\frac{eV}{kT}\right) - 1\right]\exp\left(-\frac{x}{L_p}\right) - eg_o L_p \exp\left(-\frac{x}{L_p}\right). \tag{8.44}$$

A complimentary solution can be obtained for the majority carrier current $j_n(x)$ with the total current given by $j_n + j_p = j = \text{const}$ for steady state.

The total *photocurrent* is then easily determined at any convenient position, e.g., at $x = 0$, where $j_p(x)$ has its maximum value [here $j_n(x) = 0$], yielding

$$j(V) = \frac{\mu_p kT}{L_p} p_0 \left[\exp\left(\frac{eV}{kT}\right) - 1\right] - eg_o L_p \tag{8.45}$$

the photodiode equation in this simplified model as the sum of the *dark current*, as obtained from the simple Schottky diode equation

$$j(V) = \frac{\mu_p kT}{L_p} p_0 \left[\exp\left(\frac{eV}{kT}\right) - 1\right] \tag{8.46}$$

[10] Assuming $|j_p| \ll (e\mu_p pF, \mu_p kT\mathrm{d}n/\mathrm{d}x)$.

[11] The connection of $p(x_B)$ as $p(x = 0)$ with (8.38) to determine the second boundary condition B, is not clear cut for a simple barrier. A more transparent connection of bulk and barrier is discussed in Sect. 11.1.3 for the d-type high-low heterojunction.

which is identical with (7.59) by setting the reverse dark saturation current

$$\boxed{j_0 = p_0 \frac{\mu_p kT}{L_p} = e p_0 v_{Dp}} \quad \text{with} \quad \boxed{v_{Dp} = \frac{L_p}{\tau_{p0}}.} \tag{8.47}$$

the photocurrent, that is the maximum current of photogenerated minority carriers (photocurrent)

$$\boxed{j_{\mathrm{L}} = e g_o L_p}, \tag{8.48}$$

Hence, one obtains a simple shift of the dark current by j_{L} for the *ideal photovoltaic current–voltage characteristic*

$$\boxed{j = j_0 \left[\exp\left(\frac{eV}{kT}\right) - 1 \right] - j_{\mathrm{L}},} \tag{8.49}$$

as shown in Fig. 8.4.[12]

It should be emphasized here that such a shifted diode equation which is often used to approximate the characteristics of photodiodes contains numerous approximations, that renders such discussion of limited value. Especially, the often experimentally found cross-over of photodiode and dark characteristics should be judged as an important sign that the analysis of that particular device needs to be studied in a much more detailed model. Nevertheless, the obtained shift by the photodiode current (8.48) is a valuable tool to determine the diffusion length of the minority carrier.

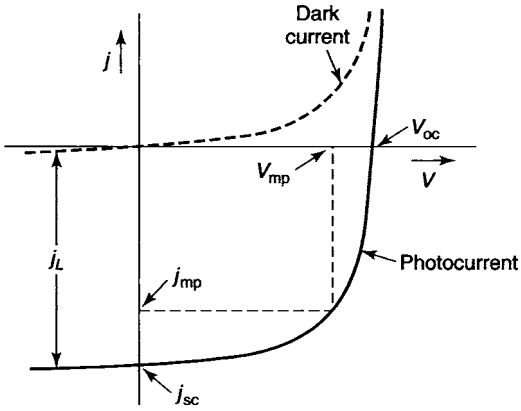

Fig. 8.4. Dark- and photodiode characteristic with the photocurrent shifted from the dark current by the saturation current $j_{\mathrm{sc}} = j_{\mathrm{L}}$. Maximum obtainable power rectangle with v_{mp} and j_{mp} shown

[12] In actuality, such simple shift is rarely observed, as often the dark- and photodiode characteristics crossover in forward bias. We will explain this behavior in Chap. 10.

8.3.1 Derived Photodiode Parameters

In contrast to passive devices which have current–voltage characteristics lying exclusively in the first and third quadrant, photodiodes (solar cells) have a major segment in the second quadrant, where electric power can be extracted directly from the device. For technical purposes this part of the characteristic is conventionally described by three parameters:

(1) the short circuit current, i.e., the maximum current that can be extracted from the device by connecting both electrodes to an ammeter with negligible internal resistance;
(2) the open circuit voltage, i.e., the maximum voltage generated by the device that can be measured between both electrodes while drawing a negligible current; and
(3) the maximum power point, i.e., the point in the characteristic from which the maximum electric power can be extracted.

From the photodiode characteristic (8.49) one obtains as short circuit current (for $V = 0$)

$$j_{\mathrm{sc}} = j_0 + j_{\mathrm{L}} \simeq j_{\mathrm{L}} \tag{8.50}$$

and as open circuit voltage (for $j = 0$)

$$V_{\mathrm{oc}} = \frac{kT}{e} \ln\left(\frac{j_{\mathrm{L}}}{j_0} + 1\right) \simeq \frac{kT}{e} \ln\left(\frac{j_{\mathrm{L}}}{j_0}\right). \tag{8.51}$$

With (8.51) one can eliminate j_0 and thereby rewrite the simple model photodiode equation (8.49) in a form containing only experimentally accessible parameters:

$$\boxed{j = j_{\mathrm{sc}} \left[\exp\left\{\frac{e(V_{\mathrm{oc}} - V)}{kT}\right\} - 1\right].} \tag{8.52}$$

The maximum power point is determined by the maximum rectangle that can be inscribed in the fourth quadrant of the characteristic (Fig. 8.4) and can obtained from the point at which the slope of the characteristic equals minus one:

$$\frac{V_{\mathrm{mp}}}{j_{\mathrm{mp}}} \frac{dj(j_{\mathrm{mp}}, V_{\mathrm{mp}})}{dV} = -1. \tag{8.53}$$

In solar cell technology another parameter is often used, the **fill factor**, which is given by

$$FF = \frac{V_{\mathrm{mp}} j_{\mathrm{mp}}}{V_{\mathrm{oc}} j_{\mathrm{sc}}}, \tag{8.54}$$

which can be derived from (8.49) and (8.53) and can be approximated by (Gray and Schwartz 1984):

$$FF \simeq \frac{\dfrac{eV_{\mathrm{oc}}}{kT} - \ln\left(\dfrac{eV_{\mathrm{oc}}}{kT} + 0.72\right)}{\dfrac{eV_{\mathrm{oc}}}{kT} + 1}. \tag{8.55}$$

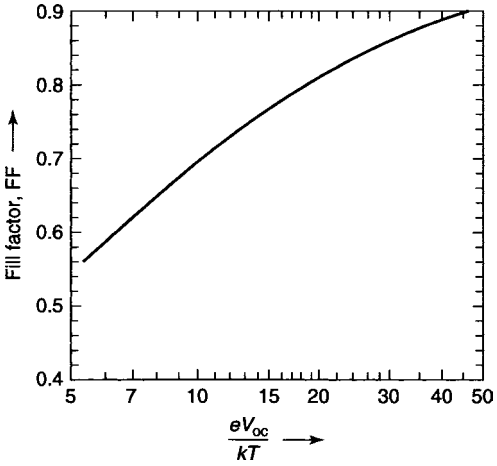

Fig. 8.5. Fill factor of an ideal photodiode as a function of the open circuit voltage according to (8.55). It lies between 55 and 80% for typical photodiodes (It is reported at 81.20% for the best CdS based multilayer solar cells (Ramasamy 1994)

The fill factor is a measure of the "squareness" of the characteristics in the fourth quadrant and is shown in Fig. 8.5 for the (simple model) "ideal" photodiode characteristic as a function of the normalized open circuit voltage.

The *power conversion efficiency* η can be derived from the above given parameters. It is the most important parameter of solar cells. This **efficiency** η is defined by the ratio of electrically generated power over the total power of light P_{in} impinging on the solar cell per unit area:

$$\boxed{\eta = \frac{V_{\text{mp}} j_{\text{mp}}}{P_{\text{in}}} = \frac{V_{\text{oc}} j_{\text{sc}} FF}{P_{\text{in}}}}. \tag{8.56}$$

8.3.2 Resistive Network Influence on the Diode Characteristics

In actual practice, photodiodes do not obey the (simple model) ideal diode equation (8.49), even though some of the better diodes come relatively close to it. There are many reasons for such deteriorating deviations, most of them related to junction or surface recombination, or to the influence of traps on transport and space-charges, as discussed in previous chapters (see, e.g., Sects. 3.2.2 and 5.2) and this is the subject of a more detailed analysis in the following chapter.

An empirical means to deal with some of the reduced diode performance is the introduction of an empirical exponential correction factor, as used in diodes, the *diode quality factor*, A which is larger than 1:

$$j = j_0 \exp\left(\frac{eV}{AkT}\right) - j_{\text{L}}. \tag{8.57}$$

The influence of the quality factor on the shape of the diode characteristics is indicated in Fig. 8.7c; it causes a reduction in the fill factor with little changes at and beyond j_{sc} and at V_{oc} (see also Sect. 3.2.2).

In addition, for some of the poly crystalline devices, rather simple series or shunt resistances[13] as shown in Fig. 8.6 can interfere with the device performance. Even though of limited and often misleading use we will show such influence here, more as a warning that with introduction of a number of parameters (justified or not) one can approximate experimental curves easily[14].

A series resistance R_s may result from insufficiently conducting electrodes, or excessive bulk material of insufficient doping. The effect of such series resistance is the tilting of the characteristic along the ascending branch and around V_{oc}, as shown in Fig. 8.7a.

A shunt resistance R_{sh} can be the result of a crystal fault or other electric pathways across the junction, possibly near surfaces or internal crystal boundaries. R_{sh} influences the slope of the characteristics near j_{sc} and simulates incomplete saturation as shown in Fig. 8.7b.

The so modified diode characteristic is given by

$$\boxed{j = j_0 \left[\exp\left\{ \frac{e(V - jR_s)}{AkT} \right\} - 1 \right] - j_s + \frac{V - jR_s}{R_{sh}}.} \tag{8.58}$$

When using these empirical correction factors, many actual characteristics can be closely approximated. This, however, may lead to erroneous conclusions about the possible presence of a network of parasitic resistors, while the actual reasons for a shape deviation from the ideal characteristic lies much deeper in the diode performance, as will be discussed in the following chapters.

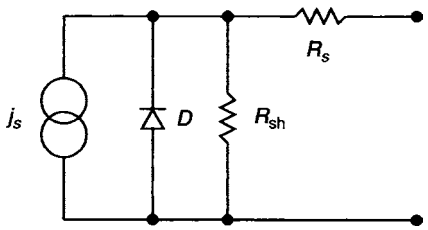

Fig. 8.6. Simple equivalent circuit of a solar cell diode D with series and shunt resistances identified

[13] Such resistances may actually exist in polycrystalline devices as paths between the electrodes through grain boundaries or as interlayers between grains and the electrodes. But their assumed existence is often overstated and can result in expensive searches for the wrong causes of such deviations from diode curve idealities in solar cell development

[14] Often the equivalent circuit is extended by other elements, such as another diode and more resistances, providing even more adjustable parameters to produce "better" (and more misleading) agreements with the experiment

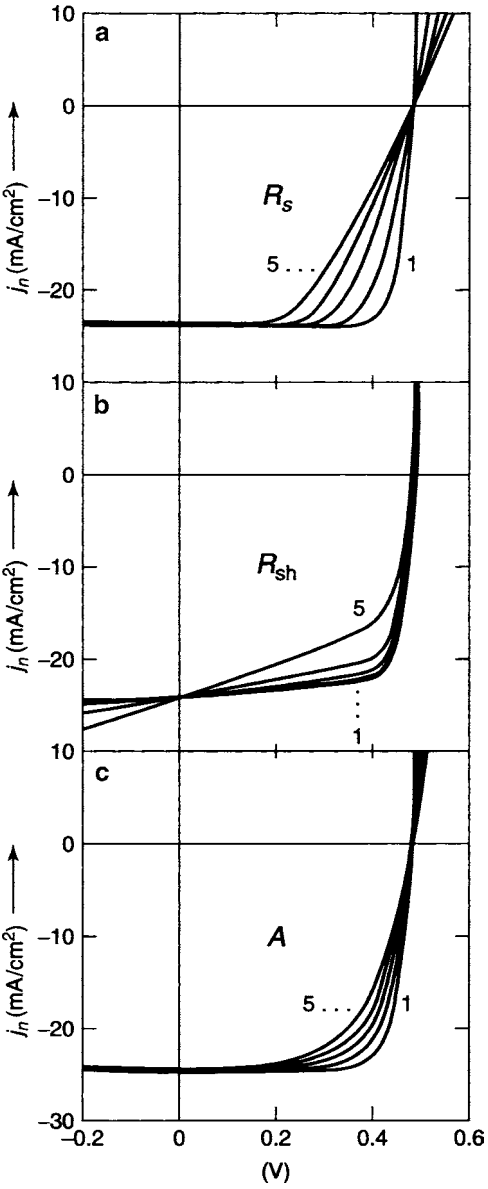

Fig. 8.7. Diode characteristics of a 1 cm^2 solar cell, modified (**a**) by a series resistance of 0, 2, 4, 6, and 8 Ohms for curves 1–5, respectively, (**b**) by a shunt resistance of 250, 200, 150, 100, and 50 Ohms for curves 1–5, respectively, and (**c**) by various diode A factors of 1 (ideal), 1.5, 2, 2.5, and 3 for curves 1–5, respectively (j_o is adjusted to keep V_{oc} = const.)

Summary and Emphasis

The photovoltaic effect is caused by a separation of photo-generated electrons and holes in the built-in field of a junction. In semiconductors this requires the diffusion of the photo-generated minority carriers to the junction where they are swept to the other side, charging this side with respect to the other side, thereby producing a photo-emf. This diffusion is controlled by a decreased minority carrier density at the bulk-to-barrier interface which, in turn, is shifted by an external bias, resulting in the photodiode characteristic.

This current–voltage characteristic has essentially the same shape as the dark-diode characteristic, but is shifted downward by the saturation diffusion current of the photogenerated minority carriers.

Following the driving force of the photo-emf, the generated carrier can transit through an external circuit, generating the photocurrent.

The photo-generated carrier density increases essentially linearly with the increasing optical generation rate, except when substantial minority carrier trapping occurs which renders this relation sublinear.

Photogeneration of minority carriers level is the initial step for generating a photo-emf and/or a photodiode current. The minority carrier density built up is controlled by a set of reaction kinetic equations which govern generation and recombination through each of the bands and defect levels of the semiconductor. The lifetime of minority carriers is controlled by a bottleneck equation involving sequential recombination of electrons and holes through recombination centers. A better understanding of this relation is the key for an improved design of photovoltaic devices.

Exercise Problems

1.(e) How deep a layer is active on both sides of a junction to produce a photocurrent in a solar cell?

2.(*) Is there an advantage to use a photoconductor rather than a semiconductor for a photovoltaic device? How would (8.7) have to be modified for a photoconductor in which the densities of photogenerated minority and majority carriers are much larger than these densities in thermal equilibrium?

3.(e) Draw a computer generated solution $n(g_o)$ and $p(g_o)$ of the polynomials given in (8.9)–(8.13) for $N_c = 10^{19}\,\mathrm{cm}^{-3}$, $N_\mathrm{a} = N_\mathrm{d} = 10^{17}\,\mathrm{cm}^{-3}$, $E_c - E_v = 0.1\,\mathrm{eV}$, and all recombination (capture) cross sections $10^{-16}\,\mathrm{cm}^2$. Plot these curves in double logarithmic scale for $10^{10} < g_o < 10^{22}\,\mathrm{cm}^{-3}\mathrm{s}^{-1}$.

4.(e) Compare the solutions obtained in solving problem number 3 with $p(g_o)$ obtained from (8.18), (8.24) (explain the factor of 2), and (8.17).

5.(*) Derive explicitly $n(g_o)$ by eliminating n_t from (8.31), using (8.26), and the relation between e_{tc} and c_{ct}.

6.(e) Express the carrier lifetimes τ_{n0} and τ_{p0} shown in (8.35) in terms of their appropriate capture coefficients.

7.(e) In (8.42), we present a general solution of the diffusion equation in terms of exponentials, while using hyperbolic trigonometric functions in Sect. 5.1.1.1, (5.8). Why? Are both representations equivalent? Why?

8.(*) Analyze the justification of the use of (8.42) for describing the boundary condition of $p(x = 0)$ that determines the constant B in (8.38), which, in turn, identifies the physically meaningful solution of the diffusion equation.

(a) Compare the Boltzmann-type solution given for minority carriers in (8.42) with the identical form of solution for majority carriers. Explain the differences to the conditions yielding the equivalent (3.12) and the exact condition under which (8.33) is fulfilled.

(b) The exact position x_B is important in defining a boundary value for p at the bulk-to-barrier interface. To set $x_B = 0$ may be justified in respect to $L_p \ll L_\mathrm{D}$, but it needs a better definition with respect to the boundary of the barrier. Develop such a definition.

9.(e) A parallel shift of the dark characteristic $j(V)$ by the photo-generated current yields an extended saturation branch in the fourth quadrant. Convince yourself by a to-scale drawing that this indeed occurs while the dark-diode characteristic increases steeply at $V > 0$. What is the simple reason for this apparent difference in shape?

10. Produce a computer solution for the fill factor as a function of V_oc of an ideal photodiode equation and determine the error to the approximation given in (8.55) and shown in Fig. 8.5.

11.(e) How much shift of V_oc would have occurred if j_0 would not have been adjusted in Fig. 8.7c. Comment on the physical significance of such V_oc changes with changing ideality factor.

12.(*) Comment on the difference of an A-factor used here and the shape factor given in Sect. 3.2.1.2. Comment on the discussion provided in Sect. 3.2.2.5.

9

The Schottky Barrier Photodiode

Summary. The Schottky barrier separates optically generated minority carriers from the majority carriers that are collected from a bulk layer, extending a couple of diffusion lengths from the barrier. As an ideal Schottky diode, however, it is unable to produce a respectable photovoltaic light-to-electric power conversion since it maintains the same majority quasi-Fermi level throughout the device to which both electrode Fermi levels are connected.

Even though it seems to be a misnomer to call these Schottky diodes actual photodiodes, since they are incapable of producing any photo emf, and if so-called Schottky barrier cells produce a photo emf, they are indeed hidden *pn*-junction cells, we have done so in the chapter heading. This was done to continue the Schottky barrier analysis from earlier chapters and introduce optical excitation to describe in a simple space charge region the effects of this additional excitation. However, we will summarize this description only briefly to explore the main differences to the exclusively thermal excitation, and then point out the reason why such photoexcitation in the Schottky diode can not produce any marked photo emf.

We have analyzed the optical generation of minority carriers, and the basic concepts of a photodiode, we now discuss the solution curves of the governing system of transport, continuity and Poisson equations for an ideal Schottky barrier device with optical excitation.

9.1 A Thin Schottky-Barrier Photodiode

In the previous chapter, we have analyzed the space charge-free part of the device in generating a photocurrent. We will now analyze this behavior within and close to a Schottky barrier. The focus on the action of the barrier layer is amplified in a "thin" device, i.e., a device of total thickness of only about twice the barrier width.

We first focus our attention to the current distribution within such a device.

9.1.1 Solution Curves of the Transport Equations

The transport equations for the Schottky barrier devices are the same as given in the previous chapters describing such devices, except that for the carrier generation an optical generation term g_o is added. that depend on the type of optical excitation may be homogeneous throughout the device, intrinsic (band-to-band excitation) or polychromatic, including excitation from levels in the band gap. Except for this influence, the solution curves show a similar behavior to the Schottky barrier device without optical excitation. Therefore, we will not discuss here these solutions in detail but only present graphically the influence of light as a shift in the distribution of minority carriers and as a split of the quasi-Fermi levels, as shown in Fig. 9.1 for a short Schottky barrier in a p-type Si device with a neutral surface at d_1.

Consequently, the spread of the quasi-Fermi levels in the bulk is "delayed" until the optically generated minority carrier density can increase significantly in the bulk, overcoming the strong recombination at the metal surface, being hindered of this recombination by its diffusion to the surface. This is shown by the shift in the spread of the quasi-Fermi levels in Fig. 9.2 from the theoretical maximum spread, shown as dashed curve, if this metal surface recombination could be neglected.

The most important feature that sets a true Schottky barrier device apart from a pn-junction device that will be discussed in the following chapter, is the fact that even for higher optical generation rates the majority quasi-Fermi level remains essentially flat throughout the entire device, as shown in Fig. 9.4. Hence, there is no emf created within the device and the Fermi levels at both electrodes are at the same potential for vanishing net current.

This is depicted in Fig. 9.4 for the computed band-model at an optical generation rate of $g_o = 10^{16}\,\mathrm{cm^{-3}s^{-1}}$. Both quasi-Fermi levels collapse at the position of the majority quasi-Fermi level without a marked jump $[E_{Fn}\left(d_1^-\right) - E_{Fp}\left(d_1^-\right) < 1\,\mu\mathrm{eV}]$. Even though there is a significant spread of the quasi-Fermi levels[1] $g_o = 10^{16}\,\mathrm{cm^{-3}s^{-1}}$ in the center of the device, both metal Fermi levels are connected to E_{Fp} which is flat throughout the device; hence, there is $< 1\,\mu\mathrm{V}$ open circuit voltage.

Only at extremely high generation rates in excess of $10^{20}\,\mathrm{cm^{-3}s^{-1}}$ can a minor open circuit voltage develop an be related to a small bending of the majority quasi-Fermi level when the "minority" carrier density can exceed the majority carrier density near the electrode, as obtained from

$$E_{\mathrm{F}}(0^-) - E_{\mathrm{F}}\left(d_1^+\right) = kT \ln\left[1 + \frac{g_o l_m}{v_p^* p_c(0^+)}\right] - kT \ln\left[1 + \frac{g_o(d_1 - l_m)}{v_p^* p_c(d_1)}\right]. \quad (9.1)$$

[1] In pn-junction devices the open circuit voltage is equal, or close to this split of the quasi-Fermi levels (see Sect. 7.2.3).

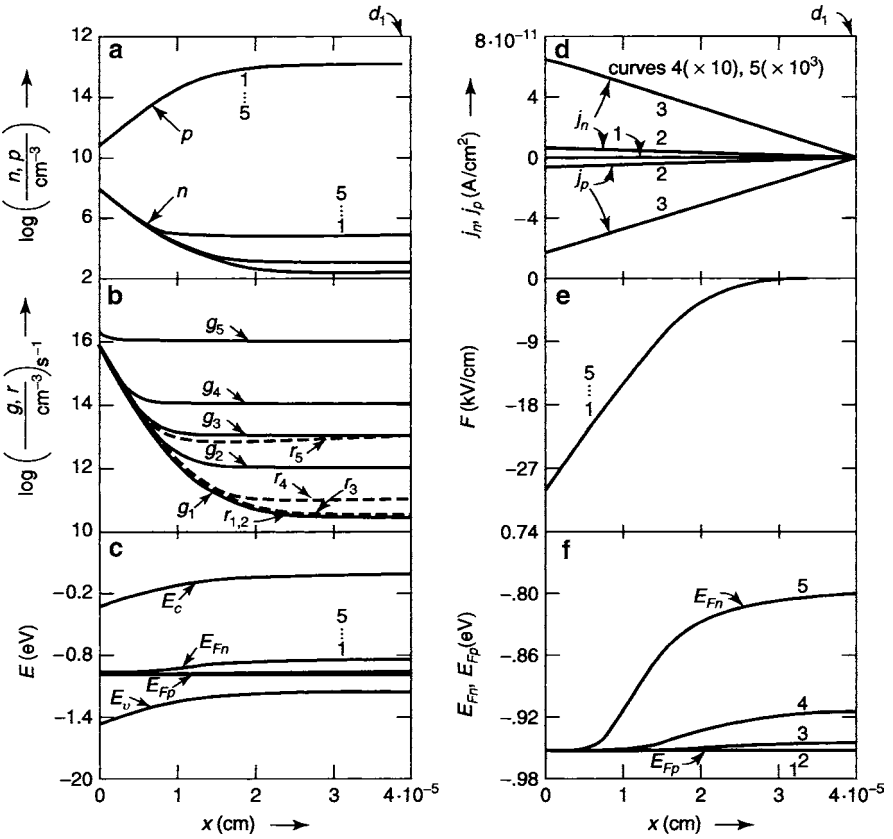

Fig. 9.1. Solution curves of (7.32)–(7.40) for a p-type Si Schottky barrier shown for zero net current; parameters are the same as given in Table 6.2. parameter is the optical generation rate; $g_o = 0$, 10^{12}, 10^{13}, 10^{14}, and $10^{16}\,\mathrm{cm^{-3}s^{-1}}$ for curves 1–5, respectively. **a**: carrier densities, **b**: generation rates, **c**: computed band model with quasi-Fermi levels, **d**: electron and hole currents, **e**: field distribution, and **f**: quasi-Fermi level distribution at an enlarged energy scale. It sold be observed that for small optical excitation rates, up to $10^{14}\mathrm{cm^{-3}}$ the minority carrier density in the bulk is little changed, even though it exceeds the thermal generation rate, since it is dominated by surface recombination. The field distribution is independent of the optical generation

This also causes a crossover of the currents, with l_m the position of the crossover of $j_n(x)$ and $j_p(x)$. The open circuit voltage, however, is still comparatively small: it is $\approx 32\,\mathrm{meV}$ at $g_o = 10^{22}\,\mathrm{cm^{-3}s^{-1}}$.

This finding is independent of the device width, as long as the type of semiconductivity does not change within the device, i.e., the majority quasi-Fermi level remains the same throughout the entire device and at the interface to both electrodes; hence, Schottky barrier photodiodes should not show any marked open circuit voltage, except for very high optical excitation.

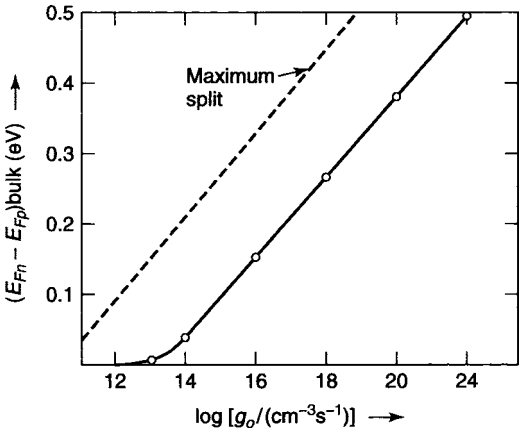

Fig. 9.2. Spread of the quasi-Fermi level in the bulk of a thin device obtained from Figs. 9.1 (*circles*) as function of the optical generation rate. Dashed curve indicates the maximum possible spread with negligible interface recombination, calculated according to (9.1)

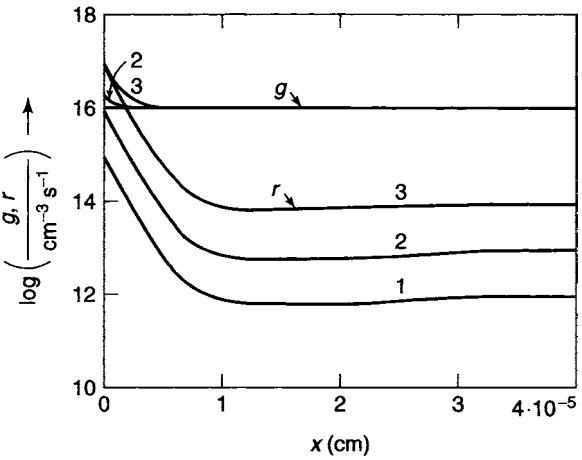

Fig. 9.3. Computed generation and recombination rates with $N_r = 10^{16}$, 10^{17}, and $10^{18}\,\text{cm}^{-3}$ for curves 1–3, respectively; $g_o = 10^{16}\,\text{cm}^{-3}\text{s}^{-1}$ and $j = 0$. Other parameters as in Fig. 9.1

The fact that experimentally some Schottky barrier devices deliver a substantial open circuit voltage indicates that such devices actually contain a thin *pn*-junction near one of the electrodes that permits switching over from one to the other majority quasi-Fermi level. We will later discuss the significance of such near-interface layers.

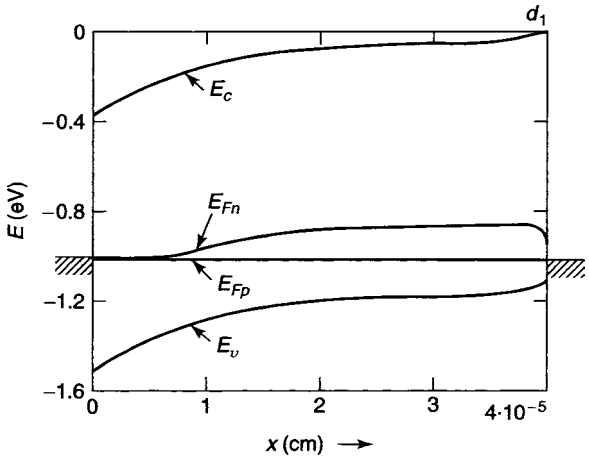

Fig. 9.4. Computed band-model for vanishing total current (open circuit condition). The left electrode produces a barrier as in Fig. 9.1, the right electrode is injecting with $e\psi_{SM,p} = 0.1\,\mathrm{eV}$; $g_o = 10^{16}\,\mathrm{cm}^{-3}\mathrm{s}^{-1}$. Connection to the metal Fermi levels is indicated outside of the figure panel

9.1.2 Current–Voltage Characteristics

The current–voltage characteristic for a thin Si-Schottky barrier device is plotted by connecting the computed voltage drop with the corresponding currents, which are used as a parameter for the set of different solutions (Fig. 9.5). Even though the barrier device is exposed to a substantial intensity of light with $g_o = 10^{19}\,\mathrm{cm}^{-3}\mathrm{s}^{-1}$, it shows a typical *dark* diode behavior with no crossing into the third quadrant. The quality factor A of this diode [see (3.72)], however. is substantially larger than one. The dashed curve shown for comparison in Fig. 9.5 is the ideal diode characteristic for otherwise the same parameters, with $A = 1$.

9.1.3 Lessons Learned from a Thin Schottky-Barrier Photodiode

The most important finding is the fact that the current–voltage characteristic of ideal Schottky barrier devices with light will not extend significantly into the fourth quadrant ($V_{\mathrm{oc}} < 1\,\mathrm{mV}$), thereby not allowing the extraction of any significant electric power from such a diode as long as the majority quasi-Fermi level does not change from one to the other carrier type.

This example illustrates the intimate interaction of interface- and bulk-related effects with the diffusion length, determining the interaction between the bulk and surface.

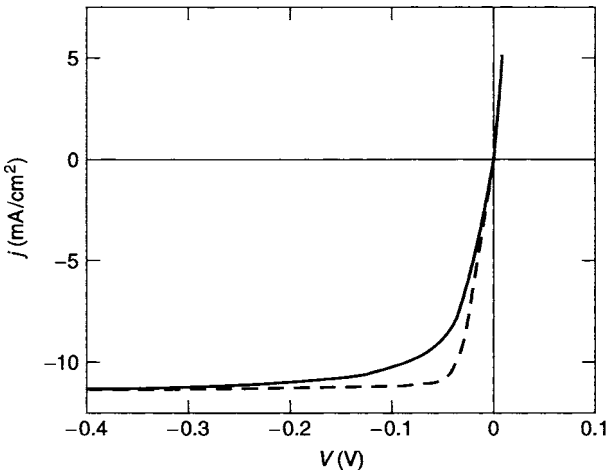

Fig. 9.5. Current–voltage characteristic for a p-type Si-Schottky barrier device for $g_o = 10^{16}\,\mathrm{cm}^{-3}\mathrm{s}^{-1}$ computed as for Fig. 9.4. Dashed curve is the ideal diode characteristic for the given saturation current of $-11.8\,\mathrm{mA/cm}^2$

9.1.4 Thicker Schottky Barrier Device

The influence of the width of the device can be estimated from the diffusion behavior of minority carriers discussed in Sect. 5.1 and combined with the results obtained for a thin device (Sect. 9.1). The solution curves can be spliced between the bulk and the junction region. In the space charge-free region, the minority carrier current is carried by diffusion only, and the majority carrier density and field are independent of optical generation, except for large injection.

When we separate the bulk from an extended barrier region at $x = 4 \times 10^{-4}\,\mathrm{cm}(= \delta)$, then the addition of bulk material beyond $x = \delta$ will raise $j_p(x = \delta) = -j_n(x = \delta)$ from zero as discussed in Sect. 9.1, to

$$j_p(x = \delta) = -j_n(x = \delta) = eg_oL_n \tanh\left(\frac{d_1 - \delta}{L_n}\right) \tag{9.2}$$

[see (5.17)], that is larger by two orders of magnitude than the gr-current in the thin device. This gr-current supplies the increased recombination current at the metal/semiconductor interface in open circuit conditions.

Most important are the increase in minority carrier density and the wider spread of the quasi-Fermi levels within the bulk of the device; these spreads approach the theoretical limit of the minority carrier density of $10^8\,\mathrm{cm}^{-3}$ in the bulk and the spread of the quasi-Fermi levels of 0.337 eV for the given generation rate ($g_o = 10^{16}\,\mathrm{cm}^{-3}\mathrm{s}^{-1}$) and minority carrier lifetime ($\tau_n = 10^{-8}\,\mathrm{s}$).

There is, however, no influence of the device width on the majority carrier distribution up to $g_o = 10^{19}\,\mathrm{cm}^{-3}\mathrm{s}^{-1}$. Therefore, $F(x)$ and hence the band

bending in the barrier remains unchanged. This behavior will only change above $g_o = 10^{19}\,\mathrm{cm}^{-3}\mathrm{s}^{-1}$, where the recombination current will start to influence the majority carrier jump of p_j/p_c at the metal boundary and thereby create then a rather small open circuit voltage.

The current–voltage characteristic for $g_o = 10^{19}\,\mathrm{cm}^{-3}\mathrm{s}^{-1}$ consequently remains the same as the current characteristic given for the thin device in Fig. 9.5.

Summary and Emphasis

A true Schottky barrier device, i.e., a device that does not change its majority carrier type is an extremely inefficient photodiode to convert optical into electric energy. The reason for this lack of conversion efficiency is the insufficient separation of minority carriers in the Schottky barrier which provides the metal-semiconductor interface with enough carriers of both types for a recombination of almost all photogenerated minority carriers. This, in turn, causes the collapse of both quasi-Fermi levels very close to the majority quasi-Fermi level, which remains nearly unchanged throughout the entire device. With the Fermi level of both electrodes connected to this majority quasi-Fermi level, no reasonable open circuit voltage can develop; therefore little excursion takes place of the current–voltage characteristics into the fourth quadrant that would be necessary for photoelectric power conversion.

Only when the collected photocurrent is high enough to saturate the recombination current at the metal semiconductor interface, some adjustments of both quasi-Fermi levels will occur at the blocking contact, and a minor open circuit voltage can be observed. This occurs only when g_o is larger than $v_p^* p_c/L_n$ for a sufficiently wide device with $d_1 > L_n$. For the given values of an ideal Si-Schottky barrier with $p_c \simeq 10^{10}\,\mathrm{cm}^{-3}$ and $L_n = 10^{-3}\,\mathrm{cm}$ it requires a minimum optical generation rate of $g_o > 10^{20}\,\mathrm{cm}^{-3}\mathrm{s}^{-1}$ to generate an open circuit voltage in excess of 25 mV.

Wider band gap semiconductors with higher barriers permit a lower majority carrier density at the metal/semiconductor interface and can result in somewhat better photodiodes. Contacts that create an inversion layer with a crossover of carrier densities within the barrier layer react in a similar fashion.

Only when doping provides a thin *pn*-layer near the metal contact changes the behavior dramatically; recombination at the barrier electrode is now shielded and large open circuit voltages can now develop.

Typical semiconductor Schottky barriers do not yield efficient photodiodes. Wider gap semiconductors, or such which have other material inter-layers between the semiconductor and the blocking electrode are essential to improve the photoelectric conversion efficiency of such devices.

Exercise Problems

1.(*) Describe qualitatively the amount of recombination current at the metal/semiconductor interface of a blocking contact in terms of the deviation of both carrier densities from thermal equilibrium when an optical excitation is present:
   (a) for zero net current (open circuit);
   (b) for reverse bias;
   (c) for forward bias.

2. Describe the difference between the blocking and an injecting contact at a neutral surface in respect to the electron and hole currents at such surfaces (interfaces).

3.(e) Develop the explicit expression for the offset from the theoretical maximum of the quasi-Fermi level spread shown in Fig. 9.2.

4.(*) At very high optical generation rates, the majority carrier distribution in the barrier region becomes modified:
   (a) Why? Give quantitative arguments.
   (b) Concurrently with these changes, the barrier height is reduced. Why?
   (c) Can you achieve a flat-band connection to a blocking contact at sufficiently high optical generation rates? Give a quantitative analysis.

5. At high optical generation rates, the minority carrier density distribution shows major deviations from the equilibrium distribution. Identify the different regions with respect to dominating drift and diffusion currents:
   (a) at open circuit conditions;
   (b) at reverse bias;
   (c) at forward bias.
   (d) How can local balance be achieved to yield the observed linear total minority carrier distribution?

6. With a blocking electrode on one side and an injecting electrode at the other side of the device:
   (a) identify the signs of the corresponding space charge regions;
   (b) the signs of the fields at both electrode interfaces; and
   (c) the slopes of the bands.

7.(*) With reverse bias, there is a cross–over of the quasi-Fermi levels between bulk and depletion region:
   (a) define exactly the position of the cross–over;
   (b) is there any further significance to this cross–over point?
   (c) does it make sense to have it corresponding to $E_{\mathrm{F}}(x)$?

10

The pn-Junction with Light

Summary. The *pn*-junction is a highly efficient means to convert optical into electrical energy.

Because of the importance of such junction devices we will spend extensive attention to their performance, using the tools we have developed in the previous chapters. In the course of these discussions, we will distinguish between a variety of such *pn*-junctions with different degrees of asymmetry in doping and material composition (heterojunctions). All of these *pn*-junctions have three important advantages compared to a Schottky barrier:

- They permit changing from one to the other majority quasi-Fermi level, thereby permitting a large increase in open circuit voltage
- they remove the surface of major recombination from the barrier (junction region), minimizing its impact on the performance of the diode
- they eliminate the divergence-free current term of the majority carriers, which causes major current leakage in the Schottky diode.

We will discuss each of these advantages in more detail below for the example of an Si *pn*-junction, and will first analyze the behavior at zero currents, i.e., open circuit condition.

10.1 Open Circuit Conditions

All of the following discussions are based on the solutions of the complete set of transport equations given in previous chapters. The interesting part of the *pn*-photodiode extends by a few Debye lengths for the space charge and by a few diffusion lengths for minority carrier collection to either side of the doping interface of the junction. In order to separate this inner part of the device from electrode effects, we first assume neutral outer boundary conditions.

Table 10.1. Main parameters used in the computation of a thin symmetric Si-diode with an abrupt junction

Parameters	$N_a = N_d$	$N_{r1} = N_{r2}$	$E_i - E_r$	n_i^*
Values Dimensions	$10^{16}\,\mathrm{cm}^{-3}$	$10^{17}\,\mathrm{cm}^{-3}$	0.10 eV	$7.03 \cdot 10^{10}\,\mathrm{cm}^{-3}$

Zero surface recombination at both outer surfaces (of $x = d_1$ and $x = d_2$) requires at open circuit condition that

$$j_n(d_1) = j_p(d_1) = j_n(d_2) = j_p(d_2) = 0. \tag{10.1}$$

For thermodynamic equilibrium, one has in addition

$$j_n(x) = j_p(x) \equiv 0 \tag{10.2}$$

throughout the device.

10.1.1 Thin, Symmetric Si-Diode with Abrupt Junction

We assume first a symmetrical thin device of double the thickness of the thin Schottky-barrier device discussed in Chap. 9.

To facilitate comparison with the results in Chap. 9, we have kept the p-type side on the right side of the device. The same set of governing equations and parameters are used as for the Si Schottky-barrier device, with the few changes listed in Table 10.1

10.1.1.1 Current Distribution in a Symmetric pn-Junction

In steady state, i.e., with optical generation $g_o > 0$, a net gr-current flows from both bulk regions toward the junction. For reasons of anti-symmetry both j_n and j_p must vanish in the center of this symmetric junction. This typical behavior is shown in Fig. 10.1, as computed for $g_o = 10^{12}\,\mathrm{cm}^{-3}\,\mathrm{s}^{-1}$ for curves 2. The figure also contains the zero current line (curve 1) for thermal equilibrium ($g_o = 0$).

The slope of the current curves depend on the net generation rate, which shows a behavior similar to that of the Schottky device in the bulk (compare the right side of Fig. 10.1 with Fig. 9.1d). However, near the center of the junction one observes a larger difference. The current density goes here through a maximum, returns to zero at the center plane of the junction and continues after changing sign to an anti-symmetric behavior at the other side of the junction. This behavior is caused by an overshoot of the recombination over the generation rate, which is typical for pn-junctions near the center plane, where the minority carriers move close to each other and have the greatest chance to recombine. The result is shown by comparison of corresponding

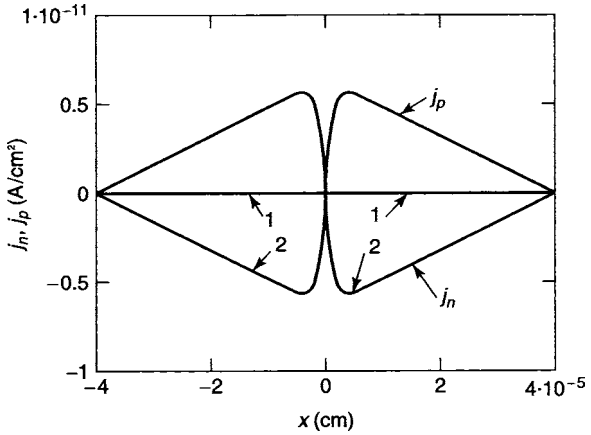

Fig. 10.1. Typical electron and hole current distributions in a thin symmetrical Si *pn*-junction device with negligible surface recombination; computed from (7.32)–(7.40) with parameters given in Table 10.1 and 10.1 and with $g_o = 0$ and $1 \cdot 10^{12}\,\mathrm{cm}^{-3}\,\mathrm{s}^{-1}$ for curves 1 and 2, respectively

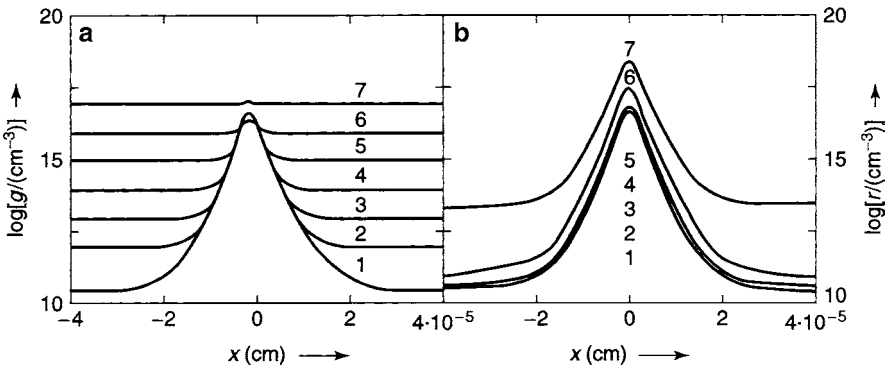

Fig. 10.2. Generation (**a**) and recombination rates (**b**) for a thin symmetrical Si *pn*-junction device computed as in Fig. 10.1 with the optical generation rate as family parameter: $g_o = 0,\ 10^{12},\ 10^{13},\ 10^{14},\ 10^{15},\ 10^{16}$, and $10^{17}\,\mathrm{cm}^{-3}\,s^{-1}$ for curves 1–7, respectively. The recombination rates of curves 1–4 lie on *top* of each other within the drawing error

curves in Fig. 10.2a, and b.[1] In Fig. 10.2a, a family of low generation rates is shown with g_o as family parameter. The constant optical excitation is superimposed on the bell-shaped thermal excitation:

$$g(x) \simeq \frac{1}{\tau_0} \frac{n_i^2}{n(x) + p(x) + n_i^*} + g_o, \tag{10.3}$$

[1] This comparison is easiest seen for curve pair 7.

with $\tau_0 = 1/(N_r c)$ and $n_i^* = 2n_i \cosh[(E_i - E_r)/kT]$; E_i is the energy of the recombination center level. The maximum of the thermal excitation (for $n = p = n_i$) is given by

$$g_{\text{th,max}} = \frac{1}{\tau_0} \cdot \frac{n_i}{2\left\{\cosh\left(\frac{E_i - E_r}{kT}\right) + 1\right\}} \simeq 1.4 \times 10^{16}\ \text{cm}^{-3}\ \text{s}^{-1}, \tag{10.4}$$

The thermal generation in the center of the junction can be neglected when the optical generation rates exceed $g_{\text{th,max}}$ (the limit of *low optical generation*—here about $10^{17}\,\text{cm}^{-3}\,\text{s}^{-1}$).

The recombination rate

$$r = \frac{1}{\tau_0} \cdot \frac{np}{n + p + n_i^*} \simeq \begin{cases} \frac{p}{\tau_0} & \text{in the } n\text{-type region} \\ \frac{n}{\tau_0} & \text{in the } p\text{-type region.} \end{cases} \tag{10.5}$$

lies below the optical generation rate in the bulk, since minority carriers are drawn into the junction for enhanced recombination here. The recombination rate lies above the optical generation rate at and near the center of the junction, since more minority carriers are now available here, supplied from the bulk. The increased[2] minority carrier density is caused by the continuity of $n(x)$ and $p(x)$ through the junction, as shown in Fig. 10.3. The enhanced recombination is localized within the central junction region of a width $\approx 10^{-5}\,\text{cm}$ (Fig. 10.1 and 10.2). This recombination, however, is rather benign compared to perfect recombination at the semiconductor/metal interface in a Schottky barrier.

Near the region where $n(x) = p(x)$, the recombination is in a steady state and open circuit conditions exceed the generation rate, a condition which is referred to as the *recombination overshoot*.

The junction net recombination compensates the bulk net generation. This general behavior should not be confused with additional junction recombination which may occur when, because of compensation in a gradient-doped homojunction, additional recombination centers (donor-acceptor pairs) are created within the region of cross-doping, an effect which further enhances the recombination overshoot, and is detrimental to the photo-diode performance; this is neglected in this section.

We will now analyze the entire set of solution curves for this Si *pn*-junction. In order to give an instructive picture of the behavior of the solution curves we have chosen an unusually large family of curves, that show a rather transparent development from small to large optical excitation rates.

[2] It is important for the understanding of this critical relation of a net junction recombination and the depletion of minority carriers from the adjacent bulk regions, to focus on current continuity that forces the transport of minority carriers to the recombination sink near the center of the junction, and results in a lemniscate shape of $j_n(x)$ and $j_p(x)$, as shown in Fig. 10.1.

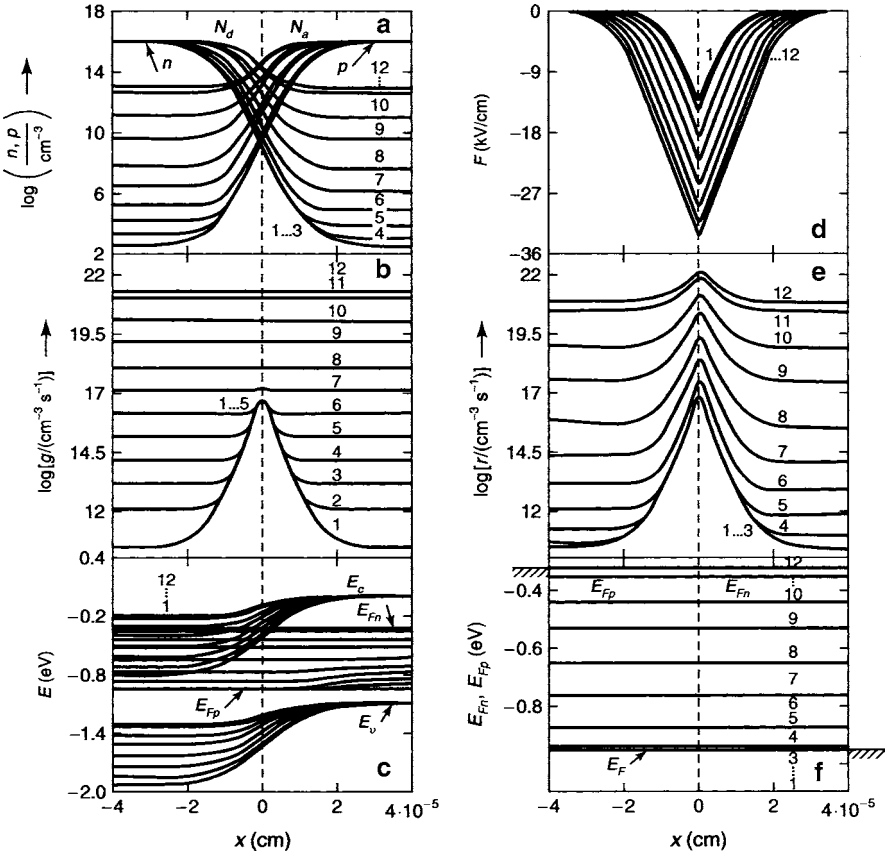

Fig. 10.3. Solution curves for a symmetrical thin Si *pn*-junction device computed as described for Fig. 10.1 with g_o as family parameter; for $N_r = 10^{11}$ cm^{-3} and $g_o =$ 0, 10^{12}, 10^{13}, 10^{14}, 10^{15}, 10^{16}, 10^{17}, 10^{18}, 10^{19}, 10^{20}, 10^{21}, and 2×10^{21} cm^{-3} s^{-1} for curves 1–12, respectively. (**a**) carrier density distribution; (**b**) generation rates; (**c**) band edges and quasi-Fermi levels; (**d**) field distribution; (**e**) recombination rates; (**f**) quasi-Fermi level distribution in expanded scale; connecting metal Fermi levels are shown for curve pair 12 adjacent to panel (**f**)

10.1.1.2 Solution Curves for Symmetric pn-Junction

The solution curves computed for this symmetric *pn*-junction in open circuit condition and for neutral surfaces are shown in Fig. 10.3 with g_o as family parameter. They show the typical *pn*-junction behavior of carrier density (panel a), field (panel d), and potential (band) distribution (panel c), including the expected spread of the quasi-Fermi levels (panel c and, in an enlarged scale, panel f).

Specifically, one observes a raise of the minority carrier densities with increasing g_o, concurring with a *decrease* in junction width, junction field, and

barrier height.[3] This typical and remarkable effect of a diminishing barrier height with increasing illumination is characteristic of any photovoltaic device and should be remembered. We will discuss its impact on the conversion efficiency later.

For vanishing bias, the barrier height is given by the diffusion voltage, which decreases with increasing optical excitation, as the minority carrier densities increase, and consequently the ratio between majority and minority carrier densities $(n_{10} \simeq N_\mathrm{d})/p_{10}$ or $(p_{20} \simeq N_\mathrm{a})/n_{20}$ is reduced:

$$V_\mathrm{D} = V_{\mathrm{D}n} + V_{\mathrm{D}p} = \frac{kT}{2e} \ln\left(\frac{N_\mathrm{d}}{p_{10}} \frac{N_\mathrm{a}}{n_{20}}\right) \tag{10.6}$$

with p_{10} and n_{20} the minority carrier densities in the space charge-free n- or p-type bulk of the device, respectively.

Quasi-Fermi Levels and V_oc. The quantitative analysis reveals some interesting details. In contrast to the Schottky barrier, the split quasi-Fermi levels are flat (except for very high optical excitation) throughout the junction and the bulk (see Fig. 10.3c and f). Consequently, the spread of quasi-Fermi levels within the device directly yields the open circuit voltage

$$V_\mathrm{oc} = \frac{1}{e}\big\{E_{Fn}(d_1) - E_{Fp}(d_2)\big\}, \tag{10.7}$$

since the metal Fermi level connects directly to the *majority* quasi-Fermi level,[4] which both quasi-Fermi levels collapse in any metal at boundary, but is not shown in this figure. The change over in a *pn*-junction device from E_{Fn} in the n-type to E_{Fp} in the p-type part of the junction, while connecting horizontally to the corresponding minority quasi-Fermi levels in the opposite part of the junction, can be seen in Fig. 10.3c and f.

The Recombination Overshoot Influence on V_oc can be seen from the fact that the minority carrier density in the bulk of this thin device is lower than expected from the $g_o\tau_0$ product because of the minority carrier drain into the junction for the enhanced recombination that becomes visible in Fig. 10.2 from the overshoot of the recombination in the center of the junction. With the reduction of the minority carrier density in the bulk, the spread of the quasi-Fermi levels is also reduced from the maximum open circuit voltage

[3] The figure shows the tendency to completely eliminate the junction barrier for a flat band connection at sufficiently high optical generation rates. Such flat band connection can be achieved at even lower optical generation rates in devices with lower doping densities and higher minority carrier life times.

[4] In contrast to the jumps of the quasi-Fermi levels at the metal interface of a Schottky barrier, the jumps for the majority quasi-Fermi levels are negligible in the *pn*-junction device when contact is made at each side with an appropriate, neutral (or injecting) contact metal.

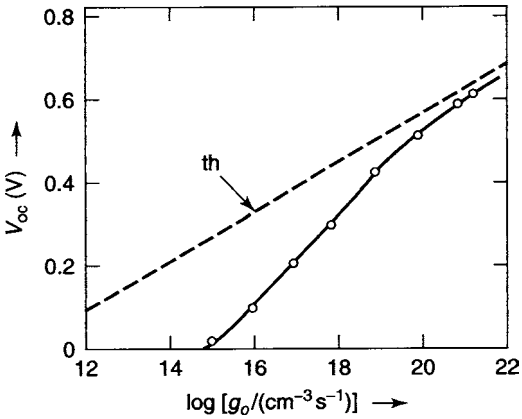

Fig. 10.4. Open circuit voltage as a function of the optical generation rate; obtained from the computation shown in Fig. 10.3 (*open circles*) *dashed line* given by (10.8).

that would be attained for vanishing recombination overshoot (here given for a symmetrical junction with $N_\mathrm{a} = N_\mathrm{d}$):

$$\boxed{V_{\mathrm{oc,max}} = \frac{1}{e}\left[E_g - kT\ln\left(\frac{N_c N_v}{N_\mathrm{a} g_o \tau_0}\right)\right] = \frac{kT}{e}\ln\left(\frac{g_o\tau_0}{n_\mathrm{th}}\right),} \tag{10.8}$$

with n_th calculated from $n_\mathrm{th} = n_i^2/N_\mathrm{a}$. $V_{\mathrm{oc,max}}$ is shown as a function of g_o in Fig. 10.4 as the dashed line. In contrast, at low optical excitation the computed spread is negligible and lies below $g_o = 10^{15}\,\mathrm{cm^{-3}\,s^{-1}}$: here almost all of the excess minority carriers are used up by recombination in the overshoot region; at higher optical generation rates V_oc starts approaching the maximum theoretical level $V_{\mathrm{oc,max}}$ but is still lower by about 130 mV at 10^{18} and by 45 mV at $10^{21}\,\mathrm{cm^{-3}\,s^{-1}}$. The actual open circuit voltage in thin symmetric devices is given by

$$V_\mathrm{oc} \simeq \frac{1}{e}\left[E_g - kT\ln\left(\frac{N_c N_v}{N_\mathrm{a} n_{10}}\right)\right] = \frac{1}{e}\left[E_g - kT\ln\left(\frac{N_c N_v}{N_\mathrm{d}\, p_{20}}\right)\right] \tag{10.9}$$

when using the computed bulk values for the minority carrier densities (from Fig. 10.3). These are shown as circles in Fig. 10.4 as taken from the $E_{Fn} - E_\mathrm{F}$ spread shown in Fig. 10.3f.

It is therefore essential to obtain the actual value of the minority carrier density in the bulk which, as indicated above, is determined by the balance between generation and recombination in the bulk minus the recombination current, which transports part of the minority carriers into the junction or to the surfaces (here neglected) for additional recombination.

We will now discuss in the following sections, the influence of changes in the recombination, including surface recombination changes in generation and doping of this symmetrical Si *pn*-photodiode.

10.1.1.3 Influence of Device Thickness

In following the same arguments presented in Sect. 9.1.4, one can represent a thicker device by simply raising the value of the electron and hole currents at the outer surfaces of the central part of the same device that was analyzed in the previous section. These minority carrier currents are given at these boundaries by the diffusion equation, neglecting any drift contribution. This neglect is justified, for $|x| > 4 \times 10^{-5}$ cm in the given example, as can be seen from Fig. 10.3d, which indicates negligible fields in this region.

In two examples of Fig. 10.5, the current was raised to 0.03 and 0.1 mA cm^{-2} at $x = \pm 4 \times 10^{-5}$ cm for curves 2 and 3, respectively. The

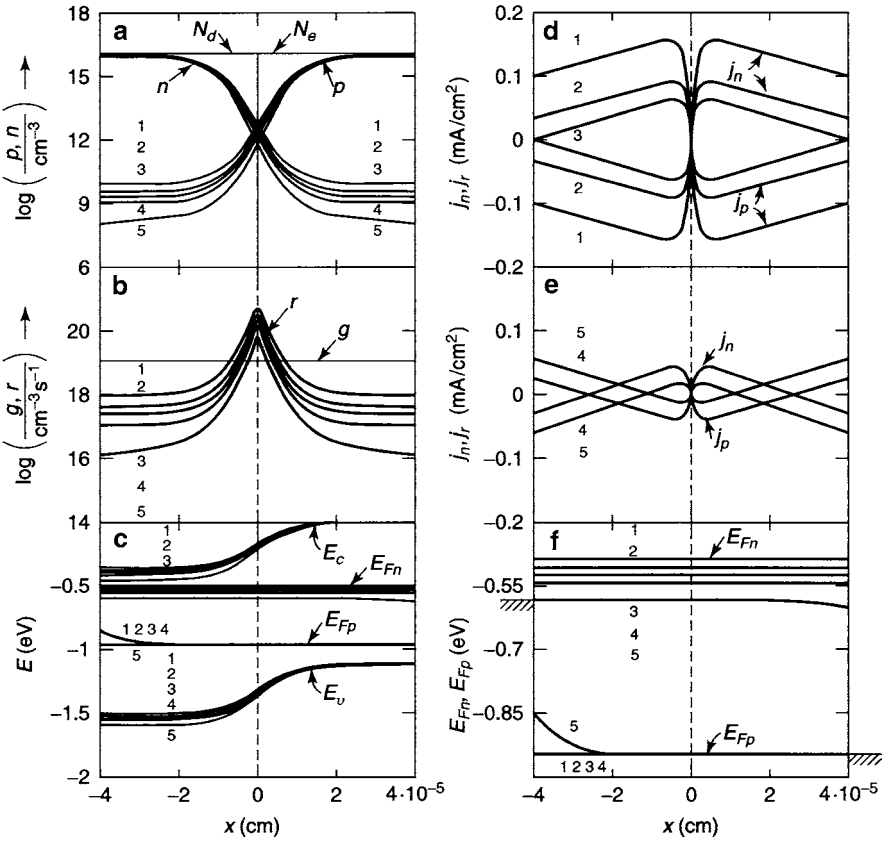

Fig. 10.5. Solution curves for a symmetric thin Si *pn*-junction device as in Fig. 10.3 for $N_r = 10^{17}$ cm^{-3} and the same optical generation rate $g_o = 10^{19}$ cm^{-3} s^{-1}, however, for various surface boundary conditions as indicated by the different currents at the surfaces in (**d**) for an increased bulk width and (**e**) for inclusion of surface recombination.(see text for more explanation

effective device thickness can be estimated by extrapolating $j_n(x)$ (or $j_p(x)$) linearly[5] to the x-value where both currents must vanish. This yields $-d_1 = d_2 = 6 \times 10^{-5}$ cm for the second and 1×10^{-4} cm for the third device.

Concurrently, with the increased device thickness, the minority carrier density and quasi-Fermi level spread increases (Fig. 10.5a, c, and f), and correspondingly the recombination overshoot heightens (Fig. 10.5b). The effect of a widened bulk region is in some aspects similar to an increase in the optical generation rate. This can be easily understood since more minority carriers are generated in the device that can be collected at the junction. Widening of the bulk also narrows the junction region, decreases the junction field and reduces the barrier height (Fig. 10.5c). This is similar to an increase in the optical excitation at a thinner device.

10.1.1.4 Influence of Surface Recombination

When surface recombination is introduced, it forces a sign change in these gr-currents near the surfaces, as minority carriers are now also drawn toward the surface where they recombine. In shorter devices with strong surface recombination, a crossover of $j_n(x)$ and $j_p(x)$ in the bulk can be seen in curves 4 and 5 in Fig. 10.5e. Curve 5 represents the shorter device, or the one with higher surface recombination. As expected, surface recombination has the opposite effect to the widening of the device bulk: it causes a reduction of the minority carrier density and the spread of quasi-Fermi levels decreases, i.e., it causes a decrease of the open circuit voltage V_{oc}. This is most dramatically seen in curve 5 of Fig. 10.5f.

Surface recombination (when within a few diffusion lengths) also widens the junction and increases the barrier height (Fig. 10.5c).

The quasi-Fermi levels remain essentially horizontal in spite of substantial changes in bulk width or surface recombination (except for curve set 5 for the minority carrier quasi-Fermi level). Their spread in the horizontal part, except for curves 5, determines again the open circuit voltage (again we have omitted the collapse of both quasi-Fermi levels to the majority quasi Fermi level) at each of the device to metal interfaces.

10.1.1.5 Influence of Recombination Center Density

In order to separate the surface influence from the important junction region, we increase the thickness of both, the p-type bulk region to more than $3L_n$ and an n-type bulk region to more than $3L_p$. We also continue to supply families of curves to show the essentially parallel shift and symmetry that is typical for symmetric junctions. The current distribution shows a barely visible slope in the bulk parts of the device, depicted in Figs. 10.6–10.8; it has

[5] This no longer holds when d_1 or d_2 become comparable to L_p and L_n.

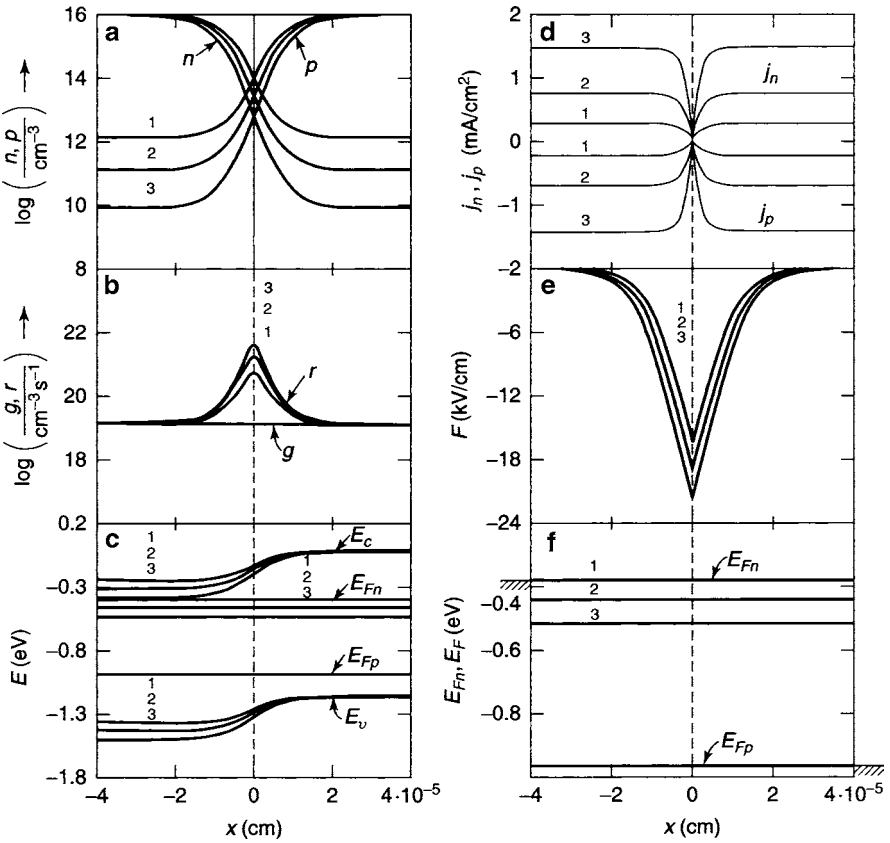

Fig. 10.6. Solution curves for a symmetric long Si *pn*-junction device computed for $g_o = 10^{19}\,\mathrm{cm}^{-3}\,\mathrm{s}^{-1}$ and with all other parameters as in Fig. 10.3. The recombination center density is the family parameter: $N_r = 10^{16},\ 10^{17}$, and $10^{18}\,\mathrm{cm}^{-3}$ for curves 1–3, respectively. The sub figures are ordered in the same fashion as in the previous figures

only the overshoot visible while the compensating region with $r(x) < g_o$ is located further in the bulk and is not displayed here in the shorter segment shown in the figure.

In Fig. 10.6, the influence of the recombination center density is depicted. With increasing $N_r = 10^{16},\ 10^{17}$, and $10^{18}\,\mathrm{cm}^{-3}$ for curves 1–3, respectively, the minority carrier density and the spread of quasi-Fermi levels decrease (Fig. 10.6a, c, and f) cause a corresponding decrease in V_{oc}. One also observes an increase in barrier width, field and diffusion potential with increasing N_r.

As an important result, one notices that the open circuit voltage now approaches closely the maximum theoretical value with decreasing recombination center density (compare Fig. 10.6f with the dashed line in Fig. 10.9).

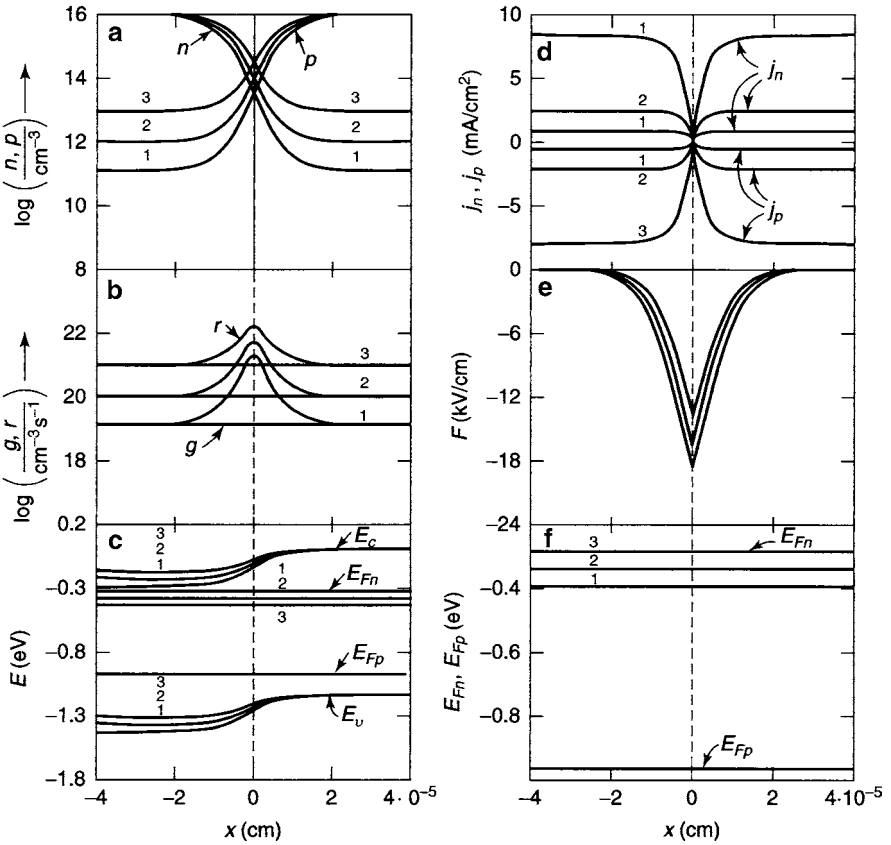

Fig. 10.7. Solution curves for a symmetric long Si *pn*-junction device computed for $N_r = 10^{17}\,\mathrm{cm}^{-3}$ and all other parameters as in Fig. 10.3. Here, the optical generation rate is the family parameter: $g_o = 10^{19}$, 10^{20}, and $10^{21}\,\mathrm{cm}^{-3}\,\mathrm{s}^{-1}$ for curves 1–3, respectively. The sub figures are again in the same fashion ordered as in the previous figure to facilitate comparison

10.1.1.6 Influence of the Generation Rate

The dependence on the optical generation rate of a device with thick bulk regions is shown in Fig. 10.7. This figure presents the increase in minority carrier density and open circuit voltage, again closely matching the theoretical maximum values. It also shows the decrease in diffusion potential and field with increasing generation rate $g_o = 10^{19}$, 10^{20}, and $10^{21}\,\mathrm{cm}^{-3}\,\mathrm{s}^{-1}$ for curves 3–1, respectively. Figure 10.7b shows that the relative overshoot ($r_{\max}/g_o$) decreases with increasing optical generation g_o. However, the maximum gr-current (Fig. 10.7d) increases in the bulk near the junction, sub linearly with g_o. We have repeated the dependence on the optical generation rate from the first figure with a much larger family of curves in order to facilitate

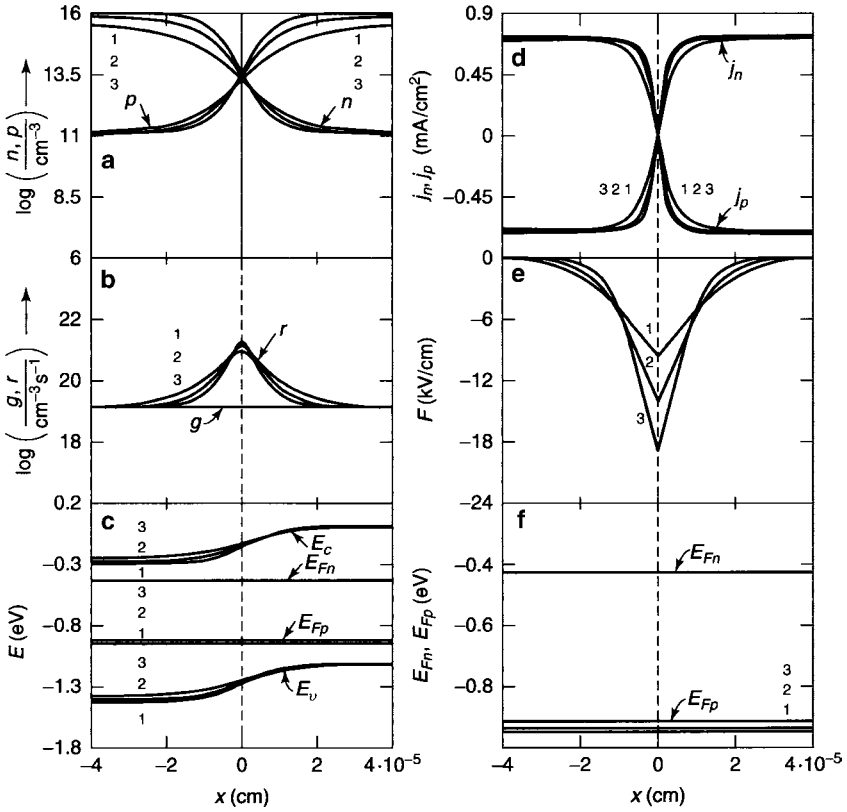

Fig. 10.8. Solution curves for a symmetric thick Si *pn*-junction device, computed as in Fig. 10.3 for $g_o = 10^{19}\,\text{cm}^{-3}\,\text{s}^{-1}$ and $N_r = 10^{17}\,\text{cm}^{-3}$. Now we have changed the doping densities as family parameter: $N_\text{a} = N_\text{d} = 3 \times 10^{15},\ 6 \cdot 10^{15}$, and $10^{16}\,\text{cm}^{-3}$ for curves 3–1, respectively. And again with the same order of the sub figures

the comparison with the somewhat similar influences of the parameters shown in the entire set of figures, however, leaving it to the observer to understand the distinct differences.

For more on high generation rate (solar concentration) of Si solar cells, see e.g., Gray et al. (1982) and a short review by Schwartz (1982).

10.1.1.7 Influence of the Doping Density

We will now discuss the influence of the doping density first for the symmetrical junction, in which the doping density is changed by equal amounts in both sides of the junction. Figure 10.8 shows the expected changes in majority carrier densities and majority quasi-Fermi level. The junction widens with decreasing doping densities: $N_\text{a} = N_\text{d} = 10^{16},\ 6 \times 10^{15}$, and $3 \times 10^{15}\,\text{cm}^{-3}$ for curves 1–3, respectively in accordance with an increased Debye length.

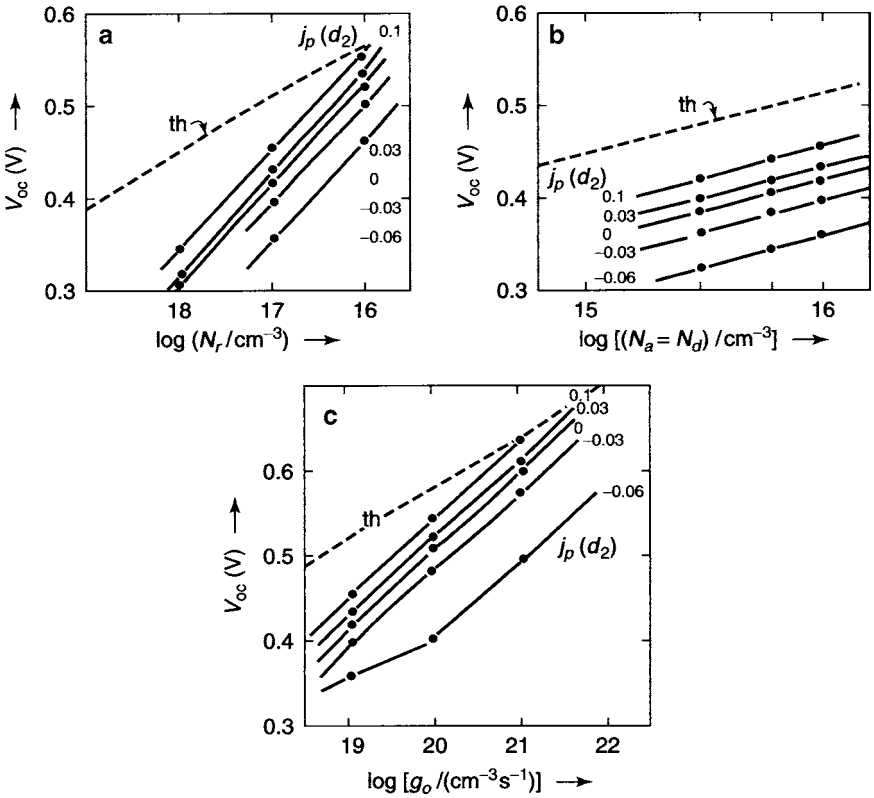

Fig. 10.9. Open circuit voltage as function of N_r, $N_\mathrm{a} = N_\mathrm{d}$, and g_o in **a, b**, and **c**, respectively. Family parameter is the hole current at $x = d_1$ and $x = d_2$ in mA cm^{-2}, representing, with increasing current, a thicker device, or, with increased negative currents, a device with a more effective surface recombination. The *dashed line* represents the maximum theoretical V_oc according to (10.8)

This widening of the junction is also observed in $r(x)$, $j_n(x)$, and $j_p(x)$ (Fig. 10.8b, d). A small decrease in the overshoot of $r(x)$ with decreasing doping follows from a decrease in the crossover densities of n and p shown in Fig. 10.8a.

The entire change is restricted to a shift of the majority quasi-Fermi level[6] while the minority quasi-Fermi level is not affected. Observe that the open circuit voltage is influenced by the doping level while all other parameters that have a more pronounced influence on V_oc are kept constant.

For more on transport equations in heavily doped devices see e.g., Lundstrom et al., 1981.

[6] The selection of E_{Fp} here as the shifted level is due to the chosen boundary condition of keeping $E_c(x = d_2) = 0$.

10.1.1.8 Parameter Dependence of V_{oc} for Insufficient Minority Carrier Supply

We will now specifically concentrate our discussion on the influence of certain parameters on the open circuit voltage. This influence shows a significant deviation from the simple diode model that was discussed in the previous chapter and can be deduced from the supply of minority carriers to the junction. When the supply of minority carriers is insufficient to compensate for the junction recombination in a thin device, or in a device with much increased recombination, the open circuit voltage is reduced, often significantly below the theoretical maximum value.

Figure 10.9 shows a summary of these changes in open circuit voltage with the device width or with surface recombination indicated by the reduced current at d_1 and d_2, as shown in Fig. 10.5d and e, or as a function of the *density of recombination centers*, as a function of *doping density* with $N_a = N_d$, and as a function of the *optical generation rate* shown in Figs. 10.9a–c, respectively. Generation and recombination rates have a larger than kT proportionality in the semilogarithmic plot; the proportionality factor can be equated to the diode ideality factor A:[7]

$$V_{oc} = \frac{1}{e}\left\{E_g - AkT \ln\left(\frac{N_c N_v}{N_a g_o \tau_{n0}}\right)\right\}. \tag{10.10}$$

This results in $A \simeq 2$ in this example for the variation of donor densities with N_r, in $A \simeq 1.5$ for the variation with g_o, and in $A \simeq 1$ for the variation with $N_a = N_d$, as shown in Figs. 10.9a, c, and b, respectively.

It is important to reflect that the deviation from $A = 1$ resides in the junction, and is caused by a more or less active recombination overshoot.

10.1.1.9 Influence of the Energy of the Recombination Center

We finally have to add a detail to the recombination traffic that can be influenced by changing the energy E_r of the recombination center, thereby changing:

$$n_i^* = 2n_i \cosh\left(\frac{E_i - E_r}{kT}\right) \tag{10.11}$$

[see (4.33)].

Such an influence is negligible as long as the recombination center resides close to the center of the band gap ($E_r \simeq E_i$). When, in the given example, the recombination center lies more than 0.1 eV from the center of the

[7] The relation (10.10) can be obtained from a simple diode equation shifted by the saturation current, using, however, the diode quality factor that was introduced in Sect. 3.2.2E.

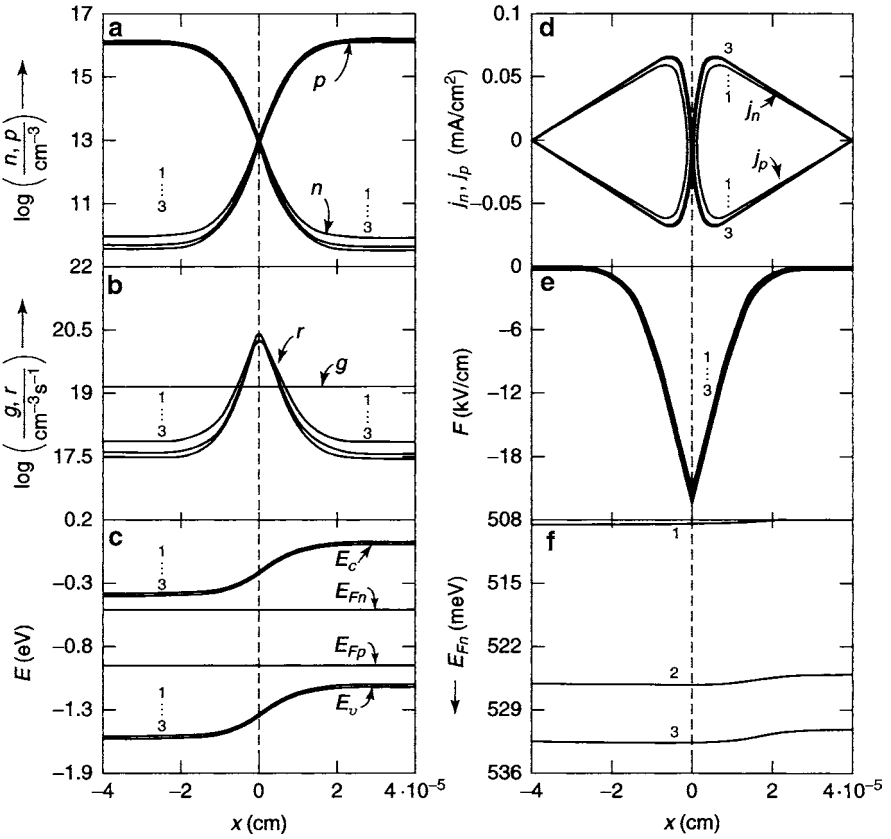

Fig. 10.10. Solution curves for a symmetric thin Si *pn*-junction as in Fig. 10.3 with $N_r = 10^{17}\,\mathrm{cm}^{-3}$; The family parameter now is the energy of the recombination center: $|E_i - E_r| = 0.25,\ 0.2$, and $0.15\,\mathrm{eV}$ for curves 1–3, respectively. Again, same arrangement of the panels for ease of comparison with the preceding figures

gap, the recombination[8] and therefore the overshoot is reduced (Fig. 10.10), consequently reducing the gr-current and improving the open circuit voltage in devices with insufficient supply of minority carriers (Fig. 10.10f).

10.2 Thin Asymmetric Si Diodes with Abrupt Junction

We now enter a more realistic description of devices that are mostly asymmetric. Again, we will start with a simple example and point out the the similarities, but now with a shift in the solution curves. After identifying the

[8] The reduction of the recombination of a center lying at a greater distance from the center of the gap is due to the more trap-like behavior by partial carrier emission into the nearest band rather than recombination.

recombination overshoot in the junction as a major factor for degrading the open circuit voltage of a symmetrical photodiode, we now extend this analysis to an asymmetrical device and systematically change one parameter at a time between the n- and p-side of the diode.

10.2.1 Recombination Through Charged Recombination Centers

The first asymmetry in the device can be introduced by simply assuming a different recombination, while the doping is left symmetrical. The recombination through centers is sensitive to their charge character. We have previously assumed that the center has the same capture cross section for electrons or holes with $s_n \simeq s_n = 10^{-16}\,\mathrm{cm}^2$, and with $c \simeq c_{cr} \simeq c_{rv} = s_n v_n = s_p v_p = 10^{-9}\,\mathrm{cm}^3\,\mathrm{s}^{-1}$. We now lift this restriction and permit $c_{cr} \neq c_{rv}$ with

$$r = \frac{c_{cr} c_{rv} N_r np}{c_{cr}(n + n_i^+) + c_{rv}(p + n_i^-)} = \frac{np}{\tau_{0p}(n + n_i^+) + \tau_{0n}(p + n_i^-)} \tag{10.12}$$

see (4.30).

We assume that the recombination center is neutral when empty, with a recombination cross section of $s_n \approx 10^{-16}\,\mathrm{cm}^2$ for electrons. After an electron is captured, the center becomes negatively charged, and a hole consequently experiences a much larger cross section, say, of $s_p \approx 10^{-14}\,\mathrm{cm}^2$. A second electron, however, experiences a repulsive center with a substantially reduced cross section, typically of $s_n' \approx 10^{-18}\,\mathrm{cm}^2$ or less. Such changing of cross sections can be taken into consideration by changing the capture coefficient, e.g., from 10^{-9} to 10^{-11} or $10^{-7}\,\mathrm{cm}^3\mathrm{s}^{-1}$ for repulsive or attractive centers, respectively.

In Fig. 10.11 a family of solution curves is shown for a variety of recombination centers with different capture coefficients for holes and electrons, as given in Table 10.2.

From a change of the capture coefficients alone, the recombination distribution becomes asymmetric as shown in Fig. 10.11b, while the minority carrier density on *both sides* of the *pn*-junction still changes symmetrically. The overshoot peak is *shifted* from the junction interface into the region with increased minority carrier recombination; correspondingly, the crossover of $j_n(x)$ and $j_p(x)$ is shifted to the shifted position.

The quasi-Fermi-level split decreases (or increases) with increasing (or decreasing) recombination reducing V_{oc} by

$$\Delta V_{\mathrm{oc}} \simeq kT \ln\left(\frac{c_{\mathrm{cr}}}{c_{\mathrm{rv}}}\right). \tag{10.13}$$

However, when the recombination rate is reduced by a factor of 100 in half of the device, the benefit to V_{oc} is smaller than that given by (10.13), as seen in

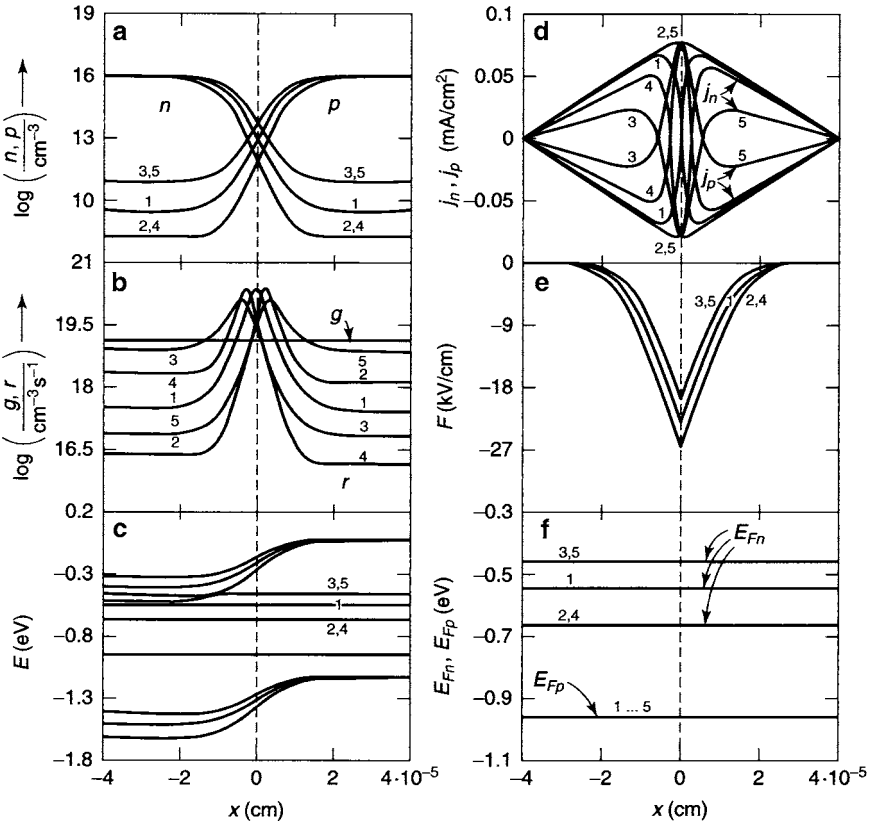

Fig. 10.11. Solution curves computed for a symmetric thin Si *pn*-junction with parameters as in Fig. 10.3, however, for different recombination coefficients for electrons and holes, as listed in Table 10.2 for *curves* 1–5.

Table 10.2. Capture coefficients used in Fig. 10.11

	Curve No.					
	1	2	3	4	5	Dimensions
c_{cr}	10^{-9}	10^{-7}	10^{-11}	10^{-9}	10^{-9}	cm^3s^{-1}
c_{rv}	10^{-9}	10^{-9}	10^{-9}	10^{-7}	10^{-11}	cm^3s^{-1}

Fig. 10.11f with a $\Delta V_{oc} = 85\,mV$ for curve set 3 and 5 vs. the deterioration by 120 mV for the curve set 2 and 4. This enhanced nonlinear behavior becomes significant whenever r approaches g_o in the left or right side of the bulk, as shown in Fig. 10.11b for curve set 3 and 5.

10.2.2 Inhomogeneous Optical Excitation

A more severe change is the introduction of an inhomogeneous optical excitation in an otherwise still homogeneous devise. The nonlinearity of $U(x)$ with changing parameters that determine the generation or recombination are modifying factors for the nonlinearity of the minority carrier density with g_o. The involved spatial dependence (and bias) makes a general analytical approximation complex; this is one of the reasons why an estimation of the actual diode A-factor is difficult.[9] We will return to such analysis in a later section.

In all practical cases, the optical generation is inhomogeneous. It is stronger near the entrance surface of light and weaker near its exit surface: the more light is absorbed at the beginning of its path, the stronger is the decrease of $g_o(x)$ with increasing x. Rather than taking a continuous, say exponential decay of $g(x)$, we introduce here a *stepwise* generation function that results in slope-breaks of the currents $j_n(x)$ and $j_p(x)$, and thereby provides some additional clues for an analysis. Curve 2 of Fig. 10.12b *simulates an exponential decay* of $g_o(x)$ As more drastic changes occur we assume a high excitation only in a thin near-surface region, which is followed by a constant and much lower excitation rate in the remainder of the device, thus simulating a direct band gap solar cell exposed to sunlight (curves 3–5) in Fig. 10.12b; also see Böer, 1986). All generation distributions are chosen so that the integrated generation rate is the same as the average homogeneous generation rate of $7.5 \times 10^{20}\,\mathrm{cm}^{-3}\,\mathrm{s}^{-1}$, that is shown as curve 1.

The results of the different step like changes of the generation rate are seen in the abrupt changes in the slopes of $j_n(x)$ and $j_p(x)$ at the left side of panel d of Fig. 10.12 with highly asymmetrical current distributions.

In contrast, the recombination distribution is not influenced (also contained in panel b as bell-shaped curve); the overshoot remains unchanged. The carrier distribution consequently stays *unchanged*.

10.2.2.1 Optical Excitation Only in a Thin Front Layer of the Device

It should be emphasized that even in the extreme case shown as curve 5 of Fig 10.12, all optical excitation occurs in the front half of the n-type region while the rest of the device is kept in the dark. The carrier and field distribution does not recognize such inhomogeneous optical excitation and remains totally symmetric. Figure. 10.13a shows the generation and recombination distributions for this example on an extended scale. It indicates the near-perfect symmetry of the recombination rate distribution in spite of the extreme asymmetry of the optical excitation near the front surface, plus a minuscule thermal excitation in the bulk.

[9] Only in a very general approximation one observes the tendency of $A \to 2$ with excessive recombination in the space charge region, and of $A \to 1$ with dominant recombination in the space charge-free bulk.

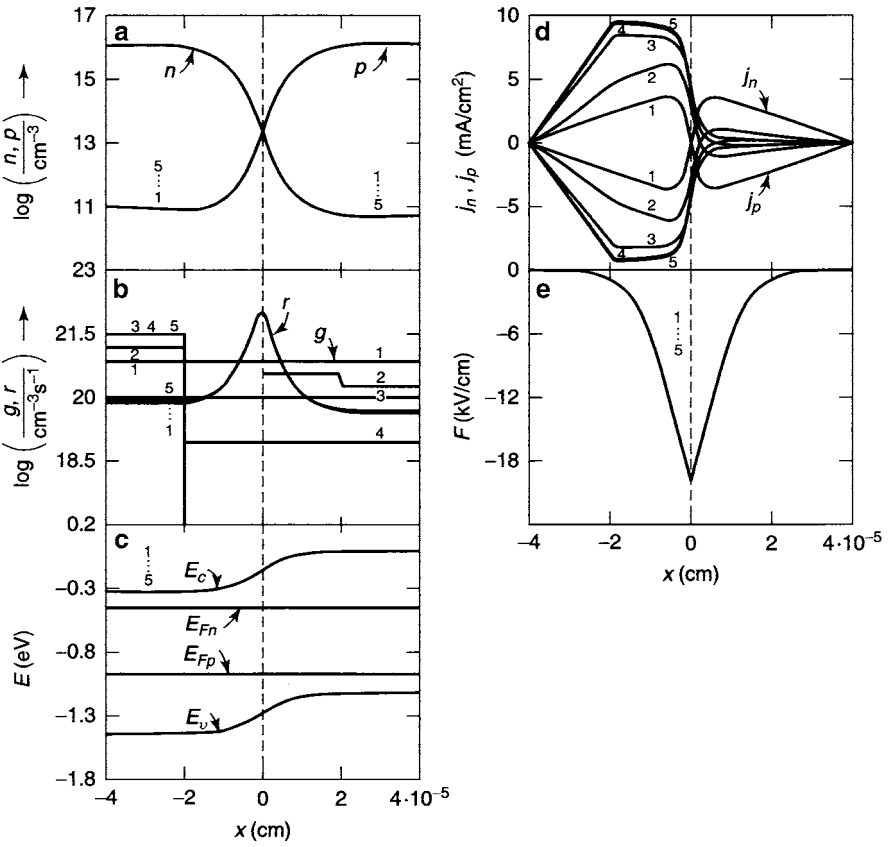

Fig. 10.12. Solution curves for a symmetric thin Si *pn*-junction as in Fig. 10.3, however, for inhomogeneous optical generation rates shown in **b**, which are normalized to the same average generation rate of $\overline{g}_o = 7.5 \times 10^{20}\ \mathrm{cm}^{-3}\,\mathrm{s}^{-1}$ as shown in curve 1

This is an excellent example to demonstrate the dominant effect of the gr-current to communicate between the two parts of the *pn*-junction, thereby effectively equalizing the carrier distribution on both sides of a symmetrical junction, as long as the device thickness is smaller than the diffusion length. The symmetry will only be disturbed when the device thickness becomes comparable to the diffusion length (see Sect. 10.3.1B).

With the carrier distribution remaining unchanged, the spread of the quasi-Fermi levels also remain the same, independent of the generation rate distribution. The spread is determined only by the total averaged generation rate. One can now revise the expression for the open circuit voltage to introduce averaged values of generation and recombination:

$$\boxed{V_{\mathrm{oc,max}} = \frac{1}{e}\left\{E_g - kT \ln \frac{N_c N_v}{N_{\mathrm{eff}}\, \overline{g}_o \overline{\tau}}\right\}} \tag{10.14}$$

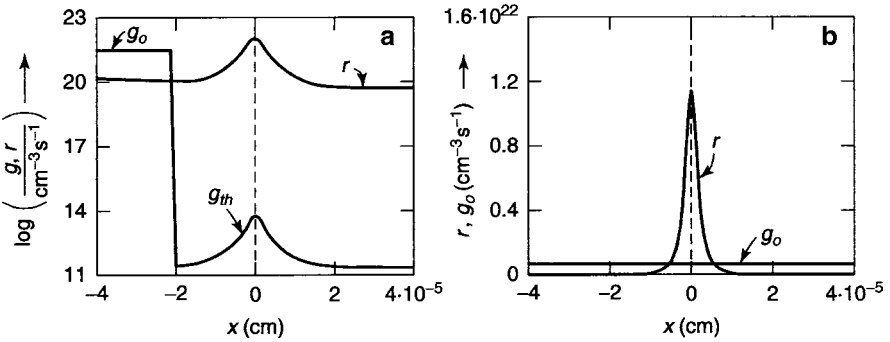

Fig. 10.13. Generation and recombination rate distributions as in Fig. 10.12 (**a**) for optical excitation in the front layer only; (**b**) for homogeneous illumination, redrawn in linear scale (same conditions as for curves 5 and 1 in Fig. 10.12, respectively).

with

$$\bar{g}_o = \frac{1}{d_2 - d_1} \int_{d_1}^{d_2} g_o(x)\mathrm{d}x \tag{10.15}$$

and

$$\bar{\tau}^{-1} = \frac{1}{d_1} \int_{d_1}^{0} \frac{1}{\tau_p}\mathrm{d}x + \frac{1}{d_2} \int_{0}^{d_2} \frac{1}{\tau_n}\mathrm{d}x \tag{10.16}$$

and with an effective donor or acceptor density

$$N_{\mathrm{eff}} = (N_{\mathrm{a}},\ N_{\mathrm{d}})_{min}. \tag{10.17}$$

In the example for homogeneous excitation, $g_o(x)$ and $r(x)$ are replotted in a linear scale in Fig. 10.13b. The recombination rate at the maximum is higher by a factor of 16 than the optical generation rate, corresponding to an effective carrier lifetime[10] of 1/8 of the bulk lifetime. Consequently, one estimates from (10.15) and (10.16) a $\bar{g}_o\bar{\tau}$ product of $\simeq 10^{11}\,cm^{-3}$, which is in reasonable agreement with the computed minority carrier density in each of the bulk regions shown in Fig. 10.12a. The open circuit voltage estimated from Eq. (10.14) is $V_{\mathrm{oc}} \simeq 498\,\mathrm{mV}$ is in agreement with the computed value of 497 mV (Fig. 10.12f, g). This value is reduced by 19 mV from the value of 516 mV estimated from the simple V_{oc} equation [Eq. (10.8)].

10.2.2.2 Thin Asymmetric Junction Design

Most *pn*-junctions are substantially asymmetric. Such asymmetry can be caused by

- Asymmetric thickness ($d_1 \neq d_2$)
- Asymmetric doping densities ($N_{\mathrm{a}} \neq N_{\mathrm{d}}$)

[10] Relating to a symmetric carrier flow from both sides of the junction.

- Asymmetric recombination center densities ($N_{r1} \neq N_{r2}$)
- Asymmetric types of recombination centers (influencing c_{ik})
- Different electrodes (influencing ψ_{MS}).

Some of the resulting effects can be estimated from the information supplied in the previous section. Quantitative answers, however, can only be obtained from actual computation, since the overshoot is determined in a nonlinear fashion from the various contributions.

Asymmetric Bulk Thickness. When the thickness of a *thin* device is increased, more material is available to absorb light, hence an increase in the number of available minority carriers will result. When increasing the thickness of only one side (here d_2 by a factor of 1.75), the resulting solution curves (Fig. 10.14a) show a symmetric increase of *both* minority carrier densities on either side of the junction. Even though the number of absorbed photons increases by a factor of 1.375 (as the increase in total device thickness) the computed minority carrier densities increase by a slightly lesser factor of ∼1.3 (Fig. 10.14A). This is caused by an increased recombination, due to the increased recombination rate plus the increased recombination overshoot (Fig. 10.14b).

The quasi-Fermi level for electrons is raised throughout the entire device by 7.5 meV according to the increase of the minority carriers; the open circuit voltage is increased by the same amount.

Asymmetric Recombination. When *surface recombination* is introduced at *one* side of this thin device (here at the right side by forming a crossover of j_n and j_p, as shown in Fig. 10.15) the minority carrier densities on both sides of the junction decrease *symmetrically* (Fig. 10.15a). Accordingly, the bulk recombination rate on both sides of the recombination overshoot decrease.

Consequently, the electron quasi-Fermi level decreases within the entire device by 10 meV, and the open circuit voltage decreases by the same amount (sub figures e and f). The junction field increases slightly (by 500 V/cm) since the junction widens by a small amount.

When asymmetric recombination is caused by a stepwise increase of the density of recombination centers from $10^{17}\,\mathrm{cm}^{-3}$ in the n-type region to $10^{18}\,\mathrm{cm}^{-3}$ in the p-type region a super linear decrease[11] by a factor of 17 of the minority carrier density in both sides of the junction (again a symmetrical decrease) is observed (Fig. 10.16). The open circuit voltage decreases by 68 mV. This indicates the difficulty of using simple approximations to estimate V_{oc} with sufficient accuracy in such a device.

Asymmetric Generation. When the generation rate is reduced by a factor of 10 in the p-type region (but the total generation rate is not normalized

[11] Even though the average increase of the recombination center density is only by a factor of 5.5.

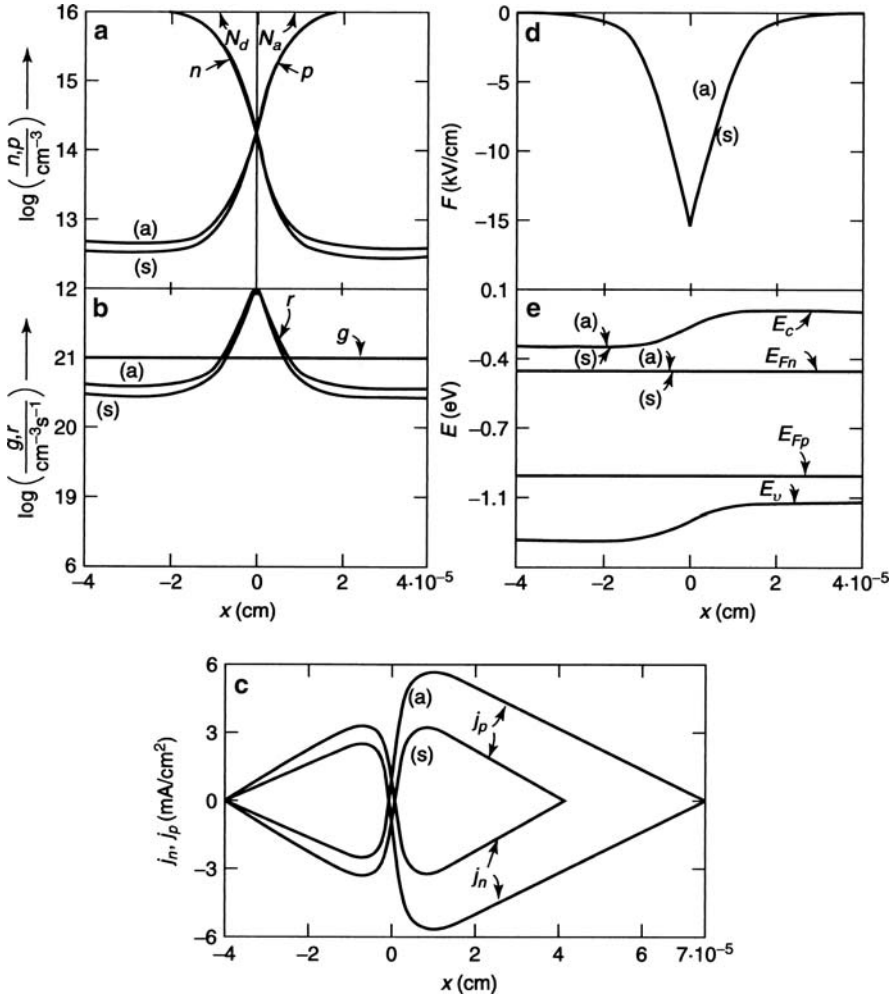

Fig. 10.14. Solution curves for a symmetric (s) (with $d_1 = d_2$) and an asymmetric (**a**) (with $d_2 \simeq 1.75\, d_1$) thin Si *pn*-junction device as indicated by the current distribution in (panel c). The new surface is at the position where $j_n(d_2) = j_p(d_2) = 0$ with $d_2 \simeq 7 \cdot 10^{-5}$ cm (this change in abscissa scale is not shown in the other panels of this figure)

to the same value as assumed before), the minority carrier density decreases in both regions by a factor of 0.4, i.e., again super linearly, compared to the expected decrease of 0.55 for an averaged lowering of the optical generation. The recombination rate of distribution again decreases *symmetrically* by the

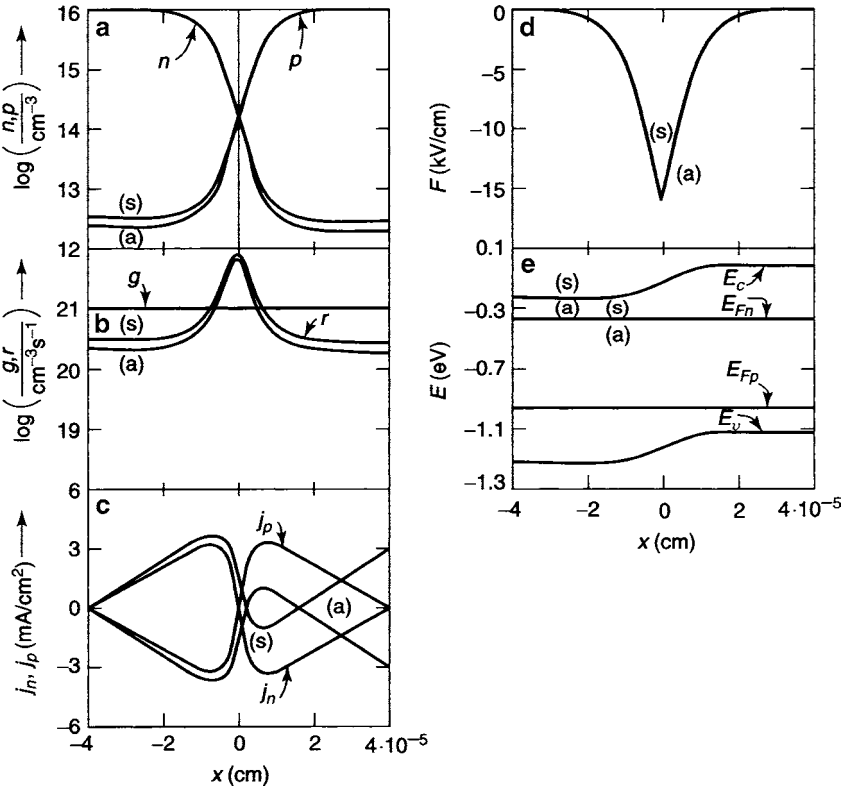

Fig. 10.15. Solution curves as in Fig. 10.14 with asymmetric solution (**a**) caused by a strong surface recombination current at the right surface (panel **c**) and (s) symmetric solution for comparison

same ratio (Fig. 10.17b).[12] The junction field is slightly increased with asymmetric decreased generation due to the widening of the junction (Fig. 10.17d). The open circuit voltage is reduced by 23 mV. When compared to a decrease of 15 mV, expected for the reduction of absorbed photons in the entire device, the increased reduction can be interpreted by an A-factor of 1.7, with $\Delta V_{\mathrm{oc}} = (AkT/e)\ln(\bar{g}/g_o)$.

10.2.3 Asymmetric Doping

Most junctions are asymmetrically doped with the thinner front side having a substantially higher dopant density. In Fig. 10.18, an example is shown in

[12] This information is complementary to the one given in Sect. 10.2.2; indicating that the solution curves for n and p and the potentials are independent of the distribution of $g_o(x)$ in thin devices, provided that the total number of absorbed photons remains the same.

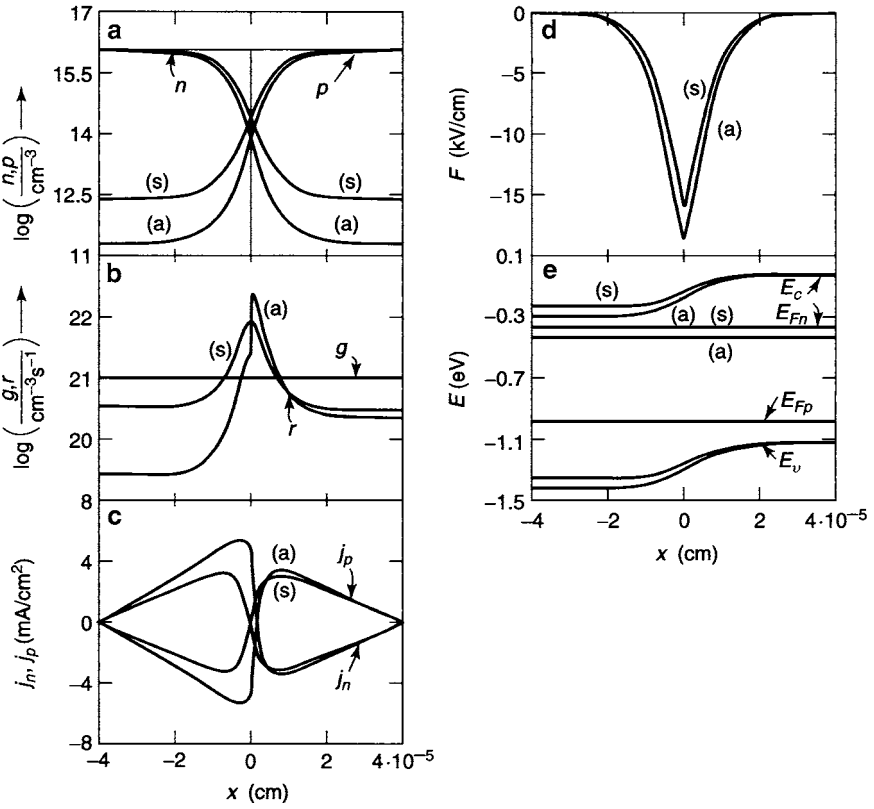

Fig. 10.16. Solution curves as in Fig. 10.14, with asymmetric solution (**a**) created by a jump in the density of recombination centers from $10^{17}\,\mathrm{cm}^{-3}$ in the n-type material to $10^{18}\,\mathrm{cm}^{-3}$ in the p-type material by a factor of 10 at $x = 0$. (s) is the symmetric solution, shown for comparison

which the donor density in the left side is increased by a factor of 100. This asymmetry shifts the peak of the recombination overshoot well into the lower doped right side, again coinciding with the position where $n = p$. Thereby, the generation current from the n-type material continues into the p-type part and increases accordingly, while the generation of current from the p-type part is reduced. As a consequence of the increased doping, there is a major increase in diffusion voltage by 120 mV.

However, the open circuit voltage is increased by only ∼12 mV. The reason for this change is a combination of two effects: the decrease in the density of minority carriers and the increase in the recombination overshoot that almost compensates (except for 12 meV) the expected spread.

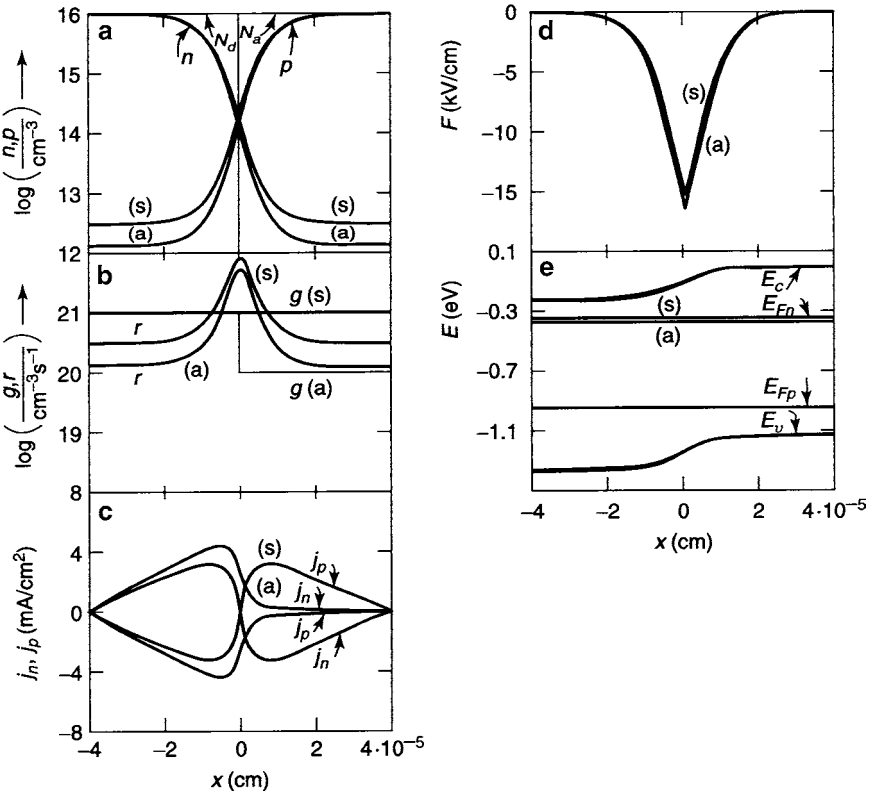

Fig. 10.17. Solution curves as in Fig. 10.14 with asymmetric solution (**a**) caused by asymmetric generation rates $g_{1,o} = 10^{21}$, $g_{2,o} = 10^{20}\,\mathrm{cm}^{-3}\mathrm{s}^{-1}$. (s) is the symmetric solution, shown for comparison

10.2.4 Thick Asymmetric Devices, Si Solar Cells

We now extend the analysis to an asymmetrically doped device with a thin, heavily doped n-type front layer[13] and a very thick ($d_2 > L_n$) p-type base. A set of solution curves is plotted in Fig. 10.19. As a consequence of the asymmetry, we now observe that the cross-over of electron and hole densities shift away from the junction interface well into the lower doped p-type material, while the peak of the electric field and the change of the space charge remains exactly at the doping interface. We shall emphasize this fact and make sure the we do not misread the position of the pn-junction as the place where $n(x)$ crosses $p(x)$ and j_n cross drift force, the electric field peaks at the junction interface (panel d).

[13] The front layer is often referred to as the emitter. We will refrain from doing so, since in solar cells the emission of minority carriers into the junction originates mostly from the much thicker base layer.

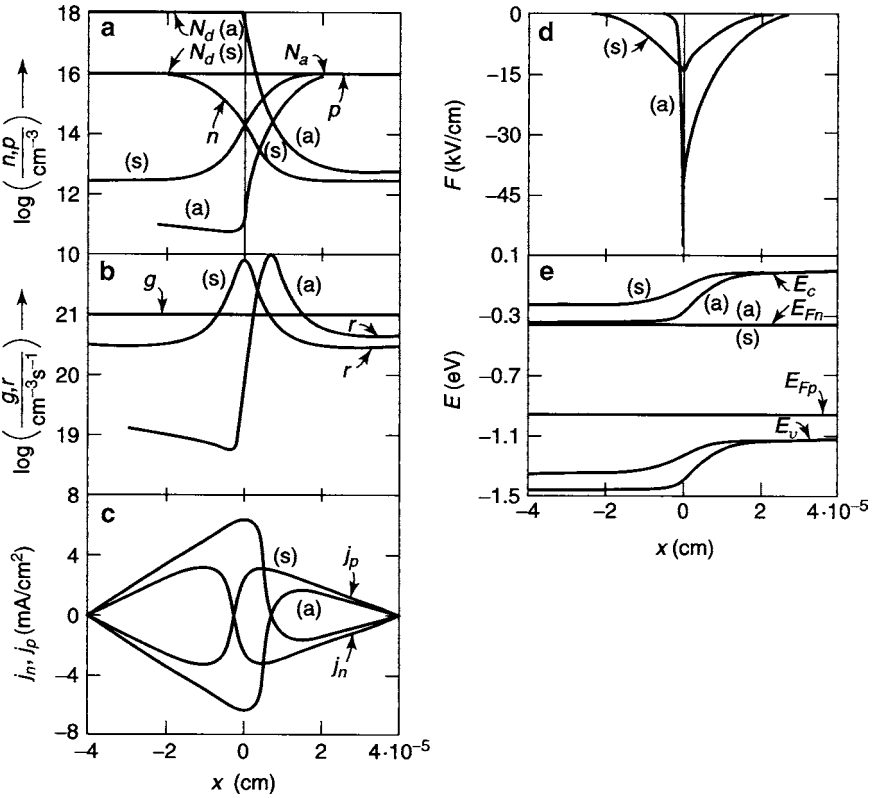

Fig. 10.18. Solution curves as in Fig. 10.14 with asymmetric solution (**a**) caused by asymmetric doping: $N_\mathrm{d} = 10^{16}$ and $N_\mathrm{a} = 10^{18}\,\mathrm{cm}^{-3}$. ($s$) is the symmetric solution, shown for comparison

We also shall point out that Fig. 10.19 has a broken abscissa at 2.5×10^{-5} cm (see arrow on top for emphasis), in order to show the behavior as well in the bulk of the junction, as close to the electrodes, which contains several interesting features that will be discussed below.

The jump of the recombination rate at the junction interface is caused by the jump in recombination center densities from $N_r = 10^{17}\,\mathrm{cm}^{-3}$ in the heavier doped n-type region to $N_r = 10^{16}\,\mathrm{cm}^{-3}$ in the lower doped p-type region. This jump, however, has negligible influence on all other solution curves since $r(x = 0) \ll g_o$.

The minority carrier density in the p-type bulk is nonmonotonic, because of electron diffusion toward the recombination overshoot and of electron out-diffusion for recombination at the outer electrode (Fig. 10.19a). In the bulk the electron density approaches its steady state value closely($g_o\tau_{n0} = n_{10}$), consequently making the recombination rate nearly equal to the generation rate here and causing near the bulk center a vanishing gr-current (Fig. 10.19c, d).

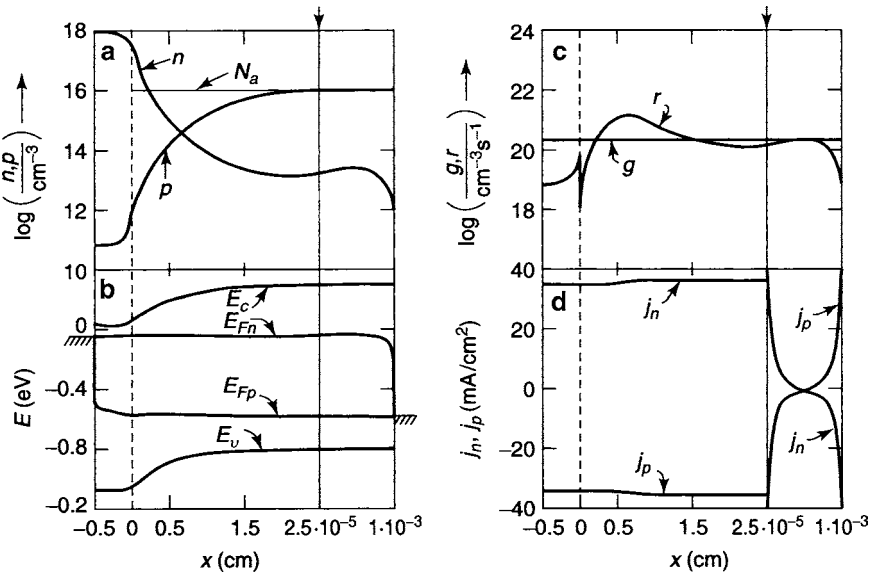

Fig. 10.19. Solution curves of a long asymmetric Si *pn*-device with complete surface recombination at both electrodes for $g_o = 2{\cdot}10^{20}\,\mathrm{cm^{-3}s^{-1}}$, $N_{r1} = 10^{17}\,\mathrm{cm^{-3}}$, $N_{r2} = 10^{16}\,\mathrm{cm^{-3}}$, and $c = 10^{-9}\,\mathrm{cm^{-3}s^{-1}}$. Observe the broken abscissa in the *p*-type bulk region (*arrow on top* of panels a and c)

Observe that closer to the right metal electrode the recombination current changes sign (Fig. 10.19d) and the electron density decreases toward the thermodynamic equilibrium value. The near-bulk recombination rate decreases below g_o, here creating a net generation rate to approach $U = g_o$, and consequently, the slope of the recombination currents toward the right electrode rapidly increases to approach the maximum slope $\mathrm{d}j_n/\mathrm{d}x = -\mathrm{d}j_p/\mathrm{d}x = eg_o$.

Because of the large width of the *p*-type bulk, the junction and the right electrode regions are well separated; a large current can flow toward the electrode without substantial reduction of the photocurrent to the junction.[14] The recombination current at the right electrode is close to the saturation current and given by:

$$-\,j_p(d_2) = j_n(d_2) \simeq eg_oL_n \simeq 40\ \mathrm{mA\ cm^{-2}}. \tag{10.18}$$

This current is dissipated as

$$j_n(d_2) = e\{n(d_2) - n_{20}^{th}\}s \simeq en(d_2)v_n^*, \tag{10.19}$$

[14] This is an artificial condition that is caused by the assumed constant optical generation rate. In actuality $g_o = g_o(x)$ and rapidly decreases from left to right. With $d_2 \gg L_n$, averaging of $g(x)$ can no longer be applied. Therefore, most of the gr-current flows toward the junction and much less is collected at the right electrode (the light enters from the left).

requiring a density of minority carriers of $n(d_2) \simeq 4 \times 10^{10}\,\mathrm{cm}^{-3}$, which is substantially larger than the thermal equilibrium density of $n_{20}^{th} \simeq 200\,\mathrm{cm}^{-3}$. Therefore, one observes a decrease of the minority carrier density from $n_{10} \simeq 10^{13}\,\mathrm{cm}^{-3}$ to $n(d_2)$ causing a corresponding decrease of the minority quasi-Fermi level near this surface, with the remaining substantial adjustment of

$$E_{Fn}(d_2) - E_\mathrm{F} = kT \ln\left[\frac{n(d_2)}{n_{20}^{th}}\right] \simeq 0.5\mathrm{eV}. \tag{10.20}$$

The majority quasi-Fermi level shows only a minute adjustment[15] at $x = d_2$ due to the negligible difference in majority carriers of $\Delta p \simeq 4 \times 10^{10}\,\mathrm{cm}^{-3}$ that is necessary to maintain the recombination current of $j_p(d_2) = -j_n(d_2)$. compared to the thermal equilibrium value of $p_{20}^{th} = 10^{16}\,\mathrm{cm}^{-3}$.

At the left electrode, the situation is somewhat different. Only a very thin layer of n-type material is available.[16] Here the minority carrier density continues to decrease immediately after passing through the junction toward the thermal equilibrium value. The slope of $p(x)$ is controlled by the minority carrier current of $\approx$35 mA cm^{-2} that is accumulated in the bulk of the p-type material. This current is lower than the saturation current by $\approx$5 mA cm^{-2} because of additional recombination in the recombination overshoot region. The recombination at the left electrode results in an adjustment of the minority carrier quasi-Fermi level of $\approx 0.5\,\mathrm{eV}$ that is nearly the same as at the right electrode.

The combined effect of minority carrier leakage to the left electrode and excess recombination because of the recombination overshoot in the junction, reduces the split of the quasi-Fermi level from[17] 0.654 eV to the computed actual split of 0.533 eV shown in Fig. 10.19 panel b. The values of the saturation current and the open circuit voltage are close to the one observed in actual solar cell in full sunlight, even though the model used here is rather crude and needs substantial refinement to describe details of the experiment.

10.3 Nonvanishing Bias

The general behavior of the solution curves in a pn-junction device with light and nonvanishing bias is qualitatively similar to a nonilluminated diode with respect to the carrier density, space charge, field, and potential distributions. A more careful quantitative analysis, however, reveals typical differences relating to the much increased minority carrier density caused by the optical

[15] From $E_\mathrm{F} - E_{Fp} = kT \ln[(p_{20} + \Delta p)/p_{20}]$, one obtains for this adjustment of the majority quasi-Fermi level approximately 10^{-8} eV.

[16] In actuality, the front is covered by a thin grid electrode, rendering this a three-dimensional problem in which most of the minority carriers a generated more than a diffusion length removed from the actual metal surface. For more see e.g. Lammert and Schwartz, 1977; Gray and Schwartz, 1984.

[17] This split is estimated in the lower doped region (see Sect. 10.2.3).

excitation. In order to discuss the main features, we will first return to a thin symmetrical *pn*-junction device with homogeneous optical generation.

10.3.1 Thin Symmetrical pn-Junction Device With Bias

Figure 10.20 shows the set of solution curves for n, p, F, g, r, j_n, j_p, μ_n, μ_p, E_c, E_v, E_{Fn}, and E_{Fp} for the same thin device discussed in Sect. 10.1.1. We have again assumed two neutral surfaces (no surface recombination) and a homogeneous generation rate of $g_o = 10^{21}\,\mathrm{cm}^{-3}\mathrm{s}^{-1}$.

Space charge, field, and electron potential distributions are determined by majority carriers only and have the same qualitative shape as without light. The corresponding currents, however, at which the junction is pulled open are increased by eight orders of magnitude from the dark current of $\sim 10^{-10}\,\mathrm{A/cm}^2$ to the photogenerated current that is in the $10^{-2}\,\mathrm{A\ cm}^{-2}$ range.

In Fig. 10.20b, the optical generation rate and a family of recombination rate distributions are shown with the total current as family parameter. With increased reverse bias, the recombination rate $r(x)$ is pulled down, yielding a larger net generation rate ($U = g_o - r$), until the maximum of $r(x)$ decreases well below g_o, i.e., rendering $U(x) \simeq g_o$ and results in reverse current saturation. This is best seen in the $j_n(x)$ or $j_p(x)$ distributions that are separated in different panels, (to avoid confusion) (Fig. 10.20c and g) which, for saturation, straighten out (curves 6), pulling all minority carriers across the junction (current saturation).

The minority carrier density decreases below $n_{10,o} = g_o\tau_p = n_{20,o} = g_o\tau_n = 10^{13}\,\mathrm{cm}^{-3}$ with increasing reverse current.[18]

The DRO-range with a strong drop of both quasi-Fermi levels (Figs. 10.20d, h, curve 6) is seen as a slowly sloping, rather straight segment of $n(x)$ and $p(x)$. This occurs between ± 0.4 and $\pm 1.8 \cdot 10^{-5}\,\mathrm{cm}$ in Fig. 10.20a. The DRO-range appears when current saturation is approached. Here, only a minor increase in currents occur (Fig. 10.20c, g), while major changes in bias are computed (Fig. 10.20d, h), as can be seen by comparing curves 5 and 6.

With forward bias, $r(x)$ is shifted upward with a net current (mostly generated in the junction region) in the forward direction. Up to $\simeq 15\,\mathrm{mA\ cm}^{-2}$, g_o remains still larger than r in the bulk region; thus, a small gr-current of minority carriers flows in the opposite direction toward the junction into the overshoot region. This part of the current is responsible for the diode quality factor $A > 1$ (see Figs. 10.20b and 10.21, curves 1). At high enough forward currents, shown for curve 0 in Fig. 10.21, the current distribution again becomes monotonic.

It is important to go over and over again of this very informative set of panels of fig. 10.20 to comprehend all detail of the discussion given above and understand the cause and result of the described behavior that is typical for such devices.

[18] The sloping of the density distribution toward the overshoot region is not visible since $(d_1, d_2) \ll (L_p, L_n)$.

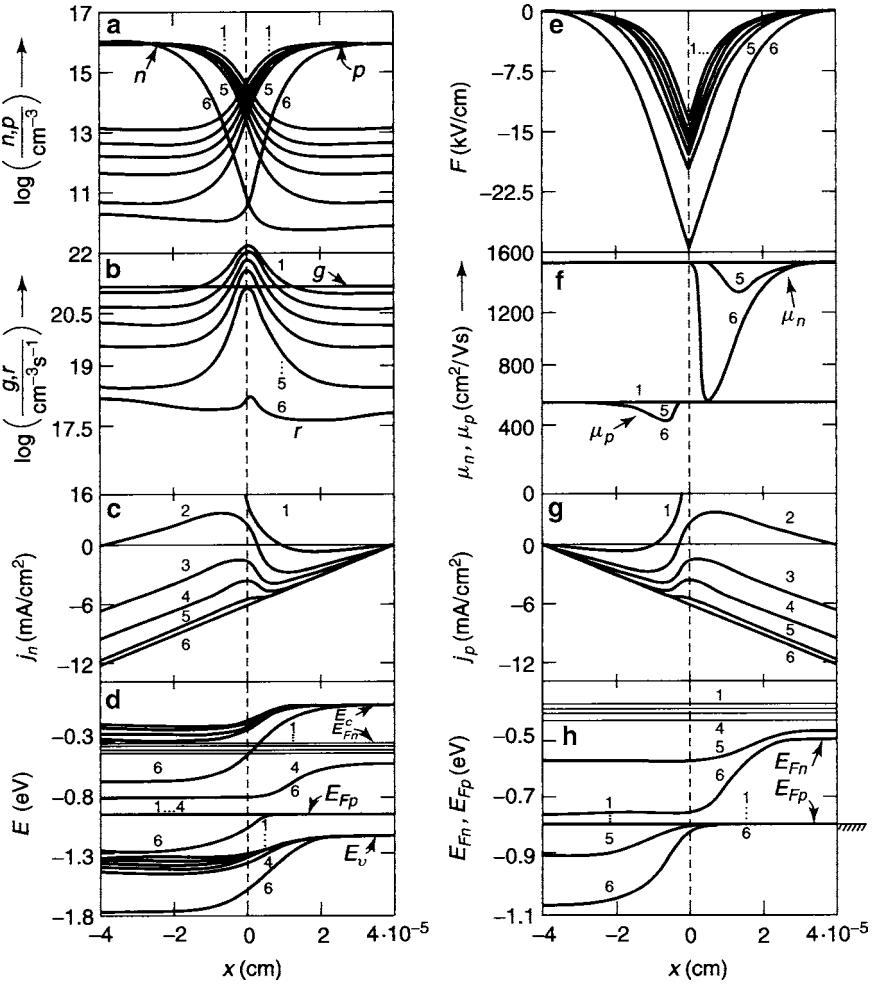

Fig. 10.20. Solution curves computed for a symmetric thin Si *pn*-junction device with neutral surfaces and $g_o = 10^{21}\,\mathrm{cm}^{-3}\mathrm{s}^{-1}$, $N_r = 10^{17}\,\mathrm{cm}^{-3}$. Total current is the family parameter: $j = 14,\ 0,\ -6,\ -10,\ -12$, and $-12.5\,\mathrm{mA\,cm}^{-2}$ for *curves* 1–6, respectively. The panel arrangement is the same as in the previous relevant sections to permit easy comparison.

With forward bias, the bell-shaped $r(x)$ distribution is maintained and determines the step like slope of $j_n(x)$ and $j_p(x)$ according to $\mathrm{d}j_n/\mathrm{d}x = er(x)$ as shown again in Fig. 10.21 that now contains a higher forward bias that was not depicted in the previous figure. With increased forward bias, $r(x)$ increases without bound and causes a stretching of $j_n(x)$ and $j_p(x)$, although with a steeper slope in the junction region (curve 0 near $x = 0$), as the bell-shaped $r(x)$ is maintained.

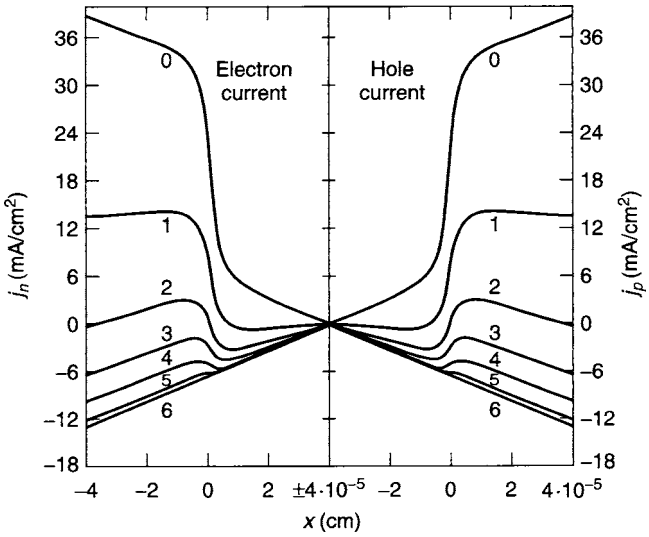

Fig. 10.21. Electron and hole current distributions computed as in Fig. 10.20; total current as family parameter (additional curve 0 obtained for 38 mA cm^{-1})

Next, we will discuss a thin asymmetric Si-photodiode which was introduced in Sect. 10.2.3 (Fig. 10.18) for vanishing bias.

10.3.1.1 Thin Asymmetric Si pn-Junction Device with Bias

In Fig. 10.22, a set of solution curves is shown for the asymmetrically doped Si *pn*-junction device with the same parameters as in Sect. 10.2.4, except for a reduced width of the lowly doped region.

In general, the solution curves show no unexpected new features, except for the field distribution that shows a spike where, near the junction interface, $n(x)$ exceeds N_a. This spike, however, has little influence on the potential distribution, except near open circuit conditions, where the area under the spike is non-negligible and causes only a slight steepening of $E_c(x)$ near the junction interface. However, the spike may have significance for field dependent effects, since it can easily exceed 60 kV cm^{-1}. But we have neglected such high-field effects in this section.

We now proceed to extend the width of the device to a more realistic thick device, with perfect surface recombination at the two electrodes.

10.3.1.2 Si-Solar Cell with Nonvanishing Bias

This device is identical with the thick, asymmetrical *pn*-junction device analyzed for zero bias in Sect. 10.2.4. A forward or reverse bias reduces or increases

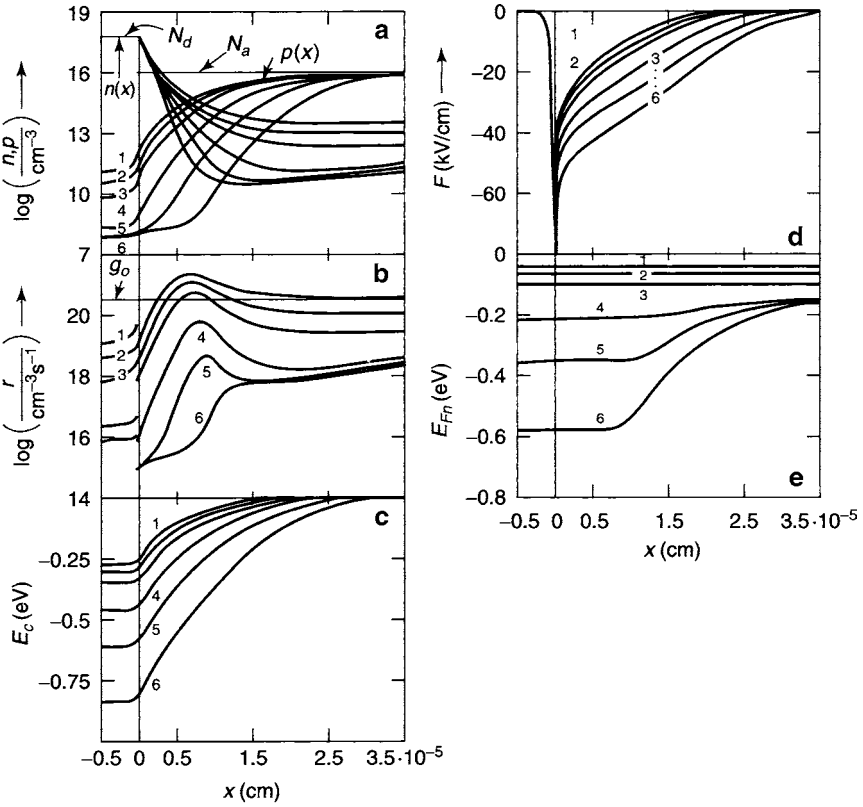

Fig. 10.22. Solution curves for a thin, asymmetrically doped Si *pn*-junction with the net current as family parameter for $j = 150,\ 0,\ -29,\ -34.5,\ -35$, and $35.6\,\mathrm{mA\ cm^{-2}}$ for curves 1–6, respectively.

the recombination rate throughout the device in a fashion similar to that in the short device discussed in the preceding section.

With sufficient *reverse bias*, $r(x)$ is reduced well below g_o throughout the entire junction region, and U becomes equal to g_o up to a few diffusion lengths from the junction and from the right surface. In thick devices ($d_2 \gg L_n$), there is a mid-bulk region of $r \simeq g_o$ (near $5 \cdot 10^{-4}\,\mathrm{cm}$ in Fig. 10.23c), with negligible U. This inactive region separates the near-junction region from the near-contact region at the right side. The former contributes to the photovoltaic effect, and the latter to the surface recombination current.

The current distribution with applied bias becomes highly asymmetric (Fig. 10.23d). A small shift in the hole current distribution, shown near $x = 0$ in an enlarged scale (Fig. 10.23e), indicates the reduction of the surface recombination current from 0.14 to $0.07\,\mathrm{mA/cm^2}$ at the left electrode when current saturation is approached. This concurs with a reduction of $p(d_1)$ from

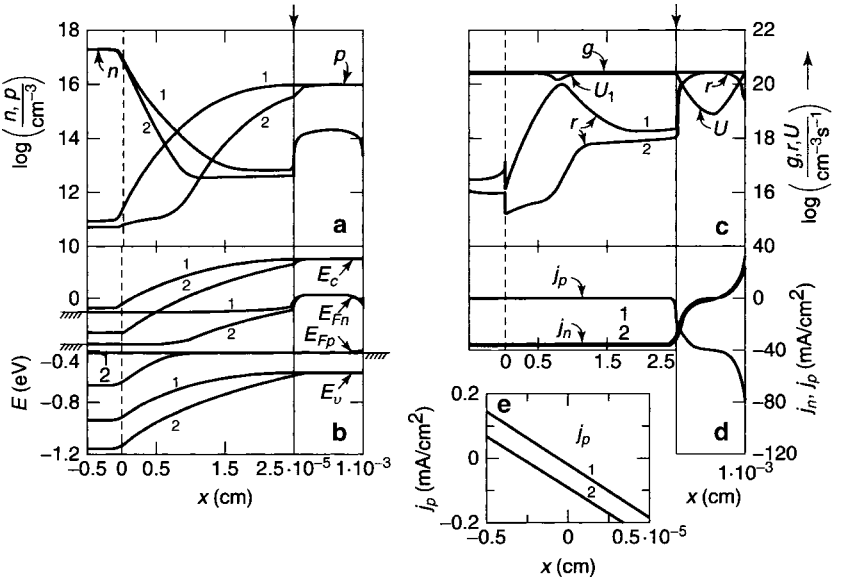

Fig. 10.23. Solution curves for an asymmetric thick Si *pn*-junction solar cell as in Fig. 10.19, however, for two reverse current cases: $j = 35$ and $37.5\,\mathrm{mA\ cm^{-2}}$, and $V = 0.365$ and $0.1\,\mathrm{V}$ for curves 1 and 2, respectively. The net generation/recombination rate U for curve 2 in the junction region coincides with g_o within the drawing accuracy, and in the region $x > 2.5\times10^{-5}\,\mathrm{cm}$ coincides with U for *curve 2* as shown. $N_{r1} = 10^{17}$, $N_{r2} = 10^{16}\,\mathrm{cm^{-3}}$ and $c = 10^{-9}\,\mathrm{cm^{-3}\,s^{-1}}$ on both sides of the junction

$1.6\times10^{8}\,\mathrm{cm^{-3}}$ to $8\times10^{7}\,\mathrm{cm^{-3}}$ in accordance with $j_p(d_1) = ev_p^* p(d_1)$. This surface recombination current, however, is negligible compared to the saturation current j_{sc} of $37.5\,\mathrm{mA/cm^2}$.

Current saturation is almost reached when the DRO-range starts appearing (Figs. 10.23a, b, curves 1 and 2). Again, a close observation of all panels of this figure to understand their discussion is most important for the understanding of the operation of a typical solar cell.

The computed current–voltage characteristic of this device is shown in Fig. 10.24 and it is very close to the ideal characteristic that is shown as dashed curve for comparison.

For more on modeling of high-efficient Si solar cells e.g., Banghart et al. (1988).

Summary and Emphasis

The *pn*-junction solar cell is an excellent device to convert optical energy into electric energy. It separates both electrodes that have a high interface recombination from the electrically active junction. The junction provides the

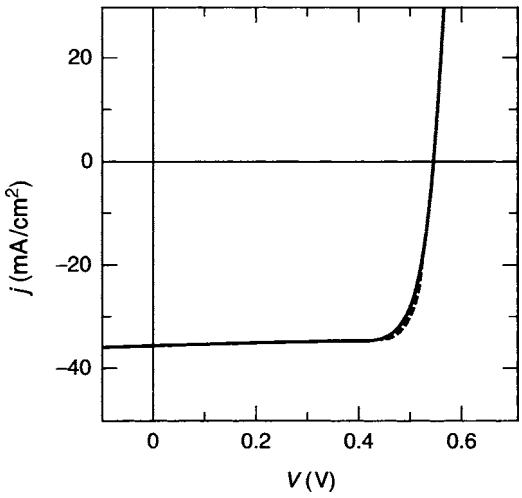

Fig. 10.24. Current–voltage characteristic obtained from solutions of Figs. 10.23. Dashed curve represents the ideal diode characteristic shifted by 37.8 mA cm^{-2}

changeover from one to the other majority quasi-Fermi level, which connects to the metal Fermi level without a marked jump, if these are neutral or injecting contacts. The spread of quasi-Fermi levels in the bulk then becomes equal to the open circuit voltage.

Intimate interaction between both sides of the junction is maintained by current continuity. It provides a flat distribution of the two quasi-Fermi levels in open circuit condition almost throughout the entire device, except for thin layers near both contacts. At each of the contacts, the minority quasi-Fermi level collapses toward the majority quasi-Fermi level that remains essentially flat.

This intimate interaction between both sides of the junction also forces one bulk region to follow symmetrically the changes in optical generation and recombination rates on the other side of the junction. This is demonstrated dramatically by the total equality of the resulting carrier distribution and Fermi level split, when, either only a thin front layer or the entire device is illuminated with the same average generation rate, provided, the device is thinner than the diffusion length.

This has significant consequences for inhomogeneous devices, in which a highly doped thin front layer also has a high density of recombination centers. These centers then deteriorate the photoelectric properties on the other side of the junction.

Within the junction, an overshoot of the recombination rate over the generation in the region, causes a net gr-current that results in a loss of V_{oc} and increases the diode ideality factor to $A > 1$.

In thick devices, the ideality factor of the photodiode approaches 1 when the bulk thickness becomes larger than about six times the minority carrier diffusion length; the barrier layer thickness is only a small fraction of the device width, and most of the light is absorbed within the active layer of the device that extends no more than two diffusion lengths from the center of the junction. However, the light that is absorbed close to the back electrode is lost for active conversion in such thick devices, since it will be used-up for back surface recombination. One therefore requires optimization for any specific three-dimensional device design.

Numerous device parameters have an influence on the photoelectric conversion efficiency of photodiodes and can be used for device optimization. Some parameters relating to recombination are still insufficiently understood, but may become decisive with specific doping for further improving the device performance by shifting the recombination overshoot into a more benign region. Sensitive balance between electrode separation from the photoelectric active region and permitting optical carrier generation close enough to the junction for near perfect minority carrier collection pose geometrical as well as electronic device design challenges.

Exercise Problems

1.(e) Show in a diagram of the type given in Fig. 8.2 the current continuity of the photocurrent of both carriers in a photodiode or Fig. 10.1.

2.(*) The recombination loss within the junction is a principal loss mechanism that forces the gr-currents to flow toward the junction even under open circuit conditions with a changeover from electron to hole current after passing through the junction. Explain in your own words
   (a) how this loss causes a reduction in the maximum open circuit voltage given by (10.8);
   (b) how this loss can be estimated;
   (c) why such a loss causes the ideality factor A to become larger than one;
   (d) how the overshoot can be reduced; and
   (e) under what circumstances the loss is further increased.

3. Relate the minimum optical generation rate which results in a measurable ($= kT/e$) open circuit voltage to the relevant device parameters. What would you do in order to increase the photodiode threshold sensitivity?

4.(e) In Fig. 10.3 several panels show less than the listed 12 curves. Point out the curves which are multiple plots on top of each other.

5.(e) Draw the actual gr-current distribution for curves 5–12 of Fig. 10.3. Use scale factors whenever appropriate to avoid multiple drawings.

6.(e) Express the theoretical maximum open circuit voltage in terms of the diffusion voltage and the optical generation rate, using. (10.8) and (10.9).

7.(e) Extend the plotted $j_n(x)$ and $j_p(x)$ curves up to the metal contact by redrawing Fig. 10.5d and e.

8.(e) Extend in Fig. 10.5 the labels for the quasi-Fermi level to $x < 0$. Explain.

9.(*) The spread between the quasi-Fermi levels is not the same when N_r is changed between 10^{16} and 10^{17} compared to the change between 10^{17} and 10^{18}.
   (a) Analyze carefully Fig. 10.6 and give your reasoning.
   (b) Why is $F(x)$ influenced by the density of recombination centers?

10.(*) Compare the change of $j_n(x)$ and $j_p(x)$ when N_r changes in steps of 10 and when g_o changes in steps of 10. Compare these stepwise changes in minority carrier densities and the split of quasi-Fermi levels. How do you explain the differences?

11.(*) Replot the recombination overshoot shown in Fig. 10.8 for three doping densities in a linear scale. Observe the significant differences and identify the reasons. Discuss the V_{oc}-dependence on doping density.

12.(r) Summarize the influence of recharging of recombination centers for V_{oc}.
   (a) How can you use this information to design more efficient photodiodes?
   (b) Compare these changes in V_{oc} with the ones obtained by changing N_r.

13.(r) Explain in your own words the insensitivity of V_{oc} on the spacial distribution of the optical generation rate shown in Fig. 10.12.

14. The generation and recombination rate distribution shown in Fig. 10.13a is grossly asymmetric. Nevertheless, V_{oc} is the same as for the symmetrical case shown in Fig. 10.13b.
   (a) Why?
   (b) Does this statement remain true when d_2 is increased to 10^{-4} cm while leaving all other parameters unchanged?
   (c) How large is V_{oc} in case (b)?

15.(*) The estimate given in (10.17) is a rather weak one. Can you improve on it?

16. In Fig. 10.16 an asymmetrical change of N_r causes a symmetrical change in the minority carrier density of both sides of the junction.
   (a) Explain.
   (a) Give the limitation for this symmetrical behavior.

17. Asymmetrical changes of $g_o(x)$ are given in Fig. 10.12 and 10.17. What are the differences? Analyze quantitatively the results with respect to V_{oc}.

18(*) In a thin device, the quasi-Fermi levels are flat within the entire device (except close to the electrodes). In a thick device, this is no longer the case, as shown in Fig. 10.19.
   (a) Give reasons for the slope of $E_{Fn}(x)$ and $E_{Fp}(x)$.
   (b) Estimate the deviations from the horizontal distribution of the quasi-Fermi levels.
   (c) Discuss the influence on V_{oc}.

19.(e) The highly asymmetric jV-characteristic of the photodiode has its basis in a similarly asymmetric $j_n(x)$ and $j_p(x)$-distribution. Explain. Discuss the limitation of the saturation current by resorting to $j_n(x)$ and $j_p(x)$ and to g_o and $r(x)$.

20.(e) Draw the jV-characteristic for the asymmetrical photodiode given in Fig. 10.22 and comment on your observation.

11

The Heterojunction with Light

Summary. Heterojunction solar cells of proper design have an advantage of producing minority carriers close to the junction when light penetrates through the wider band gap material and is absorbed close to the heterojunction and away from performance-deteriorating contacts. Such heterojunctions have the potential for higher conversion efficiencies.

A large variety of photodiodes can be formed with heterojunctions either as the photoelectrical active junction or as a means for electric control or passivation of adjacent surfaces or electrodes. We will describe here only one example in some detail to illustrate a generic type of such a behavior. We have chosen as an example, the Cu_2S/CdS solar cell[1] for which a large volume of experimental evidence is available. With these, we can illustrate the principles of the relating effects, even though the cell itself has only limited practical interest, for reasons of the high lattice mismatch that creates a high density of interface recombination centers, and for the tendency of the copper sulfide to cause cell degradation under sunlight.

In general, all material-related device parameters show a discontinuity at the heterojunction interface. Some of these discontinuities present a disadvantage; an example is the lattice mismatch that produces a dislocation field with enhanced recombination and carrier scattering. Other parameter discontinuities are benign; an example of these are the bulk carrier mobilities. Some other discontinuities may be used as an advantage, e.g., the discontinuity of the optical generation rate that permits strong optical absorption close to the heterojunction interface when the partner is a direct band gap material.

[1] We have consistently referred to this cell as a Cu_2S solar cell even though this would indicate that the copper sulfide is a chalcocite, while in actuality it is Djurleite with a stoichiometry closer to 1.98 rather than 2. This also is done in order to indicate that we do not want to use the examples discussed here as more than a possible phenomenon rather than staying too close to an actual cell in all the detail discussed here.

The discontinuity in optical excitation presents a unique opportunity to design more efficient solar cells by creating most of the minority carriers close to the junction and away from performance-deteriorating contacts or surfaces.

In general, one distinguishes a *heterojunction front wall or back wall solar cell* as devices in which most of the light is absorbed in the front region[2] or in the region behind the heterointerface, depending on whether the lower band gap material is at the front or back region of the cell. An example for the first type is the Cu_2S/CdS solar cell; an example for the second is the $CdS/CuInSe_2$ cell. Both devices are shown schematically in Fig. 11.1, with light penetrating each cell from the left.

For reasons mentioned above, we have selected only the first devices and leave the other, technically highly interesting solar cells to a more sophisticated discussion in the second volume of this book. However, we should mention here that the CdS/CdTe solar cell is another back-wall cell that recently gained significant commercial interest (for the model see Böer 2009).

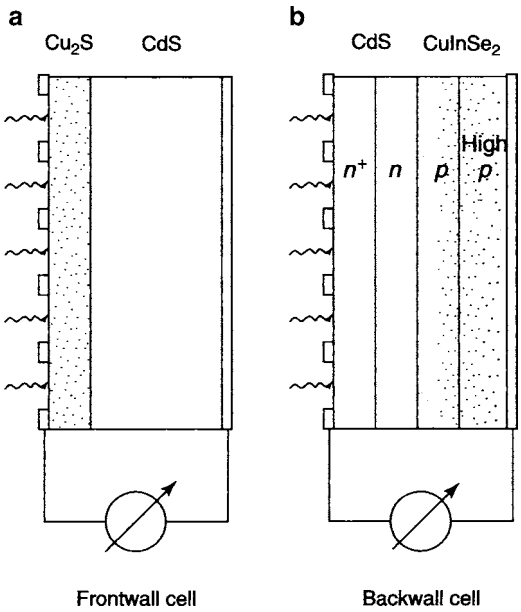

Fig. 11.1. A front wall and a back wall solar cell. Light enters from the left. Optical generation rate indicated by dots

[2] Even though as a heterojunction cell this type seems to miss the obvious advantage of optical absorption close to the heterojunction, it may still be of technical interest because of the ease of fabrication resulting in relatively inexpensive devices that may still show acceptable conversion efficiencies.

11.1 The Cu_2S/CdS Solar Cell

The Cu_2S/CdS solar cell is an example in which the region of minority carrier generation and collection is separated from the barrier region, and both regions, in principle, can be discussed individually. The highly conductive Cu_2S region in which most of the light is absorbed can be regarded as a field-free emitter of minority carriers. The adjacent CdS is much lower doped and contains almost all of the junction which, to a good approximation, can be described electronically as a Schottky barrier, however, without having the performance deteriorating metal electrode as an interface to the Cu_2S. The purpose of the CdS is to divide both types of carriers and separate the electronic active part of the device from the electrode. It is also used to limit the field[3] without requiring high purity in the junction region, as will be discussed later.

Figure 11.2 shows a simplified band model of the Cu_2S/CdS solar cell with assumed connection of the conduction bands without a jump, and a schematic sketch of the split quasi-Fermi levels with light, at open circuit conditions. The continuous $E_{Fn}(x)$ and $E_c(x)$ indicates the assumed continuity[4] of $n(x)$ at the Cu_2S/CdS interface (at $x = 0$).

A family of computed minority carrier curves $n(x)$ is shown in Fig. 11.3 for nonvanishing bias with the net current (short circuit current) as family parameter. With increased reverse bias (in this simplified model[5]), the electron

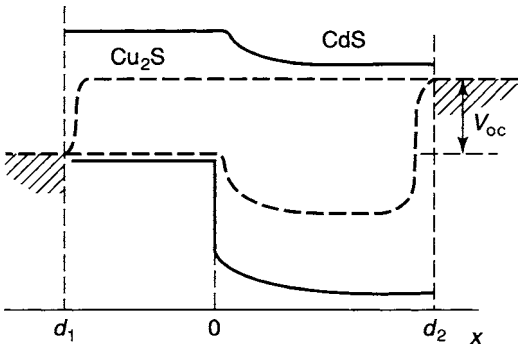

Fig. 11.2. The simplified band model of a Cu_2S/CdS heterojunction solar cell with light at open-circuit condition

[3] This is a typical characteristic of copper doped CdS by creating a high-field domain.

[4] In actuality, there may be some discontinuities, as discussed in several previous sections, which can be easily introduced but are omitted here to avoid confusion with other effects that are emphasized in this chapter.

[5] Here we assume that the conductivity in the Cu_2S is high enough that any voltage drop here can be neglected.

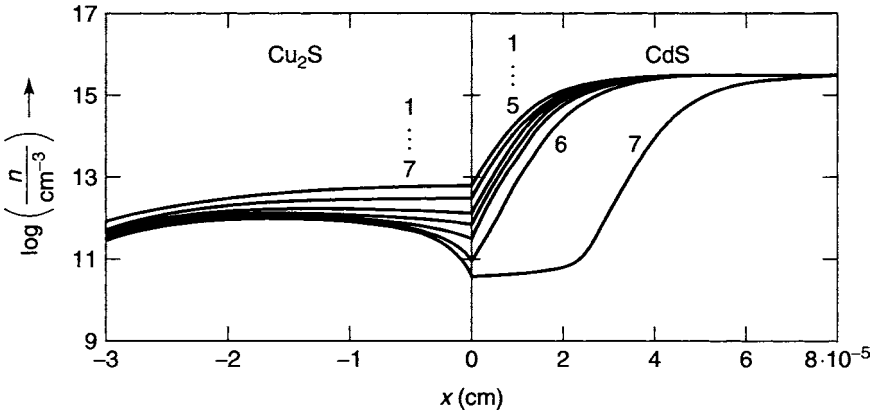

Fig. 11.3. Computed electron density distribution in the Cu_2S/CdS heterojunction solar cell assuming $n(x)$ continuity at $x = 0$ with the electron current as family parameter for $j_n = 17.3,\ 0,\ -7.5,\ -11.2,\ -12.9,\ -14.3$, and $-14.7\,\mathrm{mA\,cm^{-2}}$ for curves 1–7, respectively. Observe the abscissa break at $x = 0$

density at the Cu_2S/CdS boundary is pulled down from the CdS side of the interface, causing a gradient of $n(x)$ in the Cu_2S with consequent minority carrier diffusion toward the interface.

11.1.1 The Current–Voltage Characteristics

The relation between the applied voltage and the boundary electron density at the Cu_2S/CdS interface can be obtained explicitly from a simple Schottky barrier approximation[6] (see Sect. 8.3) with

$$n_j(x=0) = N_c \exp\left[-\frac{e(\widetilde{V}_{\mathrm{D}n} + V_{\mathrm{oc}} - V)}{kT}\right], \tag{11.1}$$

and, neglecting the small voltage drop in the highly doped Cu_2S. The diffusion current in Cu_2S is given by [Sect. 5.2.3, Eq. (5.35)] (Böer et al. 1973; Böer 1976)

$$j_n = e\frac{L_n}{\tau_n}(n_j - g_o\tau_n)\tanh\left(\frac{x_c}{L_n}\right), \tag{11.2}$$

with $x_c = x_m$ the position of the $n(x)$ maximum in Cu_2S for reverse and $x_c = x_i$ the inflection point in forward bias ($x_c \approx d_1/2$). When combining the voltage drop in the CdS barrier (11.1) with the current created in the

[6] The Schottky barrier approximation is well suited for the CdS part of the heterojunction since in the entire CdS one has $p \ll n$, and the Cu_2S is nearly degenerate, thereby acting in some respects as pseudo-electrode.

Cu_2S emitter (11.2) by eliminating n_j, one obtains directly an essentially ideal current voltage characteristic[7] (Böer, 1978)

$$j_n = eg_o L_n \left\{ \exp\left[\frac{e(V - V_{oc})}{kT}\right] - 1 \right\} \tanh\left(\frac{x_m}{L_n}\right), \tag{11.4}$$

which can be rewritten in the common form

$$\boxed{j_n = j_0 \exp\left(\frac{eV}{kT}\right) - j_s,} \tag{11.5}$$

with

$$j_0 = j_{00} \exp\left(-\frac{e\Phi}{kT}\right), \tag{11.6}$$

$$j_{00} = e\frac{L_n}{\tau_n} N_c \tanh\left(\frac{x_c}{L_n}\right), \tag{11.7}$$

$$j_s = eg_o L_n \tanh\left(\frac{x_c}{L_n}\right), \tag{11.8}$$

and

$$\Phi = \widetilde{V}_D + V_{oc}. \tag{11.9}$$

When written in this form, (11.5) with its auxiliary formulae (11.3)–(11.9), it is most instructive as it permits a distinction between the different interacting effects. These are the current generation in Cu_2S and the voltage drop in CdS, resulting in this basic photodiode characteristic. Again, this is caused by the fact that the almost degenerate, highly conductive Cu_2S acts almost exclusively to generate the photoelectric active minority carriers (electrons), and the CdS with much lower donor density has a substantially wider barrier layer with almost all the potential drop of the device generated by electron depletion and little additional photogeneration of minority carriers (that are completely neglected in this simple model). The "ideal characteristic" as obtained in this fashion contains all these approximation. It obviously needs to be modified when comparison with the experiment is desired.

Beyond this instructive example of a separation of generation and barrier effects, the Cu_2S/CdS solar cell is useful to demonstrate a variety of effects relating to the changes of space charges in the barrier, which influences the performance of solar cells, albeit here in a rather transparent form. We will explore some of these effects in the following sections, and it will become evident there as to why we have selected this heterojunction solar cell for our discussion.

[7] When using the relation

$$\widetilde{V}_{Dn} = \frac{kT}{e} \ln\left(\frac{N_c}{n_{j0}}\right) \tag{11.3}$$

and, inserting for zero current and steady state $n_{j0} = g_o\tau_n$.

11.1.2 Space Charge Effects in the Heterojunction

Changes in the development of space charges are relatively easy to follow in the Cu_2S/CdS solar cell since the junction can be described as a *single carrier* n-type Schottky barrier (see Fig. 11.3).[8] These space charges change with changing occupation of various trap levels. Such changes can be influenced by light and bias variation. We will now discuss this behavior in more detail.

11.1.2.1 Influence of Electron Traps in CdS

We now modify the previous discussion of the Schottky barrier by introducing two sets of donors with a density N_{d1} and N_{d2} and an energy E_{d1} and E_{d2}. Within the barrier layer these donors are sequentially depleted with increased reverse bias, as schematically shown in Fig. 11.4b. This causes a stepwise increase of the space charge and consequent increase in the slope of the electric field (Fig. 11.4d and f). This is compared with a conventional Schottky barrier having only one donor level and is shown in Fig. 11.4a, c, and e.

The steeper increase of the high-field region close to the barrier interface (Fig. 11.4f) results in a steeper increase of the current, as indicated in Fig. 11.4h. This can be obtained analytically from the shape factor approximation (Sect. 3.2.1.2) which yields to the current–voltage characteristics of the heterojunction

$$j = \frac{j_s \left[\exp - \left\{\frac{e(V-V_{oc})}{kT}\right\} - 1\right]}{1 + \dfrac{\varepsilon_1 v_D^*}{\varepsilon_2 \mu_{n2} F_j}}, \tag{11.10}$$

with indices 1 and 2 for Cu_2S and CdS, respectively, and v_D^* the modified diffusion velocity given by (5.41). Under conditions in which the drift velocity $\mu_{n2}F_j$ at the heterointerface is on the same order as the diffusion velocity v_D, the current becomes proportional to F_j which in turn is proportional to the square root of the bias [see (3.41)]

$$F_j = \sqrt{\frac{2eN_d}{\varepsilon_2 \varepsilon_0}(V_{oc} - V)} + F_c \tag{11.11}$$

with F_c the maximum field in open circuit conditions for a single donor model.

In the two-donor model, the space charge distribution can be approximated[9] by a gradual step function

[8] Even considering frozen-in steady state for the minority carriers in the dark and reasonable generation rates and lifetimes under sunlight, the minority carrier density within the CdS will remain well below the electron density within the entire barrier region.

[9] For a more precise evaluation of the sequential trap depletion see the corresponding Sect. 3.2.2 that deals with the dark-diode.

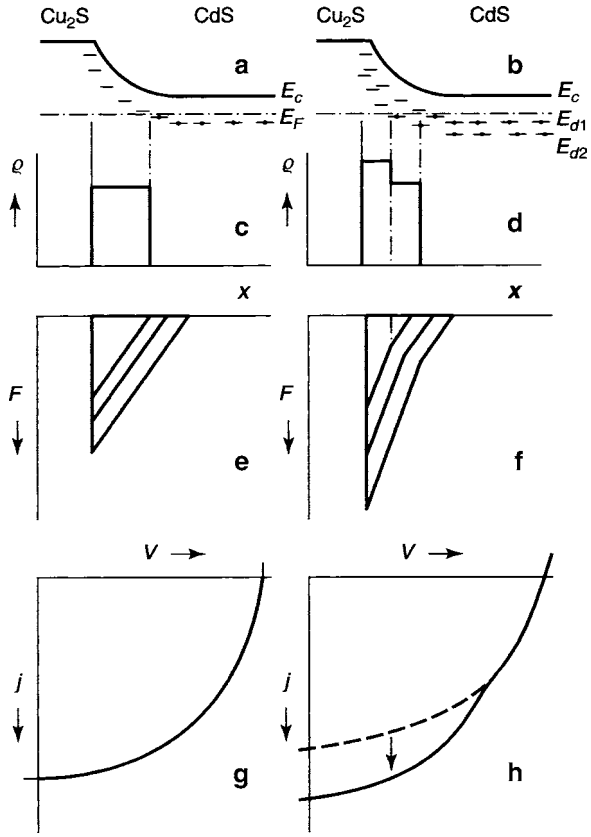

Fig. 11.4. The barrier layer at a Cu_2S/CdS heterojunction for a single donor (**a, c, e**, and **g**) and a two-donor model (**b, d, f**, and **h**). Shown are the band model for equilibrium conditions (**a** and **b**); the corresponding space charge distribution (**c** and **d**); the field distribution for three bias conditions (**e** and **f**); and the current–voltage characteristics for cell parameters resulting in an extended square-root branch (**g** and **h**) in the current voltage characteristics

$$\varrho(x) = e\left\{n(x) - N_{d1}\left[1 + 0.5\frac{N_{d2}}{N_{d1}}\left(\tanh[C\{V - (\Phi - V_2)\}]\right)\right]\right\} \qquad (11.12)$$

with $C = e/(kT)$ or $C = e/(2kT)$ dependent on the kinetics of the trap filling, and V_2 the area under the triangle of $F(x)$ up to the cross-over point at open circuit, $\Phi = V_{\mathrm{oc}} + V_{\mathrm{D}}$. As a example of the computed set of solution curves using such donor depletion function for two levels in the basic set of transport equation, one obtains the set of curves that are shown in Fig. 11.5. It shows two steps in $n(x)$, $\varrho(x)$, and indicates the field for sufficient reverse bias when the lower donor is being depleted by showing a kink and a sharply increasing slope.

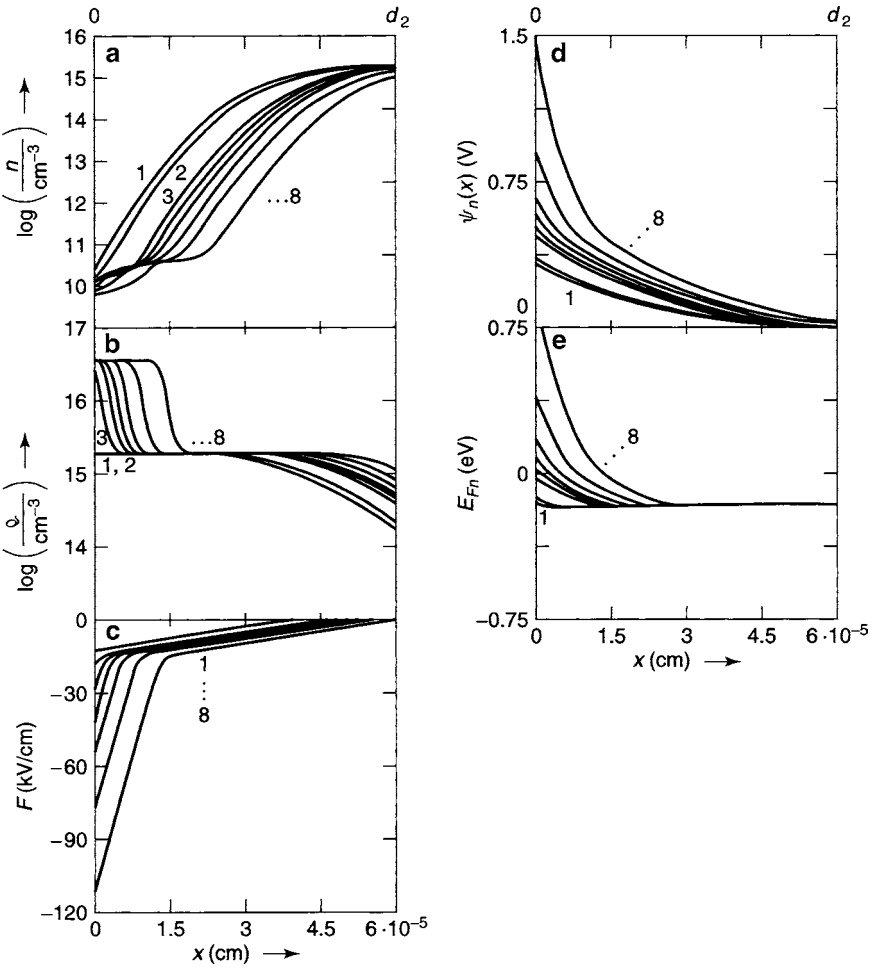

Fig. 11.5. Solution curves of (7.32)–(7.42) for a two-donor Schottky barrier model with a space charge modifying function given by (11.12) and $N_{d1} = 2 \times 10^{15}\,\mathrm{cm}^{-3}$, $N_{d2} = 5 \times 10^{16}\,\mathrm{cm}^{-3}$, $V_2 = -0.65\,\mathrm{V}$, $\Phi = 0.9\,\mathrm{V}$ and $C = -38$. Family parameter is the current with $j_n = 1, 2, \ldots, 8\,\mathrm{mA\,cm}^{-2}$ for curves 1–8, respectively

A corresponding family of **current–voltage characteristics** is shown in Fig. 11.6. These characteristics develop a step when the parameters are favorable so that an extended square root range exists, and the ratios of N_{d1} and N_{d2} as well as the ionization energies are conducive for such a step to develop, due to sequential donor depletion.

Steps are indeed occasionally observed and are usually referred to as double-diode characteristics. The case discussed here is another example of how careful one has to be in explaining an observed behavior, and how misleading a simple double diode model can be for the search to improve such

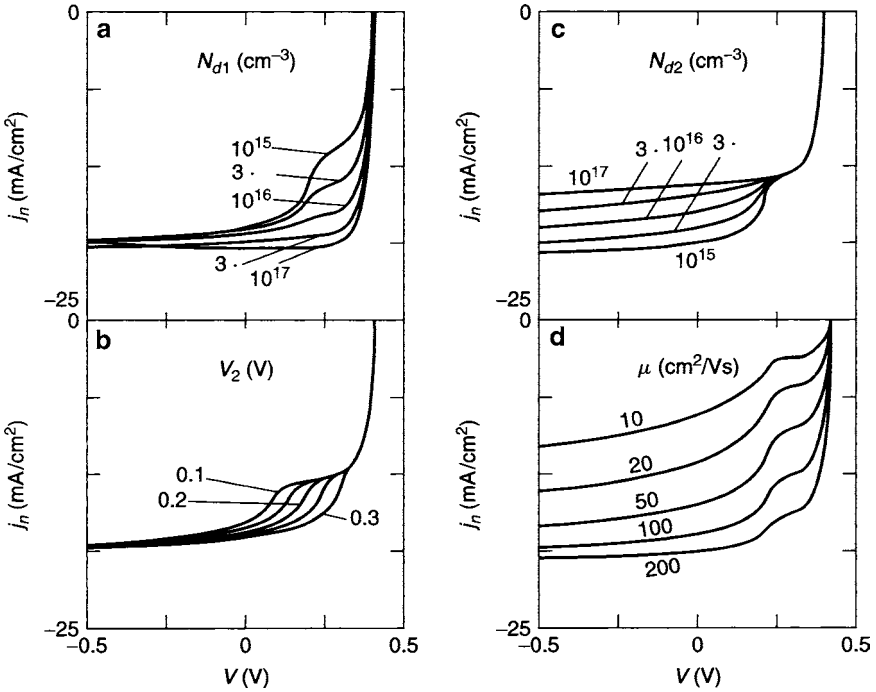

Fig. 11.6. Current–voltage characteristics computed from solution curves corresponding to the ones shown for one example in Fig. 11.5 for $N_{d1} = 2 \times 10^{15}\,\mathrm{cm}^{-3}$, $N_{d2} = 5 \times 10^{16}\,\mathrm{cm}^{-3}$, $V_2 = 0.2\,\mathrm{V}$, and $\mu_n = 100\,\mathrm{cm}^2\,\mathrm{V}^{-1}\,\mathrm{s}^{-1}$ as standard parameters while one of them is changed in steps as shown as a family parameter in each of the panels

a cell. Namely, with further cell optimization using treatments to modify the donor distribution, the steps generally disappear as the square root range vanishes and the step-like increase in field slope becomes hidden in the current saturation range.

11.1.2.2 Influence of a Compensated Layer near the Hetero-Interface

When the region close to the hetero-interface is partially compensated, a lower space charge results, thereby, the field slope is *reduced*, and the slope of the current–voltage characteristic in the DRO-range between the Boltzmann and the saturation range is also reduced.

When this compensated layer comprises only a fraction of the space charge layer, it remains fixed and cannot expand. In such devices, only a small parallel shift of the characteristic occurs, as shown in Fig. 11.7a.

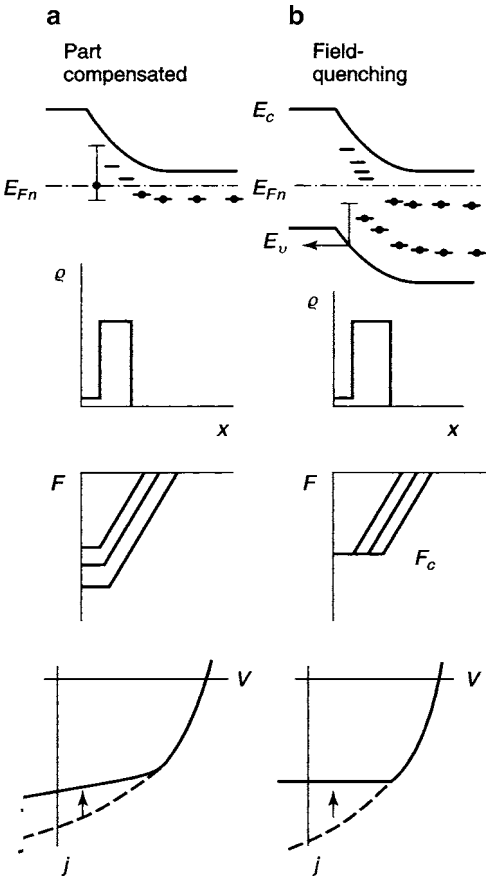

Fig. 11.7. A barrier layer which is partially compensated near the interface (**a**), or which contains Coulomb-attractive hole traps that permit field quenching above a critical field F_c (**b**) that forces total compensation at a critical field

11.1.2.3 Influence of a Field-Induced Depletion of Hole Traps

When Coulomb attractive hole traps (copper centers in CdS) close to the hetero-interface are exposed to fields in excess of the critical field for Frenkel–Poole ionization, these hole traps can be depleted by the action of the field, and the freed holes can be extracted through the adjacent hetero-interface (Fig. 11.7b). This causes a sharp reduction of the space charge and results in a reduced field slope. Consequently, a wider region becomes exposed to the ionization field (Fig. 11.7b). When the thickness of this hole-depleted region increases beyond the diffusion length, interaction of the freed holes with the electron ensemble must be considered, including modification of the recombination traffic, commonly referred to as field quenching. This is discussed in more detail below.

11.1.2.4 Influence of Field Quenching

Field quenching in optically excited CdS is well-known (Böer et al. 1968), and results in compensation by freeing holes from hole traps to recombine with electrons, thereby lowering their density (Böer 2009). This, in turn, lowers the density of positively charged centers, and can essentially eliminate the space charge in the part of the barrier where the field has reached the critical value for field quenching. It thereby limits field and current and causes a substantial widening of the barrier.[10]

A typical set of solution curves of the transport equations is shown in Fig. 11.8 which assume the onset of field quenching at $60\,\mathrm{kV\ cm^{-1}}$ and a space charge reduction from $5 \times 10^{16}\,\mathrm{cm^{-3}}$ to a compensated $(N_d - N_a)$ value of $\approx 5 \times 10^{14}\,\mathrm{cm^{-3}}$.

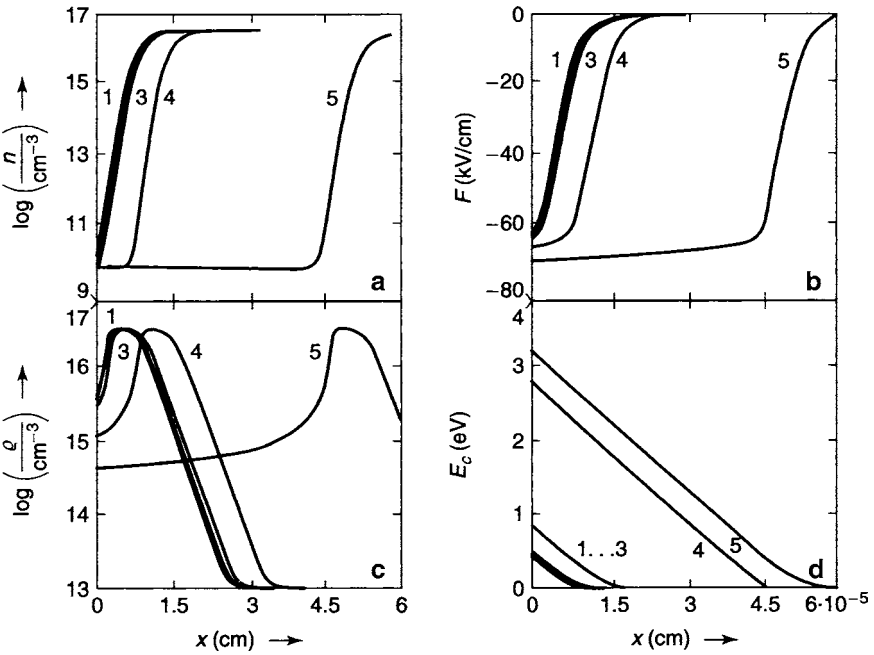

Fig. 11.8. Computed solution curves of (7.32)–(7.42) for the CdS barrier in a Cu_2S/CdS solar cell with field quenching causing an effective compensation from $N_d = 5 \times 10^{16}\,\mathrm{cm^{-3}}$ to $N_d - N_a = 5 \times 10^{14}\,\mathrm{cm^{-3}}$ at fields in excess of $60\,\mathrm{kV\ cm^{-1}}$. Family parameter is the electron current: $j_n = 2$, 5, 6, 6.3, and $6.5\,\mathrm{mA\ cm^{-2}}$ for curves 1–5, respectively

[10] Such field quenching is of interest for technical applications, since it permits working with semiconductors of lower purity, allowing less expensive fabrication methods. Without field quenching, such semiconductors would easily be driven into a range of excessive barrier fields, with detrimental influence on performance due to tunneling through the barrier, thereby creating leakage currents.

The onset of field quenching can be modeled with a step function

$$\varrho(x) = e\left[n(x) - N_{\mathrm{D}}\left\{1 - 0.5\frac{N_{\mathrm{D}} - N_A}{N_{\mathrm{D}}}\left(1 + \tanh[Q(F - F_c)]\right)\right\}\right]. \quad (11.13)$$

Field quenching is a self-compensating process that starts to become marked near the critical field F_c and frees as many holes as necessary for sufficient compensation to limiting the field slightly above F_c. If, however, during this process more acceptors than donors are depleted, the sign of the space charge is inverted, causing a decrease of the field and a reduction of the field quenching, i.e., self-stabilizing the effect.

The leveling of the field causes a rapid widening of the space-charge layer with a fast increasing voltage drop across the barrier without further lowering the carrier density at the barrier interface. This results in substantially improving current saturation with increasing compensation for curves 1–4, as shown in Fig. 11.9.

11.1.3 Kinetic Effects of Solar Cell Characteristics

The trapping or release of carriers from traps is a slow process, with a time constant, increasing exponentially with trap depth. These processes are initiated when decreasing or increasing the barrier width with changing bias. One consequently expects a hysteresis of the current–voltage characteristics when the characteristic is transversed in one or the other direction.

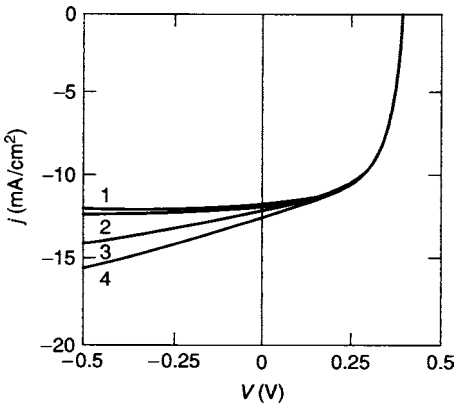

Fig. 11.9. Current–voltage characteristic for a Cu_2S/CdS solar cell with field quenching computed for $n_j = 7 \times 10^9\,\mathrm{cm}^{-3}$ $N_d = 5 \times 10^{16}\,\mathrm{cm}^{-3}$ $F_c = 1.1 \times 10^5\,\mathrm{V\,cm}^{-1}$, and $Q = 1.5 \times 10^{-4}\,\mathrm{cm\,V}^{-1}$ in (11.13) and with $(N_{\mathrm{D}} - N_A)/N_{\mathrm{D}} = 0.98$, 0.8, 0.5, and 0.2 as family parameter for curves 1–4, respectively

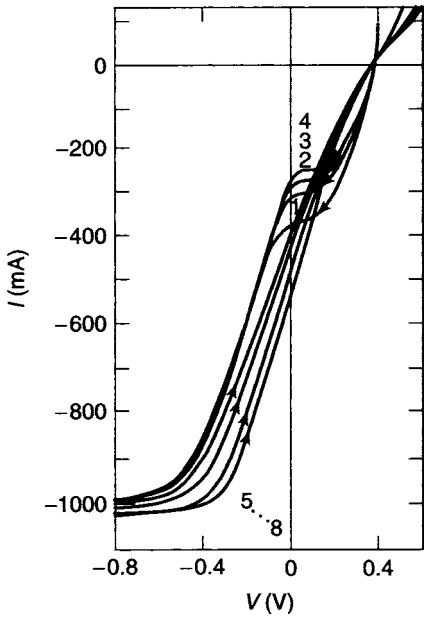

Fig. 11.10. Measured current–voltage characteristics of an insufficiently treated Cu_2S/CdS solar cell traversed in direction of the arrow after waiting 5, 10, 15, and 20 s at V_{oc} for curves 1–4, respectively, or waiting for the same times at −0.8 V for curves 5–8, respectively (after Böer (1979))

This is indeed observed in Cu_2S/CdS solar cells in characteristics with low fill-factors.[11] Examples of such hystereses are shown in Fig. 11.10. When traversed in the direction of increased reverse bias, the characteristics show the typical steps indicating deep trap depletion (Sect. 11.1.2.1). When traversed in the direction of increasing forward bias, the step disappears and an inflection point occurs at V_{oc} with a lower slope at V_{oc} the more traps were depleted while waiting longer at −0.8 V.

The filling or depleting of different types of traps can be more easily analyzed when measuring the kinetics of the voltage drop across the solar cell while maintaining a stepwise increased constant current, as discussed below.

11.1.3.1 Voltage Drop Kinetics Method

This method consists of monitoring applied voltage across the cell as a function of time that is necessary to maintain a constant current through the solar cell after the current is changed stepwise, e.g., from zero to a predetermined

[11] Only in the bias range between the Boltzmann and the saturation branch can such kinetics be observed. Otherwise, the structure of interest becomes hidden in the horizontal current saturation branch.

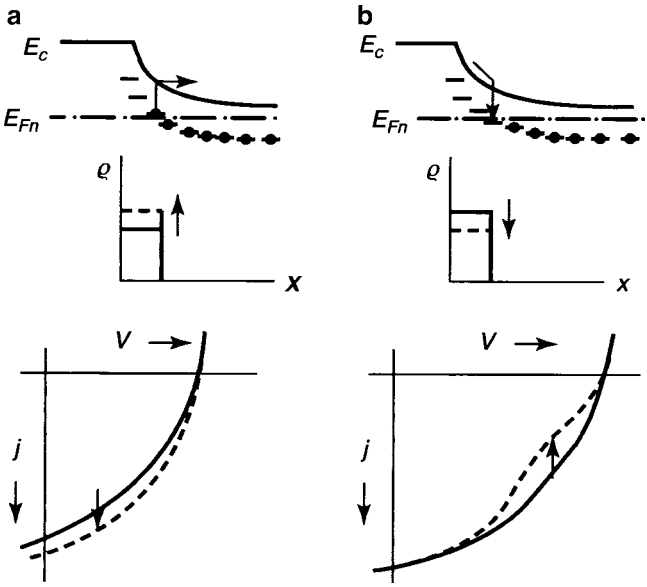

Fig. 11.11. A barrier layer kinetics with slow (thermal) trap depletion when waiting in reverse bias (**a**) and of trap filling when waiting at or near V_{oc} (**b**)

fixed value (Böer 1979). When the current is increased, the space charge is increased, caused by depletion of donors or traps that turn positive (Fig. 11.11a). Conversely, a decrease of the current causes a filling of such centers, neutralizing them and reducing the slope of the characteristic, i.e., causing the voltage drop to decrease (Fig. 11.11b).

If, however, the forced increase in current causes a depletion of acceptors or acceptor-like deep hole traps, e.g., caused by Frenkel-Poole excitation by field quenching causes a reduction in space charge by compensation and thereby an increase in the slope of the characteristics, the opposite behavior is found for depletion of donors.

The changing space charge in part of the barrier is illustrated in Fig. 11.12. In panel a we show a slow depletion of a deep electron trap with higher applied voltage, causing a reduction of the voltage drop (area under the $F(x)$-curve), as a layer with increased space charge becomes established. This results in a higher field slope near the interface that can reach the same F_j, thereby maintaining the same current.

When the critical field for field quenching is reached at the interface, the space charge-free field-quenched region with constant critical field F_c expands as shown in Fig. 11.12b. An intermittent region is created with a high field slope where deep electron traps are depleted before quenching starts.

Figure 11.13 shows corresponding experimental results. Three characteristics are given schematically in panel a. When the current is changed to a

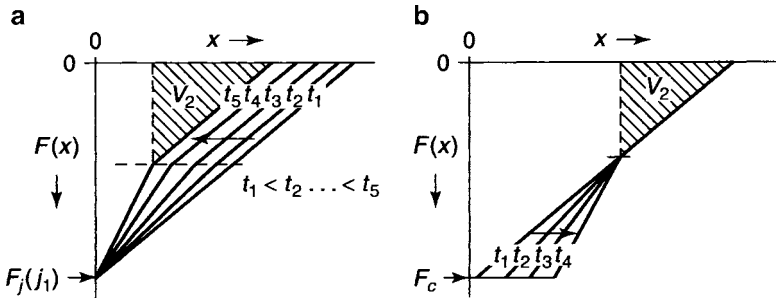

Fig. 11.12. Field distribution kinetics in a barrier layer (**a**) with gradual depletion of a deep trap; (**b**) with depletion of a deep trap, but at a field at which field quenching starts reducing the space charge near the interlayer and therefore limits the field

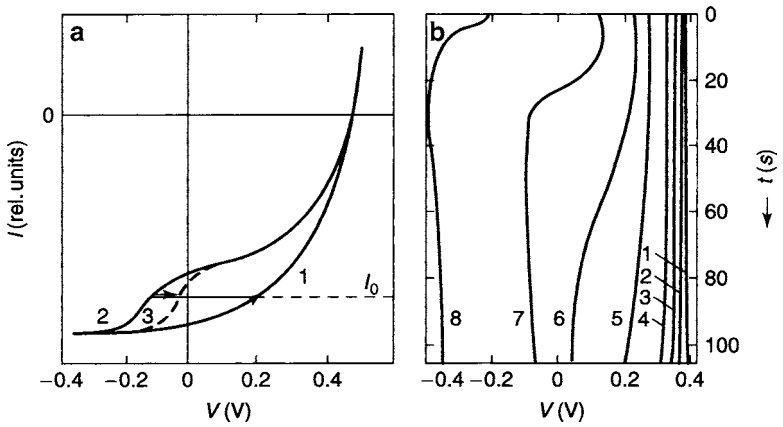

Fig. 11.13. Kinetics of the current–voltage characteristics within the DRO-range. (**a**) Three nonstationary characteristics; when constant current I_0 is maintained, the applied voltage changes in time as the characteristic develops from curves 1–3. (**b**) Voltage drop as a function of time after the current is changed from zero at V_{oc} for 2 min. to $I_0 = -530$, -600, -650, -700, -775, -800, and -820 mA for curves 1–8, respectively (after (Böer 1979))

constant value I_0, a voltage of ≈ 0.2 V is necessary to maintain this current for curve 1; however, in time the applied voltage needs to be reduced, reaching a minimum at -0.15 (curve 2), and then increased again to -0.05 V (curve 3) to maintain I_0. The actual voltage kinetics is shown in Fig. 11.13b for a Cu_2S/CdS cell that shows JV-characteristics with hysteresis similar to the one given in Fig. 11.10. The observed kinetics depends on the degree of preceding trap filling (waiting at a certain point of the characteristic), on the value of I_0, and on the temperature.

In curves 8 and 7 of Fig 11.13b, one can discern the three voltage drop ranges shown in Panel a. First a shift toward higher negative voltage,

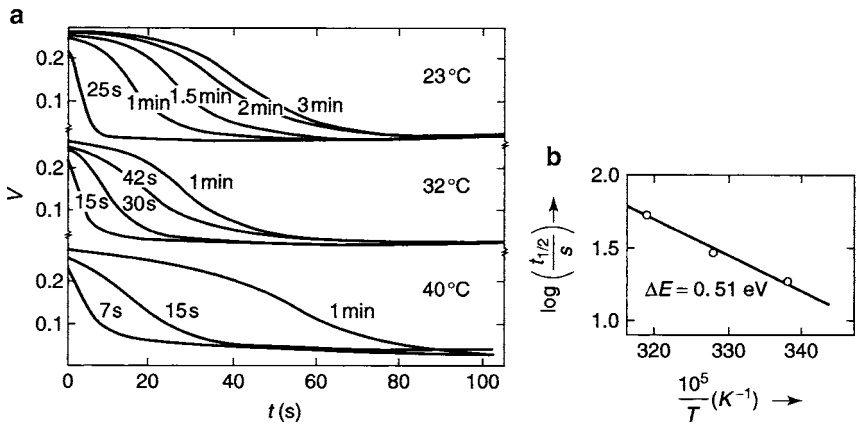

Fig. 11.14. (**a**) Voltage drop across a Cu_2S/CdS solar cell similar to the one used in Fig. 11.10 after switching from $I = 0$–860 mA at the temperatures listed in the three panels and after waiting at V_{oc} for the time indicated at each curve. (**b**) Logarithm of the half-time of the voltage decrease taken from (**a**). Curves of 1 min rest at V_{oc} are used (after Böer 1979)

indicating trap depletion; this shift is very fast, and barely resolved near $t = 0$ for curve 7. This range overlaps with the voltage decrease caused by the start of field quenching that becomes dominant near 10 s. It is then followed by a slow rise beyond 40 s; this rise is probably due to an even slower release of electrons from deeper electron traps, thereby lowering the compensation.

When waiting at V_{oc} for different lengths of time (shown as family parameter in Fig. 11.13) and then plotting the time to achieve half of the quenching obtained from the abscissa for different temperatures in a semi-logarithmic plot versus $1/T$ (Fig. 11.14b),one obtains an apparent activation energy of $\approx$0.5 eV for the filling of deep traps that makes it more time consuming for quenching, the more of these traps are filled.

The examples are given here to illustrate the sensitivity of an incompletely filled out current–voltage characteristic to trap kinetics. Any characteristic that has a substantial square-root range (indicating a DRO-range) between the Boltzmann and the current saturation range offers an opportunity to study such kinetics. For example, in this DRO-range, the current voltage characteristic relates as a simple drift current to the maximum field in the barrier

$$j_n = e\mu_n n_j F_j \quad \text{with} \quad F_j = \sqrt{\frac{2\varrho(V_{oc} - V)}{\varepsilon_2 \varepsilon_0}}, \tag{11.14}$$

which yields for the voltage drop across the solar cell for trap filling with $\varrho = e[N_d - n_d(t)]$:

$$\Delta V(t) = V_{oc} - V(t) = -\frac{j_n^2}{\frac{2e}{\varepsilon_2 \varepsilon_0}(e\mu_n n_j)^2 [N_d - n_d(t)]}. \tag{11.15}$$

In a similar fashion, the reduction of the space charge due to quenching can be analyzed.

11.1.4 Influence of Interface Recombination

A broadening of the square root branch is caused by interface recombination between Cu_2S and CdS and is probably induced by lattice mismatch resulting in a closely spaced dislocation network that creates a high density of recombination centers.

Such interface recombination provides a leakage path, diverting minority carriers that can no longer pass through the barrier as indicated in Fig. 11.15. As a result, the current is reduced by the interface recombination current and the conversion efficiency is reduced accordingly (see below).

$$j_n(x = 0^+) = j_n(x = 0^-) - en_j s_j \tag{11.16}$$

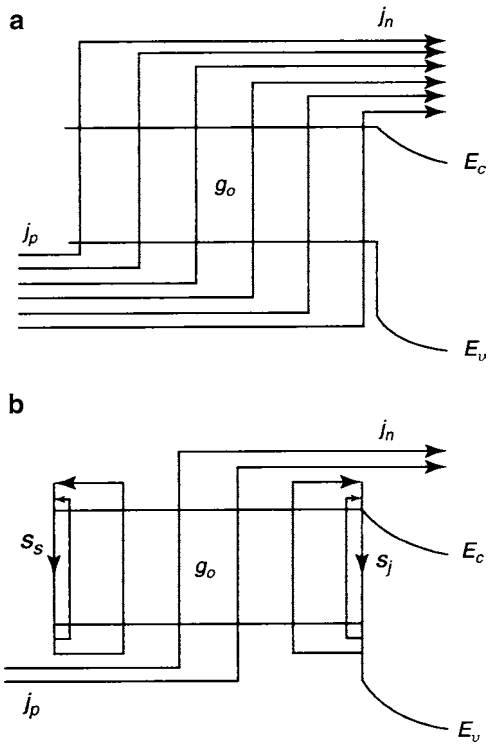

Fig. 11.15. Optically generated current (schematically) (**a**) without and (**b**) with surface and interface recombination leakage indicating the corresponding current losses. *Arrows* indicate electron transport

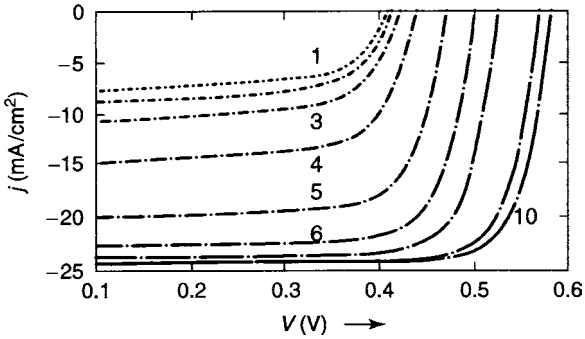

Fig. 11.16. Current–voltage characteristics obtained from (11.10) for a single donor model with $N_d = 10^{16}\,\mathrm{cm}^{-3}$, $\mu_n = 100\,\mathrm{cm}^2\,\mathrm{V}^{-1}\,\mathrm{s}^{-1}$, $\varepsilon = 10$, and $T = 300\,\mathrm{K}$ and with the interface recombination velocity as family parameter: $s_j = 10^7$, 3×10^6, 10^6, 3×10^5, 10^5, 10^4, 10^3, 10^2, 10, and 0 for curves 1–10, respectively

resulting in a reduced diode current

$$j_n = \frac{j_s \left[\exp\left\{ -\dfrac{e(V - V_{\mathrm{oc}})}{kT} \right\} - 1 \right]}{1 + \dfrac{\varepsilon_1 (v_{\mathrm{D}}^* + s_j)}{\varepsilon_2 \mu_{n2} F_j}} \tag{11.17}$$

and a corresponding reduction in the open circuit voltage

$$\Delta V_{\mathrm{oc}} = \frac{kT}{e} \ln\left(\frac{v_{\mathrm{D}}^* + s_j}{v_{\mathrm{D}}^*} \right). \tag{11.18}$$

Figure 11.16 shows a family of current–voltage characteristics computed from (11.17) with the interface recombination velocity as family parameter. This set of curves demonstrate the severity of the performance deterioration with increasing interface losses even for recombination velocities in the low $10^4\,\mathrm{cm\,s}^{-1}$ range.

11.1.4.1 Boundary Condition at the Interface

When we permit the electron density n_j to slide down at the interface, the current–voltage characteristics become modified according to the discussion of Sect. 3.2.1.2, (3.48), yielding for a planar heterointerface

$$\boxed{j_n = \frac{j_s \left[\exp\left\{ -\frac{e(V - V_{\mathrm{oc}})}{kT} \right\} - 1 \right]}{1 + \frac{\varepsilon_1 (v_{\mathrm{D}}^* + v_n^* + s_j)}{\varepsilon_2 \mu_{n2} F_j}}} \tag{11.19}$$

with v_{D}^* the modified diffusion velocity given by (5.41) and adding now in the shape factor in the denominator the much larger modified rms-velocityer modified rms-velocity of electrons $v_n^* = v_{n,\mathrm{rms}}/\sqrt{6\pi}$.

When comparing (11.19) with (11.10), one deduces that the square root branch with defect level information widens as the velocity that competes with the drift velocity increases, hence making a defect level analysis easier in the widened DRO-range.

11.1.5 Information from the Exponential A-Factor

We will now devote our attention to the Boltzmann branch near V_{oc}. We assume that a simple characteristics deterioration from a parasitic resistive network can be neglected.

The usually observed deviation from the ideal characteristic is then expressed by the *quality factor* A, as

$$j = j_0 \exp\left(\frac{eV}{AkT}\right) - j_{\mathrm{L}} \tag{11.20}$$

which, for reasons to become obvious below, we will rewrite as[12]

$$j = j_{00} \exp\left(-\frac{e\widetilde{V}_{\mathrm{D}n}}{kT}\right) \exp\left[\frac{e(V - V_{\mathrm{oc}})}{AkT}\right] - j_{\mathrm{L}}. \tag{11.21}$$

It was pointed out by Shockley et al. (1957) that a quality factor $A > 1$ can be related to junction recombination. The Cu_2S/CdS solar cell has an advantage for a simplified analysis, since the dominant junction recombination is localized at the interface and expressed as interface recombination velocity s_j. With it, the parameters of (11.21) are

$$V_{\mathrm{oc}} = V_{\mathrm{oc}}^{(0)} - \frac{kT}{e} \ln\left(\frac{v_{\mathrm{D}}^* + s_j}{v_{\mathrm{D}}^*}\right), \tag{11.22}$$

$$j_{00} = eN_{c2}(v_{\mathrm{D}}^* + s_j), \tag{11.23}$$

$$j_{\mathrm{L}} = j_{\mathrm{L}}^{(0)} \frac{v_n^*}{v_n^* + v_{\mathrm{D}}^* + s_j}, \tag{11.24}$$

with superscript (0) indicating the parameter for $s_j = 0$. The relevant energy and potential parameters are identified in Fig. 11.17.

A graphical analysis of some typical experimental results will be helpful for guiding further theoretical explanation. In Fig. 11.18, a family of current–voltage characteristics shifted by the short circuit current is shown in a semi-logarithmic scale with the light intensity as family parameter. To show the exponential relationship directly, $\ln(j + j_{\mathrm{L}})$ is plotted vs. V. In addition to

[12] Observe that we split off an exponential with the diffusion voltage that does not contain A.

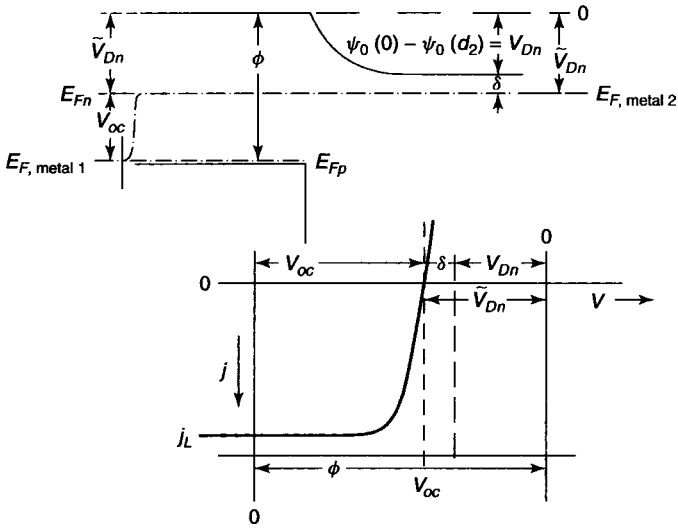

Fig. 11.17. Band model of the Cu_2S/CdS solar cell and corresponding current–voltage characteristics with potential and energy parameters identified

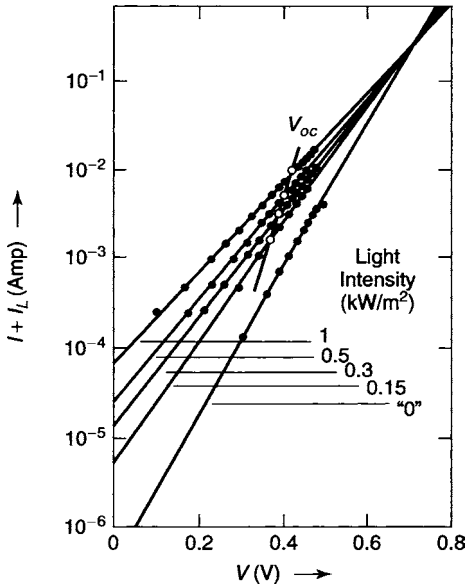

Fig. 11.18. Current–voltage characteristics shifted by the short circuit current vs. applied voltage for a Cu_2S/CdS solar cell with the light intensity, expressed in $kW\,m^{-2}$ with air mass 1 sunlight spectrum, as family parameter. Curve "0" measured without intentional illumination except for room stray light. Beyond the range indicated by dots, the measured curves deviate from the exponential law. $T = 300\,K$ (after Böer (1980))

the excellent fulfillment of the exponential law (11.20) one observes four remarkable properties:

(1) The quality factor increases with increasing light intensity;
(2) All curves intersect at a common point at about $I + I_L = 0.5\,A$ and $V = 0.7\,V$;
(3) $\ln(j_L)$ vs. V_{oc} curves also lie on a straight line, but with a different slope B, according to

$$j_L = j_0^* \exp \frac{eV_{oc}}{BkT}. \tag{11.25}$$

(4) The pre exponential factor j_0 in (11.20) is related to the saturation current j_L according to a power law

$$j_0 = a j_L^B, \tag{11.26}$$

with the exponent B identical to the slope factor in (11.25).

This can be seen from Fig. 11.19 when extending the curves from V_{oc} at a slope $e/(kT)$ and not $e/(BkT)$ (11.21). One observes a parallel shift by $\Delta \ln s_j$ as shown in Fig. 11.19a. Such a shift can be explained from

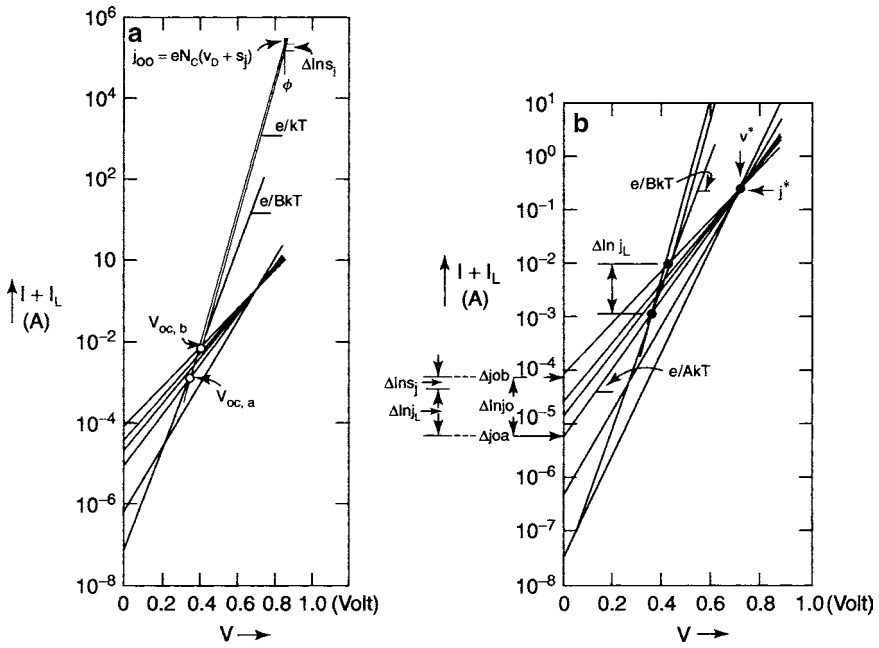

Fig. 11.19. Measured characteristics as in Fig. 11.18. (**a**) with Boltzmann solution extending from V_{oc} to Φ for two curves (**a**) and (**b**), and (**b**) highlighting the larger spread of j_0 compared to the spread of j_L, causing the fanning-out of $j(V)$ and their intersect at $(j^*,\ V^*)$

$$j_0 = en_j(V = 0)(v_{\mathrm{D}}^* + s_j) \tag{11.27}$$

that results for $s_j \gg v_{\mathrm{D}}^*$ in

$$\Delta j_0 = en_j \Delta s_j + es_j \Delta n_j \tag{11.28}$$

and can be approximated with $j_s = en_j s_j$ and $j_{\mathrm{L}} = en_j v_{\mathrm{D}}^*$ by

$$\Delta \ln j_0 \simeq \Delta \ln j_s + \Delta \ln j_{\mathrm{L}}, \tag{11.29}$$

in agreement with the geometric picture drawn in Fig. 11.19b, that yields from (11.26)

$$B \simeq \frac{\Delta \ln j_{\mathrm{L}} + \Delta \ln j_s}{\Delta \ln j_{\mathrm{L}}}. \tag{11.30}$$

The larger spreading of j_0 compared to that of j_{L} and caused by a change in j_s results in the fanning out of the characteristics $j(V)$ and causes the intersection of these curves at $j^*(V^*)$, as identified in Fig. 11.19b.

The quality factor A is related to the slope B (Böer, 1980) by

$$A = \frac{-\dfrac{eV^*}{kT}}{B \ln\left(\dfrac{j_{\mathrm{L}}}{j_{\mathrm{L}}^0}\right) - \ln\left(\dfrac{j^*}{j_0^0}\right)}, \tag{11.31}$$

and is in reasonable agreement with $A(j_{\mathrm{L}})$ obtained from the experiment.

A consistent explanation of fanning curves is a slight decrease of the interface recombination velocity (by $\Delta s_j / s_j \simeq 0.7$) when the optical generation rate, and thereby the minority carrier density at V_{oc} is increased (here by a factor of 6.7). Such a decrease of the recombination traffic with increased generation rates indicates a partial clogging of the recombination centers. The fanning of the $\log(j + j_{\mathrm{L}})$ vs. V curve can then be seen as a neat tool and sensitive indication of such partial clogging.

11.1.6 Lessons Learned from the CdS/Cu_2S Solar Cell

From a current–voltage characteristic that is not deteriorated by a network of series and shunt resistors, one can obtain separate information on

(1) The effective carrier diffusion length
(2) Carrier trapping and compensation
(3) Carrier recombination clogging

The first and the most direct information on bulk carrier diffusion length is obtained from the saturation range, according to $j_s = eg_o L_n^*$, where L_n^* may be slightly shortened from the bulk diffusion length in short devices, if competition to surface recombination is important.

The second information about the junction can be obtained from the relatively narrow range in a current–voltage characteristic between the Boltzmann and the saturation branch. Here,one can obtain kinetic effects and clues about the origin and dynamics of the space charge, such as those related to trapping of majority carriers and their slow thermal release, and of compensation from field-induced minority carrier release.

Third, the ideality factor, obtained from the Boltzmann range provides information about the recombination within the junction. Its dependence on optical excitation yields additional clues relating to possible recombination paths and nonlinear effects, such as clogging when the current–voltage characteristic is fanning-out, providing in addition to the ideality factor A a factor B relating exponentially the saturation current and the open circuit voltage.

The fact that the Cu_2S/CdS heterojunction cell provides an almost perfect separation of the junction in a wide gap semiconductor that permits easy observation of slow redistribution of carriers over traps, and that it has a dominant recombination interface with well localized interface recombination traffic, is helpful to separate the different influences experimentally.

Summary and Emphasis

The heterojunction photodiode permits the separation of various interacting effects, which helps in understanding the operation of photodiodes and solar cells and permits further device optimization.

Photodiodes with low fill-factors and extended ranges of square root bias dependence provide opportunities to analyze the influence of traps on the origin of space charges and the kinetics of trap-filling or depletion with changing bias.

Photodiodes that show different quality A-factors for the jV-characteristics and for V_{oc}, indicate a generation-rate dependent interface recombination.

A CdS-based device was selected for an extensive discussion since these devices demonstrate a great variety of possible effects that can influence their performances.

The Cu_2S/CdS that was selected was a front-wall solar cell and exemplifies an almost complete separation of the region for minority carrier generation in the emitter, and the junction region. The junction, in turn, lies almost completely in the lowly doped CdS and acts much like a Schottky barrier since holes are blocked by the large offset of the valence band at the heterointerface. It also provides a most important example for intrinsic field limitation by field quenching, which is essential for permitting the use of semiconductors with high impurity content that would otherwise cause junction leakage by tunneling in excessive fields.

Lessons learned from the CdS-based heterojunctions may be applied to the more recent heterojunctions in attempts to further optimize the performance of these devices.

Exercise Problems

1.(r) Discuss the relative advantages of back wall compared to front wall solar cells.

2.(r) List the reasons for the Cu_2/CdS solar cell to have special educational values
   (a) by clearly separating key parts of the photodiode.
   (b) Why can the junction be well approximated by a Schottky barrier?
   (c) Could this device act as a model for a metal/semiconductor Schottky barrier?
   (d) Where are the limits for such a model?

3.(∗) For the Cu_2/CdS solar cell, continuity of the electron density at the hetero-interface was assumed. In actuality this is not fulfilled.
   (a) What are the reasons?
   (b) The Fermi level must be horizontal through the interface. Can we permit a jump in $n(x)$ at the interface in thermal equilibrium or in steady state?
   (c) Is the resulting jump in $E_c(x)$ dependent on the optical excitation and on the bias?

4.(∗) Identify reasons why the mobility can influence the open circuit voltage of a photodiode.

5.(∗) Trace the reasons why the influence of the recombination center density on V_{oc} tends to be super linear, i.e., with an A-factor > 1.

6.(∗) Describe similarities and principal differences of the CdS based heterojunctions compared with the GaAs/AlGaAs heterojunction
   (a) with respect to their band structure;
   (b) with respect to the reasons why such III-V heterojunctions yield higher efficient solar cells.

A

External and Built-In Fields

Summary. There are substantial differences between an external and a built-in field. The most significant being that an external field can heat a carrier gas, while a built-in field cannot.

In the main text we have discussed the space charge, its creation and influence on the field and the potential distribution within a device. Then we have applied a voltage to the electrodes and observed the consequent changes in space charge, field, and potential distribution. We have, however, not distinguished an important difference between the part of the electric field that is induced by the applied voltage, the external field that is then superimposed on the built-in field that is due to the space charge without an external voltage. We will now point out this difference as it applies to the device heating and, as we will see later to the *entropy production*.

The *external field* is created by an external bias resulting in a surface-charge on the two electrodes with no space-charge within the semiconductor. Within a typical semiconductor, however, space-charge regions exist because of intentional or unintentional inhomogeneities in the distribution of charged donors or acceptors. This charge density ϱ causes the development of an *internal field* according to the Poisson equation:

$$\boxed{\frac{\mathrm{d}F_i}{\mathrm{d}x} = \frac{\varrho}{\varepsilon\varepsilon_0}.} \tag{A.1}$$

The acting field is the sum of both internal, subscript "i", and external, subscript "e", fields:

$$F = F_\mathrm{i} + F_\mathrm{e}. \tag{A.2}$$

External and internal fields result in the same slope of the bands. Therefore, this distinction between internal and external fields is usually not made, and the subscripts at the fields are omitted.

We will indicate in this appendix some of the basic differences between external and internal fields as they relate to carrier transport.

A.1 Penalties for a Simple Transport Model

There are, however, penalties one must pay for a general description of fields, which can best be seen from carrier heating in an electric field. *Carrier heating* is used to describe the field dependence of the mobility (see Böer, 1998) in a microscopic model. Carriers are shifted up to higher energies within a band. Consequently, their effective mass changes, it usually increases, and the scattering probability changes – most importantly, due to the fact that it becomes easier to create phonons. For all of these reasons, the mobility becomes field-dependent; it usually decreases with increasing field.

The heating *is absent in thermal equilibrium*: the carrier gas and the lattice with its phonon spectrum is in equilibrium within each volume element; thus, carrier and lattice temperatures remain the same (Stensgaard 1992). No energy can be extracted from an internal field, i.e., from a sloped band, due to a space charge *in equilibrium*.[1] This situation may be illustrated with an example, replacing electrical forces with gravitational forces: a sloping band due to a space-charge region looks much like a mountain introduced on top of a sea-level plane, the Fermi level being equivalent to the sea level. As the introduction of the mountain does little to the distribution of molecules in air, the introduction of a sloping band does little to the distribution of electrons in the conduction band. Since there are fewer molecules above the mountain, the air pressure is reduced, just as there are fewer electrons in a band where it has a larger distance from the Fermi level (Fig. A.1).

However, when one wants to conveniently integrate over all altitudes (energies) to arrive at a single number, the air pressure (or the electron density), one must consider additional model consequences to prevent winds blowing from the valleys with high pressure to the mountain top with low pressure by following only the pressure gradient. Neither should one expect a current of electrons from the regions of a semiconductor with the conduction band close to the Fermi level, which results in a high electron density, to a region with low electron density in the absence of an *external field*.

To prevent such currents in the electron-density model, one uses the *internal fields*, i.e., the built-in fields, and balances the diffusion current with an exactly compensating drift current. The advantage of this approach is the use of a simple carrier density and a simple transport equation. The penalty is the need for some careful definitions of transport parameters, e.g., the mobility, when comparing external with built-in fields, and evaluating the ensuing drift and diffusion currents when the external fields are strong enough to cause carrier heating– see for an example Liou et al. (1990), or Zhou (1994).

[1] This argument no longer holds with a bias, which will modify the space-charge; partial heating occurs, proportional to the fraction of external field. This heating can be related to the tilting of the quasi-Fermi levels (Böer 1981).

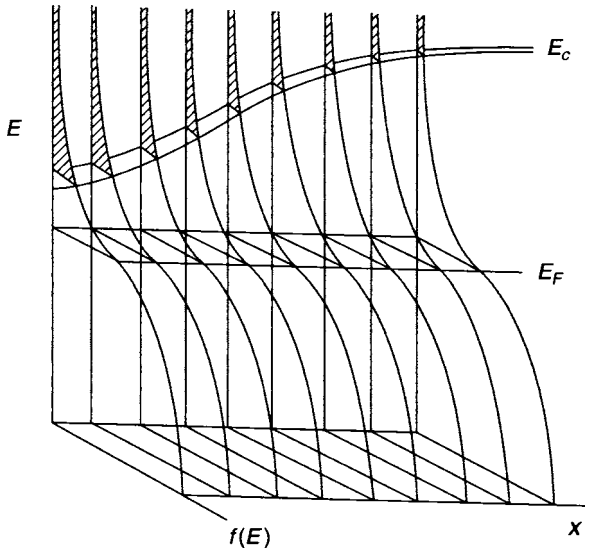

Fig. A.1. Fermi distribution for different positions in a semiconductor with a built-in field region (junction) and zero-applied bias

A.2 Built-In or External Fields

The carrier distribution and mobility are different in built-in or external fields, as discussed by e.g., Green (1982).

A.2.1 Distributions in Built-In or External Fields

The carrier distribution is determined relative to the Fermi level. For vanishing bias, the distribution is independent of the position; the Fermi level is horizontal. The distribution remains unchanged when a junction with its built-in field is introduced (Böer 1981). (For measurements of built-in fields see e.g., (Nakayama and Murayama 1999; Meintjes and Raab 1999).) The sloping bands cut out varying amounts from the lower part of the distribution, much like a mountain displaces its volume of air molecules at lower altitudes (Fig. A.1). The carrier concentration n becomes space-dependent through the space dependence of the lower integration boundary, while the energy distribution of the carrier $n(E)$ remains independent in space:

$$n(x) = \int_{E_c(x)}^{\infty} n(E)\mathrm{d}E. \tag{A.3}$$

This is similar to the velocity distribution of air molecules, which is the same at any given altitude, whether over a mountain or an adjacent plane; whereas the integrated number, i.e., the air pressure near the surface of the sloping terrain, is not. This does not cause any macroscopic air motion, since at any

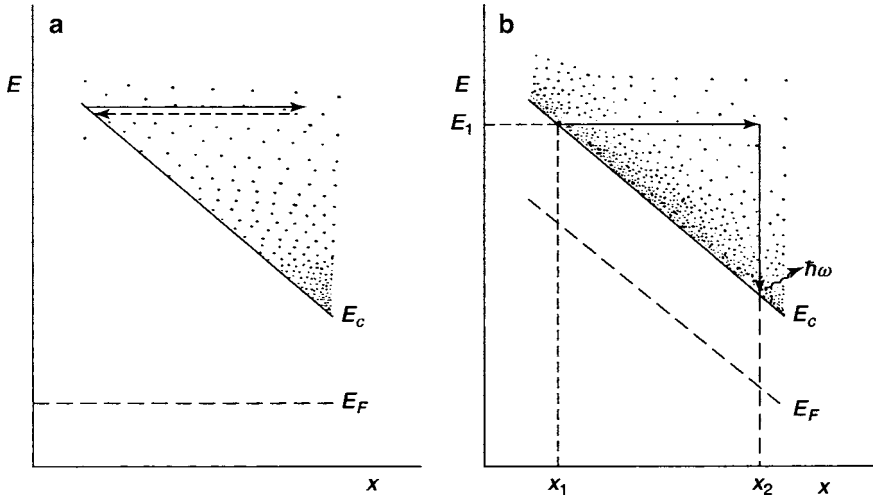

Fig. A.2. Sloping band due to (**a**) an internal (built-in) field with horizontal Fermi level; and (**b**) due to an external field with parallel sloping bands and Fermi level. The electron distribution is indicated by a *dot* distribution, and the action of field and scattering by *arrows*

stratum of constant altitude the molecular distribution is the same; hence, the molecular motion remains totally random.

In a similar fashion, electrons at the same distance above the Fermi level are surrounded by strata of constant electron density; within such strata their motion must remain random. During scattering in thermal equilibrium, the same amount of phonons absorbed by electrons are generated, except for statistical fluctuations: on an average, all events are randomized. Both electron and hole currents vanish in equilibrium *for every volume element*. Figure A.2a gives an illustration of such a behavior.

In an *external field*, however, Fermi level and bands are *tilted parallel to each other*; that is, with applied bias, the carrier distribution becomes a function of the spatial coordinate (Fig. A.2b). When electrons are accelerated in the field, they move from a region of higher density $n(E_1 - E_F)_{x1}$ to a region of lower density $n(E_1 - E_F)_{x2}$. These electrons can dissipate their net additional energy to the lattice by emitting phonons and causing lattice (Joule's) heating. In addition, while in net motion, electrons fill higher states of the energy distribution, thereby causing the carrier temperature to increase. The carrier motion in an *external field* is therefore no longer random; it has a finite component in field direction; the *drift velocity* $v_\mathrm{D} = \mu F$ and the collisions with lattice defects are at least partially *in*elastic; a net current and lattice heating result.

A.2.2 Mobilities in Built-In or External Fields

At higher fields the *carrier mobility* becomes field-dependent. The difference between the built-in and the external fields relates to the influence of carrier heating on the mobility, since the *averaging process* for determining the mobility uses the corresponding distribution functions. For instance, with an electric field in the x-direction, for the drift velocity of electrons one obtains

$$v_{\mathrm{D}} = \mu_n F_x = \bar{v}_x = \frac{\iiint v_x f(v) g(v) \mathrm{d}^3 v}{\iiint f(v) g(v) \mathrm{d}^3 v}, \tag{A.4}$$

where $g(v)$ is the density of states in the conduction band per unit volume of velocity space, and $\mathrm{d}^3 v$ is the appropriate volume element in velocity space. If F_x is the built-in field F_i, then the distribution function is the Boltzmann function $f_{\mathrm{B}}(v)$. If F_x is the external field F_{e}, the distribution function is modified due to carrier heating according to the field strength $f_{F_{\mathrm{e}}}(v)$.

The averaging process involves the distribution function, which is modified by both scattering and effective mass contributions. This is addressed in numerous papers dealing with external fields (for a review, see (Coltman and Marshal 1947; Murray and Meyer 1961); see also (Inoue et al. 1998; Schultz and Smith 1993)). In contrast, when only a built-in field is present, the averaging must be done with the undeformed Boltzmann distribution, since lattice and electron temperatures remain the same at each point of the semiconductor.

When an optical excitation is present and/or the semiconductor shows electronic conduction in multi-valley semiconductors, the resulting analysis is more complex, but resorts to the same principles as discussed earlier. For an example see Yurchenko (1993).

A.3 Device Cooling when Electric Energy Is Extracted from Devices Exited with Light

An interesting, often overlooked consequence of entropy production is the intricate interaction between external parameters such as optical excitation and applied voltages. This can be easily seen by the seemingly unrelated heating of solar cells in sun light and their electrical energy production. An uneducated observer may conclude, that such solar cells can be used to directly extract heat that is directly related to the absorption of sunlight, and in addition can extract electrical energy from the photo-voltaic effect. But both are related to each other via entropy production. When one part of the energy is extracted, e.g., the electrical energy, then the other part, the heat, must change: the solar cell must lower its temperature. Inversely, when the temperature of a solar cell is lowered, e.g., by cooling it, the solar cell electrical efficiency must increase.

We will explain this later in more detail and will give an experimental example when measuring the temperature on a solar panel before and after extracting electrical energy from it (Böer 1990).

A.3.1 Detailed Energy Balance

To obtain an insight into the intricate relationship we must provide a detailed energy balance between the different parts of energies as shown in Fig. A.3 and expressed by

$$E_{\text{in}} = E_{\text{opt}} + E_{\text{th}} = E_{\text{refl}} + E_{\text{PV}} + \varepsilon\sigma T^4 + h_1(T - T_s) + h_2(T - T_{\text{extr}}), \quad \text{(A.5)}$$

with E_{opt} the optical excitation energy (for solar cells exposed to sunlight this is described as *insolation*), $E_{\text{th}} = \sigma T^4$ the thermal energy from the surroundings at a temperature of $T = T_s$ and the coefficients h_1 and h_2 describing the thermal heat transfer to the surrounding and a heat extracting (cooling) medium at the other surface. ε is the emissivity from the cell. $E_{\text{refl}} = \kappa E_{\text{opt}}$ with κ the optical reflectivity, and $E_{\text{PV}} = \eta E_{\text{opt}}$ with η the photo-voltaic efficiency of the cell. σ is the Stephan Boltzmann constant $5.67 \times 10^{-8}\,\text{W m}^{-2}\,\text{K}^{-4}$. Without extraction of electrical energy (open switch S in Fig. A.3) we obtain for the cell temperature T_1 the implicit equation

$$E_{\text{opt}}(1 - \kappa) + \sigma T_{\text{extr}}^4 = (\varepsilon_1 + \varepsilon_2)\sigma T_1^4 + h_1(T_1 - T_s) + h_2(T_1 - T_{\text{extr}}) \quad \text{(A.6)}$$

with ε_1 and ε_2 the emissivity from the front and the back surface of the cell, respectively.

When closing the switch S and extracting electrical power from the cell at maximum power point, we obtain a similar equation, except for now including

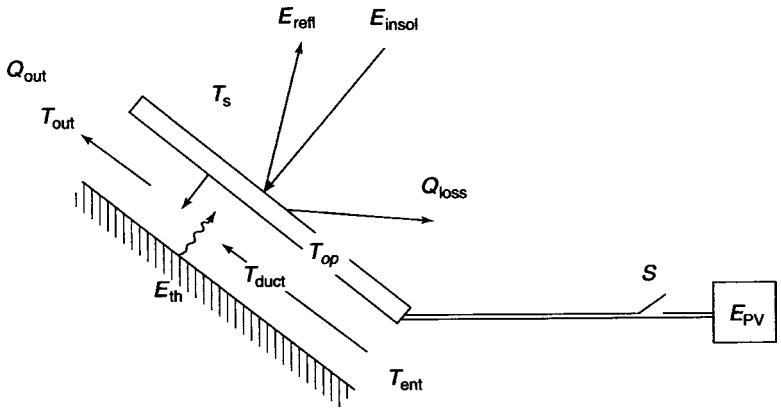

Fig. A.3. Energy balance of a solar cell within a hybrid collector. The energy input is given by the insolation E_{opt} and the thermal radiation composed of the thermal radiation from the surrounding front and the back. The useful energy is divided between the electrical energy E_{PV} and the heat out Q that is the sum of the heat radiated out from the front Q_{loss} and the extracted heat Q_{extr}, here assumed to be from air in an air duct below the cells at a temperature T_{duct} (averaged), heating the air from the inlet at T_{ent} to the temperature at the outlet T_{out}. During the operation, the temperature of the cell is increased to T_{op}, that is more precisely distinguished in the text between T_1 and T_2 without and with extraction of electrical power

the extracted electrical energy, and specifically using the efficiency η that has now to be evaluated at the lower cell temperature T_2[2]

$$E_{\rm opt}(1-\kappa-\eta)+\sigma T_{\rm extr}^4=(\varepsilon_1+\varepsilon_2)\sigma T_2^4+h_1(T_2-T_s)+h_2-T_{\rm extr}). \quad \text{(A.7)}$$

Since most of these parameters are known to a reasonable degree, (A.6) and (A.7) can be used to obtain the reduction of the cell temperature when electric energy is extracted.

In a simple first approximation the temperature difference can be obtained from subtracting (A.6) from (A.7) and developing the Stephan Boltzmann part with the approximation $T1^4-T_2^4=\left(T_1^2+T_2^2\right)(T_1+T_2)(T_1-T_2)\simeq 4T_{\rm op}^3(T_1-T_2)$, with the average operational temperature $T_{\rm op}\simeq(T_1+T_2)/2$. This yields for the cooling of the cell with electrical power extraction

$$\Delta T=\frac{T_1-T_2}{4\varepsilon T_{\rm op}^3+h_1+h_2}=\eta E_{\rm opt}. \quad \text{(A.8)}$$

The estimated temperature differences for solar panels as estimated from (A.8) are given in Fig. A.4 for typical parameter values and for an insolation of 1,000 W cm^{-2} as a function of the cell efficiency and lie between 4 and 20 °C.

In an actual setting of a solar roof on the Guest house of Solar Knoll in Kennett Square, PA, (Böer 2001) the rise and fall of the temperature of the solar cells in the panels on the roof was measured with the thermo-couples and registered after switching off and switching on, respectively, of the electric

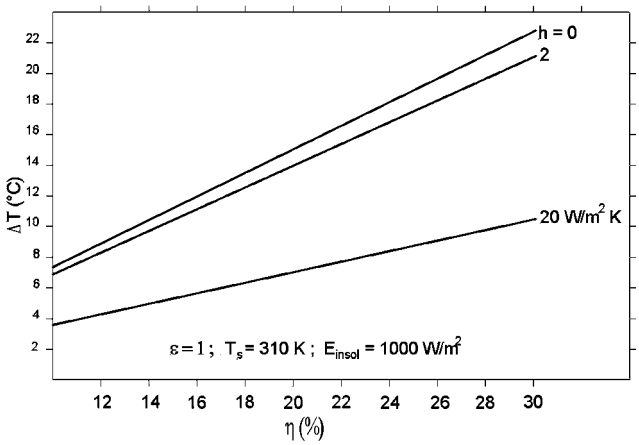

Fig. A.4. Cooling temperature difference of a solar cell when exposed to sunlight at 1,000 W cm^{-2} with an electric load at maximum power point as a function of the cell efficiency. Other parameters are given in the figure

[2] The PV efficiency depends on the temperature and increases with decreasing temperature.

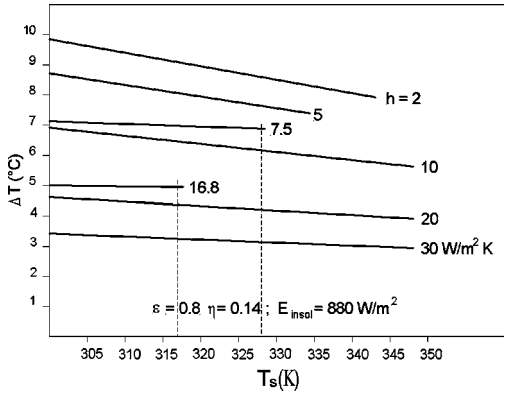

Fig. A.5. Temperature difference from cooling when electric power is extracted from a solar panel calculated from (A.8) after stationarity is reached at an insolation of 880 W m^{-2} as a function of the outside temperature. The average heat transfer coefficient h is family parameter. The values 7.5 and 16.8 are indicated corresponding to the measured cooling temperatures at calm and 10 m s^{-1} wind velocity

load tuned close to the maximum power point. With 14% conversion efficiency of the panel and on a hazy day with 880–900 W m^{-2}, the cooling or heating takes about 10 min to become stationary as shown in the lower curves of Fig. A.5.

The values of the heat transfer coefficients can be estimated from the family of curves for different heat transfer coefficients in Fig. A.5 that shows the calculated cooling temperature ΔT as a function of the outside temperature T_s and an estimated $\varepsilon = 0.8$ at an insolation of 880 W cm^{-2}. From the measured values of ΔT of 7° one obtains a heat transfer coefficient of about 7.5, and a few minutes later when the wind velocity has picked up from calm to 10 m s^{-1} of about 10.8 W cm^{-2} K^{-1}.

Even though these temperature differences are relatively small in normal solar panel operation and are not reported, they can be substantial when solar concentration is used and cell efficiencies are higher. They are estimated to exceed 100°C with cells of 20% efficiency when exposed to a sunlight concentration of 1,000 (Böer 1990).

Summary and Emphasis

In this chapter we have indicated the difference between an external field, impressed by an applied bias and the built-in field, due to space-charge regions within the semiconductor. The external field causes carrier heating by shifting and deforming the carrier distribution from a Boltzmann distribution to a distorted distribution with more carriers at higher energies within the band.

In contrast, the built-in field leaves the Boltzmann distribution of carriers unchanged; the carrier gas remains unheated at exactly the same temperature as the lattice at every volume element of the crystal, except for statistical fluctuations.

On the other hand, the extraction of electrical power causes a reduction of the temperature of any photo-voltaic device that is exposed to light. Here again the entropy of the system has to be carefully evaluated.

The important consequence of the difference between external and built-in fields is the difference in determining the field dependence of the mobility, which requires an averaging over carriers with different energies within the band. For a built-in field, the averaging follows a Boltzmann distribution; in an external field, there are more electrons at higher energies, and the distribution is distorted accordingly. This can have significant impact for the evaluation of device performances when high fields are considered.

With light, the extraction of electric power causes the temperature of a photo-voltaic device to decrease.

B

Generalized Transport Equations

As a generalized set of transport equations one may start from

$$j_n = n\mu_n \nabla E_{Fn} - L_n \nabla T, \tag{B.1}$$

$$j_p = p\mu_p \nabla E_{Fp} - L_p \nabla T. \tag{B.2}$$

The first term contains the generalized drift and diffusion, the second term describes temperature effects, such as the Seebeck-effect. Within an isotropic material and at constant temperatures this set of equations reduces to

$$j_n = n\mu_n \nabla E_c + eD_n \nabla n - eD_n \nabla_\zeta n, \tag{B.3}$$

$$j_p = p\mu_p \nabla E_v + eD_p \nabla p - eD_p \nabla_\xi p \tag{B.4}$$

with $\zeta = E_c - E_{Fn}$ and $\xi = E_{Fp} - E_v$. The diffusion constants are related to the carrier mobility by the generalized Einstein relations:

$$eD_n \equiv \frac{n}{\frac{\mathrm{d}n}{\mathrm{d}\zeta}}\mu_n \quad \text{and} \quad eD_p \equiv \frac{p}{\frac{\mathrm{d}p}{\mathrm{d}\xi}}\mu_p. \tag{B.5}$$

The gradients of n and p for constant ζ and ξ, respectively, are given by

$$\nabla\zeta = \int_0^\infty f^0 \nabla_W g_c(W, \mathbf{r})\mathrm{d}W, \tag{B.6}$$

$$\nabla\xi = \int_{-\infty}^0 f^0 \nabla_W g_v(W, \mathbf{r})\mathrm{d}W. \tag{B.7}$$

For parabolic bands, (B.6) reduces to

$$\nabla\zeta = \frac{3n}{2}\nabla \ln\left(\frac{m_n}{m_0}\right), \tag{B.8}$$

indicating that electrons tend to move in direction of an increasing effective mass.

With graded semiconductors one needs to include a quasi-drift term that takes into consideration the sloping of the bands due to the composition grading, χ, yielding as an explicit transport equations:

$$j_n = en\mu_n F_{bi} - n\mu_n \nabla\chi + eD_n \nabla n - 1.5n\mu_n kT\nabla\frac{m_n}{m_0}, \tag{B.9}$$

$$j_p = ep\mu_p F_{bi} + p\mu_p \nabla(E_g + \chi) - eD_p \nabla p - 1.5p\mu_p kT\nabla\frac{m_p}{m_0}. \tag{B.10}$$

For more and citation of the original literature see Marshak (1989).

B.1 Modified Poisson Equation

The Poisson equation relates the potential to the space charge in the semiconductor. When the dielectric function becomes position-dependent, an additional term appears in the Poisson equation:

$$\varepsilon\varepsilon_0\nabla^2\psi + \nabla\varepsilon\cdot\nabla\psi = -\varrho(\mathbf{r}) = -e\left(p - n + N_\mathrm{d} - N_\mathrm{a} - \sum n_{ti}\right) \tag{B.11}$$

with $\sum n_{ti}$ the sum of all net negatively charged traps minus the positively charged traps. In the book we have used the electron potential that relates to the potential as $\psi = -\psi_n$.

B.2 Continuity Equation

The continuity equations for electrons and holes depend on the local density of recombination centers and traps directly, and they are given by

$$\frac{\partial n}{\partial t} = G_n(\mathbf{r}) - R_n(\mathbf{r}) + \frac{1}{e}\nabla\cdot\mathbf{j_n}, \tag{B.12}$$

$$\frac{\partial p}{\partial t} = G_p(\mathbf{r}) - R_p(\mathbf{r}) - \frac{1}{e}\nabla\cdot\mathbf{j_p}. \tag{B.13}$$

In addition, the local balance in traps need to be considered, to account for all recharging of centers, which enter the Poisson equation and modify the generation and recombination traffic by storing part of the free carriers.

There are just a few examples of extensions of the governing system of equation to handle a large variety of possible modifications of the simple *pn*-junction discussed in this book.

A Few Words at the End

A few words at the end of this text may be in order. We have guided you through the many fields of space charge effects in solids and even in the two

appendices we introduced you to some more sophisticated parts of the basics. We have shown how space charges are created and how they are influenced by internal device parameters, such as doping and external surfaces, such as electrodes. We have shown how these space charges change under the influence of an external electric field or with light excitation. We have guided you through the set of main equation that determines the basic behavior of such space charge distributions, the transport equations, the continuity equations and the Poisson equation. Though this set cannot be integrated with a polynomial in well-tabulated functions, its solutions are accessible through numerical integration, and we have done this for numerous examples. These examples have guided you step by step into more and more complex devices and analyzed the different phenomena involved.

Even though we have reserved more sophisticated parts of the discussion and more complex devices for the following book on *Advanced Aspects of Space Charge Effects in Solids*, we have added a few sections within the book and the Appendices at the end to give some insight into some of the intricacies that you may want to remember when discussing the actual devices and their behavior.

It may be worth after you have come to the end of these pages, to return once more to all the major parts of the book with their emphases and conclusions, to keep in your mind, the tools that are necessary to analyze the operation of any semiconductor device in more detail – beyond describing it by an empirical network of diodes and resistors that may give you enough adjustable parameters to explain almost any current–voltage characteristics but also provides you with ample opportunities for misleading and expensive judgments.

Bibliography

Agarwal SC (1995) Bull Mater Sci 18:669

Agranovich VM, Dubovsky OA, Basko DM, La Rocca GC, Bassani F (2000) J Lumin 85:221

Agrawal BK, Agraval S, Srivastava R (1999) Surf Sci 424:232

Akiyama H (1998) J Phys: Condens Matter 10:3095

Albrecht S, Reining L, Sole RD, Onida G (1998) Phys Rev Lett 80:4510

Aliev GN, Datsiev RM, Ivanov SV, Kop'ev PS, Seisyan RP, Sorokin SV (1996) J Cryst Growth 159:523

Andersen OK (1973) Solid State Comm 13:133–136

Anderson PW (1958) Phys Rev 109:1492

Aono R, Kuemmerl L, Haarer D (1993) Jpn J Appl Phys Part 1 32:5248

Aono M, Katayama M, Nomura E (1992) Nucl Instr Meth (1992) B64:29

Aroutiounian VM, Ghoolinian MZh (2000) Proc SPIE 4060:124

Auciello O (1994) Pulsed laser ablation-deposition and influence on film characteristics. In: Hurle (ed) Handbook of crystal growth. North Holland, Amsterdam

Aulbur WG, Jonsson L, Wilkins JW (2000) Solid State Phys 54:1–218; Ehrenreich H, Spaepen F (eds) Academic Press, New York

Aydinli A, Gasanly NM, Yilmaz I, Serpenguzel A (1999) Semicond Sci Tech 14:657

Baeri P, Campisano SU (1994) Rapid solidification of silicon by pulsed laser annealing. In: Hurle (ed) Handbook of crystal growth. North Holland, Amsterdam

Bagraev NT, Bertolotti M (1990) J Non-Cryst Solids 125:58

Banghard EK (1988) Proc 20th IEEE Photovoltaic Specialists Conference, Las Vegas, p 717

Baranovskii SD, Doerr U, Thomas P, Naumov A, Gebhardt W (1994) Solid State Comm 89:5

Basol BM, VK Kapur (1990) IEEE Photovoltaic Specialists Conference, p 546

Bauer S, Rosenauer A, Link P, Kuhn W, Zweck J, Gebhardt W (1993) Ultramicroscopy 51:221

Baume P, Kubacki F, Gutowski J (1994) J Cryst Growth 138:266

Bauser E (1994) Atomic mechanisms of LPE. In: Hurle (ed) Handbook of crystal growth. North Holland, Amsterdam

Baylac B, Marie X, Amand T, Brusseau M, Barrau J, Shekun Y (1995) Surf Sci 326:161

Beeby JL, Hayes TM (1989) J Non-Cryst Solids 114:253
Berg A, Brough L, Evans JH, Lorimer G, Peaker AR (1992) Semicond Sci Tech 7:263
Bergman L, Nemanich RJ (1996), Annu Rev Mater Sci 26:551
Bimberg D, Grundmann M, Ledenstov NN (1999) Quantum dot heterostructures. Wiley, UK
Blasse G, Grabmaier BC (1944) Luminescent materials. Springer, Berlin, pp 170–193
Böer KS (1979) J Appl Phys 50:5356
Böer KW (1965) Phys Rev 139 A:1949
Böer KW (1976) Phys Rev B 13:5373
Böer KW (1976) Phys Stat Sol (a) 49:13
Böer KW (1977) Phys Stat Sol (a) 40:355
Böer KW (1981) J Appl Phys 51:4518
Böer KW (1985) Ann Physik 42:371
Böer KW (1990) Survey of semiconductor physics, vol I, Ist edn. Van Nostrand Reihold, New York
Böer KW (2001) Phys Stat Sol 184:201
Böer KW (2000) Survey of semiconductor physics, vol II, 2nd edn. Wiley, New York
Böer KW (2009) Phys Stat Sol 206:2489
Böer KW, Dussel GA (1970) Phys Stat Sol 30:375, 391
Böer KW, Tamm G (2004) J Solar Energy 34:102
Böer KW, Voss P (1968) Phys Rev 171:899
Böer KW, Dussel GA, Voss P (1968) Phys Rev 169:700 and 170:703
Böer KW, Stirn RJ, Dussel GA (1973) Phys Rev B 1433, 1443
Bohm JA Lüdge, Schröder W (1994) Crystal growth by floating zone melting. In: Hurle (ed) Handbook of Crystal Growth. North Holland, Amsterdam
Bohm M, Hennecker F, Hofstaetter A, Luh M, Meyer BK, Scharmann A, Condratiev OV, Korzhik MV (1998) Radiat Eff Defects Solid 150:413
Bonnet D (ed) (1992) Thin film solar cells, Int J Sol Energ 12:1–4
Borse PH, Deshmuk N, Shinde RF, Date SK, Kulkarni SK (1999) J Mater Sci 34:6087
Bouhelal A, Albert JP (1989) Solid State Comm 69:713
Bouhelal A, Albert JP (1993) Phys B: Condens Matter 6:255
Bradley AL, Doran JP, Hegarty J, Stanley RP, Oesterle U, Houdre R, Ilegems M (2000) J Lumin 85:261
Branchu S, Pailloux E, Garem H, Rabier J, Demenet JL (1999) Phys Stat Sol (A) 171:59
Briggs D, Seah MP (1990) Practical surface analysis, 2nd edn vol 1. In: Auger and x-ray photoelectron spectroscopy. Wiley, Chichester
Briggs D, Seah MP (1992) Practical surface analysis, 2nd edn vol 2. In: Ion and neutral atom spectroscopy. Wiley, Chichester
Brochard S, Rabier J, Grilhe J (1998) EPJ Appl Phys 2:99
Broser I (1967) In: Aven M, Prener JS (eds) Physics and chemsitry of II-VI compounds. North Holland, Amsterdam
Broser I (1998) Physicalische Blätter 54:935
Broser I, Kallmann H (1947) Z Naturf 2a:439
Broser I, Herfort L, Kallmann H, Martius U (1948) Z Naturf 3a:6
Bube RH (1992) Electronic properties of semiconductors. Cambridge University Press, Cambridge, UK

But'ko VG, Tolpygo KB (1983) Sov Phys Semicond 17:1135
Butler KH (1980) Fluorescent lamp phosphors. The University of Pennsylvania Press, University Park
Byrappa K (1994) Hydrothermal growth of crystals. In: Hurle (ed) Handbook of crystal growth. North Holland, Amsterdam
Cardona M, Ley L (eds) Topics in applied physics, vol 26. Springer, Berlin
Chakraborty PK, Biswas JC (1997) J Appl Phys 82:3328
Chavez-Pirson A, Ando H, Saito H, kanbe H (1994) Appl Phys Lett 64:1759
Chemla DS (1999) Semiconductors and semimetals, vol 58. Academic Press, New York, Chapter 3
Chen N (2000) Diffusion and Defect Data. Part A: Defect and Difusion Forum 183:85
Chen R (1969) J Appl Phys 40:570
Chen TP, Chen LJ, Huang TS, Guo YD (1992) Semiconduct Sci Tech 7:300
Cheng Y (1993) L Phys D: Appl Phys 26:1109
Cheyssac P, Sterligov VA, Lysenko SL, Kofman R (1999) Phys Stat Sol (A) 175:253
Cho GC, Kütt WA, Kurz H (1990) Phys Rev Lett 65:764
Cho SM, Lee HH (1994) J Appl Phys 75:3199
Clark RJH, Hester RE (eds) (1998) Spectroscopy for surface science. Wiley, New York
Collins CL, Yu PY (1984) Phys Rev B 30:4501
Coltman JW, Marshal F-H (1947) Nucleonics 1:58
Conwell EM (1967) High-field transport in semiconductors. Academic Press, New York
Cotal HL, Maxson JB, McKeever SWS, Cantwell E (1994) Appl Phys Lett 64:1532
Crljen Z (2000) J de Physique IV:JP, 10:Pr5-351
Cundiff ST, Steel DG (1992) IEEE J Quant Electron 28:2423
Czajkovski G, Dressler M, Bassani F (1997), Phys Rev (B): Condens Matter 55:5243
Dahan F, Fleurov V (1994) J Phys Condens Matter, 6:101
Dahan P, Fleurov V, Kikoin KA (1995) Mater Sci Forum 196:755
Dai-sik Kim and Peter Y, Yu (1990) Phys Rev Lett 64:946
Damen TC, Vina L, Leo K, Cunningham JE, Shah J, Sham LJ (1992) Proc SPIE 1677:220
Davidov VYu, Subashiev AV, Cheng TS, Foxon CT, Goncharuk LN, Smirnov AN, Zolotareva RN (1998) Mater Sci Forum 264–268:1371
Davis JR, Nazare K (1994) Mater Sci Forum 143 105
Davydov VYu, Subashiev AV, Cheng TS, Foxon CT, Goncharuk IN, Smirnov AN, Solotareva RV, Ludyn WV (1998) Mater Sci Forum 264:1371
De Raedt H, Lagendijk A, de Vries P (1989) Phys Rev Lett 62:47
De Souza MM, Amaratunga GAJ (1994) Comput Mater Sci 3:69
Di Bartolo B (1984) Energy transfer processes in condensed matter. Plenum Press, New York
Dimitruk NL, Barlas TR, Pidlisnyi EV (1993) Surf Sci 293:107
Dimoulas A, Leng J, Giapis KP, Georgakilas A, Halkias G, Christou A (1993) Appl Surf Sci 63:191
DiVentra M, Peressi M, Baldereschi A (1996) Phys Rev B: Condens Matter 54:5691
Djordjevic BR, Thorpe MF, Wooten F (1995) Phys Rev B 52:5685
Donegan JF, Doran JP, Stanley RP, Hegarty J, Feldman RD, Austin RF (1985) Appl Surf Sci 50:321
Dong J, Drabold DA (1998) Phys Rev Lett 80:1928

Drabold DA (1996) Amorphous insulators and semiconductors. In: Thorpe MF, Mitkova MI (eds) NATO ASI Series, vol 23 p 405
Drabold DA et al. (1994) Phys Rev B 49:16415
Drabold DA, Nakhmanson S, Zhang X (2001) In: MF Thorpe, Tichy L (eds). Properties and applications of amorphous materials Kluwer, Dordrecht p 221
Dreyhsig J (1998) J Phys Chem Solid 59:31
Dubey S, Ghosh S (1997) J de Physique I 7:1445
Dussel GA, Böer KW (1970) Phys Stat Sol 39:375
Dussel GA, Böer KW, Stirn RJ (1973) Phys Rev 7:1443
Ebert W, Vescan A, Borst TH, Kohn E (1994) IEEE Electron Device Lett 15:289
Efros AL, Rodina AV (1989) Solid State Comm 72:645
Esser AE Runge, Zimmermann R, Langbein W (2000) Phys Stat Sol A 178:489
Esser N, Kopp M, Haier P, Richter W (1993) J Electron Spectro Relat Phenom 64–65:85
Estreicher SK, Jones R (1994) Appl Phys Lett 64:1670
Fahrenbruch AL, Bube RH (1983) Fundamentals of solar cells. Academic Press, New York
Fan TW, Qian JJ, Wu J, Lin LY, Yuan J (2000) J Cryst Growth 213:276
Farber BYa, Lunin Yul, Nikitenko VI, Orlo VI (1991) Proceeding 4th International Meeting on Gettering and Defect Engineering in Semiconductor Technology, GADEST'91, Oct. 1991, 311
Feenstra RM (1994) Surf Sci 299:965
Feher G (1998) Foundation of modern EPR, Chapter H. Eaton Gr, Eaton SS, Salikov KM (eds) World Science, Singapore
Feklisova O, Yarkin N, Yakimov Eu, Weber J (1999) Phys B: Condens Matter 273:235
Feng PK (1999) Surf Sci 429:L469
Feng S (1990) Scattering and localization of classical waves in random media. World Scientific, Singapore
Figlarz M, Gerand B, Delahaye-Vidal A, Dumont B, Harb F, Coucou A, Fievet F (1990) Solid State Ionics 43:143
Fijol JF, Holloway PH (1996) Crit Rev Solid State Mater Sci 21:77
Fleurov V, Dahan F (1995) Proc SPIE 2706:296
Foxon CT (1994) Principle of molecular beam epitaxy. In: Hurle (ed) Handbook of Crystal Growth North Holland, Amsterdam
Franceschetti A, Zunger A (1997) Phys Rev Lett 78:915
Franz W (1958) Z Naturforsch 13A:484
Frenkel JI (1938) Phys Rev 54:647
Fricke C, Neukirch U, Heitz R, Hoffmann A, Broser I (1992) J Cryst Growth 117:783
Fricke C, Hetiz R, Lummer B, Kutzer V, Hoffmann A, Broser A, Taud W, Heuken M (1994) J Cryst Growth 138:815
Fritsch J, Arnold M, Eckl C, Honke R, Pavone P, Schroeder U (1999) Surf Sci 427–428:58
Fritzsche H (1997) Mater Res Soc Symp Proc 467:19
Fromer NA, Schuller C, Chemla DS, Shahbazyan TV, Perakis IE, Maranowski K, Gossard AC (2000) Conf Quantum Electronics and Laser Science (QELS), Technical Digest May 7–12, p 174
Froyen S, Wood DM, Zunger A (1987) Thin Solid Films, 183:33

Ganichev SD, Ziemann E, Prettl W, Istratov AA, Weber ER (1999) Mater Res Soc Symp Proc 560:239
Garcia-Cristobal A, Cantarero A, Trallero-Giner C, Cardona M (1998) Phys B: Condens Matter 263:809
Gartia RK, Singh ST, Singh ThSC, Mazumdar PS (1992) J Phys D: Appl Phys, 25:530
Geisz JF et al (2008) Appl Phys Lett 93:123505
Gerthsen D, Ponce FA, Anderson GB (1989) Phil Mag A: Phys Condens Matter, Defects and Mechanical Properties, 59:1045
Gilmer GH (1993) Atomic scale models of crystal growth. In: Hurle (ed) Handbook of crystal growth. North Holland, Amsterdam
Girlanda R, Savasta S, Quattropani A (1994) Solid State Comm, 90:267
Glicksman ME, Marsh SP (1993) The dendrite. In Hurle (ed) Handbook of Crystal Growth. North Holland, Amsterdam
Gorczyca I, Svane A, Christensen NE (1997) Solid State Comm 101:747
Gordienko YuE, Borodin BG, Smuglii VI (1998) Telecomm Radio Eng 52:47
Gray PE (1967) Physics of electronics and circuit models. Wiley, New York
Gray JL, Schwartz RJ (1984) 17th IEEE Photovoltaic Specialists Conference, Kissimee, FL, p 1297
Gray JL, Schwartz RJ, Lundstrom MS, Nasby RD (1982) Proc. 16th IEEE Photovoltaic Specialists Conference, San Diego, CA, p 437
Green MA (1982) Solar cells Prentice-Hall, NJ
Green MA (1997) Proc 26th IEEE Photovoltaic Specialists Conference, Las Vegas, p 717.
Green MA, Emery K, Hishikawa Y, Warta W (2009) Progr Photovoltaic: Res Appl 17:85
Greulich-Weber S (1997) Phys Stat Sol (A) 162:95
Gross EF, Permogor SA, Reznitz AN, Usarov EN (1974) Sov Phys Semiconduct USSR 7:844
Guissi S, Bindi R, Iacconi P, Jeambrun D, Lapraz D (1998) J Phys D: Appl Phys 31:137
Gunn JB (1963) Solid State Comm 1:88
Gutakovski AK, Fedina LL, Aseev AL (1995) Phys Stat Sol (A) 150:127
Gutsche E, Lange H (1964) Proc VII International Conference on Semiconductor Physics, Paris, p 129
Haefke H, Hofmeister H, Krohn M, Panov A (1991) J Imag Sci 35:164
Hamakawa Y (1999) Appl Surf Sci 142:215
Hao M, Sugahara T, Sato H, Morishima Y, Naoi Y, Romano LT, Sakai S (1998) Jpn J Appl Phys (2) 37:L291
Hasegawa H (1999) Japanese J App Phys Part I 38:1098
Hasegawa T, Hotate K (1999) Proc SPIE 3860:306
Hass M (1967) Lattice reflections In: Optical properties of II-V compounds, semiconductors and semimetals 3:3
Hedin L, Lundqvist S (1969) Solid State Phys 23; Seitz F, Turnbull D, Ehrenreich H (eds) Academic Press, New York
Heitz R, Hoffmann A, Broser I (1992) Opt Mater 1:776
Helleman A (1999) Science 284:24
Henisch HK (1984) Semiconductor contacts. Clarendon Press, Oxford, UK
Henry CH, Logan RA, Merrit FR (1978) J Appl Phys 49:3530

Higman JM, Bude J, Hess K (1991) Comput Phys Comm 67:93
Hirayama H, Asahi H (1994) MBE with gaseous source. In: Hurle (ed) Handbook of crystal growth. North Holland, Amsterdam
Hofstadter R (1948) Phys Rev 74:100
Holzl J, Schulte FK (1979) Springer tracts in modern physics. Höhler G (ed). Springer, Berlin pp 1–150
Honold AL, Schultheis L, Kuhl J, Tu CW (1989b) Ultrafast phenomena VI. Yajima T, Yoshihara K, Harris CB, Shionoya S, Springer Ser Chem Phys 48. Springer, Berlin, p 307
Honold A, Schultheis L, Kuhl J, Tu CW (1989a) Phys Rev B 40:6442
Horiguchi S (1990) Superlattice Microst 23:355
Huber DL (1982) J Lumin 27:333
Hurle DTJ (ed) (1994) Handbook of crystal growth. North Holland, Amsterdam
Hurle DTJ (ed) (1994a) Thin films and epitaxy. In: Handbook of crystal growth, vol 3. North Holland, Amsterdam
Hurle DTJ, Cockayne B (1994) Czochralski growth. In: Hurle (ed) Handbook of crystal growth. North Holland, Amsterdam
Hvam JM, Lyssenko VG, Schwab H (1992) J Cryst Growth 117:773
Hvam JM, Langbein W, Borri P (1999) Proc SPIE 3624:40
Hybertson MS, Loui SG (1985) Phys Rev Lett 55:1418
Ibach H (1991) Electron energy loss spectrometer: The technology of high performance. Springer, Berlin
Illekova E, Cunat Ch (1994) J Non-Crys Solids 172:597
Inoue K, Minami F, Kato Y, Yoshida K, Era K (1992) J Cryst Growth 117:738
Inoue M, Suzuki K, Amasuga H, Nakamura M, Mera Y, Takeuchi S, Maeda K (1998) Ultramicroscopy 75:5
Irmer G, Herms M, Monecke J, Volicek V, Gregora I (1993) Solid State Comm 87:99
Iwai Y, Yano M, Hagiwara R, Inoue N (1992) Surf Sci 267:434
Jackson JD (1999) Classical electrodynamics, 2nd ed. Wiley, New York
Jacobini C, Canali C, Ottoviani G, Cluaraula AA (1977) Solid State Electr 20:71
Jagla EA, Prestipino S, Tosatti E (2000) Surf Sci 454:608
Jaros M, Hagon PL, Wong KB (1989) Vacuum 41:712
Jensen KF (1994) Transport phenomena in vapor phase eptitaxy. In: Hurle (ed) Handbook of Crystal Growth. North Holland, Amsterdam
Joannopoulos NF, Meade RD, Winn JN (1995) Photonic crystals: Molding the flow of light. Princeton University Press, NJ
Joannopoulos NF, Villeneuve PR, Fan S (1997) Photonic crystals: Putting a new twist on light. Nature (London) 386:143
John S (1993) Photonic band gaps and localization. Souklouis CM (ed) Plenum Press, New York, p 1
Jones ED, Modine NA, Allerman AA, Fritz IJ, Kurtz SA, Wright AF, Tozer ST, Wei X (1999) Proc SPIE 3621:52
Justo JF, Bulatov VV, Yip S (1997) Scripta Mater 36:707
Kaldis E, Piechotka M (1994) Bulk crystal growth by physical vapor transport. Hurle (ed) Handbook of crystal growth North Holland, Amsterdam
Kalt H (1994) J Lumin 60:262
Kalt H (1996) Optical properties of III-V semiconductors. The influence of multivalley band structure. Springer, Berlin
Kamieniecki E (1990) Proc Electrochem Soc 90:1856

Kaplan TA, Mahanti SD (eds) (1995) Electronic properties of solids using cluster methods. Plenum Press, New York
Karafyllidis Y, Hagouel P, Kriezis E (1900) Microelectron J 21:41
Kassah K, Bouarissa N (2000) Solid State Electron 44:501
Keldysh LV (1958) Sov Phys JETP (Engl Transl) 4:665
Kevan SD (ed) (1992) Angle resolved photoemission, theory and current applications. Elsevier, Amsterdam
Kim DS, Yu PY (1991) Phys Rev B 43:4158
Kim DS, Shah J, Cunningham JE, Damen TC, Schäfer W, Hartmann M, Schmitt-Rink S (1992a) Phys Rev Lett 68:1006
Kim DS, Shah J, Damen TC, Schäfer W, Jahnke F, Schmitt-Rink S, Köhler K (1992b) Phys Rev Lett 69:2725
Kim TG, Wang X-L, Ogura M (2000) Jpn J Appl Phys Part I 39:2516
King RR et al (2007) Appl Phys Lett 90:183516
Kisker DW, Kuech TF (1994) Organo-metallic vapor phase epitaxy: principles and practices. In: Hurle (ed) Handbook of crystal growth. North Holland, Amsterdam
Klemens PG (1966) Phys Rev 148:845
Kobayashi Y, Kouzo K, Kamimuro H (1999) Solid State Comm 109:583
Kohno M, Matsubara H, Okada H, Hirae S, Sakai T (1998) Jpn J Appl Phys 1 37:5800
Kolev PV, Deen MJ, Kierstead J, Citterio M (1999) IEEE Trans Electron Dev 46:204
Kono S, Nagasawa N (1999) Solid State Comm 110:159
Kreissl J, Schulz H-J (1996) J Cryst Growth 161:239
Kudlek GH, Pohl UW, Fricke Ch, Heitz R, Hoffmann A, Gutowski J, Broser I (1993) Phys B: Condens Matter 185:325
Kung P, Zhang X, Walker D, Saxler A, Piotrowski J, Rogalski A, Razeghi M (1995) Appl Phys Lett 67:3792
Kuo L-H, Salamanca-Riba L, Hofler GE, Wu B-J, Haase MA (1994) Proc SPIE 2228:144
Kütt WA, Albrecht W, Kurz H (1992) IEEE J Quant Electron 28:2434
Kutzer V, Lummer B, Heitz R, Hoffmann A, Broser I, Kutz E, Hommel D (1996) J Cryst Growth 159:776
Kuwamura Y, Yamada M (1996) Jpn J Appl Phys 35:6117
Laasonen K et al (1993) Phys Rev B47:10142
Lagendijk A, van Tiggelen BA (1993) Phys Rep 270:143
Lambrecht WRL (1997) Solid State Electron 41:195
Lambrecht WRL, Limpijumnong S, Rashkeev S, Segall B (1999) Mater Sci Forum 338:545
Lammert MD, Schwartz RJ (1977) IEEE Trans Electron Dev ED-24:337
Larson P, Mahanti SD, Kanatzidis MG (2000) Phys Rev B61:8162
Laval M, Moszynski M, Alemand R, Comoreche E, Guinet P, Odru R, Vacher J (1983) Nucl Instr Meth 206:169
Lecoq P (1995) Proc Int Conf Inorg Scint, Delft Univ Press, p 52
Lee PA, Ramakrishna TV (1985) Rev Mod Phys 57:287
Lee CD, Kim HK, Park HL, Chung CH, Chang SK (1991) J Lumin 48:116
Lee KF, Ahmad HB (1996) Optic Laser Tech 28:35
Leo K, Wegener M, Shah J, Chemla DS, Göbel EO, Damen TC, Schmitt-Rink S, Schäfer W (1990) Phys Rev Lett 65:1340
Lewis LJ, Mousseau N (1998) Comp Mater Sci 12:210

Lin L, Chen NF, Zhong X, He H, Li C (1998) J Appl Phys 84:5826
Lindefelt U, Persson C (1999) Mater Sci Forum, 338(I):719
Liou JJ, Wong WW, Juan JS (1990) Solid State Electron 33:845
Liu QZ, Lau SS (1998) Solid State Electron 42:677
Lockwood JD (1999) Phase Transitions 68:151
Lugli P, Bordone P, Reggiani L, Rieger M, Kocevar P, Goodnick SM (1989) Phys Rev B 39:7852
Lugli P, Bordone P, Molinari E, Rücker H, de Paula AM, Maciel AC, Ryan JF, Ryan MCJ, Tathan MC (1992) Hot carriers in semiconductor nanostructures: Physics and applications, Shah J (ed) Academic, Boston, p 345
Lundstrom MS, Schwartz RJ, Gray JL (1981) Solid State Electron 24:159
Maes W, De Meyer K, van Overstraeten R (1990) Solid State Electron 33:705
Magonov SN (1996) Surface analysis with STM and AFM: Experimental and theoretical aspect of image analysis. VCH, Weinheim, New York
Mahan GD (1997) Solid State Phys 51, eds. Ehrenreich H, Spaepen F, Academic Press, New York
Mahanti SD, Varma CM (1970) Phys Rev Lett 25:1115
Malpuech G, Kavokin A, Langbein W, Hvam JM (2000) Phys Rev Lett 85:650
Malyshkin V, McGurn AR, Leskova TA, Maradudin AA, Nieto-Vesperinas M (1997) Waves in Random Media 7:479
Marder MP (1998) Condensed matter physics. Wiley Interscience, New York
Markevich VP, Murin LI, Sekiguchi T, Suezawa M (1997) 258:627
Markvart T, Parton DP, Peters JW, Willoughby AFW (1994) Mater Sci Forum 143:1381
Marshak AH (1959) IEEE Trans Electron Dev 36:1764
Mazurak Z (1993) Opt Mater 2:101
McCoy JM, Korte U, Maksym PA, Meyer-Ehmsen G (1992) Surf Sci 24:417
McGurn AR (1990) Surf Sci Rep 10:357
McGurn AR (1999) Phys Lett A 251:322; and Phys Lett A 260:314
McGurn AR (2000) Phys Rev B 61:13235
McKeever SWS (1985) Thermoluminescence of solids. Cambridge University Press, Cambridge
Meilwes N, Spaeth J-M, Emtsev VV, Oganesyan GA (1994a) Semicond Sci and Tech, 9:1346
Meilwes N, Spaeth J-M, Goetz W, Pensl G (1994b) Semicond Sci Tech 9:1623
Meintjes EM, Raab RE (1999) J Optic A: Pure Appl Optic 12:146
Mendik M, Ospelt M, von Kaenel H, Wachter P (1991) Appl Surf Sci 50:303
Milnes AG, Feucht DL (1972) Heterojunctions and metal-semiconductor junctions. Academic Press, New York
Mioc SL, Garland JW, Bennett BR (1996) Semicond Sci Technology 11:521
Misra S (1999) Transition ion data tabulation. In: Poole CP, Farach HA (eds) Handbook of electron spin resonance 2:155
Mita Y, Ide T, Katase T, Yamamoto H (1997) J Lumin 72:959
Moench W (1994) Surf Sci 299:928
Moench W (1997) Appl Surf Sci 117–118:380
Mollenauer LF, Stolen RH, Islam H (1985) Experimental demonstration of soliton propagation in long fibres: Loss compensated by Raman gain, Optic Lett 10:229–231

Monberg E (1994) Bridgeman and related growth techniques. In: Hurle (ed) Handbook of crystal growth. North Holland, Amsterdam
Moretti G (1998) J Electron Spectros Relat Phenom 95:95
Morgenstern M, Wittneven C, Dombrowski R, Wiesendanger A (2000a) Phys Rev Lett 84:5588
Morgenstern M, Haude D, Gudmonsson V, Wittneven C, Dombrowski R, Steinebach C, Wiesendanger R (2000b) J Electron Spectros Relat Phenom 109:127
Mott NF (1999) Metal-insulator transitions. Taylor and Francis, London
Mousseau N, Barkema GT (2000) Phys Rev B 61:1898
Müller EW (1951) Z Phys 131:136
Müller G (1988) Crystals, growth, properties, applications, vol 12. Springer, Berlin
Murray RB Meyer A (1961) Phys Rev 122:815
Mutaftschief B (1993) Nucleation theory in handbook of crystal growth, Hurle (ed) North Holland, Amsterdam
Nabiev RF, Popov YuM (1985) Soviet Physics – Lebedev Institute Reports 2:31
Nag BFR (1980) Electron transport in compound semiconductors. Springer, Berlin
Nakayama T, Murayama M (1999) J Cryst Growth 214:299
Nataka H, Uddin A, Otsuka E (1992) Semicond Sci Tech 7:1266
Neudeck GW (9183) The pn-junction diode. Addison Wesley, Reading, MA
Neugroschel A, Sah CT (1996) Electron Lett 32:2280
Neukirch U, Broser I, Rass R (1990) J Cryst Growth 101:743
Ning XJ, Huvey N (1996) Phil Mag Lett 74:241
Nunoya N, Nakamura M, Yasamoto H, Tamura S, Arai S (2000) Jpn J Appl Phys 39:3410
Oh J-E, Ma W-S, Kim D-Y, Kang T-W (1990) Appl Phys Comm 10:267
O'Leary SK (1999) Solid State Comm 109:589
Opanowicz A (1995) Phys Stat Sol (A) 148:K103
Ozawa L (1990) Cathodoluminescence. VCH, Weinheim
Ozturk E, Straw A, Balkan N (1994) Superlattice Microst 15:165
Patel KD, Modi BP, Srivastava R (1997) Proc SPIE 3316:1225
Petrillo C, Sacchetti F, Di Fabrizio E, Cricenti A, Selci S (1991) Solid State Comm 77:83
Pfeiffer G, Zhou W, Lee JM, Yang CY, Sayers DE, Paesler MA (1994) Solid State Ionics 39:99
Piekara-Sady L, Kispert LD (1994) ENDOR spectroscopy vol 5. In: Poole CP, Farach HA (eds) Handbook of electron spin resonance. I American Institute of Physics Press, New York
Pines AS (1982) Light scattering in solids Cardona M (ed). Springer, Berlin
Pirouz P (1989) Scripta Metall 23:401
Pisani C, Dovesi R, Roetti C (1988) Hartree-Fock ab-initio treatment of crystalline systems. Lecture Notes in Chemistry, vol 48, Springer, Heidelberg
Pocholle J-P, Papuchon M, Raffy J, Survivre E (1990) Revue Technique Thomson 22:187
Polezhaev VJ (1984) Crystals, growth, properties, applications 10. Springer, Berlin
Poole CP, Farach HA (1994) Data sources 1. In: Poole CP, Farach HA (eds) Handbook of electron spin resonance. I American Institute of Physics Press, New York
Poole HH (1921) Philos Mag 42:488
Prince MB (1955) J Appl Phys 26:534

Pritchard J (1979) In: Roberts MW, Thomas JM (eds) Chemical physics of solids, 7. Chemical Society p 166
Racko J, Donoval D, Barus M, Nagel V, Grmanova A (1992) Solid-State Electr 35:913
Ramasamy P (1994) Kinetics of electrocrystallization. In: Hurle (ed) Handbook of crystal growth. North Holland, Amsterdam
Ramos LE, Sipahi GM, Scolfaro MLR, Enderlein R, Leite JR (1997) Superlatt Microst 22:443
Redfield D, Bube R (1995) Mater Sci Symp Proc 325:335
Repins I, Contreras MA, Egaas B, DeHart C, Scharf J, Perkins CL, To B, Noufi R (2008) Progress in Photovoltaics: Res Appl 16:235
Rheinlaender B, Borgulova J, Kovac J, Gottschalch V, Waclavec J (1997) Phys Stat Sol (A) 164:95
Rice A, Jin Y, Ma XF, Zhang X-C, Bliss D, Larkin J, Alexander M (1994) Appl Phys Lett 64:1324
Ridley BK (1997) Electrons and phonons in semiconductor multilayers. Cambridge University Press, Cambridge, UK
Riviere JC, Myhra S (eds) (1998) Handbook of surface and interface analysis: Methods of problem solving. Marcel Dekker, New York
Robinson IK, Tweet DJ (1992) Rep Progr Phys 55:599
Rockett A, Birkmire RW (1991) J Appl Phys 70:81
Rodnyi P (1997) Physical processes in inorganic scintillators. CRC Press, Boga Raton
Ruf T, Wald K, Yu PY, Tsen KT, Morkoc H, Chan KT (1993) Superlatt Microst 13:203
Ruf T, Belitzky VL, Spitzer J, Sapega VF, Cardona M, Ploog K (1994) Solid State Electron 37:609
Sah CT, Noyce RN, Shockley W (1957) Proc IRE 45:1228
Sahyun MRV, Sharma DK, Serpone N (1995) J Imag Sci Techn 39:377
Sakurai T, Sakai A, Pickering HW (1989) Atom probe field ion microscopy and its applications. Academic Press, New York
Sankin VI, Stolichnov IA (1994) JETP Letters 59:744
Sarig S (1994) Fundamentals of aqueous solution growth. In: Hurle (ed) Handbook of crystal growth. North Holland, Amsterdam
Schaefer W, Boehne G, Sure T, Ulbrich RG (1990) J Lumin 45:211
Schappe RS, Walker T, Anderson LW, Lin CC (1996) Phys Rev Lett 76:4328
Schottky W (1939) Z Phys 113:367
Schmidt KH, Linder N, Doehler GH, Grahn HT, Ploog K, Schneider H (1994) Phys Rev Lett 72:2769
Schmidt TM, Fazzio A, Caldas MJ (1995) Mater Sci Forum 196:273
Schmitt OM, Banyai L, Haug H (2000) J Lumin 87:168
Schmitt-Rink S, Chemla DS, Miller DAB (1989) Adv Phys 38:89
Schrepel C, Scherz U, Ulrici W, Thonke K (1997) Mater Sci Forum 258:1075
Schultheis L, Kuhl J, Honold A, Köhler K, Tu CW (1986a) Phys Rev Lett 57:1797
Schultheis L, Honold A, Kuhl J, Köhler K, Tu CW (1986b) Phys Rev B 34:9027
Schultheis L, Honold A, Kuhl J, Köhler K, Tu CW (1986c) Superlattice Microst 2:441
Schultz S, Smith DR (1993) In: Photonic band gaps and localization. Soukoulis CM (ed) Plenum Press, New York, p 305

Schultz O, Glunz SW, Willeke GP (2004) Progress in Photovoltaics: Res and Application 12:553
Schumacher JO, Altermatt PP, Heiser G, Aberle AG (2000) Sol Energ Mater Sol Cell 65:95
Schwarz RJ (1982) Sol Cell 6:17
Seeger K (1999) Semiconductor Physics, 6th edn. Springer Se Sol State Sci, Springer Berlin
Seitz F (1940) The modern theory of solids. McGraw Hill, New York
Shah J (1996a) Ultrafast spectroscopy of semiconductors and semiconductor nanostructures. Springer, Berlin, p 207
Shah J (1996b) Ultrafast spectroscopy of semiconductors and semiconductor nanostructures. Springer, Berlin, p 218
Shah J (1996c) Ultrafast spectroscopy of semiconductors and semiconductor nanostructures. Springer, Berlin, p 217
Shanker J, Bhende WN (1986) Phys Stat Sol (B) 136:11
Sheik-Bahae M, Wang J, van Stryland EW (1994) IEEE J Quant Electron 30:249
Sheng (1990) Scattering and locaization of classical waves in random media. World Scientific, Singapore
Shinozuka Y (1999) Mater Res Symp Proc 588:309
Shionoya S (1991) Met Forum 15:132
Shockley W (1950) Electrons and holes in semiconductors. Van Nostrasnt, Princeton, NJ
Siegman HC, Meyer F, Erbudak M, Landolt M (1984) Spin-polarized electrons in solid state physics. In: Hawkes (ed) Advances in electronics and electron physics. 62 Academic press, Orlando, pp 1–62
Silver M, Pautmeier L, Baessler H (1989) Solid State Comm 72:177
Simmons JH, Pagano SJ, Downie LK, Potter BG, Simmons CJ, Boulos EN, Best MF (1994) J Non-Cryst Solids 178:166
Singh DJ (1994) Planewaves pseudopotentials and the LAPW method. Kluwer, Dordrecht
Small MB, Giess EA, Ghez R (1994) Liquid phase epitaxy. In: Hurle (ed) Handbook of Crystal Growth. North Holland, Amsterdam
Smith GC (1994) Surface analysis by electron spectroscopy. Plenum Press, New York
Soares EA, de Carvalho VE, Nascimento VB (1999) Surf Sci 431:74
Sobolev NA, Shek EI, Kurbakov AI, Rubinova EE, Sokolov AE (1996) Appl Sci (A): Mater Sci Process 62:259
Spaeth J-M, Meise W, Song KS (1994) J Phys Condens Matter 6:3999
Spenke E (1969) Electronic semiconductors. McGraw Hill, NewYork
Srivastava GP (2000) Vacuum 57:121
Stalmans L, Poortmans J, Bender H, Caymax M, Said K, Vazsonyi E, Nijs J, Mertens R (1998) Progress in Photovoltaics: Research and Applications 6:233
Stensgaard I (1992) Rep Prog Phys P55:989
Stier O, Bimberg D (1997) Phys Rev B 55:9740
Stöhr J (1988) In X-ray absorption, principles, techniques, applications of EXAFS, SEXAFS, and XANES Prins R, Koningsburger DC (eds) Wiley, New York, p 443
Stolz H (1994) Proc SPIE 2142:170
Stratton R (1969) J Appl Phys 40:4582

Street RA (1991) Hydrogenated amorphous silicon. Cambridge University Press, Cambridge, UK
Street RA, Mott NF (1975) Phys Rev Lett 35:1293
Stroscio J, Kaiser W (1992) Scanning tunneling microscopy. Academic Press, New York
Struck CW, Fonger WH (1991) Understanding luminescence spectra and efficiency using W_p and related functions. Springer, Berlin
Sturge MD (1982) Excitons, Rashba ET, Sturge MD (eds) North Holland, Amsterdam
Suetaka W (1995) Surface infrared and raman spectroscopy. Plenum Press, New York
Sugai S (1991) Jpn J Appl Phys Part 2 Letters 30:116
Suntola T (1994) Atomic layer epitaxy. In: Hurle (ed) Handbook of crystal growth. North Holland, Amsterdam
Swistacz B (1995) J Electrost 36:175
Sze SM (1981) Physics of semiconductor devices. Wiley, New York
Sze SM (1985) Semiconductor devices, Wiley, New York
Szuszkievicz W, Dybko K, Dynowska E, Witkowska B, Jouanne M, Julien C (1998) Mater Sci Eng B: Solid State Mater Adv Tech B55:1
Talanina IB (1996) Institute of physics, Conference Series 126:273
Talanina IB (1998) NATO ASI series, Series B, Physics 241:179
Talanina IB, Collins MA, Agranovich VM (1993) Solid State Comm 88:541
Tanaka K (1998) Jpn J Appl Phys Part 1 37:1747
Tanaka K, Nakayama Si (1999) Jpn J Appl Phys Part 1 38:3986
Tani T (1989) Fuji Film, Res Dev 34:37
Tani T (1991) Fuji Film, Res Dev 36:14
Tani T (1995) J Imag Sci Tech 39:386
Tani T, Yoshida Y (1996) Proc IS&T Annual Confer May 1996, p 212
Tatarchenko VA (1994) Shaped crystal growth. In: Hurle (ed) Handbook of crystal growth. North Holland, Amsterdam
Tathan M. Shayegan (1992) Semicond Sci Tech 7:B116
te Nijenhuis J, van der Wel PJ, van Eck ERH, Giling LJ (1996) J Phys D: Appl Phys 29:2961
Thomas DE, Hopefield JJ, Augustyniak WN (1965) Phys Rev 140:A202.
Thonke K, Schliesing R, Teofilov N, Zacharias H, Sauer R, Zaitsev AM, Kanda H, Anthony TR (2000) Diam Relat Mater 9:428
Thorpe MF, Djordejevic BR, Jacobs DJ (1996) In: Thorpe MF, Mitkova MI Amorphous insulators and semiconductors. NATO ASI Series 3. High Technology – 23:289
Tolk NH, Traum MM, Tully JC, Madey TE (eds) (1983) Desorption induced by electronic transitions, DIET I, Springer, Berlin
Torres VJB, Oberg S, Jones R (1997) Mater Sci Forum 258–263:1063
Toyoda K, Tsujibayashi T, Hayashi T (2000) Radiat Defects Solid 150:477
Tsen KT (1993) Int'l J Mod Phys B 7:4165
Tsong TT, Liou V, McLane SB (1984) Rev Sci Instr 55:1246
Tsuo YS, Xiao Y, Heben MJ, Wu X, Pern FJ, Deb SK (1993) IEEE Photovoltaic Specialists Conference, p 287
Tyagi SD, Singh K, Ghandhi SK, Borrego JM (1991) IEEE Photovoltaic Specialist Conference p 172

Valle F, Bogani F (1991) Phys Rev B 43:12049
Van de Walle CO, Neugebauer J (1996) Mater Res Soc Symp Proc 449:861
van der Eerden JP (1993) Crystal growth mechanism. In: Hurle (ed). Handbook of crystal growth. North Holland, Amsterdam
van der Heijden AEDM, van Rosmalen GM (1994) In: Hurle (ed) Handbook of crystal growth. North Holland, Amsterdam
van der Veen JF (1985) Surf Sci Rep 5:199
van Halen (1994) Proc IEEE Int Symp Circuits Syst 1:403
Vanderbilt D (1990) Phys Rev B41:7893
Vanderschaeve G (1996) Diffusion and Defect Data (B): Solid State Phenomena, 59:145
Varshneya AK, Seeram AN, Swiler DR (1993) Phys Chem Solid 34:179
Vashishta P, Kalia RK, Nakano A, Li W, Ebbsjo I (1996) In: Thorpe MF, Mitkova MI Amorphous insulators and semiconductors. NATO ASI Series 3. High Technology – 23:151
Vickerman JC (ed) (1997) Surface analysis: the principal techniques. Wiley, Chichester, New York
Vinogradov EA, Leskova TA, Ryabov AP (1994) Optic Spectros 76:278
Vodopyanov KL, Graener H, Phillips CC, Furguson IT (1991) Institute of Physics Conference Series 126:349
Völkl J (1994) Stress in the cooling crystal. Hurle (ed) Handbook of crystal growth. North Holland, Amsterdam
Wagner HP, Lehman J, Hahn B (1995) J Lumin 66:84
Wang CW, Wu CH (1992) Solid State Electron 35:1771
Wang TH, Ciszek TF, Schuyler T (1991) J Cryst Growth 109:155
Wang ZL (1996) Reflection electron microscopy and spectroscopy for surface analysis. Cambridge University Press, Cambridge
Ward AJ (1999) Contemp Phys 40:117
Watanabe H (1994) Halogen transport epitaxy. In: Hurle (ed) Handbook of crystal growth. North Holland, Amsterdam
Weber D, Petri W, Woggon U (1997) Phys Rev B1: Condens Matter 55:12 848
Weber MJ, Monchamp (1973) J Appl Phys 44:5495
Weiss S, Mycek MA, Bigot J-Y, Schmitt-Rink S, Chemla DS (1992) Phys Rev Lett 69:2685
Wender SA (1983) IEEE Trans Nucl Sci NS-30:1539
Wiersma DS, Bartolini P, Lagendijk A, Righini R (1997) Nature 390:671
Williams F (1977) J Electrochem Soc 124:C107
Williams F, Karteuser E, Evrard R (1980) Phys Rev B 21:648
Williamson D (1999) Proc Mat Res Soc 557:251
Wolf EL (1975) Solid State Phys 30
Wolf T, Ulrici W, Cote D, Clerjaud B, Bimberg D (1993) Mater Sci Forum 143:317
Wong B, Kitai A, Jessop P (1990) Proc SPIE 1398:242
Woodruff DP (1986) Rep Prog Phys 49:683
Woodruff DP, Delchar TA (1994) Modern techniques of surface science. Cambridge University press, Cambridge.
Wooten F, Weaire D (1991) Solid state physics, Ehrenreich H, Turnbull D (ed). Academic Press, New York, 40:2
Worzala H, Jost KH (1990) Solid State Ionics 39:9

Yablonovitch E (1993) Photonic band gaps and localization, Soukoulis CM (ed) Plenum Press, New York, p 207
Yablonovitch E (1987) Phys Rev Lett 58:2059
Yablonovitch E, Gmitter TJ, Meade RD, Rappe AM, Brommer KD, Joannopoulos JD (1991) Phys Rev Lett 67:3380
Yah Z, Naritsuka S, Nishinaga T (1999) J Cryst Growth. 203:25
Yamaguchi M, Morifuji M, Kubo H, Taniguchi K, Hamaguchi C, Gmachl C, Gornik E (1994) Solid State Electron 37:839
Yamaguchi M, Koyama K, Suemoto T, Mitsunaga M (1998) J Lumin 76:681
Yang J, Guha S (1999) Proc Mat Res Soc 557:239
Yarykin N, Cho CR, Zuhr R, Rozgonyi G (1999) Phys B: Condens Matter 273:485
Yeh P (1988) Optical waves in layered media. Wiley, New York
Yi J, Wallace R, Palmer J, Anderson WA (1994) Sol Energ Mater and Sol Cells 33:145
Yoshimoto M, Ozasa K, Kajimoto A, Matsunami H (1991) J Cryst Growth 115:265
Yu PY, Cardona M (1999) Fundamentals of semiconductors: physics and material properties, 2nd ed. Springer, Berlin, Chap. 7
Yuan P, Hansing CC, Anselm KA, Lenox CV, Nie H, Holmes Jr AL, Streetman BG, Campbell JC (2000) IEEE J Quant Electron 36:198
Zangwill A (1988) Physics at Surfaces. Cambridge University Press, Cambridge
Zhao GY, Ishakawa H, Jiang H, Egawa T, Jimbo T, Umeno M (1999a) Jpn J Appl Phys Part 2 38:L993
Zhao J, Wang A, Green MA (1999b) Progres in Photovoltaics 7:471
Zheng J, Allen JW (1994) J Cryst Growth 138:504
Zhou X (1994) Sol State Electron 37:1888
Zimmermann H, Boyn R, Lehr MU, Schulz H-J, Rudolph P, Kornack J-Th (1994) Semicond Sci Tech 9:1598
Zoorob MF, Chariton MDB, Parker GJ, Baunberg JJ, Netti MC (2000) Nature 404:740
Zou J, Cockayne DJH (1995) Mater Sci Forum 189:279

Index

A-factor donor distributions, 74
nn-junction, 18
pn-junction, 36, 227
pn-junction near electrodes, 222

A-factor, diode, 244
A-factor, information from, 283
A-factor, two-donor model, parameter variation, 74
abrupt Ge pn-junction, 179
abrupt pn-junction, 171, 179
abrupt space-charge distributions, 15
abrupt step-junction, 17
absolute electrostatic electron potential, 3
absorption coefficient, direct, indirect band gap, 205
accessible to outside probing, 24
accumulation region, 19
accuracy of Schottky approximation, 49
acting field, 289
additional junction recombination, 230
air mass, 97
alternating current, 28
ambipolar diffusion approximation, 166
amorphous and disordered semiconductors, 33
applied bias, 26
applied bias drops across barrier, 175
applied voltage, 23, 25
asymmetric doping, 249
asymmetric generation, 247
asymmetric junction, 172, 175
asymmetric recombination, 247
asymmetric Si diode, abrupt junction, 241
asymmetric space charge double layer, 10
asymmetrical device, 242
asymmetrical profiles, 10
asymmetrically doped device, 182, 251
atomic force microscope, 2
attainment of equilibrium, 96
attractive centers, 242
Auger recombination, 208
average generation rate, 97
average homogeneous generation, 244
averaging process, 293

back-to-back depletion layers, 172
back-to-back Schottky barriers, 171
balance equations, 206
balance of electrons, holes, 207
ballistic versus diffuse transport, 3
band and defect level model, 203
band edge follows the electron potential, 5
band edge step, 6, 8
band edge, Fermi level, space charge, 21
band model of Cu_2S/CdS, light, 267
band model, compensation, Schottky barrier, 78
band model, optical excitation, trapping, recombination, 203
band model, Schottky barrier, 56, 152
band-model, 103
band-model with quasi-Fermi and demarcation lines computed, 158

band-to-band recombination, 162
band-to-band transition, 97
barrier becomes triangular, 99
barrier behavior, 66
barrier field, 47
barrier height, 179, 232, 235
barrier layer kinetics, schematics, trap depletion, 278
barrier layer schematics, compensated, field quenching, 274
barrier layer schematics, single, two-donor, 271
barrier layer thickness, donor density, 46, 47
barrier lowering, 98
barrier width, 47, 197, 236
barrier with optical excitation, 77
barrier, optical excitation, field quenching, 80
basic photodiode characteristic, 269
bell-shaped $r(x)$ distribution, 256
benefit to V_{oc}, 242
bias drops in DRO-range, 65
bias drops, entire across barrier, 175
bias-dependent step size, 183
birth and death rates, 109
block-shaped space charge, 182
blocking electrode, 36, 42
blowing over of surplus carriers, 35
Boltzmann distribution, 46, 62, 293
Boltzmann gas, 179
Boltzmann range, 46, 183
Boltzmann region, 55, 62, 185, 186
Boltzmann region for minority carriers, 156
Boltzmann solution, 51, 55, 156
bottleneck equation, 208, 209
boundary between p- and n-type region, 180
boundary condition, 18, 57, 152, 176, 180, 211, 282
boundary conditions at the contact, 15
boundary conditions, changing, cause and effect, 153
boundary densities shifted, 150
box-like space charge profile, 172
breakdown fields, 2
built-in field, 171, 289, 291
built-in field region, 201
built-in field, Fermi distribution, 291
built-in field, sloping band, 292
built-in fields, critical remarks, 291
built-in fields, measurements, 291
bulk currents saturated, junction current small, 190
bulk gr-current, 190
bulk region, 166

capacitance, 175, 179
capacitor, 175
capture coefficients used, Si diode, 243
capture coefficients, table, 243
capture cross section, 96, 103, 242
capture transition, 95
carrier accumulation, 162
carrier collection, 115
carrier density distribution curves, current, 154
carrier density distribution, Ge, Schottky barrier, 156
carrier density generated by light, 207
carrier depletion, 105
carrier distribution, 104
carrier distribution, field, 135
carrier generation, 94
carrier heating, 186, 290
carrier heating only in DRO-region, 186
carrier heating within junction, 185
carrier injection, 33, 35, 115
carrier inversion layer, 163
carrier leakage, 28
carrier lifetime, 85, 109, 110
carrier lifetime limitation, 36
carrier lifetime, two-carrier semiconductor, 110
carrier mobility, 195, 293
carrier recombination, 94
carrier surplus, 105
carrier transport equation, 16
carrier transport through, 93
carrier trapping, 209
carriers leak out, 15
carriers redistributed, 94
carriers, mutually created, 208
CdS/Cu_2S solar cell, lessons learned, 286
change of capture parameters, 113
character of collection, 132

characteristic, 29
characteristic length, 133
characteristic time constant, 109
characteristics deterioration, 283
charge character of center, 106
charge distributions change abruptly, 6
charge neutrality, 11
charge-free field-quenched region, 278
charge-neutral region, 9
charged lattice defects, 5
charged traps, 300
charges split between electrodes, 20
classical diode equation, 56
classical Schottky barrier, 41
clogging of recombination centers, 286
clogging of recombination path, 112
collecting barrier, 131
collection efficiencies, diffusion length, 131
collection efficiencies, surface recombination, 131
collection efficiency, 129, 130
comparing external with built-in fields, 290
compensated intrinsic semiconductors, 111
compensated layer, hetero-interface, 273
compensated Schottky barrier, optical excitation, field quenching, 81
compensated semiconductors, 77
compensating charge at electrodes, 11
compensation, 273, 280
compensation from diffusion current, 26
compensation is partially lifted, 204
compensation is restored, 80
competing transitions need to be considered, 206
composition grading, 300
computed lifetime distribution, 111
computed solutions, 49
computer generated solution curves, 179
conductivity, 25
constant field, 12
constant lifetimes, 111
continuity condition, 93
continuity equation, 151, 202, 210, 300
continuity of the electrostatic potential, 172
Coulomb attractive center, lowering barrier, 98
Coulomb relation, 1
Coulomb-attractive acceptors, 80
Coulomb-attractive centers, 75, 98
Coulomb-attractive centers depleted, 76
Coulomb-repulsive centres, 103
counterbalanced by carrier drift, 16
critical electron density, 79
critical field, 80
critical field quenching, 278
cross section, centre, 103
cross-doping, 230
crossover and the current continuity, 107
crossover in junctions, 93
Cu_2S emitter, 269
Cu_2S/CdS diode, field distribution, kinetics, trap depletion, 279
Cu_2S/CdS interface, 267
Cu_2S/CdS jV, measured, fanning out, 285
Cu_2S/CdS solar cell, 267
Cu_2S/CdS, band model, jV, 284
Cu_2S/CdS, electron density distribution, computed, 268
Cu_2S/CdS, jV characteristics, donor density, 273
Cu_2S/CdS, jV characteristics, solar cell, field quenching, 276
Cu_2S/CdS, jV, light intensity, 284
Cu_2S/CdS, jV, measured, untreated Cu_2S/CdS, 277
Cu_2S/CdS, kinetics, jV characteristics, 279
Cu_2S/CdS, Schottky model, two-donor barrier, 272
Cu_2S/CdS, solar cell solution curves, field quenching, 275
Cu_2S/CdS, voltage drop kinetics, temperature, 280
current continuity equation, 116
current density maximum, 228
current density, antisymmetric, 228
current dependent interface density, 57
current distribution, 124, 136, 220, 257, 258
current distribution thin slab, 128

current distribution, thick/thin slab, 123
current equation, 85
current generation, increment, 107
current is carried by diffusion only, 59
current ranges within the junction, 183
current rectification, 28
current saturation, 64, 66, 73
current saturation, excellent, 276
current saturation, lack of, 195
current term, Schottky barrier, 53
current through a semiconductor, 4
current–voltage characteristic, 27, 34, 55, 66, 86, 194, 197, 223
current–voltage characteristic of simplified junction, 175
current–voltage characteristic, analytic approximation, 69
current–voltage characteristic, shape of, 190
current–voltage Characteristic, three contributions, 178
current–voltage characteristics, 28, 35, 60, 69, 109, 179, 188, 195, 268, 270, 272, 283
current–voltage characteristics, double-donor, 69
current–voltage characteristics, Si, GaAs pn-diodes, 198
current–voltage characteristics modified, 282
current-driven devices, 27
currents, *nn*-junction, 49
currents, Ge, Schottky barrier, 158
currents, spatial distribution, 190
curve shapes, 179

d_1, 148, 166
d_2, 246
dark current, 211
dark saturation current, 212
dark- and photodiode characteristic, 212
Dawson's integral, 51, 53
Dawson's integral approximation, 51
dc component, 28
Debye length, 32, 44, 46, 47, 62, 143, 156
decrease of the interface recombination, 286
deep acceptors, 80
degenerate region, 17
demarcation line, 93, 102, 103, 111, 160, 162
demarcation line for electrons, 102
demarcation lines separate, 105
density of states, effective, 23
density-of-state distribution, 195
dependence on optical generation, 237
depletion deep centers, field, 76
depletion layer, width, 197
depletion of deep level, gradual, 68
depletion of deeper donor, 69
depletion of donors, 65
depletion region, 19, 172
depletion-type model, 171
detailed balance, 100
detailed balance equation, 79
detailed balance principle, 95
deviation from the ideal characteristic, 88
device thickness, influence, 234
dielectric constant, 4, 32
diffusion and drift currents, 48
diffusion current, 16, 115, 132, 176
diffusion current equation, 118, 234
diffusion equation for minority carriers, 132, 210
diffusion equation solution, 117
diffusion length, 36, 85, 86, 107, 117, 119, 122, 133, 136, 178, 189, 190, 193, 210, 223, 245, 274
diffusion of minority carriers, predominant, 185
diffusion potential, 46, 173, 175, 183, 197, 232
diffusion velocity, 118, 130
diffusion velocity, effective, 84, 87
diffusion-limited current, 87
diffusion-limited diode jV, 61
diffusion-limited Schottky diode equation, 60
diode characteristic, unfavorable, 158
diode characteristics, 41, 216
diode characteristics, solar cell, shunt/series R, 216
diode current, 282

diode equation, 56
diode ideality factor, 73, 214, 240
diode jV, nonideal, 65
diode jV, two-donor model, 66
diode leakage current, 115
diode performance, 217
diode-type shape, 188
direct band gap semiconductors, 96
direct band gap solar cell exposed to sunlight, 244
discontinuities, 265
distribution functions, 293
distribution of recombination centers, 195
distribution of the band edges, 5
distributions of electric field, 4
divergence-free contribution, 109
divergence-free current, 137–139, 144, 186, 195
divergence-free electron current, 158
divergence-free hole current, 159
divergence-free majority-current, 108, 144
divergence-free minority carrier currents, 187
DO-current of minority carrier, 186
DO-range, 185
DO-range for minority carriers, 161
DO-region, 185, 192
donor density, 29, 32
donor distribution, 66, 73, 74
donor-acceptor pairs, 230
donors are sequentially depleted, 270
doping boundary, 15
doping density, influence Si-diode, 238
doping gradient, 42, 195, 196
doping inhomogeneities, 17
doping interface, 36
doping, increased diffusion voltage, 250
double layer, 20
double-diode characteristics, 272
double-donor barrier, 66
downstream diffusion length, 133, 136
drift and diffusion currents, 46, 144
drift current, 16, 25, 31, 34, 137
drift current of majority carriers, 116
drift enhanced diffusion length, 36
drift length, 133
drift velocity limitation, 57
drift, diffusion currents, nn-junction, 26
drift-assisted gr-current, 132
drift-current-limited Schottky barriers, 56
drift-limited jV, nc, 57
drift-limited Schottky diode equation, 60
DRO range is reached, 69
DRO region, carrier heating, 186
DRO-range, 63, 68, 73, 75, 88, 185, 255, 259, 273, 280
DRO-range easily identified, 63
DRO-range for majority carriers, 161
DRO-range width, 164
DRO-region, 63, 163, 186
DRO-regions for electrons and holes, 185
dyn, 1

effective carrier lifetime, 246
effective device thickness, 235
effective diffusion length, 134, 136, 138
effective diffusion velocity, 85, 86, 88, 124, 132
effective mass, 23
effective mass change, 290
effective work function, 41
efficiency of Photovoltaic effect, 201
electric field, 2
electric field at the metal/semiconductor interface, 46
electric fields, built-in, 289
electric fields, external, 289
electrochemical potential, 22, 25, 65
electrode recombination, 190
electron and hole density crossings, 162
Electron and hole gr-current distribution, 160
electron boundary condition, heterojunction, 83
electron current then increases linearly, 107
electron demarcation line, 102, 103
electron density distribution, 49
electron density distribution, Schotty barrier, jn, 54
electron diffusion, 31
electron diffusion potential, 22, 44, 47
electron gr-current, 160

electron lifetime, 110
electron out-diffusion, 252
electron population, 109
electron potential distribution, 172
electron potential, metal/semiconductor interface, 58
electron transitions, 95
electron trap, 95, 100, 101
electron traps, CdS, influence, 270
electron, hole current, junction region, 176
electron, hole distribution, 152
electron, hole traps, 100
electron–hole pairs, 93
electron-fields, 25
electron-hole inter-relation, 143
electronic active, separate from electrode, 267
electrons leak-out, 36
electrons trapped, Poisson equation, 36
electrostatic electron potential, 18, 21, 25, 44, 64
electrostatic force, 2
electrostatic potential, 4
electrostatic potential difference, 2
electrostatic relations, 1
eliminate the space charge, 275
eliminating the field spike, 21
emitter, 251
energy distribution, carrier, 291
equilibrium density of majority carriers, 35
equilibrium minority carrier current, 109
equivalent circuit of a solar cell, 215
exact solution and Schottky approximation, 54
exact solution, two-donor barrier, 69
exact solutions, 46
example set of parameters, 151
excess electrons, 109
excess recombination, 254
excitation mechanisms, 93
excitation transition, 95
expansion, compression of barrier, bias, 55
exponent B identical to the slope factor, 285
exponential correction factor A, 73
exponential decay, 109
exponential distribution of capture coefficients, 33
extended barrier region, 224
extended transport equations, 198
external bias, 101
external field, 289, 290, 292, 293
external field, Fermi level, 292
external force, 104
extraction of any significant electric power, 223

fanning-out, 285
Fermi energy, 23
Fermi function, 68
Fermi level, 22, 23, 37, 69, 95, 111, 290, 291
Fermi level of adjacent metal, 183
Fermi level splits, 105
Fermi–Dirac statistics, 23
Fermi-level, probing, point contact, 23
Fermi-potential, current density, 23
field and diffusion potential, 236
field at barrier interface, 56
field distribution, 21, 67, 69
field distribution, triangular, 6, 182
field excitation, multiple donors, 75
field inhomogeneities, 4
field ionization, 75, 98
field quenching, 274, 278, 280
field quenching in optically excited CdS, 275
field quenching is a self-compensating process, 276
field quenching onset, 276
field quenching permits larger voltage drop, 80
field slope hidden in saturation range, 273
field spike, 6, 257
field triangle, 21
field, energy distribution, 5
field-enhanced-diffusion equation, 133
field-free region, 36
field-induced depletion, hole traps, influence, 274
field-ramp, 11
fields, 20
fill factor, 213, 214

fill factor of an ideal photodiode, 214
filled out current–voltage characteristic, 280
filling of traps, 277
flat-band connection, 139, 180
flip sign of space charge, 15
fluctuations, 104
forward bias, 19, 20, 109, 146, 178
forward current, 22
forward current distribution, 183
fourth quadrant, 223
Frenkel–Poole, 80, 97
Frenkel–Poole effect, 76, 98, 99
Frenkel–Poole ionization, 75, 274
Frenkel-Poole depletion, 77
Frenkel-Poole excitation, 80, 278
front wall, back wall solar cell, schematics, 266
frozen-in carrier distribution, 193
frozen-in steady state, 270

g/r-rates, optical generation, 222
Gauss' law, 2
Ge barrier parameters, 144
Ge diode, carrier distribution, currents, 189
Ge pn-junction, j-distribution, 187
Ge, diode band, Fermi-level distribution, 192
Ge, g,r,U-distribution, current, 167
Ge, gr-current, Schottky, bias, 161
Ge, jV characteristic, computed, 190
Ge, pn-diode, jn and jp, bias, 191
Ge, pn-junction, jV, gr, surface recombination, 188
Ge, pn-junction, solution curves, 165, 181
Ge, Schottky, bias, 159
Ge, Schottky, demarcation, quasi Fermi-levels, 158
Ge, space-charge, field, potential distribution, Schottky, 155, 164
Ge/metal interfaces, 183
general solution behavior, 164
generalized drift and diffusion, 299
generalized Einstein relation, 299
generalized set of transport equations, 299
generation and recombination, 93
generation and recombination rates, 222
generation and recombination, enhanced with light, 202
generation current, 176, 177, 250
generation function, multistep, 244
generation rate for thermal excitation, 145
generation rate, bulk and barrier, 145, 146
generation rate, influence Si diode, 237
generation rate, optical, 240
generation, recombination, and net gr-rates, 108, 109, 116, 136, 147, 177
governing set of differential equations, 31, 44, 151, 179
governing system of transport, continuity and Poisson equations, 219
gr-current, 119–121, 126, 128, 132, 138, 139, 145, 159, 167, 186, 188, 190, 195, 235, 241
gr-current distribution, 167
gr-current distribution, current collection, 119
gr-current in the thin device, 224
gr-current n,p, Schottky, current, 160
gr-current, bias, 130
gr-current, limit value, 189
gr-current, schematics, 148
gr-current, surface recombination, 124
gr-rates, reverse saturation, 185
graded band gap semiconductors, 25
graded composition, 195
graded semiconductors, 300
gradual depletion, 71
granular texture of space charge, 3
graphical analysis, 283

heavy-doping, 195
heterojunction back wall, 266
heterojunction front wall, 266
heterojunction interface, 83, 265
heterojunction similar to Schottky barrier, 82–84
heterojunction, high-blocked, nonideal, 89
high injection, 195, 203
high–low junction, 17

high-blocked heterojunction, 82, 83, 85, 86
high-field effects, 195
higher reverse bias, 162
hole currents, 136, 292
hole currents, bias, field, 137
hole demarcation line, 103
hole density distribution maximum, 126
hole density distribution, inflection point, 127
hole lifetime, 110
hole quasi-Fermi level, 103
hole trapping, 206
hole traps, 101, 206
hole-depleted region, 274
hybrid collector, 294
hysteresis of current–voltage characteristics, 276

ideal characteristics, 60, 88, 214, 223, 269
ideal current saturation, 195
ideal high-blocked heterojunction diode equation, 85, 86
ideal photovoltaic characteristic, 212
ideality factor, 90, 287
ideality factor A a factor B, 287
image forces, 47
impact ionization, 75, 99
inactive bulk region, 128
inactive region, 258
increased recombination, 247
increasing effective mass, 299
incremental electron current, 106
incremental hole current, 107
indirect band gap semiconductors, 96, 97
inflection point of $n(x)$, 48
influence of doping density, 239
inhomogeneous doping, 15
inhomogeneous optical generation, 244
injected current, 33
injected electrons, 36
injecting contact, 34
injection, 115
integration of Poisson's equation, 20
interaction between the bulk and surface, 223
interdependence of primary variables, 31
interface recombination current, 281
interface recombination provides a leakage path, 281
interface recombination velocity, 87, 283
interface recombination, influence, 281
internal field, 289, 290
intricate interrelationship of the different junction variables, 195
intrinsic carrier density, 105
intrinsic energy level, 106
intrinsic recombination, 162
inversion layer, 36
ionisation rate per unit path length, 99

Joule's heating, 292
jump occurs in the valence band at the interface, 82
junction, 291
junction capacitance, 175
junction field, 179, 235
junction field, triangular, 182
junction model in steady state, 174
junction recombination, 283
jV between Boltzmann and saturation, 287
jV with hysteresis, 279
jV, Cu_2S/CdS, single donor model, interface recombination, 282
jV, two-donor model, DRO range, expanded abscissa, 72
jV-characteristics, nn-junction, 27

kinetic parameters, 96
kinetics of solar cells, 276
kinetics of the voltage drop, 277
knee development in characteristic, 71

l_2, 11
large optical generation, 111
lattice mismatch, 87, 281
leakage current, 87, 188, 275
leaking-out of minority carriers, 36
leveling of the field, 276
lifetime, 107, 206
lifetime of electrons, 78
light pass through atmosphere, 97
limit the field, 267

limits field and current, 275
linear doped junction, 196
local balance in traps, 300
local currents, 94
long device, 177
low critical fields, 75
low injection, 203
low optical generation, 230
low recombination rate, 204
luminescence, 100

majority carrier current, 211
majority carrier density, 203
majority carrier heating, 186
majority carrier injection, 35
majority carriers, 115
majority quasi Fermi levels, two with junction, 185
maximum current at inflection point, 48
maximum field, 44, 47, 175, 182
maximum gr-current, 119, 188
maximum of the thermal excitation, 230
maximum optically generated minority current, 129
maximum power point, 213
maximum power rectangle, photocurrent shifted, 212
maximum slope, currents, 48
maximum value of the field, 196
measured characteristics, 285
medium width device, 164
metal contact, 41
metal surface, 58
metal surface dipole layer, 58
metal work function, 36
metal–semiconductor boundary, 41
metal-semiconductor contact, 36
metal/semiconductor work function, 42
metal/semiconductor barrier, 86
metal/semiconductor boundary, 57
metal/semiconductor interface, 41, 65, 67, 69, 84, 150, 161, 190
metallurgical interface, 182, 186
minority and majority currents, 93
minority carrier current, 115, 137, 210
minority carrier density, 112, 125, 233
minority carrier density at the surface, 122
minority carrier density distribution, 118, 123, 135
minority carrier depletion, 162
minority carrier diffusion equation, 117
minority carrier diffusion length, 143
minority carrier distribution, boundary condition, 116, 128
minority carrier distribution, optical carrier generation, 126
minority carrier distribution, surface recombination, 129
minority carrier emission from thick base, 251
minority carrier gradients, 116
minority carrier heating, 186
minority carrier injection, 36, 197
minority carrier lifetime, 110, 206, 224
minority carrier limits recombination, 106
minority carrier relation at metal/semiconductor interface, 150
minority carrier, surface recombination, 123, 127
minority carriers, 93, 185, 203, 247
minority carriers in junction devices, 93
minority quasi-Fermi level jump, 254
mismatch dislocation, 265
missing charges, 20
mixed boundary condition, 153
mobility, 32
modified Boltzmann range, 62, 63, 68, 71, 77
modified boundary condition, 60
modified diffusion velocity, 282
modified diode characteristic, 73, 85, 88, 215
modified Poisson equation, 300
modified Schotty barrier, 57, 60
monochromatic light, 97
more generalised set of equations, 196
multi-valley semiconductors, 293
multistep generation function, 244
mutually created carriers, 208

n and p crossing, ignore, no junction, 163
n,p, independent on g(x), 249
n,p-distribution, equilibrium, 152

n,p-slopes, current, 153
n-type Ge slab, 115
n-type Schottky barrier, 143
near-contact region, 258
near-interface layer, significance, 222
near-junction region, 258
near-surface regions, 128
net charge of the double layer, 20
net current, 12, 105, 292
net drop-off of carriers, 109
net generation or recombination through such centers, 105, 228, 255
net generation rate step like, 147
net gr-rate U, 145, 210
net recombination, 106, 110
net thermal generation, 106
net transport of carriers, 104
network of parasitic resistors, 215
neutral contact, 164
neutral contact, flat band connection, 163
neutral interlayer, 37
neutral outer boundary conditions, 227
neutrality condition, 206–209
neutrality over the junction, 16
nn-junction by unintentional doping inhomogeneities, 31
nn-junction, n-distribution, mobility, 31
no influence of the device width on the majority carrier distribution, 224
nondegenerate case, 95, 101
nondegenerate semiconductors, 104
nonideal characteristic, 63
nonideal high-blocked heterojunction characteristic, 87
nonlinearity of characteristics, 31
nonohmic behavior, 28
nonvanishing bias, 254
nonvanishing currents, 49
notation of incremental current, 106
numerical integration, 18

one-dimensional Poisson equation, 4
open circuit Schottky barrier, 223
open circuit voltage, 213, 220, 227, 232, 233, 235, 241, 245, 247, 250
open circuit voltage maximum, 236
open circuit voltage reduction, 282
open circuit voltage, small, Schottky device, 225
opportunities for designing new devices, 195
optical absorption coefficient, 96
optical carrier generation, 107
optical constant, 195
optical excitation, 36, 101, 132, 201, 210, 293
optical excitation gr-currents, 125
optical excitation rates, 97, 107, 111, 202, 228
optical injection, 36
optical minority carrier generation, 138, 204
optically generated gr-current, 131
optically-generated carriers, 79
optically-generated excess carriers, 78
out-diffusion, 31
out-diffusion toward electrode, 254
overshoot of recombination, 228, 232
overshoot peak is shifted, 242

parallel shift of the characteristic, 273
parameters of computation, space charges, 18
parameters used for computation, 42
parameters, Ge-barrier, 144
parasitic resistive network, 283
partial clogging, 286
passivation, 265
penetration depth, 97
perfect recombination, 163
perfect recombination at the interface, 157
perfect separation of the junction, 287
performance deterioration, 282
permitting separation of variables, 22
phonons, 292
photo-emf, 204
photodiode equation, 213
photoconductors, 101, 203
photoconductors sensitized, 204
photocurrent, 204, 211, 212, 219
photocurrent, solar cell, interface leakage, 281
photodiode, 219, 265
photodiode current, 115, 209
photodiode model, 202

photogenerated current, 255
photogenerated minority carriers, 201, 209
photon flux, 96
photovoltaic current–voltage characteristic, 212
photovoltaic device, schematics, 204
photovoltaic effect, 201, 258
physically meaningful solution, 18
pn-junction, 111
pn-junction, capacitance, measurement, 176
pn-junction, carrier heating, 186
pn-junction, linear doping, built-in fields, 196
pn-junction, schematics space charge, field, 173, 174
pn-junction, symmetric, 231
pn-junction, thin, symmetric, current distribution, 228
pn-photodiode, Si, 227
point charges, 1
Poisson equation, 3, 33, 36, 44, 48, 151, 289
Poisson equation, decoupling, 44
polychromatic excitation, 97
polychromatic light, 97
position of pn-interface, 180
position-dependent material parameters, 195, 198
potential barrier, 8, 58
potential distribution, 4, 7, 44, 182
potential drop, 9
potential notation, barrier, 68
potential step disappears, 22
power conversion efficiency, 214
pre-breakdown effects, 64
pseudo-electrode, 268
pure generation current, 120
pure recombination current, 121

quality factor A, 74, 197, 223, 283
quality factor A is related to the slope B, 286
quality factor increases with increasing light, 285
quality factor, diode, 178
quasi Fermi level for holes, above qF-level for electrons, 162
quasi Fermi levels, demarcation lines, 103
quasi-equilibrium approximation, 205
quasi-Fermi level is flat, 157
quasi-Fermi level pinning, 206
quasi-Fermi level, spread, optical excitation, 222
quasi-Fermi levels, 23, 65, 93, 101, 102, 105, 160, 183, 206, 208, 247
quasi-Fermi levels collapse, 161, 164, 220
quasi-Fermi levels collapse at metal surface, 150
quasi-Fermi levels collapse at the majority quasi-Fermi level, 183
quasi-Fermi levels in DO-region, 192
quasi-Fermi levels independent of generation rate distribution, 245
quasi-Fermi levels remain essentially horizontal, 235
quasi-Fermi levels remain spread, 191
quasi-Fermi-level split, 242
quasi-neutrality, 20
quenching, 79
quenching of optically excited, 80

r_2, 3
random walk, 117
range of electron traps, 104
reaction kinetic discussion, 201
reaction kinetic equation, 109, 202, 209
recombination, 100
recombination at both electrodes, 253
recombination center energy, 240
recombination center is neutral, 242
recombination center, energy, influence Si diode, 240
recombination center, one-level, 202
recombination centers with different capture coefficients, 242
recombination centers, density, 240
recombination centers, influence, Si-diode, 235
recombination centre, 101, 104–106, 111, 207, 300
recombination contribution, 194
recombination current, 87, 178, 193, 195, 225, 254
recombination current at electrode, 189

recombination current changes sign, 253
recombination current toward electrode, 253
recombination current, junction, 176
recombination currents at electrodes, small, 190
recombination distribution, 244
recombination leakage current, 193
recombination overshoot, 230, 235, 247, 252
recombination overshoot, influence on V_{oc}, 232
recombination path, 103
recombination path, saturated, 206
recombination rate of distribution, 248
recombination rates, 145, 192
recombination surface, 121, 150
recombination traffic, 202, 274, 300
recombination transition, 102
recombination, asymmetric, 247
rectification, 80
rectifier characteristics, circuit diagram, 28
redistribution of carriers, 202
reduced diode performance, 214
relative error, barrier field, Schottky, 49
relative error, Schottky approximation, 51
relative overshoot, 237
repulsive center, 242
resistive network, diode characteristic, 214
restore the uncompensated case, 77
restore thermal equilibrium, 125
reverse bias, 19, 20, 63, 77, 138, 146
reverse bias, no hole traps, 162
reverse current, 22
reverse current saturation, 125, 179, 189, 255
reverts back to an uncompensated semiconductor, 79
Richardson–Dushmann electron emission, 59

saturation current, 85, 125, 193, 210, 253, 254, 259, 285
saturation diffusion current, 177
saturation range, 63
Schottky approximation, 42, 44, 49, 268
Schottky barrier, 42, 79, 82, 83, 105, 115, 118, 139, 143, 172, 186, 219, 230, 267
Schottky barrier behavior, 42
Schottky barrier computed, 43
Schottky barrier device, 65, 163, 222
Schottky barrier with two carriers, 150
Schottky barrier with two donor levels, 70
Schottky barrier, carrier heating, 186
Schottky barrier, current, 52
Schottky barrier, exact, approximation, 45
Schottky barrier, field quenching, 79
Schottky barrier, partially compensated, 77
Schottky barrier, two donor, jV, extended bias, 71
Schottky barriers, back-to-back, 171
Schottky barriers, n_c, 50
Schottky characteristic does not extend into forth quadrant, 223
Schottky device, 228
Schottky device, thick, 224
Schottky diode, 193
Schottky diode equation, 211
Schottky diode equation, modified, 60, 62
Schottky diode, lessons learned, 223
Schottky diode, no open circuit voltage, 220
Schottky relation, 182
Schottky–Read–Hall centres, 105
Schottky-approximation, 46, 172
Schottky-type solution, 182
Schubweg, 133
Seebeck-effect, 299
semiconductor surface probing, 24
semiconductor, photoconductor, typical, 203
semiconductor/metal interface, 230
separation of different current contributions, 139
separation of injection and generation currents, 138
sequential donor-depletion, 65
series or shunt resistances, 215
series resistance limitation, 197
series-resistance, 13, 195, 215

series-resistance limited, 31
set of solution curves, 189
shape factor, 61, 62, 64, 76, 85, 88
shape factor approximation, 270
shape factor, diode, 62
shape factor, two-donor diode, 72
shape of current–voltage characteristic, 195
shape of solution, not bias- dependent, 55
shape of the diode characteristics, 215
shielding, 4
Shockley-Read-Hall centre, 105
Shockley-Read-Hall centre, composition, 108
short circuit current, 213
shunt resistance, 215
Si diode, asymmetric bulk, 247
Si pn-diode, symmetric, thick, doping density, 238
Si pn-junction symmetric, current, 256
Si pn-junction symmetric, recombination coefficients, 243
Si pn-junction, asymmetric, asymmetric doping, 252
Si pn-junction, asymmetric, surface recombination, 249, 253
Si pn-junction, current–voltage characteristic, 260
Si pn-junction, g and r-rates, illumination, 246
Si pn-junction, jump in recombination centers, 250
Si pn-junction, n,p distribution, current, 257
Si pn-junction, reverse current, 259
Si pn-junction, symmetric and asymmetric, thin, 248, 251
Si pn-junction, symmetric, energy of recombination centers, 241
Si pn-junction, symmetric, inhomogeneous optical excitation, 245
Si pn-junction, symmetric, recombination center density, 236
Si pn-junction, symmetric, surface boundary conditions, 234
Si pn-junction, thin, asymmetrically doped, current, 258
Si pn-junction, thin, symmetrical, generation, recombination current, 229
Si pn-junction, thin, symmetrical, n,p currents, 229
Si Schottky photodiode, ideal real jV, 224
Si solar cells, thick, asymmetric, 251
Si, GaAs diode, bias, jV, 198
Si, open circuit voltage, computation, 233
Si, pn-diode, long, symmetric, generation rate, 237
Si, pn-junction, solution curves, 231
Si, Schottky barrier, solution curves, zero current, 221
Si-diode, jV, computed, 194
Si-diode, parameters, table, 228
Si-homojunction, 193
Si-pn junction, open circuit voltage, 239
Si-solar cell with bias, 257
significance of basic junction variables, 31
simple diode equation shifted by the saturation current, 240
simplified *pn*-junction model, 171
simplified junction model in steady state, 174
simplified model photodiode, 210
simplified pn-junction, 178
single carrier n-type Schottky barrier, 270
single layer, 11
single space charge layer, 11
singular point, 18
sinusoidal space-charge double layer, 5
six boundary conditions, 18
sliding of the minority carrier density, 83
sloping of the bands, 300
slow depletion of trap, 278
slow redistribution of carriers over traps, 287
solar cell efficiency, history, 205
solar cells, 204
solid-to-vacuum surfaces, 59
solution curves spliced, 224
space charge, 2, 41
space charge distribution, step like, 6

space charge double layer, field spike, band edge step, 6
space charge limited current in amorphous sc., 33
space charge recombination, 196
space charge with neutral interlayer, 9
space charge, asymmetric, 10
space charge, asymmetric, two surface charges, 12
space charge, compensating surface charge, 11
space charge, neutral interlayer, 9
space charge, sinoidal, 5
space charges in insulators, 1
space–charge region, 104
space-charge distribution, 4, 20
space-charge double layer, 6, 13, 58
space-charge layer, 21
space-charge limited current, 33–35, 37
space-charge limited current equation, 34
space-charge profiles, 5
space-charge region, 15, 66, 289
space-charge-free, 21
spectroscopy of local states, 33
split between drift and diffusion currents, 183
split of the quasi-Fermi levels, 185, 224, 232
square root behavior, 63
square root branch, 63, 64, 281, 283
squareness of the characteristics, 214
static dielectric constant, 4
statistical fluctuations, 3, 104
steady state, 93, 100, 101, 206
steady state nonequilibrium, 104
steady-state electron density, 31
steepening of the characteristic, 73, 77
step like behavior of the currents, 185
step like increase in depletion, 69
step like recombination rate behavior, 146
step-like doping distribution, 15
steps are observed in jV, 273
stepwise increase of $\varrho(x)$, 66
sunlight excitation, 97
superposition, 97
supply of minority carriers, 240
surface boundary condition, 122
surface charge, 20
surface recombination, 121, 124, 144, 161, 180, 186, 188–190, 195, 214, 233, 235, 240, 247, 258
surface recombination current boundary condition, 121
surface recombination perfect, 257
surface recombination velocity, 125, 126, 130
surface recombination, influence, Si-diode, 235
surface treatments, 195
surplus carriers, 35
symmetric *pn*-junction, 231, 255
symmetric minority carrier change on both sides of pn-junction, 247
symmetrical thin device, 228
system of governing differential equations, 144
system of governing equations be simplified, 28

temperature dependence of space-charge limited currents, 33
The shape of the current–voltage characteristic, 190
theory of space-charge limited currents, 33
thermal carrier generation, 193
thermal electron velocity, 86
thermal equilibrium, 85, 96, 102, 104, 290
thermal equilibrium, restore, 125
thermal excitation, 95, 100, 111, 132, 202
thermal excitation, bell-shaped, 230
thermal ionization, 210
thermal velocity, 125
thermodynamic equilibrium, 25, 101, 104
thick *pn*-junction device, 189
thin *pn*-junction device, 34, 188
thin asymmetric junction, 246
thin asymmetric Si-photodiode, 257
thin device, example solution, 154
thin grid electrode, 254
thin Schottky barrier photodiode, 219
thin symmetric *pn*-junction, 255
thin symmetric devices, 233

three-dimensional problem, 254
tightly bound centres, 103
time-invariant equations, 179
total current, 25, 144, 189
total current distribution, 187
total current equation, 151
total current, including drift and diffusion, 25
total diffusion potential, 183
total gr-contribution, 160
total hole current, 136
total incremental current, 107
transition coefficient, 95, 100
transition probability, 99
transition rate, 95
transitions between localised states, 100
transitions communicate between two bands, 101
transitions communicates with the same band, 101
transitions, localized/nonlocalized states, 94
transport and Poisson equations, 41, 165
transport equation, 156
transport equations for both carriers, 151
trap, 101
trap depletion, 276, 280
trap distribution, 37
trap filling, 279
trap kinetics, 280
trap population, 96, 100
trap-controlled space-charge-limited current, 36
trap-free case, 37
trapped carriers, 207
trapping, 100
traps as storage reservoirs, 208
traps, recombination centres, 101
triangular space charge layer, 182
triple layer, 58
tunnel ionisations, 97
tunneling, 99
two-carrier model, 144
two-donor model, 69, 270
two-donor Schottky barrier, 67
typical transitions, 94

U: net gr-rate, 210
uncompensated charges, 2
uncompensated donors, 15
upstream diffusion length, 133

V_{oc} parameter influence, 240
vacuum diode, 33
vacuum permittivity, 1
van Roosbroek assumption, 166
voltage difference, 23
voltage drop across the solar cell for trap filling, 280
voltage drop kinetics method, 277
voltage drop, main portion, 161
voltage kinetics, 279

widening of the barrier, 80, 275
wider device solutions, 165
work function between metal and semiconductor, 59
work function, Schottky barrier, Ge, 168

zero current solution, 46